



VYSOKÉ UČENÍ TECHNICKÉ V BRNĚ  
BRNO UNIVERSITY OF TECHNOLOGY



FAKULTA STAVEBNÍ  
ÚSTAV MATEMATIKY A DESKRIPTIVNÍ GEOMETRIE

FACULTY OF CIVIL ENGINEERING  
INSTITUTE OF MATHEMATICS AND DESCRIPTIVE GEOMETRY

## VÝPOČTOVÉ MODELOVÁNÍ VÝVOJE POŠKOZENÍ V MATERIÁLECH SE SLOŽITOU VNITŘNÍ STRUKTUROU POMOCÍ METODY KONEČNÝCH PRVKŮ

COMPUTATIONAL MODELLING OF FAILURE DEVELOPMENT IN MATERIALS WITH  
COMPLEX INTERNAL STRUCTURE USING FINITE ELEMENT METHOD

HABILITAČNÍ PRÁCE  
HABILITATION THESIS

AUTOR PRÁCE  
AUTHOR

Ing. VLADISLAV KOZÁK, CSc.

BRNO 2021

## Abstrakt

Účelem předkládané habilitační práce je ukázat výsledky studia zaměřeného na vznik poškození heterogenních materiálů, zvláště na problematiku modelování vzniku a šíření trhliny. Ve čtyřech kapitolách jsou ukázány výsledky práce pomocí komentovaných autorových publikací. V první kapitole je věnována pozornost přímé aplikaci metody konečných prvků na odlišné typy materiálů s cílem nalezení kritických parametrů určujících chování materiálů při poškozování. Druhá kapitola kombinuje elastoplastické výpočty pomocí MKP a vybrané parametry pro tzv. přístup kritického článku. Třetí kapitola je věnována aplikaci mechaniky poškození a dvěma možnými přístupy, jak modelovat vznik a šíření trhliny pomocí úprav v systémech MKP. Poslední čtvrtá kapitola je věnována cementovým vláknovým kompozitům a hledání nových metod pro jejich přesnější modelování zejména v oblasti koncentrátoru napětí, respektive před čelem trhliny.

Jako autor chci poděkovat všem bývalým kolegům z Ústavu fyziky materiálů AV ČR, v.v.i., kteří se podíleli na publikacích. Pro vznik této práce byla důležitá dlouholetá spolupráce s profesorem Jiřím Valou z Ústavu matematiky a deskriptivní geometrie FAST VUT, který mé zaměření přiblížil k problémům stavební mechaniky.

## Summary

The purpose of the presented habilitation thesis is to show the results of a study focused on the occurrence of damage heterogeneous materials, especially on the issue of modeling crack formation and propagation. At four chapters the results of the work are presented using annotated author's publications. In the first chapter attention is paid to the direct application of the finite element method to different types of materials in order to finding critical parameters determining behavior of materials at damage. The second chapter combines elastoplastic calculations using FEM and selected parameters for the so-called critical article approach. The third chapter is devoted to the application of damage mechanics and two possible approaches to model the origin of a crack propagation through modifications in FEM systems. The last fourth chapter is devoted to cement fiber composites and the search for new methods for their more accurate modeling, especially in the field stress concentrator, respectively ahead of the crack tip.

As an author, I would like to thank all former colleagues from the Institute of Physics of Materials CAS, who participated in the publications. Cooperation with Professor Jiří Vala from the Department of Mathematics and Descriptive Geometry of the Faculty of Civil Engineering was important for the creation of this work, which brought my focus closer to the problems of structural mechanics.

# Obsah

Abstrakt	2
Obsah	3
1 Úvod	4
2 Teoretické základy	6
2.1 Použití metody metody konečných prvků na řešení nestandardních úloh . . . . .	6
2.2 Historie lokálního přístupu . . . . .	7
2.3 Modelování šíření trhliny . . . . .	9
2.4 Vláknové kompozity pro stavebnictví a XFEM . . . . .	12
3 Vlastní výsledky - komentář publikovaných prací	15
3.1 Přímé aplikace MKP . . . . .	15
3.2 Lokální přístup . . . . .	18
3.3 GTN model a použití kohezních prvků . . . . .	20
3.4 Modelování porušení stavebních kompozitů . . . . .	24
4 Shrnutí dosažených výsledků	28
5 Literatura	29
6 Publikace autora 1990-2021	32
7 Vybrané články komentované v práci	39

# 1 Úvod

S vývojem nových zařízení a komponent je v dnešní době stále více spojována otázka zajištění bezpečnosti jejich provozu a predikce jejich životnosti. V případě konstrukcí může být přímo závislá na výskytu defektů, které mohou vzniknout již v etapě výroby nebo během provozu. Jedním z konceptů, které jsou využívány v konstrukci a hodnocení bezpečnosti, je soubor teorií a metod označovaný jako lomová mechanika. Tento vědní obor spojující v sobě mechaniku kontinua s materiálovým inženýrstvím, popisuje chování defektů, např. trhlin, v konstrukcích. Jedná se o komplikovaný vztah defekt-napětí-materiál. Lepším pochopením těchto vztahů lze dosáhnout úspor u nových konstrukcí nebo prodloužení životnosti stávajících konstrukcí.

Snahou lomové mechaniky je popis, popřípadě predikce chování těles obsahujících vadu často typu trhliny. Trhliny mohou v mnoha případech vést až k úplnému porušení konstrukce v důsledku vzniku lomu. Existují dva základní přístupy pro odvození podmínek okamžiku iniciace nestabilního šíření trhliny. Podstatou prvního je aplikovatelnost teorie nejslabšího článku, druhý model uvažuje kumulaci poškození v průběhu zatěžování. Porušování konstrukčních materiálů je chápáno jako kontinuální proces, u kterého dochází ke vzájemnému prolnutí stádií plastické deformace, nukleace a iniciace trhlin. Koncové stádium ve vývoji porušování těles, které je předmětem zkoumání lomové mechaniky je šíření trhlin (nestabilní nebo stabilní). Cílem presentovaných prací bylo, jak zjistit vzájemné vztahy mezi fyzikálními zákonitostmi a vlastní fyzikální podstatou procesu porušování na straně jedné a teorií mechaniky kontinua na straně druhé.

Současné studie se zaměřují na rozpracování druhého z výše uvedených problémů. Je jím zmíněná transferabilita materiálových charakteristik. Rozdílné lomové houževnatosti můžeme změřit při odlišných konfiguracích zkušebních těles a defektů. Důvodem nesouladu je skutečný stav rozložení napětí v okolí defektu a různý rozsah plastické deformace. Nejenom tyto skutečnosti komplikují použití lomové mechaniky v praxi, uvedenému problému je věnována kapitola zaměřená na problematiku lokálního přístupu. Ta ukazuje koncepci odlišnou od standardní lomové mechaniky a pokouší se definovat mechanismus porušení veličinami nepopisujícími globální napěťové pole, ale veličinami vycházejícími ze znalosti rozložení napětí/deformace v celém tělese.

Mezi efektivní nástroje, které přispívají k objasnění hledaných vztahů, patří modely, jež využívají numerických metod. V předložené práci se vychází většinou z použití metody konečných prvků (dále MKP), mnohdy na hranicích použitelnosti klasických software MKP, detailněji v kapitole přímých a nepřímých aplikací MKP. Nové metody převážně v oblasti modelování poškození jsou soustředěny ve třetí kapitole, která je věnována modelování šíření trhliny jak pomocí mechaniky poškození (použita modifikace Gursona-Tvergaard-Needlemana) či použití kohezních prvků implementovaných pomocí uživatelské subroutiny do systému Abaqus. Používání kompozitních materiálů s cementovou maticí a výztužnými vlákny rozličného původu pro konstrukční účely si vynucuje věrohodnou výpočtovou predikci jejich mechanických vlastností, především nebezpečí postupného vzniku mikrotrhlin a makrotrhlin. V poslední kapitole komentovaných prací je ukázána možnost de-

terministické výpočtové predikce tohoto fyzikálního procesu s využitím kvazistatického viskoelastického materiálového modelu a kohezních kontaktů, metody časové diskretizace a rozšířené metody konečných prvků pro dvourozměrné úlohy.

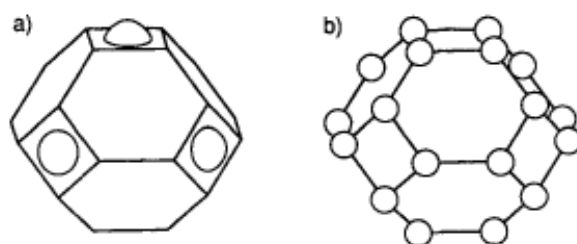
Prosazování netradičních materiálů, konstrukcí a technologií v moderním stavebnictví vyžaduje i nové přístupy k vyšetřování jejich fyzikálních vlastností, při nichž se nelze spoléhat na ty osvědčené. Simulace chování materiálových vzorků, konstrukčních prvků i staveb jako celku se stává nezbytnou.

## 2 Teoretické základy

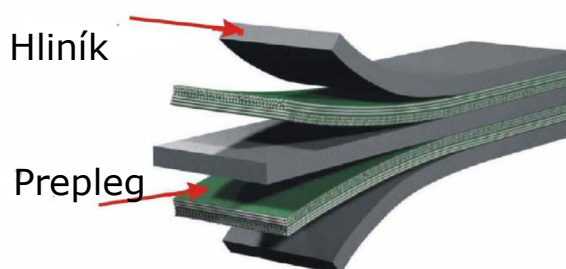
Tato kapitola si klade za cíl uvést čtenáře do řešené problematiky a naznačit některé otázky, na které se autor této práce snaží navázat v kapitole věnované vlastním výsledkům.

### 2.1 Použití metody metody konečných prvků na řešení nestandardních úloh

Zde jsou specifikovány teoretické podklady pro první kapitolu věnovanou komentovaným publikovaným pracím. První skupina se zaměřuje na speciální problémy modelování creepového chování materiálů, speciálně na procesy probíhající při stlačování kovového prášku či při zatěžování kompozitů s kovovou maticí. Druhou skupinu představují vláknové lamináty GLARE, jež byly vyvíjeny pro modernizaci letadel Airbus. Třetí skupina je věnována konvergenci elastoplastických úloh při zatěžování těles s ostrou trhlinou. Všechny skupiny používají k výpočtu standardní systémy, tj. Ansys a Abaqus. Na rozdíl od následujících kapitol jsou tyto systémy používány přímo bez zasahování do standardních softwarů.



Obrázek 2.1: Model uzavřené pórovitosti (a) nový model, (b) dle literatury [7].

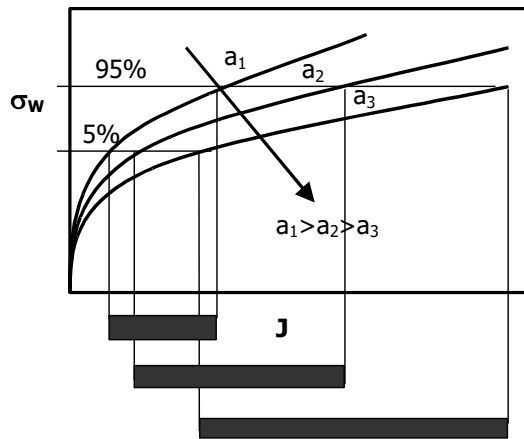


Obrázek 2.2: Struktura sklolaminátu GLARE, převzato z [en.wikipedia.org/GLARE](http://en.wikipedia.org/GLARE).

Slinování (anglicky sintering) je proces zhutňování a formování pevné hmoty materiálu teplem nebo tlakem, aniž by se roztavil do bodu zkapalnění. Slinování probíhá přirozeně v ložiscích minerálů nebo jako součást výrobního procesu používaného s kovy, keramikou, plasty a jinými materiály. Jako základní fyzikální procesy je nutno vyzvednout viskózní tok přes hranice zrn a difúzi po hranicích zrn, struktury jsou s uzavřenou pórovitostí, jak je naznačeno na obr. 2.1, při modelování této úlohy se vycházelo z prací [27] a [9].

Sklolaminátový epoxid vyztužený hliníkem (GLARE, Glass Laminate Aluminum Reinforced Epoxy) je laminát z kovového vlákna (FML, Fiber Metal Laminate) složený z několika velmi tenkých vrstev kovu (obvykle hliníku) proložených vrstvami preplegu ze skleněných vláken, spojených dohromady maticí, jako je epoxid. Při modelování pomocí MKP byla řešena otázka kritických směrů namáhání a iniciace vzniku trhliny při nízko-cyklové únavě. Strukturu materiálu, nyní velmi využívaného v letectví, například v [39], vidíme na obr. 2.2.

V této kapitole je proveden i úvod do problematiky numerického výpočtu veličiny označované v experimentální oblasti jako lomová houževnatost, která je spojována s maximálním napětím před čelem trhliny a v komentovaných pracích je jí věnována významná pozornost. Různé konfigurace těleso/defekt vedou k rozdílným napěťově/deformačním stavům (rozdílná úroveň plastické deformace), viz [28] a [35]. Z aplikačních důvodů, viz obr. 2.3, byla snaha zavést dvouparametrovou lomovou mechaniku tak, aby byla možná transformace stanovených veličin na jednoparametrový popis pomocí  $K$ ,  $J$ . Podmínky na špičce trhliny, které lze těmito veličinami popsat, jsou označovány jako stav small-scale yielding (SSY) či large-scale yielding (LSY), viz [40].



Obrázek 2.3: Predikovaný rozptyl lomové houževnatosti, převzato z Přílohy B1.

V rámci deformační teorie plasticity s předpokladem izotropního zpevnění pro Misesovu podmínku plasticity byly uvažovány podmínky rovinné deformace a rovinné napjatosti pro případ plastického chování materiálu s mezí kluzu  $\sigma_0$  a exponentem deformačního zpevnění  $n$ , jehož vlastnosti jsou popsány ve formě mocninné závislosti mezi napětím a deformací typu Ramberg-Osgood [8].

## 2.2 Historie lokálního přístupu

Tento přístup, zejména v případě štěpného porušení, koreluje pravděpodobnost porušení s distribucí napětí před čelem trhliny. Přestože je vznik porušení predikován z lokálního napětí, jsou apriori v tzv. Weibullově napětí zahrnuty efekty jako: ztráta „constraintu“ (někdy v české literatuře označován jako stísnění, viz obr. 2.5), charakter zatěžování, tepelně indukovaná napětí atd. Metodika lokálního přístupu (dále LP) je silným nástrojem pro predikci životnosti komponent. Nutnost pečlivého a přesného určení napětí/deformace v uvažovaném tělese je nezbytná.

## 2.2. HISTORIE LOKÁLNÍHO PŘÍSTUPU

Princip je založen na předpokladu, že existuje malý, ale konečný objem materiálu, který obsahuje množinu rovnoměrně rozložených defektů [3] a [8]. Problém křehkého porušení se redukuje na nalezení kritického defektu. Úvahy dodržují předpoklad iniciace prasknutím křehké částice, respektive tzv. kritického článku. Nechť existuje buňka o objemu  $V_0$ , která takovýto defekt obsahuje. Beremin [3] uvedl pravděpodobnost nalezení trhliny o délce  $l_0$  až  $l_0 + dl_0$  ve tvaru

$$p(l_0)dl_0 = \alpha/l_0^\beta dl_0, \quad (2.1)$$

kde  $\alpha$  a  $\beta$  jsou materiálové charakteristiky. Jestliže v objemu  $V_0$  elementární buňky působí napětí  $\sigma$ , pak je možné pravděpodobnost porušení vyjádřit v integrálním formě

$$p(\sigma) = \int p(l_0)dl_0, \quad (2.2)$$

kde integrujeme od kritické velikosti defektu  $l_c$ . Nechť první materiálová charakteristika je  $m = 2\beta - 2$ , potom po zavedení  $\sigma_u$  obdržíme pravděpodobnost porušení  $p(\sigma)$  ve formě

$$p(\sigma) = (\sigma/\sigma_u)^m, \quad (2.3)$$

kde pro  $\sigma_u$  platí, že je to materiálová konstanta, pokud se neprojeví vliv teploty. Úvahy se doposud týkaly jedné elementární buňky. Pro popis chování celého tělesa je nutné najít integrální vyjádření pravděpodobnosti porušení. Takto popsané chování odpovídá matematicky teorii slabého článku, která považuje systém za řetěz, který se poruší v okamžiku porušení jedné buňky. Po úpravě do formy

$$p(\sigma, V) = 1 - \exp((-V/V_0)(\sigma/A)^\beta), \quad (2.4)$$

což je obecný zápis pravděpodobnosti porušení jako funkce napětí, a po zavedení Weibullova napětí lze zapsat celkovou pravděpodobnost porušení ve tvaru

$$p_f = 1 - \exp(-(\sigma_w/\sigma_u)^m), \quad (2.5)$$

kde Weibullovo napětí je dáno vztahem

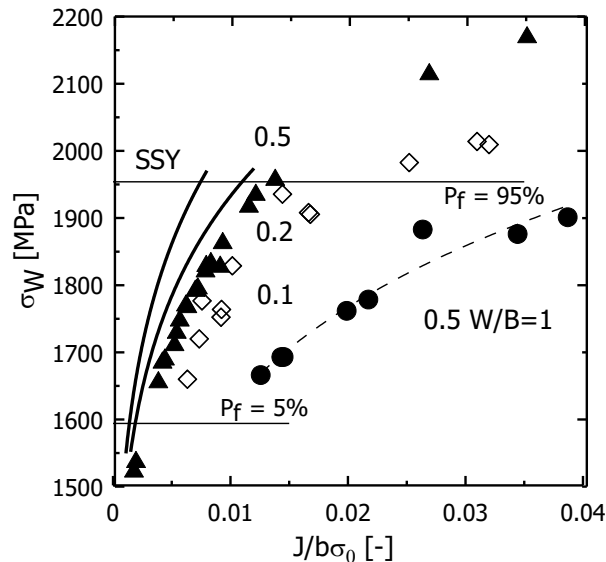
$$\sigma_w = \left[ \int \sigma_1^m (dV/V_0) \right]^{1/m}. \quad (2.6)$$

Parametr  $m$  charakterizuje rozptyl a  $\sigma_u$  je napětí pro 63 % pravděpodobnost porušení,  $dV$  je objem, kde působí napětí  $\sigma_1$ . Tyto parametry jsou obvykle nezávislé na geometrii zkušebního tělesa. Elementární objem  $V_0$  se často nahrazuje veličinou  $\lambda$ , která je definována jako

$$\lambda = V_0^{1/3}. \quad (2.7)$$

Nezbytným krokem před zahájením výpočtu je přesné stanovení závislosti skutečné napětí/skutečná deformace při zvolené teplotě. Pro výpočet distribuce napětí/deformace v testovaných tělesech je možné použít některou z implementací metody konečných prvků, např. systémy Ansys, Abaqus aj. Dle [3], [1] či [8] jsou lokální parametry nezávislé na geometrii zkušebního tělesa [26]. Poslední fází procedury je iterační proces hledání lokálních parametrů. Jedná se o hledání 2 parametrů (v pozdějších pracích 3, viz například Příloha B6, neboť se zavádí prahová hodnota napětí pro iniciaci porušení) Weibullova rozdělení. To popisuje chování materiálu v závislosti na aplikovaném napětí  $\sigma_w$ . Dříve

doporučovaná metoda nejmenších čtverců je pak později zaměněna za metodu maximální věrohodnosti. V literatuře se však objevují hodnoty lokálních parametrů, které se navzájem liší, srov. [14] a [19]. Kapitola zaměřená na komentář vlastních prací se bude věnovat i tomuto nesouladu.



Obrázek 2.4: Princip přenositelnosti lomové houževnatosti, převzato z Přílohy B2.

Jednou z prvních prací, které se zabývaly řešením problému vlivu geometrie na lomovou houževnatost v kontextu lokálního přístupu, bylo experimentálně-výpočtové řešení [23], kde byla snaha transferovat lomovou houževnatost z těles o tloušťce 5,2 a 9,6 mm na těleso 20 mm; původ této myšlenky lze nalézt v [13]. Významným prvkem při použití těchto modelů je inherentní zahrnutí „constraint“ efektu na lomovou houževnatost, viz obr. 2.4. Pokud budeme sledovat jeho vliv [14], např. způsobený poklesem poměru  $a/W$ , na tvar závislosti  $J - \sigma_w$ , dojdeme k následujícímu závěru, že se zápornějším  $Q$  získává křivka plošší charakter [33].

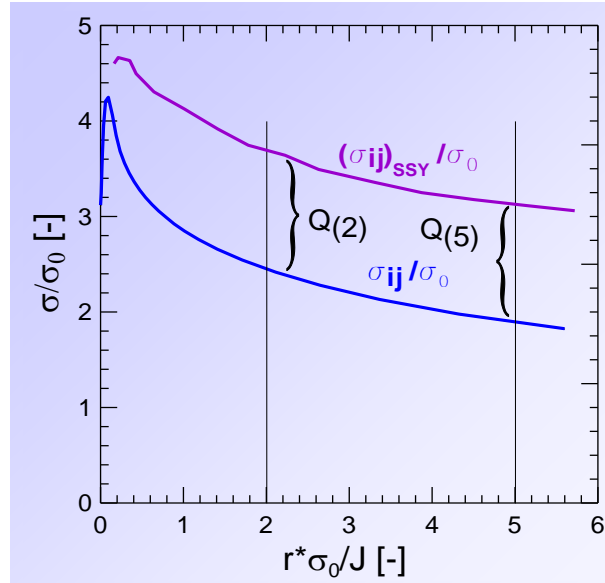
Definici parametru „constraint“ a postup pro jeho určení lze vypořádat z obr. 2.5,  $\sigma_{SSY}$  se někdy označuje  $\sigma_{ref}$ . Index 2 nebo 5 určuje polohu, kde se parametr  $Q$  počítá,  $\sigma_0$  je mez kluzu.

### 2.3 Modelování šíření trhliny

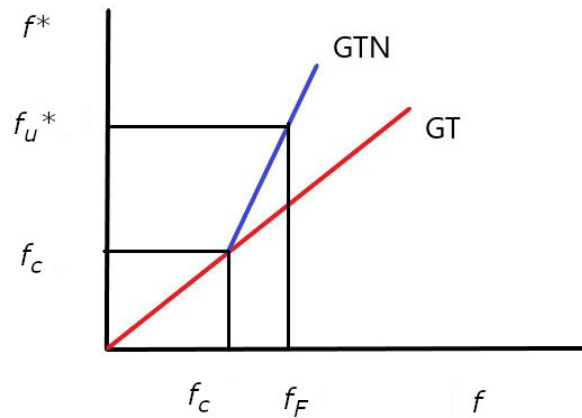
V průběhu šedesátých let se postupně vytvářely teorie, které byly schopny popsat chování těles s trhlinou s uvažováním plastické zóny většího rozsahu, a přiblížit se tak reálnějším podmínkám vznikajících při zatěžování těles s trhlinou.

V současnosti existuje několik postupů, které lze využít k řešení problému simulace šíření trhliny pomocí MKP. Mezi první a nejstarší patří modelování stabilního růstu trhliny s využitím metody uvolňování uzlů. Druhou možností představuje metoda „mizení“ elementů, v jejímž rámci jsou zahrnuty i nejnovější přístupy využívající kohezní elementy, které jsou vlastně zobecněním kontaktu. Podrobněji budou rozebrány obě výše zmiňované metody.

### 2.3. MODELOVÁNÍ ŠÍŘENÍ TRHLINY



Obrázek 2.5: Určení parametru „constraint“, převzato z Přílohy A5.



Obrázek 2.6: Definice modelu poškození Gurson-Tvergaard-Needleman.

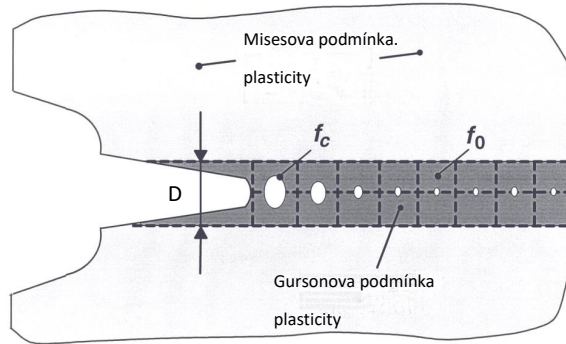
První úpravu původní Gursonovy rovnice navrhuje Tvergaard [37]. Na základě vyhodnocení provedených experimentů doporučuje zavést dva (resp. tři) volitelné parametry  $q_1, q_2, q_3$ , obvykle  $q_1 = 1, 5, q_2 = 1, q_3 = q_1^2$ . Rozbor chování těchto parametrů byl proveden v [40]. Zde  $\sigma_{YS}$  je skluzové napětí materiálu matrice,  $\sigma_m$  je střední (hydrostatické) napětí a  $f$  je objemový podíl dutin. Rozdíl mezi původním modelem a modifikovaným je znázorněn na obr. 2.6, schematická situace před čelem trhliny na obr 2.7. Tvar tzv. kompletního modelu je zapsán v následující rovnici, viz [6], nebo přesněji jako uživatelská procedura pro Abaqus ve [42]:

$$\Phi = \frac{2}{3} \frac{S_{ij} S_{ij}}{\sigma_{YS}^2} + 2q_1 f \cosh \left( \frac{3}{2} \frac{q_2^2 \sigma_m}{\sigma_{YS}} \right) - (1 + q_3 f^2) = 0. \quad (2.8)$$

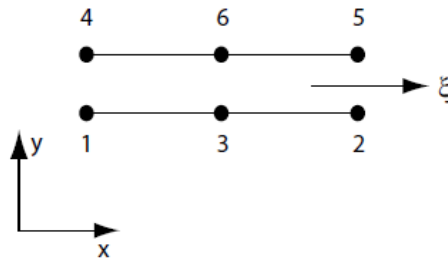
Zavedením efektivního objemového podílu dutin  $f^*$  se tedy v této rovnici  $f$  transformuje na  $f^*$ , kde pro  $f$  větší než  $f_c$  se doplní rovnice (2.8) podle předpisu

$$f^* = f_c - \frac{f_u^* - f_c}{f_F - f_c}(f - f_c), \quad (2.9)$$

kde  $f_c$  je kritický objem, při kterém dojde ke spojování dutin,  $f_F$  je objem dutin při konečném poškození a  $f_u^* = 1/q_1$ .



Obrázek 2.7: Schema modelů poškození před čelem trhliny, převzato z přílohy C2.



Obrázek 2.8: Schematický tvar kohezního prvku pro 2D.

Problematice přenositelnosti se věnoval [13], později [34] a [25], kalibrací [11]. Z aplikačních prací je třeba upozornit na [20] a [44].

Dalším typem prvků pro modelování šíření trhliny jsou prvky kohezní. Ty se původně vyvinuly z kontaktních prvků a využívají myšlenky separace materiálu se vznikem nových povrchů [36]. Prakticky se jedná o určitý fenomenologický popis, který nám charakterizuje chování materiálu pomocí tzv. trakčně separačního zákona, díky němuž pak můžeme predikovat lokální porušení; schematický tvar kohezního prvku pro 2D geometrii je na obr. 2.8.

Existuje několik možností, jak implementovat kohezní zákon do komerčního systému MKP. V předložené práci se vychází z dlouholetých zkušeností s komerčním systémem Abaqus, který umožňuje relativně snadné psaní vlastních uživatelských procedur pro případ některých speciálních typů poškozování, nových typů prvků, či uživatelskému ovládání některých možností systému. Právě možnost psaní uživatelské procedury UEL (User's Element) se stala základem pro vytvoření a implementaci procedury pro trakčně separační zákon. Obecný tvar tohoto zákona lze nalézt v [31] či v [15]. Prvotní verze je uvedena na obr. 2.9, tento trakčně separační zákon byl dále modifikován, jak bude uvedeno v kapitole věnované komentáři k vybraným vlastním výsledkům.

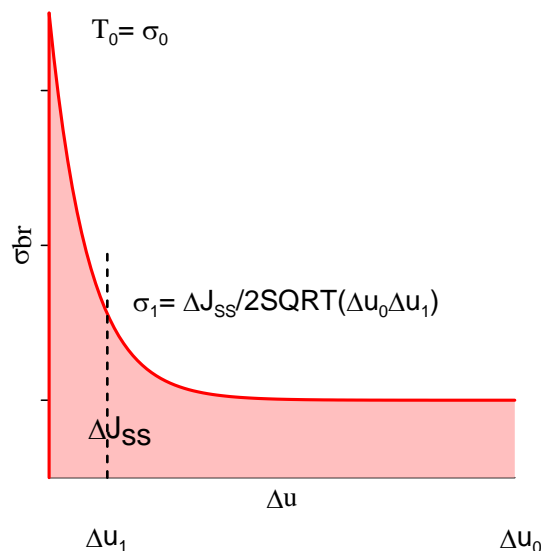
## 2.4 Vláknové kompozity pro stavebnictví a XFEM

Vláknocementové kompozity patří do třídy perspektivních betonů s vyšší mechanickou odolností proti vzniku trhlin. To umožňuje jemnější a ekonomičtější konstrukci; je tedy nutný nový pohled na vytváření stavebních konstrukcí či nahrazení ocelové konstrukce. Tyto konstrukce vystavené zatížení mohou mít za následek napětí v tělese překračující pevnost materiálu, a tím vést k postupnému selhání. Taková selhání jsou často iniciována povrchovými nebo blízkými povrchovými trhlinami, což snižuje pevnost materiálu.

Samostatný závažný problém přitom představuje nastavení materiálových parametrů na makroskopické úrovni, podpořené vhodnými experimenty, jsou-li k dispozici aspoň nějaké informace o struktuře materiálu, např. o nahodilých či záměrně preferovaných směrech vláken; problémům tohoto druhu s důrazem na nedestruktivní či málo invazivní zkušební metody (zejména rentgenografické, tomografické a elektromagnetické, pracující se stacionárním magnetickým či s harmonickým elektromagnetickým polem) se podrobně věnuje [4].

Pro praktické výpočty lze použít metodu časové diskretizace a rozšířenou metodu konečných prvků (anglicky eXtended Finite Element Method, zkráceně XFEM), viz obr. 2.11, pracující s adaptivním obohacováním množiny bazových funkcí poblíž singularit [32]. Tato metoda (včetně řady svých modifikací s vlastními názvy a označeními) má již poměrně bohatou historii; o pokroku v posledních letech se lze přesvědčit porovnáním zakladatelských prací [2] a [17] s [12] a [16]. Obecnější postup pro náhodně orientovaná vlákna předkládá [5], příklad reálného rozložení v drátkobetonu je v obr. 2.10.

Vznik mikrotrhlin [4] lze zohlednit zavedením součinitele porušení na základě přístupu modifikující pole napětí a pracujícího s nelokálním Eringenovým modelem [10], schematický diagram popisující výpočet napětí před čelem trhliny je znázorněn na obr. 2.12. O rozhraních mezi maticí a vlákny, ale i uvnitř matrice, případně i vláken, v závislosti na postupně aktivovaných makrotrhlinách, se většinou předpokládá, že je lze popsat kohezním modelem podle [30], [29] či [22].

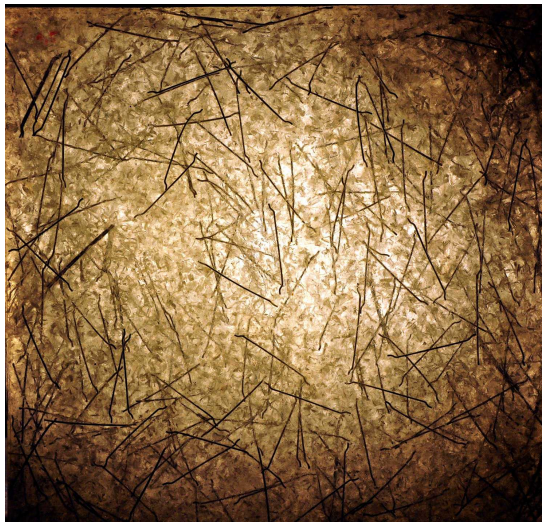


Obrázek 2.9: Trakčně separační zákon pro vláknové kompozity.

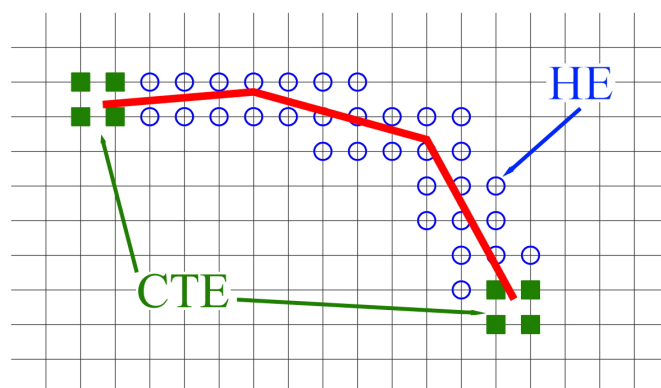
Aplikace XFEM je schopna potlačit nevýhody v simulaci šíření soudržných trhlin; musí však zvládnout neexistenci ostré singularity na špičce trhliny se složitějším odvozením požadovaných napětí z posunů. Kompletní výpočetní model by měl obecně zahrnovat vznik a šíření trhlin, jejich přemostění vlákny, ztrátu soudržnosti mezi vlákny a matricí, jejich vzájemné klouzání třením a destrukci vláken; speciální funkce jsou nutné např. pro singularity napětí v případě otevírání a zavírání trhlin. Schema šíření trhliny přes původní prvky MKP je representováno na obr. 2.11.

Jednotný přístup překlenující měřítko pokrývající elastické a plastické chování spolu s lomem a dalšími defekty vede k konceptu strukturované deformace, viz [24].

Uvažováním o modelech založených na mikromechanice se získají makro-konstitutivní rovnice jednosměrných nebo náhodně rozložených vláken vyztužených materiálů s přihlédnutím k možnosti formování a šíření trhlin v matrici, jakož i k oddělování a lámání vláken. Výpočtový model je nakonec použit v numerických simulacích, aby bylo možné nastínit jeho spolehlivost při hodnocení jak fenoménu interakce vlákno-matice, tak schopnosti



Obrázek 2.10: Radiografický snímek rozložení vláken v drátkovém kompozitu, převzato z Přílohy D1



Obrázek 2.11: Schema šíření trhliny pro XFEM, zkratka HE označuje „Heaviside Enrichment“, CTE „Crack Tip Enrichment“.

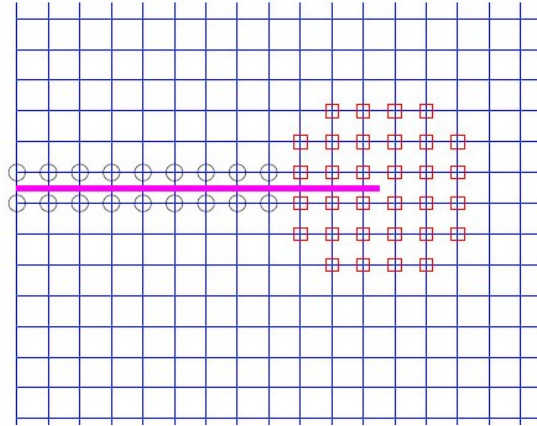
## 2.4. VLÁKNOVÉ KOMPOZITY PRO STAVEBNICTVÍ A XFEM

předpovědi selhání lomu u vláknových kompozitů. Mechanické chování kompozitů s křehkou maticí vyztužených vlákny, s důrazem na cementové kompozity, bude zkoumáno na základě jak diskontinuitního přístupu, tak modifikovaných přístupů založených na MKP.

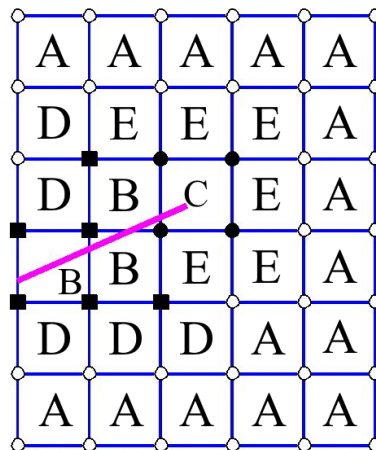
V XFEM je síť nezávislá na vnitřní hranici, jako jsou materiálová rozhraní a trhliny. Tyto interní hranice obvykle způsobují slabé nebo silné diskontinuity pole proměnných, které budou zohledněny v XFEM začleněním „enrichment“ funkcí do standardní aproximace MKP. V rámci XFEM je aproximace v prvku pro viskoelastické těleso s trhlinou vyjádřena rovnicí ve tvaru dle [43]

$$\mathbf{u}^h(\mathbf{x}) = \sum_{i \in C_A} N_i(\mathbf{x}) \mathbf{u}_i + \sum_{j \in C_S} N_j(\mathbf{x}) H_j(\mathbf{x}) \mathbf{a}_j + \sum_{K \in C_T} N_K(\mathbf{x}) \sum_{m=1}^4 \Phi_K^m(\mathbf{x}) \mathbf{c}_K^m, \quad (2.10)$$

kde  $C_A$ ,  $C_S$ ,  $C_T$  jsou množiny bodů odpovídající obr. 2.13,  $H(\mathbf{x})$  je Heavisidova funkce. Zjednodušeně řečeno první člen odpovídá standardní metodě konečných prvků, druhý realizuje vznik trhliny a třetí kritérium vzniku, přičemž  $\Phi_K^m$  reprezentuje lokální situaci před čelem trhliny.



Obrázek 2.12: Výpočet napětí před čelem trhliny pro nelokální přístup.



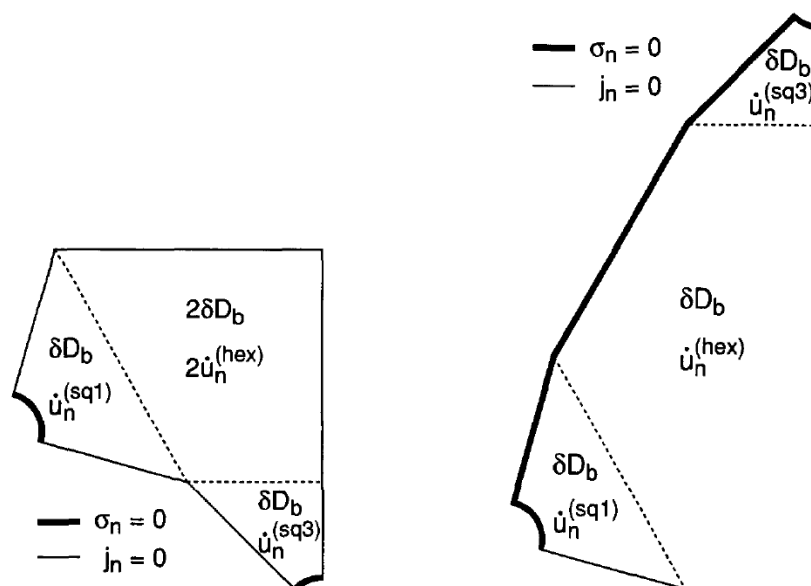
Obrázek 2.13: Ilustrace „enrichment“ funkce, prázdné kruhové uzly patří do  $C_A$ , plné do  $C_T$  a plné hranaté do  $C_S$ .

### 3 Vlastní výsledky - komentář publikovaných prací

Habilitační práce je sestavena jako komentář 26 vybraných článků publikovaných na mezinárodních konferencích, v impaktovaných a recenzovaných časopisech. V následující kapitole budou komentovány práce, která jsou zařazeny v Příloze. Výsledky jsou rozděleny do čtyř oblastí. Společným nosným problémem pro všechny kapitoly je využití metody konečných prvků pro různé aplikace. Největší prostor je věnován problematice modelování poškození pro několik druhů materiálů.

#### 3.1 Přímé aplikace MKP

Jak již bylo uvedeno v teoretické části, viz obr. 2.1, při řešení úlohy Příloze A1 se snažíme model zjednodušit pro jeho modelování ve 2D. To vede na určení čtyř zatěžovacích případů, více viz Příloha A1; první dva jsou charakterizovány v obr. 3.1. Numerické vý-



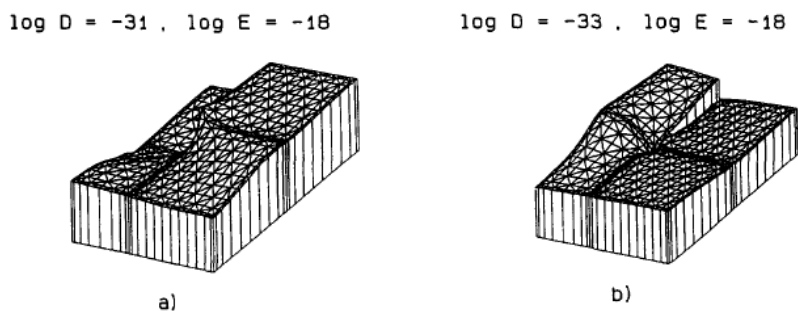
Obrázek 3.1: Jednotková buňka pro zatížení 1 a 2.

počty difúzních polí na povrchu tetrakaidekahedronu se určují pro následující případy: (i) Jednosměrné prodloužení ve směru [001]. V tomto případě je jedinou nenulovou složkou rychlosti deformace  $\dot{\epsilon}_{33}$ . Cílem je vypočítat potřebná napětí která způsobí tuto deformační rychlost. (ii) Smyk na (100) rovinách ve směru [010]. Pak jsou pouze nenulová deformační rychlost a složky napětí  $\dot{\epsilon}_{12} = \dot{\epsilon}_{21}$  a  $\sigma_{12} = \sigma_{21}$ . (iii) Izostatické zatěžování se střední rychlostí deformace  $\dot{\epsilon}_m = \dot{\epsilon}_{11} = \dot{\epsilon}_{22} = \dot{\epsilon}_{33}$  vede k hydrostatickému napěťovému stavu se střední hodnotou  $\sigma_m$ . (iiii) Creep ve směru [001] bez pórů, kdy předepíšeme složky rychlosti defor-

### 3.1. PŘÍMÉ APLIKACE MKP

mace  $\dot{\epsilon}_{33} = -2\dot{\epsilon}_{11} = -2\dot{\epsilon}_{22}$ . Jak později ukázaly citace této práce, navržený model přesněji charakterizuje chování keramických a kovových prášků při jednoosém zatěžování.

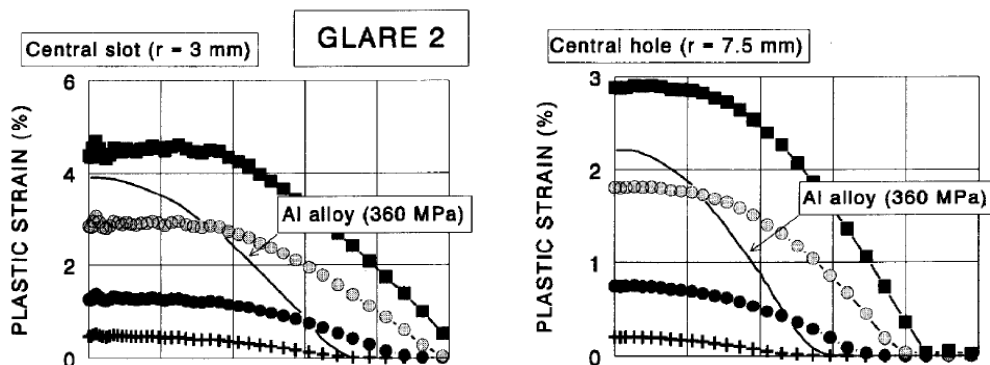
Na tuto práci navazuje Příloha A2, kdy se podařilo vytvořit funkční model pro kompozity s kovovou maticí zpevněnou krátkými vlákny či karbidy křemíku. Jedná se o vhodný materiál pro letectví, zejména o nahrazení titanu, či automobilový průmysl, zvláště pro návrhy motorů. Důležitou úlohu zde hraje difúze po hranicích zrna a pokluzu po hranicích. Příklady výsledků modelování pro logaritmus koeficientu difúze po hranicích zrn  $D$



Obrázek 3.2: Rozložení napětí  $\sigma_{22}$  v oblasti stacionárního creepu různé vlastnosti rozhraní zpevnění/matrice, převzato z Přílohy A2.

a rychlost pokluzů  $E$  jsou na obr. 3.2.

Problematice dalších druhů kompozitů, tentokrát sklolaminátu GLARE, lze nalézt v Příloze A3 a A7.



Obrázek 3.3: Ekvivalentní plastická deformace ve Al vrstvě laminátu GLARE pro různé velikosti iniciátoru napětí, převzato z Přílohy A3.

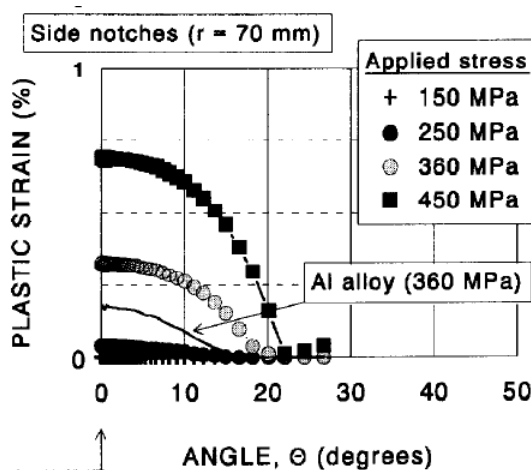
Výpočty společně s metalografií prokázaly, že první mikrotrhliny v rozích na krajích vnitřních Al vrstev. Během dalšího zatěžování vznikají nové mikrotrhliny ve vnitřních kovových vrstvách nehledíc na předchozí trhliny v materiálu. Nakonec začnou vznikat trhliny v povrchových vrstvách, viz obr. 3.3 a 3.4.

V Přílohách A4, A5, A6 je hledána kritická zóna před čelem trhliny či vrubem. Ta může být ovlivněna tvarem trhliny a určuje lomové chování komponenty. Je konfrontován deterministický přístup (princip kritického napětí Příloha A4) s pravděpodobnostním přístupem v Příloze A5 a A6. Numerické elastoplastické výpočty MKP slouží jako podpůrný nástroj pro interpretaci fyzikální podstaty probíhajících mikromechanických procesů. Ukázalo se, že tato lokální zóna není citlivá na změnu lomového mechanismu a velikost kritického napětí lze brát jako materiálovou charakteristiku. Rovněž pro ko-

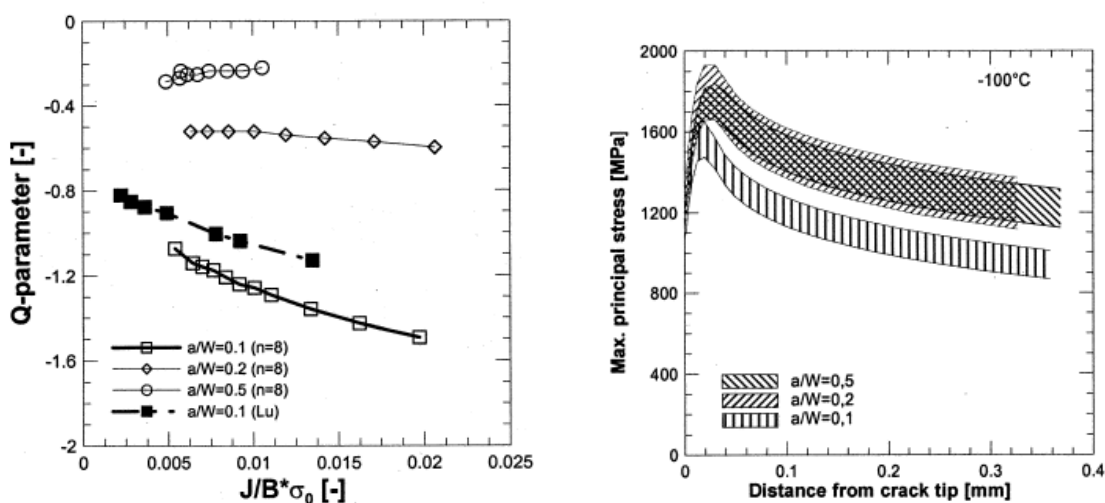
### 3. VLASTNÍ VÝSLEDKY - KOMENTÁŘ PUBLIKOVANÝCH PRACÍ

reálnější predikci lomového chování je nutno využívat možnosti víceparametrové lomové mechaniky. Tu lze, zejména  $J, Q$  přístup, využít i pro vysvětlení metod využívajících statistických přístupů. Určení těchto parametrů znamenalo přesnější výpočet pole napětí a deformace před čelem trhliny, a tedy pro vysokou úroveň plastické deformace použití deformační teorie plasticity či prodloužení závislosti skutečného napětí na skutečné deformaci mimo hodnoty získané přímým měřením. Příklad korektního výpočtu lze najít na obr. 3.5, kde je ukázán i případný rozptyl maximálního hlavního napětí  $\sigma_1$  a výpočet „constraint“ pro různé tloušťky zkušebního tělesa. Symboly  $a, W, B$  označují postupně délku trhliny, šířku zkušebního tělesa a jeho tloušťku. Zajímavým zjištěním je, že  $\sigma_1$  před čelem trhliny pro krátké trhliny  $a/W = 0,1$  je výrazně nižší než pro ostatní konfigurace.

Řešení problémů lomové mechaniky je založeno na znalosti deformačně-napěťových charakteristik před čelem trhliny. V případě hodnocení chování komponent obsahujících trhlínu určuje elasticko-plastická lomová mechanika přesně vztah mezi maximálním přípustným vnějším zatížením a parametry komponenty (rozměry tělesa, materiálové vlastnosti, velikost a polohu trhliny). MKP představuje vhodný nástroj pro získání přehledu roz-



Obrázek 3.4: Aplikované napětí pro řešení úlohy laminátu GLARE, převzato z Přílohy A3.



Obrázek 3.5: J-Q diagram a maximální hlavní napětí versus vzdálenost od čela trhliny, převzato z Přílohy A5.

### 3.2. LOKÁLNÍ PŘÍSTUP

ložení polí deformací a napěťových polí v analyzovaném modelu. Poloměr zaoblení čela trhliny se pohyboval kolem  $r = 0,01$  mm.

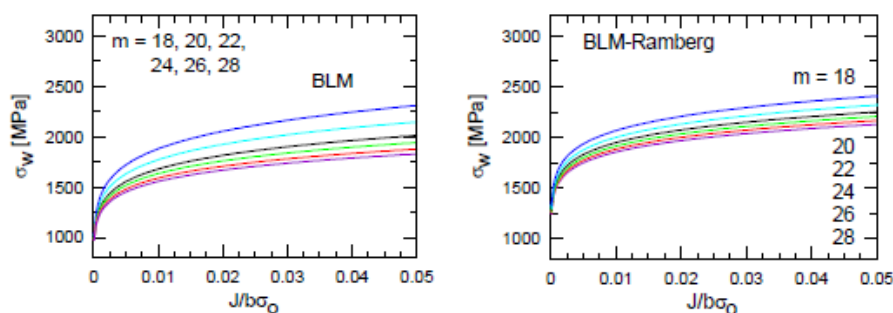
### 3.2 Lokální přístup

V přílohách B1 a B2 lze najít komentované výsledky věnované určování lokálních parametrů na tělesech s různým poloměrem vrubu a tělesech s trhlinou. V počátečních pracích jsme vycházeli z literárního rozboru a používali dvouparametrový přístup, tj. použití parametrů  $m$  a  $\sigma_u$ , později, zejména v B6 a B7, tříparametrový model zavedením  $\sigma_{th}$ . Ze závěrů je nutno zdůraznit, že lokální parametry jsou geometricky závislé, a to s tendencí klesající poloměr zaoblení – rostoucí parametr  $m$ . Situace je však složitější, jak již bylo zmíněno; hlavním problémem je stanovení vlastní distribuce napětí. V oblasti podléhající rozsáhlé plastické deformaci dochází k nukleaci mikrodefektů, které svojí existencí mění napěťové pole, viz tabulka 3.6. Na úrovni současných metod experimentálních i výpočtových nejsme schopni tento efekt identifikovat. Proto jsou pro stanovení lokálních parametrů doporučovány tělesa s malým gradientem napětí, u kterých je větší procesní zóna, a celkově je tak možné ovlivnění výpočtu okrajovými podmínkami nižší. Doporučená velikost hrany použitých prvků pro MKP se stanovuje tak, aby v elementární buňce bylo tak 10 možných vzniků defektů. To pro případ  $\lambda = 100 \mu\text{m}$  znamená velikost hrany prvku méně než  $2 - 6 \mu\text{m}$ .

Příklad testů určování lokálních parametrů na rotačních tělesech s různým poloměrem vrubu,  $\sigma_0$  označuje mez kluzu. Většina příloh označených B1-B7 se však věnuje problému

U notch 0.2 mm						
	~11300		~6500		~3500	
$\sigma_{th}/\sigma_0$	m	$\sigma_u$	m	$\sigma_u$	m	$\sigma_u$
0	65.6	1340	64.6	1343	63.3	1350
1	65.6	1340	64.6	1343	63.3	1350
1.5	65.6	1340	64.6	1342	63.3	1350
U notch 0.7 mm						
0	17.0	2485	16.9	2491	16.8	2506
1	17.0	2484	16.9	2491	16.8	2506
1.5	16.9	2489	16.9	2494	16.8	2508
U notch 1. mm						
0	18.2	2117	17.8	2145	17.8	2146
1	18.2	2117	17.8	2146	17.8	2146
1.5	18.2	2120	17.8	2148	17.7	2149

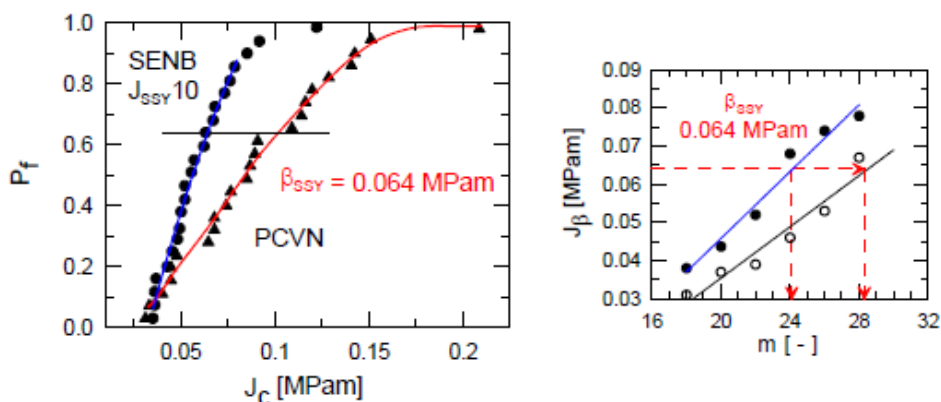
Obrázek 3.6: Vliv velikosti sítě a poloměru vrubu pro rotační tělesa, převzato z Přílohy B1.



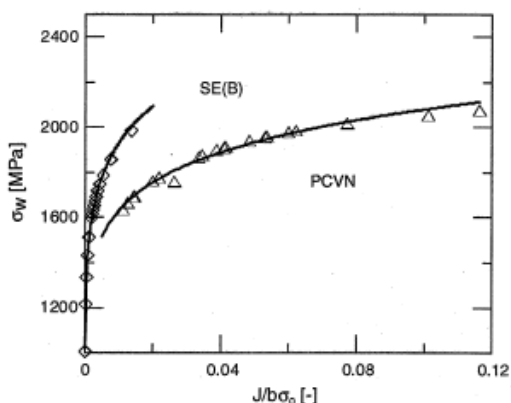
Obrázek 3.7: Diagram Weibulova napětí a navržený TSM pomocí MBL, převzato z Přílohy B3.

### 3. VLASTNÍ VÝSLEDKY - KOMENTÁŘ PUBLIKOVANÝCH PRACÍ

přenositelnosti lomových charakteristik a lokální parametry jsou určovány na tělesech s trhlinou. Bylo zjištěno, že přenos funguje pro tělesa se stejným tvarem koncentrátoru napětí. Technika tvorby diagramu TSM, (Toughness Scaling Method), viz obr. 3.7, je testována v Příloze B2 a B3; přehled je v Příloze B5, viz obr. 3.9.



Obrázek 3.8: Kalibrace lokálních parametrů, převzato z Přílohy B3.



Obrázek 3.9: Kalibrovaný TSM diagram, převzato z Přílohy B5.

Kroky postupu kalibrace použité pro TSM jsou následující, viz Příloha B3 a obr. 3.8:

- Vytvořit pravděpodobnostní diagram hodnocení ( $P_f = f(J_c)$ ) pro dvě geometrie.
- Provézt výpočet MKP pro testované těleso a podmínky SSY.
- Weibullové stanovení napětí pro testované těleso a podmínky SSY.
- Oprava omezení podle nejslabší tloušťky dle postupu ESIS E-1921.
- Nechť  $t_{SSY}$  a  $t_A$  označuje tloušťku pro SSY a pro konfiguraci A, pak je  $J_{SSY} = 1.8 + (t_A/t_{SSY})^2(J_c - 1.8)$ .
- Určíme  $b$ . Většinou se předpokládá hodnota  $b = 2$ , což znamená, že korigovaná lomová houževnatost vyhovuje Weibullovu rozdělení s exponentem rovný dvěma. Parametr  $\beta$  definuje hodnotu při 63% pravděpodobnosti porušení, což vede na

$$\left(\frac{J}{\beta}\right)^2 = \left(\frac{\sigma_w}{\sigma_u}\right)^m. \quad (3.1)$$

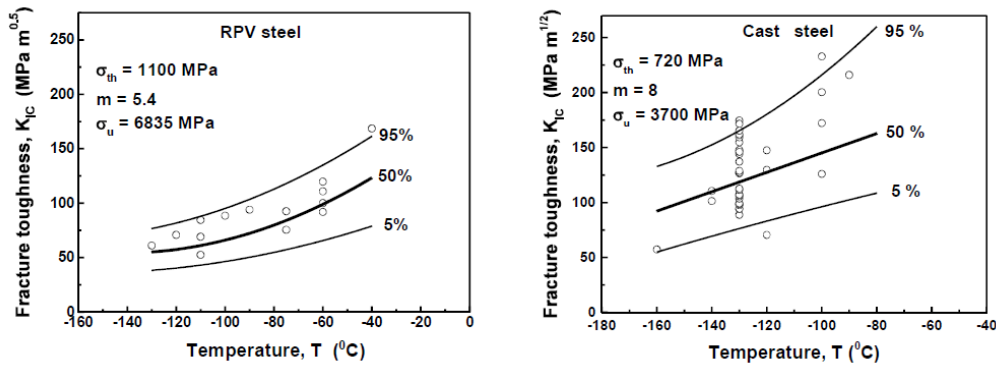
### 3.3. GTN MODEL A POUŽITÍ KOHEZNÍCH PRVKŮ

Podle modelu štěpného lomu polykrystalických kovů navrženého v [18] a verifikovaného v přílohách B6 a B7 je hodnota prahového napětí  $\sigma_{th}$  určena minimálním napětím  $\zeta_{Cmin}$  odpovídajícím nestabilitě prasklého nukleakčního jádra. Potom lze prahovou hladinu stresu popsat rovnicí

$$\sigma_{th} = \frac{\zeta_{Cmin}}{1 + tJ_{\zeta_{11}}}, \quad (3.2)$$

kde  $t$  (tolerance)  $\approx 0,3$  a  $\zeta_{Cmin}$  pro oceli  $\approx 0,13$ .

Výsledné predikce jsou ukázány na obr. 3.10 či podrobněji v přílohách B6 a B7. Jedná se o přenos z malého tělesa s trhlinou (PCVN) na těleso standardních rozměrů (SENB).



Obrázek 3.10: Predikované lomové houževnatosti pro 2 typy ocelí, převzato z Přílohy B7.

### 3.3 GTN model a použití kohezních prvků

Hlavní důraz je kladen na možnost predikce chování tělesa s trhlinou za předpokladu deformačně řízeného mechanismu porušování. Tento úkol ve skutečnosti představuje využití hybridní metodologie spojující numerické modelování, experiment a mikroskopické pozorování v jeden poměrně složitý celek. Experimentální data použitá pro modelování lze nalézt převážně v práci [40]. Výsledky predikce jak pro model GTN, tak pro použití kohezních prvků, byly ověřovány pomocí experimentálně získaných tzv.  $J - \Delta a$  neboli  $J - R$  křivek.

Stručně řečeno, přílohy C1 až C3 jsou zaměřeny na modelování šíření trhliny oběma metodami. Využívají možností programových systémů Abaqus a Warp3D a věnují se spíše vlivu jednotlivých parametrů v modelech na korektní predikci šíření trhliny. Jako modelový materiál byla zvolena kovaná ocel, kde díky tvárnému porušení se mohlo využít obou předložených metod.

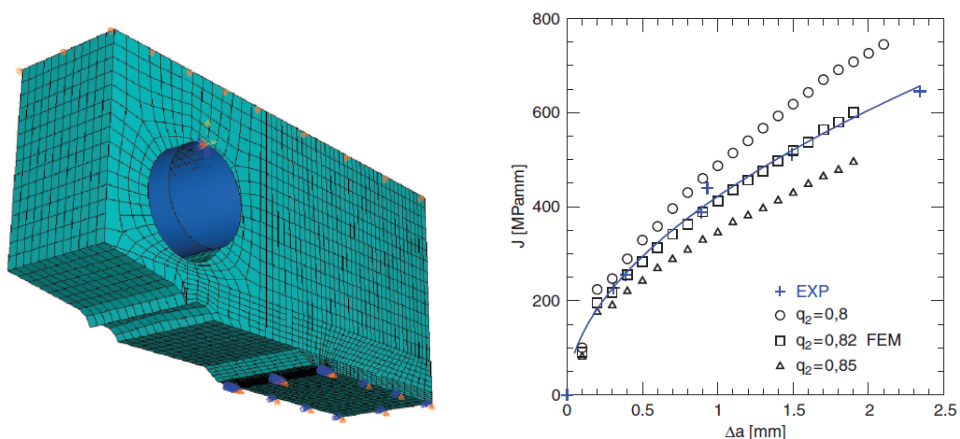
Přílohy C4 až C7 ukazují modelování šíření trhliny pro jinou třídu materiálů. Jedná se o kompozity zpevněné vlákny SiC se skelnou maticí. Z velikostního pohledu jsme o řády níže a zde návrh trakčně separačního zákona vyžaduje ještě více pochopení fyzikální podstaty probíhajících dějů. Proto byla vyvinuta uživatelská procedura v jazyce Fortran, která byla implementována do komerčního systému Abaqus.

Na obr. 3.11 jsou prezentovány výsledky pro experimentální ocel a je testován vliv parametru  $q_2$  pro model GTN na tvar predikce, podrobněji na obr. 3.12.

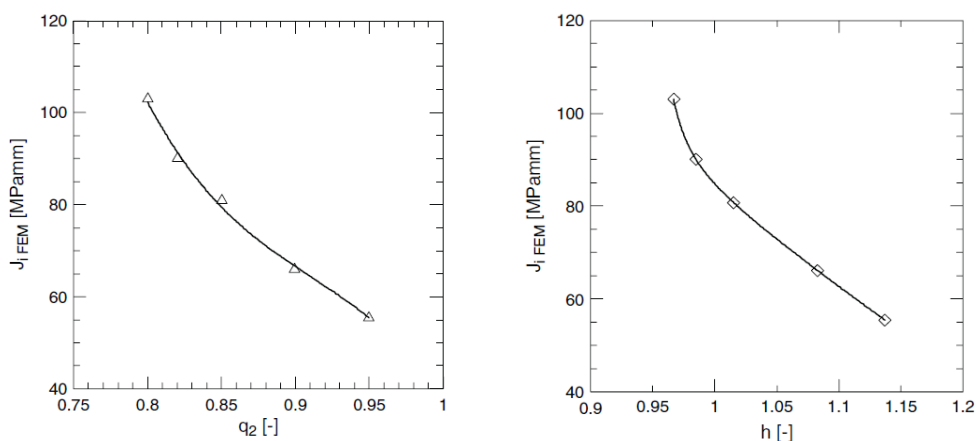
V Příloze C1 a C2 lze je uvedeno porovnání obou metod modelování šíření trhliny pro experimentální ocel, viz obr. 3.13. Za zásadní výsledek v případě modelování šíření

### 3. VLASTNÍ VÝSLEDKY - KOMENTÁŘ PUBLIKOVANÝCH PRACÍ

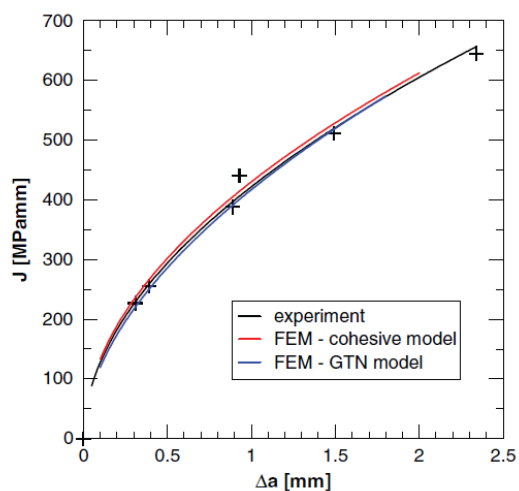
trhliny je považována nutnost kalibrace základních parametrů  $q_1$  a  $q_2$  modelu GTN, což



Obrázek 3.11: Zkušební CT těleso a predikce J-R křivky pro experimentální ocel, převzato z Přílohy C2 a C1.



Obrázek 3.12: Vliv parametru  $q_2$  a faktoru triaxiality  $h$  na hodnotu  $J$ , převzato z Přílohy C2.

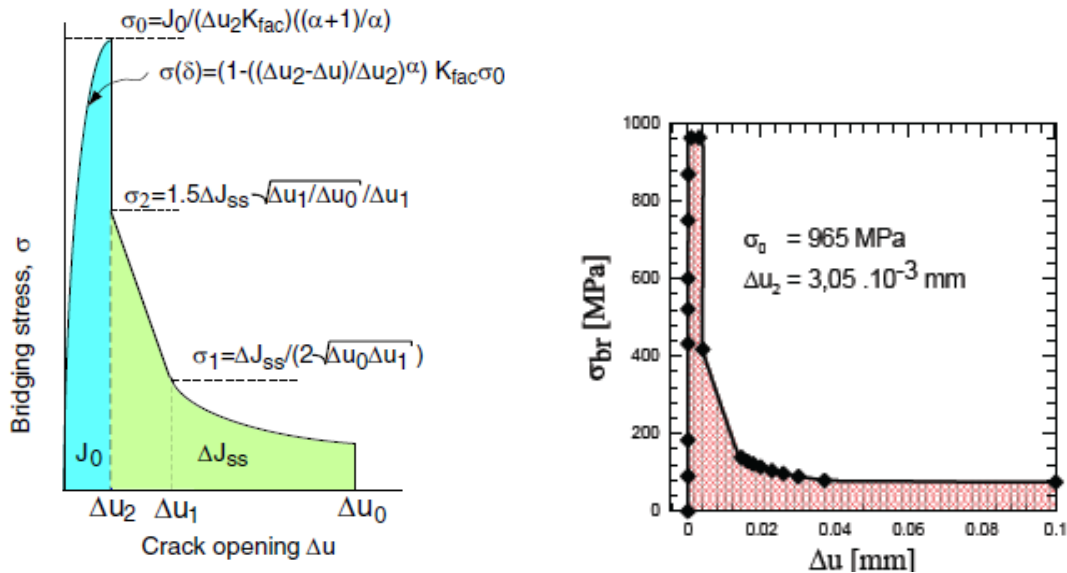


Obrázek 3.13: Určení J - R křivky pro obě metody, převzato z Přílohy C2.

### 3.3. GTN MODEL A POUŽITÍ KOHEZNÍCH PRVKŮ

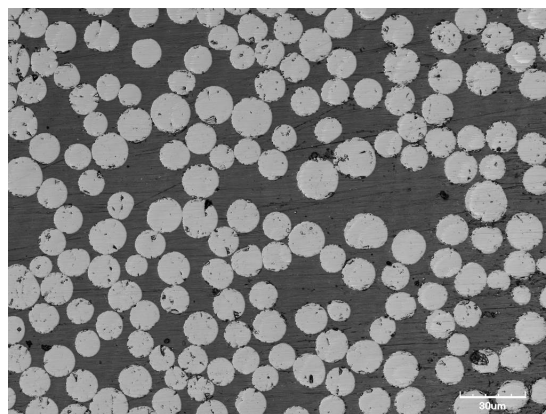
lze pozorovat nejen na obr. 3.13; nutno je také poukázat na přesné modelování závislosti skutečné napětí - skutečná deformace, viz Příloha C2.

Pro případ modelování kompozitů se skelnou maticí, jejichž příprava je ukázána v Příloze C5, byl použit speciální tvar trakčně separačního zákona, který byl matematicky popsán v Příloze C6. Příklad kalibrace trakčně separačního zákona je podrobně popsán v Příloze C4.



Obrázek 3.14: Kalibrace trakčně separačního zákona pro SiC, převzato z Přílohy C4.

Materiál použitý pro modelování přemostňovacích napětí byl komerčně dostupný kompozit z borosilikátové skelné matrice vyztužené vlákny *SiC* Nicalon (viz 3.15). Vlastnosti skleněné matrice, *SiC* vláken a kompozitu byly následující: Youngův modul 63, 198, 118 GPa, Poissonův číslo 0,22, 0,20, 0,21, pevnost v tahu 60, 2750, 600-700 MPa. Pro modelování růstu trhlin byla použita následující experimentálně stanovená data:  $J_0 = 6200 \text{ J/m}^2$ ,  $J_{ss} = 18500 \text{ J/m}^2$ ,  $\Delta u_c = 0,1 \text{ mm}$ ,  $\Delta u_1 = 0,013 \text{ mm}$ . Kalibrovaná data a konečný tvar překlenovacího zákona lze vidět na obr. 3.14.



Obrázek 3.15: Snímek mikrostruktury borosilikátového skla, převzato z Přílohy C4.

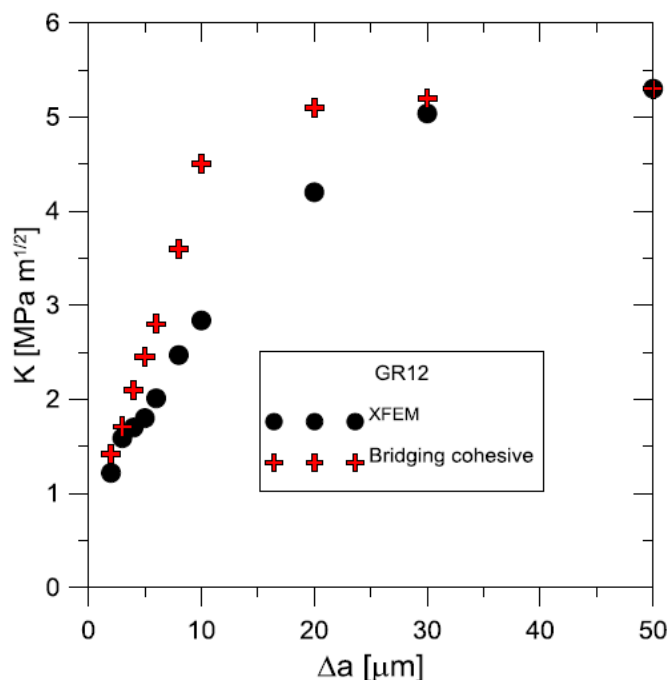
Finální modelování pro kompozit s  $Si_3N_4$ , viz Příloha C7, je prezentováno na obr. 3.17. Následující tabulka 3.16 ukazuje různé modifikace testovaných kompozitů. V práci je uveden výsledek modelování pro variantu A a srovnání predikce pro standardní XFEM

### 3. VLASTNÍ VÝSLEDKY - KOMENTÁŘ PUBLIKOVANÝCH PRACÍ

s výsledky získanými pomocí kohezních prvků. Tvar křivky pro speciálně kalibrovaný trakčně separační zákon lépe vystihují experimentální pozorování.

material	GR12 A	SKF B	GR25 C	GR36 D
$\Delta J_{ss}$ [J/m <sup>2</sup> ]	64	77	67	108
$\Delta_c$ [μm]	0.30	0.30	0.35	0.35
$\Delta_1$ [μm]	0.08	0.055	0.045	0.045
$dJ_0$ [J/m <sup>2</sup> ]	21	24	24	25
$\sigma_0$ [MPa]	1063	1590	1350	1590

Obrázek 3.16: Materiálové charakteristiky pro návrh trakčně separačního zákona pro  $Si_3N_4$ , převzato z Přílohy C7.



Obrázek 3.17: Predikce J-R křivky pomocí XFEM a kohezních prvků, převzato z Přílohy C7.

Na základě aplikace na konkrétní materiál  $Si_3N_4$  lze konstatovat:

- Mechanismy přemostění trhlin mohou poskytnout podstatné zvýšení houževnatosti.
- Saturace v křivce  $J - R$  byla pro modelování XFEM dosažena podstatně později, obvykle pro délku trhlin větší než 20 μm. Použitý model XFEM byl bez začlenění přemostujícího mechanismu.
- Saturace v křivce  $J - R$  byla dosažena pro soudržné modelování obvykle pro trhlínu pro délku v intervalu 10 - 15 μm. Pravděpodobný je brzký začátek skutečného přemostění; kvůli numerickým oscilacím mohou být získané hodnoty  $K$  menší.

### 3.4. MODELOVÁNÍ PORUŠENÍ STAVEBNÍCH KOMPOZITŮ

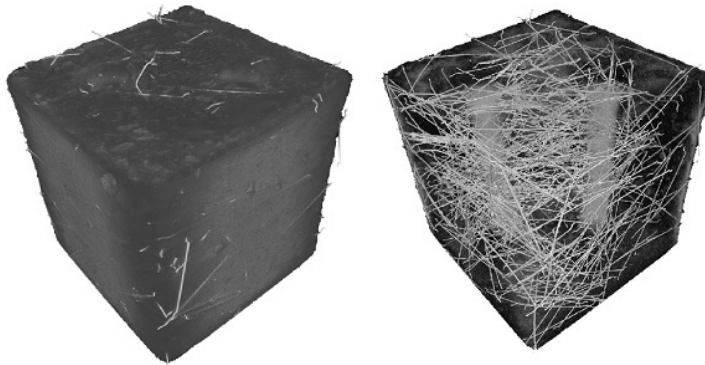
- Získané parametry pro trakčně separační zákon (přemostění) umožnily predikci  $J - R$ ; pro přesnou předpověď se jeví jako nezbytné určit alespoň maximální napětí  $\sigma_0$  experimentálně.

### 3.4 Modelování porušení stavebních kompozitů

Nedestruktivní testování struktury materiálu nabízí zpracování obrazu (2D rentgenové, 3D tomografické), stacionární magnetické a nestacionární elektromagnetické přístupy. I v případě vláknobetonu, nejčastěji používaného kompozitu s (téměř) náhodně distribuovanými vlákny používanými ve stavebnictví, je kontrola nad objemovým podílem a orientací vláken dosud možná pouze při výrobě čerstvé vláknobetonové směsi. Přidání vláken může významně zlepšit mnoho technických vlastností betonu, zejména lomové houževnatosti, pevnosti v tlaku, rázové houževnatosti a životnosti konstrukcí. Navíc v tahu také se zvyšuje pevnost, únavová pevnost a schopnost odolat praskání.

Výpočtová homogenizace makroskopického materiálu [38] se opírá o semi-analytické směšovací vzorce pro speciální tvary vláken (přijatelné zejména pro jejich nízké objemové podíly), o dvouškálovou homogenizaci periodických struktur nebo o alternativní výsledky z asymptotické analýzy ( $G$ -konvergenci,  $H$ -konvergenci,  $\Gamma$ -konvergenci atd.), až po velmi obecné (deterministické i stochastické) výsledky pro  $\sigma$ -konvergenci na homogenizačních strukturách s četnými otevřenými problémy, srov. [32]. Žádoucí je jednotný přístup zohledňující makroskopické a mikroskopické měřítko, pokrývající elastické a plastické chování společně s degradací a lomem.

Přílohy D1 a D2 se tedy věnují testování a hledání struktury vláknového kompozitu, konkrétně drátkobetonu. Z hlediska modelování metodou konečných prvků je řešen zásadní problém, tj. stanovení reprezentativního objemu RVE (v angličtině Representative Volume Element) pro korektní výpočet, jak naznačuje obr. 3.18.



Obrázek 3.18: Rentgenografický snímek betonového vzorku o hraně 150 mm, axonometrický pohled na povrch a dovnitř vzorku, viz Příloha D1.

Stejně jako u zjednodušeného modelového příkladu, vycházejícího z úvah podrobně rozebraných v Příloze D3, můžeme pro potřebu výpočtového modelování vyjít z abstraktního (obecně nelineárního) kvazistatického problému

$$\langle G(\dot{u}), v \rangle + \langle A(u), v \rangle = \langle F, v \rangle, \quad (3.3)$$

kde závorky odkazují na jistá duální přiřazení (v nejjednodušších případech skalární součiny) pro reflexivní a separabilní Banachovy prostory  $V$ ,  $v \in V$  označuje potřebnou virtuální veličinu, například posunutí vztahené k referenční konfiguraci. Tečka zde naznačuje

### 3. VLASTNÍ VÝSLEDKY - KOMENTÁŘ PUBLIKOVANÝCH PRACÍ

parciální derivaci podle času,  $F$  je lineární funkcional  $A(\cdot)$  a  $G(\cdot)$  jsou (spíše speciální) zobrazení definované na  $V$ ; naším cílem je, aby abstraktní funkce  $u$ , zobrazující jistý časový interval, splňovala v každém čase  $t$  integrální rovnici (3.3) a mimoto vyhovovala jistým předepsaným (zejména okrajovým a počátečním) podmínkám. Hlavní obtížnost hypotetického přímého přístupu souvisí s nelinearitou  $A(\cdot)$ .

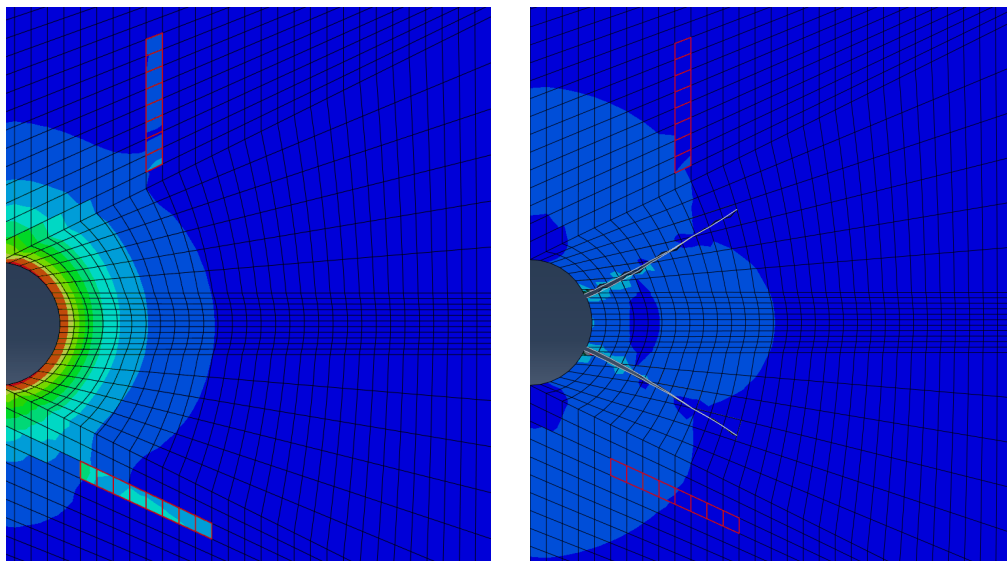
Rovnici (3.3) však lze metodou časové diskretizace (díky konvergenčním vlastnostem Rotheho posloupností) převést na tvar

$$\langle G(u_s - u_{s-1}), v \rangle + h \langle A(u_{s-1}, u_s), v \rangle = \langle F_s, v \rangle, \quad (3.4)$$

kde  $u_s$  a  $u_{s-1}$  aproximují neznámou abstraktní funkci  $u$  v diskrétních časech  $t = sh$  a  $t = (s-1)h$ , stejně jako  $F_s$  v případě neznámé  $F$ ; zde  $s \in \{1, \dots, m\}$  pro  $m = \tau/h$ , kde  $\tau$  je délka uvažovaného časového intervalu ( $0 \leq t \leq \tau$ ), přičemž potřebujeme limitní případ  $h \rightarrow 0$ , tedy  $m \rightarrow \infty$ . Po doplnění některých dodatečných podmínek a použitím normy  $\|\cdot\|$  v prostoru  $V$  dostaneme

$$\|u_s\|^2 + \sum_{r=1}^s \|u_r - u_{r-1}\|^2 \leq c \left( \|u_0\|^2 + h \sum_{r=1}^s \|F_r\|^2 \right), \quad (3.5)$$

kde  $c$  je generická konstanta; odtud je mj. zřejmá klesající norma  $\|u_m - u_{m-1}\|$  pro  $m \rightarrow \infty$ .



Obrázek 3.19: Modelování šíření trhliny pro prosté použití XFEM, viz Příloha D3.

Jelikož (3.4) představuje v každém kroku lineární úlohu, ale stále v nekonečněrozměrném prostoru  $V$ , je nutná další výpočetní diskretizace (kromě velmi speciálních konfigurací se známými analytickými nebo semianalytickými řešeními). Takovou diskretizaci lze naznačit podobně jako (2.10) ve tvaru

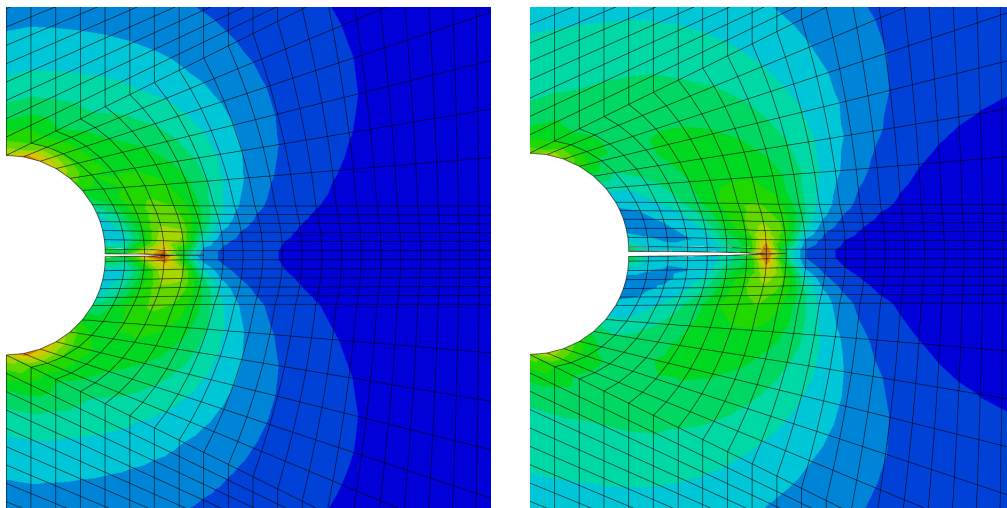
$$u_{si}(x) = u_{sia}\psi(x) + u_{sib}\psi_b(x) + u_{sic}\psi_c(x), \quad (3.6)$$

kde první člen obsahuje standardní tvarovou funkci na  $\Omega$ , druhý „enrichment“ tvarovou funkci na  $\Theta$  a třetí kohezní „enrichment“ tvarovou funkci pro rozhraní.

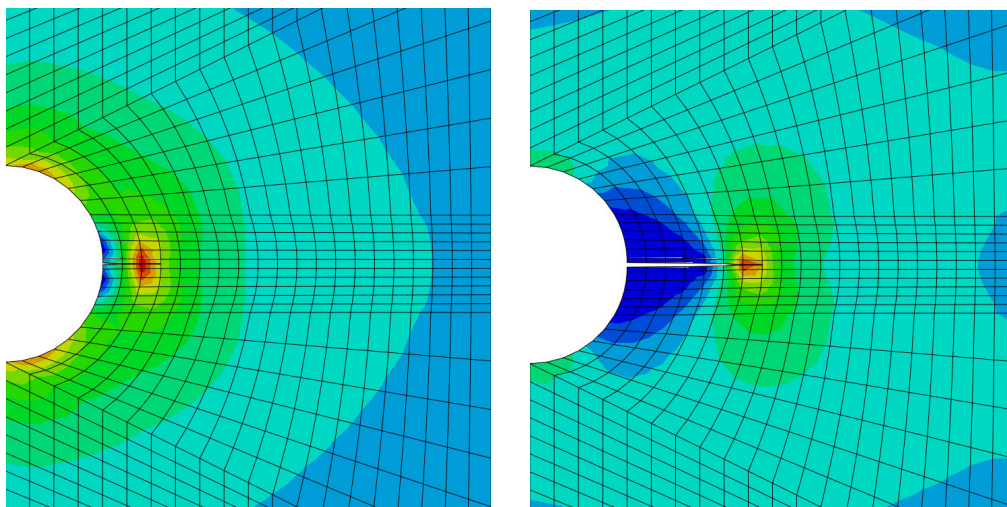
### 3.4. MODELOVÁNÍ PORUŠENÍ STAVEBNÍCH KOMPOZITŮ

Pro výpočetní modelování byl vybrán vzorek s cementovou matricí a ocelovými vlákny, viz Příloha D3. Numerické výsledky ukazují plošné šíření trhlin v porušeném tělese v závislosti na umístění vlákna a vlastnostech materiálu. Výztužný účinek vláken hraje významnou roli ve směru šíření trhlin, viz obr. 3.19: levý ukazuje počáteční stav, pravý rozběhnutou trhlínu, která se vyhýbá vláknům.

Výpočtový model pro prakticky nejdůležitější případ cementových kompozitů obsahujících krátká záměrně nebo kvazi-náhodně orientovaná ocelová, keramická, resp. polymerní vlákna s jejich primárním potlačením některých složek napětí, je zaveden v Příloze D4 a D5, přičemž podrobnější matematická formulace je v Příloze D5. Jeho numerický přístup se opírá o upravenou metodu „eXtended Finite Element“, kde lze použít jako kritérium vzniku trhliny kohezní trakční separační zákon. To představuje implementaci nějakého nelokálního konstitutivního vztahu napětí a napětí integrálního typu. Pak je věnována pozornost zejména Eringenovu modelu pro generování multiplikativního faktoru poškození, související kvazi-statické analýze, existenci slabého řešení odpovídajícího okrajového a počátečního hodnotového problému s parabolickým systémem parciální diferenciální rovnice a konvergenci algoritmu založeného na 3 typech Rotheho posloupnosti.



Obrázek 3.20: Mazarsův model, viz Příloha D5.



Obrázek 3.21: Aplikace homogenizačních postupů, viz Příloha D5.

### 3. VLASTNÍ VÝSLEDKY - KOMENTÁŘ PUBLIKOVANÝCH PRACÍ

Navržený postup tedy kombinuje možnosti několika přístupů pro modelování šíření trhliny ve vláknových kompozitech. Primární je metoda XFEM, napětí před čelem trhliny se přepočítává podle nelokálního přístupu, v celém tělese dle exponenciálního zákona porušení. Na následujících obr. 3.20 a obr. 3.21 jsou prezentovány některé výsledky z Přílohy D5.

## 4 Shrnutí dosažených výsledků

Předložená práce ukazuje možnosti metody konečných prvků pro modelování různých typů materiálů s odlišnou mikrostrukturou. Všechny úlohy mají společnou myšlenku: na základě pochopení fyzikální podstaty probíhajících procesů využít mnohdy omezené možnosti komerčních systémů. Tam, kde to jde, provést modifikaci či implementaci upraveného konstitutivního vztahu nebo se pokusit naprogramovat nový prvek do systému. Většina modelovaných úloh řešila problémy viskoelastivity, elastoplasticity či zobecnění kontaktu. Komentované práce by však nevznikly bez spoluautorů, kteří se spíše věnují experimentální oblasti výzkumu.

Problematika predikce lomového chování pomocí Weibulova napětí  $\sigma_w$  byla velmi perspektivní pro třídu ocelí využívaných pro jaderný průmysl. Bylo zjištěno, že odvození a použití těchto parametrů musí proběhnout nezbytně pro tělesa s podobným tvarem koncentrátoru napětí. Později, dle výsledků v publikovaných pracích, se ukázala spíše možnost použít  $\sigma_w$  pro přenositelnost naměřených hodnot lomové houževnatosti na malých tělesech na tělesa standardní velikosti, tedy řešit vliv velikosti a geometrie tělesa na vznik a šíření trhliny. Jediným problémem se jeví velmi plochá křivka transformačního diagramu TSM. Zajímavé a praktické pro technickou praxi je zavedení prahové hodnoty napětí  $\sigma_{th}$  ve vzorci pro výpočet  $\sigma_w$ . Tento parametr vyžaduje dobré znalosti o příčinách a mikromechanismech vzniku oblasti poškození před čelem trhliny pro daný typ materiálu.

Následující kapitola používající model GTN pro tvárné poškození ukázala velmi dobré výsledky při predikci  $J - R$  křivky. Získané výsledky také prokázaly, že některé parametry tohoto modelu jsou závislé na geometrii a velikosti tělesa. Z hlediska konvergence byl také otestován a ověřen technický postup při návrhu tvarů prvků použitých před čelem trhliny, což lze nalézt v některých komentovaných pracích. Zároveň si autor této práce vyzkoušel postupy pro návrh trakčně separačního zákona a návrh a implementaci tzv. kohezních prvků do systému na bázi metody konečných prvků. Tyto zkušenosti byly využity při práci s několika druhy vláknových kompozitů jak na bázi skelné, tak i cementové matrice.

Poškození vláknových kompozitů je ve velké míře určeno chováním trhliny na rozhraní odlišných materiálů. To bylo ukázáno již v úvodní kapitole pro úlohy v oblasti creepu a snad nejvíce v poslední kapitole věnované stavebním kompozitům. Autor se zde pokusil na základě dlouholetých zkušeností kombinovat některé známé postupy; zatím získané výsledky mohou být motivací pro následný výzkum. Ukazuje se, že řešení těchto úloh je z matematického pohledu velmi náročné a řešitelnost či konvergence výpočtových algoritmů pro komplexní chování těchto úloh nebyla mnohdy formálně verifikována. To by opětovně mohlo být námětem dalšího výzkumu v blízké budoucnosti.

## 5 Literatura

- [1] Anderson, T. L., Dodds, R. H., A framework for predicting constraint effects in shallow notched specimens, *TWI Paper 30*, (1992).
- [2] Babuška, I., Melenk, J. M., The partition of unity method, *International Journal for Numerical Methods in Engineering* 40, (1997), 727–758.
- [3] Beremin, F. M., A Local Criterion for Cleavage Fracture of a Nuclear Pressure Vessel Steels *Metalurgical Transactions* 14A, (1983), 2277–2287.
- [4] Bouhala, L., Makradi, A., Belouettar, S., Kiefer-Kamal, H., Frères, P., Modelling of failure in long fibres reinforced composites by X-FEM and cohesive zone model *Composites Part B* 55, (2013), 352–361.
- [5] Brighenti, R., Scorza, D., Numerical modelling of the fracture behaviour of brittle materials reinforced with unidirectional or randomly distributed fibres, *Mechanics of Materials* 52, (2012), 12–27.
- [6] Brocks, W., Klingbeil, D., Künecke, G., Sun, D. Z., Application of the Gurson model to Ductile tearing Resistance, *TM STP 1244*, Second Volume, (1995), 232–252.
- [7] Cooks, A. C. F., The structure of constitutive law for sintering of fine grained materials, *Acta Metallurgica et Materialia* 42/7, (1994), 2191–2210.
- [8] Dodds, R. H., Shih, C. F., Anderson, T. L., Continuum and micromechanics treatment of constraint in fracture, *Int. Journal of Fracture* 64, (1993), 101–133.
- [9] Dragone, T. L., Nix, W. D., Geometric factors affecting the internal stress distribution and high temperature rate of discontinuous fibre reinforced metal, *Acta Metallurgica et Materialia* 38/10, (1990), 1941–1953.
- [10] Eringen, A. C., Theory of Nonlocal Elasticity and Some Applications, Princeton University Press (1984), technical report 62.
- [11] Faleskog, J., Gao, X., Shih, C. F., Cell Model for Nonlinear Fracture Analysis-I. Micromechanics Calibration, *Int. Journal of Fracture* 89, (1998), 355–373.
- [12] Fries, T. P., Belytschko, T., The intrinsic XFEM: a method for arbitrary discontinuities without additional unknowns, *International Journal for Numerical Methods in Engineering* 68, (2006), 1358–1385.
- [13] Folch, L. C. A., Burdekin, F. M., Application of coupled brittle-ductile model to study correlation between Charpy energy and fracture toughness values, *Engineering Fracture Mechanics* 63, (1999), 57–80.

- [14] Gao, X., Ruggieri, C., Dodds, R. H., Calibration of Weibull stress parameters using fracture toughness data, *International Journal of Fracture* 92, (1998), 175–200.
- [15] Hillerborg, A., Modeer, M., Peterson, P. E., *Cement and Concrete Research* 6, (1976), 773–782.
- [16] Jirásek, M., Damage and smeared crack models, *Numerical Modeling of Concrete Cracking* (Hofstetter, G., Meschke, G., eds). Springer: CISM International Centre for Mechanical Sciences 532, (2011), 1–49.
- [17] Khoei, A. R., *Extended Finite Element Method: Theory and Applications*, J. Wiley and Sons, Hoboken, (2015).
- [18] Kotrechko, S. A., Meshkov, Yu., Dlouhý, I., *J. of Theoretical and Applied Fracture Mechanics* 51, (2011), 255.
- [19] Koppenhoefer, K. C., Dodds, R. H. Loading Rate Effect on Cleavage Fracture of pre-Cracked CVN Specimens: 3-D studies, *Engineering Fracture Mechanics* 58, (1997), 249–270.
- [20] Landes, J. D., Application of a J-Q Model for Fracture in the Ductile-Brittle Transition, *Fatigue and Fracture Mechanics* Vol. 27, ASTM STP 1296, (1997), 27–40.
- [21] Lemaitre, J. A., A Continuous Damage Mechanics Model for Ductile Fracture, *Journal of Eng. Materials and Technology* 107, (1985), 83.
- [22] Li, X., Chen, J., An extensive cohesive damage model for simulation arbitrary damage propagation in engineering materials, *Computer Methods in Applied Mechanics and Engineering* 315, (2017), 744–759.
- [23] Minami, F., Brückner-Foit, A., Munz, D., Trollidiner, B., Estimation procedure for the Weibull parameters used in the local approach, *Int. Journal of Fracture* 54, (1992), 197–210.
- [24] Morandotti, M., Structured deformations of continua: theory and applications, *Continuum Mechanics Focusing on Singularities (CoMFoS)*, II – 16th Conference in Fukuoka ,Springer, (2016), 125–138.
- [25] Moskovic, R., Modelling of fracture toughness data in the ductile to brittle transition temperature region by statistical analysis, *Engineering Fracture Mechanics* No. 69, (2001), 511–530.
- [26] Mudry, F., Di Fant, M., A Round-Robin on the Measurement of Local Criteria for Fracture, *BCR Report EUR 15352EN*, ECSC, (1994).
- [27] Nečas, J., Hlaváček, I., *Mathematical theory of elastic and elastoplastic bodies: An introduction*, Elsevier Amsterodam, (1991).
- [28] Niu, L., Chehimi, C., Pluvinage, G., Stress field near large blunted V-notch, *Engineering Fracture Mechanics* 49, (1994), 325–335.

- [29] Park, K., Paulino, G. H., Roesler, J. R., Cohesive fracture model for functionally graded fiber reinforced concrete, *Cement and Concrete Research* 40, (2010), 956–965.
- [30] Pike, M. G., Oskay, C., XFEM modeling of short microfiber reinforced composites with cohesive interfaces, *Finite Elements in Analysis and Design* 106, (2005), 16–31.
- [31] Rabinowitch, O., *Engineering Fracture Mechanics* 75, (2008), 2842–2859.
- [32] Roubíček, T., *Nonlinear Partial Differential Equations with Applications*, Birkhäuser, Basel (2013).
- [33] Ruggieri, C., Dodds, R. H., A transferability model for brittle fracture including constraint and ductile tearing effects: a probabilistic approach, *International Journal of Fracture* 79, (1996), 309–340.
- [34] Seok, C. S., Kim, S. Y., Effect of specimen configurations on the fracture resistance curve, *Nuclear Engineering and Design* 214, (2002), 47–56.
- [35] Sih, G. C., Ho, J. W., The role of microstructure in brittle fracture behaviour of low alloy tempered bainitic steel, *Mater. Science Engineering A*, (1997), 723–726.
- [36] Sorensen, B. F., Jacobsen, T. K., *Composites: Part A* 29 A, (1998), 1443–1451.
- [37] Tvergaard, V., Needleman, A., Analysis of the Cup-Cone Fracture in a Round Tensile Bar, *Acta Metalurgica* 32, (1984), 157–169.
- [38] Vala, J., Structure identification of metal fibre reinforced cementitious composites, *Algoritmy*, 20th Conference on Scientific Computing in Podbanské, (2016), 244–253.
- [39] Vašek, A., Vogelesang, L. B., Mechanism and mechanics of damage and failure, *ICF11*, Poitiers, (1996), 1685–1690.
- [40] Vlček, L., Numerická analýza tětes s trhlinou, *doktorská práce*, (2004), VUT Brno.
- [41] Wiesner, C. S., The Local Approach to Cleavage Fracture, *Concepts and applications*, TWI, (1996).
- [42] Zhang, Z. L., A complete Gurson model, *Nonlinear Fracture and Damage Mechanics*, ed. M. H. Aliabadi, (2001), 223–248.
- [43] Zhang, H. H., Rong, G., Li, L. X., Numerical study on deformation in a cracked viscoelastic body with the XFEM, *Eng. Analysis with Boundary Elements* 34, (2010), 619–624.
- [44] Zhu, X. K., Jang, S. K., J-R curves corrected by load-independent constraint parameter in ductile crack growth, *Eng. Fracture Mechanics* 68, (2001), 285–301.

## 6 Publikace autora 1990-2021

### 1990-1995

1. Kozák, V., The influence of an a priori crack for the development of the intergranular creep fracture process in steel 18Cr10Ni, *Metallic Materials* 2, 28, (1990), 140-151, IF 0,568.
2. Kozák, V., Malý, J., Elastoplastická napěťová a def. Analýza vzorku s V vrubem při zkoušce tříbodovým ohybem, *Inženýrská mechanika* 3, (1993), 46-52.
3. Riedel, H., Kozák, V., Svoboda, J., Densification and creep in the final stage of sintering, *Acta Metallurgica et Materialia* 42, (1994), 3093-3103, IF 1,297.
4. Malý, J., Kozák, V., Determination of the critical stress Cr-Mo-V steel using FEM, *Metallic Materials* 32, (1994), No. 2, 159-169, IF 0,568.
5. Vala, J., Svoboda, J., Kozák, V., Modelling discontinuous metal-matrix composite behaviour under creep conditions, *Scripta Metallurgica et Materialia* 30, Issue 9, (1994), 1201-1206, IF 0,600.
6. Malý, J., Kozák, V., Elastoplastic stress-strain analysis for V-notch specimen of the Cr-Mo-Mo rotor steel, *Euromat 94*, Budapest, (1994), 912-916.
7. Vala, J., Kozák, V., Numerical modelling of creep flow in discontinuoud metal matrix composites, *Numerical Modelling in continuum mechanics II*, Praha, (1994), 290-298.
8. Kozák, V., Malý, J., Evaluation of critical fracture stress using FEM, *Numerical Methods in Continuum Mechanics*, Stará Lesná, Slovakia, (1994), 330-336.
9. Dlouhý, I., Kozák, V., Peculiarities in fracture behaviour of duplex steel, *Euromat'95*, Italy, 605-608.

### 1996-2000

1. Dlouhý, I., Kozák, V., Válka, L., The susceptibility of local parameters to steel microstructure, *Journal de Physique IV* 6, Issue C6, (1996), 205-214, IF 0,368.
2. Dlouhý, I., Procházková, A., Kozák, V., Characteristics of fracture behaviour of duplex steels in transition region, *Proc. European Conference of Fracture ECF 11*, Poitiers, (1996).
3. Dlouhý, I., Kozák, V., Válka, L., Holzmann, M., The susceptibility of local parameter on steel microstructure evaluated using Charpy type specimen, *Proc. MECAMAT'96*, Fontainebleau, Brittle Fracture Oral Section, (1996), 22-32.
4. Holzmann, M., Kozák, V., Dlouhý, I., Použití lokálního přístupu při posuzování mezního stavu křehkého porušení komponent s vruby a defekty, *Int. Conference Engineering Mechanics'96*, Svatka, (1996), 51-56.
5. Kozák, V., Dlouhý, I., Hozmann, M., Aplikace lokálního přístupu při posuzování mezního stavu křehkého porušení na duplexní oceli, *Int. Conference Engineering Mechanics' 97*, Vol. I, Svatka, (1997), 29-34.
6. Kozák, V., Dlouhý, I., Local approach and FEM in brittle fracture prediction, *Proc. Numerical Methods in Continuum Mechanics*, Slovakia, Stará Lesná, (1997), 256-260.

7. Orlová, A., Kuchařová, K., Kozák, V., Shear creep testing of copper crystals, *Microstructure and processing* 233, Issue 1-2, (1997), 50-55, IF 0,896.
8. Kozák, V., Dlouhý, I., Holzmann, M., Crack effects on the fracture behaviour in the duplex steels, *Structural Mechanics in Reactor Technology SMIRT 14* 4, Lyon, (1997), 681-688.
9. Vašek, A., Polák, J., Kozák, V., Fatigue crack initiation in fibre-metal laminate GLARE2, *Microstructure and Processing* 234, (1997), 621-624, IF 0,896.
10. Kozák, V., Dlouhý, I., Application of a local approach to the evaluation of the critical state, *Fractography 97*, Slovakia, (1997), 175-180.
11. Kozák, V., Holzmann, M., Novák, A., Prediction of fracture toughness using scaling methodology and the local approach, *VII Int. Conference Numerical Methods in Continuum Mechanics*, Stará Lesná, Slovakia, (1998), 253-258.
12. Holzmann, M., Kozák, V., Dlouhý, I., Master curve methodology and fracture behaviour of the cast steel, *European Conference on Fracture ECF 12*, Sheffield, (1998), 823-828.
13. Dlouhý, I., Kozák, V., Holzmann, M., Micromechanical aspects of brittle failure initiation, *Experimental Mechanics '98*, 11th Int. Conference, Oxford, UK, (1998), 1191-1196.
14. Kozák, V., Dlouhý, I., Local approach and FEM in brittle fracture prediction, *Computer Assisted Mechanics and Eng. Science* 5, (1998), 193-198.
15. Novák A., Kozák V., Application of local approach to the prediction of fracture behaviour of steel, *Engineering Mechanics* 5, No. 3, (1998), 203-206.
16. Holzmann, M., Dlouhý, I., Kozák, V., Možnosti aplikace koncepce Master křivky pro hodnocení lomové houževnatosti C-Mn oceli na odlitky, *Konstrukční materiály "99*, Bratislava, (1999), 73-82.
17. Novák A., Kozák V., Application of local approach to the prediction of fracture behaviour of manganese cast steel, *Junior Euromat '98*, Lausanne, Switzerland, September (1998), 100.
18. Pluvinage, G., Azari, Z., Kozák, V., Effect of ferritic microstructure on local damage zone, *Theoretical and Applied Fracture Mechanics* 31, (1999), No. 2, 149-156, IF 1,391.
19. Novák, A., Kozák, V., Dlouhý, I., Stochastické modely křehkého porušení, *Inženýrská mechanika '99*, Svatka, ČR, 403-409.
20. Dlouhý, I., Kozák, V., Holzmann, M., Fracture resistance of cast steel for spent nuclear fuel, *Conference Case Histories on Integrity*, Milan, (1999), 267-276.
21. Kozák, V., Holzmann, M., Dlouhý, I., Fracture toughness transferability: From the standard 1T specimens to the pre-cracked Charpy specimen, *CMEM IX*, Sorrento 99, Italy, (1999), 87-96.
22. Kozák, V., Holzmann, M., Dlouhý, I., The fracture behaviour of the cast steel and its prediction using the local approach, *5th Int. Conference on Structural Mechanics in Reactor Technology SMiRT 15* Vol. V, Seoul, (1999), 71-78.
23. Holzmann, M., Dlouhý, I., Kozák, V., Possibilities of master curve application for fracture toughness assessment of CMn cast steel, *Zváranie - Svařování* 48, (1999), 221-225.
24. Kozák V., Novák A., Dlouhý I., The Transferability of Fracture Toughness Characteristics, *Numerical Methods in Continuum Mechanics 2000*, (VIII. Inter. Confer.), (2000), Liptovský Ján, SR, (sk. 64-1, 64-10), publikace na CD.

25. Kozák V., Dlouhý I., Novák A., Scaling effect evaluation in brittle fracture (Book of Abstracts II – General Session, pp. 411), *4th Euromech – Solid Mechanics Conference*, Metz, (2000) (sb. na CD).

26. Dlouhý, I., Holzmann, M., Kozák, V., Možnosti použití malých zkušebních těles při hodnocení lomového chování CMn oceli na odlitky, *Zváranie - Svařování* 49, (2000), 256-260.

27. Dlouhý, I., Kozák, V., Fracture resistance of cast ferritic steel for container of spent nuclear fuel, *Ninth International Conference Pressure Vessel Technology*, Sydney, (2000), 461-468.

28. Dlouhý, I., Kozák, V., Holzmann, M., Micromechanical aspects of constraint effect in steel for containers of spent nuclear fuel, *EUROMAT 2000 2*, (2000), Tours, Francie, 1409-1414.

29. Kozák V., Novák A., Local parameters susceptibility checkup using fracture toughness data, *European Conference on Fracture ECF 13*, (2000), San Sebastian, Španělsko, 183-188.

## 2001-2005

1. Vlček, L., Kozák, V., Numerické a experimentální určení lomových charakteristik u těles s trhlinou pro tříbodový ohyb, *Výpočtová mechanika*, (2001), Nečtiny, 417-424.

2. Dlouhý, I., Holzmann, M., Kozák, V., Současné koncepce hodnocení křehkolomových vlastností charakteristik ocelí, *konference Predikce mechanických vlastností materiálů na základě strukturních charakteristik*, Nové Město, (2001), 247-259.

3. Lisek, L., Kozák, V., *Engineering Mechanics*, Svratka, (2001), 1-8.

4. Dlouhý, I., Chlup, Z., Kozák, V., Holzmann, M., Fracture toughness transferability - from small to full scale specimens, *Charpy Centenary Conference*, Poitiers, Francie, (2001), 817- 824.

5. Dlouhý, I., Chlup, Z., Kozák, V., Constraint effects at brittle fracture initiation in cast ferritic steel, *Conference Fracture and Damage Mechanics FDM*, Milan, Italy, (2001), 245-250.

6. Kozák, V., Dlouhý, I., The transferability of fracture toughness characteristics from point a view of the integrity of components with defects, *Computational Methods and Experimental Measurements (CMEM 2001)*, Alicante, Španělsko, (2001), 757-766, invited lecture.

7. Kozák, V., Novák, A., Probabilistic local approach based on the notched tensile specimen data, *Notch effects in Fatigue and Fracture*, NATO Science Series, Series II: Mathematics, Physics and Chemistry, Vol 11, Kluwer Academic publishers Dordrecht-Boston-London, The Netherlands, edited by G. Pluvinage and M. Gjonaj, (2001), 147-159, invited lecture.

8. Kozák, V., Holzmann, M., Dlouhý, I., The Transferability of brittle fracture toughness characteristics, *Structural Mechanics in Reactor Technology SMIRT 16*, (2001), Washington, DC, Proc. on CD, paper 1079.

9. Dlouhý, I., Kozák, V., Toughness scalling model applications, *Transferability of fracture mechanical characteristics*, Nato-Science Series II-Mathematics Physics and Chemistry, 78, (2002), 195-212.

10. Kozák, V., Vlček, L., Constraint phenomena on the pre-cracked specimen: numerical and experimental evaluation, *ECF 14*, Cracow, (2002), 251-259.

11. Kozák, V., Janík, A., The use of the local approach for the brittle fracture prediction, *Transferability of fracture mechanical characteristics*, Nato-Science Series II-Mathematics Physics and Chemistry, 78, (2002), 105-122.
12. Vlček, L., Chlup, Z., and Kozák, V., Problems in Q-parameter calculation, NATO Science Series: Mathematics, Physics and Chemistry 78, *Transferability of Fracture Mechanical Characteristics*, ed. Dlouhý, (2002), 79-92.
13. Kozák, V., Dlouhý, I., Holzmann, M., The fracture behaviour of cast steel and its prediction based on the local approach, *Nuclear Engineering and Design*, (2002), Elsevier Science, 67-73, IF 0.546.
14. Dlouhý, I., Kozák, V., Chlup, Z., Fracture toughness transferability - from small to full scale specimens, *New Trends in Fatigue and Fracture*, Francie, Metz, (2002).
15. Kozák, V., Vlček, L., Constraint phenomena in pre-cracked specimens and Weibull stress model for cleavage fracture, *Key Engineering Materials* 251-252, (2003), 409-414, IF 0,250.
16. Kozák V., Vlček L., The Weibull stress parameters calibration upon the toughness scaling model between cracks having different constraint, *International Conference on Structural Mechanics in Reactor Technology SMIRT 17*, (2003). Paper G03-2.
17. Kozák, V., Vlček, L., Influence of constraint effect on transferability of fracture mechanics characteristics, *Engineering Mechanics (2003)*, Praha: Institute of Theoretical and Applied Mechanics, čl. 321.
18. Kozák V., Vlček L., Parameters identification for GTN model and their verification on the CrMo4 steel, *Materials Structure and Micromechanics of Fracture*, (2004), 48.
19. Dlouhý, I., Chlup, Z., Kozák, V., Constraint effects at brittle fracture initiation in a cast ferritic steel, *Engineering Fracture Mechanics* 71, Issue 4-6, (2004), 873-883, IF 1,615.
20. Holzmann, M., Kozák, V., Lomová houževnatost lité nízkolegované CrNiMo oceli s bainitickou strukturou, *Kovové materiály*, Roč. 42, č. 6 (2004), 384-398, IF 0,765.
21. Dlouhý, I., Chlup, Z., Kozák, V., Fracture toughness transferability - from small to full scale specimens, [Přenositelnost lomové houževnatosti z malých těles na tělesa standardních rozměrů.], *Fracture Damage of Structural Parts*, Ostrava: VŠB TU Ostrava, (2004), 53-60.
22. Kozák, V., On the challenging FEM application field in the fracture mechanics, *4. Matem. Workshop FAST VUT Brno*, (2005), 10 stran on CD.
23. Kozák, V., Vlček, L., The Weibull stress parameters calibration upon the toughness scaling model between cracks having different constraint, *Nuclear Engineering and Design* 235, (2005), 1889-1896, IF 0,889.
24. Kozák, V., Vlček, L., Parameters identification for GTN model and their verification, *Materials Science Forum* 482, (2005), 335-338.
25. Vlček, L., Kozák, V., The influence of the triaxiality in the stable crack growth modelling using GTN model, *Proceedings International Conference of Fracture ICF 11*, Torino Italy, (2005), on CD ID 5650.

#### 2006-2010

1. Kolář, P., Kozák, V., Mikulec, L., Aplikace kohezního modelu pro tvárné porušení, *Problémy lomové mechaniky VI.*, Brno, (2006), 33-42.

2. Kozák, V., Použití kohezních prvků pro modelování šíření trhliny, *Výpočty konstrukcí metodou konečných prvků*, Brno, (2006), 80-91.
3. Kozák, V., The outlook of the cohesive zone approach, *5th Mathematical workshop*, on CD ROM + Book of abstracts 75, Brno, (2006).
4. Kozák V., Dlouhý I., J-R curve prediction using cohesive model and its sensitivity to a material curve, *Structural Mechanics in Reactor Technology SMIRT 19*, Toronto (2007), paper G06/4, 8 pages on CD.
5. Kozák, V., Dlouhý, I., Chlup., Z., Cohesive zone model and GTN model collation for ductile crack growth, *Int. Conference Material Structure and Micromechanics of Fracture MSMF 5*, (2007), Brno, 4 pages.
6. Kozák, V., Ductile crack growth modeling using cohesive zone approach, *Int. Conference Computational Modeling and Experiment of Composites Material with Micro and Nano Structures*, May 28/31, (2007), Liptovský Mikuláš, Slovak Republic, 7 pages on CD.
7. Kozák, V., Dlouhý, I., Chlup, Z., Cohesive zone model and GTN model collation for ductile crack growth, *Materials Science Forum* 567-568, (2008), 145-148.
8. Kozák, V., Cohesive zone modelling, Numerical Analysis and Applied Mathematics, *International Conference ICNAAM 2008*, Edited by T. E. Simos, G. Psihoyios and Ch. Tsitouras, (2008) Americal Institute of Physics, CP1048, 328-331.
9. Kozák V., Ductile crack growth modelling using cohesive zone approach, *Computational Modelling and Experiments*, Computational Methods in Applied Science 9, Springer, (2008), 191-208.
10. Pokluda, J., Kondo, Y., Kozák, V., et al., Microstructural interpretation of effective fatigue: Threshold of structural steels, *17 European Conference on Fracture (ECF17)*, CE 170019, (2008).
11. Chlup, Z., Harrer, W., Kozák, V., Conecrack development during ball on the three ball test, *17 European Conference on Fracture (ECF17)*, CE 170001 (2008).
12. Kozák, V., Dlouhý, I., A crack growth modelling in materials with heterogeneous microstructure, *17 European Conference on Fracture ECF17*, CE 170388, (2008).
13. Vala, J., Šťastník, S., Kozák, V., Computational thermomechanical modelling of early age silicate composites, AIP conference proceedings, Crete, Vol. 1168, *ICNAAM (2009)*, 232-235.
14. Dlouhý, I., Chlup, Z., Kozák, V., et al., Fracture behaviour of TiAl intermetallics, *Damage and Fracture mechanics*, Springer, Ed. T. Boukharouba, M. Elboujdaini, G. Pluvinage, (2009), 265-274.
15. Vala, J., Šťastník, S., Kozák, V., Numerical prediction of strains and stresses in early- age massive concrete structures, *Forum Statisticum Slovacum*, (2009), č. 3, 101-112.
16. Chlup, Z., Dlouhý, I., Kozák, V., Interfacial characterisation in transparent spinel matrix reinforced by SiC fibre, *Key Engineering Materials* 409, (2009), 252-259.
17. Kozák, V., Cohesive zone models in materials with various microstructures, *ICF12 12th International Conference on Fracture*, (2009), Ottawa, Canada, T26.004.
18. Kozák, V., Chlup, Z., Long fibre composite modelling using cohesive user's elements, AIP Conference proceedings 1281, *ICNAAM (2010)*, ed. T. Simos, paper 621.
19. Chlup, Z., et al., Properties of modified polysiloxane based ceramic matrix for long fibre reinforced composite materials, *Plastics Rubber and Composites* 40, Issue 6-7, (2010), 380-385. IF 1,543.

**2011-2015**

1. Strachota, A., et al., Preparation of Silicon Oxycarbide Composites, *Acta Physica Polonia A* 120, Issue 2, (2011), 326-330, IF 0,875.
2. Vala, J., Šťastník, S., Kozák, V., Micro and macro-scale thermomechanical modelling of bulk deformation in early age cement based materials, *Key Engineering Materials* 465, (2011), 111-114.
3. Kozák, V., Chlup, Z., Modelling of fibre matrix interface of brittle matrix long fibre composites by application of cohesive zone method, *Key Engineering Materials* 465, (2011), 231-234.
4. Kozák, V., Chlup, Z., Long fibre composite modelling using cohesive approach, *Computational Modelling of Fracture and Failure of Materials and Structures*, Barcelona, Conference Proceedings, 50-54.
5. Kotrechko, S., Mamedov, S., Dlouhý, I., Kozák, V., Use of local approach for prediction of the irradiation effect on fracture toughness of pressure vessel steel, *Key Engineering Materials* 465, (2011), 568-573.
6. Chlupová, A., Kozák, V., Fatigue crack growth and delamination in fiber metal laminate (GLARE), *18th International Conference Engineering Mechanics*, (2012), Svratka, 79-536.
7. Kozák, V., Chlup, Z., Bridging law shape for long fibre composites and its finite element construction, *Algoritmy 2012*, Slovakia, 1-10.
8. Strachota, A., Černý, M., Chlup, Z., Kozák, V., Optimization of sol-gel/pyrolysis routes to silicon oxycarbide glasses, *Journal of Non-Crystalline Solids* 358, (2012), 2771-2782, IF 2,600.
9. Kozák, V., Chlup, Z., Crack Growth Modelling in the Silicon Nitride Ceramics by Application of the Cohesive Zone Approach, *Key Engineering Materials* 592-593, (2014), 193-196, IF 0,300.
10. Kozák, V., Chlup, Z., Microindentation test modelling in the silicon nitride ceramics by application of the cohesive zone approach, *Conference Fracture and Damage Mechanics FDM 14*, (2014), Ponta Delgado Azores, Portugal, Conference Proceedings, 149.
11. Vala, J., Hobst, L., Kozák, V., Non-destructive detection of metal fibres in cementitious composites, *Advances in Engineering Mechanics and Materials*, (2014), 125-128.
12. Kozák, V., Chlup, Z., Microindentation test modelling in the silicon nitride ceramics by application of the cohesive zone approach, *Key Engineering Materials* 627 (2015), 329-332, IF 0,260.
13. Vala, J., Hobst, L., Kozák, V., Detection of metal fibre composites based on signal and image processing approaches, *WSAS Transaction on Applied and Theoretical Mechanics* 10, (2015), 39-46.
14. Vala, J., Kozák, V., Modelling of cohesive crack growth of the brittle and quasi-brittle fracture of structural materials, *Advances in Mathematical and Computational Methods*, (2015), 49, No. 1, 44-51.

**2016-2021**

1. Vala, J., Jarošová, P., Kozák, V., On the computational analysis of damage of quasi-brittle materials using integral-type nonlocal models, *International Journal of Applied Physics*, (2019), roč. 4, č. 1, 8-13, IF 0,810.

2. Vala, J., Kozák, V., Computational analysis of quasi-brittle fracture in fibre reinforced cementitious composites, *Theoretical and Applied Fracture Mechanics* 107, (2020), No. 1, 5501-5510, IF 3,021.
3. Kozák, V., Chlup, Z., Padělek, P., Dlouhý, I., Prediction of traction separation law of ceramics, using iterative finite element method, *Solid State Phenomena* 258, (2017), 186-189.
4. Kotrechko, S., Gryshchenko, V., Kozák, V., Dlouhý, I., Method of threshold stress determination for local approach to cleavage factor, *Solid State Phenomena* 258, (2017), 281-285.
5. Kotrechko, S., Zatsarna, O., Kozák, V., Dlouhý, I., Threshold fracture stress: theory and application, *Procedia Structural Integrity* 23, (2019), 413-418.
6. Vala, J., Kozák, V., Computational analysis of quasi-brittle fracture in fibre reinforced cementitious composites, *Procedia Structural Integrity* 23, (2019), 328-333.
7. Vala, J., Kozák, V., K možnostem výpočtové predikce kvazikřehkého porušení cementových kompozitů rozšířenou metodou konečných prvků, *Maltoviny 2019*, Brno, FAST VUT, (2019), 5-13.
8. Vala, J., Kozák, V., Jarošová, P., On a computational approach to micro- and macro-modelling of damage in brittle and quasi-brittle materials, *International Journal of Mechanics*, (2020), roč. 14, č. 1, 185-197.
9. Vala, J., Kozák, V., Výpočtové modelování šíření trhlin v kvazikřehkých kompozitních materiálech, Prague: Institute of Mathematics, CAS, (2020), 20-28.
10. Vala, J., Kozák, V., Jedlička, M., Scale bridging in computational modelling of quasi-brittle fracture of cementitious composites, In ICBM 2020, *Solid State Phenomena*, (2021), in print, 6s.
11. Vala, J., Kozák, V., Jarošová, P., On the nonlocal computational modelling of damage in brittle and quasi-brittle materials, *Proceedings of CSCC 2020*, Sofia: IEEE Conference Publishing Services (CPS), (2021), 174-183.
12. Vala, J., Kozák, V., Nonlocal damage modelling of quasi-brittle composites, accepted for publication *Applications of Mathematics*, January (2021), in print, IF 0,544.

## 7 Vybrané články komentované v práci

A1 Riedel, H., Kozák, V., Svoboda, J., Densification and creep in the final stage of sintering, *Acta Metallurgica et Materialia* 42, (1994), 3093-3103, IF 1,297.

A2 Vala, J., Svoboda, J., Kozák, Čadek., J., Modelling discontinuous metal-matrix composite behaviour under creep conditions, *Scripta Metallurgica et Materialia* 30, Issue 9, (1994), 1201-1206, IF 0,600.

A3 Vašek, A., Polák, J., Kozák, V., Fatigue crack initiation in fibre-metal laminate GLARE2, *Microstructure and Processing* 234, (1997), 621-624, IF 0,896.

A4 Pluvinage, G., Azari, Z., Kozák, V., Effect of ferritic microstructure on local damage zone, *Theoretical and Applied Fracture Mechanics* 31, (1999), No. 2, 149-156, IF 1,391.

A5 Vlček, L., Chlup, Z., and Kozák, V., Problems in Q-parameter calculation, NATO Science Series: Mathematics, Physics and Chemistry 78, *book Transferability of Fracture Mechanical Characteristics*, ed. Dlouhý, (2002), 79-92.

A6 Kozák, V., Vlček, L., Influence of constraint effect on transferability of fracture mechanics characteristics, *Engineering Mechanics*, (2003), Praha: Institute of Theoretical and Applied Mechanic, čl. 321.

A7 Chlupová, A., Kozák, V., Fatigue crack growth and delamination in fiber metal laminate (GLARE), *18th International Conference Engineering Mechanics*, (2012), Svratka, 531-536.

B1 Kozák V., Novák A., Dlouhý I., The Transferability of Fracture Toughness Characteristics, *Numerical Methods in Continuum Mechanics 2000*, (VIII. Inter. Confer.), (2000), Liptovský Ján, SR, (sk. 64-1, 64-10), publikace na CD.

B2 Kozák, V., Dlouhý, I., The transferability of fracture toughness characteristics from point a view of the integrity of components with defects, *Computational Methods and Experimental Measurements (CMEM 2001)*, Alicante, Španělsko, (2001), 757-766, invited lecture.

B3 Kozák, V., Vlček, L., Constraint phenomena on the pre-cracked specimen: numerical and experimental evaluation, *ECF 14*, Cracow, (2002), 251-259.

B4 Kozák, V., Dlouhý, I., Holzmann, M., The fracture behaviour of cast steel and its prediction based on the local approach, *Nuclear Engineering and Design*, (2002), Elsevier Science, 67-73, IF 0.546.

B5 Kozák, V., Vlček, L., The Weibull stress parameters calibration upon the toughness scaling model between cracks having different constraint, *Nuclear Engineering and Design* 235, (2005), 1889-1896, IF 0,889.

B6 Kotrechko, S., Gryshchenko, V., Kozák, V., Dlouhý, I., Method of threshold stress determination for local approach to cleavage factor, *Solid State Phenomena* 258, (2017), 281-285.

B7 Kotrechko, S., Zatsarna, O., Kozák, V., Dlouhý, I., Threshold fracture stress: theory and application, *Procedia Structural Integrity* 23, (2019), 413-418.

C1 Kozák, V., Vlček, L., Parameters identification for GTN model and their verification, *Materials Science Forum* 482, (2005), 335-338.

C2 Kozák V., Ductile crack growth modelling using cohesive zone approach, *Computational Modelling and Experiments*, In: Computational Methods in Applied Science 9, Springer, (2008), 191-208, kapitola v knize.

C3 Kozák, V., Dlouhý, I., Chlup, Z., Cohesive zone model and GTN model collation for ductile crack growth, *Int. Conference Material Structure and Micromechanics of Fracture MSMF 5*, (2007), Brno, 4 pages.

C4 Kozák, V., Chlup, Z., Modelling of fibre matrix interface of brittle matrix long fibre composites by application of cohesive zone method, *Key Engineering Materials* 465, (2011), 231-234.

C5 Strachota, A., et al., Preparation of Silicon Oxycarbide Composites, *Acta Physica Polonia A* 120, Issue 2, (2011), 326-330, IF 0,875.

C6 Kozák, V., Chlup, Z., Bridging law shape for long fibre composites and its finite element construction, *Algoritmy 2012*, Slovakia, 1-10.

C7 Kozák, V., Chlup, Z., Padělek, P., Dlouhý, I., Prediction of traction separation law of ceramics using iterative finite element method, *Solid State Phenomena* 258, (2017), 186-189.

D1 Vala, J., Hobst, L., Kozák, V., Non- destructive detection of metal fibres in cementitious composites, *Advances in Engineering Mechanics and Materials*, Athens: EUROPEMENT, (2014), 125-128.

D2 Vala, J., Hobst, L., Kozák, V., Detection of metal fibre composites based on signal and image processing approaches, *WSAS Transaction on Applied and Theoretical Mechanics 10*, (2015), 39-46.

D3 Vala, J., Kozák, V., Computational analysis of quasi-brittle fracture in fibre reinforced cementitious composites, In 9th International Conference Materials Structure and Micromechanics of Fracture (MSMF9), *Procedia Structural Integrity*, (2019), 328-333.

D4 Vala, J., Kozák, V., Computational analysis of quasi-brittle fracture in fibre reinforced cementitious composites, *Theoretical and Applied Fracture Mechanics* 107, (2020), No. 1, 5501-5510, IF 3,021.

D5 Vala, J., Kozák, V., Nonlocal damage modelling of quasi-brittle composites, *Applications of Mathematics*, January (2021), to appear, IF 0,544.

A1 Riedel, H., Kozák, V., Svoboda, J., Densification and creep in the final stage of sintering, *Acta Metallurgica et Materialia* 42, (1994), 3093-3103, IF 1,297.



## DENSIFICATION AND CREEP IN THE FINAL STAGE OF SINTERING

H. RIEDEL<sup>1</sup>, V. KOZÁK<sup>2</sup> and J. SVOBODA<sup>2</sup>

<sup>1</sup>Fraunhofer-Institut für Werkstoffmechanik, Wöhlerstraße 11, D-79108 Freiburg, Germany and

<sup>2</sup>Institute of Physical Metallurgy, Academy of Sciences of the Czech Republic, Žitkova 22, 61662 Brno, Czech Republic

(Received 9 August 1993; in revised form 19 January 1994)

**Abstract**—Densification and creep by grain boundary diffusion is modelled for the late stage of sintering. The grain structure is described as a regular array of tetrakaidekahedra with pores at each grain boundary between next-nearest neighbors. The diffusion problem on the surface of the tetrakaidekahedron is solved numerically using the heat-conduction option of the finite element code ANSYS. From the calculated normal stresses on the boundary facets one assembles the macroscopic constitutive behavior. Since the assumed grain shape is the Wigner–Seitz cell of the body-centered cubic lattice, the resulting viscosity tensor has cubic symmetry. Isotropic bulk and shear viscosities are obtained by applying the procedures developed for the elasticity theory of polycrystals. The resulting bulk viscosity is well approximated by a closed-form solution developed previously. Due to the pronounced cubic anisotropy of the model, the isotropic shear viscosity cannot be determined unambiguously. The model includes the effect of viscous grain boundary sliding. The influence of surface diffusion on the sintering rate is also explored.

### 1. INTRODUCTION

The uniaxial pressing of ceramic or metallic powders generally leads to powder compacts with inhomogeneous density distributions. Such inhomogeneities result in shape distortions during sintering. There have been attempts to predict the shape of the sintered part by finite element simulation of the pressing and sintering processes with the goal of adjusting the shape of the pressing tools and the pressing schedule such that the final part assumes the required shape (e.g. [1–6]). The shape evolution during sintering may depend sensitively on the constitutive behavior under multiaxial stresses. Especially, if the sintering material can be described as linear viscous, the ratio of the shear to the bulk viscosity,  $G/K$ , is an important factor. Classical sintering theories (e.g. [7–9]) are usually not concerned with the question of shear loading of material elements and hence do not provide estimates of the shear viscosity  $G$ . Only recently the problem was addressed in connection with the desire to analyze stresses and distortions during inhomogeneous sintering, either for simple geometries [10–13] or for complex parts [1–6].

In this paper, a model for closed porosity is presented with grain boundary diffusion being the assumed transport mechanism. This is justified for fine-grained materials at not too high temperatures, and in the absence of liquid phases. Grain boundary sliding is described by a linear relation between shear stress and sliding speed. Surface diffusion on the pore surfaces is assumed to be fast enough that the pores

develop near-equilibrium shapes after pore closure. However, the free energy dissipated by surface diffusion is taken into account in the thermodynamic balance equation. The resulting retardation of sintering is treated in Section 6.

Since grain boundary diffusion is governed by a linear relation between displacement rate and stress, the macroscopic constitutive equation will be a linear viscous law. In the isotropic case the general form is

$$\dot{\epsilon}_{ij} = \frac{\sigma'_{ij}}{2G} + \delta_{ij} \frac{\sigma_m - \sigma_s}{3K}. \quad (1)$$

Here,  $\dot{\epsilon}_{ij}$  and  $\sigma_{ij}$  are the strain rate and stress tensors, the prime denotes the deviator,  $\sigma_m$  is the mean (or hydrostatic) stress,  $\sigma_s$  is the sintering stress,  $\delta_{ij}$  is the Kronecker symbol, and  $G$  and  $K$  are the shear and bulk viscosities, respectively. The aim of a micromechanical model is to specify  $G$ ,  $K$ ,  $\sigma_s$ , which depend on the relative density  $\rho$ , on the dihedral angle  $\psi$  and on the arrangement of the grains. The dihedral angle is defined by  $\cos \psi = \gamma_b / (2\gamma_s)$ , where  $\gamma_s$  and  $\gamma_b$  are the surface and grain boundary energies per unit area, respectively.

Micromechanical models were developed for open porosity by various working groups assuming either viscous flow of the grains [14, 15] or grain boundary diffusion [16–18] as the governing transport mechanism. The  $G/K$  ratio is obtained by these models as 0.6, if the particle contacts are randomly oriented and if they have no spatial correlation. If there is a short-range order in the particle arrangement, for example a body-centered cubic particle packing over small

distances, the  $G/K$  ratio is found to be smaller, and a value of 0.27 was advocated in [18]. Experimental values tend to be larger and often exceed the value 0.6, which is considered to be an upper bound in the models. This is an unresolved problem.

For closed porosity, a three-dimensional model for sintering and diffusion creep was developed by Pan and Cocks [19] using a bounding theorem. Similarities and differences between their model and the present model will be pointed out in the following sections. One of the main differences is that Pan and Cocks ignore the cubic anisotropy of the model and derive the shear response for a special orientation only. In this paper, the full anisotropic response is derived and averaging methods are applied to find isotropic averages for the shear viscosity.

## 2. DESCRIPTION OF THE MODEL

### 2.1. Geometry

The pore configuration analyzed in this paper is shown in Fig. 1(a) in comparison with the one studied by Pan and Cocks [19] [Fig. 1(b)]. Both approaches use a periodic, body-centered cubic (b.c.c.) array of tetrakaidekahedral grains, but Pan and Cocks place the pores on the 24 grain corners, while we consider pores on the six square facets of the grains. Their choice corresponds to the classical picture [7], while ours is motivated by the investigation of equilibrium shapes of the open pore space and the evolution of the pores at the transition to closed porosity [17].

### 2.2. Grain boundary diffusion

Grain boundary diffusion is described by the equations

$$j_i = \frac{\Omega \delta D_b}{kT} \nabla_i \sigma_n \quad (2)$$

$$\nabla_i j_i = -\dot{u}_n \quad (3)$$

$$\nabla^2 \sigma_n = -\frac{kT}{\Omega \delta D_b} \dot{u}_n \quad (4)$$

where the first gives the vector of the flux density,  $j_i$ , as a function of the gradient of the chemical potential,  $\Omega \sigma_n$ , the second is the continuity equation and the third follows by combining the previous two. The symbols are:  $\dot{u}_n$  is the relative displacement rate of touching grains normal to the contact area,  $\nabla_i$  is the

gradient operator,  $\sigma_n$  is the normal component of the stress acting on the grain boundary,  $\Omega$  is the atomic volume,  $\delta D_b$  is the grain boundary diffusion coefficient,  $k$  is the Boltzmann constant and  $T$  is the absolute temperature. The summation convention is applied for repeated vector and tensor indices  $i, j$  in equation (3) and in the rest of the paper.

### 2.3. Grain boundary sliding

Grain boundary sliding at a rate  $\dot{u}_t$  is assumed to result in a tangential force

$$F_t = \eta A \dot{u}_t \quad (5)$$

where  $A$  is the area of the grain facet (excluding the area occupied by pores) and  $\eta$  is a viscosity coefficient for sliding. In Section 4, the effect of viscous grain boundary sliding is neglected, but it will be included in Section 5.

## 3. THE SINTERING STRESS

The sintering stress,  $\sigma_s$ , can be calculated in advance without solving the diffusion problem. A preliminary expression for the sintering stress was derived in [17] for the present configuration. However, since [17] was concerned primarily with open porosity, an inaccuracy in the derivation of the sintering stress for closed pores on two-grain junctions remained undetected.

A porous polycrystalline solid is in equilibrium, if the applied mean stress, which is then called the sintering stress, balances the internal surface and interface tension forces

$$\sigma_s dV = \gamma_b dA_b + \gamma_s dA_s \quad (6)$$

where  $dV$  is a virtual change of the volume of the unit cell, and  $dA_b$  and  $dA_s$  are the associated changes of the grain boundary area and surface area, respectively.

For one unit cell  $A_b = 4A_6 + 3A_4$  and  $A_s = 3A_p$ , where  $A_6$ ,  $A_4$  and  $A_p$  are the areas of one hexagonal and one square facet and of the surface of one pore, respectively. After division of equation (6) by  $dt$  one obtains time derivatives, which are given by the geometrical relations

$$\begin{aligned} \dot{A}_6 &= 3\sqrt{3}a^2\dot{\epsilon}_m \\ \dot{A}_4 &= 2a^2\dot{\epsilon}_m - 2\pi \sin^2 \psi r \dot{r} \\ \dot{A}_s &= 24\pi(1 - \cos \psi)r \dot{r} \\ \dot{V} &= 3V\dot{\epsilon}_m. \end{aligned} \quad (7)$$

Here  $\dot{\epsilon}_m$  is the mean strain rate,  $a$  is the edge length of the tetrakaidekahedron, which is related to its volume by  $V = 8\sqrt{2}a^3$ , and  $r$  is the radius of curvature of the pore surface, which is related to the volume of one pore,  $V_p$ , by

$$V_p = F_v(\psi)r^3 \text{ with } F_v = \frac{2\pi}{3}(2 - 3\cos \psi + \cos^3 \psi). \quad (8)$$

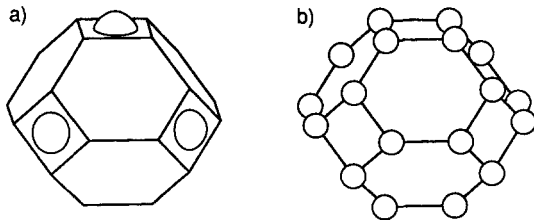


Fig. 1. Alternative configurations of closed porosity. (a) Present work, (b) Pan and Cocks [19].

With these relations equation (6) yields the sintering stress

$$\sigma_s = \frac{2\gamma_s}{R} \left( \frac{9F_v}{4\pi} \frac{\rho}{1-\rho} \right)^{1/3} + \frac{2\sqrt{3}+1}{4} \left( \frac{3\rho}{\pi} \right)^{1/3} \frac{\gamma_b}{R}. \quad (9)$$

Here the relative density,  $\rho$ , was introduced, which is related to the pore volume by  $1-\rho = 3V_p/V$ ;  $R$  is the radius of the sphere having the same material volume as a grain, i.e.  $V = (4\pi/3)R^3/\rho$ . In [17] the second term is missing from equation (9). This term results from the fact that the surface of the whole unit cell shrinks during densification, while the first term accounts for the changes of the surface and grain boundary areas at the pore tip.

4. SOLUTION OF THE DIFFUSION PROBLEM

4.1. Overview

The diffusion problem on the surface of the tetrakaidekahedron is solved in the following way. The macroscopic strain rate tensor is considered to be known. Four different cases of prescribed straining are treated in the (numerical) analysis. From the strain rate the normal displacement rates on the grain boundary facets are calculated. Further, the smallest possible unit cells for the solution of the diffusion equation (4) are identified and boundary conditions are specified. Then equation (4) is solved numerically using the heat-conduction option of the finite-element program ANSYS. The normal displacement rate is analogous to the heat production rate, the normal stress is analogous to the temperature, and  $\Omega \delta D_v/kT$  plays the role of the thermal conductivity. The finite element program generates solutions for the distribution of the normal stress,  $\sigma_n$ . Integrating (numerically) over the facets gives the forces transmitted by each facet. From these forces the macroscopic viscosity tensor is assembled by the same method that was applied for open porosity in [15, 18]. Finally the cubic viscosities are averaged to obtain isotropic values.

4.2. Displacement rates

The normal displacement rate on a grain contact area with unit normal vector  $n_i$  is given by

$$\dot{u}_n = n_i r_j \dot{\epsilon}_{ij} \quad (10)$$

where  $r_j$  is the vector connecting the grain centres. The macroscopic strain rate tensor is considered to be prescribed. The response of the material in terms of stress is calculated in the following section.

The cubic axes of the tetrakaidekahedron are normal to the square facets, and we choose a Cartesian coordinate system aligned with the cubic axes. Then the normal unit vectors on the square facets are  $\{100\}$ , and those on the hexagonal facets are  $(1/\sqrt{3})\{111\}$ . The notation with the parentheses implies all possible permutations of the components including +1 and -1. The vectors  $r_j$  are all parallel to the

corresponding  $n_j$ , and their magnitude, for the hexagonal and square facets, respectively, is

$$|r_j| = 2R \left( \frac{\rho_0}{\rho} \right)^{1/3} \quad (11)$$

$$|r_j| = 2R \frac{2}{\sqrt{3}} \left( \frac{\rho_0}{\rho} \right)^{1/3}. \quad (12)$$

Here  $\rho_0$  is the density of the b.c.c. sphere packing, i.e.  $\rho_0 = \pi \sqrt{3}/8 = 0.68$ . For  $\rho = \rho_0$  the distance between nearest neighbor spheres is  $2R$ , and that between next-nearest neighbors in  $2/\sqrt{3}$  times larger.

4.3. Loading cases

The numerical calculations of the diffusion fields on the surface of the tetrakaidekahedron are performed for the following four loading cases.

(1) *Unidirectional extension in [001] direction.* In this case the only nonzero strain rate component is  $\dot{\epsilon}_{33}$ . The aim is to calculate the stresses needed to cause this strain rate. Equation (10) gives the normal displacement rates on the grain facets. The result, together with those of the other loading cases, will be summarized at the end of this section.

The diffusion equation (4) is solved numerically with these prescribed displacement rates on the unit cell shown in Fig. 2. It comprises a quarter of a hexagonal facet, a quarter of a square facet with (100) orientation and an eighth of the square facet with (001) orientation. These facets are shown in Fig. 3 tilted into the plane of drawing. The circular arcs represent the edges of the pores, which were omitted from Fig. 2 for simplicity.

The unit cell is chosen such that, because of the symmetry of the problem, no matter flows across the outer boundary, except into the pores. At the edge of the pores, continuity of the chemical potential demands that  $\sigma_n = 2\gamma_s/r$ . This stress is set equal to zero in the computation since it leads to an additive

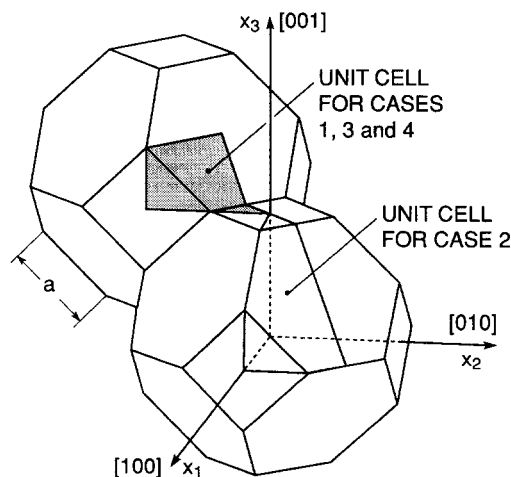


Fig. 2. Unit cells for the treatment of the diffusion problems.

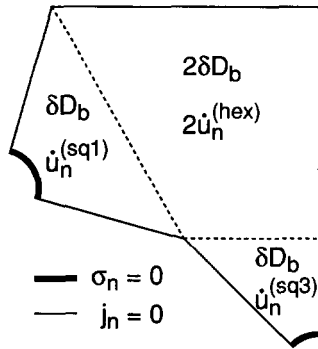


Fig. 3. Unit cell for loading case (1). All facets are shown in one plane.

term, the sintering stress, which is already known from equation (9).

Further, at the border line between hexagonal and square facets the normal components of the flux density must obey  $j_n^{(sq)} + 2j_n^{(hex)} = 0$ , since at each edge of the grain two equivalent hexagonal facets meet with one square facet. In the numerical model this requirement is met by doubling the "thickness" of the hexagonal facet, i.e. by artificially doubling  $\delta D_b$  and  $\dot{u}_n$ . Then the flux density is continuous and the stress is calculated correctly. The resulting forces on the grain facets and the cubic moduli are given later.

(2) *Shear on (100) planes in [010] direction.* The only nonzero strain rate and stress components are now  $\dot{\epsilon}_{12} = \dot{\epsilon}_{21}$  and  $\sigma_{12} = \sigma_{21}$ . The resulting displacement rates are obtained from equation (10) and they are listed at the end of this section.

The unit cell for the numerical solution of the diffusion equation must be larger than in the previous loading case. It is shown in Fig. 2 and, plotted on a plane, in Fig. 4. It comprises one half of a hexagonal facet, a quarter of the square facet with (100) orientation, and one eighth of the square facet with (001) orientation. At the triple grain junctions, the flux does not branch in this loading case, but flows continuously from one facet to one of the others, while the third does not exchange matter with the first two. The boundaries on the right and at the bottom of Fig. 4 are characterized by zero normal flux, while at the boundaries on the left  $\sigma_n = 0$  because of the symmetry of the loading. At the edges of the pores, one prescribes  $\sigma_n = 0$  also.

(3) *Isostatic loading.* Isostatic loading with a mean strain rate  $\dot{\epsilon}_m = \dot{\epsilon}_{11} = \dot{\epsilon}_{22} = \dot{\epsilon}_{33}$  leads to a hydrostatic stress state with mean stress  $\sigma_m$ . This loading case could be obtained by superposition from case (1), so that a separate numerical analysis would not be necessary. However, the redundancy in numerical calculations can be used to test their consistency. In fact, the bulk moduli calculated from loading cases (1) and (3) agree to within 0.01%.

In the numerical calculation the same unit cell was used as in loading case (1), although a smaller cell would have been sufficient because of the higher symmetry.

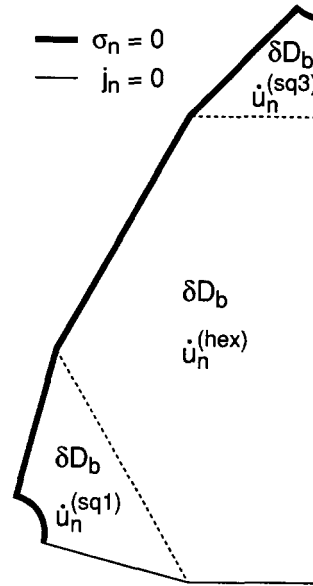


Fig. 4. Unit cell for loading case (2). All facets are shown in one plane.

(4) *Creep in [001] direction without pores.* In the absence of pores, loading cases (1) and (3) cannot be prescribed since the material is incompressible. In this case, we prescribe the strain rate components  $\dot{\epsilon}_{33} = -2\dot{\epsilon}_{11} = -2\dot{\epsilon}_{22}$ . The unit cell for the finite element calculation is the same as in loading case (1). An arbitrary stress value can be prescribed at any location and we choose  $\sigma_n = 0$  in the center of the square facets with normals in  $x_1$  and  $x_2$  directions. The choice of the stress boundary condition specifies the hydrostatic stress, which, however, plays no role for deviatoric creep.

*Summary of the displacement rates.* The displacement rates following from equation (10) for the four loading cases are given in Table 1 in nondimensional form,  $\dot{u}_n$ , which is defined by

$$\dot{u}_n = \dot{u}_n 2R \left( \frac{\rho_0}{\rho} \right)^{1/3} \dot{\epsilon} \quad (13)$$

where  $\dot{\epsilon}$  means  $\dot{\epsilon}_{33}$ ,  $\dot{\epsilon}_{12}$ ,  $\dot{\epsilon}_m$  and  $\dot{\epsilon}_{33}$  in cases (1), (2), (3) and (4), respectively.

#### 4.4. Finite element solution

Figure 5 shows the grids used in the finite element solution of the diffusion equation (4) with the  $\dot{u}_n$ -values and boundary conditions specified in the preceding section. Eight-noded isoparametric quadrilaterals are used with  $3 \times 3$  integration points.

Table 1. Dimensionless displacement rates on square facets with normals in  $x_3$ -direction (sq3) or in  $x_1$ - or  $x_2$ -directions (sq1) or (sq2), and on hexagonal facets (hex)

Loading case	$\dot{u}_n^{(sq3)}$	$\dot{u}_n^{(sq1)} = \dot{u}_n^{(sq2)}$	$\dot{u}_n^{(hex)}$
(1) $\dot{\epsilon}_{33} \neq 0$	$2/\sqrt{3}$	0	1/3
(2) $\dot{\epsilon}_{12} \neq 0$	0	0	$\pm 2/3$
(3) $\dot{\epsilon}_m \neq 0$	$2/\sqrt{3}$	$2/\sqrt{3}$	1
(4) $\dot{\epsilon}_{33} = -2\dot{\epsilon}_{11}$	$2/\sqrt{3}$	$-1/\sqrt{3}$	0

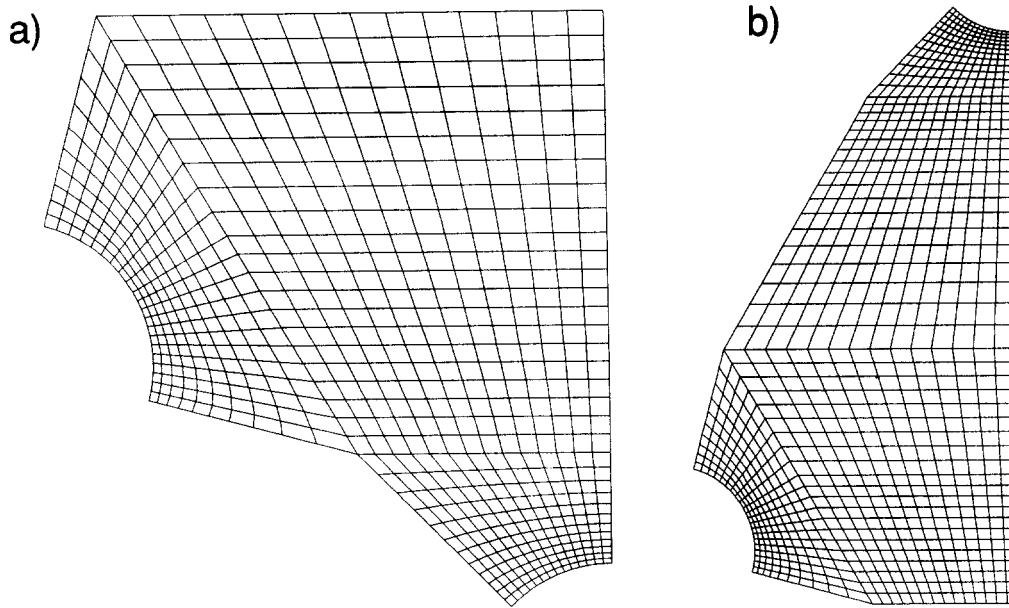


Fig. 5. Finite element grids on the unit cells.

Computations were carried for four different pore sizes  $r_p/(\sqrt{2}a) = 0, 0.1, 0.2$  and  $0.3$ ;  $r_p$  is the pore radius in the grain boundary. Table 2 gives the corresponding values of the area fraction of the square grain facets covered by pores,  $\omega = \pi r_p^2/a^2$ , and the corresponding relative densities,  $\rho$ ;  $\rho$  and  $\omega$  are related by

$$\omega = \pi \sin^2 \psi \left( \frac{8\sqrt{2}(1-\rho)}{3F_v} \right)^{2/3}. \quad (14)$$

Figure 6 shows the distribution of the normal stress,  $\sigma_n$ , on the grain boundaries. The stress is given in units of  $kTR^3\dot{\epsilon}/(\Omega \delta D_b \rho)$ . The iso-stress lines correctly exhibit kinks, where they intersect triple grain lines with discontinuities in  $\delta D_b$  and  $\dot{u}_n$ . The flux vector is normal to the isostress lines. Considering the isostatic case [Fig. 6(c)], the isostress lines are nearly circular, so that the flow is approximately radial around the centers of the square and hexagonal facets. Hence the approximation of radial flow made in [18] is expected to yield good estimates for the bulk viscosity (see Section 5.3).

Figure 6(d) shows the stress distribution under creep conditions in the absence of pores. Again the flow pattern on the square facet normal to the tensile axis is nearly radial. Contrary to this (numerical) observation, Pan and Cocks [19] assume a parallel flow field to describe deviatoric creep. Hence it is not surprising that their result for the strain rate is found

to differ markedly from the numerical result shown below.

Table 3 shows the dimensionless forces on the boundary facets, which are obtained by integration of the stress over the facets. The nondimensional force  $\hat{F}_n$ , is defined by

$$F_n = \hat{F}_n \left( \frac{\rho_0}{\rho} \right)^{2/3} \frac{kTR^5 \dot{\epsilon}}{\Omega \delta D_b \rho} \quad (15)$$

where  $\dot{\epsilon}$  has the same meaning as before, namely  $\dot{\epsilon}_{33}$ ,  $\dot{\epsilon}_{12}$ ,  $\dot{\epsilon}_m$  and  $\dot{\epsilon}_{33}$  in the four loading cases. The slight difference of the order 0.1% between sq3 and sq1 in the isostatic case arises from the asymmetry of the finite element grid. It can be considered as a measure of the accuracy of the finite element results.

#### 4.5. Macroscopic stresses and viscosities

The macroscopic stresses are calculated most easily by equating the work rates (per volume) done by the macroscopic stresses and by the contact forces

$$\sigma_{ij} \dot{\epsilon}_{ij} = \frac{1}{2V} \sum_k F_n^{(k)} \dot{u}_n^{(k)}. \quad (16)$$

Here  $V = (4\pi/3)R^3/\rho$  is the volume of the tetrakaidekahedron, including the pore space, the sum extends over all facets of the grain, and the factor 1/2 is needed since each facet is shared by two grains.

The work rate on the left-hand side of equation (16) can be written as  $\sigma \dot{\epsilon}$ , where  $\sigma$  means  $\sigma_{33}$ ,  $2\sigma_{12}$ ,  $3\sigma_m$  and  $\sigma_{33} - \sigma_{11}$  in the four loading cases, and  $\dot{\epsilon}$  was given earlier. Using the dimensionless forms of  $F_n$  and  $\dot{u}_n$  in equation (16) and dividing by  $\dot{\epsilon}$  gives the stress

$$\sigma = \left[ \frac{3\sqrt{3}}{32} \sum_k (\dot{u}_n^{(k)} \hat{F}_n^{(k)}) \frac{kTR^3}{\Omega \delta D_b \rho} \right] \dot{\epsilon} \quad (17)$$

 Table 2. Area coverage,  $\omega$ , and relative density,  $\rho$ , for which the finite element calculations are carried out

$r_p/a$	$\omega$	$\rho$ (for $\psi = 60^\circ$ )	$\rho$ (for $\psi = 90^\circ$ )
0	0	1	1
$0.1\sqrt{2}$	0.0628	0.9985	0.9969
$0.2\sqrt{2}$	0.2513	0.9879	0.9749
$0.3\sqrt{2}$	0.5655	0.9592	0.9152

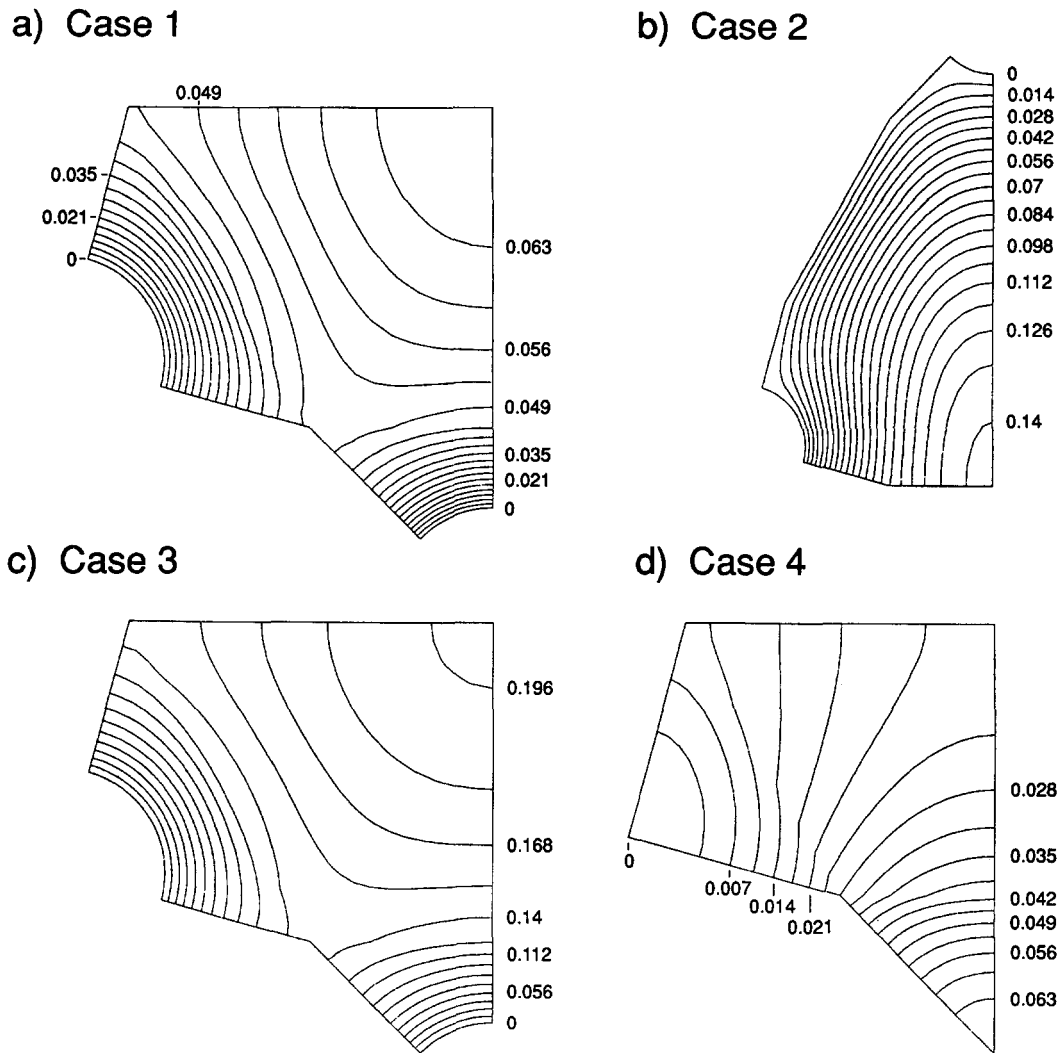


Fig. 6. Lines of constant normal stress for the loading cases (1)–(4). The lines are equidistant in stress.

where  $\sigma$  and  $\epsilon$  have the above meaning. The term in square brackets specifies the viscous moduli, as shown next.

For cubic anisotropy, the linear viscous relations are

$$\sigma_{33} = C_{11}\epsilon_{33} \quad \sigma_{11} = C_{12}\epsilon_{33} \quad (18)$$

$$\sigma_{12} = 2C_{44}\epsilon_{12} \quad (19)$$

$$\sigma_m = 3K\epsilon_m \quad (20)$$

$$\sigma_{33} - \sigma_{11} = \frac{3}{2}(C_{11} - C_{12})\epsilon_{33} \quad (21)$$

for the four loading cases, respectively. The  $C_{ij}$ 's are the cubic viscosities, and  $K = (C_{11} + 2C_{12})/3$  is the bulk viscosity.

Comparison of equations (18)–(21) with equation (17) shows that the expression in square brackets in equation (17) gives  $C_{11}$ ,  $C_{44}$ ,  $K$  and  $(3/2)(C_{11} - C_{12})$  if evaluated for the four loading cases. Additionally,  $C_{12}$  can be obtained from loading case (1), either by directly equilibrating the facet forces with  $\sigma_{11}$  or by superimposing the solution with  $\epsilon_{11} \neq 0$ , which is obtained from case (1) by an exchange of  $x_1$  and  $x_3$ . It remains to carry out the sum in equation (17) over the six square facets and the eight hexagonal facets of a tetrakaidekahedron to obtain the cubic viscosities.

Table 3. Dimensionless normal forces on grain facets

Loading case	$r_p/a$	$\hat{F}_n^{(sq3)}$	$\hat{F}_n^{(sq1)} = \hat{F}_n^{(sq2)}$	$\hat{F}_n^{(hex)}$
(1) Uniaxial extension ( $\epsilon_{33} \neq 0$ )	$0.1\sqrt{2}$	0.140405	0.120572	0.528873
	$0.2\sqrt{2}$	0.046543	0.038928	0.271125
	$0.3\sqrt{2}$	0.009184	0.007761	0.129573
(2) Shear ( $\epsilon_{12} \neq 0$ )	0	0	0	$\pm 0.449787$
	$0.1\sqrt{2}$	0	0	$\pm 0.435817$
	$0.2\sqrt{2}$	0	0	$\pm 0.393674$
	$0.3\sqrt{2}$	0	0	$\pm 0.323005$
(3) Isostatic	$0.1\sqrt{2}$	0.381398	0.381631	1.586608
	$0.2\sqrt{2}$	0.124438	0.124375	0.813366
	$0.3\sqrt{2}$	0.024694	0.024712	0.388726
(4) Creep in $x_3$ direction	0	0.096127	0.014112	0.107621

## 5. RESULTS

## 5.1. The cubic viscosities

The procedure described above leads to the cubic viscosities, which are given in dimensionless form according to

$$C_{ij} = \hat{C}_{ij} \frac{kTR^3}{\Omega \delta D_b \rho}. \quad (22)$$

The same normalization is used for  $K$  and  $G$ . Table 4 shows the results.

Apparently, the Cauchy relation,  $C_{12} = C_{44}$ , is not fulfilled by the values shown in Table 4. This is because the forces on the facets are not independent but are coupled by the diffusion fluxes from one boundary to another. In the case of open porosity with isolated contacts the Cauchy relation is fulfilled [18].

In an isotropic material  $2C_{44} = C_{11} - C_{12}$ . Inspection of Table 4 shows that the present model yields a strong cubic anisotropy. The factor  $2C_{44}/(C_{11} - C_{12})$  varies from 5.5 for the fully dense material to 152 for  $r_p/a = 0.3\sqrt{2}$ , while for an isotropic material the factor is 1.

## 5.2. Inclusion of sliding forces

So far grain boundary sliding was assumed to occur freely without any resistance. Now sliding forces as described by equation (5) are taken into account. To achieve this one notes that the contributions of normal and tangential forces on grain facets are additive in their effect on the cubic viscosities [18]. The contribution of tangential forces can be taken from the analysis of isolated grain contacts (equation (20) of [18]). Only the contact area needs to be adjusted to the situation of closed porosity. The total cubic viscosities are then

$$\begin{pmatrix} C_{11} \\ C_{12} \\ C_{44} \end{pmatrix} = \frac{kTR^3}{\Omega \delta D_b \rho} \begin{pmatrix} \hat{C}_{11} \\ \hat{C}_{12} \\ \hat{C}_{44} \end{pmatrix} + \frac{\eta R}{4} \left( \frac{\rho_0}{\rho} \right)^{1/3} \begin{pmatrix} 4 \\ -2 \\ 1 + \frac{2}{\sqrt{3}}(1 - \omega) \end{pmatrix}. \quad (23)$$

The first term arises from the normal forces with the  $\hat{C}_{ij}$ 's from Table 4, while the second arises from the tangential forces. The voided area fraction of the square facets,  $\omega$ , was related to the density in equation (14).

Table 4. Dimensionless cubic viscosities and bulk viscosity

$r_p/a$	$\hat{C}_{11}$	$\hat{C}_{12}$	$\hat{K}$	$\hat{C}_{44}$	$\hat{C}_{11} - \hat{C}_{12}$
0	$\infty$	$\infty$	$\infty$	0.05622	0.02050
$0.1\sqrt{2}$	0.28166	0.27424	0.27671	0.05448	0.00742
$0.2\sqrt{2}$	0.13486	0.13199	0.13295	0.04921	0.00287
$0.3\sqrt{2}$	0.05955	0.05902	0.05920	0.04038	0.00053

 Table 5. Normalized bulk viscosities  $\hat{K} = K\Omega \delta D_b \rho / (kTR^3)$ . Comparison of an analytical estimate with the numerical results

$r_p/a =$	$0.1\sqrt{2}$	$0.2\sqrt{2}$	$0.3\sqrt{2}$
$\hat{K}$ from equation (24)	0.282	0.139	0.065
$\hat{K}$ numerical	0.277	0.133	0.059

 5.3. Comparison with an analytical estimate for  $K$ 

In [18] the bulk viscosity was estimated by assuming circular symmetric diffusive flow on all grain facets. The result was

$$K = \frac{kTR^3}{18\Omega \delta D_b \rho} \left( -2 \ln \omega - \frac{33}{64} + \omega - \frac{\omega^2}{16} \right) \quad (24)$$

with  $\omega$  from equation (14). Table 5 shows a comparison between the bulk viscosities calculated numerically and those calculated from equation (24).

The relative difference between the analytical and numerical results is small. It ranges from less than 2% for small porosities to about 10% for the largest pores considered. Hence, equation (24) can be used as a convenient approximation for the bulk viscosity.

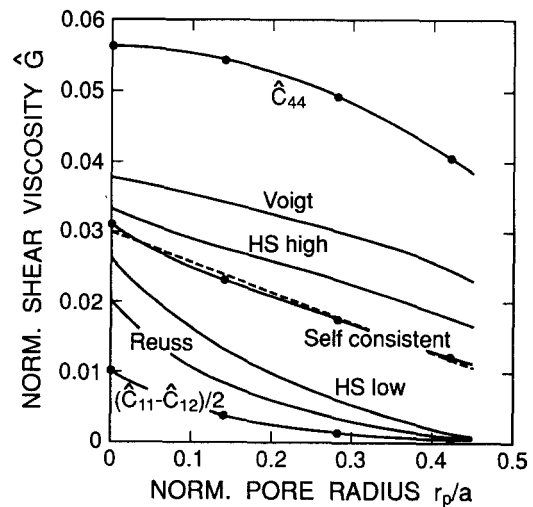
 5.4. Isotropic averages for  $G$ 

To obtain the isotropic shear viscosity the methods used in polycrystalline elasticity theory are applied, as in the case of open porosity [18]. The results are shown in Fig. 7 for the case that  $\eta = 0$ . As a consequence of the high anisotropy of the model the bounds lie considerably apart. Kröner's [20] self-consistent estimate, which lies between the Hashin-Shtrikman [21] bounds, is considered to be the best estimate. It is approximated by

$$\hat{G} = 0.0300 - 0.0432r_p/a \quad (25)$$

which is shown in Fig. 7 as a straight dashed line.

The  $G/K$  ratio, calculated with the self-consistent estimate for  $G$ , has the values 0, 0.065, 0.116 and


 Fig. 7. Normalized cubic shear viscosities  $\hat{C}_{44}$  and  $(\hat{C}_{11} - \hat{C}_{12})/2$  and estimates for the normalized isotropic shear modulus,  $\hat{G}$ . HS = Hashin-Shtrikman bounds [21].

0.197 for the values of  $r_p/a = 0, 0.1\sqrt{2}, 0.2\sqrt{2}$  and  $0.3\sqrt{2}$ , respectively.

### 5.5. Uniaxial creep without pores

In order to compare the present results with those of Pan and Cocks [19] for creep of fully dense material, we consider uniaxial tension, i.e. the only nonzero stress component is  $\sigma_{33}$ . If one considers the case with tension along one of the cubic axes, one obtains the strain rate from equation (17) with  $\sigma = \sigma_{33}$  and the term in square brackets  $= (3/2)(C_{11} - C_{12})$ , which is taken from Table 4. Then

$$\dot{\epsilon}_{33} = 272 \frac{\Omega \delta D_b \sigma_{33}}{kTd^3}. \quad (26)$$

Here the distance between opposite square facets,  $d$ , was used, which is related to  $R$  by  $d = (4/\sqrt{3})R\rho_0^{1/3}$  for the fully dense material [from equation (12)]. Pan and Cocks [19] use the same quantities and obtain a numerical factor 153 instead of 272. (Their result in [22], a factor 554, was numerically incorrect.) With the self-consistent isotropic average of  $G$ , one obtains the uniaxial creep rate

$$\dot{\epsilon}_{33} = \frac{\sigma_{33}}{3G} = 88 \frac{\Omega \delta D_b \sigma_{33}}{kTd^3}. \quad (27)$$

Coble's [23] classical analysis gave a numerical factor 148. A comparison of equations (26) and (27) shows that the cubic axes are exceptionally soft directions for tension, and the average creep rate is three times smaller.

## 6. INFLUENCE OF SURFACE DIFFUSION ON THE BULK VISCOSITY

The pore shape was assumed in this paper to be the equilibrium shape consisting of spherical caps. This assumption is certainly justified if surface diffusion is very fast compared to grain boundary diffusion. However, a recent (theoretical) observation [24] indicated that an approximation based on equilibrium pore shapes yields results with a wide range of validity even for very slow surface diffusivities.

In [24] sintering of a hexagonal array of wires was modelled numerically for arbitrary mean stresses,  $\sigma_m$ , and for arbitrary ratios of  $\delta D_s/\delta D_b$  (where  $\delta D_s$  is the surface diffusion coefficient).

In analogy to cavity growth under tensile stresses [25] it was found that equilibrium pore shapes prevail, if the applied stress does not exceed a few times the sintering stress, nearly irrespective of the value of  $\delta D_s/\delta D_b$ . At higher compressive stresses and small  $\delta D_s/\delta D_b$  ratios, the material flowing out of the grain boundary into the pore forms extrusions. This is the analogue to the crack-like mode of cavity growth under high tensile stresses [25]. It appears that the range of validity of the equilibrium mode is larger under compressive than under tensile stress.

In [24] an additional important finding was made, which had not been discovered previously in connection with cavity growth. The numerical results for the pore shrinkage rates can be reproduced accurately by a quasi-equilibrium theory, which differs from the conventional equilibrium theory solely by the contribution of surface diffusion to the dissipation rate, which was previously neglected. This additional dissipative term may reduce the shrinkage rate by a large factor compared to the conventional equilibrium theory and it leads to accurate results (compared to the numerical solutions), as long as the pore shape globally resembles the equilibrium shape with possibly large deviations of the curvature near the pore tip. This condition of near-equilibrium shapes is fulfilled for nearly arbitrary  $\delta D_s/\delta D_b$  ratios, including very small ones, as long as the compressive stress does not exceed a few times the sintering stress. In situations of inhomogeneous sintering this prerequisite is always granted.

There is no obvious reason that this quasi-equilibrium theory, which was verified in [24] for a two-dimensional problem, should not be applicable analogously to the present three-dimensional problem. The shrinkage rate is derived from the thermodynamic principle that the negative rate of change of the Gibbs free energy must be equal to the dissipation rate due to the diffusive fluxes. The rate of change of the Gibbs free energy is, for hydrostatic loading

$$-\dot{G}_{\text{tot}} = 3V\sigma_m\dot{\epsilon}_m - 2\gamma_s \int_{A_s} \kappa v_n dS - 6(2\sqrt{3} + 1)a^2\dot{\epsilon}_m\gamma_b. \quad (28)$$

The first term results from the work rate of the macroscopic stress, the second accounts for the change of the surface area and of the grain boundary area due to the pore shrinkage, and the third describes the change of the energy of the grain boundaries surrounding the shrinking unit cell as pointed out in Section 3. The integral extends over the pore surface area pertaining to one grain, and  $v_n$  is the velocity of the pore surface away from the center of curvature due to the plating or removal of material. The formulation of the capillary terms in equation (28) is an equivalent alternative to the formulation in Section 3.

Within the quasi-equilibrium approximation, the integral on the pore surface is evaluated in the same way as in the equilibrium theory, namely by setting  $\kappa = \text{const}$ , so that the integral becomes  $\int \kappa v_n dS = \kappa \dot{V}$ , and the sintering stress is obtained in exactly the same form as in the equilibrium theory, equation (9). As shown in [24] for the two-dimensional case this approximation leads to accurate results for the sintering rate in a wide range of conditions.

The equality of the negative rate of the free energy and the dissipation rate gives

$$3V(\sigma_m - \sigma_s)\dot{\epsilon}_m = R_b + R_s \quad (29)$$

where  $R_b$  and  $R_s$  are the contributions of grain boundary diffusion and surface diffusion to the dissipation rate. The evaluation of the dissipation rates is described in the Appendix. The bulk viscosity is obtained as a sum of two terms, one arising from grain boundary diffusion  $K_b$ , and the other from surface diffusion  $K_s$ ,

$$K_{\text{tot}} = \frac{kTR^3}{\Omega \delta D_b \rho} \left( \hat{K}_b + \frac{\delta D_b}{\delta D_s} \hat{K}_s \right) \quad (30)$$

where the hat indicates the normalized quantities, as before. The first contribution was given in Table 4, or, approximately by equation (24), while the latter is derived in the Appendix with the result

$$\hat{K}_s = g_0 + g_1 \omega + g_2 \omega^2 \quad (31)$$

with

$$g_0(\psi) = \frac{1}{9} \frac{-48 \ln \cos \frac{\psi}{2} - 12 + 6 \cos \psi + 14 \cos^2 \psi - 9 \cos^3 \psi + \cos^5 \psi}{(2 + \cos \psi)^2 (1 - \cos \psi)^4} \quad (32)$$

$$g_1(\psi) = \frac{1}{18} \frac{3 + \cos \psi}{(2 + \cos \psi)(1 + \cos \psi)} \quad (33)$$

$$g_2(\psi) = \frac{1}{144} \frac{2 + \cos \psi}{(1 + \cos \psi)^2} \quad (34)$$

The  $g$ 's are only moderately dependent on  $\psi$ . For  $\psi = 60^\circ$  is  $g_0 = 0.088$ ,  $g_1 = 0.052$ ,  $g_2 = 0.0077$ . Also  $\hat{K}_s$  does not vary strongly with  $\psi$  nor with  $\omega$ , and a typical value is  $\hat{K}_s = 0.102$  for  $\psi = 60^\circ$  and  $\omega = 0.251$ . This is the same order of magnitude as  $\hat{K}_b$  (which is 0.133 for  $\omega = 0.251$  according to Table 4).

Hence the contribution of surface diffusion to the bulk viscosity can only be neglected, if  $\delta D_s / \delta D_b \gg 1$ , but it contributes substantially if  $\delta D_s / \delta D_b$  is of the order 1, and it dominates if  $\delta D_s / \delta D_b$  is small. As pointed out earlier, equation (30) can be expected to be a good approximation even for very small  $\delta D_s / \delta D_b (\ll 1)$ , unless the compressive stress becomes too large. More precise criteria for the range of validity are not yet available, but they can be developed in analogy to the analysis of cavity growth [25].

## 7. DISCUSSION

The preceding analysis of the densification and creep process was based on a specific grain and pore geometry with pores on the two-grain junctions between next-nearest grain neighbors. This geometry was motivated by a previous investigation on the evolution of equilibrium pore shapes [17], which indicated that this configuration is more likely to occur than the configuration with pores on the grain corners. The latter configuration was investigated by Pan and Cocks [19]. A comparison of their results with ours illustrates the influence of the pore

configuration on the viscosities. From their equation (44) one obtains the bulk viscosity, which in our notation is

$$K = \frac{\pi k T R^3}{108 \Omega \delta D_b \rho} \left\{ -2.45 \ln \left( \frac{r_p}{a} \right) - 2.69 + 5.40 \left( \frac{r_p}{a} \right)^2 - 3.53 \left( \frac{r_p}{a} \right)^4 \right\} \quad (35)$$

For spherical pores on the 24 grain corners, pore radius and relative density are related by

$$\frac{r_p}{a} = \left( \frac{\sqrt{2}}{\pi} (1 - \rho) \right)^{1/3} \quad (36)$$

Comparison of equations (24) and (35) shows that the bulk viscosity is about four times smaller for the

configuration with pores on the 24 grain corners than for that with pores on the six square facets; the comparison is made for the same relative density, and  $\psi = 90^\circ$  is used, i.e.  $F_v = 4\pi/3$ .

Pan and Cocks [19] also consider the case of deviatoric creep in the [001] direction. Their result for the viscosities is, in our notation

$$\hat{C}_{11} - \hat{C}_{12} = \frac{\pi}{18} \left[ 0.209 - 4.41 \left( \frac{r_p}{a} \right)^2 + 12.5 \left( \frac{r_p}{a} \right)^3 - 10.8 \left( \frac{r_p}{a} \right)^4 \right] \quad (37)$$

Table 6 shows a comparison with our results for the same relative densities.

The two models should agree for  $\rho = 1$ , when no pores are present in either model. The difference which actually occurs corresponds to the ratio 274/153 given previously and is probably due to the inaccuracy caused by the flow pattern assumed by Pan and Cocks for the deviatoric case.

Once pores are present, the difference between the two models increases to about a factor 4 (for 0.3% porosity) and a factor 16 (for 8.5% porosity). It is not clear to what extent the difference is due to the different configurations or to inaccuracies of Pan and Cocks' estimate. No estimate for  $C_{44}$  nor for the isotropic average,  $G$ , is given by Pan and Cocks, so that no comparison is possible.

Table 6. Values of  $\hat{C}_{11} - \hat{C}_{12}$  for two pore configurations;  $\psi = 90^\circ$  is assumed

	$\rho = 1$	$\rho = 0.9969$	$\rho = 0.9747$	$\rho = 0.9152$
Pan and Cocks	0.0365	0.0296	0.0177	0.00854
Present work	0.0205	0.0074	0.0029	0.00053

## 8. CONCLUSIONS

Densification and creep by grain boundary diffusion are described by a linear viscous constitutive equation with compressibility and a sintering stress. The bulk and shear viscosities and the sintering stress are derived for a specific configuration of closed porosity. The diffusion problem is solved numerically using the finite element method. Since the assumed grain geometry, a tetrakaidekahedron, implies a b.c.c. symmetry, one primarily obtains cubic viscosity constants.

From the cubic viscosities the isotropic bulk viscosity,  $K$ , is easily obtained, since it is equal to the cubic bulk viscosity. An analytical approximation for  $K$  [18] is confirmed, which shows that  $K$  diverges logarithmically, when full density is approached. To calculate the isotropic shear viscosity,  $G$ , the methods of polycrystalline elasticity theory are applied. However, the result remains somewhat ambiguous, since, as a consequence of the pronounced anisotropy of the model, the Hashin–Shtrikman bounds lie considerably apart. If the self-consistent method is assumed to give the best estimate, the  $G/K$  ratio drops from about 0.22 at pore closure to 0 at full density. The latter value is a necessary consequence of the fact that the material becomes incompressible.

A comparison with an analysis of Pan and Cocks [19], who studied a different pore configuration, shows that the material becomes much more compliant (i.e.  $K$  and  $G$  drop), if the same pore volume is distributed on two times more, smaller and more closely spaced pores.

*Acknowledgement*—The authors would like to thank the Deutsche Forschungsgemeinschaft for financial support under contract Ri 329/18-1.

## REFERENCES

1. M. Abouaf, J. L. Chenot, G. Raison and B. Baudin, *Int. J. Num. Methods Engng.* **25**, 191 (1988).
2. J. L. Chenot, in *Numerical Methods in Industrial Forming Processes, NUMIFORM '89*, (edited by E. G. Thompson, R. D. Wood, O. C. Zienkiewicz and H. Samuelson), pp. 11–16, A. A. Balkema, Rotterdam (1989).
3. A. Jagota, K. R. Mikeska and R. K. Bordia, *J. Am. Ceram. Soc.* **73**, 2266 (1990).
4. K. Mori, in *Numerical Methods in Industrial Forming Processes, NUMIFORM '92*, (edited by J. L. Chenot, R. D. Wood and O. C. Zienkiewicz), pp. 69–78. A. A. Balkema, Rotterdam (1992).
5. H. Riedel and D. Z. Sun, in *Numerical Methods in Industrial Forming Processes, NUMIFORM '92* (edited by J. L. Chenot, R. D. Wood and O. C. Zienkiewicz), pp. 883–886. A. A. Balkema, Rotterdam (1992).
6. A. C. F. Cocks and Z. Z. Du, *Acta metall. mater.* **41**, 2113 (1993).
7. R. L. Coble, *J. appl. Phys.* **32**, 787 (1961).
8. E. Arzt, *Acta metall.* **30**, 1883 (1982).
9. A. S. Helle, K. E. Easterling and M. F. Ashby, *Acta metall.* **33**, 2163 (1985).
10. A. G. Evans, *J. Am. Ceram. Soc.* **65**, 497 (1982).
11. R. Raj and R. K. Bordia, *Acta metall.* **32**, 1003 (1984).
12. C. H. Hsueh, A. G. Evans, R. M. Cannon and R. J. Brook, *Acta metall.* **34**, 927 (1986).
13. R. K. Bordia and G. W. Scherer, *Acta metall.* **36**, 2393 (1988).
14. G. W. Scherer, *J. Non-Cryst. Solids* **34**, 239 (1979).
15. A. Jagota, P. R. Dawson and J. T. Jenkins, *Mech. Mater.* **7**, 255 (1988).
16. R. M. McMeeking and L. T. Kuhn, *Acta metall. mater.* **40**, 961 (1992).
17. J. Svoboda, H. Riedel and H. Zipse, *Acta metall. mater.* **42**, 435 (1994).
18. H. Riedel, H. Zipse and J. Svoboda, *Acta metall. mater.* **42**, 445 (1994).
19. J. Pan and A. C. F. Cocks, *Acta metall. mater.* **42**, 1215 (1994).
20. E. Kröner, *Z. Physik* **151**, 504 (1958).
21. Z. Hashin and S. Shtrikman, *J. Mech. Phys. Solids* **10**, 343 (1962).
22. A. C. F. Cocks and J. Pan, in *Creep and Fracture of Engineering Materials and Structures* (edited by W. Wilshire and R. W. Evans), pp. 41–51. The Institute of Materials, London (1993).
23. R. L. Coble, *J. appl. Phys.* **34**, 1679 (1963).
24. J. Svoboda and H. Riedel, Quasi-equilibrium sintering for coupled grain-boundary and surface diffusion, IWM-Report M9/93, submitted to *Acta metall. mater.*
25. T.-J. Chuang, K. I. Kagawa, J. R. Rice and L. B. Sills, *Acta metall.* **27**, 265 (1979).

## APPENDIX

*Evaluation of the Dissipation Rate*

It is the aim of this appendix to derive the contribution of surface diffusion to the bulk viscosity. The dissipation rate by grain boundary diffusion,  $R_b$ , need not be evaluated, since it leads to the bulk viscosity already derived in Sections 4 and 5 by other means. The dissipation rate by surface diffusion is defined as

$$R_s = \frac{kT}{\Omega \delta D_s} \int_{A_s} j_s^2 dS \quad (\text{A1})$$

where  $j_s$  is the surface flux density and the integral extends over the six halves of the pores surrounding the unit cell.

The surface flux that yields a sequence of equilibrium pore shapes with decreasing radius of curvature,  $r$ , is derived by considering the hatched volume shown in Fig. A1. In terms of the angle  $\alpha$ , the hatched volume is

$$v^* = \frac{\pi}{3} (2 - 2 \cos \alpha - \sin^2 \alpha \cos \psi) r^3. \quad (\text{A2})$$

Its value changes by the surface flux entering the hatched volume and by the motion of the grains, the so-called jacking effect

$$\dot{v}^* = -2\pi r \sin \alpha j_s + \frac{\dot{r}}{2} \pi r^2 \sin^2 \alpha. \quad (\text{A3})$$

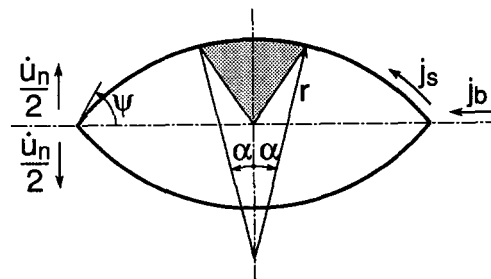


Fig. A1. Illustration of the calculation of the surface flux density.

Combining these equations gives the flux density

$$j_s = \frac{r}{2} \left[ (2 \cot \alpha - \frac{2}{\sin \alpha} + \sin \alpha \cos \psi) \dot{r} + \sin \alpha \frac{\dot{u}_n}{2} \right]. \quad (\text{A4})$$

The dissipation rate on the six half pore surfaces belonging to one grain is

$$R_s = \frac{6kT}{\Omega \delta D_s} \int_0^\psi j_s^2 2\pi r^2 \sin \alpha \, d\alpha \quad (\text{A5})$$

If  $j_s$  is inserted from equation (A4), one obtains  $R_s$  in the form

$$R_s = \frac{3\pi k T r^4}{\Omega \delta D_s} \left[ I_0 \dot{r}^2 + I_1 \dot{r} \frac{\dot{u}_n}{2} + I_2 \left( \frac{\dot{u}_n}{2} \right)^2 \right] \quad (\text{A6})$$

where the  $I$ 's are integrals over  $\alpha$  which can be evaluated in closed form

$$I_0 = -16 \ln \cos \frac{\psi}{2} - 4 + 2 \cos \psi + \frac{14}{3} \cos^2 \psi - 3 \cos^3 \psi + \frac{1}{3} \cos^5 \psi \quad (\text{A7})$$

$$I_1 = 2 - \frac{16}{3} \cos \psi + 4 \cos^2 \psi - \frac{2}{3} \cos^4 \psi \quad (\text{A8})$$

$$I_2 = \frac{2}{3} \cos \psi + \frac{1}{3} \cos^3 \psi. \quad (\text{A9})$$

Only isostatic loading is considered here. Then  $\dot{r}$  and  $\dot{u}_n$  are determined by the mean strain rate

$$\dot{r} = \frac{V \dot{\epsilon}_m}{3F_v r^2} \quad (\text{A10})$$

$$\dot{u}_n = (2V)^{1/3} \dot{\epsilon}_m. \quad (\text{A11})$$

Hence  $R_s \propto \dot{\epsilon}_m^2$ , and the contribution of surface diffusion to the bulk viscosity is  $K_s = R_s / (9V \dot{\epsilon}_m^2)$  with  $R_s$  from equations (A6)–(A11). The result in the main text is obtained after  $r$  is expressed by  $r_p$  through  $r_p = r \sin \psi$ ,  $r_p$  is replaced by  $a\sqrt{(\omega/\pi)}$ ,  $a$  is expressed by the volume  $V$  of the grain,  $V$  is expressed by the grain radius  $R$ , combinations of the  $I$ 's are formed to give the  $g$ 's and equation (22) is used for the normalization of  $K$ .

A2 Vala, J., Svoboda, J., Kozák, Čadek., J., Modelling discontinuous metal-matrix composite behaviour under creep conditions, *Scripta Metallurgica et Materialia*, Vol. 30, Issue 9, (1994), 1201-1206, IF 0,600.



MODELLING DISCONTINUOUS METAL MATRIX COMPOSITE BEHAVIOR  
UNDER CREEP CONDITIONS:  
EFFECT OF INTERFACE DIFFUSIONAL MATTER TRANSPORT AND INTERFACE SLIDING

J. Vala, J. Svoboda, V. Kozák and J. Čadek  
Institute of Physical Metallurgy, Academy of Sciences of Czech Republic  
Žižkova 22, 61662 Brno, Czech Republic

(Received September 23, 1993)  
(Revised January 18, 1994)

Introduction

Discontinuous metal matrix composites, i.e. metals or solid solution alloys reinforced with ceramic particulates or short fibers, are an important class of structural materials. Although they do not belong to the heat or creep resistant group, they frequently retain strength at high temperatures. This holds particularly true for discontinuous aluminium alloy matrix composites reinforced by silicon carbide particulates or short fibers. Hence, they are candidates for replacing aircraft components now made of titanium or for use at automobile engine components or, possibly, for other applications. This is why the high temperature creep of these composites has been extensively studied in the last decade [1-9].

However, our understanding of the rather unusual creep behavior in the discontinuous aluminium and aluminium matrix composites is far from satisfactory. Similarities in the different matrix materials suggest that very strong applied stress, as well as very strong temperature dependence of the creep strain rate usually observed, are not caused by the matrix, but rather are determined by the particulate or short fiber reinforcement.

Several suggestions have been made to explain the unusual creep behavior of discontinuous metal matrix composites. Some authors [6,10,11] suggested direct load transfer as the source of such behavior. However, the load transfer to the reinforcement still results in a creep law for the composite which expresses the same stress and temperature dependence of the creep strain rate as that for the matrix.

Other suggestions [12-14] involve some form of non-continuum (dislocation) mechanics analysis to describe the effect of reinforcement and of course, attempts have also been made to combine the "continuum mechanics load transfer approach" with the "non-continuum (dislocation) mechanics approach" [9-15].

Once discontinuous reinforcement is introduced into the metallic matrix, a great number of interfaces is created. Via these interfaces, stress directed diffusional matter transport can take place and contribute to measured creep strain rate, thus lowering the creep strength of the composite. Also, interface sliding will contribute to the overall creep strain rate. Consequently, in an extreme case, the creep strength of the composite may be even lower than that of the matrix if the diffusional paths are not long enough and the sliding interfaces are numerous; such can be the case of reinforcement of a "subcritical" size.

Rösler and Evans [16] seem to be the first to point out that the interface reactions must be taken into account in any detailed analysis of creep behavior of discontinuous (metal matrix) composites.

In the present paper, continuum mechanics analysis along the line of that performed by Dragone and Nix is extended, incorporating the above mentioned processes of stress directed diffusional matter transport along reinforcement/matrix interfaces and sliding.

Theoretical Analysis

The strain and stress analysis of material is based on the assumption of the plane strain and on the periodicity of geometric and physical characteristics. Let us consider a domain

$$\Omega = (0, H) \times (0, L) \times (0, \delta)$$

and its subdomains

$$\Omega^1 = (0, h) \times (0, l) \times (0, \delta) ,$$

$$\Omega^2 = \Omega \setminus \Omega^1$$

in the 3-dimensional Euclidean space (the orthogonal system of coordinates  $x$  is used),  $h, l, H, L, \delta$  ( $h < H, l < L$ ) are positive numbers and  $\bar{M}$  always means the closure of a set  $M$  in this space. The following notation (the symbols (...)) for open and  $\langle \dots \rangle$  for closed intervals are applied) is clear from Fig.1:

$$\begin{aligned} \Lambda^1 &= (0, H) \times \langle L, L \rangle \times (0, \delta) , & \Lambda^2 &= \langle H, H \rangle \times (0, L) \times (0, \delta) , \\ \omega^1 &= (0, h) \times \langle l, l \rangle \times (0, \delta) , & \omega^2 &= \langle h, h \rangle \times (0, l) \times (0, \delta) , \\ \Gamma^1 &= (0, H) \times \langle 0, 0 \rangle \times (0, \delta) , & \Gamma^2 &= \langle 0, 0 \rangle \times (0, L) \times (0, \delta) , \\ \gamma^0 &= \omega^1 \cap \omega^2 , & \gamma^1 &= \omega^2 \cap \Gamma^1 , & \gamma^2 &= \omega^1 \cap \Gamma^2 . \end{aligned}$$

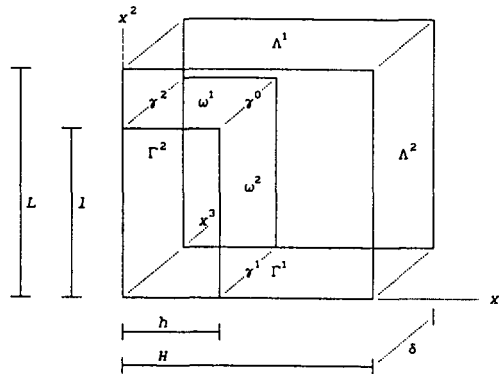


Fig.1: Geometrical configuration

Let us assume that  $\Omega^1$  and  $\Omega^2$  contain a homogeneous isotropic material that can be described by means of the serial viscoelastic model with one linear elastic and one special power-law viscous component. Let  $S$  and  $T$  be the spaces of admissible hydrostatic and deviatoric stresses on  $\Omega^1$  and  $\Omega^2$ , and let  $V$  be the space of admissible velocities on  $\Omega^1$  and  $\Omega^2$  respecting the plane strain

$$\epsilon^{33}(v) = 0 ,$$

where the usual notation from the linear theory of elasticity

$$\forall i, j \in \{1, 2, 3\} \mid \epsilon^{ij}(v) = \frac{1}{2} (\partial v^i / \partial x^j + \partial v^j / \partial x^i)$$

is applied, together with the boundary conditions

$$\begin{aligned} v^2(\Gamma^1) &= 0 , & \forall a, b \in \bar{\Lambda}^1 \mid v^2(a) &= v^2(b) , \\ v^1(\Gamma^2) &= 0 , & \forall a, b \in \bar{\Lambda}^2 \mid v^1(a) &= v^1(b) . \end{aligned}$$

Let  $\mathcal{Q}$  be the space of admissible normal loads on  $\omega^1$  and  $\omega^2$  continuous in  $\gamma^0$  satisfying the boundary condition

$$q(\gamma^1) = q(\gamma^2) = 0 ,$$

and  $\mathcal{P}$  the space of admissible tangential loads in directions  $x^1$  on  $\omega^1$  and  $x^2$  on  $\omega^2$ . (The more precise definitions, together with some existence results, have been presented in [17]; a more thorough study concerning these mathematical problems is being prepared.)

Let  $\epsilon^e, \epsilon^c$  be the elastic and non-elastic strain parts ( $\epsilon = \epsilon^e + \epsilon^c$ ) and  $u$  the displacements (time integrals of velocities  $v$ ) on  $\Omega^1$  and  $\Omega^2$ . The constitutive relations for materials in  $\Omega^1$  and  $\Omega^2$  are given by

$$\begin{aligned} \epsilon^e(u) &= A\sigma + B\tau & (\text{Hooke law}) , \\ \epsilon^c(v) &= C|\tau|^{N-1}\tau & (\text{Norton law}) . \end{aligned}$$

where  $A, B, C, N$  are material parameters (in general, with different values on  $\Omega^1$

and  $\Omega^2$ ). Let  $v^{ij}$  be the traces of  $v^i$  from  $\Omega^j$  on  $\omega^1$  and  $\omega^2$  for every  $j \in \{1, 2\}$  and  $i \in \{1, 2, 3\}$ ; let us assume  $v^{31} = v^{32}$ . The properties of the interface  $\omega^1$  and  $\omega^2$  are given by phenomenological relations

$$\begin{aligned} v^{i1} - v^{i2} &= -\partial(D\partial q/\partial x^j)/\partial x^j && \text{on } \omega^j && \text{(equation of interface diffusion),} \\ v^{i1} - v^{i2} &= Ep && \text{on } \omega^j && \text{(equation of interface sliding),} \end{aligned}$$

where  $i, j \in \{1, 2\}$  and  $i \neq j$ , and  $D$  has close relation to the diffusion coefficient on the interface and  $E$  characterizes the interface sliding. The principle of virtual velocities together with these relations generate the equations of evolution

$$\begin{aligned} \forall \tilde{\sigma} \in S & \mid [\tilde{\sigma}, A\delta] - [\tilde{\sigma}, \varepsilon(v)] = 0, \\ \forall \tilde{\tau} \in T & \mid [\tilde{\tau}, Bt] + [\tilde{\tau}, C|\tau|^{k-1}\tau] - [\tilde{\tau}, \varepsilon(v)] = 0, \\ \forall \tilde{q} \in Q & \mid \langle \tilde{q}, Dq \rangle - \langle \tilde{q}, v \rangle^n = 0, \\ \forall \tilde{p} \in P & \mid \langle \tilde{p}, Ep \rangle - \langle \tilde{p}, v \rangle^t = 0, \\ \forall \tilde{v} \in W & \mid [\varepsilon(\tilde{v}), \sigma + \tau] - \langle \tilde{v}, q \rangle^n - \langle \tilde{v}, p \rangle^t = \langle \tilde{v}, r \rangle, \end{aligned} \quad (*)$$

where the time-variable function  $r$  (one constant for any fixed time) describes the development of the normal external load; for illustration, if all stresses are smooth enough, the last equation implies

$$\int_{\Lambda^1} (\sigma^{22} + \tau^{22}) d\mu^2 = H\delta r.$$

The unknown variables (with zero values in initial time) in (\*) are the hydrostatic and deviatoric stresses  $\sigma$  and  $\tau$  ( $|\tau|$  is the symbol for the norm of  $\tau$  in the Euclidean space of real square matrices of order 3), and the velocities  $v$  defined on  $\Omega^1$  and  $\Omega^2$ , and the normal loads  $q$  defined on  $\omega^1$  and  $\omega^2$ . All these variables are abstract functions mapping the time interval into the corresponding one of the function spaces  $S, T, W, Q, P$ . For the 2- and 3-dimensional Lebesgue measures  $\mu^2, \mu^3$  the short notation

$$\begin{aligned} [\varphi, \psi] &= \sum_{i,j=1}^3 \int_{\Omega} \varphi^{ij} \psi^{ij} d\mu^3 \text{ for suitable functions } \varphi, \psi, \\ \langle \tilde{q}, Dq \rangle &= \int_{\omega^1} (\partial \tilde{q} / \partial x^1) D(\partial q / \partial x^1) d\mu^2 + \int_{\omega^2} (\partial \tilde{q} / \partial x^2) D(\partial q / \partial x^2) d\mu^2, \\ \langle \tilde{q}, v \rangle^n &= \int_{\omega^1} \tilde{q} (v^{21} - v^{22}) d\mu^2 + \int_{\omega^2} \tilde{q} (v^{11} - v^{12}) d\mu^2, \\ \langle \tilde{v}, q \rangle^n &= \int_{\omega^1} (\tilde{v}^{21} - \tilde{v}^{22}) q d\mu^2 + \int_{\omega^2} (\tilde{v}^{11} - \tilde{v}^{12}) q d\mu^2, \\ \langle \tilde{p}, v \rangle^t &= \int_{\omega^1} \tilde{p} (v^{11} - v^{12}) d\mu^2 + \int_{\omega^2} \tilde{p} (v^{21} - v^{22}) d\mu^2, \\ \langle \tilde{v}, p \rangle^t &= \int_{\omega^1} (\tilde{v}^{11} - \tilde{v}^{12}) p d\mu^2 + \int_{\omega^2} (\tilde{v}^{21} - \tilde{v}^{22}) p d\mu^2, \quad \langle \tilde{v}, r \rangle = \int_{\Lambda^1} \tilde{v}^2 r d\mu^2 \end{aligned}$$

is used.

As the standard finite element packages do not handle the system (\*), and we have no information about the available software solver of (\*), the original algorithm searching for an approximate solution of (\*) was developed and the corresponding PC programs [18] were written. The Rothe method of discretization in time was used to find the solution of (\*) as the limit of the solutions of certain systems of integral equations containing only 5 time-independent unknown functions corresponding to  $\sigma, \tau, v, q, p$ . The integrals in these equations were simplified with help of finite and boundary element techniques; the resulting system of algebraic equations was solved by standard numerical methods.

### Results of modelling

Let us consider the material parameters  $A, B$  in the form

$$A = (1-2m)/e, \quad B = (1+m)/e,$$

where  $e$  is the Young modulus and  $m$  the Poisson coefficient, and let the development of the external load be described by the relations

$$\begin{aligned} r &= \frac{1}{2}(1 - \cos(\alpha t))r^* \text{ for } t \leq t^*, \\ r &= r^* \text{ for } t \geq t^*, \end{aligned}$$

where  $r^*, t^*, \alpha$  are certain time-independent parameters and  $t$  is the time variable. The following figures show the results obtained by the above mentioned software for the values of elastic and creep characteristics

$e = 470 \cdot 10^9 \text{ Pa}$  on  $\Omega^1$ ,       $e = 68,3 \cdot 10^9 \text{ Pa}$  on  $\Omega^2$ ,  
 $m = 0,17$  on  $\Omega^1$ ,       $m = 0,345$  on  $\Omega^2$ ,  
 $C = 0$  on  $\Omega^1$ ,       $C = 1,1 \cdot 10^{-15} \text{ s}^{-1} \text{ Pa}^{-4}$  on  $\Omega^2$ ,  
 $N = 0$  on  $\Omega^1$ ,       $N = 4$  on  $\Omega^2$ ,

and of interface diffusion and sliding characteristics  
 $D = 10^{-\varphi} \text{ m s}^{-1} \text{ Pa}^{-1}$  where  $\varphi \in \{26, 28, 30, 31, 32, 33, 34, 36, 38, 40\}$ ,  
 $E = 10^{-\psi} \text{ m s}^{-1} \text{ Pa}^{-1}$  where  $\psi \in \{18, 19, 20, 21, 22\}$ ,  
 for the geometrical configuration given by the distances  
 $h = 0,2 \cdot 10^{-5} \text{ m}$ ,  $l = 0,5 \cdot 10^{-5} \text{ m}$ ,  $H = 0,5 \cdot 10^{-5} \text{ m}$ ,  $L = 1,0 \cdot 10^{-5} \text{ m}$   
 (under the assumption of plane strain for arbitrary  $\delta$ ) and for the external  
 load development characteristics  
 $r^* = 8 \cdot 10^7 \text{ Pa}$ ,  $t^* = 10000 \text{ s}$ ,  $\alpha = 0,0002\pi \text{ s}^{-1}$ .

The results are presented for times when the processes have become stationary. Figure 2 shows the macroscopic creep rate for various values of  $D$  and  $E$ . The upper and lower dashed lines correspond to the creep rate of non-reinforced matrix and composite without diffusion and sliding at reinforcement/matrix interface ( $D = 0$ ,  $E = 0$ ), respectively. A similar calculation was performed by Dragone and Nix [6]. From the figure it can be seen that the range of three orders of magnitude of  $D$  and  $E$  values decide significantly on reinforcement effect. This can be positive (for low  $D$  and  $E$ ) or negative (for high  $D$  and  $E$ ). The critical values of  $D$  and  $E$  (at which the dependence of creep rate on  $D$  and  $E$  is strongest) can be shifted by changing the size of reinforcement. Higher critical values of  $D$  and  $E$  correspond to larger reinforcement sizes.

Figures 3a-e show the steady state stress distribution  $\sigma^{22}$ . In Fig. 3a relatively high values of  $D$  and  $E$  are chosen. The local values of  $\sigma^{22}$  are

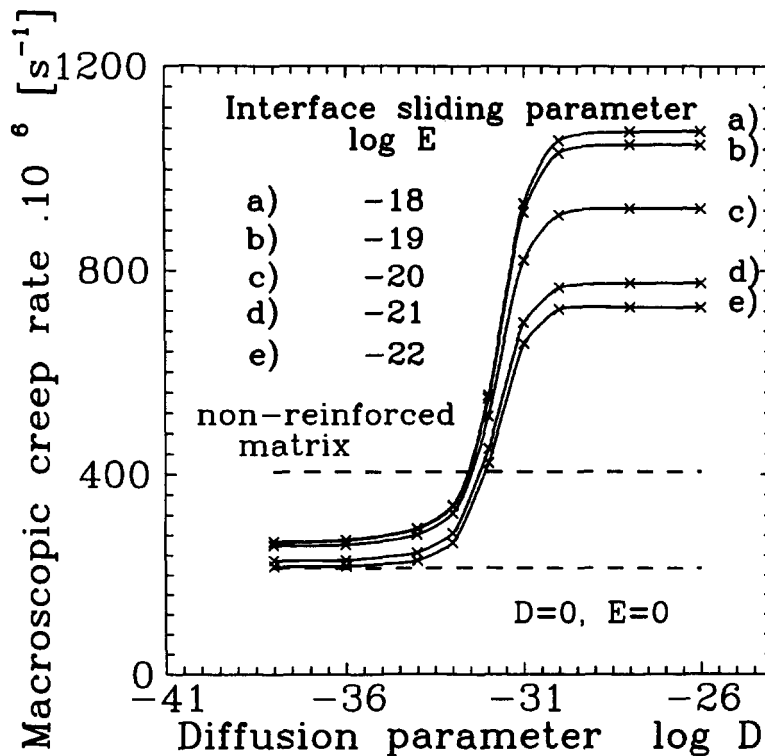
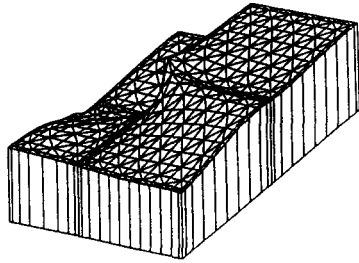


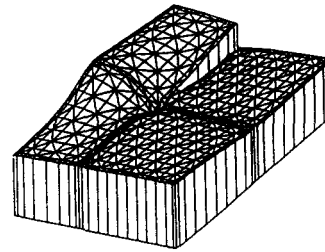
Fig. 2: Steady state macroscopic creep rate for various reinforcement/matrix interface properties

$\log D = -31, \log E = -18$



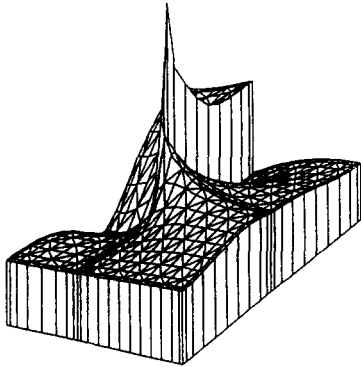
a)

$\log D = -33, \log E = -18$



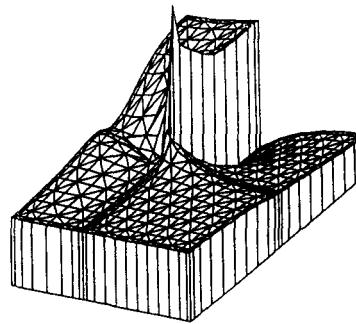
b)

$\log D = -31, \log E = -22$



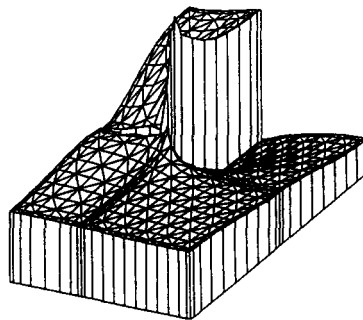
c)

$\log D = -33, \log E = -22$



d)

$D = 0, E = 0$



e)

**Fig.3: Steady state distribution  $\sigma^{22}$  for various reinforcement/matrix interface properties**

higher in the matrix than in the reinforcement. Owing to very active matrix/reinforcement interface diffusion and sliding, the stress component normal to the matrix/reinforcement interface is nearly constant and the tangential one is nearly zero. This results in nearly hydrostatic stress in the reinforcement. A decrease of  $D$  by two orders of magnitude causes the reinforcement effect to become positive (Fig. 3b). The next two figures (Figs. 3c and 3d) show a considerable change of stress distribution when  $E$  is lowered by four orders of magnitude. Figure 3e for  $D = 0$  and  $E = 0$  was computed in standard finite element method and it is similar to Fig. 3d. The oscillations of the stress field are significantly less in our computations than in those obtained by Dragone and Nix [6]. The reason is that we used simple triangular finite elements, while Dragone and Nix used more complicated finite elements designed for smooth stress fields.

The present method may represent an important tool for better understanding the creep behavior of discontinuous metal matrix composites. Varying the size, the shape and the content of reinforcement, the structure of the composite can be adjusted to have optimal creep properties.

Of course the method requires further improvement. First of all it is necessary to introduce local hardening and softening terms into the creep equation of the matrix. It may be expected that this would help to explain some of the experimentally observed facts not yet interpreted. In the next step, damaging processes associated with stress concentrations should be addressed.

#### Summary

The continuum mechanics analysis of creep behavior of metal matrix composite is presented in this paper. The analysis includes elasticity, power law creep and diffusional matter transport and sliding along the reinforcement/matrix interfaces. The solution of the problem requires development of original mathematical and numerical methods. The present results indicate a significant influence of reinforcement/matrix interface properties on macroscopic behavior of the composite as well as on stress distribution in the composite under creep conditions.

#### Remark

The authors would appreciate any possibility of cooperation in the field of the present theory.

#### References

- [1] V.C.Nardone and J.R.Strife, Metall.Trans. 18A (1987) 109
- [2] T.G.Nieh, K.Xia and T.G.Langdon, J.Eng.Mater.Technol. 110 (1988) 77
- [3] T.Morimoto, T.Yamako, H.Lilholt and M.Taya, J.Eng.Mater.Technol. 110 (1988) 70
- [4] K.T.Park, E.J.Lavernia and F.A.Mohamed, Acta Metall.Mater. 38 (1990) 2149
- [5] F.A.Mohamed, K.T.Park and E.J.Lavernia, Mater.Sci.Eng. A 150 (1991) 21
- [6] T.L.Dragone and W.D.Nix, Acta Metall.Mater. 38 (1990) 1941
- [7] T.L.Dragone and W.D.Nix, Acta Metall.Mater. 40 (1992) 2781
- [8] J.Čadek, V.Šustek and M.Pahutová, Mater.Sci.Eng., in press
- [9] A.Dlouhý, N.Merk and G.Eggeler, Acta Metall.Mater., submitted for publication
- [10] V.C.Nardone and K.M.Prewo, Scr.Metall. 20 (1986) 43
- [11] N.Sørensen, A.Needleman and V.Tvergaard, Mater.Sci.Eng. A 158 (1992) 129
- [12] M.Volgesang, R.J.Arsenault and R.M.Fisher, Metall.Trans. 11A (1986) 379
- [13] R.J.Arsenault and M.Taya, Acta Metall. 35 (1987) 651
- [14] R.J.Arsenault, Key Eng.Mater. 79-80 (1993) 265
- [15] N.Shi, B.Wilner and R.J.Arsenault, Acta Metall.Mater. 40 (1992) 2841
- [16] J.Rösler and A.G.Evans, Mater.Sci.Eng. A 153 (1992) 438
- [17] J.Vala, Equadiff 8 (Comenius University Bratislava) Abstracts (1993) 222
- [18] J.Vala and V.Kozák, research report 845/992, Inst.Phys.Metall.Brno (1993)

A3 Vašek, A., Polák, J., Kozák, V., Fatigue crack initiation in fibre-metal laminate GLARE2, *Microstructure and Processing* 234, (1997), 621-624, IF 0,896.

## Fatigue crack initiation in fibre-metal laminate GLARE 2

A. Vašek \*, J. Polák, V. Kozák

*Institute of Physics of Materials, Academy of Sciences of the Czech Republic, Žitkova 22, 616 62 Brno, Czech Republic*

Received 5 February 1997; received in revised form 7 March 1997

### Abstract

Fatigue crack initiation in notched plates made of fibre-metal laminate GLARE 2 was studied under constant stress amplitude loading using light and scanning electron microscope. Fatigue crack initiation mechanism observed in notched laminates was found different from the mechanism typical for monolithic materials. Stress and plastic strain finite element calculation was used to discuss the anomalous fatigue crack initiation in fibre-metal laminates. © 1997 Elsevier Science S.A.

*Keywords:* Fatigue crack initiation; GLARE 2; Finite element calculations

### 1. Introduction

Fibre-metal laminates (FML) are a new type of structural materials used for light weight structures [1,2]. Application of FML GLARE 2 is motivated by its excellent fatigue resistance and weight savings with respect to the traditional Al-alloys. In structural parts where the final failure may occur in the presence of a relatively short crack (e.g. riveted lap joints or attachment lugs), the period of crack initiation can determine the fatigue life. Unlike the relatively frequent works concerning behaviour of long-cracked FMLs (e.g. [3,4]), studies focused to the fatigue crack initiation in this type of material are still rare. The necessity to consider the period of crack initiation for fatigue life prediction of multi-layered FML structural parts has been emphasised by Vašek and Vogelesang [5]. Different features of fatigue crack initiation and early crack growth in notched GLARE 2 with respect to monolithic Al-alloy notched bodies were noted by Vašek et al. [6].

The aim of this paper is to show the results of a recent study of fatigue crack initiation in GLARE 2 notched plates and explain the anomalous initiation mechanism in this type of material.

### 2. Experimental

FML GLARE 2 consists of 0.3 mm thin high strength 2024-T3 Al-alloy layers which alternate with 0.25 mm thin epoxy-resin layers reinforced by unidirectional glass fibres (prepregs). The laminate plates were prepared by a stacking up of total 12 Al-alloy and 11 prepreg layers and by a subsequent curing in an autoclave cycle at temperature 120°C under pressure (10 bars) for 90 min. A total of three different notches were milled in the rectangular plates of 200 × 50 mm: Central slot with radius  $r = 3$  mm and width 15 mm ( $K_t = 3.2$ ), central hole with radius  $r = 7.5$  mm ( $K_t = 2.4$ ) and two side notches with radius  $r = 70$  mm and depth 7.5 mm each ( $K_t = 1.2$ ). Specimen surface in the notch area including the lateral side was mechanically polished to enable an observation of fatigue cracks since their initiation.

The specimens were loaded in an electro-hydraulic fatigue machine MTS under constant stress amplitude control with a sine cycle and cycle ratio  $R = 0.04$ . Maximum net-section stress was 150, 250, 360 and 450 MPa in individual tests. During loading the notch area was observed to find the first fatigue cracks. The loading continued until a surface crack extended up to 10 mm.

\* Corresponding author. Tel: +420 5 7268344; fax: +420 5 41218657; e-mail: vasek@ipm.cz

3. Results

SEM observation of the notch area from the lateral side showed that nucleation of microcracks in inner metal layers preceded the fatigue crack initiation on the laminate surface. Cracks in the inner Al layers initiated predominantly at the edge of the metal sheet adjacent to the prepreg layer region where the unidirectional fibres were cut by the notch (Fig. 1). In the notch root area where the fibres are intact, the microcrack occurrence was relatively poor.

After test termination the specimens with developed cracks were subjected to a successive layer-by-layer milling-off procedure to reveal a distribution of fatigue cracks in inner metal sheets. Number of cracks in individual metal layers, their length and position were measured. Lower number of cracks was found in the surface layers than in inner ones, however average crack length was higher in the surface layers (Fig. 2).

On the contrary to the common situation in a monolithic material, where location of crack initiation is expected in the notch root, fatigue cracks in GLARE 2 nucleate at a position which significantly deviates from the notch root. The deviation was measured as an angle  $\Theta$  between the notch root position ( $\Theta = 0$ ) and the crack initiation position on the notch edge contour. Deviation of crack initiation positions,  $\Theta$ , varied between 0 and 25° on both sides from the notch root depending on the applied stress and notch radius. Most probable position of crack initiation  $\Theta_p$ , what is an angle between the notch root and the position where the crack occurrence is maximum, was evaluated. Fig. 3 shows that fatigue cracks in laminates with sharper notches and under higher loads take place at higher angles  $\Theta$ .

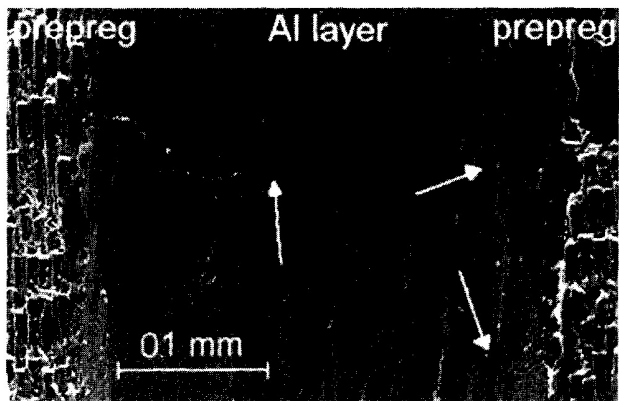


Fig. 1. Nucleation of microcracks at the edges of an inner Al layer of GLARE 2 laminate.

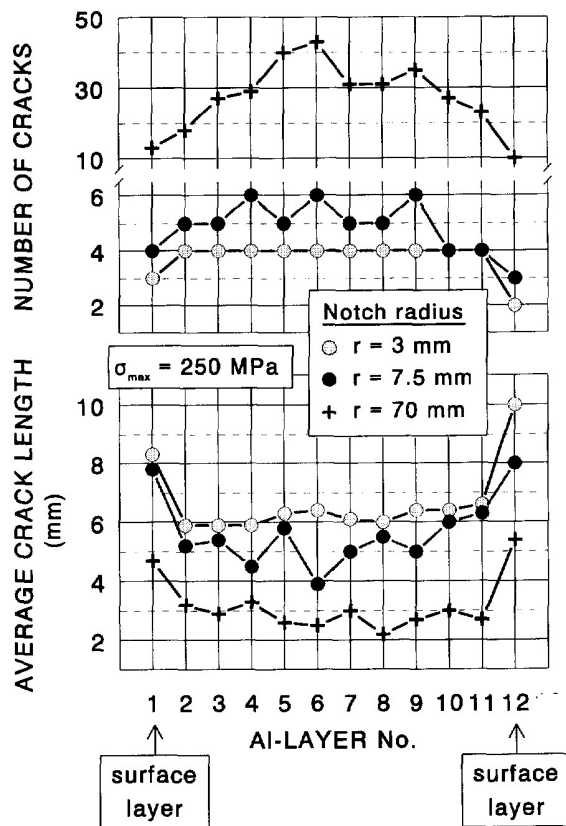


Fig. 2. Number of cracks and average crack length in individual Al layers of notched GLARE 2 laminate (12 Al-alloy layers and 11 prepreg layers).

4. Finite element calculations

Through-thickness distribution of residual stresses present in the in Al layers after thermal curing of the laminate was modelled by means of elastic 3-dimensional ANSYS finite element analysis using brick elements SOLID45. The results showed that residual stresses in Al layers are positive and higher in inner layers with respect to the outer ones. The maximum residual stress was reached at the sheet edges.

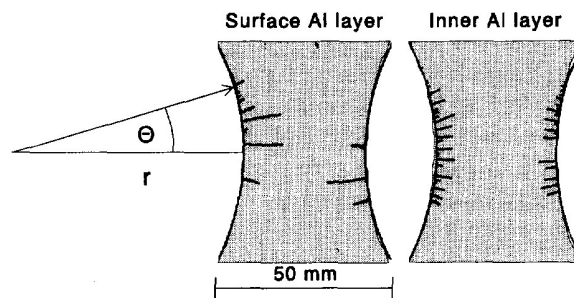


Fig. 3. Fatigue cracks in a surface and central Al layer of the laminate with two side notches. ( $\sigma_{max} = 250$  MPa). Angle  $\Theta$  defines position of a crack at the notch contour.

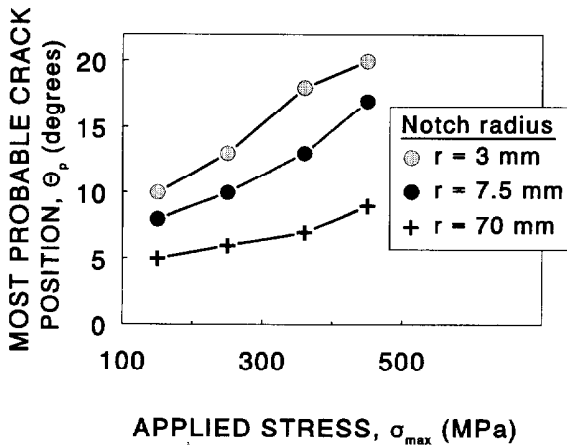


Fig. 4. Most probable position of fatigue crack initiation in notched GLARE 2 laminates.

Elastic-plastic 2-dimensional ABAQUS finite element analysis using shell elements (SR85 and STRI65) was adopted to calculate monotonic plastic strain in notched specimens. Plastic strain at the notch contour was plotted in Fig. 4 versus angle  $\Theta$ . Relatively large notch area in the GLARE 2 specimens undergoes high plastic strain. The affected area is larger in laminates with a smaller notch radius and under higher applied stress Fig. 5.

5. Discussion

The presence of the residual stress, which is higher in inner Al layers and reaching the maximum at the sheet edge, increases the local plastic strain developed by an applied load. First fatigue microcracks thus initiate at the edge of inner Al sheets. The microcracks grow fast through the thickness of the sheet. Growth of microcracks through the laminate thickness is restricted by fibres in prepreg layers bridging the crack from both sides. During further loading new microcracks nucleate in inner metal layers independently on the cracks already present in the laminate. Later, some cracks arise also in the surface layer. Conditions for crack growth are more favourable in the surface layers where stress intensity factor is reduced only by one prepreg layer and cracks can propagate easier than in inner metal layers. It results in a lower number of cracks initiated in the surface layers.

The wide angle interval of crack initiation positions corresponds to the relatively large area of high plastic strain on the notch contour. Moreover some additional contribution to the local plastic strain has to be taken into account. Steps on the prepreg surface made by fibres broken-off during notch contour milling pro-

duce an increase in the local shear stress in the prepreg layer which results in the high local stress and strain concentration in the metal sheets. First steps arise in some distance from the notch root and border a small flat face with intact fibres. In this area the crack initiation is less probable than in the area with steps made by the cut fibres.

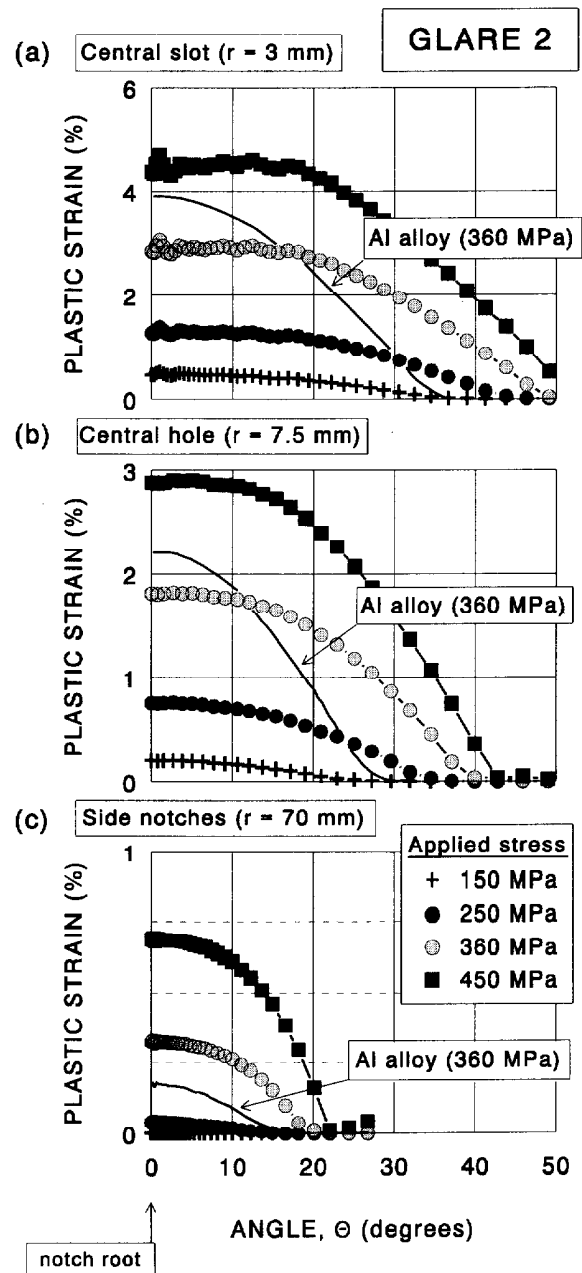


Fig. 5. Equivalent plastic strain in Al layers of GLARE 2 laminate at the notch contour for different notch radii and different net-section stresses calculated by means of a finite element analysis.

## 6. Conclusions

Scanning-electron and light microscopy study of fatigue crack initiation in notched GLARE 2 specimens loaded under higher stress amplitudes yield the following conclusions:

(1) Mechanism of fatigue crack initiation in notched FMLs differs from that in monolithic materials.

(2) Initiation of fatigue cracks in the laminate surface is preceded by earlier nucleation of a number of microcracks in inner metal layers.

(3) Fatigue cracks start to grow separately in individual metal layers. The number of cracks is higher in the inner Al layers while the cracks grow faster in the surface layers.

(4) Fatigue cracks are located in a wide interval of angles  $\Theta$  on both sides from the notch root position. Most probable crack initiation position varied in the interval  $\Theta = 5\text{--}20^\circ$  depending on applied stress and a notch radius.

## Acknowledgements

This work was financially supported by the Grant Agency of the Czech Republic (Grant No. 101/96/0319) and by the NATO Scientific Affairs Division, Brussels (Grant No. HTECH.LG.941331). These supports are gratefully acknowledged.

## References

- [1] L.B. Voegesang, J.W. Gunning, *Mater. Design* 7 (1986) 287–300.
- [2] A. Beukers et al. (Eds.), *Fatigue of Aircraft Materials*, Delft University Press, Delft, 1992.
- [3] R.O. Ritchie, *Mat. Sci. Eng. A103* (1988) 15–28.
- [4] M. Papakyriacou et al., in K.H. Schwalbe and C. Berger (eds.), *ECF10—Structural Integrity: Experiments, Models and Applications*, Berlin 1994, Engineering Materials Advisory Services, Warley, Vol. II (1994) 1193–1199.
- [5] A. Vašek, L.B. Voegesang, in U. Meier (ed.), *SAMPE Europe—Success of Materials by Combination*, Basel, 1996, SAMPE Europe, Niederglatt/ZH, (1996) 437–449.
- [6] A. Vašek et al., in J. Petit (ed.), *ECF11—Mechanism and Mechanics of Damage and Failure*, Poitiers 1996, Engineering Materials Advisory Services, Warley, (1996) 1685–1690.

A4 Pluinage, G., Azari, Z., Kozák, V., Effect of ferritic microstructure on local damage zone, *Theoretical and Applied Fracture Mechanics* 31, (1999), č. 2, 149-156, IF 1,391.



ELSEVIER

Theoretical and Applied Fracture Mechanics 31 (1999) 149–156

theoretical and  
applied fracture  
mechanics

www.elsevier.com/locate/tafmec

## Effect of ferritic microstructure on local damage zone distance associated with fracture near notch

G. Pluvinage<sup>a</sup>, Z. Azari<sup>a</sup>, N. Kadi<sup>a</sup>, I. Dlouhý<sup>b,\*</sup>, V. Kozák<sup>b</sup>

<sup>a</sup> *Laboratoire de Fiabilité Mécanique, Université de Metz-ENIM, Ile du Saulcy, 57045 Metz, France*

<sup>b</sup> *Institute of Physics of Materials, Academy of Sciences, Žitkova 22, 61662 Brno, Czech Republic*

### Abstract

A deterministic approach is used to analyze cleavage failure near the notch root by application of a local fracture criterion. Micromechanism of fracture is assessed using finite element calculations. Two ferritic microstructures have been selected; they differ significantly in the carbide thickness as the fracture data scattered widely. Local damage zones are calculated from the normal stress distributions and compared with those from the notch root to the location of failure initiation. To this end, the static three-point bend Charpy V-notch specimens were used. Microfractography identifies the local damage zone distances and their locations with reference to the prevailing microstructures. © 1999 Elsevier Science B.V. All rights reserved.

### 1. Introduction

Stress triaxiality and plastic strain are known to affect the fracture initiation conditions [1]. The stress criterion can be used to explain the onset of unstable crack growth. Stress concentration near notches introduces hydrostatic state of stress with trends to cause embrittlement [2].

For low alloy structural steels in the lower shelf region, it is generally known that crack starts to propagate, when the local fracture stress  $\sigma_f$  is exceeded by the normal stress  $\sigma_{yy}$  ahead of the notch [3]. In order for the cleavage micromechanism to prevail in ferritic grain and/or carbide particles, the local tensile stress would presumably have to be higher over some characteristic distance. For blunted notches, this condition can be depicted

from the maximum on the normal stress distribution curve. For sharp notches such as crack, the characteristic distance tends to play a deciding role [4].

For the afore-mentioned steel, the origin of fracture initiation is frequently associated with the cleavage of ferritic subgrains. Microscopic cleavage initiation involves several successive events [5–7]: slip induced separation of ferrite grains; inter- or trans-granular cracking of carbide particles; and microcracking of cleavage plane across subgrain boundaries. Fracture stress is defined as a local material parameter characterizing the microscopic resistance against cleavage. Such a parameter was shown to be independent of temperature, hydrostatic stress, and strain rate [5]. The value of this stress is strongly affected by the microstructure [8–11] and the relations used for quantifying the results.

Stochastic models have been developed in Refs. [12–14] to explain the fracture characteristics in

\* Corresponding author. Fax: +420 541 218 657; e-mail: idlouhy@ipm.cz

relation to the distribution of brittle particles. The different size crack nuclei in the changing stress gradient field ahead a sharp crack appears to compete with one another. The deterministic approach assumes that initiation corresponds to the site of local maximum stress where microcracks would presumably form in a small volume in the plastic zone ahead of the crack. A sufficiently large volume of material ahead of the crack could be found to contain a particle that would nucleate cleavage. That corresponds to  $\sigma_{yy} > \sigma_f$ , a condition for crack growth.

The aim of the present contribution is to determine the local damage zone distance from the normal stress distribution near the notch root. Explained also is the relationships between this distance as computed and those measured from the fracture surface of two materials different fracture behavior.

## 2. Background

The elastic and elastic-plastic normal stress near the notch root tend to decrease with increasing distance. Analysis has shown in Ref. [15] such a behavior given in Fig. 1. Three zones may be identified.

Region I – the normal stress is nearly constant and/or increasing to a maximum  $\sigma_{yy}^{max}$ .

Region II – an intermediate transition zone.

Region III – a pseudo stress singularity type of distribution can be identified:

$$\sigma_{yy} = \frac{K_\rho}{(2\pi r)^\alpha} \tag{1}$$

The parameter  $K_\rho$  characterizes the stress intensity at the notch root zone III. It is associated with failure initiation. The exponent  $\alpha$  determines the order of stress singularity for  $\sigma_{yy}$ . It has been evaluated [16] for a wedge notch where an energy density was defined as the governing fracture parameter. A local damage zone distance is defined to represent the distance from the notch tip to the boundary between zone II and III in Fig. 2. It is denoted by  $X_{ef}$  which is assumed to be:

- greater than the plastic zone diameter;
- cylindrical in shape and to coincide with the diameter of the process volume; and
- localized in a high stress region in which the stress gradient is not too high.

Let the relative stress gradient  $\chi$  be determined by

$$\chi = \frac{1}{\sigma_{yy}(x)} \frac{d\sigma}{dx} \tag{2}$$

It can be evaluated in terms of the distance from the notch root for each normal stress distribution. To emphasize, the local damage zone distance should be localized in a region with a small gradient so that the minimum of  $\chi$  could be considered. It corresponds to the upper bound of zone II

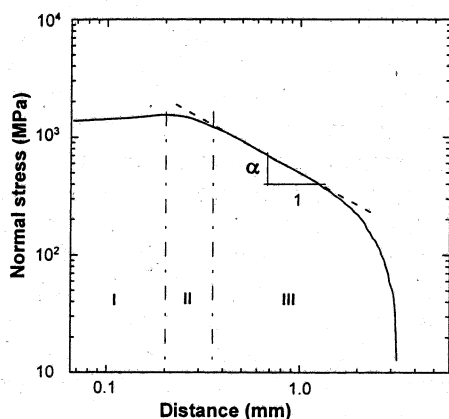


Fig. 1. Variations of normal stress with distance from notch root.

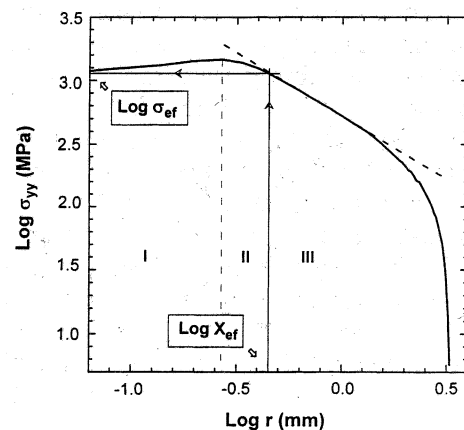


Fig. 2. Log-log plot of normal stress distribution for defining the local damage zone.

while the distance to the notch root corresponds to the effective distance  $X_{ef}$ . The corresponding normal stress  $\sigma_{ef}$  is as given in Fig. 2.

According to the present approach, fracture is assumed to initiate from a notch when  $\sigma_{ef} > \sigma_f$  acting over the distance  $X_{ef}$  that corresponds to the minimum stress gradient curve,  $\chi_{min}$ . Since the distance  $\chi_{ef}$  might be affected by the microstructure, experimental results are needed to analyze the assumed criterion.

### 3. Experimental procedures

#### 3.1. Material characteristics

A CrMoV rotor steel is used for the experiments. Its chemical composition can be found in Table 1. Two types of microstructures are selected.

They consist of ferrite with fine carbides (FC-bainite tempered for 2 h at 680°C) and ferrite with coarse carbides (CC-bainite tempered for 10 h at 72°C). The microstructure material parameters are given in Table 2. A more detailed of the material description is given in Ref. [11]. In Table 2,  $d_{AG}$  is the original austenitic grain size,  $d_p$  the packet size, and  $d_c$  the mean value of the carbide size. Here,  $d_c(c)$  falls into the 95% percentile of carbide diameter distribution. Moreover, HV10 is the Vickers hardness,  $R_p(0.2)$  the yield strength,  $R_m$  the ultimate tensile strength, and CVN the Charpy V-notch impact energy at room temperature. FATT stands for the fracture appearance transition temperature corresponding to the temperature at which 50% of the fracture surface has a

fibrous appearance. Temperature dependency of CVN the impact energy were also observed.

#### 3.2. Mechanical testing

Tensile properties and true stress–strain curves have been determined using cylindrical specimens with a diameter of 6 mm. Data are taken for a temperature range of  $-196$  to  $200^\circ\text{C}$  at a cross-head speed of 2 mm/min. The lower yield stress value  $R_{eL}$  corresponds to the 0.2% proof stress  $R_p(0.2)$ . Temperature dependency of fracture toughness is also evaluated for precracked three-point bend specimen for a cross head speed of 1 mm/min. The dimensions are 25 mm thick with a loading span of 120 mm. Refer to [11,17] for the evaluation of the fracture properties. The Charpy V-notch specimen has a root radius of 0.25 mm. The temperature in the lower shelf region corresponds to that below the general yield transition temperature  $t_{GY}$  at which the fracture force and general yield force coincide. Data for seven bend specimens were obtained for each material. Recorded are the maximum force  $F_M$ , the fracture force  $F_{FR}$ , and the general yield force  $F_{GY}$  for the selected temperature of interest.

#### 3.3. Fractography

For the CVN specimens tested below the general transition temperature  $t_{GY}$ , the distances between the fracture initiation sites and the notch root were found using the scanning electron microscope (SEM). The location through the thickness of the specimen was also obtained. Assessed also is the effect of microstructure on cleavage nucleation, i.e., the origin of failure initiation. Microstructural parameters were determined by SEM on sections perpendicularly to the fracture surfaces. Thin foils and carbide extraction replicas were also examined.

Table 1  
Chemical composition of CrMoV steel of rotor by wt%

C	Mn	Si	P	S	Cr	Mo	V
0.23	0.64	0.28	0.022	0.028	1.23	0.55	0.16

Table 2  
Microstructural parameters for CrMoV steel

State	Tempering	$d_{AG}$ ( $\mu\text{m}$ )	$d_p$ ( $\mu\text{m}$ )	$d_c$ ( $\mu\text{m}$ )	$d_c(c)$ ( $\mu\text{m}$ )	HV10	$R_p(0.2)$ (MPa)	$R_m$ (MPa)	CVN impact energy (J)	FATT ( $^\circ\text{C}$ )
FC	680°C/2 h/AC	29	15	0.09	0.09	278	771	886	18	110
CC	720°C/10 h/AC	29	12	0.17	0.17	200	511	644	51	50

#### 4. Finite element calculations

The stress distribution near a V-shaped notch is obtained from a finite element calculation for the Charpy specimen at  $-80^{\circ}\text{C}$  for FC and  $-150^{\circ}\text{C}$  for CC in the lower shelf region. The plane strain condition is assumed for the incremental elastic–plastic analysis [17] with the Von Mises yield condition. The software package corresponds to ANSYS 5.1 (IPM) and CASTEM 2000 (LFM). Determined are  $X_{ef}$ ,  $\sigma_{ef}$  and  $\sigma_f^*$  (cleavage fracture stress) while  $r_c$  and  $r_{c\ min}$  were measured.

#### 5. Discussion of results

##### 5.1. Fracture behaviour of CVN bend specimens

Displayed in Fig. 3(a) and (b) are the variations of the general yield force  $F_{GY}$ , the fracture force

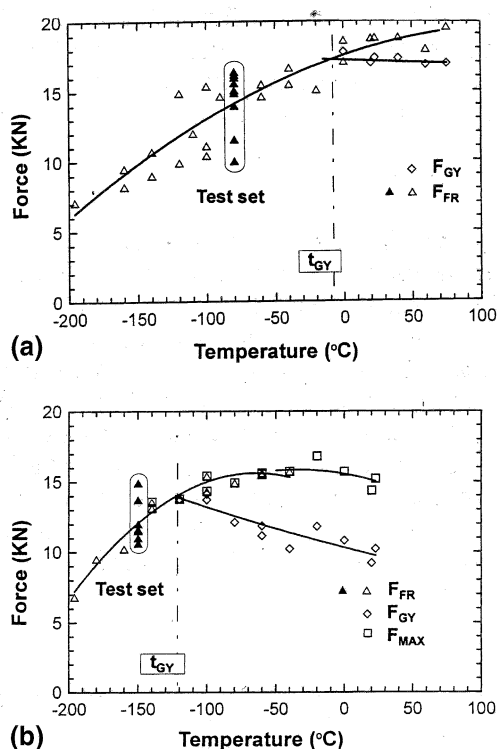


Fig. 3. Temperature dependency of forces obtained from CVN specimen data. (a) FC microstructure, and (b) CC material.

$F_{FR}$ , and the maximum force  $F_{max}$  with temperature. The solid data points are those obtained in this study. For coarse carbides (CC), lower general yield force  $F_{GY}$  are obtained for lower general yield transition temperature,  $t_{GY}$ . Such a trend prevailed for both materials. This includes the shift of the transition region to higher temperatures and decrease of resistance against brittle fracture for the CC material [11].

The afore-mentioned findings are supported by the fractographic observations.

At lower magnification, the fracture surface of the CVN bend specimen exhibited macroscopic river patterns. For the microstructure with fine carbides, this pattern originates from a small spot on the fracture surface, Fig. 4(a) which contains one or a few cleavage facets. For microstructure with coarse carbides, the river patterns are traced to the initiation region Fig. 5(a). In both cases, the centre of the river pattern was assumed to coincide with the origin of cleavage initiation.

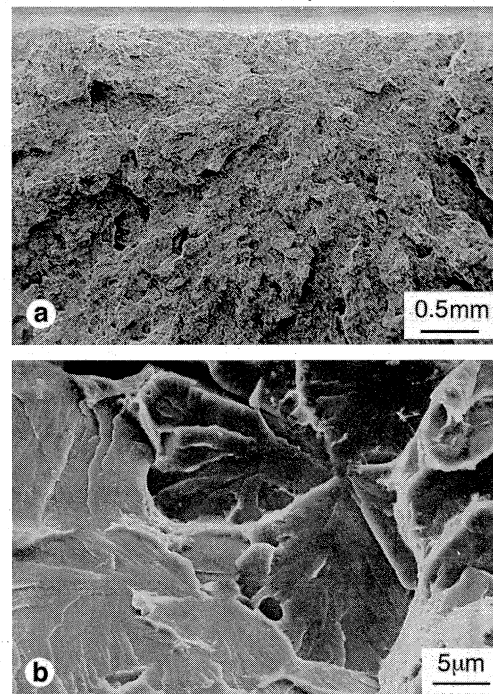


Fig. 4. Fracture appearance of CVN specimen. (a) FC material at  $-80^{\circ}\text{C}$  and (b) detail of nucleating facet.

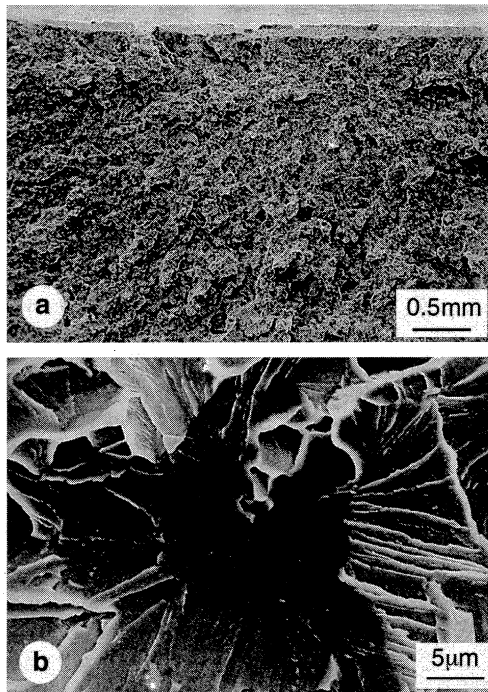


Fig. 5. Fracture appearance of CVN specimen. (a) CC material at  $-150^{\circ}\text{C}$  and (b) detail of nucleating facet.

At higher level of magnification, four fracture initiation sites could be identified:

- (i) For the FC microstructure, no distinct initiation site were found on one cleavage facet, Fig. 4(b). The average facet size was about  $20\text{--}30\ \mu\text{m}$ . Dislocation micromechanisms of cleavage were assumed.
- (ii) Two or three facets arrangement were found at the initiation site. A facets had no clear initiation site. Cleavages starting from grain boundaries or triple points were assumed.
- (iii) Facets with one large or with a few smaller inclusions appear to be located in the middle of the facet.
- (iv) Cleavage facets with carbide particles correspond to an increase of metal content in particles in comparison with the matrices. The presence of carbide were assumed to be the cause of cleavage initiation. This is observed in heavy temperature microstructures for coarse carbides, Fig. 5(b).

With an increase of carbide diameter, significant changes in the cleavage micromechanism and macroscopic appearance of fracture surface were observed. The fracture appearance changes morphology with a single initiation site in Fig. 6(a) for FC materials to one with more multiple initiation sites in Fig. 6(b) for CC materials. The cause of dislocation is assumed for initiation cleavage in FC while carbide is the cause for cleavage in CC materials. The former corresponds to the weakest link concept. That is the failure of one weak link leads to an unstable fracture. Fracture of materials with the CC microstructure correlates well with the concept of critical damage sites. With sufficient number of damage sites activated, unstable cleavage failure will presumably follow.

### 5.2. Local damage zone

The critical of minimum stress gradient being assumed to prevail in a localized region of high stress. Eq. (2) has been applied to determine the local damage zone distance  $X_{ef}$ . The corresponding stress distributions are displayed in Fig. 7 on a logarithmic scale for both materials. In both cases, the value for  $X_{ef}$  is greater than the plastic zone diameter. The local damage zone distance can be found in Table 3 for steel with the finer carbides (FC) and Table 4 for steel with the coarse carbide particles (CC).

A comparison of the calculated local damage distance with that measured are plotted in Fig. 8. They are within a scatter band of  $\pm 0.1\ \text{mm}$  which

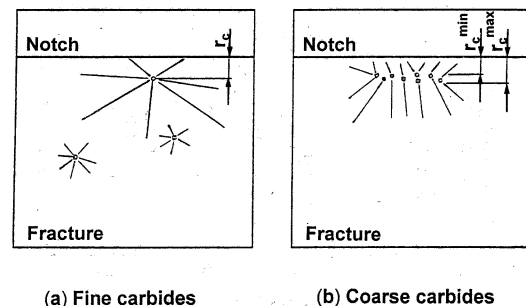


Fig. 6. Initiation micromechanism. (a) FC material (weakest link) and (b) CC material (damage accumulation).

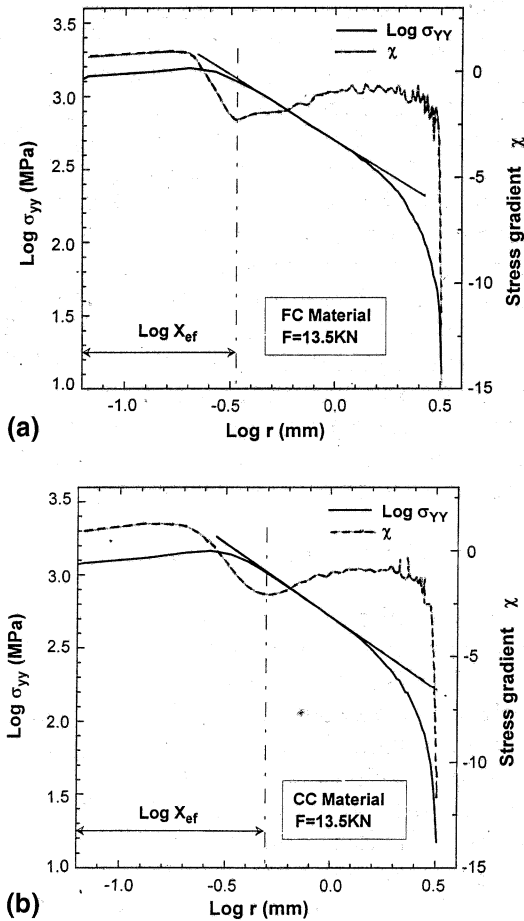


Fig. 7. Stress distribution at notch root together with stress gradient versus distance from notch tip (a) for FC material and (b) for CC material.

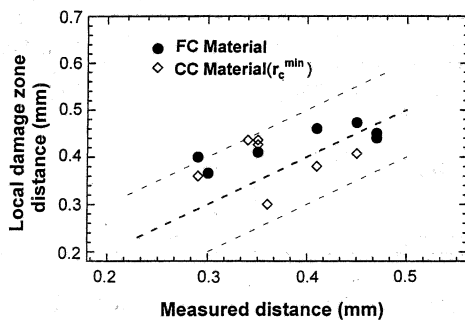


Fig. 8. Calculation distance,  $X_{ef}$ , and measured distance  $r_c$  from notch root for FC and CC material.

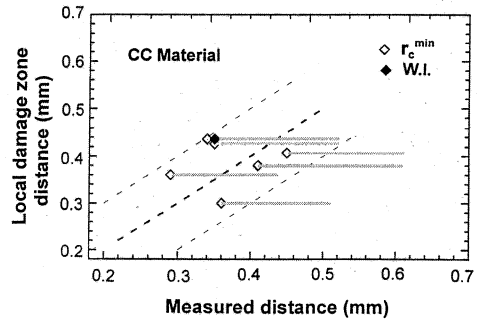


Fig. 9. Calculation distance  $X_{ef}$  versus measured minimum distance of initiation site  $r_c^{min}$  from notch root for CC material.

indicates that the agreement between analysis and test is good. Referring to Fig. 9, the horizontal scatter bars represent the width of initiation region which corresponds to the distances  $r_c^{min}$  and  $r_c^{max}$  in Fig. 6. In almost all cases, the mean and maximum values are outside of the scatter band of  $\pm 0.1$  mm. The solid data point in Fig. 9 represents the weakest link micromechanism of initiation.

### 5.3. Damage zone stress

Damage zone  $\sigma_{ef}$  corresponds to the distance  $X_{ef}$  in Fig. 2. Their values are summarized in Tables 3 and 4. For comparison, the local tensile stress  $\sigma_f^*$  (and the distance  $r_c^{min}$  and  $r_c^{max}$  are also given. This gives a correlation between  $X_{ef}$  and  $r_c$  as shown in Fig. 8.

For the FC microstructure, the mean value of  $\sigma_{ef}$  is 1206 Mpa which compares well with the local tensile stress of 1310 Mpa at fracture. Similarly, for the CC microstructure,  $\sigma_{ef}$  equals to 991 Mpa and the local tensile stress is 1001 Mpa.

## 6. Conclusions

Experimental support is provided for the local damage zone distance as a criterion of fracture initiating from notches. Two microstructures are considered for cleavage type of fracture. Stress gradient near notches is found to play an important role in the initiation of brittle fracture.

Good correlation is found for the calculated and measured values of the local damage zone

Table 3  
Fracture parameter data for FC material

Specimen number	$F_{FR}$ (kN)	$r_c$ (mm)	$X_{ef}$ (mm)	$\sigma_f^*$ (Mpa)	$\sigma_{ef}$ (Mpa)	$\alpha$ (–)
43	11.6	0.30	0.37	1109	924	0.89
22	12.5	0.29	0.40	1288	1000	0.91
27	13.5	0.35	0.41	1212	1120	0.92
45	14.7	0.47	0.44	1413	1270	0.94
36	14.9	0.47	0.45	1226	1300	0.94
25	15.6	0.41	0.46	1466	1400	0.95
20	16.0	0.45	0.47	1460	1430	0.96

Table 4  
Fracture parameter data for CC material

Specimen number	$F_{FR}$ (kN)	$r_c^{\min}$ (mm)	$r_c^{\max}$ (mm)	$X_{ef}$ (mm)	$\sigma_f^*$ (Mpa)	$\sigma_{ef}$ (Mpa)	$\alpha$ (–)
34	10.2	0.36	0.51	0.300	1089	990	0.85
10	11.6	0.29	0.44	0.360	1203	1070	0.89
8	12.0	0.41	0.61	0.380	1010	1110	0.9
7	13.1	0.45	0.61	0.407	1106	1230	0.93
13	13.3	0.35	0.52	0.426	1285	1250	0.93
15	13.7	0.34	0.52	0.436	1320	1290	0.95
9	14.4	0.35	0.436	0.436	1328	1360	0.96

distance. The data lie within a scatter band of  $\pm 0.1$  mm. The damage zone stress compares well with the cleavage fracture stresses.

The local damage zone does not appear to be sensitive to change in fracture mechanism from one of the weakest link to that of damage accumulation.

#### Acknowledgements

This work is supported by Barrande project Nr. 97022. Acknowledgement is also due to the Research Grant Agency of the Czech Republic under grant number 101/96/K264.

#### References

- [1] J.H. Chen, G.Z. Wang, Z. Wang, L. Zhu, Y.Y. Gao, Further study on the scattering of the local fracture stress and allied toughness value, *Met. Trans.* 22A (1991) 2287–2296.
- [2] L. Niu, C. Chehimi, G. Pluvinage, Stress field near a large blunted V-notch and application to the concept of the critical notch stress intensity factor to the fracture toughness of very brittle materials, *Engrg. Fract. Mech.* 49 (N3) (1994) 325–335.
- [3] R.O. Ritchie, J.F. Knott, J.R. Rice, On the relationship between critical tensile stress and fracture toughness in mild steel, *J. Mech. Phys. Solids* 21 (1973) 395–410.
- [4] A.J. Krasovsky, G. Pluvinage, Minimal resistance of engineering materials to brittle fracture as predicted by local approach, *J. de Physique III 6 (C6)* (1996) 215–244.
- [5] J.F. Knott, Effects of notch depth on the toughness of mild steel, in: P.L. Pratt (Ed.), *Proceedings of the Second International Conference On fracture*, Brighton, 1969, pp. 205–218.
- [6] T. Lin, A.G. Evans, R.O. Ritchie, Stochastic modelling of the independent role of particle size and grain size in transgranular cleavage fracture, *Met. Trans.* 18A (1987) 641–651.
- [7] A. Mathin-Meizoso, Modelling cleavage fracture of bainitic steels, *Acta Metall. Mater.* 42 (1994) 2057–2068.
- [8] E. Smith, The nucleation and growth of cleavage microcracks in mild steel. in: *Proceedings of the Conference on Physical Basis of Yield and Fracture*, Institute of Physics, Oxford, 1996, pp. 36–45.
- [9] N.J. Petch, The influence of grain boundary carbide and grain size on the cleavage strength and impact transition temperature of steel, *Acta Metal.* 34 (1986) 1387–1394.
- [10] P. Bowen, J.F. Knott, Some observations on the assessment of short, sharp cracks at the roots of blunt notches, and their effect on brittle fracture, *Internat. J. Fract.* 28 (1985) 103–117.
- [11] I. Dlouhý, V. Kozák, M. Holzmann, The susceptibility of local parameters to steel microstructure evaluated using charpy type specimen, *J. de Physique III C 6* (1996) 205–214.

- [12] D. Curry, Influence of hydrostatic tension on cleavage fracture of bainitic pressure vessel steel, *Met. Sci.* 16 (1982) 435–440.
- [13] F.M. Beremin, A local criterion for cleavage fracture of nuclear pressure vessel steel, *Metall. Trans.* 14A (1983) 2277–2287.
- [14] B. Strnadel, Modelling of fracture events in structural steels, Thesis for Doctor of Science Degree, Technical University of Ostrava, 1995.
- [15] G. Angot, G. Pluinage, About Notch Fracture Mechanics. in: *Proceedings of the Second Copernicus Workshop Influence of Local Stress and Strain Concentrators on the Reliability and Safety of Structures*, 1996, pp. 37–47.
- [16] G.C. Sih, J.W. Ho, Sharp notch fracture strength characterized by critical energy density, *J. Theoret. Appl. Fract. Mech.* 16 (1991) 179–214.
- [17] L. Válka, M. Holzmann, I. Dlouhý, The role of microstructure in brittle fracture behaviour of low alloy tempered bainitic steel, *Mater. Sci. Engrg. A* 234–236 (1997) 723–726.

A5 Vlček, L., Chlup, Z., and Kozák, V., Problems in Q-parameter calculation, NATO Science Series: Mathematics, Physics and Chemistry 78, book *Transferability of Fracture Mechanical Characteristics*, ed. Dlouhý, (2002), 79-92.

## PROBLEMS IN Q-PARAMETER CALCULATIONS

L. VLČEK, Z. CHLUP, V. KOZÁK

*Institute of Physics of Materials, Academy of Science of the Czech Republic, CZ-61662 BRNO, Žižkova 22*

**Abstract:** The present work deals with determination of the sensitivity detached parameters describing fracture behaviour of body with crack with respect to the character change of true stress-strain curve. The typical low carbon cast steel stress-strain curve with dominant region of Lüders deformation was exerted. This paper presents the consideration on the change judgement of J-integral and Q-parameter as the base parameters of two parameters fracture mechanics. The attention is paid on the influence of deformation hardening exponent of the idealised true stress-strain material curve described by the Ramberg-Osgood relation to Q-parameter. All computations are based on the 3D elastic-plastic analyses using FEM and supported by mechanical tests.

**Keywords:** stress-strain curve, deformation hardening, J-integral, Q-parameter, finite element method

### 1. Introduction

It seems that for transferring fracture-mechanical data from test specimens to exposed real constructions or to its monitored parts, it is necessary to use two-parameter fracture approach. This requirement involved large investigations, which are considered of the constraint influence near the crack tip to fracture behaviour. Recent extensive investigations on crack tip constraint effects provide a necessity of testing various constraint configurations, such as shallow-cracked SEN(B) specimens. The present paper is contributing to assessment of the influence of constraint effect near the crack tip to fracture parameters.

Determining static fracture toughness of SEN(B) specimens is one of the basic fracture mechanics test. As a result of this test are significant values of static fracture toughness, which depends upon temperature. It must be emphasised that the most important values are critical K-value, in case of using linear-elastic fracture mechanics and critical value of J-integral, in case of using elastic-plastic fracture mechanics. Subsequently we confine our investigation to elastic-plastic material behaviour.

Standard assessments of elastic-plastic fracture behaviour in large engineering structures using laboratory specimen data employ a one-parameter characterization of loading and toughness, most commonly the J-integral or the corresponding value of the Crack Tip Opening Displacement (CTOD). Fracture toughness measured on one specimen size can be directly at some circumstances transformed to another geometry. This approach can be valid only in the case of small scale yielding (SSY).

Experimental measurements have shown significant elevations in the elastic-plastic fracture toughness in the transition region for shallow crack specimens of ferritic steels. This apparent increased toughness of ferritic steels has enormous practical implication in defect assessment. Elastic-plastic stress fields along the crack front depend strongly on the specimen geometry, size, loading mode and material flow properties. A more realistic description of crack tip stress and deformations fields has been developed. Approaches are based on two-parameter characterization of crack tip fields, such T-stress and Q-stress. In both approaches, J sets the magnitude of near tip deformation, while the second parameter characterizes the level of stress triaxiality. These J-T and J-Q approaches retain contact with traditional fracture mechanics. Laboratory measurements on the specimens with varying crack length (changing the relation  $a/W$ ) and with the same ligament showed increasing values of fracture toughness expressed using  $J_c$  versus decreasing crack length. Following the idea of Sumpter [1], Kirk and Dodds [2] investigated several possibilities of J-integral and CTOD estimation for SEN(B) specimens with shallow crack. Presented results summing up that critical values of J-integral and CTOD obtained on SEN(B) specimens with different crack length are comparable due to establishing parameter  $\eta_p$ , where  $J = J_{el} + J_{pl}$  and  $J_{pl} = \eta_p U_p / Bb$ . This parameter is depended on ratio  $a/W$  and represents the influence of crack length on fracture toughness. For standard crack length is  $\eta_p = 2$ .

For fracture toughness valuation on the basis of two-parameter fracture mechanics the evaluation of parameters, which expresses this constraint ahead the crack tip in our case Q-parameter, is critical. Several approaches exist:

- a) On the base of experimentally determined dependence  $J_c$  on  $a/W$  the Q calculation comes after from numerically given stress fields received by FEM for every analysed body separately. This approach is time consuming due to experimental work and next modelling and computation.
- b) Statistical approach using so called local approach [3]. We limit our focus to a stress controlled, cleavage mechanism for material and adopt the Weibull stress ( $\sigma_w$ ) as the local parameter to describe crack-tip conditions. Unstable crack propagation occurs at a critical value of ( $\sigma_w$ ) which may be attained prior to or following some amount of stable, ductile crack extension [4].
- c) Function  $J_c(Q)$  can be found on the basis of so called toughness scaling models. The procedure focuses on an application of the micromechanical model to predict specimen geometry and crack effects on the macroscopic fracture toughness  $J_c$ . Dodds [5] and Anderson [6]. The procedure requires attainment of equivalent stressed volumes ahead of a crack front for cleavage fracture in different specimens. The D-A model does not reflect such variations, with equal weight attributed to all material volumes having  $\sigma_1/\sigma_o > \sigma_c$ . This can be done e.g. on the base of Weibull stress, because the Weibull stress incorporates both the effects of stressed volume (as in the D-A model) and the potentially strong changes in the character of the near tip stress fields due to constraint loss and ductile crack extension [7].

The present analyses are generally based on the FEM calculations. To obtain the correct values of stress-strain fields using real materials model seems to be fundamental for effective numerical analysis. As an experimental material manganese cast steel was used (ČSN 42 2707). Two procedures, how to approximate the stress-strain curve, were used. The first model describes how to more precisely express the real curve

(experimentally determined) using the incremental theory of plasticity. The curve can be divided into three basic parts. The initial part is linear elastic, next is the part of dominant Lüders deformation and the last part for deformation hardening. The second model is based on the deformation theory of plasticity and constitutes continual hardening material.

The change estimation dependence of J integral and Q parameter on the material stress-strain curve can be very expressive. Therefore this study describes a computational framework to quantify the influence of the stress-strain approximation to the J integral values and Q parameter. The stress is put onto the ability of using the deformation theory of plasticity, which actually describes not correctly the materials with dominant yield stress area, with comparison to incremental theory of plasticity. The reason why to use this approximation is given by the capability of finite elements to transport the high values of plastic strain. The next problem, which is solved, is the selection of proper value of deformation hardening exponent to the stress-strain field ahead the crack tip and to the force-displacement diagram.

## 2. Q-parameter Theory and its Determination

Two-parameter approaches to elastic-plastic fracture mechanics were introduced to remove some of the conservatism inherent in the one-parameter approach based on the J integral and to account for observed size effect on fracture toughness. This paper presents the consideration on the change judgement of J-integral and Q-parameter as the base parameters of two-parameter elastic-plastic fracture mechanics. Q-parameter is the second parameter in two-parameter approach and it is used for describing constraint effect near the crack tip. In accordance with [8], [9] Q-parameter is defined at point  $\theta=0$ ,  $r=2J/\sigma_0$  as the participation of difference stress field  $(\sigma_{ij})_{diff}$  and yield stress  $\sigma_0$ :

$$Q = \frac{(\sigma_{ij})_{diff}}{\sigma_0} = \frac{(\sigma_{ij}) - (\sigma_{ij})_{ref}}{\sigma_0} \quad (1)$$

It is possible to say [10], [15] that difference stress field is constant in region  $r < J/\sigma_0$ ,  $5J/\sigma_0 >$  for  $\theta \leq \pi/2$ . This stress value is difference between real stress fields, which are obtained usually from numerical analyzes, and reference stress field. Different methods of the Q-parameter computation are given by using different types of reference stress fields. The most commonly used approaches for obtaining reference stress field values are boundary layer method (BLM) [10], [12] and method that is based on using HRR solution. The second one arises from works of Hutchinson [13], Rice and Rosengren [14], who generalized Williams' solution (for linear elastic material) into nonlinear hardening material. Its behavior is determined by deformation theory of plasticity.

### 2.1. HRR SOLUTION

Determination technique of the difference stress field is based on elastic-plastic solution of the specimen with crack. Thus, the real stress  $(\sigma_{ij})$  near the crack tip is given as an

approximate stress in case that sufficiently fine mesh was used. In accordance with [9] the difference stress field is given by the relation:

$$(\sigma_{ij})_{diff} = (\sigma_{ij}) - (\sigma_{ij})_{HRR} \quad (2)$$

where  $(\sigma_{ij})_{HRR}$  is the reference field stress. Values of the reference stress are tabulated as a function of stress intensity factor  $K_I$ , yield stress  $\sigma_0$  and deformation hardening coefficient  $n$ . The value of the Q-parameter is:

$$Q = \frac{(\sigma_{\theta\theta}) - (\sigma_{\theta\theta})_{HRR}}{\sigma_0} \quad (3)$$

Advantage of this method is the fact that  $(\sigma_{\theta\theta})_{HRR}$  values are tabulated, but only for a small range of specimens with simple geometry. To the contrary the disadvantage of this method could be the fact that the material behavior is not described well.

## 2.2. BOUNDARY LAYER METHOD (BLM)

BL method is suitable for any types of geometry configurations. This method is based on analysis of the maximal principal stress ahead of the crack tip using finite element method (FEM). The small local analyzed area with the crack is removed from the whole body (*Figure 1*). The size of the area has to be chosen efficiently because of generating small scale yielding (SSY) conditions on the boundary of this area. The boundary conditions are given by displacements from elastic solution of the whole body [10]:

$$u = \frac{K_I(1+\nu)}{E} \sqrt{\frac{r}{2\pi}} \cos \frac{\theta}{2} (3 - 4\nu - \cos \theta) \quad (4)$$

$$v = \frac{K_I(1+\nu)}{E} \sqrt{\frac{r}{2\pi}} \sin \frac{\theta}{2} (3 - 4\nu - \cos \theta) \quad (5)$$

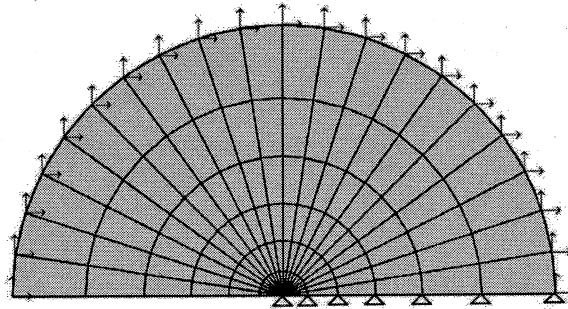


Figure 1. Schema of BL model

where  $u$ ,  $v$  are displacements in directions of  $X$  and  $Y$  in Cartesian system of coordinates,  $K_I$  is stress intensity factor, which was determined from Rice's  $J$  integral,  $E$  is Young's modulus and  $\nu$  is Poisson's ratio.

As follows the elastic-plastic calculation for the whole body with crack is solved to obtain values of the "real" stress. The difference stress field is given by:

$$(\sigma_{ij})_{diff} = (\sigma_{ij}) - (\sigma_{ij})_{SSY} \quad (6)$$

where  $(\sigma_{ij})$  is real stress in the specimen, which is determined by using elastic-plastic FEM solution and  $(\sigma_{ij})_{SSY}$  is reference stress field, which is determined from BLM calculation. In accordance with works of [9] and [10] there are two definitions for  $Q$ -parameter computation:

$$Q = \frac{(\sigma_{\theta\theta}) - (\sigma_{\theta\theta})_{SSY}}{\sigma_0}, \quad Q_m = \frac{(\sigma_m) - (\sigma_m)_{SSY}}{\sigma_0} \quad (7, 8)$$

for  $\theta=0$ ,  $r=2J/\sigma_0$ , where  $(\sigma_{\theta\theta})$  is stress in cylindrical system of coordinates and for  $\theta=0$  it is the same value as  $(\sigma_{yy})$  in Cartesian system of coordinates and

$$\sigma_m = \frac{1}{3}(\sigma_{xx} + \sigma_{yy} + \sigma_{zz}) \quad (9)$$

where  $\sigma_{xx}$ ,  $\sigma_{yy}$ ,  $\sigma_{zz}$  are stresses in particular axis in Cartesian system of coordinates.

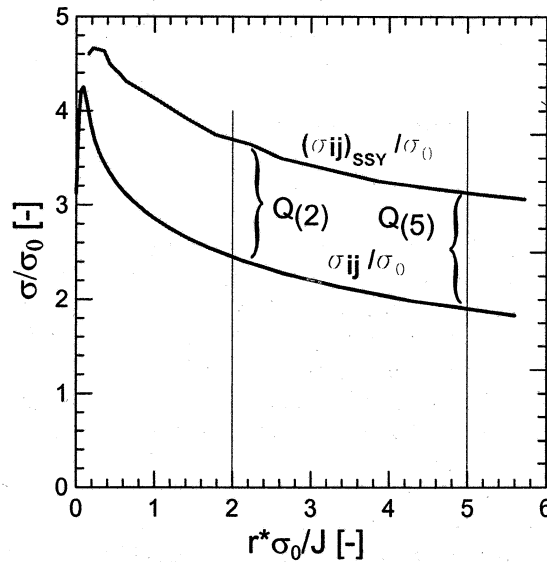


Figure 2. Schema of  $Q$ -parameter determination

The theory said that  $Q$ -parameter value is constant on defined interval, but in fact the distance between  $Q_{(2)}$  and  $Q_{(5)}$  have to be less than 10 % (see Figure 2).

### 3. Problem and Aim Formulations

For numerical simulation it is necessary to determine model geometry, boundary and load conditions, as well as the way of material model. Three sets of SEN(B) specimens were tested and modelled. The geometry of the specimens is shown in *Figure 3* and its characteristic dimensions are in the TABLE I (all values are in mm).

TABLE I. Dimensions of test specimen

	$a/W=0.1$	$a/W=0.2$	$a/W=0.5$
L	120	140	250
B	25	25	25
W	26	30	50
a	2.5	7	25.25
l	104	120	200

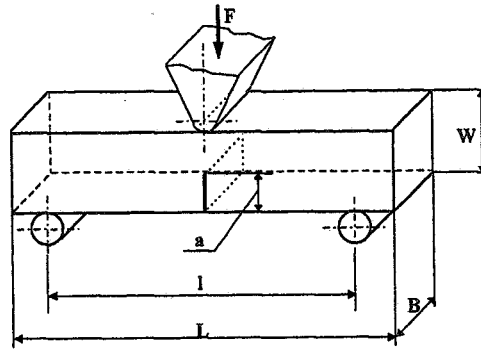


Figure 3. The test specimen

The generalised material behaviour considered in this study is that typically found in low carbon steels. The elastic part is followed by a perfect plateau (this part is commonly called Lüders deformation) and part with work hardening (see *Figure 4*). There are two ways in computational system Abaqus, which can be used for describing material behaviour. The first one is to use deformation theory of plasticity. This material model is trouble-free for numerical calculations. In that case Ramberg-Osgood well-known relation defines material. The second one describes material by using incremental theory of plasticity.

The main question is to show the influence of the stress-strain curve approximation on the fracture parameters. The aim of presented work is confrontation of fracture parameters, which are used for assessment pre-cracked bodies in three-point bending. Attention is paid on the influence of deformation hardening exponent to the history of the idealised true stress-strain material curve.

#### 4. Experiments and Modelling

As an experimental material C-Mn cast steel was used. This material was modelled as homogenous and isotropic with elastic constants  $E=2,05 \cdot 10^5$  MPa and  $\nu=0.3$ . The average value of yield stress was 360 MPa. The testing temperature was  $-100$  °C.

In the case of using incremental theory of plasticity the curve  $\sigma$ - $\epsilon$  was modelled by 23 points, which were connected to linear parts. These points belong to experimental measured stress-strain curve.

In the case of using deformation theory of plasticity material was described by Ramberg-Osgood relation:

$$\frac{\epsilon}{\epsilon_0} = \frac{\sigma}{\sigma_0} + \alpha \left( \frac{\sigma}{\sigma_0} \right)^n \quad (10)$$

where  $n$  is hardening exponent,  
 $\alpha$  is hardening coefficient,  
 $\epsilon_0$  is yield strain,  
 $\sigma_0$  is yield stress.

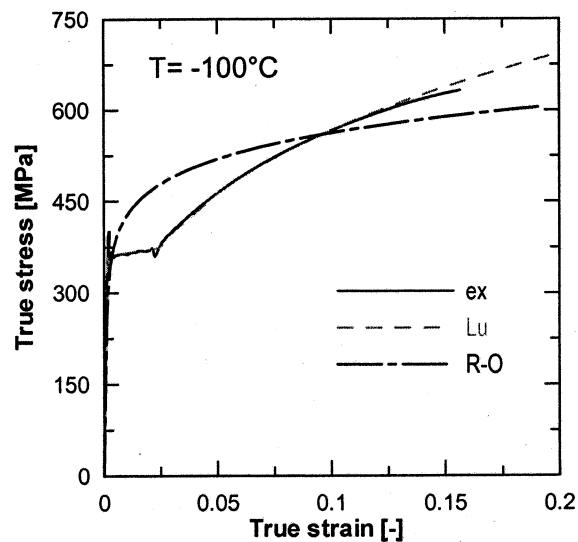
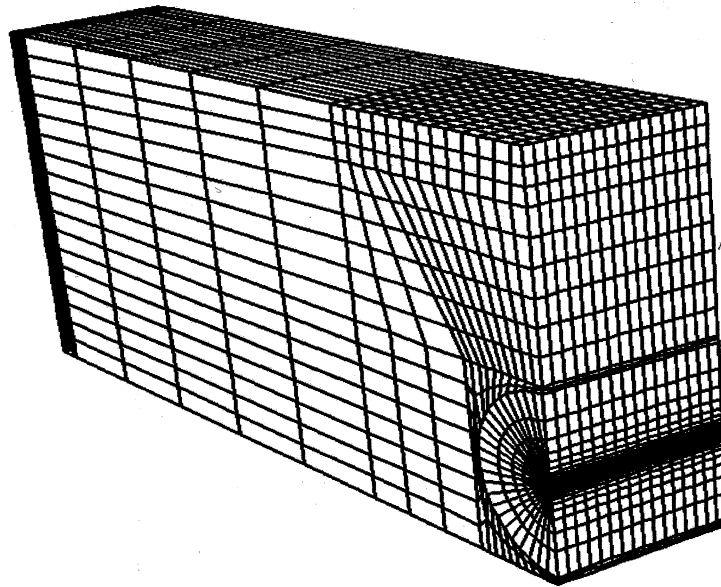


Figure 4. True stress-strain curve

All computations are based on 3D elastic-plastic analysis using FEM, concretely Abaqus version 6.1. 3D model of specimen is shown in the Figure 5. It is only one quarter of real body because of using two planes of symmetry. Models were meshed with eight-node hybrid elements provided by the finite element code Abaqus. 15 680 of elements (C3D8H) were used, which means 17884 nodes. The figure below (Figure 6) shows the detail with the crack. All solutions have to be evaluated at a distance of  $cJ/\sigma_0$  ahead of the crack tip ( $c=1-5$ ). This region of interest is very small and stress and strain

gradients are steep. Hence, a very fine mesh is required. Element size is increased as the radial distance is increased from the crack front.

Outer radius of the area (*Figure 6*) is 0.1 mm and the crack tip radius was 0.01mm. Twelve elements were used for dividing this radius. Thus the characteristic element length was  $8,3 \cdot 10^{-4}$  mm. Ten elements in the direction of thickness were used.



*Figure 5.* 3D model with mesh

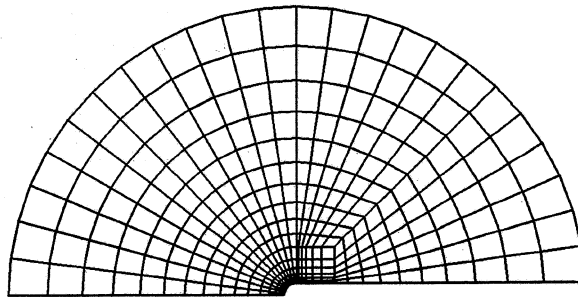


*Figure 6.* Detail of the crack tip

The real system consists of the specimen, the punch and rollers. These three parts are in contact and that is why the contact between the specimen and punch and between rollers was modelled. The length of elementary face and contact pressure were determined. 3D contact solutions need a long time for computation and that is why the equivalent pressure was applied on the equivalent face (*Figure 7*).

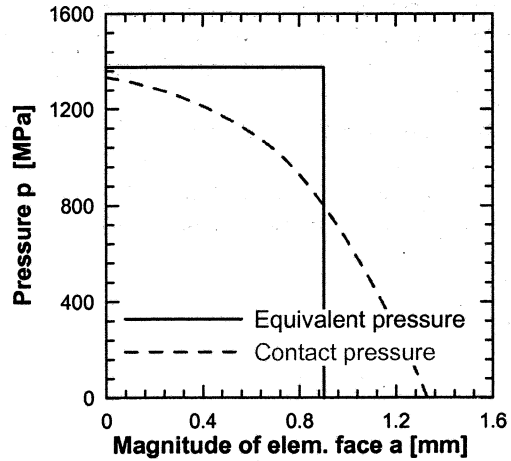


Figure 7. Contact and equivalent pressures ( $a/W=0.2$ )

Four calculations were solved for range of value  $n$  in case of using deformation theory of plasticity because of choosing the proper value  $n$ . In the *Figure 8* there are force-displacement curves for various numerical calculations. The bolt-dashed lines indicate high and low experimental dependencies. It seems that all progressions for linear area (force value to 40kN) are in good agreement with experimental values. To the contrary force-displacement relations are rather different for area with overvalue forces.

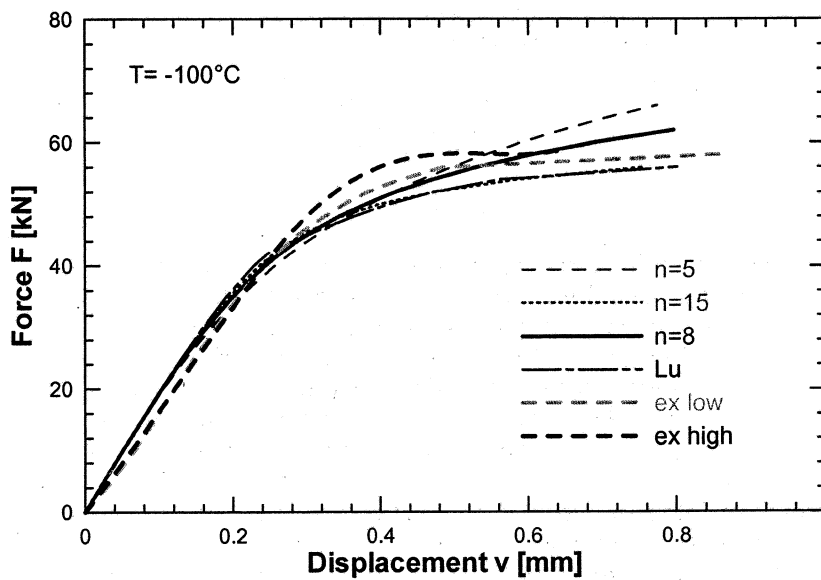


Figure 8. Force-displacement relation

The selection of proper value  $n$  was based on comparing the relations between force and displacement. After that value of hardening exponent  $n=8$  was applied as the best fit, as well as the value of hardening coefficient  $\alpha=1$ . Hence the model of continual hardening material was determined. Its behaviours are very similar as with real material with Lüders strain region. Fracture forces were in interval 35, 65, 75 kN for specimens with ratio  $a/W=0.5, 0.2, 0.1$ . In the case of modelling material behaviour by incremental theory of plasticity fracture forces were too high and solutions were not converged because of destruction of small elements near the crack tip due to achievement high values of plastic strain.

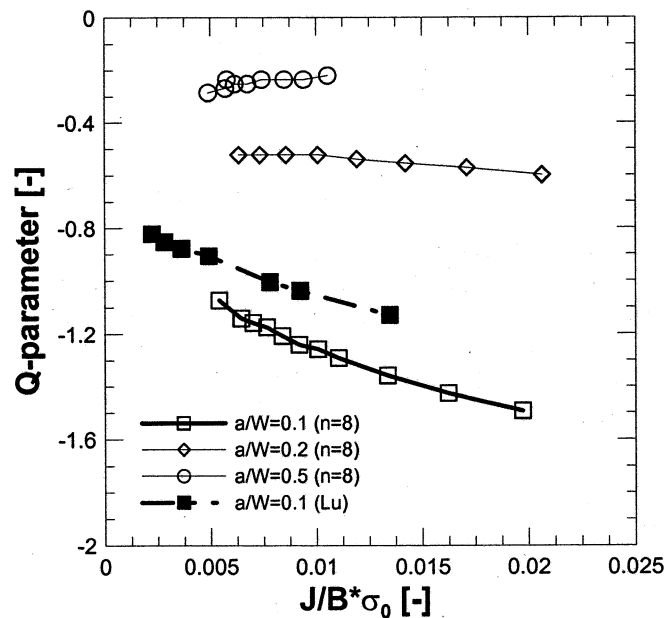


Figure 9. J-Q diagram

Results from numerical calculations are compared in the *Figure 9*. Apparently, there are differences between Q-values due to using two ways of modelling the same material. In this case, the incremental theory of plasticity could not be right because of numerical errors, which appeared near the crack tip. It must be emphasised, that Q-parameter value determined as odds between real stress from elastic-plastic solution and reference stress normalized by yield stress value could be taken as parameter for assessment bodies with crack, but only in case, that the same theory of plasticity and the same material stress-strain curve will be used.

Relation in the *Figure 10* was constructed for check calculation of the influence of the specimen geometry to maximal principal stress near the crack tip distribution. Distribution regions of maximal principal stresses from numerical calculations were constructed for fracture forces interval. Essentially, when the applied force increases, the global stress level increases as well. As to differences in maximal principal stresses

between specimens, at first maximal principal stress increases when crack length decreases ( $a = 25$  mm ( $a/W = 0.5$ ) and  $a = 7$  mm ( $a/W = 0.2$ )). After that the maximal principal stress decreases in case of specimen with shallow crack  $a = 2.5$  mm ( $a/W = 0.1$ ).

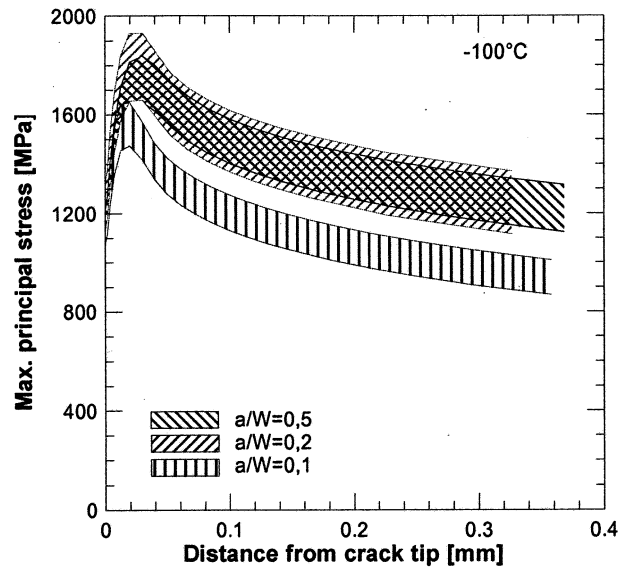


Figure 10. Maximal principal stresses vs. crack tip distance

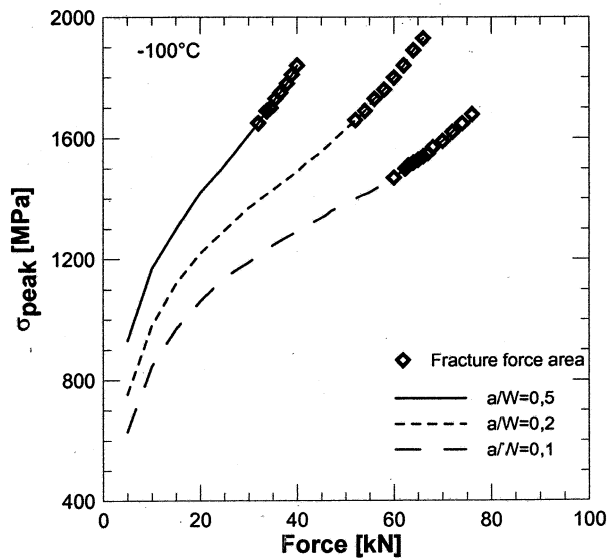


Figure 11. Force-stress relation

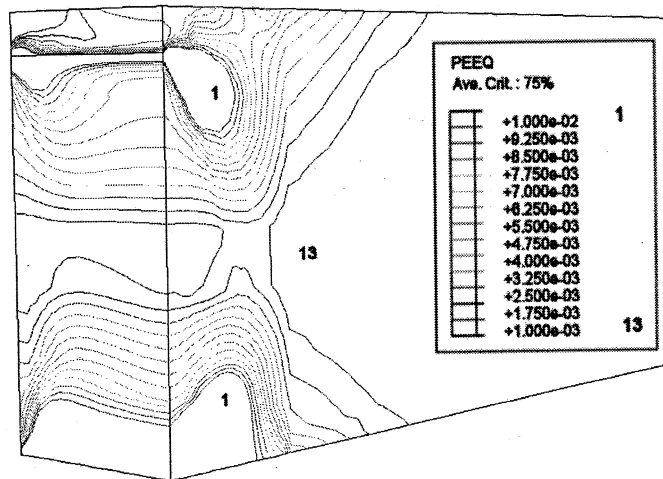
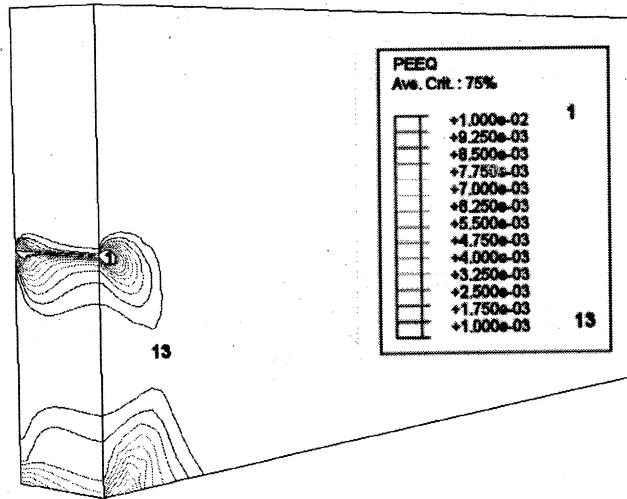


Figure 12. Plastic deformation for standard ( $a/W=0.5$ ) and small ( $a/W=0.1$ ) specimens

For better understanding stress trends ahead of the crack tip the relation between maximal stress values and fracture force level was constructed (*Figure 11*). These trends are given by changing boundary conditions near the crack tip. There are no changes in the direction of specimen thickness, because the same thickness of specimen and yield stress value is maintained. The same situation is in the direction of crack propagation, because the same ligament is sustained too. The main serious change is reducing material volume against of crack propagation direction. Plastic zone monitoring is remarkably interesting for systematic and complex assessment in sphere of elastic-plastic fracture mechanics. It stands to reason, that larger plastic zone appeared in case of shallow crack due to higher fracture forces. The magnitude of the plastic zone decreases with increasing crack length. Account of stress decreasing in case of shallow crack is not unambiguous. But the main difference between standard and small specimens is shown in the *Figure 12*. The plastic deformation is still closed in material of standard specimen, but to the contrary plastic deformation flows on the surface of small specimen and stress relaxation process is available.

## 5. Conclusions

It could be said that on the basis of numerical stress-strain analyses bodies with crack it may be possible to determine suitable substitution of "real" material by continuously hardening material model. This material model is trouble-free for all numerical applications. Remarkably significant is the fact that using of deformation theory reduced computational time more than ten times. Results obtained from incremental method could be remarkably inaccurate arising high plasticity near the crack tip. It must be stressed, that Q-parameter value determined as odds between real stress from elastic-plastic solution and reference stress normalized by value  $\sigma_0$  could be taken as parameter for assessment bodies with crack, but only in the case, that the same theory of plasticity and the same material stress-strain curve will be used in all solved problems. A new important piece of knowledge is the fact that the maximal principal stress ahead of the crack tip for the short crack specimen ( $a/W = 0.1$ ) is markedly lower to the other crack lengths. Geometric changes of specimens advert to possible change of the critical fracture stress. This hypothesis was sustained by fractography analysis of fracture surfaces, which extend approximately the same distances of initiation areas in all solved geometries.

## Acknowledgements

*This research was financially supported by grant 101/00/0170 Grant Agency of the Czech Republic and by project Nato SfP 972655 .*

## References

1. Sumpster, J. D. G. (1987)  $J_c$  Determination for Shallow Notch Welded Bend Specimens, *Fatigue and Fract. of Eng. Mater. Struct.* **10**, 479-493.

2. Kirk, M. T. and Dodds, R. H. (1993) J and CTOD Estimation Equations for Shallow Crack in Single Edge Notch Bend Specimens, *Journal of Testing and Evaluation* **21**, 228-238.
3. Beremin (1983) A Local Criterion for Cleavage Fracture of a Nuclear Pressure Vessel Steels, *Metallurgical Transaction*, **14A**, 2277-2287.
4. Kozák, V., Dlouhý, I. (1998) Local Approach and FEM, *Computer Assisted Mech. and Eng. Sci.* **5**, 193-198.
5. Dodds, R. D., Shih, C. F., Anderson, L. (1993) Continuum and Micromechanics Treatment of Constraint in Fracture, *Int. Journal. of Fract.* **64**, 101-133.
6. Dodds, R.H., Tang, M., Anderson, L. (1995) *ASTM STP 1299*, 101-133.
7. Ruggieri, C., Dodds, R. D. (1996) A Transferability Model for Brittle Fracture Including Constraint and Ductile Tearing Effects: a probabilistic approach, *International Journal of Fracture* **79**, 309-340.
8. Shih, C. F., O'Dowd, N. P. (1994) Two-Parameter Fracture mechanics: Theory and Applications, *Fracture Mechanics, ASTM STP 1207*, 21-47, 379-386.
9. Henry, B. S., Luxmoore, A. R. (1997) The Stress Triaxiality Constraint and the Q-Value as a Ductile Fracture Parameter, *Eng. Fracture Mech.* **57**, 375-390.
10. Nevalainen, M., Dodds, R.H. (1995) Numerical Investigation of 3-D Constraint Effects on Brittle Fracture, SE(B) and C(T) Specimens, *Int. J. of Fract.* **74**, 131-161
11. Shih, C. F., O'Dowd, N. P., Kirk, M. T. (1993) A Framework for Quantifying Crack Tip Constraint, Constraint Effects in Fracture, *ASTM STP 1171*, 2-20.
12. Landes, J. D. (1997) Application of a J-Q Model for Fracture in the Ductile-Brittle Transition, *Fatigue and Fracture Mechanics* **27**, *ASTM STP 1296*, 27-40.
13. Hutchinson, J. W. (1968) Singular Behaviour at the End of Tensile Crack Tip in a Hardening Material, *Journal of the Mechanics and Physics of Solids*, 13-31.
14. Rice, J. R., Rosengren, G. F. (1968) Plane Strain Deformation Near a Crack Tip in a Power-Law Hardening Material, *J. of the Mech. and Physics of Solids*, 1-12.
15. Anderson, T. L. (1995) *Fracture Mechanics Fundamentals and Applications, Second Edition CRC Press.*
16. Hibbit, Karlsson & Sorenson Inc. (2000) *ABAQUS User's Manual, Version 6.1.*
17. O'Dowd, N. P. (1995) Applications of two Parameter Approaches in Elastic-Plastic Fracture Mechanics, *Engineering Fracture Mechanics* **52**, 445-465.
18. Boothmann, D. P., Lee, M. M. K., Luxmoore, A. R. (1997) A Shallow Crack Assessment Scheme for Generalised Material Behaviour in Bending, *Engineering Fracture Mechanics* **57**, 493-506.
19. Zhang, Z. L., Thaulow, C., Hauge, M. (1997) Effects of Crack Size and Weld Metal Mismatch on the Haz Cleavage Toughness of Wide Plates, *Engineering Fracture Mechanics* **57**, 653-664.
20. Kim, Y. J., Schwalbe, K. H. (2001) On the Sensitivity of J Estimation to Materials' Stress-Strain Curves in Fracture Toughness Testing Using the Finite Element Method, *Journal of Testing and Evaluation* **29**, 18-30.
21. Chlup, Z. (2001) *Disertation, ÚFM AV ČR*
22. Pavankumar, T. V., Chattopadhyay, J., Dutta, B. K., Kushwaha, H. S. (2000) Numerical investigation of crack-tip constraint parameters in two-dimensional geometries, *Int. Journal of Pressure Vessels and Piping* **77**, 345-355.
23. Betegón C., Hancock J. W. (1991) Two-parameter Characterization of Elastic- Plastic Crack-Tip Fields, *Journal of Applied Mechanics* **58**, 104-110.

- A6 Kozák, V., Vlček, L., Influence of constraint effect on transferability of fracture mechanics characteristics, *Engineering Mechanics (2003)*, Praha: Institute of Theoretical and Applied Mechanic, čl. 321.

## INFLUENCE OF CONSTRAINT EFFECT ON TRANSFERABILITY OF FRACTURE MECHANICS CHARACTERISTICS

L. Vlček<sup>1</sup>, V. Kozák<sup>2</sup>

**Summary:** *This paper presents the consideration on the change judgement of  $J$ -integral and  $Q$  parameter as the base parameters of two-parameter elastic-plastic fracture mechanics. An extensive set of non-linear 3D FEM analyses of SE(B) specimens deals with crack front conditions, which are characterised in terms of  $J$ - $Q$  trajectories. Results of numerical simulations provide "effective" thickness, which can be used in statistical approaches.*

### 1. Úvod

Mezi základní materiálové charakteristiky ocelí patří hodnota lomové houževnatosti. Z inženýrského hlediska je houževnatost významnou vlastností konstrukčních materiálů, kterou lze obecně definovat jako schopnost materiálu absorbovat energii před porušením, a proto jsou lomy podle energetické náročnosti rozděleny na houževnaté a křehké. Závislost lomové houževnatosti na teplotě lze na ose teplot obecně rozdělit na tři základní oblasti. Oblast dolních prahových hodnot (křehké porušení) přechází v tranzitní oblast, po které následuje oblast horních prahových hodnot (tvárné porušení). V každé oblasti je lomová houževnatost reprezentována svou střední hodnotou, které odpovídá příslušný rozptyl, přičemž nejmenší rozptyl hodnot lomové houževnatosti připadá na oblast dolních prahových hodnot a při posunu směrem k vyšším teplotám se rozptylový pás zvětšuje. V současné době obecně existuje několik přístupů ve zpracování naměřených dat, jejichž společným cílem je co nejpřesněji popsat a vyhodnotit teplotní průběh lomové houževnatosti ať již se jedná o jednotlivé oblasti (ČSN 42 03 47 1991, Wallin 2000) nebo o celou teplotní závislost (Moskovic 2001).

K velice často používaným materiálům v dosavadní technické praxi patří materiály s nízkou a střední pevností. S výhodou se oceli s nízkou a střední pevností používají na výrobu mostních konstrukcí a nejrůznějších technologických zařízení (zejména tlakové nádoby určené pro petrochemický průmysl). Stále větší důležitosti pak nabývá použití těchto ocelí v oblasti jaderné energetiky. Jedná se o výrobu tlakových nádob jaderných reaktorů a s nimi souvisejícími potrubními soustavami a v poslední době především o výrobu kontejnerů, které jsou určeny pro přepravu radioaktivního materiálu. Mechanismy porušování

<sup>1</sup> Ing. Libor Vlček: Ústav fyziky materiálů AVČR, Žižkova 22; 616 62 Brno; +420 532 290 336 a Ústav mechaniky těles FSI VUT v Brně, Technická 2; 616 69 Brno; e-mail: [vlcek@ipm.cz](mailto:vlcek@ipm.cz)

<sup>2</sup> Ing. Vladislav Kozák, CSc., Ústav fyziky materiálů AVČR, Žižkova 22; 616 62 Brno

těchto materiálů spadají zejména do tranzitní oblasti, ve které se mohou vyskytovat oba typy lomů. Z hlediska hodnocení lomového chování je porušení materiálu křehkým lomem považováno za velice významné. Trhлина se po překročení své kritické velikosti začne šířit bez potřeby dodávané vnější energie rychlostí zvuku vlivem akumulované elastické energie celé soustavy. Předmětem předložené práce je zkoumání vlastností C-Mn oceli na odlitky, která byla navržena pro výrobu kontejneru určeného k přepravě radioaktivního materiálu. Výsledně byla stanovena lomová houževnatost u těles s různou délkou trhliny namáhaných tříbodovým ohybem-tělesa  $SE(B)$ . Na základě experimentálně zjištěné tranzitní závislosti modelové oceli byla vytipována dolní část tranzitní oblasti, kde dochází k porušení v důsledku nestabilního štěpného lomu. Hodnoty lomové houževnatosti ve výše zmíněné oblasti jsou reprezentovány hodnotami  $J$ -integrálu, které vykazují značný rozptyl. Pro homogenní materiály lomová houževnatost není konstantou, ale obecně závisí i na geometrické konfiguraci tělesa s trhlinou, tedy na rozměrech zkušební tělesa, délce, poloze a orientaci trhliny a zatěžovacích podmínkách. Již dříve bylo prokázáno, že rozhodujícím aspektem při hodnocení lomového chování těles je mikromechanismus porušování. V případě porušení nestabilním štěpným lomem je za rozhodující parametr brána velikost maximálního hlavního napětí v určité vzdálenosti před čelem trhliny, avšak za předpokladu, že mikromechanismus tohoto lomu se řídí podle teorie nejslabšího článku. V souladu s požadavkem komplexního hodnocení vlastností C-Mn oceli na odlitky byly kromě potřebných experimentů provedeny numerické výpočty za použití metody konečných prvků. V rámci numerických simulací byly vytvořeny výpočtové modely založené na teorii konečných deformací (finite strain) s cílem nejvíce se přiblížit „reálnému“ nesingulárnímu rozložení napětí před čelem trhliny. Možnost získání nesingulárního průběhu napětí před čelem trhliny je v současnosti považována za základní předpoklad při posuzování mikromechanismů porušování. Přestože je v předložené práci uvažováno porušení nestabilním štěpným lomem ukazuje se, že rozsah plastické zóny před čelem trhliny je natolik velký, že není možné použít teorie lineární elastické lomové mechaniky. Veškeré numerické výpočty byly provedeny s uvažováním elasticko plastického chování materiálu na prostorových modelech. Cílem práce je (s využitím MKP) posouzení přenositelnosti a korekce lomové mechanických dat mezi standardními tělesy pro statickou zkoušku tříbodovým ohybem, která splňují podmínku malých plastických deformací před čelem trhliny (podmínka SSY) a malými tělesy s trhlinou.

## 2. Materiál a metodika experimentu

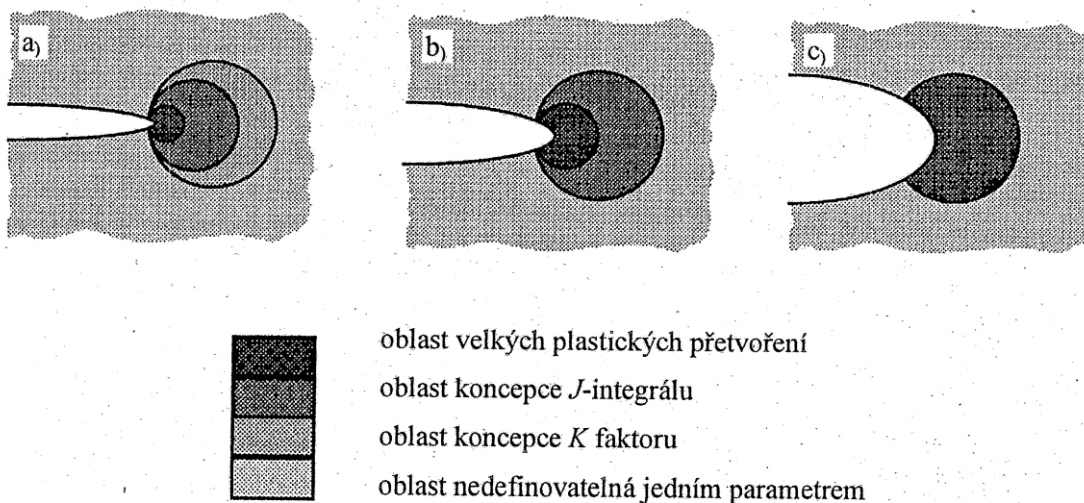
Pro experimentální účely byla použita nízkouhlíková manganová ocel na odlitky (ČSN 42 27 07). Nejprve byly provedeny tahové zkoušky na poměrných válcových tyčích s počáteční měřenou délkou  $L_0 = 30$  mm a průměrem zkoušené délky  $d = 6$  mm. Pro měření prodloužení bylo použito extenzometru. Rychlost pohybu příčniku byla vždy  $2 \text{ mm} \cdot \text{min}^{-1}$ . Potřebná závislost skutečného napětí na skutečné deformaci (pro MKP výpočty) byla stanovena ze získaných záznamů síly a prodloužení.

Následně byla určena lomová houževnatost u tří typů zkušebních těles s trhlinou pro tříbodový ohyb. První typ představovala standardní tělesa s rozměry  $25 \times 50 \times 220$  mm, poměr délky trhliny k výšce tělesa byl  $a/W \sim 0.5$ . Předmětem druhého typu byla tělesa o rozměrech  $25 \times 30 \times 120$  mm s poměrem  $a/W \sim 0.2$ . Tělesa s rozměry  $25 \times 26 \times 104$  mm a poměrem  $a/W \sim 0.1$  tvořily třetí typ zkušebních těles. Geometrie těles byla záměrně zvolena tak, aby jednotlivé typy těles byly mezi sebou geometricky podobné, přičemž ve všech zkoumaných případech byla zachována stejná velikost nosného průřezu zkušební tělesa-ligamentu.

Všechny typy těles byly zkoušeny při rychlosti pohybu příčnicku  $1 \text{ mm} \cdot \text{min}^{-1}$ . Tahové zkoušky i zkoušky lomové houževnatosti byly prováděny v kryostatu za teploty  $-100^\circ\text{C}$  v parách tekutého dusíku.

### 3. Vliv constraint na lomovou houževnatost

Přímým důsledkem deformačně zpevňujících procesů v materiálu je vznik plastické deformace v okolí čela trhliny. Následuje intenzivní růst plastické deformace před čelem trhliny, čímž může dojít ke změně původních podmínek—běžně označované jako podmínky malých plastických deformací (SSY—Small Scale Yielding) na podmínky nové—podmínky velkých plastických deformací (LSY—Large Scale Yielding). Podmínky LSY musí být chápány ve smyslu vztahu k rozměrům trhliny, a tedy v žádném případě nepředstavují výskyt plastické deformace ve velkém objemu materiálu vzorku. Rozdíl mezi oběma podmínkami je ilustrativně zobrazen na obr. 1. V takovém případě rozložení napěťového pole již nelze popsat pomocí jediného globálního parametru ( $K$  faktorem při uvažování LEELM nebo  $J$ -integrálem v případě EPLM). Pro popis pole napětí se používá dvouparametrová lomová mechanika. V případě aplikace EPLM je kritická hodnota  $J$ -integrálu v okamžiku iniciace spojena vždy s určitou hodnotou  $Q$  parametru.  $Q$  parametr je chápán jako míra posuzující stupeň triaxiality napětí na čele trhliny vzniklé v důsledku stísnění plastické deformace a obecně je označován pojmem constraint (O'Dowd, Shih 1992). Byla navržena  $J$ - $Q$  formulace (O'Dowd, Shih 1991), která nám charakterizuje vlivy constraint na napěťové pole,  $J$  je  $J$ -integrál popisující deformační chování a  $Q$  je faktor vyjadřující multiaxialitu napětí před čelem trhliny. Měření lomové houževnatosti na tělesech s postupně se zkracující délkou trhliny (klesající poměr  $a/W$ ) ukázala růst lomové houževnatosti vyjádřené pomocí  $J_c$ . Prakticky všechny modely (např. Al-Ani, Hancock 1991, Faleskog 1995) iniciace křehkého porušení předpokládají, že rozhodující pro trigenerování tohoto lomu je průběh a hodnota maximálního hlavního napětí.



Obrázek 1 Možné stupně zplastizování před čelem trhliny: stav SSY(a), elasticko-plastické podmínky (b), stav LSY (c)

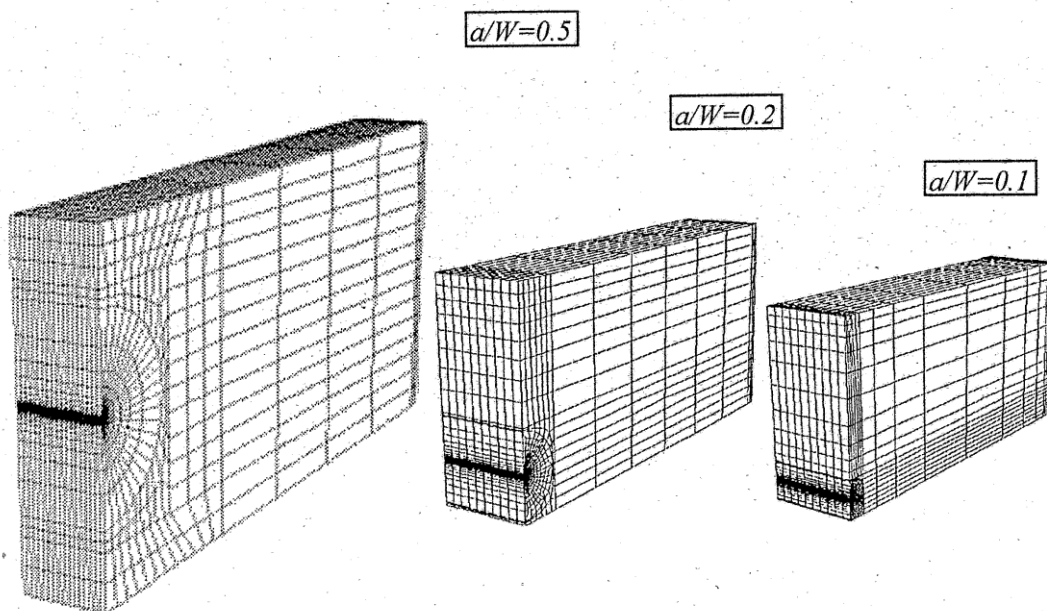
Růst  $J_c$  je pak spojen s poklesem  $\sigma_I$  u čela trhliny (Dodds, Shih, Anderson, 1993). To poukazuje na nezbytnost zavedení dalšího parametru, který vyjadřuje relaxaci maximálního hlavního napětí u čela trhliny.

#### 4. Numerické modelování

Řešení problémů lomové mechaniky je založeno na znalosti deformačně-napětových charakteristik před čelem trhliny. V případě hodnocení chování komponent obsahujících trhlínu, elasticko-plastická lomová mechanika přesně určuje vztah mezi maximálním přípustným vnějším zatížením a parametry komponenty (rozměry tělesa, materiálové vlastnosti, velikost a poloha trhliny). Metoda konečných prvků (MKP) představuje vhodný nástroj pro získání přehledu rozložení polí deformací a napětových polí v analyzovaném modelu. Pro řešení problému byl zvolen programový systém Abaqus 6.1. S využitím dvou rovin symetrie byla modelována čtvrtina reálného tělesa s trhlínou o poloměru zaoblení čela  $r = 0.01\text{mm}$ . Pro následnou diskretizaci celé oblasti bylo zapotřebí 15680 prvků typu C3D8, což představuje 17884 uzlů. Charakteristická délka prvku na čele trhliny byla  $8,3 \cdot 10^{-4}\text{mm}$ . Veškeré výpočty byly provedeny až do hodnot lomové síly, které odpovídaly jednotlivým zkušební tělesům. Uniaxiální (tahovou) křivku napětí-deformace popisuje Rambergova-Osgoodova rovnice:

$$\frac{\varepsilon}{\varepsilon_0} = \frac{\sigma}{\sigma_0} + \alpha \left( \frac{\sigma}{\sigma_0} \right)^n, \quad (1)$$

Materiál zkušebních těles byl považován za izotropní a homogenní s elastickými konstantami  $E=2,05 \cdot 10^5\text{ MPa}$ ,  $\mu=0.3$ . Střední hodnota meze kluzu byla  $\sigma_0=360\text{ MPa}$  a exponent deformačního zpevnování  $n=8$ , koeficient deformačního zpevnování  $\alpha=1$

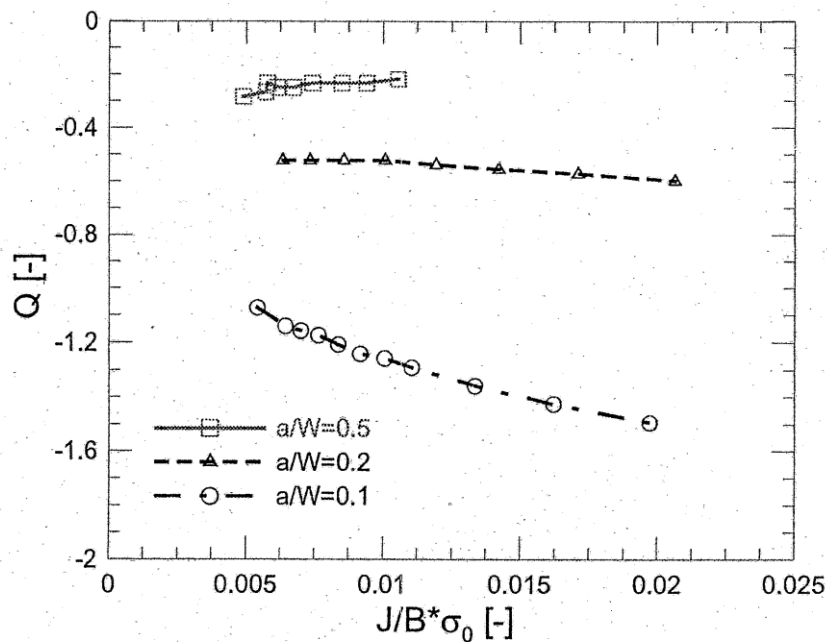


Obrázek 2 3D modely těles

Výsledkem analýz MKP modelů bylo získání průběhů hodnot maximálního hlavního napětí před čelem trhliny u všech typů modelovaných těles. Dále byly stanoveny hodnoty  $J$ -integrálu v celém průběhu zatěžování a hodnoty maximálních posunutí uzlů ve směru působícího zatížení. Veškeré výpočty byly následně porovnány s experimentálně získanými závislostmi síla-přemístění síly s cílem ověření správnosti numerických simulací. Hodnoty  $Q$  parametru byly stanoveny na základě definice (Shih, O'Dowd 1994);  $Q$  parametr je definován v bodě  $\theta=0$ ,  $r=2J/\sigma_0$  jako podíl diferenciálního pole napětí a meze kluzu:

$$Q = \frac{(\sigma_{ij})_{diff}}{\sigma_0} = \frac{(\sigma_{ij}) - (\sigma_{ij})_{ref}}{\sigma_0} \quad (2)$$

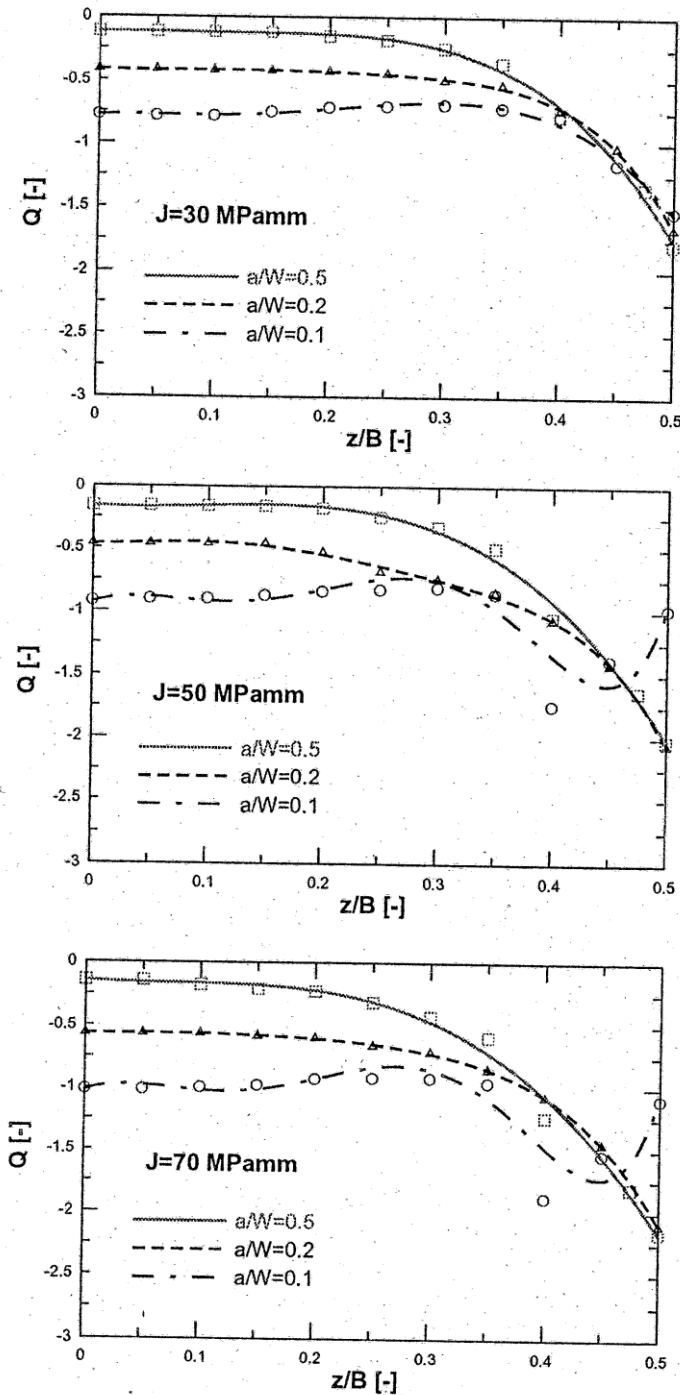
Diferenční pole napětí lze podle (Nevalainen, Dodds 1995, Anderson 1995) v oblasti  $r = \left\langle \frac{J}{\sigma_0}, 5J/\sigma_0 \right\rangle$  a pro  $\theta \leq \pi/2$  považovat za konstantní. Jde o rozdíl mezi skutečnou napjatostí, kterou získáme z numerické analýzy, a referenčním polem napětí. Mezi nejběžněji používaný přístup vhodný k získání hodnot napětí referenčního pole patří metoda okrajové vrstvy (Landes 1997, Nevalainen, Dodds 1995).



Obrázek 3  $J$ - $Q$  závislost získaná pro tři konfigurace tělesa a trhliny

Z obrázku 3 je patrné, že se zkracující se délkou trhliny dochází ke zvyšování hodnot  $Q$  parametru. Důvody změn v jednotlivých průbězích hodnot  $Q$  parametru je třeba hledat v souvislosti s určitými změnami rozložení hlavních napětí, která přísluší jednotlivým zkušebním tělesům (tedy poměrům  $a/W$ ). Byl pozorován patrný pokles křivky maximálního hlavního napětí v závislosti na vzdálenosti od čela trhliny ve směru šíření u tělesa s nejkratší délkou trhliny. Tento trend vývoje je způsoben změnou okrajových podmínek v okolí čela trhliny. Ve směru tloušťky tělesa k žádné změně nedochází, protože je stále stejná. Obdobně je tomu ve směru šíření trhliny, kde je vždy stejná velikost nosného příčného průřezu. Jedinou

závažnou změnou je zmenšování množství materiálu v protisměru šíření trhliny se zkracující se její délkou. Napjatost v tělese vzniká teprve až jako důsledek projevu plastické deformace. Zřetelně větší plastická oblast u tělesa s nejkratší délkou trhliny se dala očekávat v důsledku vyšších zatěžovacích sil. S klesající délkou trhliny se oblast stejných hodnot plastické deformace prodlužuje a sklání směrem ke směru šíření trhliny. Velikost plastické zóny se s



Obrázek 4 Průběhy  $Q$  parametru po tloušťce tělesa

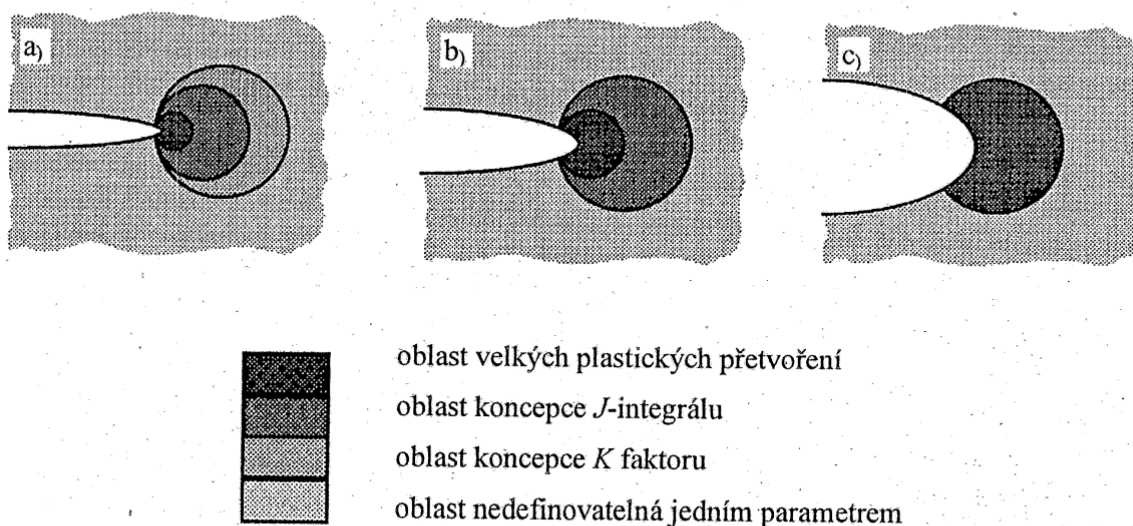
vzrůstající délkou trhliny zmenšuje. U těles s  $a/W=0.1$  a  $0.2$  je velikost plastické zóny pro nejnižší lomové síly srovnatelná. Vysvětlení poklesu napětí u těles s nejkratší trhlinou ve srovnání s ostatními tělesy není jednoznačné, ale vše nasvědčuje tomu, že oblast plastické deformace u tohoto tělesa „prorůstá“ až na povrch, čímž dochází k větší relaxaci napětí, než když kdyby plastická oblast zůstala „uzavřená“ v tělese. Výše uvedené metody numerického modelování a poznatky získané na  $SE(B)$  tělesech byly použity pro možnosti hodnocení přenositelnosti lomové mechanických dat z nestandardních těles ( $a/W=0.1$ ,  $0.2$ ) na standardní tělesa ( $a/W=0.5$ ), která splňují podmínky malých plastických deformací (SSY). Na základě mikromechanických modelů (Anderson, Dodds 1991) aplikovaných pro popis procesu porušování u čela trhliny, lze transformovat globální parametr naměřený na tělese jedné geometrie na těleso jiné geometrie (tzv. Toughness Scaling Model – TSM).

Důležitou otázkou spojenou s 3D modelováním je stanovení vlivu konečných rozměrů tělesa na hledané lomové charakteristiky. Jedná se zejména o vliv konečné tloušťky tělesa na průběhy  $J$ -integrálu tzn. určit oblast dominance rovinné napjatosti (RN) resp. rovinné deformace (RD). Pro posouzení vlivu konečné tloušťky tělesa (efekt out of plane constraint) na průběhy hodnot  $Q$  parametru v blízkosti čela trhliny byly zkonstruovány závislosti na obr. 4. Na svislých osách jsou vyneseny hodnoty  $Q$  parametru spočtené podle vztahu

Všechny typy těles byly zkoušeny při rychlosti pohybu příčnicku  $1 \text{ mm} \cdot \text{min}^{-1}$ . Tahové zkoušky i zkoušky lomové houževnatosti byly prováděny v kryostatů za teploty  $-100^\circ\text{C}$  v parách tekutého dusíku.

### 3. Vliv constraint na lomovou houževnatost

Přímým důsledkem deformačně zpevňujících procesů v materiálu je vznik plastické deformace v okolí čela trhliny. Následuje intenzivní růst plastické deformace před čelem trhliny, čímž může dojít ke změně původních podmínek-běžně označované jako podmínky malých plastických deformací (SSY-Small Scale Yielding) na podmínky nové-podmínky velkých plastických deformací (LSY-Large Scale Yielding). Podmínky LSY musí být chápány ve smyslu vztahu k rozměrům trhliny, a tedy v žádném případě nepředstavují výskyt plastické deformace ve velkém objemu materiálu vzorku. Rozdíl mezi oběma podmínkami je ilustrativně zobrazen na obr. 1. V takovém případě rozložení napěťového pole již nelze popsat pomocí jediného globálního parametru ( $K$  faktorem při uvažování LELM nebo  $J$ -integrálem v případě EPLM). Pro popis pole napětí se používá dvouparametrová lomová mechanika. V případě aplikace EPLM je kritická hodnota  $J$ -integrálu v okamžiku iniciace spojena vždy s určitou hodnotou  $Q$  parametru.  $Q$  parametr je chápán jako míra posuzující stupeň triaxiality napětí na čele trhliny vzniklé v důsledku stísnění plastické deformace a obecně je označován pojmem constraint (O'Dowd, Shih 1992). Byla navržena  $J$ - $Q$  formulace (O'Dowd, Shih 1991), která nám charakterizuje vlivy constraint na napěťové pole,  $J$  je  $J$ -integrál popisující deformační chování a  $Q$  je faktor vyjadřující multiaxialitu napětí před čelem trhliny. Měření lomové houževnatosti na tělesech s postupně se zkracující délkou trhliny (klesající poměr  $a/W$ ) ukázala růst lomové houževnatosti vyjádřené pomocí  $J_c$ . Prakticky všechny modely (např. Al-Ani, Hancock 1991, Faleskog 1995) iniciace křehkého porušení předpokládají, že rozhodující pro trigenerování tohoto lomu je průběh a hodnota maximálního hlavního napětí.



Obrázek 1 Možné stupně zplastizování před čelem trhliny: stav SSY(a), elasticko-plastické podmínky (b), stav LSY (c)

vzdálenost iniciačních míst u všech zkoumaných geometrií. Výsledky získané z MKP byly použity pro konstrukci TSM diagramu. Snižování efektivní tloušťky se zatížením u všech typů těles není překvapivé. Více zajímavým se může jevit fakt, že největší efektivní tloušťky je dosaženo v případě tělesa s poměrem  $a/W=0.1$ , i když rozdíly oproti ostatním tělesům jsou velmi malé. Důvody jsou shledány v geometrii příčného průřezu. Průběh efektivní tloušťky u tělesa s  $a/W=0.2$  naznačuje, že projevy „out of plane constraint“ jsou v cílovém chování těles s trhlinou protikladem projevům „in plane constraint“, a proto u čtvercových průřezů může být déle držena oblast  $J-Q$  dominance ve směru tloušťky tělesa.

## 6. Poděkování

Tato práce vznikla za podpory grantu GAAV ČR č. S 2041001.

## 7. Literatura

- Al-Ani, A. M., Hancock, J. W. (1991) J-dominance of short cracks in tension and bending, *J. of the Mechanics and Physics of Solids*, Vol. 39, No. 1, pp. 23-43.
- Anderson, T. L. (1995) Fracture Mechanics Fundamentals and Applications, *Second Edition CRC Press*
- Anderson, T. L., Dodds, R. H. (1991) Specimen size requirements for fracture toughness testing in the ductile-brittle transition region, *J. of Testing and Evaluation*, Vol. 19, pp. 123-134.
- ČSN 42 03 47, (1991) Lomová hůževnatost kovov pri statickom zaťaženi
- Dodds, R. D., Shih, C. F., Anderson, T. L. (1993) Continuum and Micro-Mechanics Treatment of Constraint in Fracture, *Int. Journ. of Fract.*, Vol. 64, pp. 101-133.
- Faleskog, J. (1995) Effects of local constraint along three-dimensional crack fronts-a numerical and experimental investigation, *J. of the Mechanics and Physics of Solids*, Vol. 43, No. 3, pp. 447-493.
- Landes, J. D. (1997) Application of a J-Q Model for Fracture in the Ductile-Brittle Transition, *Fatigue and Fracture Mechanics*, Vol. 27, ASTM STP 1296, pp. 27-40.
- Moskovic, R. (2001) Modelling of fracture toughness data in the ductile to brittle transition temperature region by statistical analysis, *Engineering Fracture Mechanics*, No. 69, pp. 511-530.
- Nevalainen, M., Dodds, R.H. (1995) Numerical Investigation of 3-D Constraint Effects on Brittle Fracture, SE(B) and C(T) Specimens, *Int. J. of Fract.* Vol. 74, pp. 131-161.
- O'Dowd, N. P., Shih, C. F. (1991) Family of crack-tip fields characterized by a triaxiality parameter-I. structure of fields, *J. of the Mechanics and Physics of Solids*, Vol. 39, No. 8, pp. 989-1015.
- O'Dowd, N. P., Shih, C. F., (1992) Family of crack-tip fields characterized by a triaxiality parameter-II. fracture applications, *J. of the Mechanics and Physics of Solids*, Vol. 40, No. 5, pp. 939-963.
- Shih, C. F., O'Dowd, N. P. (1994) *Two-Parameter Fracture mechanics: Theory and Applications*, Fracture Mechanics, *ASTM STP 1207*, pp. 21-47, 379-386.
- Wallin, K. (2000) Master curve analysis of the "Euro" fracture toughness dataset, *Eng. Fracture Mech.*, Vol. 69, pp. 451-481.

A7 Chlupová, A., Kozák, V., Fatigue crack growth and delamination in fiber metal laminate (GLARE), *18<sup>th</sup> International Conference Engineering Mechanics*, (2012), Svratka, 531-536.

## FATIGUE CRACK GROWTH AND DELAMINATION IN FIBER METAL LAMINATE (GLARE) DURING LOADING WITH POSITIVE MEAN STRESS

A. Chlupová\*, V. Kozák\*\*

**Abstract:** *The aim of the paper is to present the results of a study on the damage of fiber metal laminate (GLARE) subjected to the low cycle fatigue loading with positive mean stress. The fatigue crack initiation and growth was observed on the surface of notched specimens and then the individual layers of fatigued specimens were removed by chemical etching and polishing to obtain data about cracks length and delamination shape and area. Mechanism of initiation and crack growth in this type of materials differs from homogeneous monolithic materials. The fatigue life in term of number of cycles to crack initiation depending on amplitude of local plastic deformation and local stress in the notch root was evaluated.*

**Keywords:** *Fatigue, laminate, crack initiation, crack growth, delamination*

### 1. Introduction

Fibre metal laminates (FMLs) were developed at Delft University of Technology in Netherlands (Roebroeks 1991). These hybrid laminates consist of fibre reinforced plastic layers, so-called prepregs alternating with metal sheets of aluminium alloy. This combination connects outstanding fatigue resistance and high strength properties of glass fibre composite and ductility of metal layers.

FMLs can be strengthened by different kinds of fibres (Chlupova 2002). Material in this study with commercial name GLARE contains as reinforcing fibres the high strength S-glass fibres. For the metal sheets, the aluminium alloy 2024-T3 of thickness 0.4 mm is used (Prasilova 1998).

The concept of hybrid materials was developed primary for aviation applications (Vasek 1999) and presently is used as a fuselage of Airbus A380 (Hinrichsen 2002); nevertheless it can have very wide range of employment as a material for automotive and ship industry, wind power plants, sports, up to unusual applications such as manufacturing of music instruments or prosthesis in medicine.

FMLs possess different kinds of properties and their anisotropy allows tailoring material exactly according to the stress-strain fields acting in particular structural part (Chlupova et al. 2001). Basic mechanical properties such as strength and stiffness are comparable to conventional materials. The other properties like impact and fire resistance, formability, manufacturability, reparability, weight savings, low costs of production etc. offer in many cases significant advantages and are in the centre of attention (Yaghoubi 2012, Moussavi-Torshizi 2010, Park 2010). The drawback of this material can be seen in the lack of knowledge, i.e. due to insufficient data and information about material characteristics the designers aren't able to make the right decisions at design of structural parts and hesitate to apply FMLs for broader industrial applications.

The aim of this work is to present results obtained at study of fatigue properties of one kind of FML. Contrary to the monolithic metal materials the GLARE exhibits among others longer fatigue life and extremely elongated stadium of fatigue crack propagation which makes this material safer and damage tolerant. Zehnder in his work compared two types of materials: 1) homogeneous material and 2) layered material made of metal and plastics laminas without fibres, show that plastic layers operate as a barrier and a kind of bridging element (Zehnder1997). The glass fibre layers in GLARE can

---

\* Ing. Alice Chlupová, Ph.D.: Institute of Physics of Materials, Academy of Sciences of the Czech Republic, Žitkova 22; 616 62, Brno; CZ, e-mail: [prasil@ipm.cz](mailto:prasil@ipm.cz)

\*\* Ing. Vladislav Kozák, CSc.: Institute of Physics of Materials, Academy of Sciences of the Czech Republic, Žitkova 22; 616 62, Brno; CZ, e-mail: [kozak@ipm.cz](mailto:kozak@ipm.cz)

therefore even more improve the mentioned barrier and bridging effect. Glass fibre layers have very positive effect on postponing of initiation and on retardation of propagation of already initiated fatigue cracks. This fact elongates efficiently fatigue life and increases safety of structural parts made of this kind of material (Prasilova 1998).

## 2. Experiment

Material used for investigation: GLARE 2 have unidirectional fibre orientation. Flat specimens having dimensions 200x50mm and thickness:  $t = 1.4, 3.1$  and  $6.5$  mm (i.e. with number of layers 3/2, 6/5 and 12/11) were provided with different kind of notches: specimens with central semicircular or circular notch or two side shallow notches with stress concentration factor  $K_t = 1.2, 2.4$  and  $3.2$ .

The cyclic loading was performed in force control regime, i.e. different levels of stress amplitudes were chosen with parameter of asymmetry of  $R = 0.04$ . Specimens were loaded by computer controlled servohydraulic testing machine MTS 880 at room temperature. Maximum applied stress in cycle  $\sigma_{max}$  varied from 90 to 450 MPa in individual test.

Fatigue crack initiation and growth was observed in-situ on the surface of notched specimens. The surface metal layer at the notch root area was mechanically grinded and polished before the loading to facilitate observation of crack initiation and growth. Observation and measurement of crack length during loading was performed using microscope QUESTAR QM-100 and CCD camera. The data acquisition during loading was performed. Loading was terminated at length of surface layers about 10 mm or at number of cycles  $10^6$ . After test termination the destructive analysis was performed. Individual layers of laminate were removed by means of chemical etching and mechanical grinding and polishing. A level of material degradation inside of laminate was evaluated (i.e. for cracks the number, length, place and direction of growth were investigated; for delamination the size and shape were assessed).

## 3. Results

FMLs are very complex material which means that damage in this type of material is even more complex problem. The damage can occur at different levels as is seen in Fig. 1.

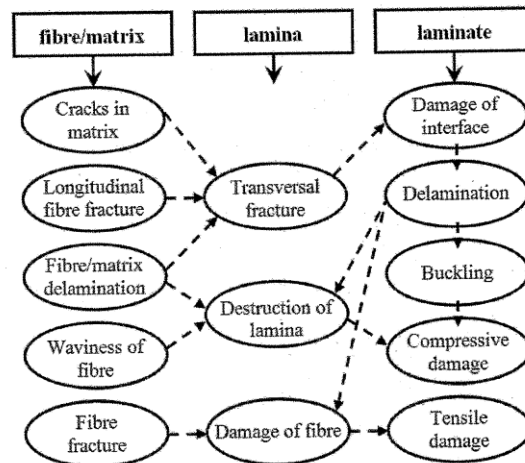


Fig. 1: Different types and levels of damage in hybrid laminates.

Mechanism of initiation and crack propagation differs from the mechanism of initiation in homogeneous monolithic materials. Fatigue cracks initiate first in metal layers in inner layers of laminate. The cracks initiated always at metal prepreg interface even in case of surface metal layer. The latest is the initiation in surface layers nevertheless the crack growth on surface of specimen was the fastest. The crack front in FMLs is not continuous, it is created by crack fronts in individual layers laying usually not in one plane and with the maximum length on the surface of specimen. It is

different from the crack front in monolithic metal materials where it is continuous, in one plane and curved with maximum length inside of material.

The initiation place is usually under some angle from the notch root (Fig. 2a). The deflection depends on the type of notch and applied stress (in case of central circular hole it was about 7 to 12 degree at lower applied stresses and 5 to 20 degree for higher applied stresses). The wide range of deflection angles of crack initiation place is connected mainly to: 1) fibre structure with intact fibres directly in the notch root which prevent crack initiation and 2) cut fibres acting as defects are situated at certain angle. Between areas of continuous and cut fibres i.e. outside the notch root there is a high level of shear stress on fibre-matrix interface and high level of interlaminar elastic and plastic deformations. The initiation in the notch root is therefore less probable (see Fig. 2b).

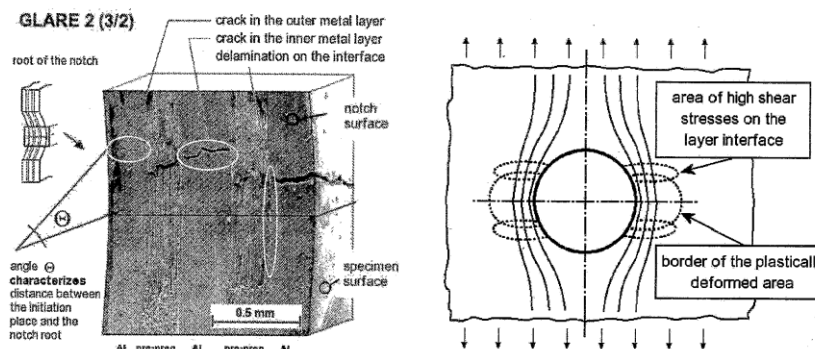


Fig. 2: a) Deflection of crack initiation angle and b) shear stress in the fibre reinforced lamina with circular notch.

Shortly after initiation the cracks are radial i.e. they grow perpendicularly to the edge of the notch. After some propagation period (approximately when cracks reach length corresponding to the notch radius) the cracks deflect to the direction perpendicular to applied loading. From comparison of situation inside and on surface of laminate it is obvious that number of cracks in metal layers inside of laminate is bigger and crack length is smaller.

Number of cycles to crack initiation  $N_{in}$  and to elongation to defined length  $N_f$  were evaluated in dependence on applied stress level. Obtained results for different notch and different thickness of specimens from unidirectional material GLARE 2 are shown in Fig. 3.

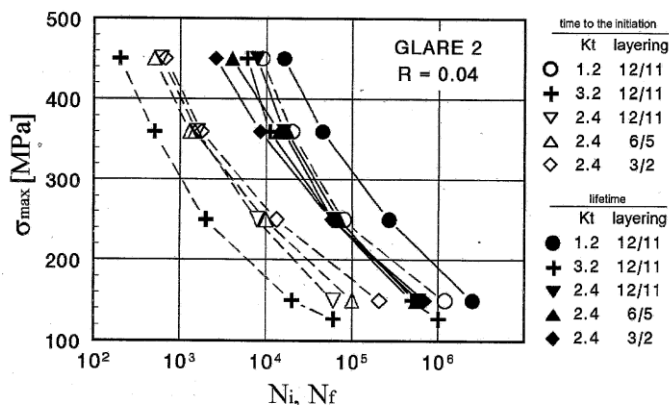


Fig. 3: Number of cycles to crack initiation and up to end of testing for specimens with different lay-up and different notches.

Measured data were then used for finite element method calculation of local plastic deformation in the notch root  $\epsilon_{pl}$ . At calculations in 2D analysis by means of ABACUS software the elasto-plastic behaviour of metal layers and internal stresses in unidirectional laminate GLARE 2 were taken into account (Chlupová, 2001). A plastic deformation in metal layers was calculated according to experimentally measured monotonic hardening curve of aluminium alloy 2024-T2, the residual

stresses caused by laminate preparation method were taken into account. Results of FEM calculations of plastic deformation for specimen with central circular notch are graphically represented in Fig. 4.

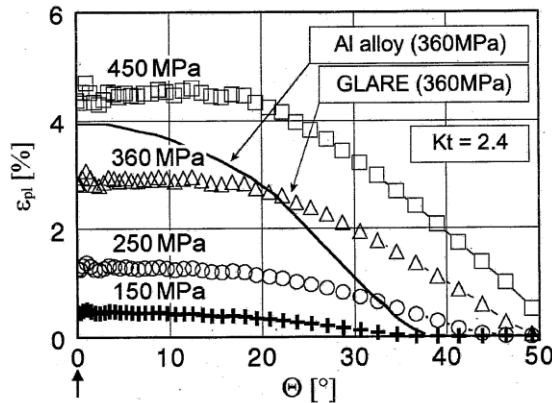


Fig. 4: Results of FEM calculations for specimen with central circular notch.

Calculated amplitude of local plastic deformation in aluminium layers in the notch root was then displayed in dependence of number of cycles to initiation (see Fig. 5a). As it is seen from the plot, all data points obtained for different stress concentration factors  $K_t$  lie on one curve.

$$\epsilon_{a,pl,l} = 0,036 \cdot N_{in}^{-0,214} \tag{1}$$

Amplitude of local plastic deformation in notch root can be therefore considered to be the parameter determining number of cycles to fatigue crack initiation in notched specimens from the material GLARE, similarly like in the case of homogeneous materials (Polák 1991).

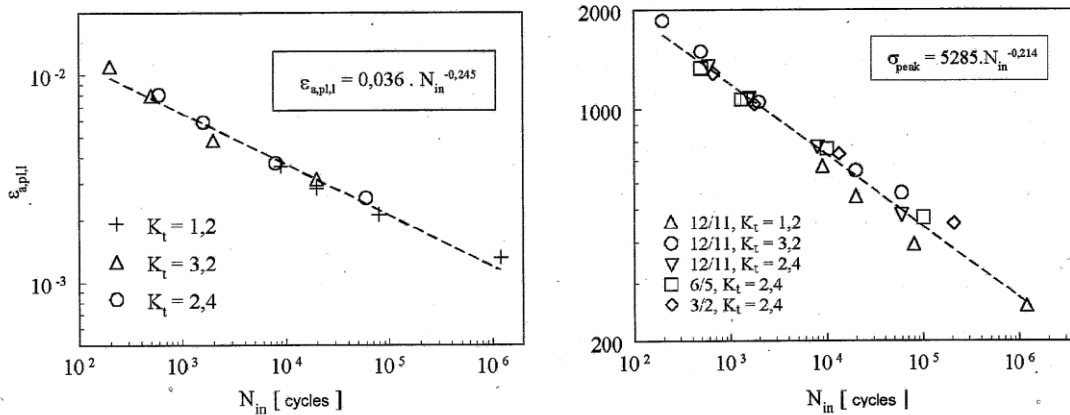


Fig. 5: Dependence of number of cycles to crack initiation ( $N_{in}$ ) on a) amplitude of local plastic deformation in the notch root and b) local peak stress in aluminium layers the notch root of specimen.

Local plastic deformation in the notch root is induced by local stress  $\sigma_{peak}$ , which is given by maximum applied stress  $\sigma_{max}$ . The value of local stress can be calculated using stress concentration factor in metal layers  $K_{t,Al}$  and internal residual stress in metal layers  $\sigma_{r,Al}$  as follows:

$$\sigma_{peak} = \sigma_{max} K_{t,Al} + \sigma_{r,Al} \tag{2}$$

In the Fig. 5b there is the dependence of number of cycles to initiation on calculated local peak stress according to equation (2) for different thicknesses and different notch factors together with approximation of data by power function:

$$\sigma_{peak} = 5285 \cdot N_{in}^{-0,214} \tag{3}$$

Relationship between  $N_{in}$ ,  $K_{t,Al}$ ,  $\sigma_{r,Al}$  and  $\sigma_{max}$  given by eq. (2) and (3) explains experimentally observed lower number of cycles to crack initiation in thicker laminates. In laminates with higher number of layers (12/11) due to curing cycle in autoclave the higher tensile residual stress in metal layers are present, i.e it results in higher level of local stress in the notch root  $\sigma_{peak}$  and consequently the lower number of cycles to crack initiation. This trend is more pronounced for lower levels of applied stress  $\sigma_{max}$ .

Delamination is one kind of damage in laminates which is related to crack initiation and growth (see Fig. 6a). Delamination for this type of material has nearly elliptical shape. The delamination size can be thus characterised by ratio  $b/l$ , where  $l$  is crack length and  $b$  is the height of delamination in the notch root. These two parameters are also axis of “half-ellipse” which can be used as a good approximation of delamination shape. The appearance of delaminated areas on the resin rich surface of prepreg after removing of metal layer with four cracks in specimen loaded at maximum applied stress 450 MPa are exhibited in Fig. 6b.

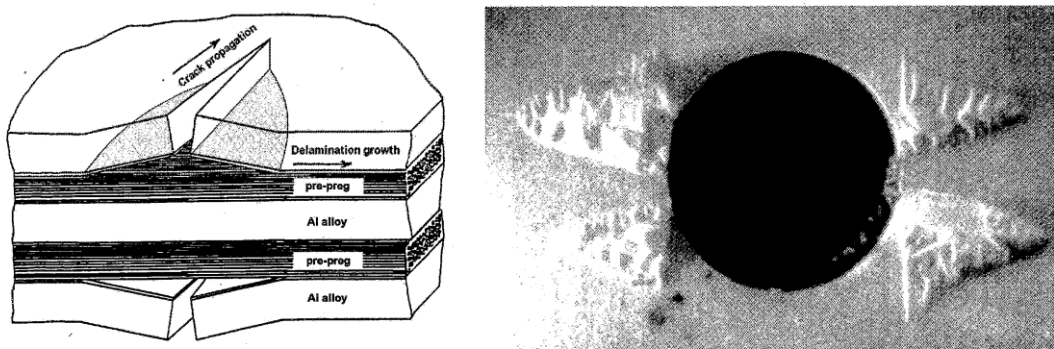


Fig. 6: a) Scheme of relationship between crack growth, delamination and fibres bridging the opening crack; b) real shape and range of delamination.

As soon as the crack in metal layer is initiated simultaneously the delamination appears as a result of shear stresses on layers interface. The size of delamination depends on many factors such as crack length, crack growth rate, fibres properties and fibres volume fraction but predominantly on quality of adhesion on interface. The presence of delamination of certain size is essential to create optimal conditions for outstanding fatigue resistance; nevertheless a judging of effect of adhesion quality is difficult due to its antagonistic influence on delamination. Strong adhesion results in small delamination. In the extreme: in the case of no delamination, the length of fibres actively acting on crack closure would be so small that crack wouldn't open and crack would stop. On the other hand at these conditions the loading of short part of fibres would be so enormous that it would cause the failure of fibres. The right function of fibres and their bridging effect wouldn't be thus possible. Weak adhesion results in big delamination and significant decrease of bearing capacity. In the extreme: it would cause debonding of laminate along the fibre-matrix interface. In that case the transfer of loading through shear stresses from metal to prepreg layers and vice versa wouldn't be possible.

#### 4. Conclusions

Fatigue behaviour of fibre metal laminates containing as a reinforcing material glass fibres was studied. It was found that FMLs exhibit different mechanism of initiation and growth of fatigue cracks than homogeneous monolithic metallic materials. Cracks initiate first inside of laminate, exhibits shorter period of crack initiation and strongly elongated period of crack growth. Number of cracks initiated from the notch is higher and the place is transferred out of the root of notch.

The situation in inner and outer layers of laminate differs slightly – the initiation in inside layers is earlier, nevertheless the growth is slower than on surface. Prepreg acts as an effective barrier against crack growth from one layer to another. Cracks thus grow separately and independently. Crack growth was monitored in relation to growth direction and growth rate.

Relations for prediction of number of cycles to crack initiation and fatigue life of notched specimens from laminate were specified. The dependence of initiation on local plastic deformation and/or local stress in the notch root of metal layers was evaluated.

The delamination for both types of material (GLARE2 and GLARE 3) was found to be dependent on type of material, crack length and location in the metal-prepreg interface closer or farther from the specimen surface.

Delamination area is proportional to crack length, which induced it. Range of delamination is affected by level of shear stresses at metal-prepreg interface. It was found that the shape of delamination in material GLARE can be approximated by an ellipse. The higher is the level of maximum applied stress the higher range of delamination it evokes. The proper function of laminate, i.e. bridging effect of reinforcing fibres on growing crack, can be assured only by optimum strength of adhesion which causes suitable delamination area.

### Acknowledgement

Financial support of projects GACR 106/09/1954 and RVO 68081723 is acknowledged.

### References

- Chlupova, A. (2001) Fatigue behavior of laminate composites, *Ph.D. Thesis*, Technical University of Brno.
- Chlupova, A., Heger, J., Vasek, A. (2001) Fatigue crack initiation and early growth in GLARE 3 fiber metal laminate subjected to mixed tensile and bending loading. *Acta Polytechnica* Vol. 41, pp: 33–36.
- Chlupova, A. & Dymacek, P. (2002) Mechanical behaviour of hybrid laminates with carbon fibers. *Metallic Mater.* Vol. 40, pp. 195–208.
- Hinrichsen, J. (2002) The material down-selection process for A3XX, *Around Glare: A new aircraft material in context*, pp 127-144.
- Moussavi-Torshizi, S.E., Dariushi, S., Sadighi, M., Safarpour, P. (2010) A study on tensile properties of a novel fiber/metal laminates, *MatSciEng A*, Vol. 527, pp: 4920-4925.
- Park, S. Y., Choi, W. J., Choi, H. S. (2010) A comparative study on the properties of GLARE laminates cured by autoclave and autoclave consolidation followed by oven postcuring, *Int. Journal of advanced manufacturing technology*, Vol. 49 pp: 605-613.
- Polak, J. (1991) *Cyclic Plasticity and Low Cycle Fatigue Life of Metals*, Academia, Praha.
- \* Prasilova, A. & Vasek, A. (1998) Retarding effect of reinforcing fibers on early crack growth in fatigued notched laminate GLARE2, *Engineering Mechanics*, Vol. 5, No.3, pp. 219-223.
- Roebroeks, G.H.J.J. (1991) Towards GLARE – the development of a fatigue insensitive and damage tolerant aircraft material. *Ph.D. Thesis*, Delft University of Technology.
- Vasek, A., Dymacek, P. & Vogelesang, L.B. (1999) Fatigue strength of L610-P wing-fuselage attachment lug made of glare 2 fibre-metal laminate, *Fatigue design and reliability*, Vol. 23, pp: 73-81.
- Yaghoubi, A.S., Liu, Y., Liaw, B. (2012) Stacking Sequence and Geometrical Effects on Low-Velocity Impact Behaviors of GLARE 5 (3/2) Fiber-Metal Laminates, *Journal of thermoplastic composite materials* Vol. 25 pp: 223-247.
- Zehnder, A. T., Swenson, D.V., Pienkos, T.J. (1997) Polymer reinforcements for retarding fatigue crack growth in metals, *International journal of fracture*, Vol. 84, pp: 307-323.

- B1 Kozák V., Novák A., Dlouhý I., The Transferability of Fracture Toughness Characteristics, *Numerical Methods in Continuum Mechanics 2000*, (VIII. Inter. Confer.), (2000), Liptovský Ján, SR, (sk. 64-1, 64-10), publikace na CD.

# The Transferability of Fracture Toughness Characteristics

V. Kozák\*, A. Novák and I. Dlouhý

*Institute of Physics of Materials  
Academy of Sciences of the Czech Republic, Žitkova 22, 616 62 Brno  
e-mail:kozak@ipm.cz*

## Abstract

Fracture toughness transition behavior of C-Mn cast steel intended for fabrication of large transport and storage container for spent nuclear fuel (ŠKODA 440/84) has been carried out. The fracture resistance has been assessed using data from static tests of the bend CVN and pre-cracked (PCVN) specimens and from the axisymmetric notched tensile specimens. Local material parameters have been calculated arising from Beremin approach. Accepting this approach to the analysis of local criteria for cleavage fracture the location  $\sigma_u$  and shape parameters  $m$  were calculated using FEM for notched tensile bars having various type of geometry. The first one was the tensile specimen with the same circumferential notch the same as for Charpy (CVN), the other three types were U geometry with radii 1; 0.7; 0.2 mm. The fracture toughness scaling diagram based on the local approach has been generated.

## 1. Introduction

The aim of the paper can be seen in using the Beremin conception [1] of local approach to fracture resistance assessment. The local approach uses internal microscale variables related to the material damage evolution in order to predict initiation of macroscale cracks in an elastic plastic regime. This methodology has been an invaluable complement for classical fracture mechanics which is based on a single parameter for characterizing fracture but not reproduce the transitional behavior satisfactory. The local approach consists of application of finite element calculation using very fine mesh to predict fracture. The use of Weibull statistics for modeling of defect distribution over characteristic volume of material under a critical state of stress allows the probability of general unstable fracture to be predicted. The main steps are determination of the first principal stress at the experimentally obtained load level at fracture, calculation of the Weibull stresses at fracture and an iterative maximum likelihood procedure for distribution parameters of the Weibull stress. The effort is concentrated on (i) the use of notched tensile bars and (ii) small test specimen (Charpy V notch or pre-cracked CVN) for fracture toughness temperature diagram determination including scatter characteristics.

Transport and storage containers for spent nuclear fuel have to ensure the safe enclosure of a radioactive material and must meet stringent requirements on safety. They must ensure the storage of radioactive material safely for expected container lifetime and also in the case of the most severe accident loading and earthquake shock. The container should be highly resistant to temperature and radiation embrittlement. Škoda Nuclear Machinery (Czech Republic) has introduced new design of a container for spent nuclear fuel. The cast design is based on thick walled pipe with bolted lids, both fabricated from cast low alloyed steel with ferritic microstructure.

For the safe enclosure of the radioactive material during transportation it must be shown that the crack extension will not occur. For the safe storage additional embrittling effects should be taken into account. Brittle fracture can occur under specific combination of temperature, mechanical and environmental loading conditions. When assessing if the material satisfies the demand on container resistance against catastrophic failure the following key problems have to be addressed from the fracture mechanical point

of view: (i) the transferability of fracture toughness data measured on small specimens to the component of much larger dimensions. And (ii) the prediction with a good probability of brittle fracture in case of the most severe accident loading and in case of radiation embrittlement.

## 2. Theoretical background of the local approach

In the local approach to cleavage fracture, the probability distribution ( $P_f$ ) for the fracture stress of a cracked solid at a global level  $K_I$  or  $J$  is assumed to follow a two-parameter Weibull distribution [1,2] in the form:

$$P_f(\sigma_w) = 1 - \exp\left[-\left(\frac{\sigma_w}{\sigma_u}\right)^m\right], \quad (1)$$

the stress integral over the fracture process zone is denoted  $\sigma_w$  and is termed the Weibull stress. This stress is defined by

$$\sigma_w = \left[ \frac{1}{V_0} \int \sigma_1^m dV \right]^{1/m}, \quad (2)$$

where  $m$  is so-called Weibull slope,  $V_0$  is a reference volume, the integral is computed over the plastic zone, and  $\sigma_1$  is the first principal stress. The parameters  $\sigma_u$  and  $m$  of the Weibull stress  $\sigma_w$  at fracture are material parameters, i.e. independent of the stress state of materials, but may depend on the temperature. The first principal stress values are obtained from ABAQUS stress analysis and the Weibull stress is integrated element by element.

The determination of two parameters  $m$  and  $\sigma_u$  has to be performed iteratively as  $\sigma_w$  depends on the parameter  $m$ . This can be done by the least square method or preferably by the maximum likelihood procedure, e.g. [2,3],  $\sigma_u$  can be determined by the following equation

$$\sigma_u = \left( \frac{1}{N} \sum_{j=1}^N (\sigma_w^{(j)})^m \right)^{1/m}. \quad (3)$$

## 3. Material and experiment

Manganese cast steel has been utilized for experiments having a chemical composition in wt % given in Tab. 1. Škoda Company has supplied the material as a component part produced for attest of the container of nuclear spent fuel. To guarantee the microstructure of specimens used for the static test to be the same as that of an inner part of cast body the computer simulation of cooling of semi-product has been used. The heat treatment was done in the laboratory of ŠKODA Research Ltd. and as the result of this modeling was the scheme how to cut this experimental plate in size 55 x 90 x 250 mm from which three tested bodies were produced (in size 50 x 25 x 240 mm) for brittle fracture experiments. The size of semi-product was the compromise between the cooling rate for cooling simulation and furnace capacity.

True stress-strain curves have been measured using cylindrical specimens with a diameter of 6 mm being loaded over a temperature range of  $-196^\circ\text{C}$  to  $-60^\circ\text{C}$  at cross-head velocity of  $2 \text{ mm}\cdot\text{min}^{-1}$ . Standard FEA – ABAQUS 5.8 was used to model elastoplastic behaviour for tensile notched specimens.

Fracture toughness data were measured using a standard 25 mm thick specimen with  $a/W$  ratio of 0.5 loaded in the 3-point bending. Small pre-cracked Charpy type specimens have been also tested in the same temperature range. For one selected temperature in lower shelf region (below temperature  $T_{GY}$  at which  $F_{FR}$  and  $F_{GY}$  coincides on their temperature dependencies) a range of round tensile-notched bars were tested to obtain data for statistical local approach procedure treatment.

	<b>C</b>	<b>Mn</b>	<b>Si</b>	<b>P</b>	<b>S</b>	<b>Cr</b>	<b>Ni</b>	<b>Cu</b>	<b>Mo</b>	<b>V</b>	<b>Ti</b>
ČSN	Max	1	0,2	Max.	Max.	Max.	Max.	Max.	Max.	Max.	Max.
	0,12	1,6	0,5	0,03	0,02	0,3	0,4	0,3	0,15	0,03	0,05
melt	0,1	1,11	0,36	0,01	0,015	0,11	0,28	0,28	0,03	-	-
plate	0,09	1,18	0,37	0,01	0,025	0,12	0,29	0,29	0,03	0,001	0,002

	<b>W</b>	<b>Sn</b>	<b>Al</b>	<b>Nb</b>	<b>Co</b>	<b>As</b>	<b>Sb</b>
Plate	0,01	0,055	0,038	0,004	0,012	0,012	0,0095

Table 1: The chemical composition of manganese cast steel.

#### 4. Numerical modeling

Accepting the Beremin approach and ESIS methodology [4] to the analysis of local criteria for cleavage fracture the location  $\sigma_u$  and shape parameters  $m$  were calculated using FEM for notched tensile bars having various type of notch geometry (Table 2). The first one was the tensile specimen with the same circumferential notch as for Charpy (CVN), the other three types were U-notch geometry with radii 1;0.7;0.2 mm. Statistics were made at least for 20 replicated experiments in all cases. The influence of geometry and quality of mesh for FEM is presented in the Table 4 ( $V_0 = (100e-6)^3 \text{ m}^3$ ,  $\sigma_{th}/\sigma_0 = 1$ ).

The intrinsic model for notched bars is proposed with respect to symmetry as a half of bar. The axisymmetric elements CAX6 from Abaqus FEM [5] package are being used. In case of Charpy body the C3D8I elements were applied and due to symmetry the fourth part of body was solved. Approximately the same element size ahead the crack tip in the region 1 mm is being used because the data from this region are mainly exerted for determination of Weibull stress. The radii of notch was divided at least into 20 parts. The principal stress distribution at the maximum fracture force can be seen in Figure 1.

<b>Geometry</b>	<b>No. of elements</b>	<b>No. of nodes</b>	<b>No. of plastic elements</b>	<b>No. of plastic nodes.</b>	<b>Steps</b>	<b>CPU time [min]</b>
V notch	8243	16784	7625	12234	17	48
U 1 mm	10279	20784	8747	16234	20	56
U 0.7 mm	8755	17836	7765	15788	14	39
U 0.2 mm	11303	22966	9645	18496	15	54

Table 2: FEM mesh for various geometry

For the following step of modeling the right setting of determined material characteristics of the cast steel is necessary. As can be seen in [6], at tests temperatures the stress – strain curve has the region where the Lüders deformation is dominating. Therefore the standard relations seems to be not appropriate for the modeling. Incorrectness of standard Ramberg-Osgood or exponential description and then necessity to use piecewise linear description expressed in case of modeling the body with a crack. The dependence measurement the true stress true strain provides the information below the values of

deformation 0.15-0.2. After some numerical tests and their comparison with experiments, the next expression in Tab. 3 were applied.

Yield stress	$\varepsilon < 0,002434 - 0,03981 >$	$\sigma = 695,6 * \varepsilon + 496$	at $-160^{\circ}\text{C}$
hardening	$\varepsilon < 0,03981 - 0,9 >$	$\sigma = 1151 * \varepsilon^{0,2436}$	$E = 205\ 000\ \text{MPa}$
Yield stress	$\varepsilon < 0,0017512 - 0,02429 >$	$\sigma = 562,2 * \varepsilon + 361$	at $-100^{\circ}\text{C}$
hardening	$\varepsilon < 0,02429 - 0,9 >$	$\sigma = 1110 * \varepsilon^{0,2921}$	$E = 205\ 000\ \text{MPa}$

Table 3: Material properties

The presented results for geometry which can be seen in Fig. 1 show the plastic size difference as to region where the maximal principal stress is dominant. For the sharp notch the localization is close to notch tip, but for the notch with big radius is distributed in bigger profile. To verify each experiment and its numerical results the checkup of the elongation and the contraction was done. The example of this procedure can be seen in Fig. 2.

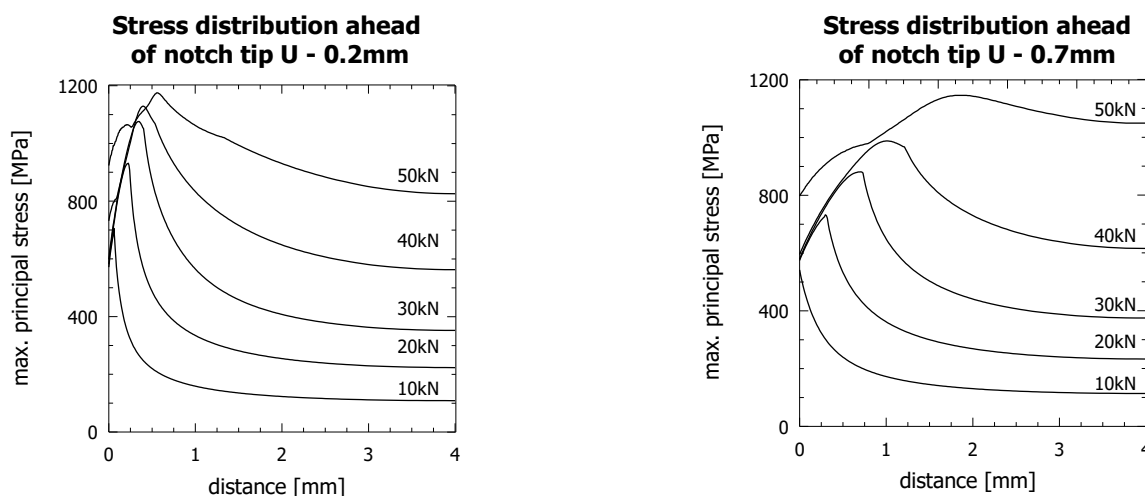


Fig. 1: Stress distribution ahead of notch tip

In case when the measured and computed values are compared the quality is different for various geometry. This discrepancy can be explained by two factors. The first one is caused by the variability of yield stress and length of Lüders deformation, the second one by the different level of plastic deformation size. The both factors put forth at the same time by the comparison of data record force – elongation for various tested body geometry. This discrepancy is due to own measurement of elongation where the Lüders deformation plays the dominant role. This phenomenon was observed at experiments for which the dependence force – contraction was measured. In case U notch 0.7 mm the accordance was nearly perfect and we can raise a presumption that the computation in place of local deformation is less sensitive with respect to variability of material characteristics given by static tensile test, especially for the material in inhomogeneities such as can be found in cast steel.

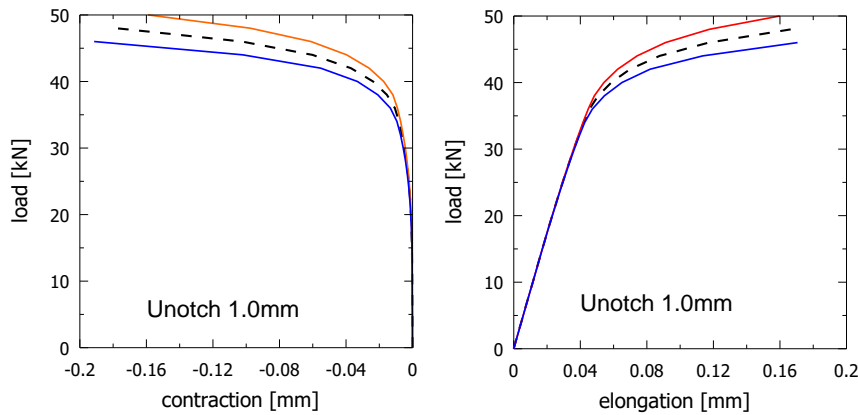


Fig. 2: Elongation and contraction for U notch = 1 mm, the mean value is received from FEM, outer values corresponds to the maximum and minimum of the fracture force

To determine the local parameters it is very important how to modify the base statistical data set. After the surface fracture inspection it is needful to omit these experiments whose character is unmatched to the weakest link theory. A selection is based on the usage of scanning digital camera and the following processing on a personal computer. The investigation showed that the right criterion for selection can come from the following relation  $\sigma_w = f(\varepsilon_p)$ , kde  $\varepsilon_p = -2 \ln(d/d_0)$ . Example of a such dependence is on the Fig. 3. The reference volume  $V_0$  is prescribed in [4] to be  $0.001 \text{ mm}^3$ . This value relates to microstructure dimensions as well to the element size of the FE mesh. The acceptable choice is this where the curve is linear. It means that in our test set in case U notch with radius 1 mm and 0.7 mm the valid data are for the deformation greater then 4 %, but for the specimen with U notch 0.2 mm from 0.3 %.

The next problem solved in this paper is if the quality of the FE mesh size has some influence on the generated local parameters. As can be seen e.g. in Tab. 4, the influence of this is nearly insignificant. Establishing  $\sigma_{th}/\sigma_0$  the influence of process zone was tested. But this aspect is insignificant for the same geometry too. Another problem is the difference in obtained local parameters for different notch diameter. The quality of generated local parameters can be seen in Fig. 4.

<b>U notch 0.2 mm</b>						
	~11300		~6500		~3500	
$\sigma_{th}/\sigma_0$	m	$\sigma_u$	m	$\sigma_u$	m	$\sigma_u$
0	65.6	1340	64.6	1343	63.3	1350
1	65.6	1340	64.6	1343	63.3	1350
1.5	65.6	1340	64.6	1342	63.3	1350
<b>U notch 0.7 mm</b>						
0	17.0	2485	16.9	2491	16.8	2506
1	17.0	2484	16.9	2491	16.8	2506
1.5	16.9	2489	16.9	2494	16.8	2508
<b>U notch 1. mm</b>						
0	18.2	2117	17.8	2145	17.8	2146
1	18.2	2117	17.8	2146	17.8	2146
1.5	18.2	2120	17.8	2148	17.7	2149

Table 4: The influence of the mesh size and of the used process zone

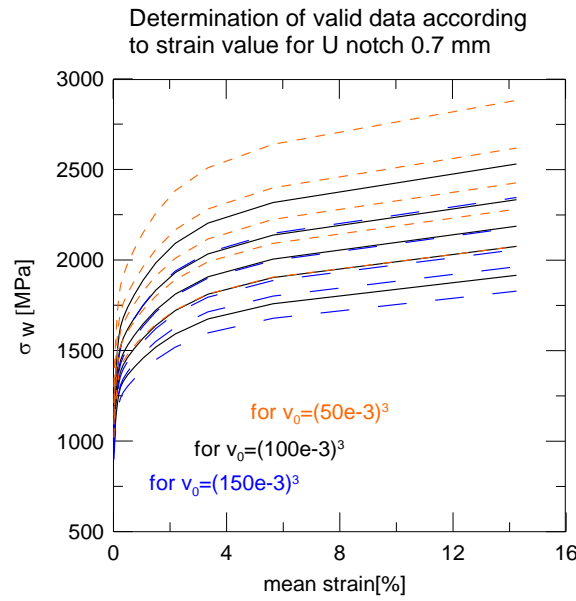


Fig 3 : The valid data determination,  $v_0$  is given in  $\text{mm}^3$

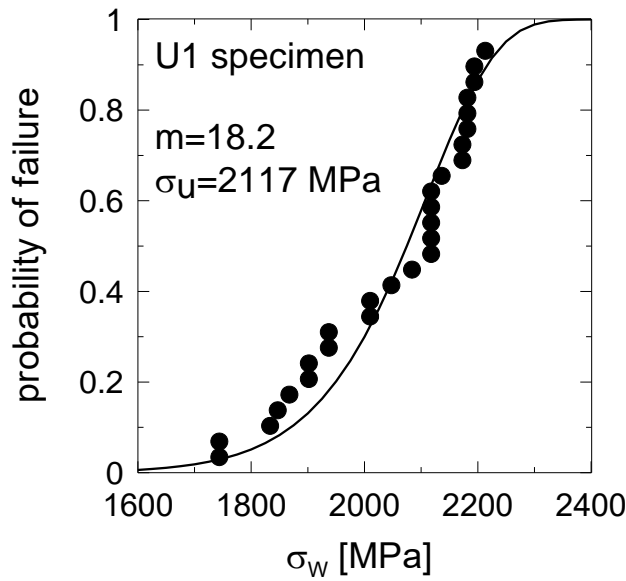


Fig 4: Probability of failure for  $m=18$ ,  $\sigma_u=2117 \text{ MPa}$

### 5. Local parameters and fracture toughness scaling diagram

The development of methodology for prediction of fracture behavior of components and structures has great practical meaning and one can suppose the new European norms setting and standard procedures for valuation of integrity of construction. E.g. using the Charpy pre-cracked specimens indicates to be very perspective for valuation of material degradation in nuclear industry.

The soundness of structures is usually ensured on the basis of several relatively well accepted rules. These rules are supposed to be able to assess the integrity for complex engineering applications on the base of exact measurement in laboratory, evaluation of received data according to standards and their transferability to components and structures. The most recent investment proved that e.g. the well-used characteristics as the fracture toughness cannot be generally used to the arbitrary geometry of body. The

new methods of experimental and theoretical fracture mechanics should be provide the right rules to solve it. Based on this concept, some works from seventies and eighties years are trying to predict values of  $K_{IC}$  and relations between  $K_{IC}$  and absorbed energy CVN. Values developed by linear or elastic plastic fracture mechanics are used for assessment of defect tolerance from a global view. At present, latest approaches can be characterized mostly by the knowledge of micromechanics and micromechanisms of failure. More recently the approach to the problems has been developed. This is the local approach which relies upon the fact that it is possible to model macroscopic fracture behavior of defected components in terms of local fracture criteria. This statistical approach, the methodology of local material parameters measurement using notched tensile specimens and some prediction of brittle fracture behavior prediction were worked out during solution of this problem. It is important to emphasize that local approach methodology has wider spectrum of approaches than were incorporated in Beremin model and others.

The results demonstrates the strong dependence of crack-tip field on the specimen geometry, mainly induced by shallow cracks and remote loading – the constraint phenomena is being studied. As can be seen in literature the Weibull stress  $\sigma_w$  seems be as a suitable near-tip parameter to describe the coupling of the remote loading with a micromechanical model incorporating the statistics of microcracks (weakest link philosophy). Then one can used it to prediction of critical parameters of the fracture initiation for the various cracks length and geometry of body. The material parameters received then make possible to use the J – Q stress field for the determination of the critical value of J integral  $J_c$  versus Q parameter. This dependence  $J_c - Q$ , incorporating the probability of failure, is more precise then the result based on model of critical fracture stress. The result received can more precisely describe the behavior of bodies with cracks and better study the problems of transferability of some fracture parameter from one body geometry to another.

The first one methodic of transferability of the fracture toughness was studied on the pre-cracked Charpy specimens and standard bodies (1T). The Dodds and Anderson [7] have proposed to quantify the relative effects of constraint variation on the cleavage fracture toughness in the form toughness-scaling model . They approached lost of constraint by postulating the material volume ahead of the crack front over which the principal stress exceeds a critical value as a local fracture criterion without respect for the J integral value. The first one studies can be found out in same woks, where as principal can be regarded: (i) the Dodds and Anderson approach , (ii) the Koppenhofer approach , (iii) the Minami and others [8, 9, 10].

(i) The method is getting from the philosophy of diagram construction  $J_o/b\sigma_o$  versus  $J_{FE}/b\sigma_o$ , where b is body thickness and  $\sigma_o$  is yield stress. The principle is to transfer from tested geometry, where the elasto-plastic fracture toughness is measured, to small scale yielding state (SSY). (ii) These method demonstrate the dependence of Weibull stress  $\sigma_w$  on the crack-tip stress triaxility and the transfer diagram  $\sigma_w$  versus computed value of  $J_{FE}$  is being constructed. The idea is to used to same value of probability of failure. In the beginning we have to determine the local parameters, m and  $\sigma_u$ , and compute  $\sigma_w$  of bodies of various geometry. (iii) This approach is modified Koppenhofer method and the construction  $\ln(\ln(1/P_f))$  versus  $\sigma_w$  is generated.

The results demonstrates the strong dependence of crack-tip field on the specimen geometry, mainly induced by shallow cracks and remote loading – the constraint phenomena is being studied. As can be seen in [9] the Weibull stress  $\sigma_w$  seems to be as a suitable near-tip parameter to describe the coupling of the remote loading with a micromechanical model incorporating the statistics of microcracks (weakest link philosophy). Then one can use it in the prediction of critical parameters of the fracture initiation for the various cracks length and geometry of body. The material parameters received [10,11] then make possible to use the J – Q stress field for the determination of the critical value of J integral  $J_c$  versus Q parameter. This dependence  $J_c - Q$ , incorporating the probability of failure, is more precise than the result based on model of critical fracture stress [8]. The result received can more precisely describe the behavior of bodies with cracks and better study the problems of transferability of some fracture parameter from one body geometry to another. The transformation diagram for three SENB geometry and pre-cracked Charpy was determined and is presented in Fig. 5 and the calculation matrix in Tab. 5.

Geometry	Size [mm]	Nodes	Layers	Calculation
Charpy a/W = 0.5	10x10x55	16300	15	11
Charpy a/W = 0.5	10x10x55	35400	30	1
a/W = 0.1	25x26x104	27800	15	9
a/W = 0.2	25x30x120	23900	15	10
a/W = 0.5	25x50x200	16200	15	1

Geometry	a1	a2	a3	a4	a5	a6	a7	a8	a9	a10	a11
Charpy a/W = 0.5	4.65	4.8	4.9	4.95	5	5.05	5.1	5.2	5.25	5.3	5.55
a/W = 0.1	2	2.22	2.3	2.4	2.5	2.7	2.8	3.2	3.7		
a/W = 0.2	4.7	5.5	6	6.15	6.3	6.5	7	7.2	7.4	7.6	
a/W = 0.5	25										

Table 5: Calculation matrix

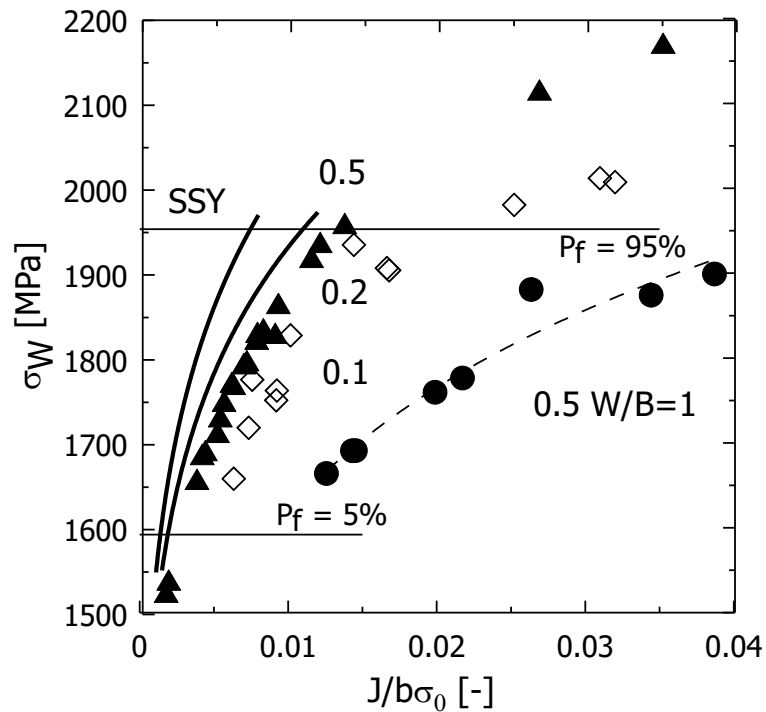


Fig. 5: Fracture toughness scaling diagram for the manganese cast steel

Scatter band can be generally described as can be seen in Fig. 6. We can say that the bigger is the crack length the bigger is the scatter band.

## 6. Conclusion

The main results obtained in this work can be summarized into the following points:

- The Beremin model with strain correction (slightly adapted) is used for the calculation of  $\sigma_w$ . The iterative procedure using the maximum likelihood theory was applied and the geometry effect for various notch radius of tensile bars is observed.
- The local parameters generated on the geometry with U notch 0.2 mm, V notch 0.25 mm and on the Charpy specimen give practically the same values.

- The valid local parameters are received on test specimens with notch radius 0.7 and 1 mm, where the character of maximum principle stress distribution has no influence on the microstructure inhomogenities which can be found in the cast steel.
- The fracture toughness scaling diagram based on the local approach for three geometry was determined and used for the transformation of data received on small pre-cracked specimens. Other experiments are currently being carried out to test this approach.
- The influence of the crack length on the scatter band has been observed, prediction on  $a/W = 0.5$  and SSY (small scale yielding) can be seen in the Fig.8.

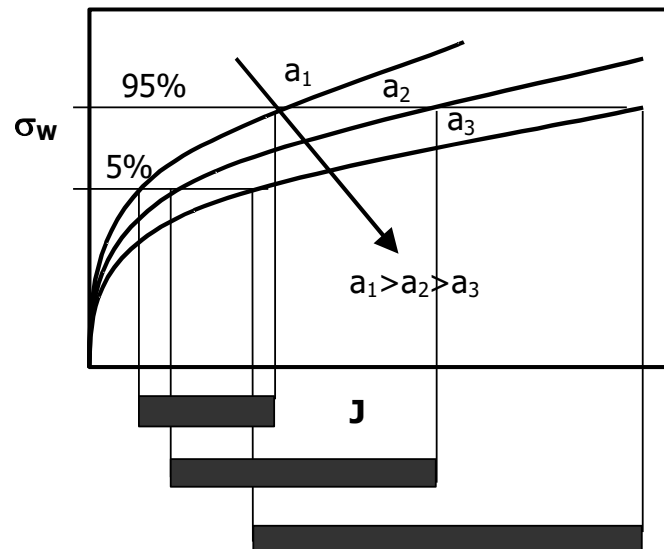


Fig.6: Fracture toughness scaling diagram based on the Weibull stress

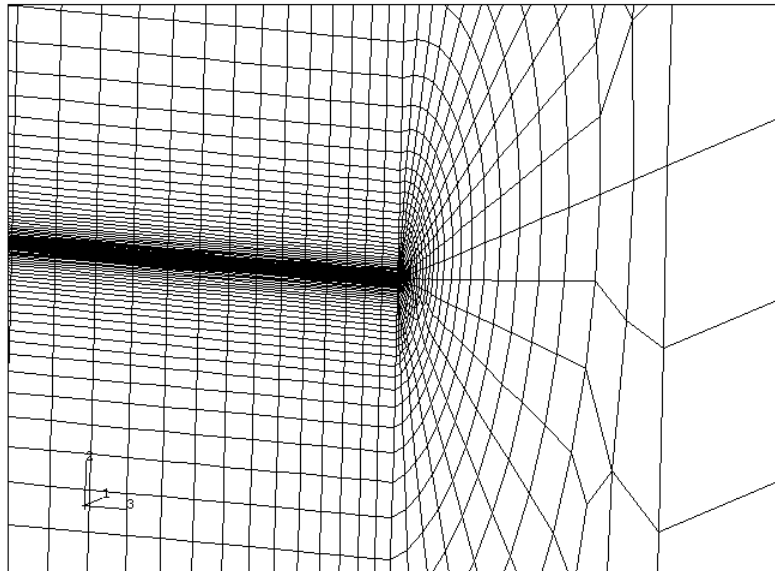


Fig. 7: Detail of mesh tip

## Acknowledgements

This research was financially supported by grant No. A2041003 Grant Agency of the Academy of Sciences of Czech Republic and by grant No. 101/00/0170 of the Grant Agency of the Czech Republic.

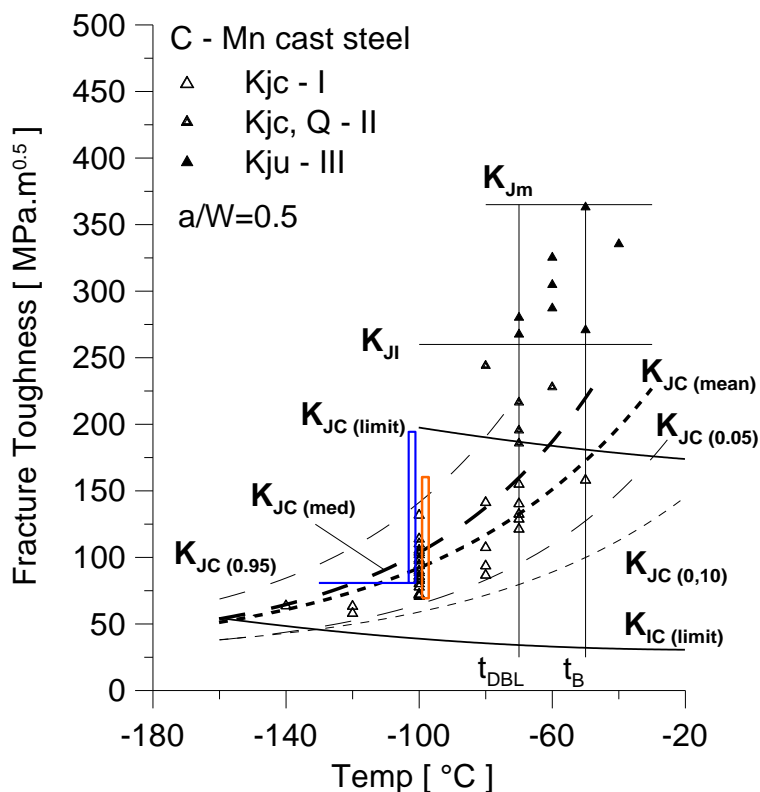


Fig. 8: FT prediction for a/W=0.5 and SSY

## References

- [1] Beremin, F. M., Metal. Trans. A, Vol. **14A**, 2277, 1983.
- [2] Riesch-Opperman, H., Bruckner-Foit, A., Weistraba, *Wissenschaftliche Berichte FZKA 6155*, M. Forschungszentrum Karlsruhe, Germany, 1998.
- [3] Gao, X., Ruggieri, C., Dodds, R., H., Calibration of Weibull stress parameters using fracture toughness data, *Int. J. of Fracture* **92**, 175, 1998.
- [4] ESIS P 6 98, Procedure to measure and calculate materials parameters for the local approach to fracture using notched tensile specimens.
- [5] Hibbit, Karlsson & Sorensen Inc., Abaqus 5.8.14, Users manual, 1999.
- [6] Kozák, V., Dlouhý, I., Holzmann, M., The fracture Behavior of the Cast Steel and Its Prediction Using the Local Approach, *SMIRT-15*, Seoul, Korea, Vol. **V**, pp. 71-78, 1999.
- [7] Ruggieri, C., Dodds, R., H., Wallin, K., (1998), *Eng. Fract. Mechan.* Vol. **60**, pp. 14-36, 1998.
- [8] Shih, C., F., O'Dowd, N., P., (1992): Shallow Cracks Fracture Mechanics, *Toughness Test and Applications*, Cambridge, conf. TWI, Abington Publ., P31.
- [9] Koppenhoefer, K., C., Dodds, R., H., *Eng. Fracture Mechanic*, Vol **58**, pp. 224 – 270, 1997.
- [10] Ainswort, R., A., O'Dowd, R., H.,: Constraint in the failure assessment diagram approach for fracture assessment, *Journal of Pressure Vessel Technology*, Trans. of ASME, Vol. **117**, pp. 260-297, 1995.
- [11] Kozák, V., Holzmann, M., Dlouhý, I., Fracture toughness transferability: From the standard 1T specimen to the pre-cracked Charpy specimen, *Computational Methods and Experimental Measurements IX*, Sorrento, Italy, pp.87-96. 1999.

- B2 Kozák, V., Dlouhý, I., The transferability of fracture toughness characteristics from point a view of the integrity of components with defects, *Computational Methods and Experimental Measurements (CMEM 2001)*, Alicante, Španělsko, (2001), 757-766, invited lecture.

# The transferability of fracture toughness characteristics from point a view of the integrity of components with defects

V. Kozák & I. Dlouhý

*Institute of Physics of Materials, Academy of Sciences of the Czech Republic, Žitkova 22, 616 62 Brno, Czech Republic*  
Email: kozak@ipm.cz

## Abstract

*In this work, the use of the Weibull stress as a measure of the failure probability of cracked body is tested. Fracture of large engineering structures and conventional safety assessment and integrity of components and structures still remains a top field of research in the experimental and the theoretical fracture mechanics. Weibull stress seems to be a parameter for prediction of cleavage failure of cracked bodies and the study is focused to assess the effects of constraint loss on cleavage fracture toughness ( $J_c$ ). To quantify the relative effects of constraint variation on the cleavage fracture toughness the form of the toughness-scaling model based on the Weibull stress  $\mathbf{s}_w$  is investigated. Local material parameters have been calculated arising from Beremin approach. It is based on weakest link assumption and incremental fracture probability, which depends not only on the maximum principal stress, but also on the equivalent plastic strain. Accepting this approach to the analysis of local criteria for cleavage fracture the location  $\mathbf{s}_u$  and shape parameters  $m$  were calculated using FEM for notched tensile bars having various type of geometry. The aim of the paper can be seen in fracture toughness correction from various specimen geometries to small scale yielding (SSY). The fracture resistance has been assessed using data from static tests of the bend specimens and from the axisymmetric notched tensile specimens. The standard finite element method package Abaqus was applied and the manganese cast steel considered for storage and transport container for spent nuclear fuel (SKODA) was selected as an experimental material.*

## 1 Introduction

Transport and storage containers for spent nuclear fuel have to ensure the safe enclosure of a radioactive material and must meet stringent requirements on safety. They must ensure the storage of radioactive material safely for the expected container lifetime and also in the case of the most severe accident loading and earthquake shock. The container should be highly resistant to temperature and radiation embrittlement. Škoda Nuclear Machinery (Czech Republic) has introduced a new design of container for spent nuclear fuel. The cast design is based on thick walled pipe with bolted lids, both fabricated from cast low-alloyed steel with ferritic microstructure.

For the safe enclosure of the radioactive material during transportation it must be shown that the crack extension will not occur. For the safe storage additional embrittling effects should be taken into account. Brittle fracture can occur under specific combination of temperature, mechanical and environmental loading conditions. When assessing if the material satisfies the demand on container resistance against catastrophic failure the following key problems have to be addressed from the fracture mechanical point of view: (i) the transferability of fracture toughness data measured on small specimens to the component of much larger dimensions. And (ii) the prediction with a good probability of brittle fracture in case of the most severe accident loading and in case of radiation embrittlement.

## 2 Theoretical background of the local approach

Cleavage fracture is a sequential process involving crack initiation and propagation. Crack nucleation occurs in most steels at brittle grain boundary particles (e.g. carbides) due to stress concentration caused by the dislocations pile-ups at these particles. This explains the experimental fact that local plastic deformation always preceded cleavage fracture. The local approach for cleavage is based on the weakest link concept (see Fig. 1) which postulates that failure of the body of a material containing a large number of statistically independent volumes is triggered by the failure of one of the reference volume [1]. In Ref. [2], the reference volume  $V_0$  was identified as a material volume related to likelihood of finding cracked carbide. In a finite element analysis it is kept to be constant and to be computed Weibull stress independent of the finite element mesh used the size of the element in the plastic zone ahead the crack tip must be smaller than size of  $V_0$ .

In the local approach to cleavage fracture, the probability distribution ( $P_f$ ) for the fracture stress of a cracked solid at a global level  $K_I$  or  $J$  is assumed to follow a two-parameter Weibull distribution [1,2] in the form:

$$P_f(\mathbf{s}_w) = 1 - \exp\left[-\left(\frac{\mathbf{s}_w}{\mathbf{s}_u}\right)^m\right]. \quad (1)$$

The stress integral over the fracture process zone is denoted  $\sigma_w$  and is termed the Weibull stress. This stress is defined by

$$\sigma_w = \left[ \frac{1}{V_0} \int \sigma_1^m dV \right]^{1/m}, \quad (2)$$

where  $m$  is so-called Weibull slope,  $V_0$  is a reference volume, the integral is computed over the plastic zone, and  $\sigma_1$  is the first principal stress. The parameters  $\sigma_u$  and  $m$  of the Weibull stress  $\sigma_w$  at fracture are material parameters, i.e. independent of the stress state of materials, but may depend on the temperature.

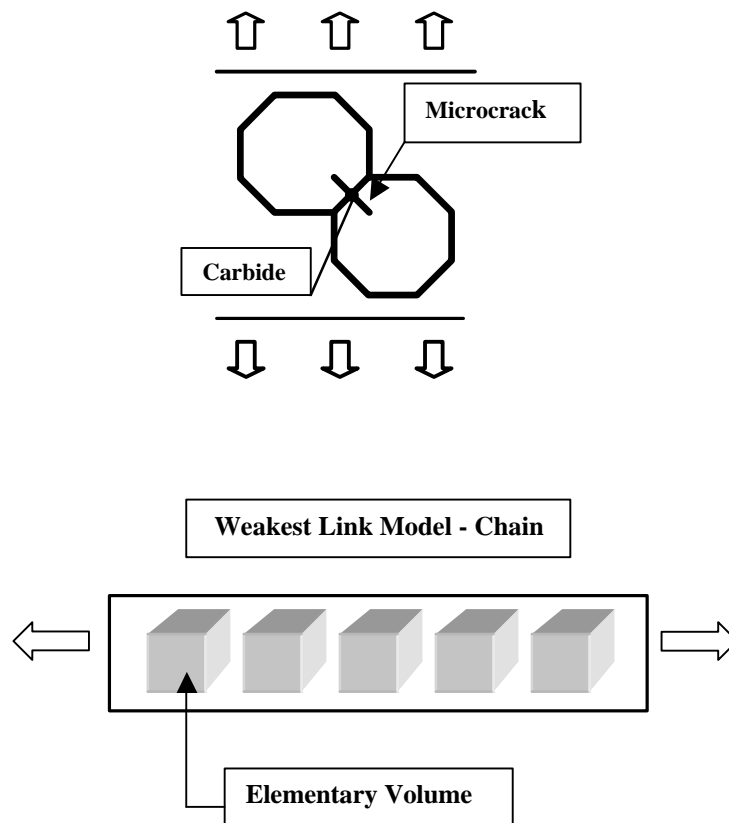


Figure1: Fundamentals of the local approach.

The determination of two parameters  $m$  and  $\sigma_u$  has to be performed iteratively as  $\sigma_w$  depends on the parameter  $m$ . This can be done by the least square method or preferably by the maximum likelihood procedure, e.g. [2,3],  $\sigma_u$  can be determined by the following equation

$$s_u = \left( \frac{1}{N} \sum_{j=1}^N (s_w^{(j)})^m \right)^{1/m} . \quad (3)$$

### 3 Local parameters and fracture toughness scaling diagram

The development of methodology for prediction of fracture behaviour of components and structures has great practical meaning and one can suppose the new European norms setting and standard procedures for valuation of integrity of construction. E.g. using the Charpy pre-cracked specimens indicates to be very perspective for valuation of material degradation in the nuclear industry.

The soundness of structures is usually ensured on the basis of several relatively well-accepted rules. These rules are supposed to be able to assess the integrity for complex engineering applications on the base of exact measurement in laboratory, evaluation of received data according to standards and their transferability to components and structures. The most recent investment proved that e.g. the well-used characteristics as the fracture toughness couldn't be generally used to the arbitrary geometry of body. The new methods of experimental and theoretical fracture mechanics should provide the right rules to solve it. Based on this concept, some works from the seventies and eighties are trying to predict values of  $K_{IC}$  and relations between  $K_{IC}$  and absorbed energy CVN (e.g. [1]). Values developed by linear or elastic plastic fracture mechanics are used for assessment of defect tolerance from a global view. At present, the latest approaches can be characterized mostly by the knowledge of micromechanics and micromechanisms of failure. More recently the approach to the problems has been developed. This is the local approach that relies upon the fact that it is possible to model macroscopic fracture behaviour of defected components in terms of local fracture criteria. This statistical approach, the methodology of local material parameters measurement using notched tensile specimens and some prediction of brittle fracture behaviour prediction were worked out during solution of this problem. It is important to emphasize that local approach methodology has wider spectrum of approaches than were incorporated in Beremin model and others.

The first one methodic of transferability of the fracture toughness was studied on the pre-cracked Charpy specimens and standard bodies (1T). The Dodds and Anderson [4] have proposed to quantify the relative effects of constraint variation on the cleavage fracture toughness in the form toughness-scaling model. They approached lost of constraint by postulating the material volume ahead of the crack front over which the principal stress exceeds a

critical value as a local fracture criterion without respect for the J integral value. The first one studies can be found out in same works, where as principal can be regarded: (i) the Dodds and Anderson approach, (ii) the Koppenhofer approach, (iii) the Minami and others [5, 6, 7].

(i) The method is getting from the philosophy of diagram construction  $J_o/b\sigma_o$  versus  $J_{FE}/b\sigma_o$ , where  $b$  is body thickness and  $\sigma_o$  is yield stress. The principle is to transfer from tested geometry, where the elasto-plastic fracture toughness is measured, to small scale yielding state (SSY). Schematic outline can be seen at Fig. 2. (ii) This method demonstrates the dependence of Weibull stress  $\sigma_w$  on the crack-tip stress triaxility and the transfer diagram  $\sigma_w$  versus computed value of  $J_{FE}$  is being constructed. The idea is to use same value of probability of failure. In the beginning we have to determine the local parameters,  $m$  and  $\sigma_w$ , and compute  $\sigma_w$  of bodies of various geometry. (iii) This approach is modified Koppenhofer method and the construction  $\ln(\ln(1/P_f))$  versus  $\sigma_w$  is generated.

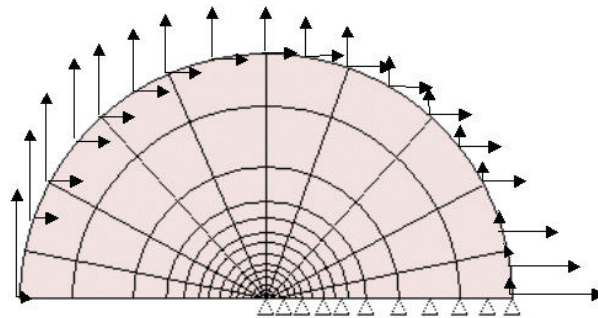


Figure 2: Schematic outline of modified boundary layer method.

#### 4 Material characteristics and experiments

Manganese cast steel has been utilized for experiments having a chemical composition in wt % given in Table 1. Škoda Company has supplied the material as a component part produced for attest of the container of nuclear spent fuel. To guarantee the microstructure of specimens used for the static test to be the same as that of an inner part of cast body the computer simulation of cooling of semi-product has been used. The heat treatment was done in the laboratory of ŠKODA Research Ltd. and as the result of this modelling the scheme how to cut this experimental plate in size 55 x 90 x 250 mm from which three tested bodies were produced (in size 50 x 25 x 240 mm) for brittle fracture experiments. The size of the semi-product was the compromise between the cooling rate for cooling simulation and furnace capacity.

True stress-strain curves have been measured using cylindrical specimens with a diameter of 6 mm being loaded over a temperature range of  $-196^{\circ}\text{C}$  to  $-60^{\circ}\text{C}$  at crosshead velocity of  $2 \text{ mm}\cdot\text{min}^{-1}$ . Standard FEA – ABAQUS 5.8 [8] was used to model elastoplastic behaviour for tensile-notched specimens.

Fracture toughness data were measured using specimens with a/w ratio of 0.5, 0.2, 0.1 loaded in the 3-point bending. The size of these specimens is given in Table 2. For one selected temperature in lower shelf region (below temperature  $T_{\text{GY}}$  at which  $F_{\text{FR}}$  and  $F_{\text{GY}}$  coincides on their temperature dependencies) a range of round tensile-notched bars were tested to obtain data for statistical local approach procedure treatment.

	C	Mn	Si	P	S	Cr	Ni	Cu	Mo	V	Ti
CSN	Max	1	0,2	Max	Max	Max	Max	Max	Max	Max	Max
	0,12	1,6	0,5	0,03	0,02	0,3	0,4	0,3	0,15	0,03	0,05
melt	0,1	1,11	0,36	0,01	0,015	0,11	0,28	0,28	0,03	-	-
plate	0,09	1,18	0,37	0,01	0,025	0,12	0,29	0,29	0,03	0,001	0,002

	W	Sn	Al	Nb	Co	As	Sb
Plate	0,01	0,055	0,038	0,004	0,012	0,012	0,0095

Table 1: The chemical composition of manganese cast steel.

Geometry	Size [mm]	Nodes	Layers	Calculation
Charpy a/W = 0.5	10x10x55	16300	15	11
Charpy a/W = 0.5	10x10x55	35400	30	1
a/W = 0.1	25x26x104	27800	15	9
a/W = 0.2	25x30x120	23900	15	10
a/W = 0.5	25x50x200	16200	15	16

Table 2: Specimens used for determination of the TSM diagram.

## 5 Numerical determinations of local parameters and TSM

Accepting the Beremin approach and ESIS methodology [9] to the analysis of local criteria for cleavage fracture the location  $\sigma_0$  and shape parameters  $m$  were calculated using FEM for notched tensile bars having various type of notch geometry. The first one was the tensile specimen with the same circumferential

notch as for Charpy (CVN), the other three types were U-notch geometry with radii 1; 0.7; 0.2 mm. Statistics were made at least for 20 replicated experiments in all cases.

The intrinsic model for notched bars is proposed with respect to symmetry as a half of bar. The axisymmetric elements CAX6 from Abaqus FEM [8] package are being used. In case of Charpy body the C3D8I elements were applied and due to symmetry the fourth part of body was solved. Approximately the same element size ahead the cracks tip in the region 1 mm is being used because the data from this region are mainly exerted for determination of Weibull stress. The radii of notch were divided at least into 20 parts. The quality FEM approximation can be seen from Table 3.

Geometry	No. of elements	No. of nodes	No. of plastic elements	No. of plastic nodes.
<b>V notch</b>	8243	16784	7625	12234
<b>U 1 mm</b>	10279	20784	8747	16234
<b>U 0.7 mm</b>	8755	17836	7765	15788
<b>U 0.2 mm</b>	11303	22966	9645	18496

Table 3: FEM mesh for notched specimens.

To determine the local parameters it is very important how to modify the base statistical data set. After the surface fracture inspection it is needful to omit these experiments whose character is unmatched to the weakest link theory. A selection is based on the usage of scanning digital camera and the following processing on a personal computer. Some data were received using scanning electron microscopy. In all cases carbides were found at the cleavage origin; example can be seen in Fig. 3. The investigation showed that the right criterion for selection can come from the following relation  $\sigma_w = f(\epsilon_p)$ , kde  $\epsilon_p = -2 \ln(d/d_0)$ . The acceptable choice is this where the curve is linear. It means that in our test set in case U notch with radius 1 mm and 0.7 mm the valid data are for the deformation greater then 4 %, but for the specimen with U notch 0.2 mm from 0.3 %.

The material parameters received then make possible to use the J – Q stress field for the determination of the critical value of J integral  $J_c$  versus Q parameter. This dependence  $J_c - Q$ , incorporating the probability of failure, is more precise than the result based on model of critical fracture stress [5]. The result received can more precisely describe the behavior of bodies with cracks and better study the problems of transferability of some fracture parameter from one body geometry to another. The transformation diagram for three SENB geometry and pre-cracked Charpy was determined and is presented in Fig. 5.

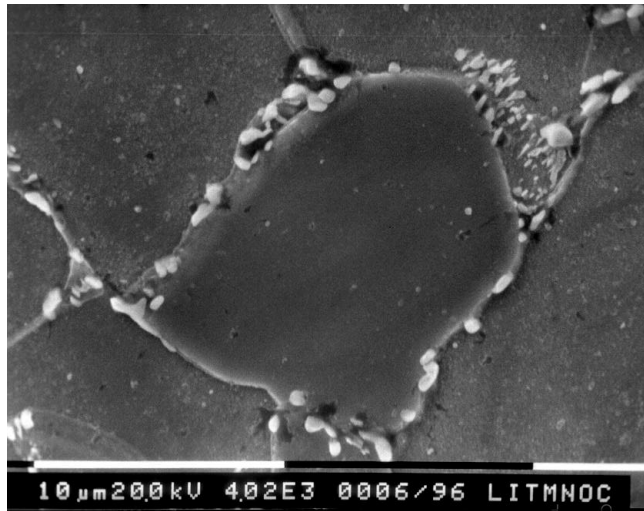


Figure 3: A carbide particle observed at the cleavage origin.

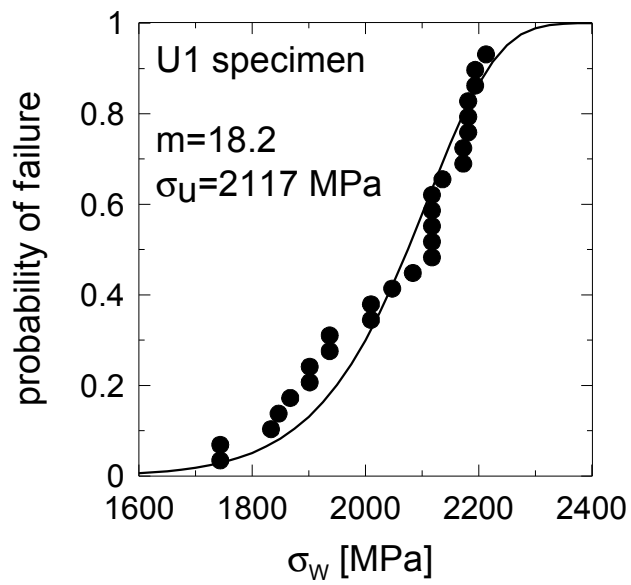


Figure 4: Probability of failure for  $m=18$ ,  $\sigma_u=2117$  MPa.

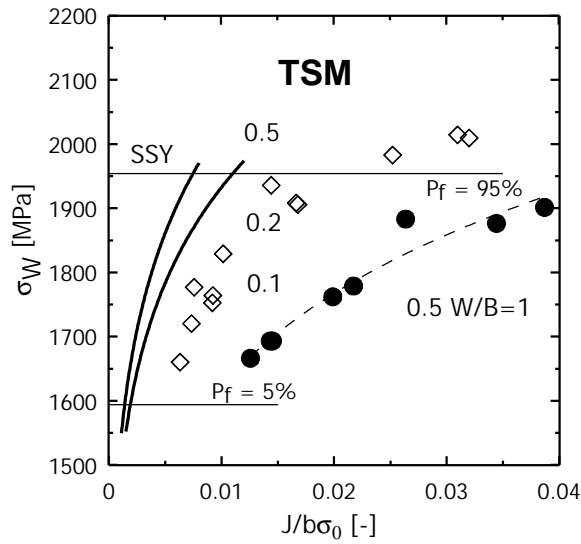


Figure. 5: Toughness scaling diagram for the manganese cast steel.

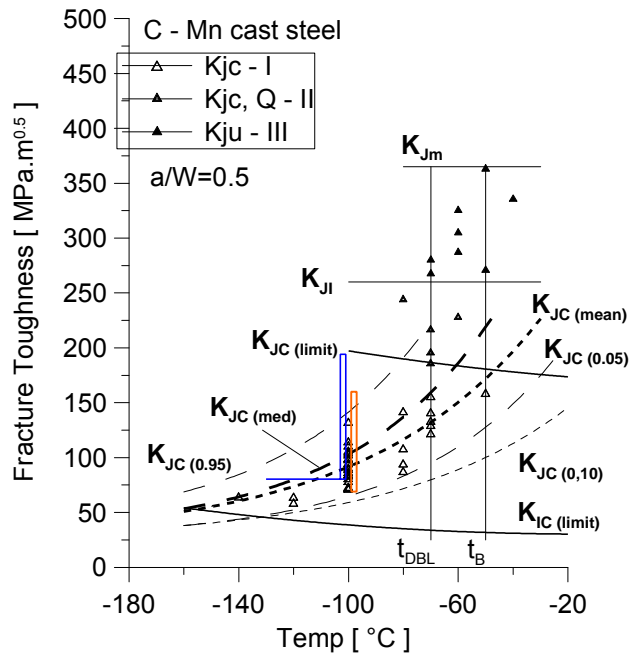


Figure. 6: FT prediction for  $a/w = 0.5$  and SSY.

## 6 Conclusion

The main results obtained in this work can be summarized into the following points:

- The Beremin model with strain correction (slightly adapted) is used for the calculation of  $\sigma_w$ .
- The valid local parameters are received on test specimens with notch radius 0.7 and 1 mm, where the character of maximum principle stress distribution has no influence on the microstructure inhomogeneities that can be found in the cast steel. For more detailed information see [10].
- The fracture toughness-scaling diagram based on the local approach for three geometries was determined and used for the transformation of data received on small pre-cracked specimens. Other experiments are currently being carried out to test this approach.
- The influence of the crack length on the scatter band has been observed, prediction on  $a/W = 0.5$  and SSY can be seen in the Fig. 6.

## Acknowledgements

This research was financially supported by grant 101/00/0170 Grant Agency of the Czech Republic and by project Nato SfP 972655 (Kontakt ME 303).

## References

- [1] Beremin, F. M., Metal. Trans. A, Vol. 14A, 2277, (1983).
- [2] Riesch-Opperman, H., Bruckner-Foit, A., Weistraba, *Wissenschaftliche Berichte FZKA 6155*, M. Forschungszentrum Karlsruhe, Germany, (1998).
- [3] Gao, X., Ruggieri, C., Dodds, R., H., Calibration of Weibull stress parameters using fracture toughness data, *Int. J. of Fracture* 92, 175, (1998).
- [4] Ruggieri, C., Dodds, R., H., Wallin, K, (1998), *Eng. Fracture. Mechanics*. 60, pp. 14-36, (1998).
- [5] Shih, C., F., O'Dowd, N., P., (1992): *Shallow Cracks Fracture Mechanics, Toughness Test and App.*, Cambridge, conf. TWI, Abington Publ., P31.
- [6] Koppenhoefer, K., C., Dodds, R., H., *Eng. Fracture Mechanic* 58, pp. 224 – 270, (1997).
- [7] Ruggieri C., Gao X., Dods, R., H., Transferability of elastic-plastic fracture toughness using Weibull stress approach, *Eng. Fracture. Mechanics* 67, pp. 111-117, (2000).
- [8] Hibbit, Karlsson & Sorensen Inc., Abaqus 5.8.14, Users manual, (1999).
- [9] ESIS P 6 98, Procedure to measure and calculate materials parameters for the local approach to fracture using notched tensile specimens.
- [10] Kozák, V., Dlouhý, I., Holzmann, M., The fracture Behaviour of the Cast Steel and Its Prediction Using the Local Approach, *SMIRT-15*, Seoul, Korea, Vol. V, pp. 71-78, (1999).

B3 Kozák, V., Vlček, L., Constraint phenomena on the pre-cracked specimen: numerical and experimental evaluation, *ECF 14*, Cracow, (2002), 251-259.

# Constraint phenomena on the pre-cracked specimens: numerical and experimental evaluation

Vladislav Kozák and Libor Vlcek

Institute of Physics of Materials, Czech Academy of Sciences, Brno,  
Zizkova 22, 616 62 Brno, Czech Republic

**ABSTRACT:** *An extensive investigation has been carried out on the sensitivity parameters determination describing the fracture behaviour of body with crack with respect to the character change of true stress-strain curve with dominant region of Lueders deformation. The attention is paid on the influence of hardening exponent of deformation to the history of the idealised true stress-strain material curve described by the Ramberg-Osgood relation. Above mentioned tests are used for the correct Weibull stress determination, which is as a measure of the failure probability of cracked body. The Weibull stress model for cleavage fracture of cast steel requires calibration of two micromechanics parameters ( $m$ ,  $\sigma_w$ ). Weibull stress seems to be a parameter for prediction of cleavage failure of cracked bodies and the study is focused on the assessment of the effects of constraint loss on cleavage fracture toughness ( $J_c$ ). Local material parameters have been calculated arising from Beremin approach and calibration is based on the Gao and Ruggieri approach. The aim of the paper can be seen in fracture toughness transfer and correction from pre-cracked specimens to small scale yielding (SSY) represented by 1T (SENB) specimens and their precise computation using FEM. The fracture resistance has been assessed using data from static tests of the three point bend specimens.*

## Introduction

To quantify the effects of constraint variation on the cleavage fracture toughness the form of the toughness-scaling model based on the Weibull stress  $\sigma_w$  is investigated. Method is based on weakest link assumption and incremental fracture probability, which depends not only on the maximum principal stress, but also on the equivalent plastic strain. It seems that for transferring of fracture-mechanical data from test specimens to exposed real constructions or to its monitored parts, it is necessary to use two-parameter fracture approach. This requirement involved large investigations, which are considered of the constraint influence near the crack tip to fracture behaviour. Recent extensive investigations on crack tip constraint effects

provide a necessity of testing various constraint configurations, such as shallow-cracked SEN(B) specimens.

Determining of static fracture toughness on SEN(B) specimens is one of the basic fracture mechanics test. As a result of this test are significant values of static fracture toughness, which depends upon temperature. It must be emphasised that the most important values are critical K-value, in case of using linear-elastic fracture mechanics and critical value of J-integral, in case of using elastic-plastic fracture mechanics. Subsequently we confine our investigation to elastic-plastic material behaviour.

More realistic description of crack tip stress and deformations fields has been developed. Approaches are based on two-parameter characterization of crack tip fields, such T- stress and nondimensional Q-stress. In both approaches, J sets the magnitude of near tip deformation, while the second parameter characterizes the level of stress triaxiality. These J-T and J-Q approaches retain contact with traditional fracture mechanics. Laboratory measurements on the specimens with varying crack length (changing the relation  $a/W$ ) and with the same ligament showed increasing values of fracture toughness expressed using  $J_c$  versus decreasing crack length. Following the idea of Sumpter [1], Kirk and Dodds [2] investigated several possibilities of J-integral and CTOD estimation for SEN(B) specimens with shallow crack. For fracture toughness valuation on the base two-parameter fracture mechanics the evaluation of parameters, which express the constraint ahead the crack tip in our case Q-parameter, is critical. Several approaches exist: (i) On the base of experimentally determined dependence  $J_c$  on  $a/W$  the Q calculation comes after from numerically given stress fields received by FEM for every analysed body separately. (ii) Statistical approach using so called local approach [3]. We limit our focus to a stress controlled, cleavage mechanism for material and adopt the Weibull stress ( $\sigma_w$ ) as the local parameter to describe crack-tip conditions. Unstable crack propagation occurs at a critical value of ( $\sigma_w$ ) which may be attained prior to or following some amount of stable, ductile crack extension. Function  $J_c(Q)$  can be found on the base so called toughness scaling models. The procedure focuses on an application of the micromechanical model to predict specimen geometry and crack effects on the macroscopic fracture toughness  $J_c$  Dodds [4] and Anderson [5]. The procedure requires attainment of equivalent stressed volumes ahead of a crack front for cleavage fracture in different specimens. This can be done e.g. on the base of Weibull stress, because the Weibull stress incorporates both the effects of stressed volume and the potentially strong changes in the character of the near tip stress fields due to constraint loss and ductile crack extension [6].

## Experiments and modeling

As an experimental material C-Mn cast steel was used. This material was modelled as homogenous and isotropic with elastic constants  $E=2,05.10^5$  MPa and  $\mu=0.3$ . The average value of yield stress was 360 MPa. The testing temperature was  $-100$  °C. In case of using incremental theory of plasticity the curve  $\sigma$ - $\epsilon$  was modelled by 23 points, which were connected to linear parts. These points belong to experimental measured stress-strain curve.

In case of using deformation theory of plasticity material was described by Ramberg-Osgood relation:

$$\frac{\mathbf{e}}{\mathbf{e}_0} = \frac{\mathbf{s}}{\mathbf{s}_0} + a \left( \frac{\mathbf{s}}{\mathbf{s}_0} \right)^n, \quad (1)$$

where  $n$  is hardening exponent,  $a$  is hardening coefficient,  $\epsilon_0$  is yield strain and  $\sigma_0$  is yield stress.

TABLE 1: Test specimen geometry in mm

	a/W=0.1	a/W=0.2	a/W=0.5	Pre-cracked Charpy
L	120	140	250	55
B	25	25	25	10
W	26	30	50	10
l	104	120	200	40

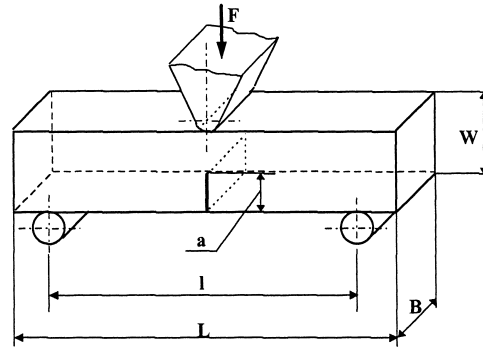
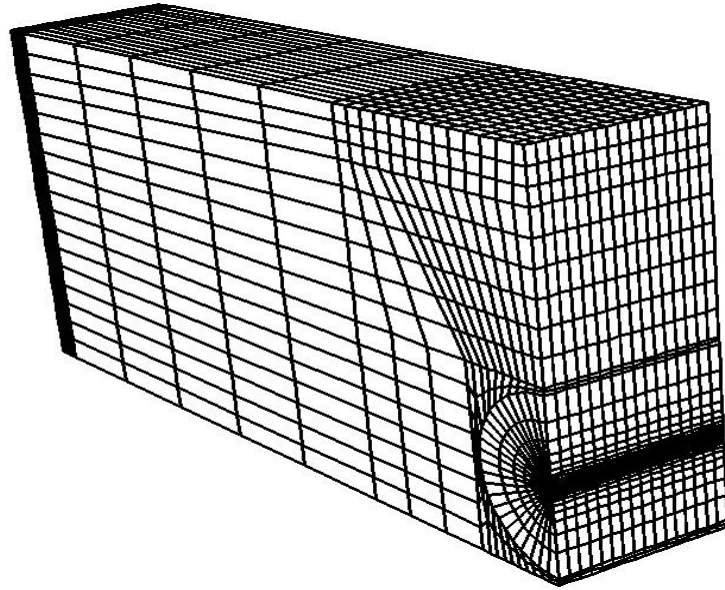


Figure 1: 3PD test

All computations are based on 3D elastic-plastic analysis using FEM, concretely Abaqus version 6.1 [7]. Example of 3D model is shown in the Figure 2, where only one quarter of real body is turned over because of two symmetry planes. Models were meshed with eight-node hybrid elements included in Abaqus. 15 680 of elements (C3D8H) were used it means 17884 nodes. The figure below (Figure 3) shows the detail around the crack. As can be seen a very fine mesh is required. Element size is increased instantly when the radial distance is increased from the crack front. Outer radius of the area (Figure 3) was 0.1 mm and the crack tip radius was 0.01mm. Twelve elements were used for dividing this radius. Thus, the characteristic

element length was  $8,3 \cdot 10^{-4}$  mm; at least ten layers of elements in the direction of thickness were used.



**Figure 2.** Example of 3D FEM mesh

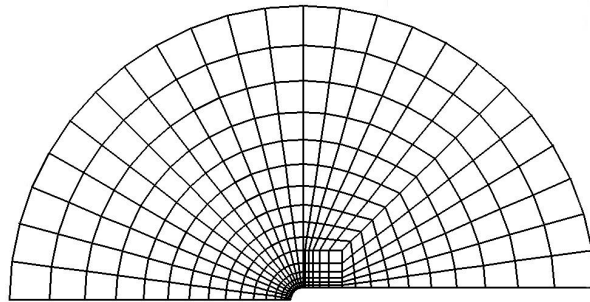


**Figure 3.** Detail of the crack tip

Four calculations were solved for range of value  $n$  in case of using deformation theory of plasticity because of choosing the proper value  $n$ . Selection of proper value  $n$  was based on comparing the relations between force and displacement. After that value of hardening exponent  $n=8$  was

applied as the best fit, as well as the value of hardening coefficient  $a=1$ . Hence the model of continual hardening material was determined. Its behaviours are very similar as with real material with Luders strain region.

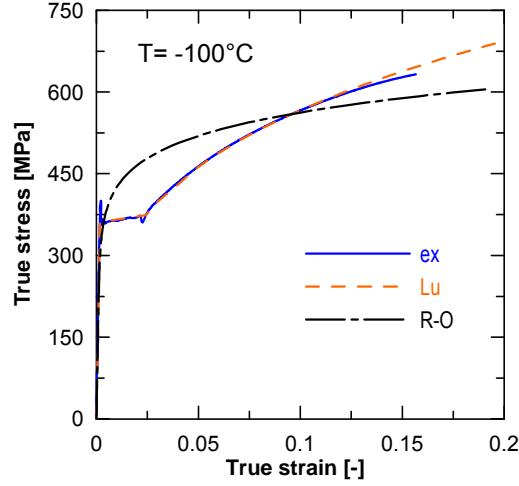


**Figure 4.** True stress strain curve and its approximation

### **Toughness scaling model based on Weibull stress**

The local approach for cleavage is based on the weakest link concept that postulates that failure of the body of a material containing a large number of statistically independent volumes is triggered by the failure of one of the reference volume [3]. In the local approach to cleavage fracture, the probability distribution ( $P_f$ ) for the fracture stress of a cracked body at a global level  $K_J$  or  $J$  is assumed to follow a two-parameter Weibull distribution [1,8] in the form:

$$P_f(s_w) = 1 - \exp\left[-\left(\frac{s_w}{s_u}\right)^m\right]. \quad (2)$$

The stress integral over the fracture process zone is denoted  $\sigma_w$  and is termed the Weibull stress. This stress is defined by

$$s_w = \left[ \frac{1}{V_0} \int s_1^m dV \right]^{1/m}, \quad (3)$$

where  $m$  is so-called Weibull slope,  $V_0$  is a reference volume, the integral is computed over the plastic zone, and  $\sigma_1$  is the first principal stress. The parameters  $\sigma_u$  and  $m$  of the Weibull stress  $\sigma_w$  at fracture are material parameters, i.e. independent of the stress state of materials, but may depend on the temperature.

The first one method of transferability of the fracture toughness was studied on the pre-cracked Charpy specimens and standard bodies (1T). Koppenhoefer and Dodds [9] have proposed to quantify the relative effects of constraint variation on the cleavage fracture toughness in the form toughness-scaling model (TSM). The first one studies can be found out in the same works, where as principal can be regarded: (i) the Dodds and Anderson approach, (ii) the Koppenhoefer approach and others. The method demonstrates the dependence of Weibull stress  $\sigma_w$  on the crack-tip stress triaxility and the transfer diagram  $\sigma_w$  versus computed value of  $J_{FE}$  is being constructed. The idea is to use to same value of probability of failure.

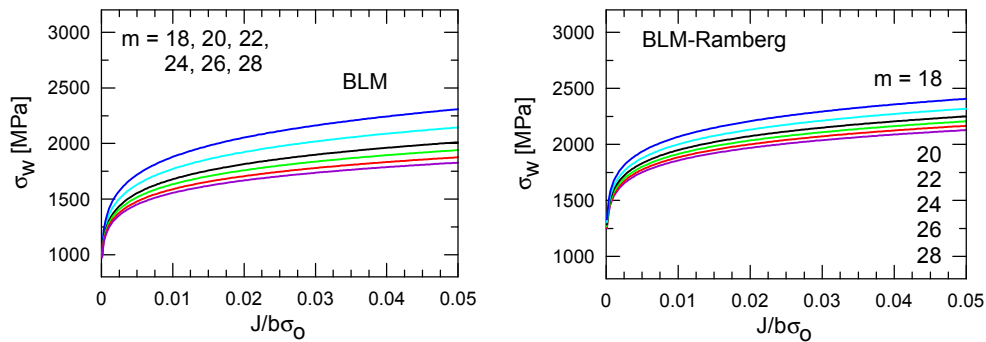


**Figure 5:** Diagram of Weibull stress determined by boundary layer method for both approximation of true stress strain curve.

*The steps of calibration procedure used for TSM:*

- Rank probability diagram ( $P_f$  versus  $J_c$ ) for two geometry is generated.
- FEM computation for tested body and SSY conditions.
- Weibull stress determination for tested body and SSY conditions.
- Constraint correction according to weakest link based thickness correction procedure of E-1921. Let  $t_{ssy}$  and  $t_A$  denote thickness for the SSY reference and configuration A, then  $J_{ssy}(i) = 1.8 + (t_A/t_{ssy})^{1/2}(J_c(i) - 1.8)$ . Results of this transformation can be seen in [10].
- Determine  $\beta$ . Assume that constrain corrected toughness values obey Weibull distribution with fixed exponent of 2. Where  $\beta$  defines

toughness value at a 63.2 percent failure probability. Equating failure probabilities leads to

$$\left(\frac{J}{b}\right)^2 = \left(\frac{s_w}{s_u}\right)^m \quad (4)$$

The plane-strain, boundary layer model [10] simplifies the generation of numerical solution for stationary cracks under SSY conditions with varying levels of constraint in Fig. 5, where the reference volume  $V_o$  equals  $(100 \mu\text{m})^3$  for convenience in all calculations.

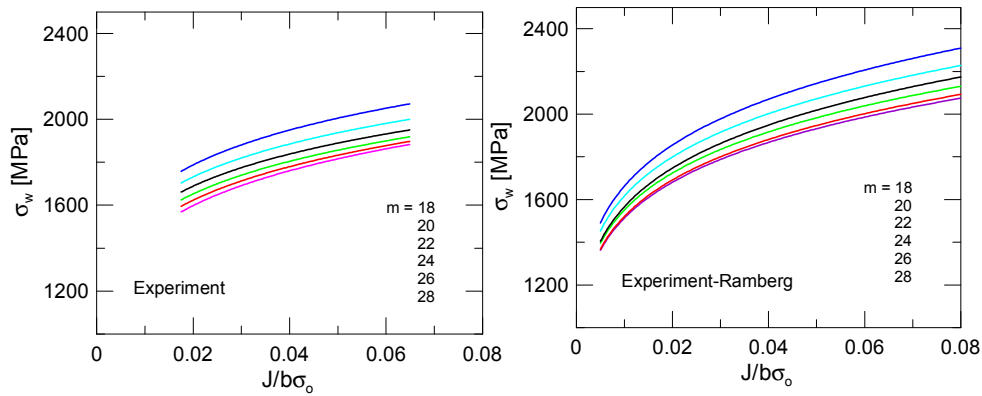


**Figure 6:** Diagram of Weibull stress determined by experimental data for both approximation of true stress strain curve.

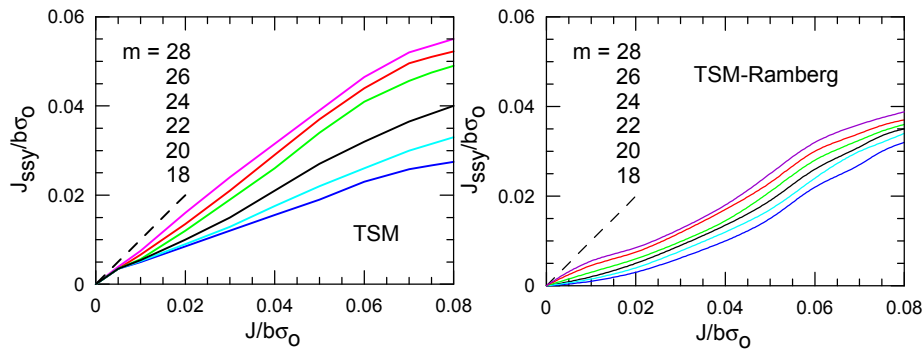


**Figure 7.** Toughness scaling diagram base dupon the Weibull stress with varying Weibull moduli for both approximation of true stress strain curve.

For the material considered in this paper  $\beta_{SSY} = 0.064 \text{ MPam}$  was determined according data presented in Fig. 8. Calibrated  $m$ -values were

found out for numerical FEM model based on the incremental theory of plasticity (very precise approximation of stress strain curve)  $m=24.1$ , for numerical model based on the deformation theory of plasticity (ramberg-Osgood)  $m=28.3$ . The estimation of calibrated  $m$ -value is clear from plot given in Fig. 9.

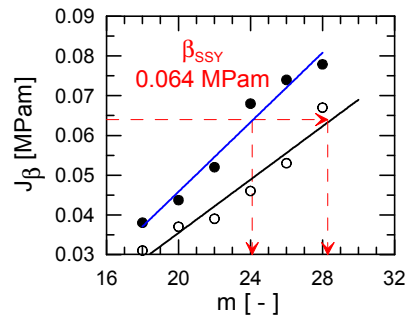
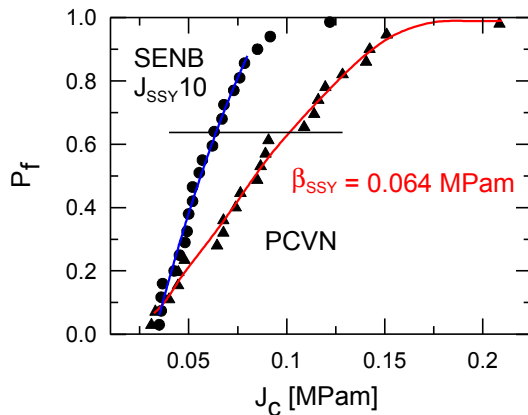


Figure 8. Rank probability diagram.

Figure 9. Calibration of Weibull stress parameter.

## Conclusions

The main results obtained in this work can be summarized into the following points:

- The Beremin model [3] was used for the calculation of  $\sigma_w$ , a reference volume  $V_o = (100 \mu\text{m})^3$  was used for all computations.
- The fracture toughness-scaling diagram based on the local approach for SSY specimen was determined and used for the transformation of data received on small pre-cracked specimens. Other computations (see Tab. 1) are currently being carried out to test this approach.
- The calibration procedure based on the work Gao, Ruggieri and Dodds presented in [8] has been applied on the cast manganese steel and calibrated  $m$ -value was found to be  $m=24.1$  for one model and 28.3 for the model base on the deformation theory of plasticity. The calibrated  $m$ -value makes the BL estimate for the toughness of the constraint corrected fracture toughness data experimentally received on PCVN specimens.
- Calibrated  $m$ -values is a bit differing to each other. It shows that a precise approximation of stress train curve is very important.

## ACKNOWLEDGEMENTS

This research was financially supported by project 101/00/0170.

## REFERENCES

1. Sumpter J. D. G. (1987)  $J_c$  Determination for Shallow Notch Welded Bend Specimens, *Fatigue and Fract. of Eng. Mater. Struct.*, Vol. 10, No. 6, pp. 479-493.
2. Kirk M. T. and Dodds R. H. (1993) J and CTOD Estimation Equations for Shallow Crack in Single Edge Notch Bend Specimens, *Journal of Testing and Evaluation*, Vol. 21, No. 4, pp.228-238.
3. Beremin (1983) A Local Criterion for Cleavage Fracture of a Nuclear Pressure Vessel Steels, *Metallurgical Transaction*, Vol. 14A, pp. 2277-2287.
4. Dodds R. D., Shih C. F., Anderson L. (1993) Continuum and Micromechanics Treatment of Constraint in Fracture, *Int. Journal of Fracture*, No. 64, pp. 101-133.
5. Dodds R.H., Tang M., Anderson L. (1995) ASTM STP 1299, pp. 101-133.
6. Ruggieri C., Dodds R. D. (1996) A Transferability Model for Brittle Fracture Including Constraint and Ductile Tearing Effects: a probabilistic approach, *International Journal of Fracture*, Vol. 79, pp. 309-340.
7. Hibbit, Karlsson & Sorenson Inc. (2000) ABAQUS User' s Manual, Version 6.1.
8. Gao, X., Ruggieri, C., Dodds, R., H., (1998) "Calibration of Weibull stress parameters using fracture toughness data", *Int. J. of Fracture* 92, pp. 175-200.
9. Koppenhoefer, K., C., Dodds, R., H., (1997) "Loading rate effects on cleavage fracture of pre-cracked CVN specimens: 3-D studies", *Eng. Fracture Mechanic* 58, pp. 224 – 270.
10. Kozák, V., Dlouhý, I., Holzmann, M., The fracture Behaviour of the Cast Steel and Its Prediction Using the Local Approach, *SMIRT-15*, Seoul, Korea, Vol. V, 1999, pp. 71-78.

- B4 Kozák, V., Dlouhý, I., Holzmann, M., The fracture behaviour of cast steel and its prediction based on the local approach, *Nuclear Engineering and Design*, (2002), Elsevier Science, 67-73, IF 0.546.



ELSEVIER

Nuclear Engineering and Design 212 (2002) 67–73

**Nuclear  
Engineering  
and Design**

www.elsevier.com/locate/nucengdes

# The fracture behaviour of cast steel and its prediction based on the local approach

Vladislav Kozák \*, Ivo Dlouhý, Miloslav Holzmann

*Institute of Physics of Materials, Academy of Sciences of the Czech Republic, Žitkova 22, 616 62 Brno, Czech Republic*

## Abstract

The master curve (MC) concept has been used for assessment of the fracture toughness transition behaviour of C–Mn cast steel intended for fabrication of large containers for spent nuclear fuel (ŠKODA). Standard fracture toughness tests using single edge notched bend specimens (SENB) with various crack lengths, the static tests of the CVN specimens and the axisymmetric notched tensile specimens have been utilised. The transferability of results received on the small pre-cracked Charpy specimens are tested here and the methodology MC is applied. For determining the reference transition temperature,  $T_0$ , which is taken as a basic material characteristic positioning the MC on the temperature axis, the large (1T) specimens are required. Additionally, the small pre-cracked Charpy-type specimens have been used for determining the fracture transition behaviour and for fracture toughness measurement and prediction. © 2002 Elsevier Science B.V. All rights reserved.

## 1. Introduction

Transport and storage containers for spent nuclear fuel have to ensure the safe enclosure of a radioactive material and must meet stringent requirements on safety. They must ensure the storage of radioactive material safely for expected container lifetime and also in the case of the most severe accident loading and earthquake shock. The container should be highly resistant to temperature and radiation embrittlement. Škoda Nuclear Machinery (Czech Republic) has introduced a new design of container for spent nuclear fuel. The cask design is based on thick walled pipe with

bolted lids, both fabricated from cast low-alloyed steel with ferritic microstructure (see Fig. 1).

The knowledge, assessment method of fracture mechanics has increased to a point where certain structural materials until now have not been considered for radioactive transport cask constructions are being proposed for these applications. For the safe enclosure of the radioactive material during transportation it must be shown that the extension of non-detected crack after fabrication will not occur. For the safe storage additional embrittling effects should be taken into account. Brittle fracture can occur under specific combination of temperature, mechanical and environmental loading conditions. When assessing whether the material satisfies the demand on container resistance against catastrophic failure the following key problems have to be addressed from the

\* Corresponding author. Tel.: +420-5-4163-6364; fax: +420-5-4121-8657.

E-mail address: kozak@ipm.cz (V. Kozák).

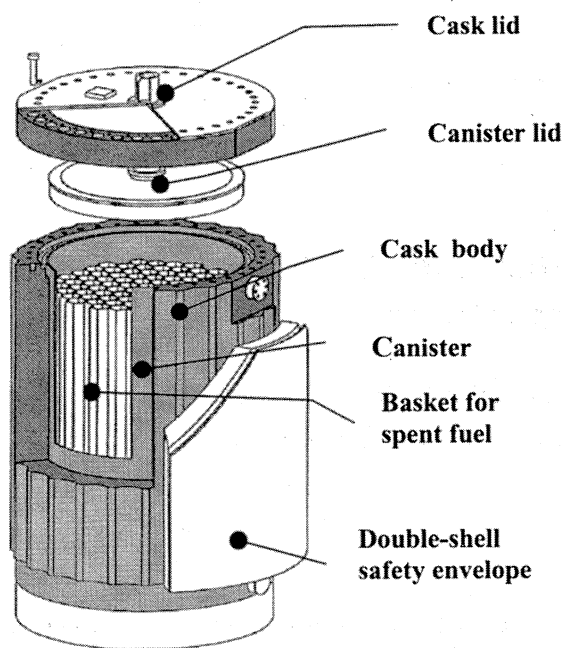


Fig. 1. Transport and storage cask ŠKODA 440/84.

fracture mechanics point of view: (i) the transferability of fracture toughness data measured on laboratory specimens to the component of much larger thickness and different geometry; and (ii) the prediction with a good probability of the brittle fracture initiation in cases of the most severe accident loading and radiation embrittlement.

## 2. Methodology

The methodology of master curve (MC) (ASTM, E1921-97, 1997) is widely used currently for transition behaviour evaluation of fracture toughness. The verification of this concept has been performed for steel of pressure vessel and weldments (Yoon, 1995; Aurich et al., 1996; Holzmann and Dlouhý, 1997; Link and Joyce, 1995; McCabe et al., 1997; Wallin, 1997a). For determining the reference transition temperature,  $T_o$ , which is taken as a basic material characteristics localising the MC on the temperature axis, the large (1T) specimens are required. But there are

structures (plants) under operation for which the transition behaviour of fracture toughness is of great interest (reactor pressure vessels, rotors, etc.) and application of MC concept would be very useful here. For these components only small specimens (Charpy V-notch) can be used for assessment of degradation, however. The effort is now concentrated on the application of small pre-cracked Charpy specimens for these purposes (Mayfield et al., 1995). Some works, mainly of Wallin (1997b) have shown that the small pre-cracked specimens can be used in determining reference temperature,  $T_o$ , and thereby making possible to apply MC concept for the integrity assessment procedure of these components. Small pre-cracked specimens and 1T SENB specimens were used to measure fracture toughness over a wide temperature range. Using the results obtained the reference transition temperatures,  $T_o$ , were determined for both types of specimens and compared with each other. Having the  $T_o$ , the MC may be drawn. Its validity for the cast steel has been discussed. Additionally, the prediction of the fracture toughness scatter of large (1T) specimens through those small pre-cracked ones using Weibull stress concept has been also performed.

## 3. Material, experimental and calculation procedures

### 3.1. Material characterisation

Manganese cast steel has been utilised for experiments having chemical composition in wt% given in Table 1. To guarantee the microstructure of specimens used for the static test to be the same as that of an inner part of cast body the computer simulation of cooling of semi-product has been used. The heat treatment was done in the laboratory of ŠKODA Research Ltd and as a result of this modeling was the scheme to cut this experimental plate in size  $55 \times 90 \times 250$  mm from which three tested bodies were produced (in size  $50 \times 25 \times 240$  mm) for brittle fracture experiments. The size of semi-product was the compromise between the cooling rate for cooling simulation and furnace capacity. Heat treatment was as fol-

Table 1  
The chemical composition of manganese cast steel

	C	Mn	Si	P	S	Cr	Ni	Cu	Mo	V	Ti
CSN	Max	1	0.2	Max.	Max.	Max.	Max.	Max.	Max.	Max.	Max.
Melt	0.12	1.6	0.5	0.03	0.02	0.3	0.4	0.3	0.15	0.03	0.05
Plate	0.1	1.11	0.36	0.01	0.015	0.11	0.28	0.28	0.03	–	–
	0.09	1.18	0.37	0.01	0.025	0.12	0.29	0.29	0.03	0.001	0.002
	W	Sn	Al	Nb	Co	As	Sb				
Plate	0.01	0.055	0.038	0.004	0.012	0.012	0.0095				

lows: 930 °C/6 h/1.5 °C min<sup>-1</sup> + 900 °C/4 h/20 °C min<sup>-1</sup> up to 600 °C/10 °C min<sup>-1</sup> up to 400 °C/air + 780 °C/4 h/20 °C min<sup>-1</sup> up to 550 °C/10 °C min<sup>-1</sup> up to 400 °C/air + 650 °C/8 h/furnace opening.

True stress–strain curves have been measured using cylindrical specimens with a diameter of 6 mm being loaded over a temperature range of –196 to –60 °C at cross-head velocity of 2 mm min<sup>-1</sup>. Standard FEA—ABAQUS 5.7 was used to model elastoplastic behaviour for tensile-notched specimens.

Fracture toughness data were measured using a standard 25 mm thick specimen with  $a/W$  ratio of 0.5 loaded in the three-point bending. Small pre-cracked Charpy-type specimens have been also tested in the same temperature range. For one selected temperature in lower shelf region (below temperature  $T_{GY}$  at which  $F_{FR}$  and  $F_{GY}$  coincides on their temperature dependencies) a range of round tensile-notched bars were tested to obtain data for statistical local approach procedure treatment.

Accepting the Beremin approach (1983) for the analysis of local criteria for cleavage fracture the location  $\sigma_u$  and shape parameters  $m$  were calculated using FEM for notched tensile bars having various types of notch geometry. The first one was the tensile specimen with the same circumferential notch as for Charpy (CVN), the other three types were U-notch geometry with radii 1, 0.7, 0.2 mm. Statistics were made for at least 20 replicated experiments in all cases. The influence of geometry is presented in Table 2. Prediction was calcu-

lated for standard cell size recommended for the cleavage fracture. Different size of process zone describing the part of plastic zone has small influence on computed local parameters. Values used for the MC are:  $m = 18$  ( $V_o = (100 \times 10^{-6})^3$  m<sup>3</sup>) see Table 2 (the best fit).

The Beremin model with strain correction (slightly adapted) is used for the calculation of  $\sigma_w$ . The iterative procedure using the maximum-likelihood theory was applied and the geometry effect for various notch radii of tensile bars is observed. The local parameters generated on the geometry with U notch 0.2 mm, V notch 0.25 mm and on the Charpy specimen give practically the same values. The valid local parameters are received on test specimens with notch radii of 0.7 and 1 mm, respectively, where the character of maximum principle stress distribution has no such influence on the microstructure inhomogenities that can be found in cast steel as in the cases of notches with a smaller diameter. For local parameters determination is inevitable to use either the specimens with notch diameter that satisfy slow gradient of principal stress or the values must be calibrated.

Table 2  
Local parameters received for various geometries (the best fit)

Geometry	$V_o = (100 \times 10^{-6})^3$ m <sup>3</sup>
$V_r = 0.25$ mm	$\sigma_u = 1409$ , $m = 45.4$
$U_r = 1.00$ mm	$\sigma_u = 2117$ , $m = 18.2$
$U_r = 0.70$ mm	$\sigma_u = 2486$ , $m = 17.0$
$U_r = 0.20$ mm	$\sigma_u = 1340$ , $m = 64.6$

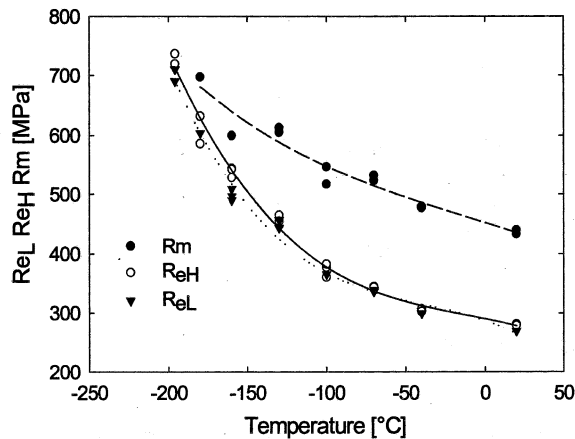


Fig. 2. Tensile properties of the cast steel.

### 3.2. Tensile properties

The temperature dependence of common tensile characteristics is given in Fig. 2. As seen the cast steel examined exhibits relatively low values of lower and upper yield stresses, respectively, and with decreasing temperature these characteristics increase very slowly (e.g. at  $-100$  °C  $Re$  is equal to only 380 MPa). With respect to small pre-cracked specimens this fact resulted in the necessity to test small specimens at very low temperatures in order to fulfil the validity condition for valid determination of  $K_{Jc}$ .

The testing at very low temperature, far below the expected reference temperature  $T_0$ , determined by means of larger 1T specimens, can lead to uncertainty in the determination of  $T_0$  (Aurich et al., 1996).

### 3.3. Fracture behaviour of 1T SENB specimens

On the basis of preliminary measurement of the fracture toughness using this type of specimen the temperature of  $-100$  °C has been chosen for determining the reference temperature  $T_0$ . Six SENB specimens were used to measure the fracture toughness values at this temperature. The  $K_{Jc}$  results obtained are given in Fig. 3. This figure serves as a check whether the basic assumption included in ASTM Standard E1921 (1997) for

determining the reference temperature  $T_0$ , i.e. whether the cast steel obeys the three parametric Weibull distribution with the Weibull modulus  $m$  being equal to 4,

$$P_f = 1 - \exp[(K_I - K_{\min}) / (K_o - K_{\min})]^m \quad (1)$$

describing the fracture toughness scatter in transition region.

Therefore the dependence of  $\ln[\ln(1/(1 - P_f))]$  versus  $\ln(K_{Jc} - K_{\min})$  for six measured  $K_{Jc}$  values was plotted in Fig. 3. As seen, the obtained value of modulus  $m$  is equal to 4.8. This value is slightly different from the value 4. To determine this dependence more precisely additional experiments are in progress. However, in spite of the small difference in  $m$ , for assessment of reference temperature  $T_0$  the procedure given in the ASTM Standard E1921 (1997) was used for the present.

$$K_o \left[ \sum_{j=1}^N (K_{Jc(i)} - K_{\min}) / (r - 0.3068) \right]^{1/4} + K_{\min} \quad (2)$$

$K_{\min} = 20$  MPa  $m^{1/2}$ , one gets for  $K_o$  the value  $K_o = 85.6$  MPa  $m^{1/2}$ .  $K_{Jc(\text{med})}$  is given by:

$$K_{Jc(\text{med})} = (K_o - K_{\min}) [\ln(2)]^{1/4} + K_{\min} \quad (3)$$

After substituting  $K_o$  and  $K_{\min}$  the value of

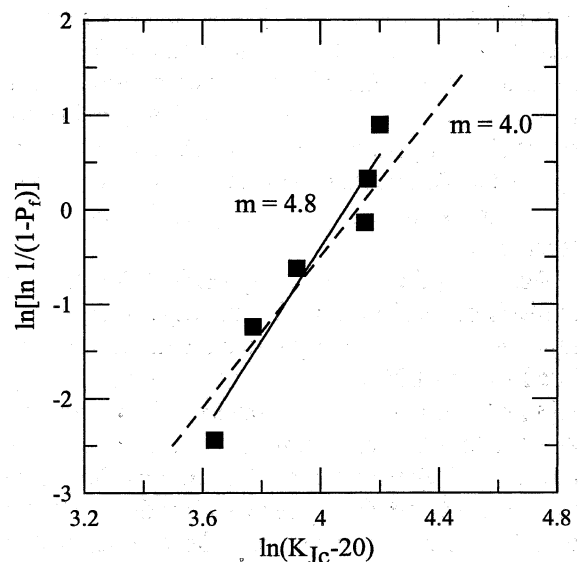


Fig. 3. Scatter of fracture toughness data.

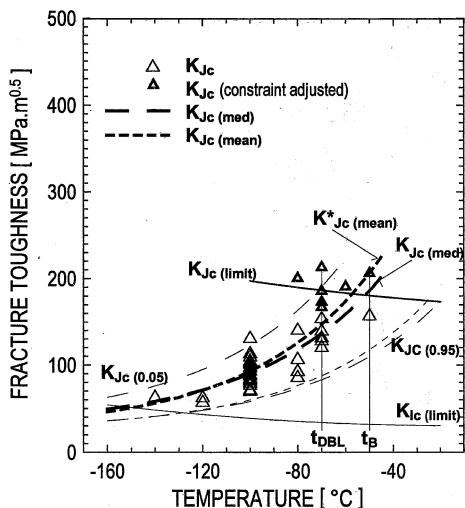


Fig. 4. Fracture toughness temperature diagram for 1T specimen.

$K_{Jc(\text{med})} = 79.8 \text{ MPa m}^{1/2}$ . Finally, utilising the equation:

$$T_o = T - \frac{1}{0.019} \ln \left[ \frac{K_{Jc(\text{med})} - 30}{70} \right] \quad (4)$$

the reference temperature  $T_o$  may be established to be  $T_o = -82 \text{ °C}$ .

The master curve for C–Mn cast steel investigated is described by:

$$K_{Jc(\text{med})} = 30 + 70 \exp[0.019(T + 82)] \quad (5)$$

Fig. 4 shows the master curve together with the tolerance bounds 5 and 95%. In this diagram the measured fracture toughness values in temperature range  $-160$  to  $-40 \text{ °C}$  are plotted. Full triangles represent data keeping the validity condition:

$$K_{Jc(\text{LIMIT})} = [(EbRe)/50]^{1/2} \quad (6)$$

The value of non-dimensional size limit parameter in Eq. (6) was taken to be 50 instead of 30 in (ASTM Standard E1921-97, 1997) based on the work of Ruggieri et al. (1998) and the discussion in subcommittee of ASTM Session (1998).

Some peculiarities of the fracture behaviour of cast steel follow from Fig. 4:

- Only for the fracture toughness values being below  $T_o + 15 \text{ °C}$  the master curve methodol-

ogy may be used to predict the fracture toughness behaviour.

- At temperature  $T_o + 26 \text{ °C}$  the sharp transition of fracture toughness to much higher values of  $K_{Jc}$  occurs. But it must be emphasised that for those specimens having these high values of  $K_{Jc}$ , the fracture was initiated by cleavage indicating that the C–Mn cast steel has large intrinsic resistance against ductile tearing.

### 3.4. Fracture behaviour of small pre-cracked Charpy specimen—PCVN

For PCVN specimens the temperature dependence of fracture toughness is given in Fig. 5. The line representing the validity condition (Eq. (6)) is plotted in the graph. Only a small number of fracture toughness data, especially the data at the temperature  $-100 \text{ °C}$ , those were intended for establishing  $T_o$ , fall below the line. Therefore data not meeting the  $K_{Jc(\text{limit})}$  were first constraint adjusted, using Dodds and Anderson toughness scaling model (Dodds and Anderson, 1991).

But only for data lying below the line labelled  $K_{Jc(\text{max})}$  DA this concept may be used, as this line represents the end of FE-3D calculation of Dodds and Anderson model as performed by Nevalainen and Dodds (1995). All constraint adjusted and

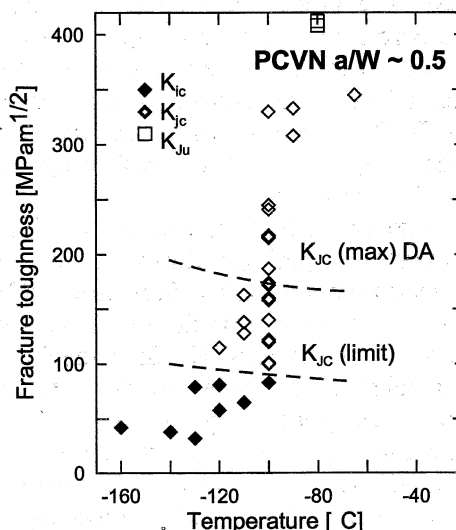


Fig. 5. Fracture toughness data from pre-cracked specimens.

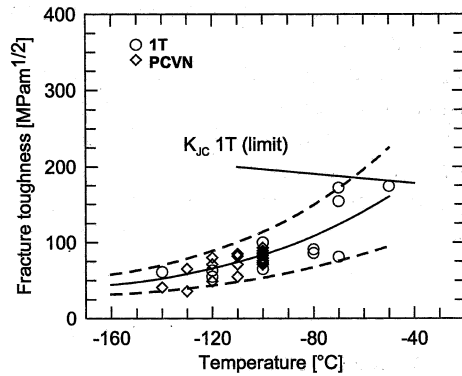


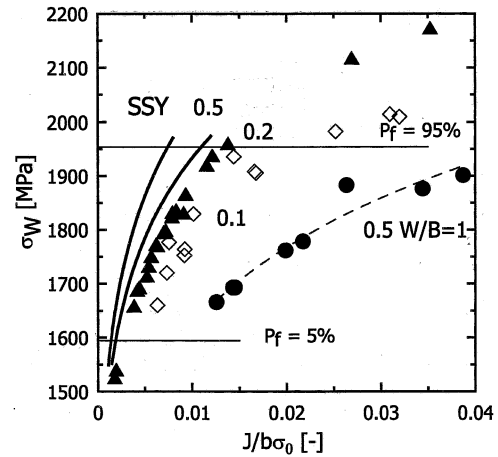
Fig. 6. FTTD from 1T and corrected PCVN data.

size corrected data using

$$K_{J_{c(1T)}} = 20 + (K_{J_{c(10)}} - 20) \left( \frac{B_{10}}{B_{1T}} \right)^{1/4} \quad (7)$$

are plotted in Fig. 6 in which MC  $K_{J_{c(\text{med})}}$  and tolerance bounds for 5 and 95% are replotted. All fracture toughness data of small pre-cracked specimens processed in such a way fall inside the scatter band of larger 1T specimens, verifying so the potency of utilising small pre-cracked specimens for the fracture toughness evaluation in the transition region. Additionally, the reference temperature  $T_0$  was established. The set of 12 PCVN specimens was used, from which only two had valid  $K_{J_c}$  values (see Fig. 5) and were only size corrected. The others were constraint adjusted and size corrected. The data obtained are shown in Fig. 6. Following the above-mentioned procedure the reference temperature  $T_0$  was estimated to be  $-78$  °C, which is in good agreement with the value of  $T_0 = -82$  °C established by means of larger 1T specimens.

It is to be noted, that the recommendation for testing the PCVN specimens for the purpose of  $T_0$  determination given in ASTM Standard E1921-97 (1997) is effectively impossible for the cast steel examined. To obtain valid  $K_{J_c}$  data required for PCVN specimens the testing would have to be carried out at very low temperatures (Fig. 5), well below the expected reference temperature  $T_0$ . This aspect could lead to the uncertainty in the estimation of  $T_0$ . The above procedure involving constraint adjustment seems to be very promising and should be verified with other steels.

Fig. 7. Relation between local  $\sigma_w$  and the global  $J$  parameters for various crack length ( $a/W$ ) for SENB specimen and pre-cracked Charpy.

Using data described in Table 2, the local approach methodology applied by Koppenhoefer and Dodds (1997), was used to transfer values of  $K_{J_c}$  received on the Charpy pre-cracked specimens to 1T specimens. After determining the local parameters, as it is mentioned in the beginning of the paper, it is important to compute variation of  $\sigma_w$  as a function of  $J$  integral for both types of specimens. Then from a given value of  $J$  integral in pre-cracked Charpy specimen it is necessary to find its corresponding  $\sigma_w$ . This value has to be transferred into the diagram for SSY specimen. The transformation diagram was computed and the data are plotted in Fig. 7, one can see the data received on bodies with various crack length ( $a/W$ ), geometry of these bodies is described in Table 3. Having used the corrected data, calculating the average values  $K_{J_{c(\text{mean})}}$  and substituting into Eq.

Table 3

The geometry of bodies used for the fracture toughness diagram determination

Geometry	Size (mm)	Nodes	Layers
Charpy $a/W = 0.5$	$10 \times 10 \times 55$	16 300	15
Charpy $a/W = 0.5$	$10 \times 10 \times 55$	35 400	30
$a/W = 0.1$	$25 \times 26 \times 104$	27 800	15
$a/W = 0.2$	$25 \times 30 \times 120$	23 900	15
$a/W = 0.5$	$25 \times 50 \times 200$	16 200	15

(4) one can get  $T_o = -80$  °C as was presented in Holzmann et al. (1998).

#### 4. Summary

The main conclusions are as follows:

- Master curve concept has been shown to be valid in the lower transition range for C–Mn cast steel.
- Fracture toughness was measured using small pre-cracked Charpy specimens and results were constraint and size corrected to the 1T SENB specimens.
- Reference temperature  $T_o$  determined using constraint adjusted and size corrected invalid PCVN data was slightly different from  $T_o$  evaluated using 1T SENB specimens.
- Fracture toughness transformation diagram based on the Weibull stress  $\sigma_w$  for bodies with various crack lengths has been determined.

#### Acknowledgements

The research was financially supported by grant No. 101/00/0170 of the Grant Agency of the Czech Republic and grant No. 972655 of Science for Peace NATO Programme.

#### Appendix A. Nomenclature

$T_o$	reference transition temperature where $K_{J_c} = 100 \text{ MPa m}^{1/2}$
$T_{GY}$	temperature, at which fracture force $F_{FR}$ equals to general yield force $F_{GY}$
$F_{FR}$	fracture force
$F_{GY}$	general yield force
$m$	shape parameter from Beremin model
$\sigma_u$	location parameter from Beremin model
$\sigma_w$	Weibull stress, $\sigma_w = [1/V_o \int \sigma_1^m dV]^{1/m}$
$\sigma_1$	maximum principal stress
$V_o$	reference volume for Beremin model

$K_{J_i}$	fracture toughness at stable crack propagation initiation (converted from $J_i$ )
$K_{J_c}$	fracture toughness at unstable crack propagation prior to 0.2 mm of crack growth (converted from $J_c$ )
$K_{J_u}$	fracture toughness at unstable crack propagation, at, or greater than, 0.2 mm crack growth (converted from $J_u$ )

#### References

- Aurich, D., et al. 1996. Safety and Reliability of Plant Tech. 22 MPA Seminar, p. 21.
- ASTM, E1921-97, 1997. Standard Test Method for the Determination of Reference Temperature  $T_o$ , for Ferritic Steels in the Transition range.
- Session of ASTM Subcommittee E 08.08, July 1998.
- Beremin, F.M., 1983. Metallurgical Transactions 14A, 2277–2287.
- Dodds, R.H., Anderson, T.L., 1991. J. Testing Evaluation 19, 123–134.
- Holzmann, M., Dlouhý, I., 1997. Zváranie 6, 219–224 (in Czech).
- Holzmann, M., Kozák, V., Dlouhý, I., 1998. ECF 12 Proceedings, vol. II, pp. 823–828.
- Koppenhoefer, K.C., Dodds, R.H., 1997. Eng. Fracture Mech. 58, 224–270.
- Link, R.E., Joyce, J.A., 1995. In: Kirk, M., Bakker, Ad (Eds.), Constraint Effect in Fracture, ASTM STP 1244. American Society for Testing Materials, Philadelphia, USA, pp. 286–315.
- Mayfield, M.E., et al., 1995. In: Kirk, M., Bakker, Ad (Eds.), ASTM STP 1244. American Society for Testing Materials, Philadelphia, USA, pp. 17–29.
- McCabe, D.E., Sokolov, M.A., Nansland, R.K., 1997. Structural Mechanics in Reactor Technology. 14th International Conference, vol. 4, division G, Lyon, France, pp. 349–356.
- Nevalainen, M., Dodds, R.H., 1995. In: KariHaloo, B.L., Mai, Y.W., Ritchie, M.I. (Eds.), Advances in Fracture Research, ICF 9. Pergamon, Amsterdam, pp. 131–161.
- Ruggieri, C., Dodds, R.H., Wallin, K., 1998. Eng. Fracture Mech. 60, 14–36.
- Yoon, K.K., 1995. J. Pressure Vessel Technol. 117, 378–382.
- Wallin, K., 1997a. In: KariHaloo, B.L., Mai, Y.W., Ritchie, M.I. (Eds.), Advances in Fracture Research, ICF 9. Pergamon, Amsterdam, pp. 2333–2344.
- Wallin, K., 1997b. In: KariHaloo, B.L., Mai, Y.W., Ritchie, M.I. (Eds.), Validity of Small Specimen Fracture Toughness Estimates Neglecting Constraint Correction, ICF 9. Pergamon, Amsterdam, pp. 519–537.

- B5 Kozák, V., Vlček, L., The Weibull stress parameters calibration upon the toughness scaling model between cracks having different constraint, *Nuclear Engineering and Design* 235, (2005), 1889-1896, IF 0,889.



Available online at [www.sciencedirect.com](http://www.sciencedirect.com)

SCIENCE @ DIRECT®

Nuclear Engineering and Design 235 (2005) 1889–1896

**Nuclear  
Engineering  
and Design**

[www.elsevier.com/locate/nucengdes](http://www.elsevier.com/locate/nucengdes)

## The Weibull stress parameters calibration upon the toughness scaling model between cracks having different constraint

Vladislav Kozák\*, Libor Vlček

*Institute of Physics of Materials, Academy of Sciences of the Czech Republic, Žitkova 22,  
616 62 Brno, Czech Republic*

Received 18 November 2004; received in revised form 6 May 2005; accepted 30 May 2005

### Abstract

An extensive investigation has been carried out on the sensitivity parameters determination describing the fracture behaviour of the body with a crack with respect to the character change of the true stress–strain curve with the dominant region of Lueders deformation. This paper presents the consideration on the change judgement of the  $J$ -integral and the constraint as the base parameters of two-parameter fracture mechanics. The Weibull stress model for cleavage fracture originally proposed by Beremin group requires calibration of two micromechanics parameters ( $m, \sigma_0$ ). The Weibull stress  $\sigma_w$  seems to be a parameter for the prediction of cleavage failure of cracked bodies and the study is focused on the assessment of the effects of constraint loss on the cleavage fracture toughness ( $J_c$ ). To quantify the effects of the constraint variation on the cleavage fracture toughness the form of the toughness scaling model based on the Weibull stress  $\sigma_w$  is investigated. Local material parameters have been calculated from Beremin approach and the calibration is performed on various approaches. Methods are based on the weakest link assumption and the incremental fracture probability, which depends not only on the maximum principal stress, but also on the equivalent plastic strain. The fracture resistance has been assessed using data from static tests of three point bend specimens.

© 2005 Elsevier B.V. All rights reserved.

### 1. Introduction

In the ductile-to-brittle transition region of ferritic steels, transgranular cleavage fracture initiated by slip-induced cracking of grain boundary carbides often triggers the brittle fracture which results in catastrophic

failure of structural components. As the results of localized character of failure mechanism and microstructural inhomogeneity, the cleavage fracture toughness is very sensitive to the local stress and its scatter is very high. Determining of the static fracture toughness on pre-cracked single-edge notched bend bars, SE(B), is one of the basic fracture mechanics test. It must be emphasised that the most important values are critical  $K$ -value, in case of using linear-elastic fracture mechanics and critical value of  $J$ -integral, in case of

\* Corresponding author. Tel.: +420 532 290 364;  
fax: +420 541 218 657.  
E-mail address: [kozak@ipm.cz](mailto:kozak@ipm.cz) (V. Kozák).

**Nomenclature**

$K_{J_i}$	the fracture toughness at stable crack propagation initiation (converted from $J_i$ )
$K_{J_c}$	the fracture toughness at unstable crack propagation prior to 0.2 mm of crack growth (converted from $J_c$ )
$K_{J_u}$	the fracture toughness at unstable crack propagation, at, or greater than, 0.2 mm crack growth (converted from $J_u$ )
$m$	the shape parameter from Beremin model
$V_0$	the reference volume for Beremin model
<i>Greek letters</i>	
$\sigma_u$	the location parameter from Beremin model
$\sigma_w$	Weibull stress
$\sigma_1$	the maximum principal stress

using elastic–plastic fracture mechanics. Subsequently, we confine our investigation to elastic–plastic material behaviour.

Laboratory measurements on the specimens with varying crack length (changing the relation  $a/W$ ) and with the same ligament showed increasing values of the fracture toughness expressed using  $J_c$  versus decreasing crack length. This problem was studied in recent works of Sumpter and Hancock (1991), Kirk et al. (1994) who investigated several possibilities of  $J$ -integral and CTOD estimation for SE(B) specimens with shallow crack. Generally, this problem can be solved on the base of two-parameter fracture mechanics, which expresses the constraint ahead the crack tip; in our case  $Q$ -parameter is critical. Several approaches exist: (i) on the base of experimentally determined dependence  $J_c$  on  $a/W$  the  $Q$  calculation comes from numerically given stress fields received by finite element method for every analysed body separately. (ii) Statistical approach using so called local approach (Beremin, 1983). We limit our focus to a stress controlled, cleavage mechanism for material and adopt the Weibull stress ( $\sigma_w$ ) as the local parameter to describe crack tip conditions. Unstable crack propagation occurs at a critical value of ( $\sigma_w$ ) which may be attained prior

to or following some amount of stable, ductile crack extension.

The aim of the paper can be seen in the fracture toughness transfer and the correction from pre-cracked specimens to small scale yielding (SSY) represented by SE(B) specimens and their precise computation using the finite element method. Some approaches were tested, see Ruggieri (2002), Gao and Dodds (2001), Kozák et al. (2001) and obtained results were compared. The fracture resistance has been assessed using data from static tests of the three points bend specimens with varying crack length and temperature. The Beremin model is used for the calculation of the Weibull stress ( $\sigma_w$ ). The standard package Abaqus for finite element method was applied and the manganese cast steel was selected as an experimental material.

## 2. Weibull fitting of data

Within this framework, it seems to determine first if the weakest link assumption for the local approach application is valid or not. Weakest link concept is the key assumption and postulates that failure of the body of a material containing a large number of statistical independent volumes is triggered by failure of one of the reference volume (Beremin, 1983). Fractography is indispensable for an appropriate interpretation of the applied model and also to ensure that basic assumption of the model with respect to the fracture mode is justified. The following assumption characterizes the microstructural and statistical model (Riesch-Opermann and Diegele, 2003):

- There is a large population of weak spots in the material.
- The failure of the material starts from and is triggered by the most dangerous weak spot.
- The weak spots are randomly distributed within the material.
- The weak spot became active within the onset of plastic deformation.
- The statistical effects of specimen size on  $K_{J_c}$  in the transition range are treated using the weakest link theory applied to the three-parameter Weibull distribution of the fracture toughness. A limit on  $K_{J_c}$  values, relative to the specimen size, is specified to

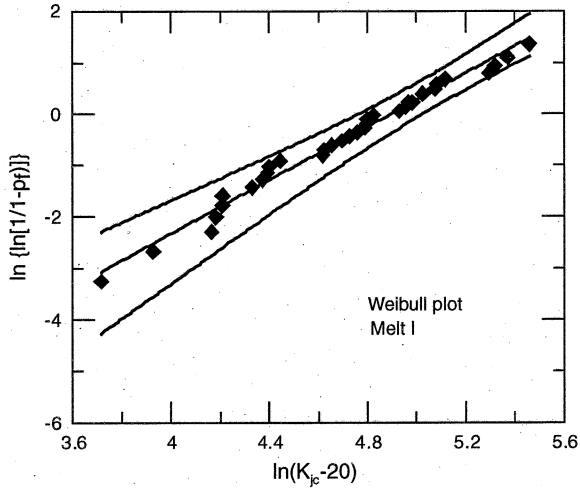


Fig. 1. Weibull plot for melt I, tolerance bounds are for 95% for reliability, temperature range <math>-160, -90>^{\circ}\text{C}</math>.

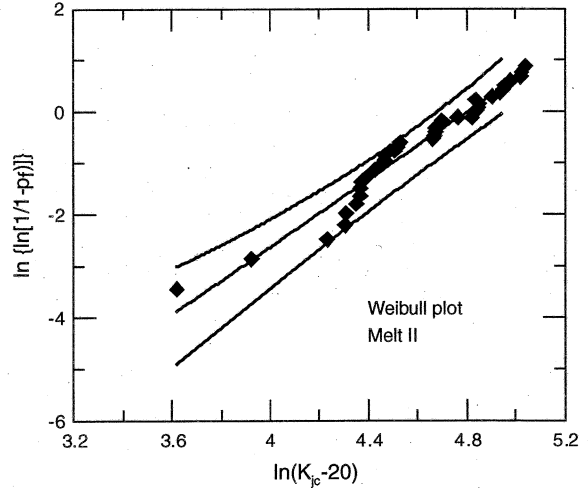


Fig. 2. Weibull plot for melt II, tolerance bounds are for 95% for reliability, temperature range <math>-160, -90>^{\circ}\text{C}</math>.

ensure high constraint condition along the crack front of the fracture (E1921-97).

The three-parameter Weibull model is used to fit the relationship between  $K_{Jc}$  and cumulative probability of failure,  $p_f$ . The term  $p_f$  is the probability for failure at or before  $K_{Jc}$  for an arbitrary chosen specimen from the population of specimens. This can be calculated from the following:

$$p_f = 1 - \exp \left\{ - \left[ \frac{(K_{Jc} - K_{\min})}{(K_0 - K_{\min})} \right]^b \right\} \quad (1)$$

where  $b$  is a shape parameter, which is assumed at given temperature to be close to 4. A scale parameter,  $K_0$ , is data fitting parameter. On the base of above-mentioned philosophy two sets of fracture toughness for melt I and melt II has been tested using the maximum likelihood method (see Figs. 1 and 2). Data points are converted to Weibull coordinates using:

$$Y_i = \ln \left\{ \ln \left[ \frac{1}{(1 - p_f(i))} \right] \right\} \quad (2)$$

where

$$p_f(i) = \frac{(i - 0.3)}{(N + 0.4)} \quad (3)$$

$N$  is number of tested specimens and  $K_{\min} = 20 \text{ MPa m}^{1/2}$ .

### 3. Material, experimental and calculation procedures

To investigate the constraint effects on 3D crack-front fields, detailed finite element analyses were performed and as an experimental material C-Mn cast steel was used. This material was modelled as homogenous and isotropic with elastic constants  $E = 2.05 \times 10^5 \text{ MPa}$  and  $\nu = 0.3$ . The values of yield stress can be seen from Figs. 3 and 4. In case of using the incremental theory of plasticity the curve  $\sigma$ - $\epsilon$  was modelled

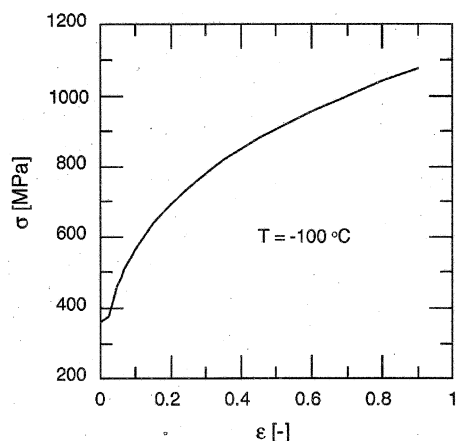


Fig. 3. True stress-strain curve for melt I.

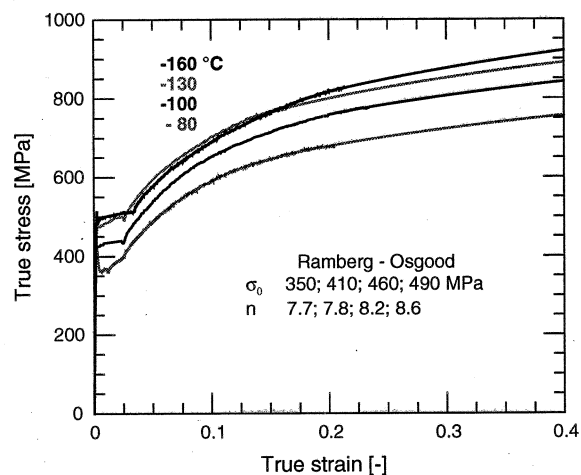


Fig. 4. True stress–strain curve for melt II.

by 23 points, which were connected to linear parts. These points belong to the experimentally measured stress–strain curve. In case of using the deformation theory of plasticity the material was described by the Ramberg–Osgood relation:

$$\frac{\varepsilon}{\varepsilon_0} = \frac{\sigma}{\sigma_0} + \alpha \left( \frac{\sigma}{\sigma_0} \right)^n, \quad (4)$$

where  $n$  is a hardening exponent,  $\alpha$  a hardening coefficient,  $\varepsilon_0$  a yield strain and  $\sigma_0$  is a yield stress.

All computations are based on the 3D elastic–plastic analysis using a finite element method, in the concrete using Abaqus version 6.1 3D model is shown in Figs. 5 and 6, where only one quarter of real body is thinking over because of two symmetry planes. Standard eight-node hybrid elements included in Abaqus were used, for example in Figs. 5 and 6 ( $a/W=0.1$ ) 15,680 of elements (type C3D8H) (17884 nodes) were utilized. Fig. 6 shows enlarged area around the crack. As can be seen a very fine mesh is required. An element size is increased when the radial distance is retreated from the crack front. Outer radius of the area was 0.1 mm and the crack tip radius was 0.01 mm. Twelve elements were used for dividing this radius. Thus, the characteristic element length was  $8.3 \times 10^{-4}$  mm; at least 10 layers of elements in the direction of thickness were used.

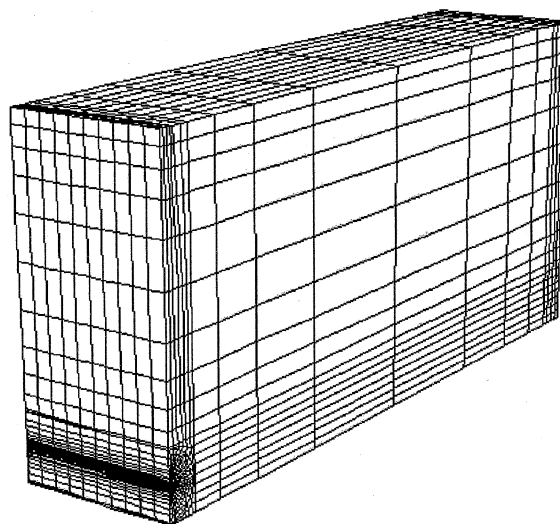
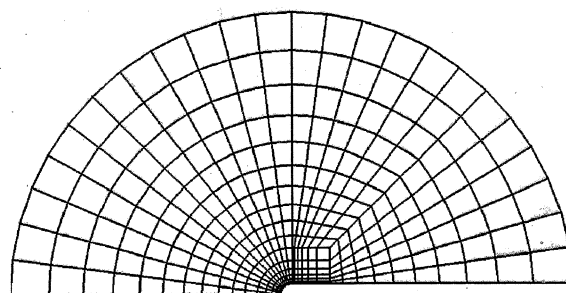
Fig. 5. Mesh for finite element analysis,  $a/w=0.1$ .

Fig. 6. Detail of the crack tip.

#### 4. Weibull stress model

The local approach for cleavage fracture is based on the weakest link concept that postulates that failure of the body of a material containing a large number of statistically independent volumes is triggered by the failure of one of the reference volume  $V_0$ . The Beremin cleavage model (Beremin, 1983) is phrased within a two-parameter Weibull description of the failure probability by

$$p_f(\sigma_w) = 1 - \exp \left[ - \left( \frac{\sigma_w}{\sigma_u} \right)^m \right]. \quad (5)$$

The volume integral over the fracture process zone is denoted  $\sigma_w$  and is termed the Weibull stress. This

stress is conventionally defined by:

$$\sigma_w = \left[ \frac{1}{V_0} \int \sigma_1^m dV \right]^{1/m}, \quad (6)$$

where  $m$  is so-called Weibull slope,  $V_0$  a reference (or characteristic) volume, the integral is computed over the plastic zone and  $\sigma_1$  is the maximum principal stress. The parameters  $\sigma_u$  and  $m$  of the Weibull stress  $\sigma_w$  at fracture are material parameters, i.e. independent of the stress state of materials, but may depend on the temperature.

### 5. The toughness scaling model

#### 5.1. Non-calibrated approach

The first method of the transferability of the fracture toughness was tested on the pre-cracked Charpy specimens and standard specimens with various  $a/W$  (Table 1). Koppenhoefer and Dodds (1997) proposed to quantify the relative effects of the constraint variation on the cleavage fracture toughness in the form of toughness scaling model (TSM). The method demonstrates the dependence of Weibull stress  $\sigma_w$  on the crack tip stress triaxility and the transfer diagram  $\sigma_w$  versus computed value of  $J$  is constructed. The idea of TSM is to use to same value of probability of failure for both specimen geometries, schematic diagram can be seen in Fig. 4. The TSM created against the laboratory data generated from tensile notched specimens can be seen in the following Fig. 7.

#### 5.2. The toughness scaling model generated using boundary layer method

Local approach parameters for Beremin model were calibrated against laboratory data using two and three-dimensional large strain elastic–plastic finite element

Table 1  
Test specimen geometry

	$a/W=0.1$	$a/w=0.2$	$a/w=0.5$	Pre-cracked Charpy
L	120	140	250	55
B	25	25	25	10
W	26	30	50	10
l	104	120	200	40

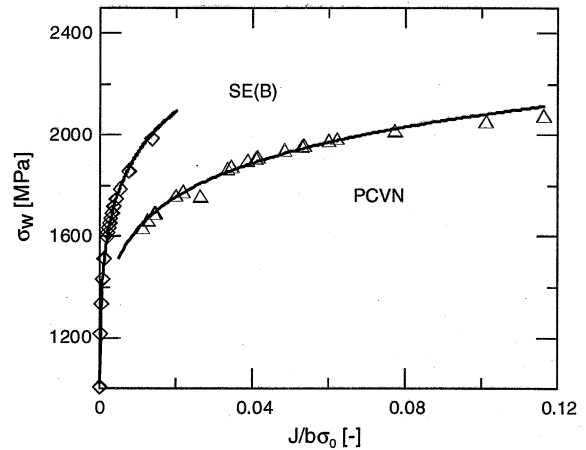


Fig. 7. The toughness scaling diagram uses  $m$ -value = 18 generated on the notched tensile specimens for melt I at  $-100^\circ\text{C}$ .

analysis (2D for SSY condition, 3D for three point bending tests). The steps of calibration procedure used for the toughness scaling model are following:

- Rank probability diagram ( $p_f$  versus  $J_c$ ) for two geometries is generated.
- The finite element analysis for tested specimens and for SSY conditions (boundary layer method).
- The Weibull stress determination for tested specimens and for SSY conditions.
- Constraint correction according to weakest link based thickness correction procedure of E1921-97. Results of this transformation can be seen in Kozák et al. (2001).
- Determine  $\beta$ . Assume that constrain corrected toughness values obey Weibull distribution with fixed exponent of 2, where  $\beta$  defines toughness value at a 63.2% of failure probability. Equating failure probabilities leads to

$$\left( \frac{J}{\beta} \right)^2 = \left( \frac{\sigma_w}{\sigma_u} \right)^m \quad (7)$$

The plane-strain, boundary layer model simplifies the generation of numerical solution for stationary cracks under SSY conditions with varying levels of constraint (for both approximation), where the reference volume  $V_0$  equals  $(100 \mu\text{m})^3$  for convenience in all calculations. For the material considered in this paper  $\beta_{\text{SSY}} = 0.064 \text{ MPa m}$  was determined according data presented in Fig. 8. Calibrated  $m$ -values were

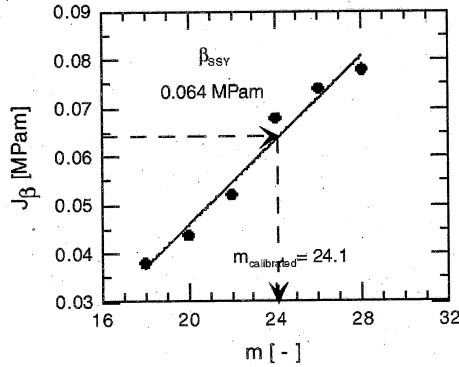


Fig. 8. Determination of calibrated  $m$ -values for melt I at  $-100\text{ }^\circ\text{C}$ .

found out for numerical finite element analysis based on the incremental theory of plasticity  $m=24.1$ . Size and constraint corrected data can be seen in Fig. 9.

5.3. Calibration procedure for Weibull modulus utilizes only one set of data \*

The last procedure described in Kirk et al. (1994) is going out from the weakest link statistic for  $J$ -integral from the Eq. (1). A central feature emerging from this model is that, under SSY condition, the scatter in the cleavage fracture toughness data is characterized by  $b=2$  for  $J_c$  values.

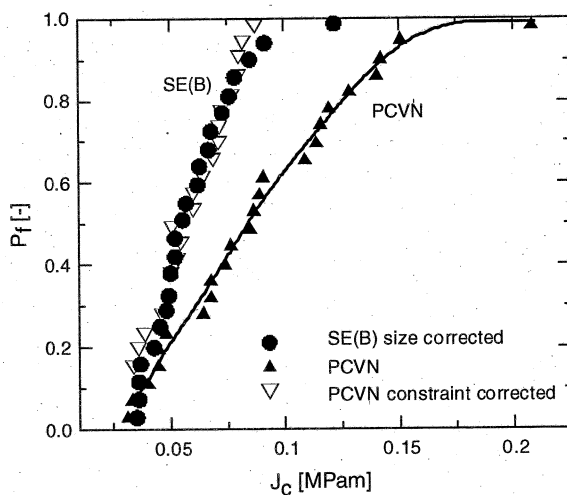


Fig. 9. Size and constraint corrected data for melt I at  $-100\text{ }^\circ\text{C}$ .

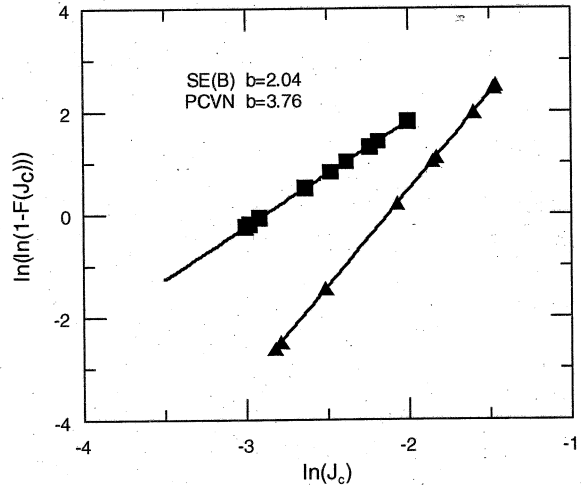


Fig. 10. Weibull plots of experimental toughness values at  $-130\text{ }^\circ\text{C}$  for melt II.

- Cleavage fracture toughness values measured from one set of high constraint standard specimens (configuration A) define  $J_0$  of the statistical distribution given by Eq. (1) (for  $J_c$ ) as the basis for the calibration; this parameter is denoted  $J_0^A$ .
- Consider now a different constraint crack configuration (configuration B) at the same temperature and loading rate. Because  $m$  is assumed to be independent of specimen geometry, the calibrated Weibull modulus is the  $m$ -value that corrects the toughness for configuration A to its equivalent characteristic toughness for configuration B, ( $J_0^A$  to  $J_0^B$  correction), denoted  $J_{0-TSM}^B$ .
- By using a thickness correction based on the weakest link statistic, parameter  $J_0^A$  is simply scaled to the characteristic toughness value for the configuration B (with different thickness), denoted  $J_{0-WLM}^B$  given by:

$$J_{0-WLM}^B = J_{min} + \left(\frac{B_A}{B_B}\right)^{(1/b)} (J_0^A - J_{min}) \quad (8)$$

where  $B_A$  and  $B_B$  denote the specimen thickness.

- The calibrated  $m$ -value for the material is defined as the value at which  $J_{0-TSM}^B = J_{0-WLM}^B$ .

Fig. 10 provides a Weibull diagram of measured toughness values for  $-130\text{ }^\circ\text{C}$  for SE(B) and pre-cracked Charpy for melt II. The straight line indi-

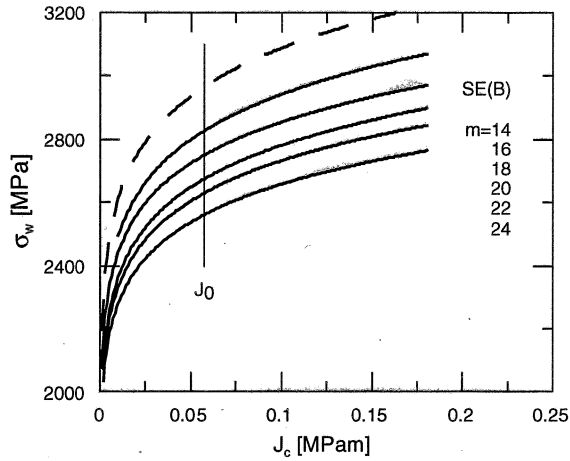


Fig. 11. Weibull stress  $\sigma_w$  for SE(B) at  $-130^\circ\text{C}$  for melt II.

icates the three-parameter Weibull distribution obtained by the maximum likelihood analysis of the data set with  $J_{\min} = 0.0018 \text{ MPa m}$  ( $K_{\min} = 20 \text{ MPa m}^{1/2}$ ). The characteristic toughness value for SE(B) is  $J_0 = 0.0557 \text{ MPa m}$  and for the pre-cracked Charpy  $J_0 = 0.138 \text{ MPa m}$ .

The calibrated  $m$ -value was found to be very close to  $m = 16$ . The principle of the calibration procedure can be seen in Figs. 11 and 12, in the following Fig. 13 one can see the result of the above-mentioned procedure, the solid symbols in this plot indicate the received data

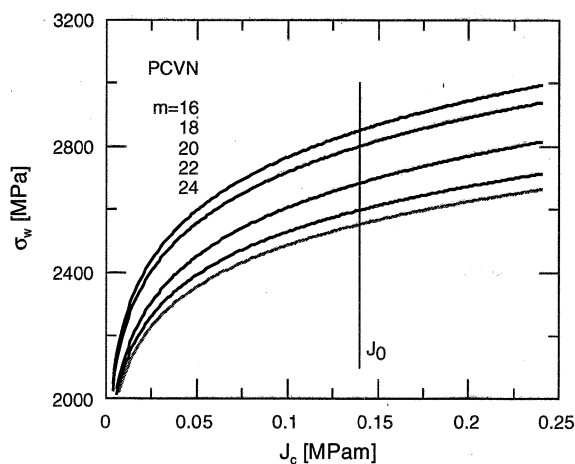


Fig. 12. Weibull stress  $\sigma_w$  for PCVN (pre-cracked Charpy) at  $-130^\circ\text{C}$  for melt II.

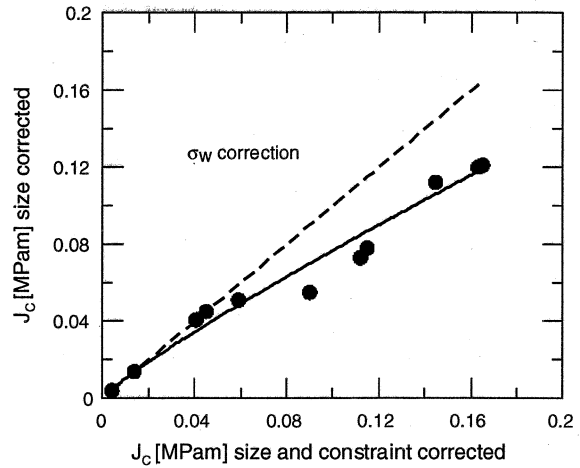


Fig. 13. Corrected data (PCVN to SE(B)) according to Weibull stress for  $m = 16$  at  $-130^\circ\text{C}$  for melt II.

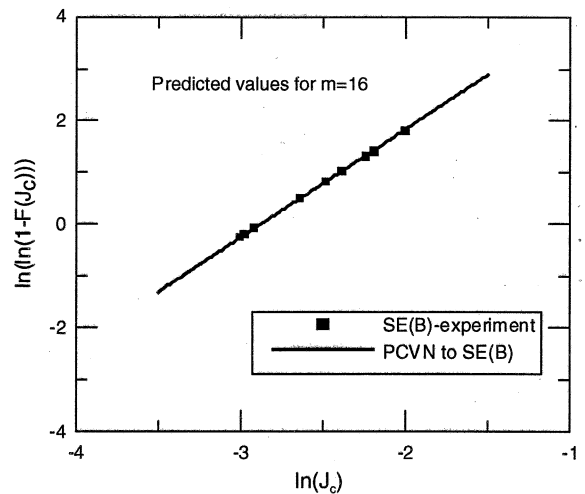


Fig. 14. Cleavage fracture prediction for the tested PCVN (pre-cracked Charpy) specimen, data transformed to SE(B) specimen.

and the constraint influence. The dashed line indicates only the size corrected data. The Weibull stress prediction for SE(B) specimen using  $m = 16$  agrees well with the experimental data as can be seen in Fig. 14.

## 6. Conclusions

This paper describes three procedures, which can be used for the toughness scaling model generation.

First procedure is procedure without  $m$  calibration and it is not too accurate. It is well-known that a direct application  $m$ -values generated on the notch specimens is controversial.

The procedure based on the small scale yielding solution gives very good results, but it is necessary to have a large amount of data and carry out a lot of computations using finite element method.

The last procedure has its origin in the master curve approach. It can be regarded to be a modified version of the second procedure; however, before generating the Weibull stress trajectories one needs to scale the  $J_0$  values. This approach is giving valuable data for the small experimental data set. According to the author recommendation the accuracy of this procedure is dependent not on the thickness ratio but the configuration A and B must have substantially different  $\sigma_w$  versus  $J$  histories computed for the same  $m$ -values.

#### Acknowledgements

This research was financially supported by project 101/02/0683 and 106/02/0745 of the Grant Agency of the Czech Republic.

#### References

- Beremin, F.M., 1983. A local criterion for cleavage fracture of nuclear pressure vessel steel. *Metall. Trans.* 14A, 2277–2287.
- E1921-97, 1997. Standard Test Method for Determination of Reference Temperature,  $T_0$  for Ferritic Steels in the Transition Regime.
- Gao, X., Dodds, R.H., 2001. Recent developments in Weibull stress model for prediction of cleavage fracture in ferritic steel. In: *Proceedings of ICF 10, Hawaii, CD ROM.*
- Kirk, M.T., Dodds, R.H., Anderson, T.L., 1994. In: J.D. Landes, D.E. McCabe, J.A. Boulet (Eds.), *Approximate Techniques for Prediction of Size Effects on Cleavage Fracture Toughness (JC)*, *Fracture Méchanics*, vol. 24, ASTM STP 1207, Philadelphia, pp. 62–86.
- Koppenhoefer, K.C., Dodds, R.H., 1997. Loading rate effects on cleavage fracture of pre-cracked CVN specimens: 3-D studies. *Eng. Fract. Mech.* 58, 224–270.
- Kozák, V., Holzmann, M., Dlouhý, I., 2001. The transferability of brittle fracture toughness characteristics. *Transactions of SMIRT 16*, Washington DC, paper 1079, CD ROM.
- Riesch-Opermann, H., Diegele, E., 2003. Towards a micro-mechanical description of the fracture behaviour for RAFM steels in the ductile-to-brittle transition regime. *J. Nucl. Mater.* 307–311P2, 179–183.
- Ruggieri, C., 2002. A New procedure to calibrate the Weibull stress modulus ( $m$ ). In: *Proceedings ECF 14, Krakow*, pp. 163–170.
- Sumpter, J.D.G., Hancock, J.W., 1991. Shallow crack toughness of HY80 welds: an analysis based on T stresses. *Int. J. Pressure Vessels Piping* 45 (2), 207–221.



B6 Kotrechko, S., Gryshchenko, V., Kozák, V., Dlouhý, I., Method of threshold stress determination for local approach to cleavage factor, *Solid State Phenomena*, Vol. 258, (2017), 281-285.

## Method of Threshold Stress Determination for a Local Approach to Cleavage Fracture

Kotrechko S.<sup>1</sup>, Gryshchenko V.<sup>1\*</sup>, Kozak V.<sup>2</sup>, Dlouhy I.<sup>2</sup>

<sup>1</sup>G.V. Kurdyumov Institute for Metal Physics of NASU, 36 Vernadsky Blvd., 03142, Kyiv, Ukraine

<sup>2</sup>Institute of Physics of Materials, Academy of Sciences of CR, Zizkova 22, Brno, Czech Republic

<sup>1</sup>serkotr@gmail.com, <sup>1\*</sup>walduk@bigmir.net, <sup>2</sup>kozak@ipm.cz, <sup>2</sup>idlouhy@ipm.cz

**Keywords:** Local approach, fracture, cleavage, threshold stress, Beremin model.

**Abstract.** The contribution is focused on a new methodology description for determination of threshold stress  $\sigma_{th}$ , as the third parameter in Beremin local approach to cleavage fracture that is using three-parameter Weibull statistics. Nature of the methodology lies in tensile testing of rounded notched specimens at liquid nitrogen temperature and corresponding calculations. Reactor pressure vessel steel was chosen as an example for the illustration.

### Introduction

Local approach (LA) to cleavage fracture appears to be a part of fracture mechanics which is based on theoretical background of both mechanical and physics of fracture. LA was established mainly by Beremin group for solution of tasks associated with statistical size effect, scatter of experimental data and prediction of temperature dependence for fracture toughness [1, 2]. Beremin version of LA is based on the assumption that probability of cleavage initiation in metals and alloys can be described sufficiently by Weibull distribution. Two alternatives of Beremin model can be recognized (i) more or less simplified two-parametric approach and (ii) three-parametric one. Applicability each of them strongly depends on the calibration procedure of Weibull parameters [1, 3]. Murdy was one of the first researchers, who suggested a comprehensive calibration procedure [3]; nowadays a few different approaches to the procedure have been developed, a detailed overview being available in [4]. The two-parametric Beremin model was established by authors [2] which is only a first approximation because it supposes finite value of fracture probability at negligible small loads, which is a contradiction to one of the main postulates of original Beremin model - impossibility of any fracture (even cleavage) without a plastic deformation (namely, at stress level less than yield stress) [5]. That reason motivated researchers Petti and Dodds [6], Bakker and Koers [7], Xia and Chang [8] to introduce threshold stress as a third parameter into Beremin model. The physical nature of threshold stress is a minimum level of stress is necessary for a cleavage initiation. Several detailed discussions about the three-parameter Weibull model and toughness scaling based on Weibull stress, were carried out in investigations [4] and [9]. Possibility of invalid calibration of the shape parameter  $m$  and the scale parameter  $\sigma_u$  in case of underestimation  $\sigma_{th}$  is one of the considerable conclusions; especially, it applies to the shape parameter  $m$ , which will be systematically overestimated [9]. According to [10], rational calibration procedure for  $\sigma_{th}$  remains an open issue nowadays.

The aim of the work is to establish a new technique for determination of threshold stress  $\sigma_{th}$ .

### Theoretical background

According to the model of cleavage fracture of polycrystalline metals proposed in [11, 13], the value of threshold stress is determined by the minimum stress  $\xi_{C\min}$  corresponding to instability of a crack nucleus. Then threshold stress level can be described by the equation:

$$\sigma_{th} = \frac{\xi_{C\min}}{1 + tJ_{\xi_{11}}}, \quad (1)$$

where  $J_{\xi_{11}}$  is a variation of microstresses (in case of polycrystalline iron  $J_{\xi_{11}} \approx 0.13$ ),  $t \approx 3$  is probability tolerance.

As it was shown in [13], up to a factor 0.8-0.9 the value of threshold stress is equal to the minimum level of cleavage fracture (figure 2) of metal  $R_{MC}$  ( $R_{MC}$  is the brittle strength) at the uniaxial tension (figure 1). Factor 0.8 corresponds to low quality steel, 0.9 - to a high quality steel.

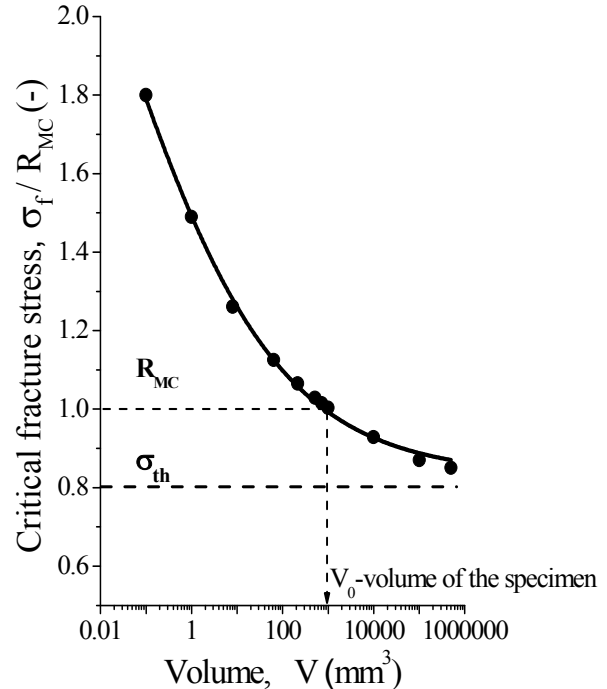
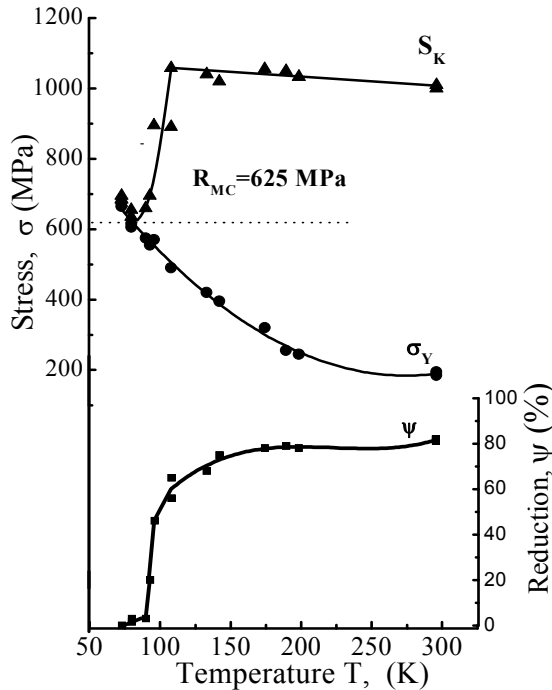


Figure 1. Temperature dependence of the main mechanical characteristics of iron:  $S_k$  is a fracture stress,  $\sigma_y$  is yield stress,  $\psi$  is reduction in area

Figure 2. Scale effect at cleavage fracture of iron:  $R_{MC}$  is brittle strength,  $\sigma_{th}$  is threshold stress

Such consequences enabled a new simplified procedure for determination of threshold stress  $\sigma_{th}$ , as the value of minimum stress of cleavage fracture  $R_{MC}$  of standard specimens at uniaxial tension. According to results of investigations [14], ductile-to-brittle-transition range for typical structural steels lies below 77K, and this means some methodological difficulties for experimental determination of  $R_{MC}$ . That's why the authors [14] ascertained experimentally a possibility of determination  $R_{MC}$ , as the value of nominal fracture stress for notched specimens at 2% plastic strain for wide range of structural steels. For this purpose, notched specimens with stress concentration radius equal to 2 mm were utilized. It means that threshold stress can be determined by uniaxial tensile testing of 5 notched specimens at 77K. Than

$$\sigma_{th} = (0.8 - 0.9) \sigma_{NF2}, \tag{2}$$

where  $\sigma_{NF2}$  is nominal fracture stress of rounded notched specimens at residual strain value 2%.

### Experimental

RPV steel 15H2NMFAA was selected as the material for tests; the chemical composition and mechanical properties of the steel are listed in Table 1 and 2, respectively.

Table 1. Chemical composition of RPV steel 15Ch2NMFAA

Material	C, [%]	Mn, [%]	Si, [%]	Ni, [%]	Mo, [%]	Cu, [%]	Cr, [%]	P, [%]	V, [%]
15Ch2NMFAA	0.06 - 0.15	0.48 - 0.97	0.26-0.33	2.070	1.120	0.530	1.820	0.007	0.100

Table 2. Mechanical properties of RPV steel 15Ch2NMFAA

Material	T, [K]	Yield strength $\sigma_Y$ , [MPa]	Ultimate strength $\sigma_{ult}$ , [MPa]	Reduction in area $\psi_K$ , [-]	Strain at fracture $e_F$ , [-]	Strain corresponding to ultimate strength $e_{ult}$ , [-]	Work hardening exponent $n$ , [-]
15Ch2NMFAA	293	610	714	0.75	1.40	0.07	0.065

The tensile tests for the smooth rounded bar specimens were executed over the temperature range from  $-196^\circ\text{C}$  till room temperature ( $+20^\circ\text{C}$ ) to determine the materials flow properties. The diameter of the gauge section of the smooth tensile specimen was 6 mm and the gage length was 30 mm. For the determination of  $\sigma_{th}$  the tensile tests using the rounded notched bar specimens were performed at  $-196^\circ\text{C}$  to obtain a nominal fracture stress and strain. In the notched specimens the diameter of the smooth section was 8 mm and the diameter of the notched section at a position of minimum cross-sectional area was 5.2 mm, the notch root radius was 2 mm. The value of the nominal fracture stress  $\sigma_{NF}$  was calculated as:

$$\sigma_{NF} = P_F / A_F, \quad (3)$$

where  $P_F$  is load at fracture,  $A_F = \pi d_F^2 / 4$  - is cross-sectional area after fracture.

The value of average strain in cross-section of notched specimen was estimated as follows:

$$e_F = \ln\left(\frac{1}{1 - \psi_F}\right), \quad (4)$$

where  $\psi_F = (d_F / d_0)^2$  - reduction in cross-sectional area,  $d_F$  is a diameter of neck after fracture,  $d_0$  - is initial diameter of a specimen.

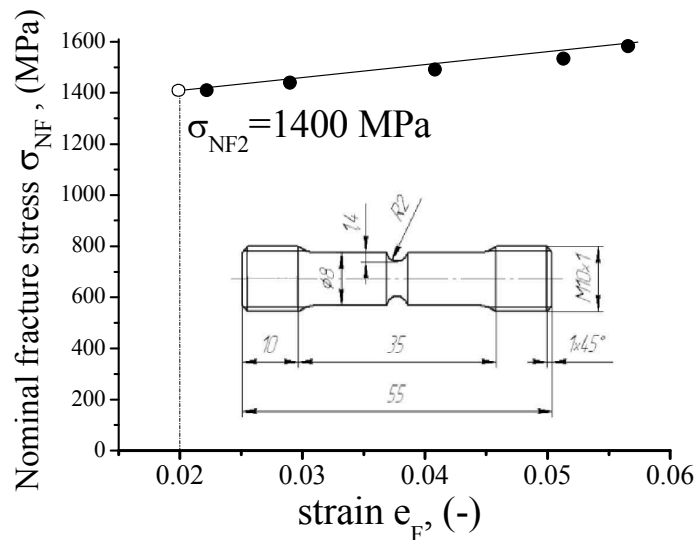


Figure 3. The dependence  $\sigma_{NF}$  of notched specimen of steel 15Ch2NMFAA on the average strain in the minimum cross-section:  $\sigma_{NF2}$  is a nominal fracture stress corresponding to 2% strain

## Discussion

According to obtained experimental results (figure 3) for investigated steel, the value of  $\sigma_{NF2}$  is 1400 MPa. Equation (2) gives the value of threshold stress  $\sigma_{th} = 1260$  MPa. Threshold stress is a material constant, and its value is determined by the distribution of ferrite grain sizes in

pure iron or by the distribution of carbide sizes in most structural steels [11,12]. In the most cases, the value of threshold stress  $\sigma_{th}$  is taken as  $2\sigma_Y$ , where  $\sigma_Y$  is yield stress at test temperature for Weibull parameters determination [14]. This approach has no physical basis; because of  $\sigma_{th}$  and  $\sigma_Y$  have a different physical nature. On the other hand, there is a need for precise determination of  $\sigma_{th}$ ; high sensitivity of shape and scale parameters in Weibull distribution to the value of threshold stress is the main reason. For example, authors [15] pointed out that for RPV steel A515-70 the shape parameter  $m$  changes significantly at different values of  $\sigma_{th}$ : for  $\sigma_{th} = 0$  the shape parameter gain value  $m = 8$ , for  $\sigma_{th} = \sigma_Y$  the value of  $m = 5$ , and for  $\sigma_{th} = 2\sigma_Y$  the value of  $m = 2.5$ . Threshold stress values  $\sigma_{th}$  for selected structural steels [16] were determined by proposed method and exhibited in Table 3. For our RPV 15Ch2NMFAA steel the similar analysis is based on the standard CT specimen data. The results are very close to literature findings,  $m$  parameter for 2 parametric local approach was determined to be 7.4, for 3 parametric local approach and data in temperature range  $<-90, -130> ^\circ\text{C}$  the shape parameter gains the value  $m = 1.9$  (at  $\sigma_{th} = 1260$  MPa).

Table 3. The main mechanical characteristics of some structural steels at 293K

Material [15]	$\sigma_Y$ , [MPa]	$\sigma_{ult}$ , [MPa]	n, [-]	$e_F$ , [-]	$\sigma_{th}$ , [MPa]
FeMn (ferrit)	317	481	0,190	1,350	1102
42CrMo4 (ferrit-perlite)	376	708	0,222	0,831	832
10Ch2MFA (tempered bainite)	491	606	0,109	1,549	1248
CrMoV (tempered bainite)	502	681	0,134	1,072	842
15Cr2NMFAA (tempered bainite)	610	714	0,065	1,400	1260
20CrNiMoV (tempered bainite)	676	801	0,097	0,836	1005
CrMoV (Tempered bainite)	779	904	0,095	0,999	1152
Lo8CrNiMo (bainite)	839	1038	0,108	0,727	1240
Lo17CrNiMo (bainite)	915	1306	0,152	0,692	1557

## Conclusions

New simplified method for determination of threshold Weibull stress is offered, namely, by uniaxial tensile tests cylindrical notched specimens at temperature 77K. Utilizing this method ensures high accuracy of determination of Weibull parameters.

## Acknowledgements

The work has been executed under the financial support of Bi-national Czech-Ukrainian Collaboration.

## References

- [1] S.R. Bordet, A.D. Karstensen, D.M. Knowles and C.S. Wiesner: Engng Fract Mech., Vol. 72 (2005), 435-452.
- [2] M. Beremin: Metall. Trans. V 14 (1983), 2277-2287.
- [3] F. Mudry: Nucl Engng Des. Vol.105 (1987), 65-76
- [4] X. Gao, C. Ruggieri and R.H. Dodds: Int.J.Fract. Vol 92 (1998), 175-200.
- [5] X. Zhang, J.F. Knott: Acta Mater. V.48 (2000), 2135-2146.
- [6] J.P. Petti and R.H. Dodds: Engng Fract. Mech. Vol. 51 (1996), 2079-2103.
- [7] R. W. Bakker and. J. Koers: Mechanical Engineering Publications, V.1 (1991), 31.
- [8] Xia Shih and F. C. Shih: J. Mech. Phys. Solids V. 44 (1996), 603-639.
- [9] X. Gao and R. H. Dodds: Int. J. Fract. V.102 (2000), 43-69.
- [10] A. Pineau: Int. J. of Fracture V.138 (2006), 139-166.

- 
- [11] S.A. Kotrechko, Yu. Meshkov, I. Dlouhy: *Theor. and Appl. Fract. Mech.* 35, 2001, 255.
  - [12] S. Kotrechko; B. Strnadel; I. Dlouhy.: *Theor. and Appl. Fract. Mech.*, 47, 2007, 2, 171-181.
  - [13] S. Kotrechko: *J. of Theoretical and Applied Mechanics*, 51 (2013), p 75-89
  - [14] S.A.Kotrechko, U.A. Polushkin, V.N.Grishchenko, S.A.Mamedov: *Metallofizika i noveishie tekhnologii*, 35, 2013, 1517-1526 (in Russian).
  - [15] C. Ruggieri: *International Journal of Fracture*, 110, 2001, 281-304.
  - [16] I. Dlouhy et al. In Bezensek; Hasegawa; Scarth eds. *Proceedings of the ASME Pressure Vessels and Piping Conference*, V. 1 Codes and standards, 2012, 101-105.

B7 Kotrechko, S., Zatsarna, O., Kozák, V., Dlouhý, I., Threshold fracture stress: theory and application, *Procedia Structural Integrity* 23, (2019), 413-418.



Available online at [www.sciencedirect.com](http://www.sciencedirect.com)

ScienceDirect

Procedia Structural Integrity 23 (2019) 413–418

Structural Integrity

Procedia

[www.elsevier.com/locate/procedia](http://www.elsevier.com/locate/procedia)

9th International Conference on Materials Structure and Micromechanics of Fracture

## Threshold fracture stress: theory and application

Sergiy Kotrechko<sup>a,b\*</sup>, Oleksandra Zatsarna<sup>a</sup>, Vladislav Kozák<sup>c</sup>, Ivo Dlouhý<sup>c</sup>

<sup>a</sup>*G.V. Kurdyumov Institute for Metal Physics, National Academy of Sciences of Ukraine, 36, Acad. Vernadsky Blvd., UA-0380 Kyiv, Ukraine*

<sup>b</sup>*National Technical University of Ukraine "Igor Sikorsky Kyiv Polytechnic Institute" 37, Prosp. Peremohy UA-03056 Kyiv, Ukraine*

<sup>c</sup>*Institute of Physics of Materials, Academy of Sciences of CR, Žitkova 22, Brno, Czech Republic*

### Abstract

The physical nature of cleavage threshold stress  $\sigma_{th}$  was considered and the technique for its experimental determination was developed. By applying data for reactor pressure vessel steel and cast low-alloyed manganese steel, it is shown that ignoring the value of  $\sigma_{th}$  gives rise to an 1.5-2 times overestimation of the shape parameter  $m$ . Within the framework of the suggested alternative of the Local Approach, temperature dependences of fracture toughness  $K_{IC}$  for probabilities of 5%, 50% and 95% were obtained for the steels. Accounting for the threshold stress  $\sigma_{th}$  a correct quantification of the temperature effect on fracture toughness values  $K_{IC}$  and proper prediction of its scatter limits in transition region is possible. In particular, it is important to take into account the threshold stress  $\sigma_{th}$  when predicting the lower envelope curve for fracture toughness  $K_{IC}$ , i.e. the  $K_{IC}$  value corresponding to a total probability of 5%.

© 2019 The Authors. Published by Elsevier B.V.

This is an open access article under the CC BY-NC-ND license (<http://creativecommons.org/licenses/by-nc-nd/4.0/>)

Peer-review under responsibility of the scientific committee of the ICMSMF organizers

**Keywords:** threshold stress; Local Approach; fracture toughness; Weibull parameters; crack nuclei; RPV steel;

Local Approach (LA) to cleavage fracture is an interdisciplinary concept enabling to predict unstable fracture of a pre-cracked body, using a local criterion for initiating a cleavage fracture in the vicinity of a crack/notch. In general, it was assumed that the LA would place fracture mechanics on a strong physical basis. Over the past three

\* Corresponding author. Tel.: +3-804-424-1352; fax: +3-804-424-2561.

E-mail address: [serkotr@gmail.com](mailto:serkotr@gmail.com)

decades, a significant number of articles have been published and a lot of conferences have been focused on this issue. However, the Local Approach didn't receive the expected utilization. This is mainly due to unnecessarily oversimplified description of the local cleavage event in conventional version of LA. Application of the Weibull two-parameter distribution, i.e. neglecting the role of threshold stress  $\sigma_{th}$  appears to be one of the unjustified simplifications of the LA to the cleavage fracture. According to experimental data, the value of  $\sigma_{th}$  for typical structural steels is about 1000 MPa [Kotrechko et al. (2017)]; therefore, the threshold stress  $\sigma_{th}$  can't be set equal to zero. One of the indirect evidences of the crucial effect of the threshold stress magnitude on the fracture characteristics is a significant change in the values of the Weibull distribution parameters at transition from two- to three-parameter distribution [Ruggieri. (2001)].

Several detailed discussions about the three-parameter Weibull stress model and toughness scaling on Weibull stress, were carried out by Gao et al. (1998) and Gao et al. (2000). Possibility of invalid calibration of shape parameter  $m$  and scale parameter  $\sigma_u$  in case of neglecting  $\sigma_{th}$  has been found one of the considerable conclusions; in particular in relation to the shape parameter  $m$ , which can be then will be systematically overestimated [Gao et al. (2000)]. According to overview of Pineau (2006), rational calibration procedure for  $\sigma_{th}$  remains an open issue nowadays. In the work of Kotrechko et al. (2001), a two-scale version of LA was proposed, in which the probability of cleavage initiation was determined by a sequential analysis of the processes of formation, instability and propagation of the crack nuclei in a polycrystalline aggregate. This made it possible to ascertain the main physical effects governing the cleavage fracture in metals and alloys, i.e. to create the physical basis of a LA.

Within the framework of two-scale version of LA this paper presents interpretation of the threshold cleavage stress of a polycrystalline metal, an experimental technique for determining the  $\sigma_{th}$  value, as well as an analysis of the effect of  $\sigma_{th}$  value on both the nature of the temperature dependence and scatter limits of fracture toughness of structural steels.

## 1. Theoretical background

From a mathematical point of view, the key element of the LA to cleavage is the Weibull distribution. Correct use of the Weibull distribution, and, accordingly, the choice of a procedure for parameters calibration of this distribution requires accounting for the quantitative features of the cleavage initiation micromechanism in metals and alloys. Most existing versions of the LA to cleavage account the fact that the crack nuclei (CN), which don't exist initially in metal, but are continuously generated during its plastic deformation, are the cause for the cleavage fracture. In a number of papers [Kotrechko (2001); Kotrechko (2013); Bordet (2005)], attention was focused on the peculiarities of the cleavage nucleation stage in the metal. It lies in the fact that only *freshly nucleated* CN can initiate cleavage. The crack nuclei that aren't unstable at the time of formation become blunt, and later don't participate in the cleavage fracture initiation. The rate of CN generation per unit volume,  $\rho$ , depends on the plastic strain level. This is important because the local plastic strain ahead of a crack / notch, may change by more than an order of magnitude. In addition, temperature has a significant effect on  $\rho$  [Kotrechko (2013)]. From a mathematical point of view, this means that the reference volume  $V_0$  ( $V_0 = 1/\rho$ ) will not be constant, as accepted in the most conventional models. Its magnitude is a function of the both local plastic strain  $\bar{\epsilon}$  and temperature  $T$ . The dependence was quantified by [Kotrechko (2013)], in analytical form, it may be approximated as follows:

$$\rho = \rho_0 - a \left( 1 - \frac{\bar{\epsilon}}{\bar{\epsilon}_c} \right), \quad \bar{\epsilon} \leq \bar{\epsilon}_c \quad (1)$$

$$\rho = \rho_0 - b \left( \frac{\bar{\epsilon}}{\bar{\epsilon}_c} - 1 \right), \quad \bar{\epsilon}_{\max} \geq \bar{\epsilon} > \bar{\epsilon}_c \quad (2)$$

where  $\bar{\epsilon}_c$  is the critical value of equivalent strain, corresponding to the maximum CN density;  $a$  and  $b$  are the coefficients;  $\bar{\epsilon}_{\max}$  is the maximum strain in approximation dependence (for ferritic steels typically  $\bar{\epsilon}_c \approx 0.02$ ;  $a = 1.498 \times 10^{13} \text{ m}^{-3}$ ;  $b = 0.124 \times 10^{13} \text{ m}^{-3}$ );  $\bar{\epsilon}_{\max} \leq 0.3 - 0.5$ .

$$\rho_0 = \rho_c \left[ 1 - \exp(-\alpha \tau_Y) \right] \quad (3)$$

$\alpha$  and  $\rho_c$  are the coefficients which determined by a calibration procedure (typical values can reach:  $\alpha \approx 0.01 - 0.04 \text{ MPa}^{-1}$ ;  $\rho_c = (1 - 8) \times 10^{13} \text{ m}^{-3}$ );  $\tau_Y$  is the thermal component of shear stress:

$$\tau_Y = 0.5 C_1 \exp[C_2 T + C_3 T \ln \dot{\epsilon}] \quad (4)$$

$\dot{\epsilon}$  is the plastic strain rate; for ferrite steels typically:  $C_1 = 1033 \text{ MPa}$ ;  $C_2 = -0.0068 \text{ K}^{-1}$ ;  $C_3 = 0.000415 \text{ K}^{-1}$ .

The threshold stress  $\sigma_{\text{th}}$  is the minimum stress of cleavage fracture. The crack nuclei have microscopic sizes, so, they become unstable under the action of tensile *microstresses*. According to Kotrechko (2013):

$$\sigma_{\text{th}} = \frac{\xi_c^{\min}}{1 + 3I_{\xi_{11}}} \quad (5)$$

where  $\xi_c^{\min}$  is the stress corresponding to crack nucleus instability of maximum length, which is most favourably oriented relatively to the direction of normal stresses;  $I_{\xi_{11}}$  is the coefficient of variation of tensile microstresses  $\xi_{11}$  (for iron and ferritic steels under tension  $I_{\xi_{11}} \approx 0.13$ ); the coefficient «3» before  $I_{\xi_{11}}$  means that  $\sigma_{\text{th}}$  is determined with a probability of 0.997.

The idea of experimental determination of the threshold stress magnitude is based on the use of a statistical scale effect for the cleavage stress. This effect manifests itself the tendency of the cleavage stress value  $\sigma_f$  to approach the level of threshold stress with increasing specimen volume (Fig. 1). The relatively high density of the crack nuclei

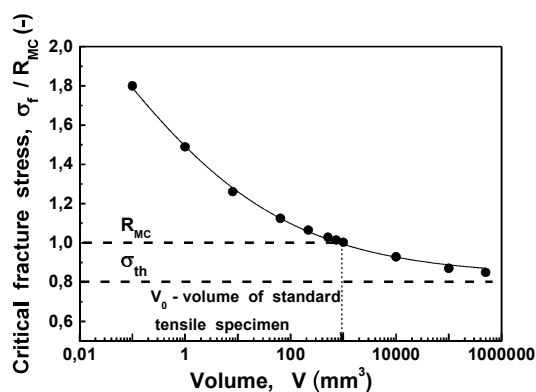


Figure 1. Scale effect at cleavage fracture of iron:  $R_{MC}$  is the brittle strength,  $\sigma_{\text{th}}$  is the threshold stress: circles designate the computer simulation findings

formed in the iron and structural steels ( $\approx 10^{13} \text{ m}^{-3}$ ) gives rise to the fact that starting from rather small volumes ( $\geq 500 \text{ mm}^3$ ) the value of  $\sigma_f$  slightly (up to 20%) exceeds the threshold level  $\sigma_{\text{th}}$ . For experimental determination of  $\sigma_{\text{th}}$ , this enables utilisation of the minimum of the cleavage fracture stress (brittle strength)  $R_{MC}$  of standard specimens at uniaxial tension within the temperature range of the ductile-to-brittle transition (Fig. 2). Unfortunately, ductile-to-brittle-transition range for typical structural steels lies below the nitrogen boiling point ( $-196 \text{ }^\circ\text{C}$ ). This means some methodological difficulties at experimental determination of  $R_{MC}$ . In this meaning, a method for determining the value of brittle strength,  $R_{MC}$ , was developed for structural steels by testing cylindrical specimens with an circumferential notch. The parameters of the notched specimen were experimentally ascertained (the maximum diameter is 8 mm, minimum - 5.2 mm, notch root radius - 2 mm), at which the nominal fracture stress for this particular specimen geometry at 2% average strain in the minimal cross-section is equal to  $R_{MC}$  with an accuracy of  $\pm 4\%$ .

Based on these ideas a technique was proposed for the experimental determination of the magnitude of threshold stress of structural steels  $\sigma_{th}$  [Kotrechko (2013)]. According to this technique:

$$\sigma_{th} = (0.75 \div 0.95) \times \sigma_{NF2}, \tag{6}$$

where the coefficient 0.75 corresponds to low strength steels, and the coefficient 0.95 – to high-strength ones;  $\sigma_{NF2}$  is the nominal fracture stress of notched tensile specimens at 2% average strain.

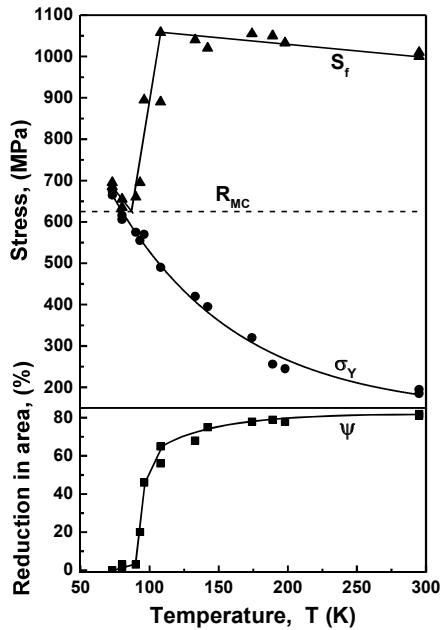


Figure 2. Temperature dependence of the main mechanical characteristics of iron:  $R_{MC}$  is the brittle strength;  $S_f$  is the fracture stress,  $\sigma_Y$  is the yield stress,  $\psi$  is the reduction in area.

For experimentally determining the value of  $\sigma_{NF2}$  it is enough to test 5-6 notched tensile specimens at the boiling point of liquid nitrogen (-196 °C) and to find the value of nominal fracture stress  $\sigma_{NF}$  at an average plastic strain in the notched section that is equal to 2%.

### 2. Results and discussion

Experimental studies were carried out on reactor pressure vessel (RPV) steel and cast low-alloyed manganese steels. Determination of the threshold stress values  $\sigma_{th}$  for these steels was performed according to the technique described above. To ascertain the parameters of Weibull distribution, standard pre-cracked specimens CT-1T made of RPV steel and 1T SENB specimens made of cast low-alloyed manganese steel were tested. The values of the shape parameter  $m$  and scale parameter  $\sigma_u$  were determined by a calibration procedure. For this purpose, the experimental values  $K_{IC}$  of the investigated steels were used (Fig. 3 (a and b)). The values  $m$  and  $\sigma_u$  were ascertained for the Weibull three- and two-parameter distribution, i.e., taking into account  $\sigma_{th}$  and at its zero value (see the table). In addition, the values  $\rho_c$  and  $\alpha$  were determined. In this case:  $\rho_c = 4 \times 10^{13} m^{-3}$ ,  $\alpha = 0.024 MPa^{-1}$ . Probability of the cleavage initiation for the finite element was taken to be zero, if the value of  $\rho$ , calculated from (2), became less or equal than 0.

Table. Mechanical properties and values of the Weibull distribution parameters

Material	$\sigma_Y$ (MPa)	$\sigma_{ul}$ (MPa)	$e_u$ (-)	$\psi$ (-)	$\sigma_{th}$ (MPa)	Three-parameter Weibull distribution		Two-parameter Weibull distribution	
						$\sigma_u$ (MPa)	$m$	$\sigma_u$ (MPa)	$m$
RPV steel	610	714	0.07	0.75	1100	6835	5.4	4895	12.2
Cast steel	319	481	0.26	0.74	720	3700	8.0	3800	13.3

Here  $\sigma_Y$  is the yield stress;  $\sigma_{ul}$  is the ultimate strength;  $e_u$  is the uniform elongation;  $\psi$  is the reduction in area;  $\sigma_{th}$  is the threshold stress;  $m$  and  $\sigma_u$  are the shape and scale parameters (values  $\sigma_Y$ ,  $\sigma_{ul}$ ,  $e_u$  and  $\psi$  are given for room temperature).

According to the data obtained, accounting for the threshold stress  $\sigma_{th}$  give rise to a significant (1.5–2 times)

decrease in the magnitude of the shape parameter  $m$ . This is in good agreement with the data of Ruggieri (2001). Based on these data, temperature dependences of fracture toughness  $K_{IC}$  for the studied steels were plotted (Fig. 3 (a and b)). The algorithm of calculations of fracture toughness and fracture probabilities is as follows:

1. For each  $j^{\text{th}}$  stage of loading  $K_I^j$ , the values of equivalent plastic strain  $\bar{\epsilon}^i$  and normal tensile stresses  $\sigma_{YY}^i$  in each  $i^{\text{th}}$  finite element were calculated using the finite elements method (software ABAQUS).
2. Further, the probability of the cleavage initiation in  $i^{\text{th}}$  element was calculated:

$$P_i = 1 - \exp \left[ - \frac{V^i}{V_0^i} \times \left( \frac{\sigma_{YY}^i - \sigma_{th}}{\sigma_u} \right)^m \right] \quad (7)$$

where  $V^i$  is the finite element volume;  $V_0^i$  is the volume per one crack nucleus ( $\frac{1}{V_0^i} = \rho^i$ , value of  $\rho^i$  was calculated according to equations (1), (2) and (3)).

3. Then, the total probability of cleavage initiation in specimen can be calculated:

$$P_\Sigma = \prod_{n=1}^{n=N} P_i(n) \quad (8)$$

where  $N$  is the number of finite elements falling into the yield region.

The step size and the number of loading stages were chosen in such a way as to obtain  $K_I$  values when the probability of cleavage initiation  $P_\Sigma$  is 5%, 50% and 95%.

Figures 3 (a and b) show the calculated temperature dependences of fracture toughness for RPV and cast steel. Also, here are experimental data for  $K_{IC}$ . According to these data, the calculated dependences describe well both the regularities of  $K_{IC}$  increase with increasing temperature  $T$  and the limits of its scatter at a constant  $T$  value. It should be emphasized that in this case, the fact is taken into account that the increase in  $K_{IC}$  is not only due to a fall in the yield strength, but also due to a decrease in the rate of generation of the crack nuclei in the vicinity of major crack tip (dependences (3) and (4)). The latter has not been accounted in the conventional concepts of local approach. This usually results in an underestimation of the slope of the  $K_{IC}$  temperature dependence. The higher the strength of steel and the higher the temperature for which  $K_{IC}$  is determined, the greater the error due to ignoring the temperature dependence of  $V_0$ .

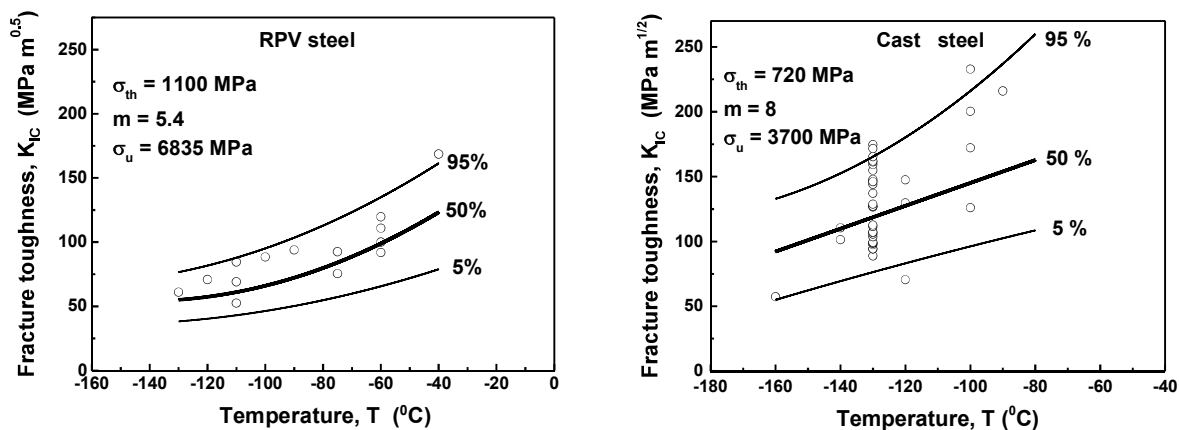


Figure 3. The temperature dependences of fracture toughness for RPV steel (a) cast low-alloyed manganese steel (b): circles designate the experimental evidence; lines are the calculation results.

According to the obtained results, taking into account the crucial role of threshold stress  $\sigma_{th}$  is especially important for correct description of the scatter limits for fracture toughness  $K_{IC}$  in transition region, as well as of its temperature dependence for small values of the fracture probability (5%), i.e. for description of the lower envelope of  $K_{IC}$ . As generally known, this is of paramount importance in predicting the integrity of the critical structural elements (reactor pressure vessels, gas pipelines etc.)

### Conclusions:

1. The relatively high density of the crack nuclei formed in iron and structural steels enables determining the value of the threshold cleavage stress from the results of testing tensile specimens with a circumferential notch of a special geometry.
2. Ignoring the threshold stress value gives rise to an overestimation of the shape parameter magnitude by 1.5 times for cast steel and 2 times for RPV steel.
3. In the Local Approach, accounting for the magnitude of threshold stress is especially important for correctly predicting the temperature dependence of the fracture toughness  $K_{IC}$  for low probabilities of fracture ( $P_{\Sigma}=5\%$  or less). This is of considerable practical importance for predicting the integrity of critical structural elements.

### Acknowledgements

This work was supported by the National Academy of Sciences of Ukraine (grants' number #0116U003048) and Bilateral Czech-Ukrainian project.

### References

- Bordet S.R., Karstensen A.D., Knowles D.M., Wiesner C.S., 2005. A new statistical local criterion for cleavage fracture in steel. Part I: Model presentation. *Engineering Fracture Mechanics* 72, 435-452.
- Kotrechko S., Stradel B., Dlouhy I., 2005. Fracture toughness prediction of cast Mn steel applying Local Approach. *Theoretical and Applied Fracture Mechanics* 12, 25.
- Kotrechko S., Meshkov Yu., 2001. Physical fundamentals of a local approach to analysis of brittle fracture of metals and alloys. *Materials Science* 37, 4, 583-597.
- Kotrechko S., 2013 The key problems of local approach to cleavage fracture *Journal of Theoretical and Applied Mechanics* 51, 75-89, Warsaw.
- Kotrechko S., Gryshchenko V., Kozak V., Dlouhy I., 2017. Methods of threshold stress determination for a Local Approach to cleavage fracture *Solid State Phenomena* 258, 281-285.
- Gao X., Ruggieri C. and Dodds R.H., 1998. Calibration of Weibull stress parameters using fracture toughness data. *International Journal of Fracture* 92, 175-200.
- Gao X. and Dodds R.H., 2000. Constraint effects on the ductile-to-brittle transition temperature of ferritic steels: a Weibull stress model. *International Journal of Fracture* 102, 43-69.
- Pineau A., 2006. Development of the local approach to fracture over the past 25 years: Theory and applications. *International Journal of Fracture* 138, 139-166.
- Ruggieri C., 2001. Influence of threshold parameters on cleavage fracture predictions using the Weibull stress model. *International Journal of Fracture* 110, 281-304.

- C1 Kozák, V., Vlček, L., Parameters identification for GTN model and their verification, *Materials Science Forum*, Vol. 482, (2005), 335-338.

## Parameters identification for GTN model and their verification on 42CrMo4 steel

V. Kozák<sup>1a</sup>, L. Vlček<sup>1b</sup>

<sup>1</sup>Institute of Physics of Materials, AS of CR, Žitkova 22, 616 62 Brno, Czech Republic

<sup>a</sup>[kozak@ipm.cz](mailto:kozak@ipm.cz), <sup>b</sup>[vlcek@ipm.cz](mailto:vlcek@ipm.cz)

**Keywords:** ductile fracture, GTN model, R-curve, vanishing elements

**Abstract.** The base of this paper is exact measurement of deformation and fracture material characteristics in laboratory, evaluation of these parameters and their application in models of finite element analysis modelling the fracture behaviour of components with defects. The base of the work is dealing with ductile fracture of forged steel 42CrMo4. R-curve is modelled by 3D FEM using WARP3D and Abaqus. Crack extension is simulated in sense of element extinction algorithms. Determination of micro-mechanical parameters is based on combination of tensile tests and microscopic observation. Input parameters for the next computation and simulation were received on the base of image analysis, namely  $f_N$  and  $f_0$ . The possibility of transferring these parameters to another specimen is discussed.

### Introduction

Classical nonlinear fracture mechanics can be understood as a mechanic of fracture for materials with inelastic deformations. It is covered by the classical theory of elastoplasticity and by the theory of viscoplasticity and based on the incremental formulation. However, constitutive equations presuppose stable behaviour to receive the convergence of modelled problem. It depends many times on the quality of used mesh in FEM and a numerical algorithm implementation. Physical reality of failure is often more complicated due to initiation, growth and nucleation of cavities; it can be characterized as damage. This damage may lead to the initiation and growth of macrocracks in a structure and to final damage of the whole structure or component. The term crack tip used in the fracture mechanics is a mathematical idealization because in the process zone ahead the crack tip new surfaces are coming up. Principally there are three approaches how to model damage, separation of materials and fracture process [1, 2]: (a) On the assumption of a small process zone, its influence is neglected and special fracture criteria are used, e.g. K, J and  $C^*$  etc. (b) We admit the creation of the new surfaces (separation) in the local area, the rest of the body is modelled using a standard element of continuum. The local area is described using cohesive models. (c) Damage is being implemented in constitutive models and accumulation of damage is processed. The advance approaches e.g. [3] enable to combine mechanics of continuum with the local behaviour of collection of atoms or on the base of molecular dynamics [4].

Micromechanical models of ductile tearing based on the damage mechanics showed themselves as a perspective way how to avoid numerical problems connected with the dependence of characteristic parameters used in the classical fracture mechanics on the size and geometry of body. The principal question is if the obtained parameters can be used without problems on the real component and predict its integrity. The procedures which can be applied on the strategy in modelling of the crack growth follow from the previous approaches. In contrast to crack growing of elastic materials, where the crack initiation is directed to the catastrophic damage of component, the presence of the ductile area leads to the stable crack growth. The crack growth can be simulated by the following way: (i) using node release techniques, where the control of the crack growth is based on the J, CTOD, CTOA (e.g. Siegele and Schmidt [5], Brocks [6]), (ii) using cohesive elements (e.g. Needleman [7], Yuang [8], Li [9]), (iii) using constitutive equations based on the damage mechanics (e.g. Needleman [10], Brocks [11], Schmidt [12], Lemaitre [13]). Within the framework

of the damage mechanics, the GTN [14] model is thought of as a micromechanical process like initiation, growth and coalescence of voids. A major item of GTN model is the yield criterion which extends von Mises yield criterion and can be expressed as:

$$\Phi = \frac{2}{3} \frac{S_{ij}S_{ij}}{\sigma_{YS}^2} + 2q_1 f^* \cosh\left(\frac{3}{2} \frac{q_2 \sigma_m}{\sigma_{YS}}\right) - \left[1 + q_3 f^{*2}\right] = 0 \tag{1}$$

$$f^* = \begin{cases} f & f_c \geq f \\ f_c - \frac{f_u^* - f_c}{f_F - f_c} (f - f_c) & f_c \leq f \end{cases} \tag{2}$$

The parameters  $q_1, q_2, q_3$  are used to adjust the model,  $\sigma_m$  is hydrostatic stress,  $\sigma_{YS}$  is yield stress,  $f^*$  is void fraction,  $f_c$  is the critical void fraction for coalescence,  $f_F$  is the final value of  $f$ ,  $f_u^* = 1/q_1$ .

**Experiments and identification of material parameters**

The basic micromechanical parameters are determined from the real tensile test combined with the finite element calculations.

f	0,0049	0,0073	0,0073	0,0083	0,0126	0,0131	0,0349
---	--------	--------	--------	--------	--------	--------	--------



Fig. 1: The tensile bar

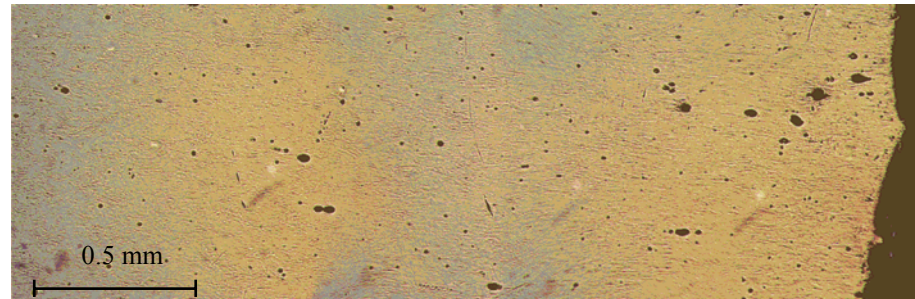


Fig. 2: Void distribution in the neck area of the round tensile bar

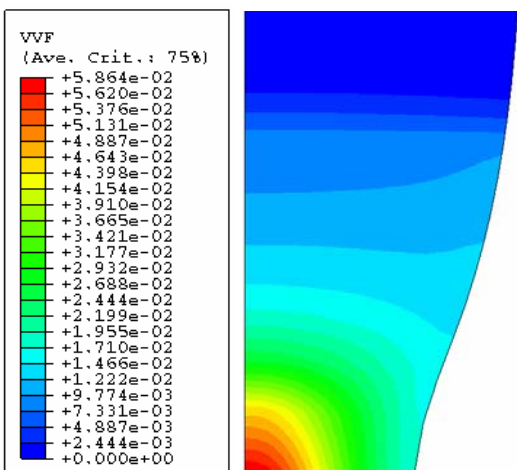


Fig. 3: Void fraction distribution for both GT and the GTN model

One can see in Fig. 2 that the  $f_F$  close to fracture surface nearly reaches the value of 0.034. As can be seen in Fig. 3, this is the value when the whole specimen is broken and this value was used for the next computations for three point bending (3PB) modelling using the approach of vanishing elements. Obtained results proved that the plastic strain distribution and void fraction distribution for the tensile tests are same for both GT and GTN model. Therefore the GT model (without void coalescence) can be used for 3PB modelling.

The simulations with varying  $f_0$  value (the initial value of  $f$ ),  $f_N$  is the nucleation parameter, are presented in Fig. 4 ( $\Delta L$  represents the elongation and  $\Delta d$  the contraction). In all computations recommended values for nucleation were used ( $\varepsilon_N=0.3$  and  $S_N=0.1$ ) and  $q_1=1.5$ ,  $q_2=1$ ,  $q_3=q_1^2$ .

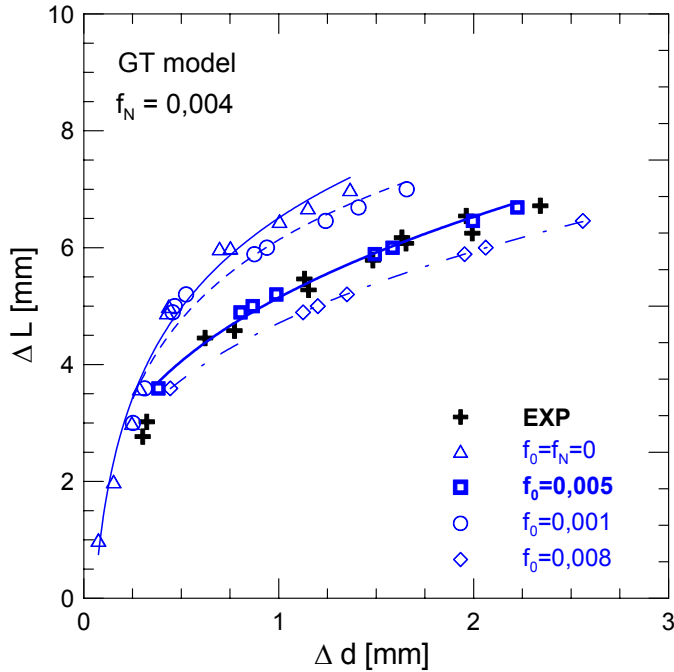


Fig. 4: The determination of  $f_0$

The values  $f_0=f_N=0$  represent the situation where only the elements without damage are used. For all finite element calculations the material parameters have been determined as  $E=210000$  MPa,  $\mu=0.3$  and actual true stress-strain curve at the room temperature has been used. The commercial code Abaqus [16] and university code WARP3D [17] were used for FEM modelling.

### Modelling of stable crack propagation

In order to perform the numerical analysis the FEM mesh was generated using two planes of symmetry for the 3PB specimen (Fig. 5). In the region of the supposed crack propagation the „vanishing elements“ (described by the dependence true stress vs. true strain plus GT parameters) were used with the characteristic size of 0.1 mm (and 0.05 mm for the second model). Number of elements was 6654 (resp. 6904) of the type C3D8. The angle of initial blunting was  $45^\circ$ , maximum increase of the crack length was 2.5 mm. The results of the FEM simulation are presented in Fig. 6 ( $q_1=1.5$ ,  $q_2$  is varying,  $q_3=q_1^2$ ).

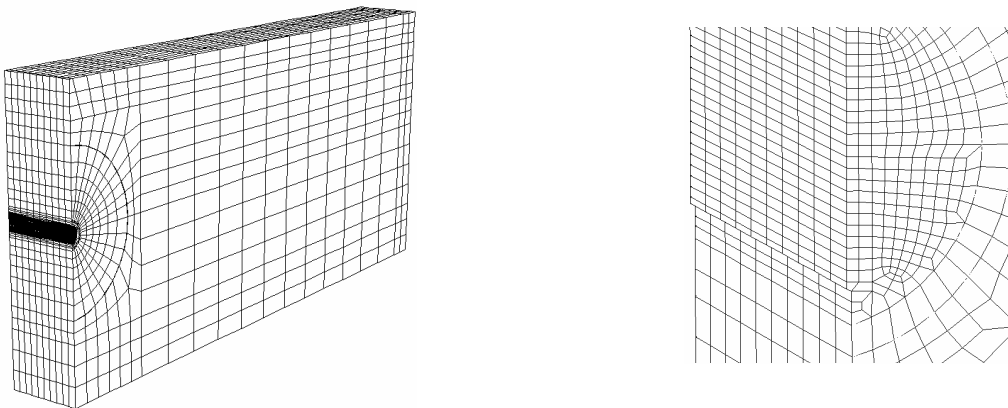
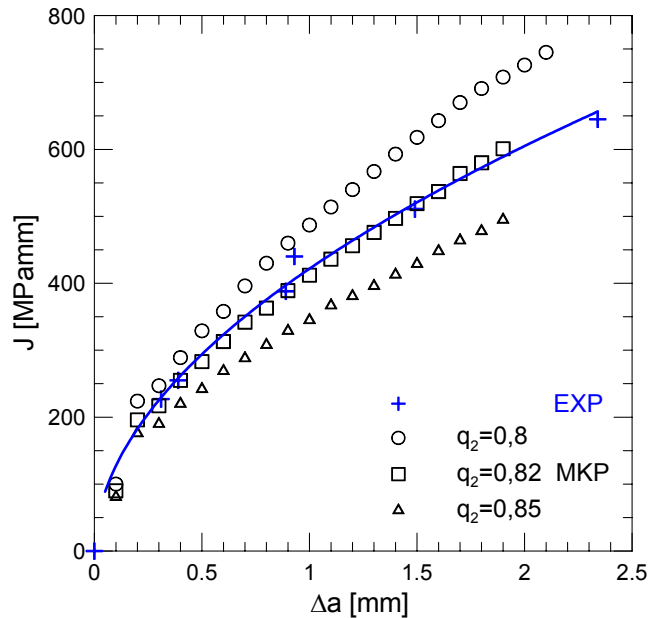


Fig. 5: FEM mesh for 3PB specimen and the detail of the crack tip

### Summary

- On the base of hybrid procedure (numerical modelling and experiment) the parameters of GT model were determined.

- Using the „vanishing elements” the ductile crack growth was simulated and the R-curve was predicted. The coincidence of the predicted curve and experimental curve is very good; to receive these results it is necessary to calibrate parameters  $q_1$  and  $q_2$  in GTN model. A more detailed discussion can be found in [15].



### Acknowledgements

This research was financially supported by project S2041001 of the Academy of Sciences of the Czech Republic and 106/02/0745 of the Grant Agency of the Czech Republic.

Fig.6: R-curve

### References

- [1] W. Brocks, et al.: report GKSS 2003/30.
- [2] N. Moes, T. Belytschko: Engng. Fracture Mechanics, 69, 2002, p. 813.
- [3] L. E. Shilkrot, R. E. Miller, W. A. Curtin: J. of Mech. and Phys. of Solids, 2004, article in press.
- [4] P.A. Klein et al.: Theoretical and Appl. Fracture Mechanics, 37, 2001, p. 99.
- [5] D. Siegele and W. Schmidt: Compu. Structures, 17, 1983, p. 697.
- [6] W. Brocks, A. Eberle, S. Fricke, H. Veith: Nuclear Eng. Design, 151, 1994, p. 387.
- [7] A. Needleman: Int. J. Fracture, 42, 1990, p. 21.
- [8] B. Yang, K. Ravi-Chandar: Int. J. Fracture, 93, p. 115.
- [9] Y. N. Li, Z. Bazant: Int. J. Fracture, 86, 1997, p. 267.
- [10] A. Needleman: J. Appl. Mech, 54, 1987, p. 525.
- [11] W. Brocks, D. Z. Sun, A. Hoenig: Int. J. Plast., 32, 1995, p. 459.
- [12] W. Schmidt et al.: Nucl. Eng. Design, 174, 1997, p. 237.
- [13] J. A. Lemaitre: J. Eng. Mater. Technology, 107, 1985, p. 86.
- [14] V. Tvergaard, A. Needleman: Acta Metal., 32, 1984, p. 157.
- [15] L. Vlček: Numerical 3D analysis of cracked specimens: Constraint parameters computations and stable crack growth modelling, PhD. Thesis, Brno, 2004.
- [16] Hibbit, Karlsson, Sorensen, Inc.: Abaqus User's Manual, Version 6.2, 2001.
- [17] Gullerud et al.: Warp3D release 14.1, University of Illinois, 2003.

C2 Kozák V., Ductile crack growth modelling using cohesive zone approach, Computational Modelling and Experiments, *In: Computational Methods in Applied Science 9*, Springer, (2008), 191-208, kapitola v knize.

# Chapter 11

## Ductile Crack Growth Modelling Using Cohesive Zone Approach

Vladislav Kozák

**Abstract** The paper studies the prediction of the crack growth of the ductile fracture of forged steel 42CrMo4. Crack extension is simulated by means of element extinction algorithms and two approaches have been compared. The first one is based on the damage model Gurson-Tvergard-Needleman (GTN) (see [12]), the second on the cohesive zone model with the exponential traction separation law. The bulk of the paper is concentrated on the cohesive zone modelling. Determination of micro-mechanical parameters is based on the combination of static tests, microscopic observation and numerical calibration procedures. The attention is paid on the influence of initial value of J-integral and the slope of R-curve ( $J-\Delta a$ ) which is modelled by 3D FEM. Based on tensile test the static elastic-plastic characterization of metals consist of the determination of the curve expressing the equivalent von Mises stress as a function of equivalent plastic strain. For ductile materials capable of undergoing large post-necking deformations, the exact material curve determination requires exact approach. The approximation suggested by Mirone [18] has appeared to be promising and valid for the structural steels.

### 11.1 Introduction

An important issue when considering failure is the observation that most engineering materials are not perfectly brittle in the Griffith sense, but display some ductility after reaching the strength limit, in which small-scale yielding, micro-cracking and void initiation, growth and coalescence take place. If the process zone is sufficiently small compared to structural dimension, linear elastic fracture mechanics can apply. If not cohesive forces that exist in the fracture zone must be taken into account.

---

Vladislav Kozák  
Institute of Physics of Materials, Academy of Sciences of the Czech Republic, 616 62 Brno,  
Žitkova 22, Czech Republic  
kozak@ipm.cz

The most powerful and natural way is to use cohesive zone model, which was introduced by Dugdale [8] and modified by Barenblatt [2] for elastoplastic fracture in ductile metals. For ductile fracture the most important parameters of the cohesive zone model appear to be tensile strength and the work of separation or fracture energy. The cohesive model is a phenomenological model and most authors take their own formulation for dependence of traction on the separation.

The crack tip, the term used very often in the fracture mechanics, is a mathematical idealization. In reality, a region of material degradation exists in some process zone. In this zone the microbehaviour becomes important for constitutive modelling. Most of the newer models developed and proposed are a bit different from Barenblatt's model in that they define the traction acting on the ligament as a function of the opening and not on the crack tip distance as Barenblatt did. The material separation and, thus, damage of the structure is described by interface elements in FE method. Using this technique, the behaviour of the material is split into two parts: the damage free continuum with arbitrary material law, and the cohesive interfaces between the continuum elements, which specify only the damage of the material.

Principally there are four approaches how to model damage, predict separation of materials and fracture process, e.g. [3] and [19]: (a) The process zone is small, its influence is neglected and than only special fracture criteria are used, e.g.  $K$ ,  $J$  and  $C^*$  etc. (b) We admit the creation of the new surfaces (separation) in the local area and the rest of the body is modelled using standard continuum element. Only local area is described using cohesive elements. (c) Damage is implemented in constitutive models and accumulation of damage is processed. (d) The advance approaches, e.g. [22] enable to combine mechanics of continuum with the local behaviour of collection of atoms on the base of molecular dynamics [14].

Micromechanical models based on the damage mechanics showed themselves as a perspective way how to avoid to numerical problems connected with the dependence of characteristic parameters used in the classical fracture mechanics on the size and geometry of body. The principal question is if the obtained parameters can be used without problems on the real component and predict its integrity. From it follow procedures which can be applied on the strategy in modelling of the crack growth. In contrast to crack growing of elastic materials, where the crack initiation is directed to the catastrophic damage of component, the presence of the ductile area leads to the stable crack growth. Crack growth can be simulated by the following way: (i) using node release techniques, where the control of the crack growth is based on the  $J$ , CTOD, CTOA, e.g. [5, 23], (ii) using cohesive elements, e.g. [17, 21, 26], and (iii) using constitutive equations based on the damage mechanics, e.g. [4, 16, 21]. Within the framework of the damage mechanics the GTN [24] model is thought of as a micromechanical process like initiation, growth and coalescence of voids. The constitutive equations which are used to describe ductile fracture processes are based on the relatively simple models which are dependent on many micromechanical parameters obtained experimentally.

## 11.2 Determination of Cohesive Parameters

Since the cohesive model is a phenomenological model, there is no evidence, which form is to be taken for the cohesive law,  $T(\delta)$  (see Fig. 11.1).

Cohesive models can be used for normal and tangential separation as well for mixed mode loading. Experiment in this paper were made only on a pure mode I crack and therefore cohesive law for mode I was applied. Cohesive law has to be assumed independently of specific material as a model of the separation process. The exponential model is used by many authors for both the ductile and the cleavage fracture [6]. An exponential relationship between the effective traction ( $T$ ) provides a decohesion model. The  $T$ - $\delta$  response follows an irreversible path with unloading always direct to origin. This model represents all the features of the separation process by: (1) the shape of the cohesive traction/separation curve ( $T$ - $\delta$ ), and (2) the local material strength by the peak traction ( $T_0$ ), and, the local ductility defined by the work of separation ( $\Gamma_0$ ) given by the area under ( $T$ - $\delta$ ) curve.

For the determination of the cohesive stress,  $T_0$  in the case of normal fracture a hybrid technique has been developed. Using conventional elastic-plastic analysis, the distribution of the axial stress across the notch section of the specimen geometry is determined for the instant of the crack initiation in the centre of specimen. At that event, the axial stress exhibits a maximum in the centre of specimen, which is supposed to be equal to  $T_0$ . The case of the standard computation by Abaqus [1] can be seen in the Fig. 11.2a and in the Fig. 11.2b (used load steps are in the Table 11.1). Approximately twelve specimens have been used and mean value 2000 MPa was determined as the  $T_0$  value ( $T_0 = 2,000 \pm 50$  MPa).

The standard CT specimens were used for  $J$ -integral determination according the ASTM 1820-99a procedure. The experimentally determined value of  $J_i$  was

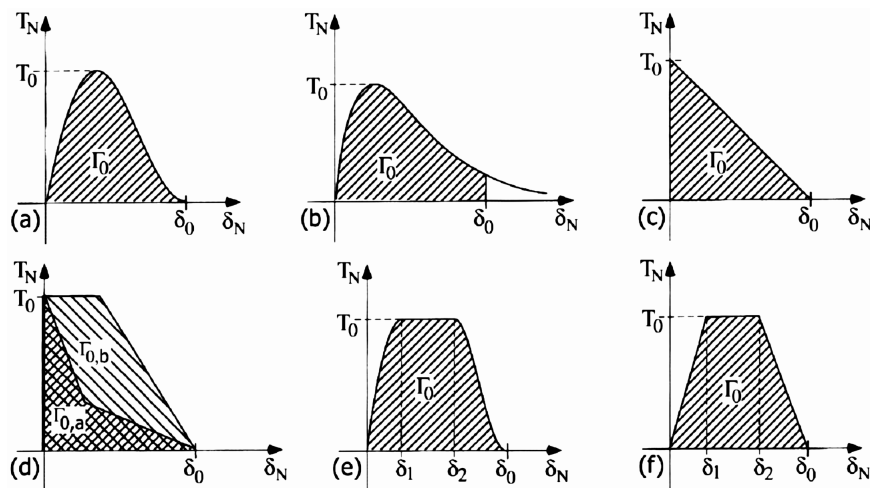


Fig. 11.1 Cohesive laws proposed for various materials

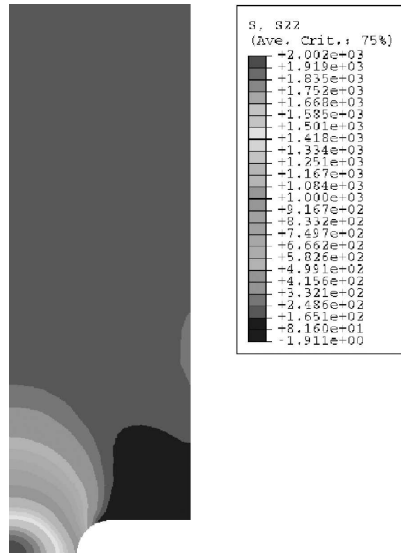


Fig. 11.2a Stress distribution for notched tensile specimen

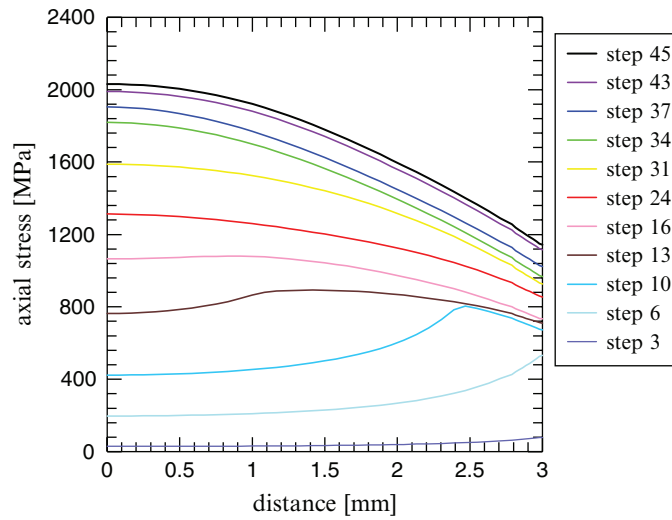


Fig. 11.2b Axial stress distribution

Table 11.1 Load steps used in Fig. 11.2b

Step	3	6	10	13	16	24
F [N]	2504.2	8000.53	16003.4	22003.6	25001.9	29002.4
Step	31	34	37	43	45	
F [N]	32,502	33675.4	33217.3	31149.1	29999.7	

found to be  $J_i = 115 \pm 5 \text{ MPa}\cdot\text{mm}$  and this value was calibrated using numerical procedure in WARP3D because of absence cohesive element carrying plasticity in Abaqus [1]. FE mesh for CT specimen can be seen in Fig. 11.3. Set of computations were applied to the calibration of the cohesive parameters used for  $J - R$  curve prediction ( $T_0, J_i$ ). Various combinations for  $T_0$  and  $J_i$  were tested. In the Fig. 11.4 the values  $J_i$  are marked as Cohe\_1, Cohe\_2 a Cohe\_3 ( $J_i = 110, 120, 130$ ) and

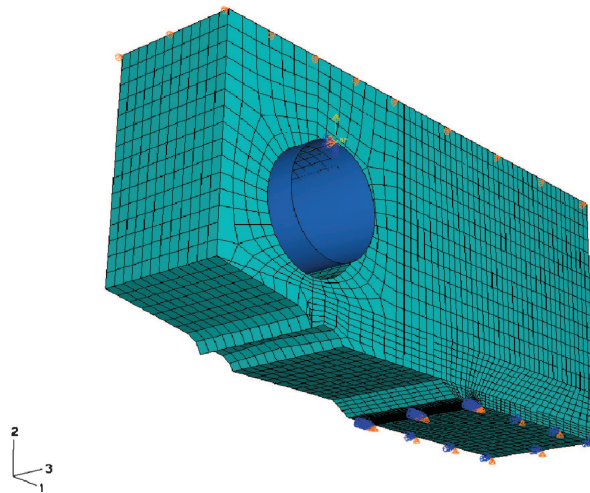


Fig. 11.3 FE mesh for CT specimen

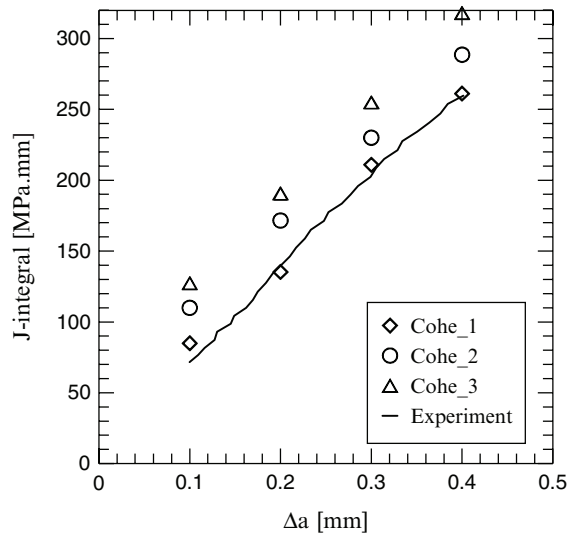


Fig. 11.4 J-R curve in the initial phase of the crack propagation

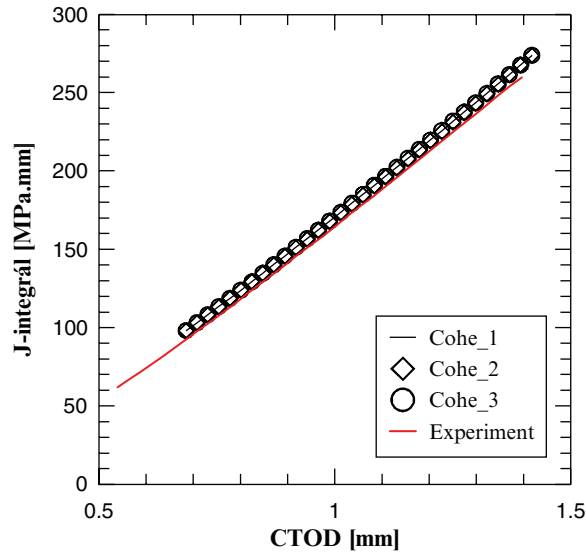


Fig. 11.5 J-CTOD curve in the initial phase of the crack propagation (data obtained from CT specimen)

received data were compared with the experimental values. The best correlation was found for first value of  $J_i = 110 \text{ MPa}\cdot\text{mm}$ . The calibration process can be seen further in the Fig. 11.5. After this procedure the input data for stable crack growth modelling have been received.

For simulation at given material curve the cohesive parameters seem to be:  $T_0 = 2,000 \text{ MPa}$  and  $J_i = 110 \text{ MPa}\cdot\text{mm}$ .

### 11.3 Stable Crack Growth Modelling Using Cohesive Elements

The experimental results of the SE(B) specimens were available in the form of the J-R diagram (J- $\Delta a$ ). The characteristic mesh size of the cohesive element was  $0.2 \times 1.4 \times 0 \text{ mm}$ . Some material curves received by the standard material tests for the same material show necessity of the diligent approach and accurate methods for the material curve determination. The best coincidence with the experimental data was in case of the material curve obtained from the tensile specimens and where the Mirone approach [18] was applied.

Using the cohesive parameters received on the notched specimens ( $T_0$ ) and  $J_i$  on the CT specimens the numerical simulation of the stable crack growth was simulated and  $J - R$  curve was predicted. By utilization of two symmetry planes (plane xy and yz) for SE(B) specimen with  $a/W = 0.5$  only one quarter of the real body was modelled. The FE mesh consists from 8,560 nodes and 7,155 element C3D8 (Abaqus 2005). For application of nonlinear cohesive element, the package Warp3D [10] was

necessary to use. In the same mesh generated in Abaqus [1] the next 180 cohesive elements *inter\_8* were added. Owing to numerical instability the loading increment from one step was decreased from 0.025 mm to 0.0025 mm (therefore more than 1,000 loading steps were applied).

Numerical modelling found strong dependence on the mesh size, especially on the mesh size in the direction in the thickness of the body. Therefore 15 various meshes for the FE modelling were applied. In Fig. 11.6 one can see detail of the crack for FE mesh used for the application of the cohesive elements.

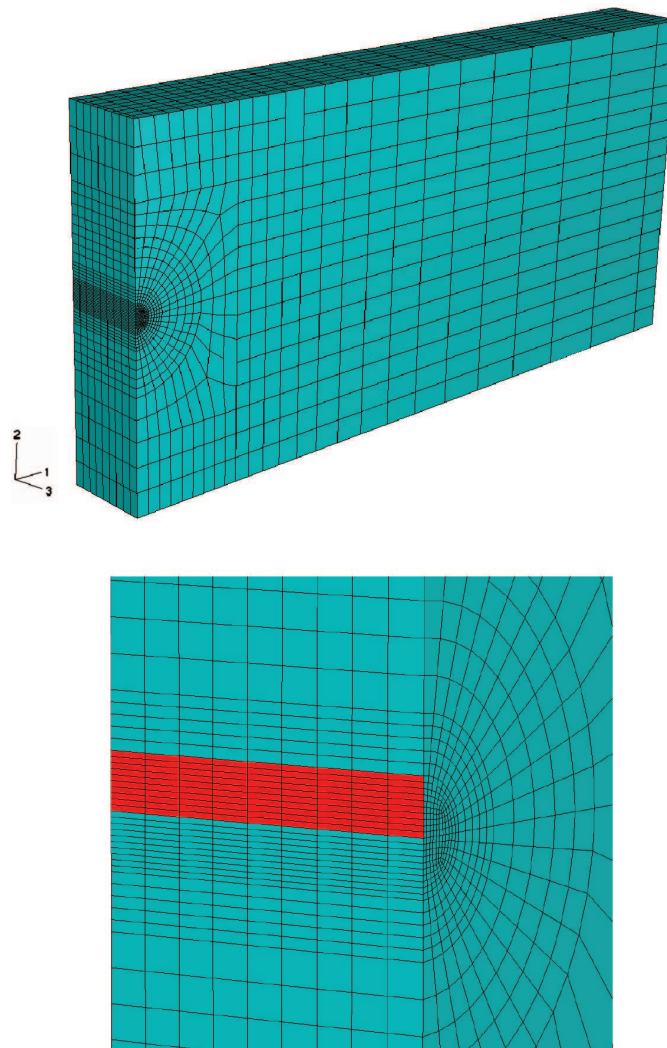


**Fig. 11.6** The FE mesh and detail of the crack tip for SE(B) specimen

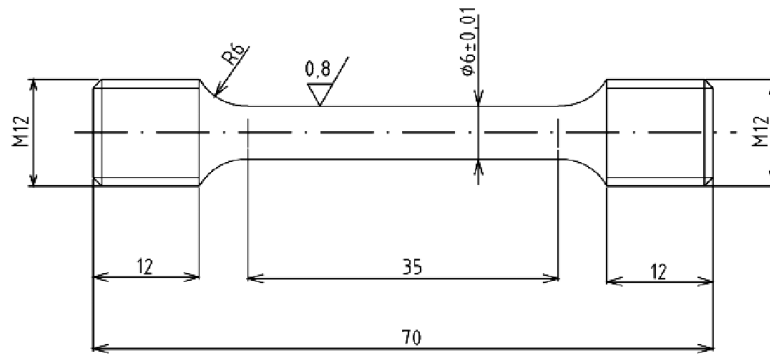


Fig. 11.7 Standard tensile specimen

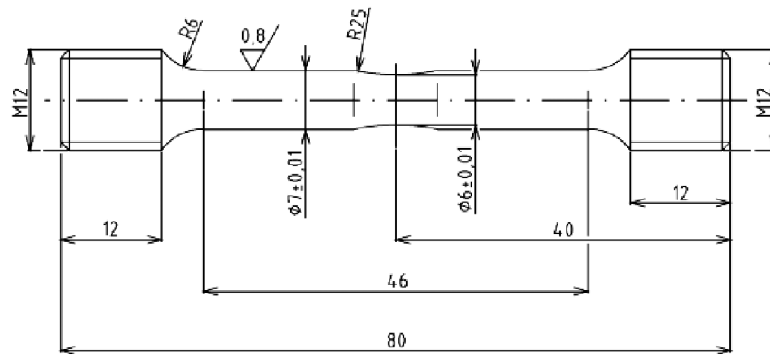


Fig. 11.8 Modified tensile specimen – waisted

To determine material curve for characterization of the elastoplastic behaviour of tested material the standard tensile experiments have been using for many years. The relation  $\sigma_{ekv}(\epsilon_{ekv})$  is found but the problem is the validity of this relation after necking. According to many experimental observations in [18] the new approximate curve in Eq. (11.1) was received for standard tensile specimens (see, Fig. 11.7) and modified tensile specimens – waisted specimens (Fig. 11.8). This Eq. (11.1) was used in our prediction of the material curve. At least 10 specimens were used in both cases; the third curve [25] was determined by standard procedure without MLR elongation. Material curves used for modelling can be seen in the Fig. 11.9 and corresponding  $J$ - $R$  curves in the Fig. 11.10. The higher values of deformation are the fitted values.

$$MLR\sigma(\epsilon_{ekv} - \epsilon_N) = 1 - 0,6058(\epsilon_{ekv} - \epsilon_N)^2 + 0,6317(\epsilon_{ekv} - \epsilon_N)^3 - 0,2107(\epsilon_{ekv} - \epsilon_N)^4 \quad (11.1)$$

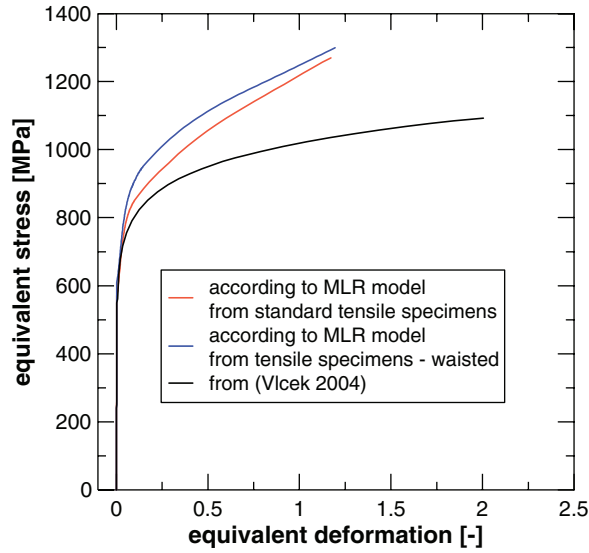


Fig. 11.9 Material curves used for modelling

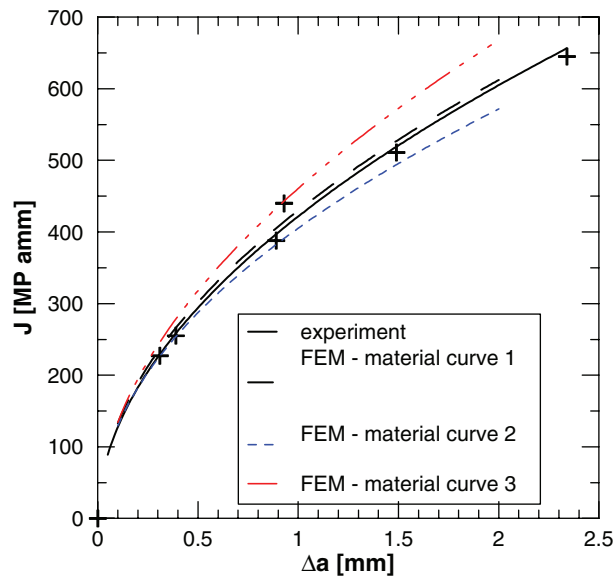
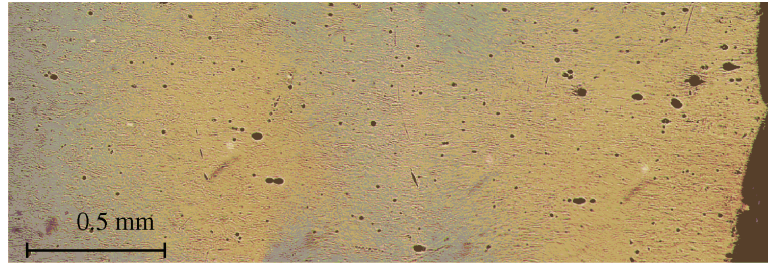


Fig. 11.10 J-R curve for various material curves

#### 11.4 Stable Crack Growth Modelling Using GTN Model

The base micromechanical parameters are determined from the real tensile test combined with the finite element calculations. Determination of micro-mechanical parameters is based on the combination of tensile tests and microscopic observation.



**Fig. 11.11** Void distribution in the neck area of the round tensile bar

The standard cylindrical specimens with a diameter of 6 mm have been tested at room temperature at crosshead velocity of  $2 \text{ mm min}^{-1}$ . From the reason for the numerical simulation the following data have been measured: force vs. elongation and force vs. contraction using optical method. The tensile specimens have been analysed as a first. The methodology for the assessment of the micromechanical parameters requires the metallographic observation not only in the area of the local change of the diameter but in the area of non-affected by the plastic deformation [15]. Half of the tensile specimen has been bisected and a die head has been separated. The two samples for optical microscopy have been prepared. Received photos have been analyzed using image analysis. Void distribution in the neck area of the round tensile bar can be seen in Fig. 11.11.

f	0.0049	0.0073	0.0073	0.0083	0.0126	0.0131	0.0349
---	--------	--------	--------	--------	--------	--------	--------

On the base of the received photos recording the contracted area it is possible to submit that in this case of ductile process the coalescence of cavities is minimal. Then the value of  $f_c$  is very close to value of  $f_F$  and the critical conditions for ductile damage is being received only by combination of growth and nucleation. One can see in Fig. 11.11 that the  $f_F$  close to fracture surface nearly reaches the value equal 0.034 and  $f_0$  the value 0.005.

Major item of GTN model is the yield criterion which extends von Mises yield criterion and can be expressed as:

$$\Phi = \frac{2}{3} \frac{S_{ij}S_{ij}}{\sigma_Y^2} + 2q_1 f^* \cosh\left(\frac{3}{2} \frac{q_2 \sigma_m}{\sigma_Y}\right) - [1 + q_3 f^{*2}] = 0 \quad (11.2)$$

$$f^* = \begin{cases} f & f_c \geq f \\ f_c - \frac{f_u^* - f_c}{f_F - f_c} (f - f_c) & f_c \leq f \end{cases} \quad (11.3)$$

The parameters  $q_1$ ,  $q_2$ ,  $q_3$  are used to adjust the model,  $\sigma_m$  is hydrostatic stress,  $\sigma_Y$  is yield stress,  $f^*$  is void fraction,  $f_c$  is the critical void fraction for coalescence,  $f_F$  is the final value of  $f$ ,  $f_u^* = 1/q_1$ .

The void volume fraction,  $f$ , which is defined as the total volume of all cavities to the volume of the body, is introduced as an internal variable to characterize the damage. Its equation consists of two terms due to nucleation and growth:

$$df = df_{\text{growth}} + df_{\text{nucl}} \text{ with } f(t_0) = f_0, \quad (11.4)$$

with  $f_0$  as the initial void volume fraction. The void growth rate is proportional to the plastic volume dilatation rate and an empirical approach for nucleation of void was proposed by [7, 11], suggested a normal distribution for void nucleation (for strain-controlled nucleation) and then we can write:

$$df_{\text{nucl}} = A d\varepsilon_p, \quad (11.5)$$

where  $A$  represents the intensity of nucleation and  $\varepsilon_p$  is equivalent plastic deformation and  $A$  is given by

$$A = \frac{f_N}{S_N \sqrt{2\pi}} \exp \left[ -\frac{1}{2} \left( \frac{\varepsilon_p - \varepsilon_N}{S_N} \right)^2 \right] \quad (11.6)$$

$\varepsilon_N$  is the mean strain for nucleation,  $S_N$  is its standard deviation,  $f_N$  is the volume fraction of void nucleating particles.

The results following from the metallographic observation in question of the absence of the coalescence stadium have been verified on the base of the finite element calculation too. An important query for the applicability of the model is whether or not the micro-mechanical parameters are dependent on the mesh size. Material affection was given by the true stress-strain curve,  $f_N = 0.04$  and the statistical model of nucleation with recommended values  $\varepsilon_N = 0.3$  and  $S_N = 0.1$  was chosen see [20] for all computations. As can be seen in Fig. 11.12, where the number of elements in the neck area is varying, one can observe the discrepancy between Fig. 11.12a and b. Next computations for more elements than 14 are giving the same curves as in Fig. 11.12b.

The influence of the initial volume fraction on the slope of elongation-contraction curve has been tested; it can be seen in Fig. 11.13. It is evident that the increasing value of  $f_0$  implicates the increasing of the value of the plastic deformation in the neck area. Reciprocally the volume fraction of void nucleating particles,  $f_N$ , has been tested and it is presented in [25].

In the framework of the stable crack growth modelling the 3D model of the standard specimen for three point bend test was created. Using two planes of symmetry only one fourth of the real body was modelled. The problem of determination of the proper mesh size ahead the crack tip was solved on the base of comparison experimentally determined force-COD curve and numerically received one (see [25]). The characteristic mesh size was initially determined to 0.5 mm, but the coincidence between experiment and the numerical data was not good. Having been used the mesh where the characteristic mesh size for crack growth area had been selected to 0.1 mm the agreement between experiment and numerical model has been markedly increased.

Using above mentioned micromechanical data and FEM software WARP3D [10] the dependence of J-integral on the ductile crack length has been received. As can be seen in Fig. 11.14 the computed curve and the experimental curve are nearly the

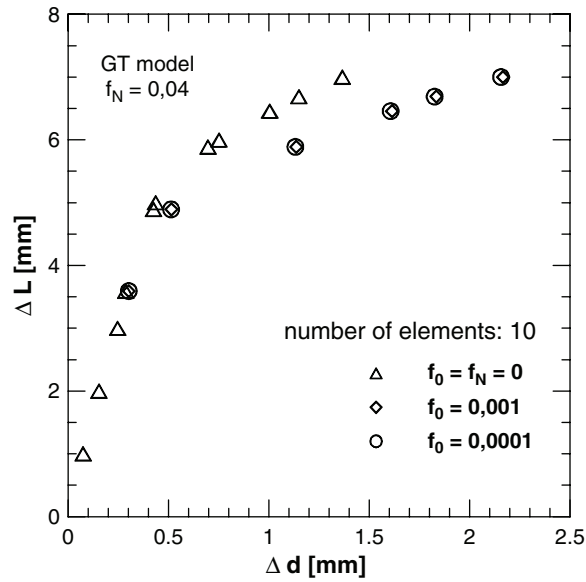


**Fig. 11.12a** The influence of the mesh size on the curve elongation-contraction

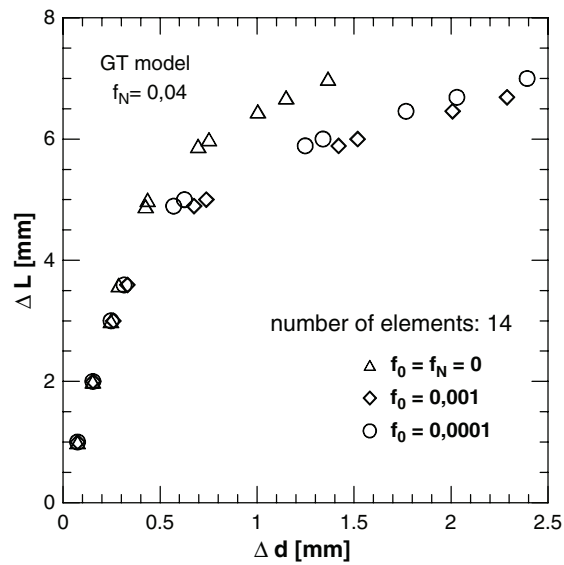


**Fig. 11.12b** The influence of the mesh size on the curve elongation-contraction

same, but the good correlation has been found due to varying of  $q_2$  parameter. The values  $q_1 = 1.5$  and  $q_2 = 1$  have been accepted for a long time as constants non-dependent on the material behaviour. Faleskog [9] as the first referred to difficulties following from the consideration of the independence of these parameters on the

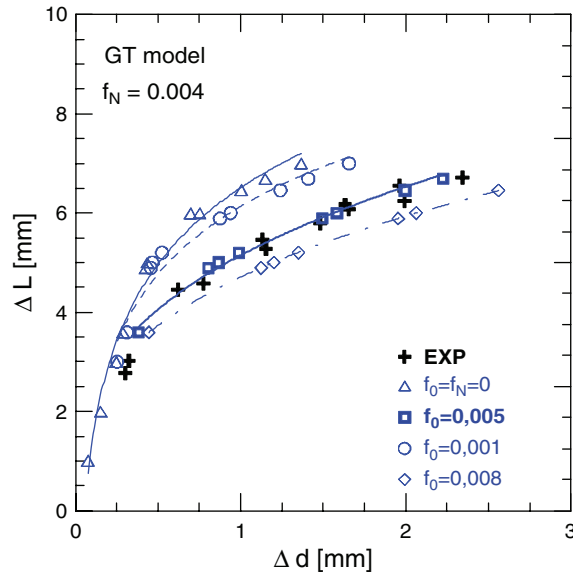


Fig. 11.13 The dependence of the elongation-contraction curve on the varying value  $f_0$

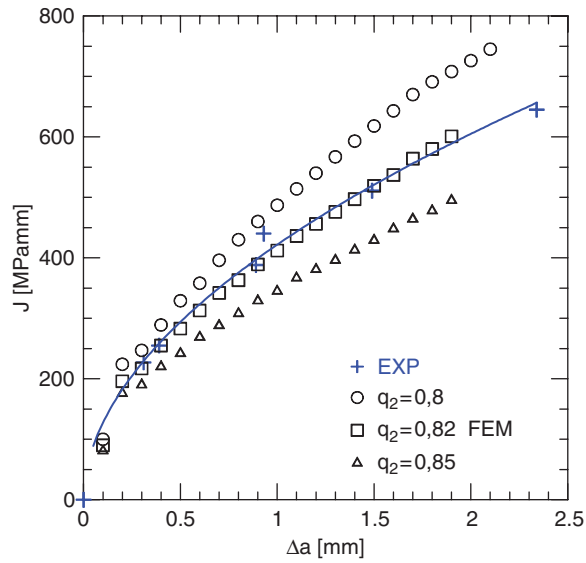
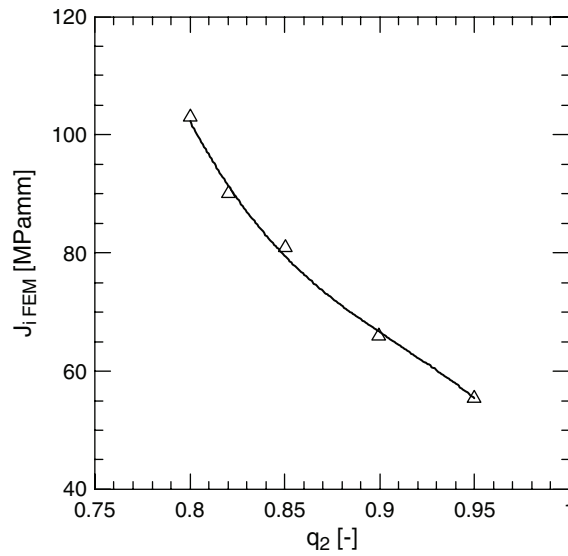


Fig. 11.14 J-R – curve

material. The new method of calibration  $q_1$  and  $q_2$  parameters is being discussed in the latest work presented by Kim [13].

In our calibration the  $q_1$  parameter is fixed and the dependence of  $q_2$  (representing the local triaxiality) on the slope of the R-curve is tested. In connection of the slope the attention has been paid on the ductile crack initiation. From

physical-mechanical point of view the value of  $J_i$  is appeared to be independent on the geometry of the body. This value can be regarded as a material characteristic and it has been determined numerically as the value when the first element vanished. This value can be denominated as a pseudo-physical and its dependence on the  $q_2$  parameter (in Fig. 11.15) and on the triaxiality factor  $h$  (in Fig. 11.16) has been



**Fig. 11.15** The dependence of  $J_{i \text{ FEM}}$  on the  $q_2$  parameter

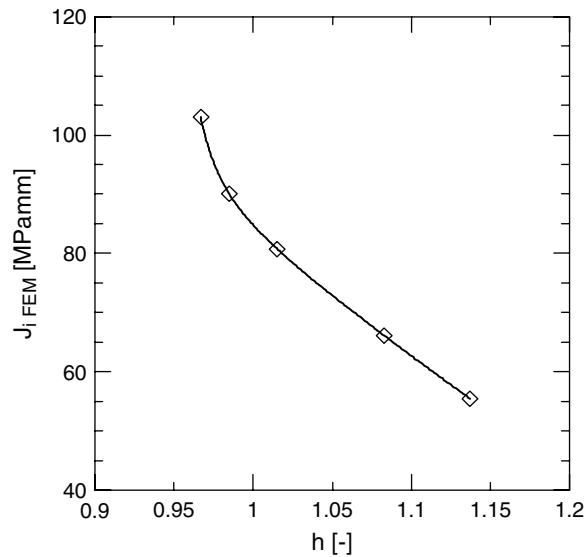


**Fig. 11.16** The dependence of  $J_{i \text{ FEM}}$  on the stress triaxiality factor

determined. As can be seen the decreasing of the local stress triaxiality leads to the increasing of the initial value of  $J_{1\text{ FEM}}$  and for our experimental steel this initiation value was markedly higher then for recommended value of  $q_2$ . The value of  $J_i$  could be dependent on the geometry of the body (from the engineering approach) and this finding is necessary to take into account in the case of transferability of the experimentally determined data to the real components.

## 11.5 Conclusions

Using of the “vanishing elements” the ductile crack growth was simulated and the R-curve ( $J$ - $\Delta a$ ) was predicted using damage and cohesive elements in case of a pure mode I. The coincidence of the predicted curve and experimental curve is very good;

- To receive these results is necessary to calibrate parameters  $q_1$  and  $q_2$  in GTN model.
- For modelling using cohesive elements the hybrid experimental and numerical procedure is used for the calibration  $T_0$  and  $\Gamma_0$ .
- Stable crack growth modelling is strongly dependent on the quality of the FE mesh. For the damage modelling the blunting crack tip is used; for the modelling using cohesive elements the thickness of these separate elements is zero and the exponential traction separation law (see Fig. 11.1b) was used. Obtained results can be seen in Figs. 11.17 and 11.18.

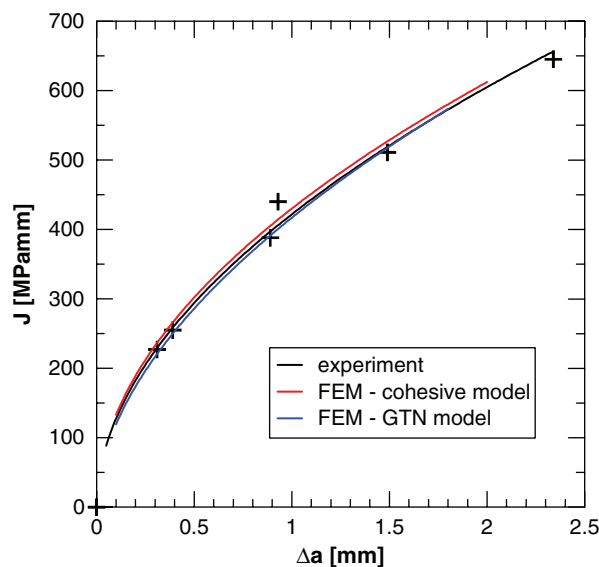
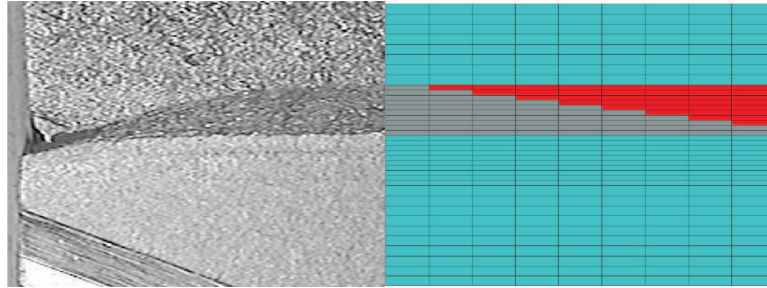


Fig. 11.17 J-R curve generated by cohesive model and by GTN model



**Fig. 11.18** The reconstruction of the crack path

- The shape of the  $J$ - $R$  curve is more determined by the material curve than by the shape of the traction separation law. The exact determination of the material curve is the key point for proper application of the cohesive zone model used for the ductile fracture.
- Three separate tensile geometries were investigated, including waisted and notched specimens. Waisted samples and standard tensile specimens were used to determine the material curve. The notched specimens have been found very suitable for the verification of the measured material curves. The shallow notch of the waisted tensile specimen allows monitoring of the diametral contraction during testing, so that the true stress could be accurately monitored. Agreement of the computed curve (using Abaqus [1]) force – deflection and force – contraction for notched specimen was excellent. Notched specimens were used for  $T_0$  determination and calibration.
- The standard CT specimens were used for  $J$ -integral determination according to the ASTM 1820–99a procedure and  $J_i$  value has been calibrated through the best fit of the calculated and measured  $J$ - $R$  curve.

**Acknowledgements** This research was supported by the grant 101/05/0493 of the Grant Agency of the Czech Republic.

## References

1. ABAQUS 6.5.4 (2005) User's manual, ABAQUS Inc.
2. Barenblatt GI (1962) The mathematical theory of equilibrium cracks in brittle fracture, Adv. Appl. Mech. 7: 55–129
3. Brocks W, Cornec A, Schneider I (2003) Computational Aspects of Nonlinear Fracture Mechanics, GKSS 2003/30: 129–203
4. Brocks W, Sun DZ, Hoening A (1995) Verification of the transferability of micromechanical parameters by cell model calculations with visco-plastic materials, Int. J. Plasticity 11(8): 971–989
5. Brocks W, Eberle A, Fricke S, Veith H (1994) Large stable crack growth in fracture mechanics specimens, Nucl. Eng. Design, 151(2–3): 387–400

- C3 Kozák, V., Dlouhý, I., Chlup, Z., Cohezive zone model and GTN model collation for ductile crack growth, Int. Conference *Material Structure & Micromechanics of Fracture MSMF 5*, (2007), Brno, 4 pages.

## Cohesive Zone Model and GTN Model Collation for Ductile Crack Growth

Vladislav Kozák<sup>1,a</sup>, Ivo Dlouhý<sup>1,b</sup> and Zdenek Chlup<sup>1,c</sup>

<sup>1</sup>Institute of Physics of Materials AS CR, Zizkova 22,  
616 62 Brno, Czech Republic

<sup>a</sup>kozak@ipm.cz, <sup>b</sup>idlouhy@ipm.cz, <sup>c</sup>chlup@ipm.cz

**Keywords:** cohesive zone model, GTN model, J-R curve prediction.

**Abstract.** The micromechanical modelling encounters a problem that is different from basic assumptions of continuum mechanics. The material is not uniform on the microscale level and the material within an element has its own complex microstructure. Therefore the concept of a representative volume element (RVE) has been introduced. The general advantage, compared to conventional fracture mechanics, is that, in principle, the parameters of the respective models depend only on the material and not on the geometry. These concepts guarantee transferability from specimen to components over a wide range of dimensions and geometries. The prediction of crack propagation through interface elements based on the fracture mechanics approach (damage) and cohesive zone model is presented. The cohesive model for crack propagation analysis is incorporated into finite element package by interface elements which separations are controlled by the traction-separation law.

### Introduction

The prediction of crack propagation through interface elements based on the fracture mechanics approach (damage) and cohesive zone model is investigated. The contribution is concentrated on qualification of the two approaches and their use for the prediction of the ductile crack growth in 42CrMo4 forged steel.

Two approaches have been selected for crack extension simulations, both built up on element extinction algorithms. The first one is based on the damage model of Gurson-Tvergaard-Needleman (GTN) [1]. The other approach arises from the cohesive zone model [4]. Determination of micro-mechanical parameters inevitable for modelling utilizes combination of results from static tests, microscopic observations and numerical calibration procedures. The attention has been paid to the influence of initial value of J-integral and the slope of R-curve which were modelled by 3D FEM using WARP3D and Abaqus. The ductile tearing process consisting of void nucleation, growth and subsequent coalescence has been represented by a traction separation law in case of the cohesive zone model. Interface elements (cohesive elements) simulating the damage development were implemented between the conventional continuum elements representing elastic-plastic properties of the material. Two cohesive parameters,  $T_0$  (cohesive strength) and  $\Gamma_0$  (cohesive energy) are supposed to describe damage and fracture of the representative volume element (RVE). The tensile bars were used for determination of the cohesive strength, and the fracture mechanics specimens (CT) for determination of the cohesive energy. The ductile crack initiation ( $J_i$ ) has to be determined by appropriate experimental method like multiple specimens technique.

The separate problem supposes elastic-plastic characterization of the steel based on tensile test. It consists mainly of the determination of the loading curve expressing the equivalent von Mises stress as a function of equivalent plastic strain. For ductile materials capable of undergoing large post-necking deformations, the determination of such material response curve determination requires an exact approach. From a number of possible approaches the solution suggested by Mirone [2] appears to be promising. The material curves introduced into calculation have been

nearly identical; however, an immaterial alteration may play a significant role in the final prediction of the crack extension.

R-curves in terms of the J-integral approach play a key role in the structural integrity assessment concept. Thus, it is important to know in depth about the effects contributing to predictions of this curve.

### Experiments and determination of material parameters

The basic *micromechanical parameters for GTN model* were determined from the measured tensile test data combined with the finite element calculations; generally 9 material parameters have been determined as described elsewhere [3]. The geometry parameters  $q_1$ ,  $q_2$ ,  $q_3$  were used to adjust the model,  $f_c$  is the critical void fraction for coalescence,  $f_F$  is the final value of void fraction,  $f_N$  is the nucleation parameter, in all computations recommended values for nucleation were used ( $\varepsilon_N=0.3$  and  $S_N=0.1$ ).

To determine material curve for characterization of the elastic-plastic behaviour of tested material the standard tensile test data have been using for many years. The relation of  $\sigma_{ekv}(\varepsilon_{ekv})$  can be determined but a key problem is the validity of this relation after necking. According to observations [2] the new approximate curve, Eq. 1, was received for standard tensile specimens and so-called waisted specimens.

$$MLR\sigma(\varepsilon_{ekv} - \varepsilon_N) = 1 - 0,6058(\varepsilon_{ekv} - \varepsilon_N)^2 + 0,6317(\varepsilon_{ekv} - \varepsilon_N)^3 - 0,2107(\varepsilon_{ekv} - \varepsilon_N)^4 \quad (1)$$

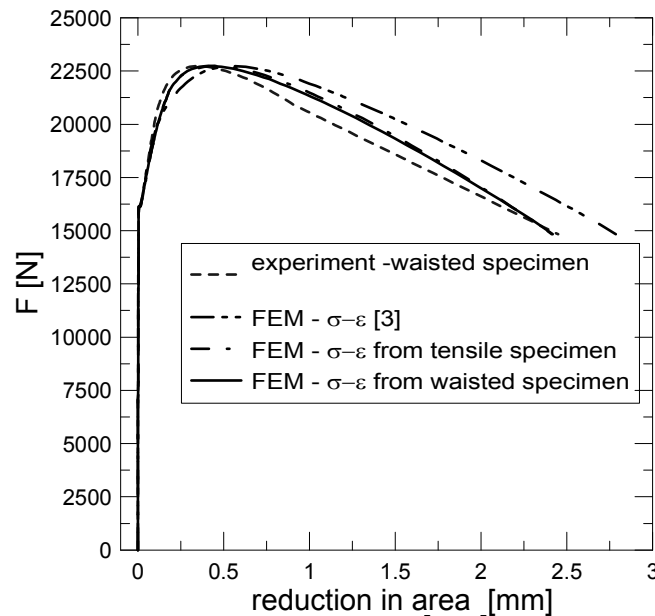


Fig. 1: Comparison of tensile test curves obtained experimentally and by FEM modelling

The *parameters for cohesive zone modelling*. For the cohesive strength,  $T_0$ , in the case of fracture in the normal direction, the hybrid technique has been developed [4]. Using conventional elastic-plastic analysis, the distribution of the axial stress across the notch section of the specimen is determined for the moment of the crack initiation in the centre of specimen. In that case, the axial stress exhibits a maximum in the centre of specimen, which is supposed to be equal to  $T_0$ . The result values were determined as the average values from a set of ten tested specimens.

The cohesive energy,  $\Gamma_0$ , has been determined by a fracture mechanics test with assumption that  $\Gamma_0$  is equal to  $J_i$  valued, i.e. the J-integral at initiation of stable crack extension. The procedure can be taken from the standard test methods and numerical calibration as can be seen in Fig.2. The standard CT specimens were used for the J-integral determination according the ASTM 1820-99a

procedure. The calibration process was applied on three combinations of values  $T_0$  and  $J_i$  marked in Tab. 1 as cohe\_1, cohe\_2, cohe\_3.

	$T_0$ [MPa]	$J_i$ [MPa.mm]	$\delta_0/2$ [mm]
Cohe_1	2000	110	0.0101
Cohe_2	2000	120	0.011
Cohe_3	2000	130	0.012

Table 1: Input parameters for traction-separation law calibration

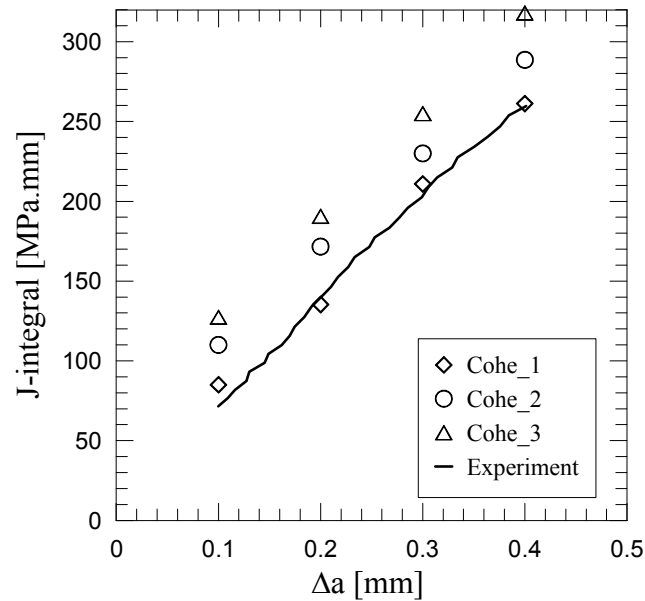


Fig.2: Traction separation law calibration by means of  $J_i$ - $\Delta a$  data (for CT specimen)

### Stable crack propagation modelling

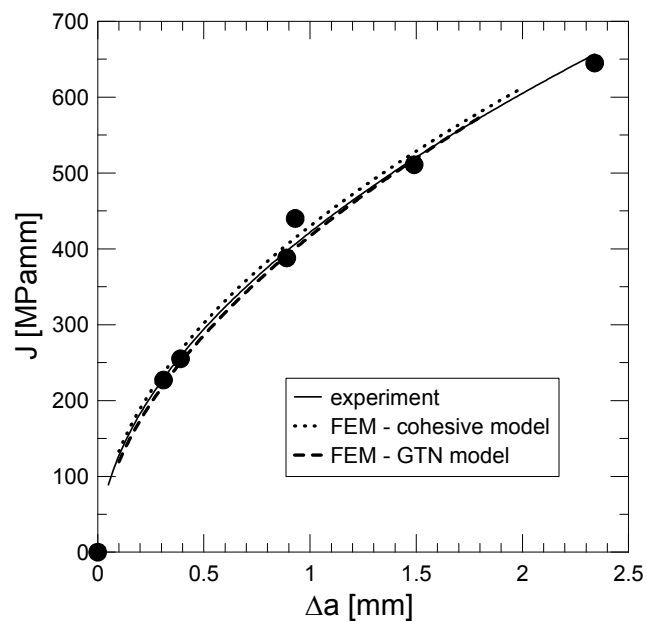


Fig.4:  $J_i$ - $\Delta a$  curve prediction for cohesive model and GTN (SE(B) specimens)

The experimental results of the SE(B) specimens were available in the form of the  $J$ - $\Delta a$  curve. The characteristic mesh size of the cohesive element was  $0.2 \times 1.4 \times 0 \text{ mm}^3$ . The dependence of the  $J$ -integral on the crack increment is illustrated in the Fig. 4. Some material curves received by the standard tensile tests for the same material show necessity of the diligent approach and accurate methods for the material curve determination. The best coincidence with the experimental data was obtained in case of the material curve adjusted by means of Mirone method from the tensile test of the standard specimen.

### Summary

The cohesive parameters for ductile crack growth have been experimentally determined and calibrated using finite element computation method. Obtained results have been compared with the GTN method. This procedure consists of a specific traction-separation law of the cohesive model and convenient method for determining the material parameters. The traction-separation law has been characterized by the constant cohesive strength,  $T_0$ , which is preceded by a steep slope and by the cohesive energy,  $\Gamma_0$ , which also characterizes the material properties in the process zone. From a numerical point a view the following findings have been made:

- The shape of the  $J$ - $\Delta a$  curve and therefore the results of crack propagation modelling is strongly controlled by the material curve (equivalent stress – equivalent strain curve). The precise determination of the material curve is the key point of the correct modelling and application of the cohesive elements. The sensitivity of the cohesive zone modelling on the material curve is higher than in case of the GTN model.
- The strong dependence of the convergence and numerical stability on the mesh size was found in both cases. The shape of the crack line for numeric stable solution is a bit different. The crack line for the GTN model is blunted, the best shape is for  $45^\circ$  chamfer of the first element. Thickness of the cohesive element is zero; therefore no bevel edge can be used.
- Determination of nine parameters for GTN model is more complicated procedure and more dependent on the experimentally determined values.
- Using of the „vanishing elements” for the ductile crack growth simulation was tested and R-curve was predicted. The coincidence of the predicted curve and experimental curve is very good due to partial calibration of numerical  $q_2$  parameter of the GTN model.
- The experimentally obtained values for the  $J_I$  received on the CT specimens must be numerically calibrated.
- The higher plasticity is in the crack tip the lower requirements are on the shape of the traction-separation curve for the cohesive zone model.

Finally, good agreement between numerical simulations and experimentally measured J-R curve was found.

### Acknowledgements

The research was financially supported by project IA A 200410502 of the Academy of Sciences of the Czech Republic and project 101/05/0493 of the Czech Science Foundation.

### References

- [1] V. Tvergaard, A. Needleman: Acta Metal., 32, (1984), p. 157.
- [2] G. Mirone: International Journal of Solids and Structures 41, (2004), p. 3545.
- [3] V. Kozák, L. Vlček: Mater. Sci. Forum Vol. 482 (2005), p. 335.
- [4] A. Cornec, I. Schneider, K.H. Schwalbe, On the practical application of the cohesive model, Engineering Fracture Mechanics, Vol. 70, (2003), pp. 1963-1987.

- C4 Kozák, V., Chlup, Z., Modelling of fibre matrix interface of brittle matrix long fibre composites by application of cohesive zone method, *Key Engineering Materials*, Vol. 465, (2011), 231-234.

## Modelling of fibre-matrix interface of brittle matrix long fibre composite by application of cohesive zone method

Vladislav Kozák<sup>1,a</sup> and Zdeněk Chlup<sup>1,b</sup>

<sup>1</sup>Institute of Physics of Materials AS CR, Žitkova 22,  
616 62 Brno, Czech Republic

<sup>a</sup>kozak@ipm.cz, <sup>b</sup>chlup@ipm.cz

**Keywords:** cohesive zone model, fibre composite, finite element user procedure.

**Abstract.** Ceramic matrix composites reinforced by unidirectional long ceramic fibre are very perspective materials. The only disadvantage of such materials is relatively high brittleness at room temperature. The main micromechanism acting as toughening mechanism is the pull out. There are other mechanisms as crack bridging, crack deflection etc. but the primer mechanism is mentioned pull out which is governed by interface between fibre and matrix. The contribution shows a way how to predict and/or optimise behaviour of composite by application of cohesive zone method using the FEM numerical package Abaqus. The presented results from numerical calculations are compared with experimental data.

### Introduction

The prediction of crack propagation through interface elements based on the fracture mechanics approach (damage) and cohesive zone model is investigated. From amount damage models the cohesive models seem to be especially perspective for practical applications [1]. Thanks to phenomenological character of cohesive models this model is adapting for various kinds of materials and damages. Cohesive models (more often) cohesive zone model (CZM) is increasingly being used to simulate fracture and fragmentation processes in metallic, polymeric, ceramic materials and composites [2]. Base principle of CZM which is using cohesive elements for crack and damage modelling is their damage while the classical continuum elements are undamaged. In terms of modelling the separation of materials is realized using cohesive elements in the boundary line between classical elements of continuum. Using cohesive models the behaviour of materials is realized by two types of elements. The former is the element for classical continuum and the latter is the connecting cohesive element. The separation of these connecting cohesive elements is computed from the displacement of neighbouring continuum elements. Generally the separation is dependent on the normal and shear stresses and their operation on the surface of separation elements [3].

The failure of composites has been investigated extensively from the micromechanical point of view. When a crack propagates in a composite material in a direction perpendicular to that of reinforced fibres, the failure process typically involves four basic mechanisms: matrix cracking, fibre/matrix debonding, fibre breakage and fibre pull-out. Critical problems in application of these materials are the interfaces between matrix and reinforcing fibres. The interface is very strip area with primary key property including the fracture toughness, strength and fracture behaviour. This interface plays the crucial role in stress transferring between reinforcement and matrix and so it determines the mechanical and fracture behaviour. The separation is given by the common influence between normal and tangential directions at the interface. Compound materials consist of two or more constituents with different properties complementing other. The degrading properties of one constituent are levelled off by better properties of the others. Damage evolution is sensitive to morphological parameters of the microstructure such as volume fraction, size and spatial distribution of reinforcements, interfacial strength and size defect. Significant improvement in discrete crack modelling has been realized with the development of extended finite element method

[X-FEM]. In this approach the domain is modelled by finite elements with no explicit meshing of the crack surfaces. The location of the crack discontinuity can be arbitrary with respect to the underlying finite element mesh and static or fatigue crack propagation simulation can be performed without the need to remesh as the crack advances [4, 5]. Combination cohesive elements and X-FEM approach seem to be a very perspective way how to model the crack growth.

### Bridging law modelling

For glass fibre composites, the interfacial properties are controlled by the sizing, which is applied to the glass fibres during manufacture. The change of sizing results in changes of these properties. This leads to the influence to the mechanical properties such as strength and fracture toughness. The concept of strength is used for characterising crack initiation in composite design, while fracture toughness determines crack growth and damage development. Bridging occurs during cracking in mode I crack growth along the fibre direction. This failure mode plays an important role during delamination of fibre composites and cracks splitting around holes and notches. The fibre bridging zone must be modelled as a discrete mechanism on its own; failure is not just controlled by the cracking at the crack tip. The failure process can be described by a bridging law, which describes the relationship between the crack opening displacement and the local bridging tractions resulting from the bridging ligaments. This paper derives the necessary basics and equations to implement these laws into the commercial finite element code ABAQUS with a cohesive user element. Different numerical adjustments of the bridging law will be discussed in detail in oral presentation. Crack aspects, such as crack opening shape and the influence of bridging law parameters, are studied based on the numerical results.

Now consider the specimen having a crack with bridging fibres across the crack faces near the tip. The bridging law  $\sigma = \sigma(\delta)$  is then taken to be identical at each point along the bridging zone. Since fibres will fail when loaded sufficiently, we assume the existence of a characteristic crack opening  $\delta_0$ , beyond which the closure traction vanishes. Shrinking the path of the J integral to the crack faces and around the crack tip gives

$$J = \int_0^{\delta^*} \sigma(\delta) d\delta + J_{TIP}, \quad (1)$$

where  $J_{TIP}$  is the J integral evaluated around the crack tip (during cracking is equal to the fracture energy of the tip,  $J_0$ ). The integral is the energy dissipation in the bridging zone and  $\delta^*$  is the end-opening of the bridging zone at the notch root. The bridging law can be determined by differentiating Eq. (1)

$$\sigma(\delta^*) = \frac{\partial J_R}{\partial \delta}. \quad (2)$$

$J_R$  is the value of J during crack growth. Initially, the crack is unbridged. Thus, by Eq. (1), crack growth initiates when  $J_R = J_{TIP} = J_0$ . As the crack grows,  $J_R$  increases in accordance with Eq. (1). When the end opening of the bridging zone  $\delta^*$  reaches  $\delta_0$ , the overall R-curve attains its steady state value  $J_{SS}$ .

### Bridging law implementation

There are a variety of possible methods for implementing cohesive laws within commercial finite element programs. The most versatile is the development and programming of cohesive elements. These elements are in most cases defined with zero thickness and prescribe stresses based on the relative displacement of the nodes of the element. Similar work has also been undertaken with spring elements (force-opening relation), although in this case there might be simplifications required when calculating the equivalent nodal spring forces from the surrounding elements. The

procedure is not straight forward when springs are connected to elements with non-linear shape functions, such as 8-noded elements.

The constitutive expression can be expressed either with a linear displacement term for  $\Delta \mathbf{u}$ , or with a coupled form, where  $\Delta \mathbf{u}$  is included with non-linear dependence. The preferred option depends on the form of the constitutive equation (Eq. 3) and its numerical implementation:

$$J_R(\delta^*) = J_0 + \Delta J_{SS} \left( \frac{\delta^*}{\delta_0} \right)^{1/2}. \quad (3)$$

Two points need to be addressed during the numerical adjustment: Removal of the stress singularity at  $\Delta u = 0$  and incorporation of the initial fracture strength  $J_0$  improved traction separation law as can be seen in Fig. 1. Parameter  $\alpha$  is in range  $\langle 1, 100 \rangle$ ,  $K_{fac} = J_0 / (\Delta u_2 \sigma_0) (\alpha + 1 / \alpha)$ .

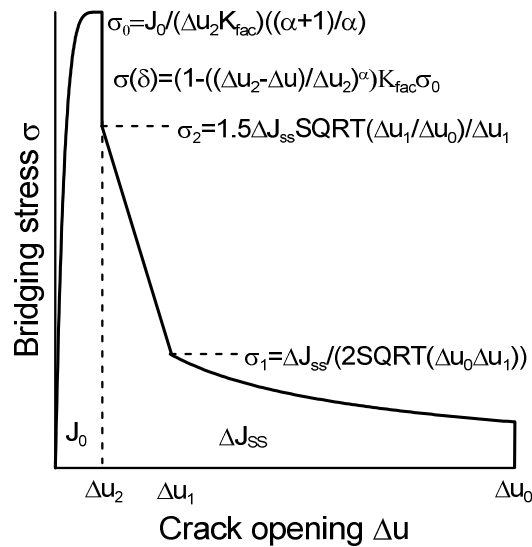


Fig.1: Traction separation (bridging) law modification

### Experiments and determination of material parameters

The material used for the bridging stresses modelling was a commercially available SiC Nicalon fibre reinforced borosilicate glass matrix composite (see Fig. 2). More information can be found in [6]; especially the prediction of bridging stresses was valuable for the cohesive model application. Properties of the glass matrix, SiC fibres and composite were: Young's modulus 63, 198, 118 GPa, Poisson ratio 0.22, 0.20, 0.21, tensile strength 60, 2750, 600-700 MPa.

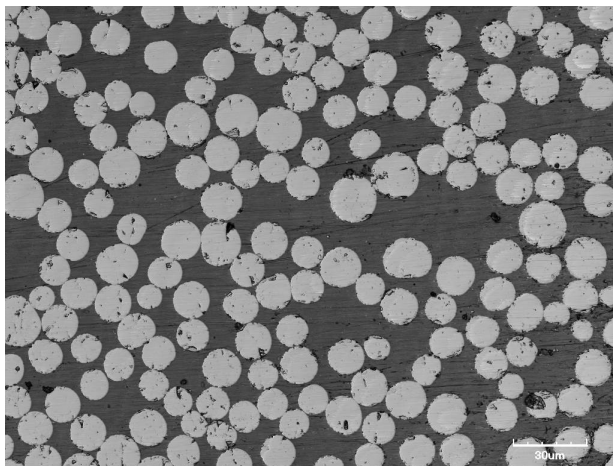


Fig. 2: Image of the microstructure

### Stable crack propagation modelling

For the crack growth modeling the following data determined experimentally were used:  $J_0 = 6200 \text{ J/m}^2$ ,  $J_{ss} = 18500 \text{ J/m}^2$ ,  $\Delta u_c = 0,1 \text{ mm}$ ,  $\Delta u_1 = 0,013 \text{ mm}$ . Calibrated data and the final shape of the bridging law can be seen on the following Fig. 3.

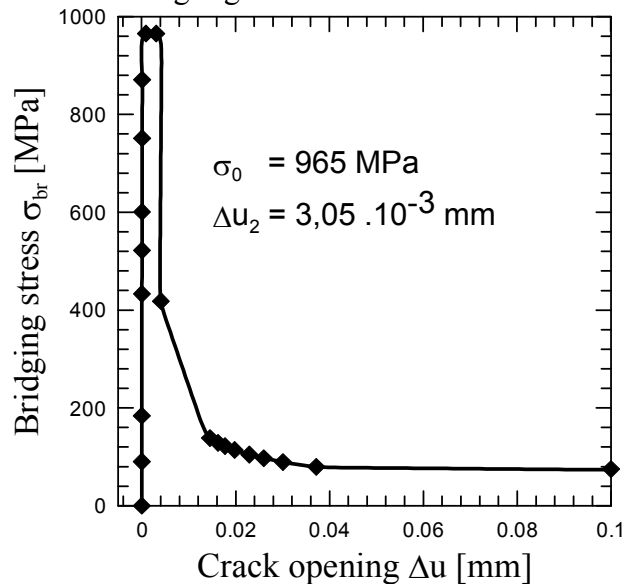


Fig. 3: Traction separation law after calibration procedure

### Summary

Special shape of the bridging law has been tested and implemented into the commercial finite element package Abaqus. The cohesive parameters for crack growth have been experimentally determined and calibrated. The traction-separation (bridging) law has been characterized by bridging stress  $\sigma_0$ , steady state value  $J_{ss}$ , crack growth initiates when  $J_R = J_{TIP} = J_0$ . The following findings have been made:

- Crack propagation and its numerical stability are strongly controlled by slope of bridging law. The precise determination of the law is the key point of the correct modelling and application of the cohesive elements.
- The strong dependence of the convergence and numerical stability on the mesh size was found. Thickness of the cohesive element is zero; therefore the sharp crack tip is used.
- Vanishing elements for the crack growth simulation were tested and numerical stable shape of the traction separation law was suggested.

### Acknowledgements

This research was financially supported by project 101/08/1304 of the Grant Agency of the Czech Republic.

### References

- [1] A. Cornec, I. Schneider and al.: Engineering Fracture Mechanics, Vol. 70 (2003), p. 1963.
- [2] V. Kozák, L. Vlček: Mater. Sci. Forum Vol. 482 (2005), p. 335.
- [3] Wiewer, M., Kabir, R., Cornec, A., Schwalbe, K.-H.: Engineering Fracture Mechanics, Vol. 74, Issue 16 (2007), p. 2615.
- [4] J.L. Asferg, P.N. Poulsen, L.O. Nielsen: International J. of Numer. Methods and Engng., Vol. 72 (2007), p.464.
- [5] E. Giner, N. Sukumar and al.: Engineering Fracture Mechanics 76 (2009), p.347.
- [6] M. Kotoul at al.: Theoretical and Applied Mechanics 49 (2008), p.158.

C5 Strachota, A., et al., Preparation of Silicon Oxycarbide Composites, *Acta Physica Polonia A*, Vol. 120, Issue 2, (2011), 326-330, IF 0,875.

# Preparation of Silicon Oxycarbide Composites Toughened by Inorganic Fibers via Pyrolysis of Precursor Siloxane Composites

A. STRACHOTA<sup>a,\*</sup>, M. ČERNÝ<sup>b</sup>, P. GLOGAR<sup>b</sup>, Z. SUCHARDA<sup>b</sup>, M. HAVELCOVÁ<sup>b</sup>, Z. CHLUP<sup>c</sup>,  
I. DLOUHÝ<sup>c</sup> AND V. KOZÁK<sup>c</sup>

<sup>a</sup>Institute of Macromolecular Chemistry, Academy of Sciences of the Czech Republic, v.v.i.  
Heyrovského náměstí 2, CZ-16200 Praha, Czech Republic

<sup>b</sup>Institute of Rock Structure and Mechanics, Academy of Sciences of the Czech Republic, v.v.i.  
V Holesovickách 41, CZ-182 09, Praha, Czech Republic

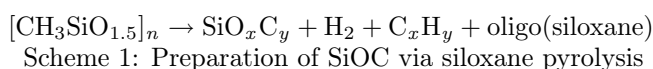
<sup>c</sup>Institute of Physics of Materials of the Academy of Sciences of the Czech Republic, v.v.i.  
Žitkova 22, CZ-61662 Brno, Czech Republic

The optimization of silicon oxycarbide (SiOC) synthesis (sol-gel/pyrolysis) is described, starting from methyltriethoxysilane, dimethyldiethoxysilane, tetraethoxysilane, ethyltriethoxysilane and propyltriethoxysilane. Variation of final elemental composition was tested via change of monomer ratios and combinations. The main aim was to achieve low weight losses during cure and pyrolysis and high micromechanical properties. Gas chromatography and mass spectroscopy was used to analyse the by-products of cure and pyrolysis, indicating a prominent role of cyclosiloxane and polyhedral oligomeric silsesquioxane (POSS) oligomers. Best results were obtained with high contents of methyltriethoxysilane in the monomers mixture.

PACS: 81.05.Je, 81.05.Mh, 82.30.Lp

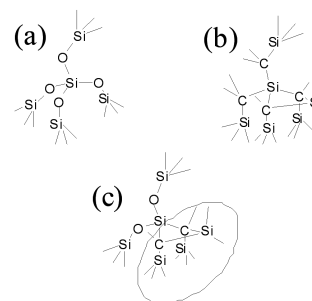
## 1. Introduction

Silicon oxycarbide (SiOC) is a hard glass which is structurally related to both silica (SiO<sub>2</sub>) and silicon carbide (SiC). It enjoys a considerable research interest, because of its high mechanical properties and refractoriness [1], interesting viscoelastic behavior at elevated temperatures [1], and not least because of an improved oxidation resistance [2–5] in comparison to SiC, due to much more efficient surface passivation with SiO<sub>2</sub>.



Attractive is the easy accessibility of SiOC via pyrolysis of siloxane resins (Scheme 1, review [6]). Even ideally homogeneous SiOC can be considered a nanocomposite, consisting of SiO<sub>2</sub>- and SiC-like structural units, as illustrated in Scheme 2. The highest SiOC homogeneity is achieved via magnetron sputtering [7, 8]. Above 1100 °C, SiOC undergoes a “micro”-phase separation into larger nanometric domains of SiC embedded in SiO<sub>2</sub> [1, 9–12]. Typical SiOC also contains turbostratic graphite [1, 4, 9] which is responsible for its black color. Only under special synthesis conditions, completely graphite-free, colorless SiOC can be prepared [13]. SiOC synthesis via

pyrolysis typically leads to porous products, so that it is difficult to obtain large, well-shaped, monolithic pieces.



Scheme 2: Symbolic representation of SiO<sub>2</sub> (a), of the denser SiC (b) and of SiOC (c) covalent networks

In previous work the authors prepared compact SiOC composites with silicate fibers, using commercial siloxane resins (repeated soaking/pyrolysis) [14–16]. It was demonstrated [17] that high amounts of iron oxide in the fibers (basalt) lead to their good pull-out behavior. Micromechanical properties of SiOC were also recently investigated [18]. In this work the focus was of non-expensive variation and optimization of SiOC synthesis using common alkoxy silanes as starting compounds.

\* corresponding author; e-mail: strachota@imc.cas.cz

## 2. Experimental

### 2.1. Chemicals

Methyltriethoxysilane, dimethyldiethoxysilane, tetraethoxysilane, ethyltriethoxysilane and propyltriethoxysilane, as well as catalyst sulfuric acid ( $\text{H}_2\text{SO}_4$  98%), sodium hydrogen carbonate and toluene were purchased from Sigma-Aldrich and used without further purification.

### 2.2. Synthesis of precursor resins

4 wt%  $\text{H}_2\text{SO}_4$  in water was mixed with the alkoxy-silane monomers so that the ratio  $\text{H}_2\text{O}/\text{OR}$  (OR = alkoxy groups from alkoxy-silanes) was equal 2.25, 1.5 and 3. The mixture was stirred for 5 min without heating (complete homogenization and heat evolution is observed), thereafter it was stirred for 25 min on a heating plate at 130 °C (evaporation of formed ethanol and of excess- and condensation-water). Finally, the raw (liquid) product was diluted by toluene to 50 wt%, and  $\text{H}_2\text{SO}_4$  was neutralised with  $\text{NaHCO}_3$  (10% excess). The toluenic resin solution was separated from the small aqueous phase formed from  $\text{H}_2\text{SO}_4$  and  $\text{NaHCO}_3$  and stored in refrigerator.

### 2.3. Resin cure and pyrolysis

Resin solutions were put into a porcelain weigh dish and first evaporated under air stream at room temperature around 15 min, yielding a viscous paste. This was further dried under vacuum at room temperature for two hours, yielding **dry non-cured resin** (weight determination). For cure, the resins were heated on air at 90 °C/h up to 250 °C, and thereafter this temperature held constant for 4h. The **pyrolysis** of the cured siloxanes to SiOC was carried out under nitrogen atmosphere by heating from 250 to 420 °C at 50 °C/h, followed by slower heating from 420 °C till 1000 °C at 10 °C/h. The cooling of the finished SiOC sample was performed at 50 °C/h.

### 2.4. Weight Loss determination

The weight loss of samples after curing, or after curing and subsequent pyrolysis was measured by weighing larger specimens (2 g) on an analytical balance, before and after the respective heating program, averages of five values were used. For recording thermogravimetric mass-loss vs. temperature curves (TGA) a *Kern EW* device was used, at a heating rate 90 °C/h, with air as purge gas.

### 2.5. Pyrolysis / Gas Chromatography / Mass Spectroscopy analysis

The cure and pyrolysis was followed using a *Trace-DSQII* gas chromatograph (GC) with quadrupole mass spectrometer from ThermoElectron, equipped with the *CDS Pyroprobe 5000* pyrolysis chamber. For every pyrolysis-GC-MS analysis, 2 mg of a powdered sample

were used. The pyrolysis was carried out in helium atmosphere for 30 s, at 160, 200, 250, 300, 400, 500, 650, 750 and 1000 °C. The silica column *TR-5MS* with a moderately polar stationary phase was used for GC: Injection temperature was 250 °C, mobile phase (helium) flow: 1.5 mL/min, injection splitting was 1:10, GC program: initial temperature: 35 °C, rate 5 °C/min, final *T*: 300 °C. Product mass spectra were assigned using a NIST library.

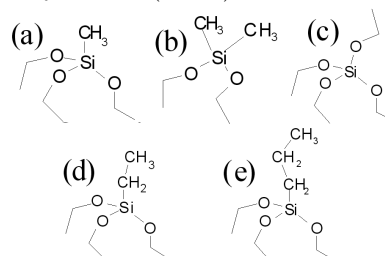
### 2.6. Micromechanical testing

The micromechanical analysis of SiOC samples was performed using a *ZWICK Z2.5* indentation tester, equipped with the micro hardness head *ZHU0.2* (200 N load cell). The depth measurement resolution was 20 nm. Experiments (repeated five times) were performed at 2 N peak load, and in accordance with the Vickers hardness test standard [19]. The unloading branch of loading curves (force vs. indentation depth) yielded the universal hardness HMs and the indentation elastic modulus  $E_{IT}$ . The indents were also measured optically using a laser confocal microscope *LEXT OLS3100* (Olympus, Japan), yielding Vickers hardness HV02.

## 3. Results and discussion

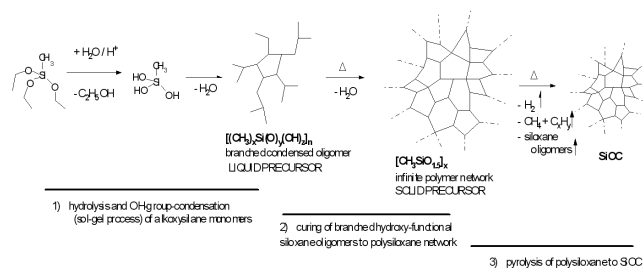
### 3.1. SiOC Synthesis procedure

Several alkoxy-silane monomers (Scheme 3), were tested in a well-controlled sol-gel synthesis of siloxane precursors to silicon oxycarbide (SiOC).



Scheme 3: Monomers: (a) = methyltriethoxysilane, “T”, (b) = dimethyldiethoxysilane, “D”, (c) = tetraethoxysilane, “Q”, (d) = ethyltriethoxysilane, “TET”, (e) = propyltriethoxysilane, “TP”

The SiOC preparation consisted of three steps (Scheme 4): **(1)** First, alkoxy-silane monomers were subjected to an acid-catalyzed sol-gel process with water (hydrolysis followed by gradual Si-OH group condensation to Si-O-Si), under heating and evaporation of the formed alcohol. OH-functional oligomeric siloxane resins were obtained, whose further condensation was stopped by catalyst neutralization and by dilution with toluene to a storable 50% solution (well suited for fiber textures impregnation); **(2)** In the second step, the precursor solution was dried and subsequently cured at 250 °C to yield an infinite network; **(3)** Finally, the cured polysiloxane was pyrolysed at 1000 °C under nitrogen to yield SiOC.



Scheme 4: The employed preparative path to SiOC.

### 3.1.1. The examination of the sol-gel step

The effect of the amount of added water in step (1) of Scheme 4 was studied first: lower than stoichiometric amount leads to an incomplete hydrolysis of the alkoxy silane. Until  $\text{H}_2\text{O} : \text{OR}$  ratio of 0.5, a complete subsequent cure to perfect polysiloxane is still possible (via OH-OR condensation), but the steps (1) and (2) of Scheme 4 proceed slower, which could be eventually an advantage (improved control of gas evolution and solidification).  $\text{H}_2\text{O} : \text{OR}$  ratios of 1.5 (low), 2.25 and 3 (high excess) were tested, taking into account evaporation losses (50%) of water. The  $\text{H}_2\text{O} : \text{OR}$  ratio of 2.25 led to optimal curing behavior and was selected as standard. Optimal reaction time for the sol-gel step (1) is around 70% of the time of gelation. At lower conversions, the resins foam during cure (usually not desired). At higher conversions, the resin storability becomes problematic.

### 3.2. Weight loss of the siloxane resins during cure and pyrolysis

Weight losses during cure and pyrolysis are illustrated in Figs. 1–3: Fig. 1 depicts a typical behavior during cure (at  $90^\circ\text{C}/\text{h}$ ). After the first scan, practically no loss occurs during the second, until  $270^\circ\text{C}$ . Above this temperature, weight loss is observed in any scan, indicating the start of pyrolysis reactions (strong above  $400^\circ\text{C}$ ). The obtained resins were compared with the commercial methylsiloxane “M130” from Lucebni zavody a.s. Kolin, Czech Republic (loss after cure and pyrolysis: 20%).

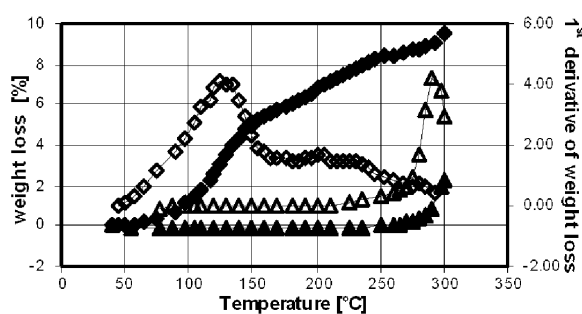


Fig. 1. Exemplary weight loss behavior during siloxane cure and the onset of pyrolysis near  $300^\circ\text{C}$ : full squares: first heating, hollow squares: derivative of the weight loss, full triangles: second heating, hollow triangles: derivative of weight loss for second heating.

As illustrated in Figs. 2 and 3, the weight losses during cure step and during pyrolysis step are similar in the

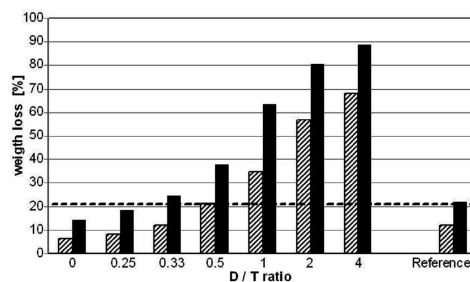


Fig. 2. Effect of bifunctional carbon-rich “D”-monomer content on the weight loss behavior of siloxane resins based on methyltriethoxysilane (trifunctional, “T”) and dimethyldiethoxysilane (bifunctional, “D”).

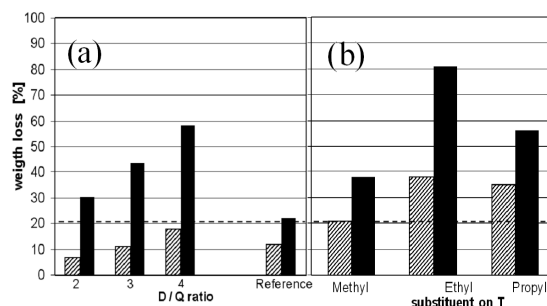
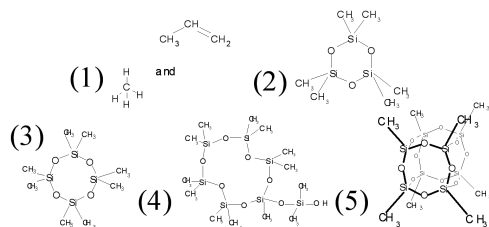


Fig. 3. (a) Effect of bifunctional carbon-rich “D”-monomer content on the weight loss behavior of siloxane resins based on tetraethoxysilane (tetrafunctional, “Q”) and dimethyldiethoxysilane (bifunctional, “D”), (b) Effect of size of the alkyl substituent on triethoxysilane units “T”, onto the weight loss of T2D1 resins.

best resins. In those with high weight losses, most of the loss often occurs already during the cure. Generally, high content of the carbon-rich repeat units “D” (from dimethyldiethoxysilane) leads to high losses.

In the series methyltriethoxysilane/dimethyldiethoxysilane ( $T/D$ ) (Fig. 2), the resins with “D”/“T” (Scheme 3) monomer ratios 0, 0.25 and 0.33 display smaller (or same) weight losses than the reference. The resin with  $D/T = 0$  has a very strong tendency to gelation, so that  $D/T = 0.25$  (“T4D1”) was ideal. The resins with  $D/T = 0.5$  to 4 display high losses, which increase with D content (suspected elimination of cyclic D oligomers - confirmed by  $GC/MS$  below). The  $Q/D$  series (Fig. 3a), in which the “T”-monomer was replaced by the cheaper and carbon-free tetraethoxysilane, “Q” (Scheme 3), showed very promising low weight losses at cure, especially for  $D/Q = 2$  and 3. Q1D2 had a high tendency to gelation, while Q1D3 is unproblematic. Unfortunately, all the  $Q/D$  resins display too high D-losses at pyrolysis.



Scheme 5: Assignment of important components of pyrolysis gases from gas chromatograms via coupling with mass spectroscopy

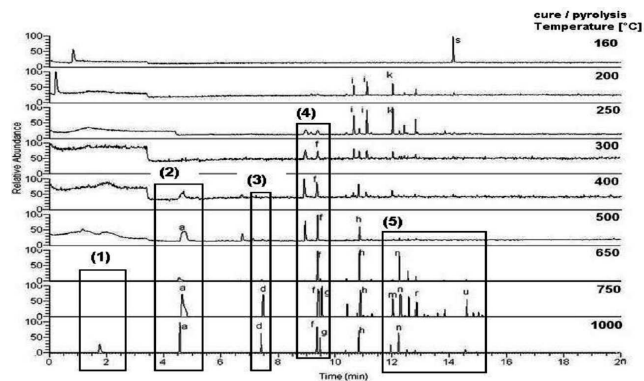


Fig. 4. Gas chromatograms of gases escaping during the cure of siloxane resins and their pyrolysis to SiOC.

**Effect of alkyl groups on “T” (trialkoxysilane) monomer on weight loss** (Fig. 3b): The variation of Si/O/C ratios via “D” (carbon-rich dimethyldiethoxysilane) content in the *T/D* and *Q/D* series was found to be rather small, due to strong elimination of *D*. Hence, the variation of carbon content was tested by introducing larger alkyl substituents on “T”. Larger alkyl groups on *T* lead to higher losses than the methyl groups, but the trend is not simple (Fig. 3 b): Ethyl groups cause a twofold increase in weight loss, if compared with methylated T2D1. *n*-Propyl groups yield a much better result, but the total loss is still higher by 30%. Obviously, the larger alkyl substituents favor the formation of volatile oligomers of *T* (see GC/MS below). With increasing substituent size (*n*-propyl), radical crosslinking and carbonization of these substituents reverse the *T*-release trend. A butyl group could possibly achieve improved weight losses, but reactive larger groups on *T* seem to be more promising.

### 3.3. GC-MS-study of pyrolysis by-products

The evolution of gaseous by-products during cure and pyrolysis of precursor siloxane resins was followed via gas chromatography coupled with mass spectroscopy (GC/MS). Figure 4 shows chromatograms of fumes evolving from a T2D1 sample pyrolysed at  $T = 160^\circ\text{C}$  to  $1000^\circ\text{C}$  (“T” corresponds to methyltriethoxysilane, “D” to dimethyldiethoxysilane monomer, the numbers give monomer ratios). Products marked in Fig. 4 were assigned via MS (Scheme 5). “D”-unit content led to release

of cyclic *D*-trimer (highly preferred) and *D*-tetramer (marked as (2) and (3), boiling points:  $134^\circ\text{C}$  and  $176^\circ\text{C}$ , respectively). *D*-rich resins (T1D1, T1D2, T1D4, Q1D4 (*Q* = tetraethoxysilane)) release cyclo-*D*3 and -*D*4 already during cure, indicating their formation during synthesis. Above  $400^\circ\text{C}$ , cyclo-*D* evolves due to pyrolysis (see literature [20, 21]). Above  $400^\circ\text{C}$ , methane and propene were detected (marked (1)), as side products of alkyl substituents pyrolysis. From moderate pyrolysis temperatures ( $300^\circ\text{C}$ ) onwards, branched cyclic *D* – *T*-oligomers marked as (4) were detected. Above  $650^\circ\text{C}$ , spherical *T*-oligomers (POSS, marked (5)) evolve, especially strongly if ethyl-substituted “T” was used.

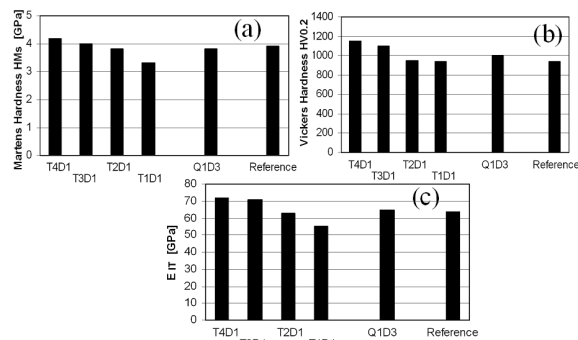


Fig. 5. Micromechanical characteristics of SiOC glasses in dependence of monomer composition: (a) Martens hardness *HMs*, (b) Vickers hardness *HV0.2*, (c) indentation Young modulus  $E_{IT}$ , “T” corresponds to methyltriethoxysilane, “Q” to tetraethoxysilane, and “D” to dimethyldiethoxysilane, numbers to monomer ratios.

### 3.4. Micromechanical testing

The quality of the SiOC glasses prepared was evaluated via micro-indentation. Regarding precursor composition, the mechanical properties showed similar but much weaker trends like weight losses. In Fig. 5, the Martens hardness *HMs* (a), the Vickers hardness *HV0.2* (b) and the indentation Young modulus  $E_{IT}$  are compared for SiOC made from T4D1, T3D1, T2D1, T1D1, Q1D3 and from the reference “M130”. The series T4D1 to T1D1 shows a moderate but clear decrease of hardness and modulus with increasing *D* content. This trend seems to correlate more with density, rather than with composition, because samples with high weight losses were typically micro-porous (“micro-foaming”). Densities, determined by weighing thoroughly powdered samples on air and in water (after being soaked for one day), range from 2.0 to 1.8 g/mL for T4D1 to T1D1 (before pyrolysis: 1.2 g/mL). Interestingly, Q1D3 displays nearly the same micromechanical properties like SiOC from the reference, in spite of Q1D3 relatively high weight loss.

#### 4. Conclusions

Silicon oxycarbide (SiOC) glasses with varying element ratio were prepared from mixtures of alkoxy silane comonomers. Combining simple monomers, linear carbon-rich dimethyldiethoxysilane with branching carbon-poor ones (methyltriethoxysilane or tetraethoxysilane) led to rather narrow variation of final SiOC composition, due to dimethyldiethoxysilane elimination upon pyrolysis. Samples with high weight losses were micro-porous. Larger alkyl groups on triethoxysilane units led to formation of volatile cage-like silsesquioxane oligomers, but also to higher substituent carbonization, hence large and polymerizable substituents on trialkoxysilane units seem to be most promising for future work.

#### Acknowledgments

The authors thank Eva Miškovská for the preparation of the larger resin batches, and the Grant Agency of the Czech Republic, Grant Nr. 106/09/1101 for the financial support.

#### References

- [1] H.J. Kleebe, Y.D. Blum, *J. Europ. Ceramic Society* **28**, 1037 (2008).
- [2] M. Narisawa, R. Sumimoto, K. Kita, *J. Mater. Sci.* **45**, 5642 (2010).
- [3] G.M. Renlund, S. Prochazka, R.H. Doremus, *J. Mater. Res* **6**, 2716 (1991).
- [4] F. Kolar, V. Machovic, J. Svitilova, L. Borecka, *Mater. Chem. Phys.* **86**, 88 (2004).
- [5] J. Brus, F. Kolar, V. Machovic, J. Svitilova, *J. Non-Crystalline Solids* **289**, 62 (2001).
- [6] C.G. Pantano, A.K. Singh, H.X. Zhang, *Journal of Sol-Gel Science and Technology* **14**, 7 (1999).
- [7] H. Miyazaki, *Jpn. J. Appl. Phys.* **47**, 8287 (2008).
- [8] J.V. Ryan, C.G. Pantano, *J. Vacuum Sc. Techn. A* **25**, 153 (2007).
- [9] J.V. Ryan, C.G. Pantano, *J. Phys., Cond. Matter* **19**, 455205 (2007).
- [10] H. Brequel, J. Parmentier, G.D. Sorar, L. Schiffrini, S. Enzo, *Nanostr. Mater.* **11**, 721 (1999).
- [11] E. Ionescu, B. Papendorf, H.J. Kleebe, F. Poli, K. Muller, R. Riedel, *J. Am. Ceramic Soc.* **93**, 1774 (2010).
- [12] E. Ionescu, B. Papendorf, H.J. Kleebe, R. Riedel, *J. Am. Ceramic Soc.* **93**, 1783 (2010).
- [13] T.A. Liang, Y.L. Li, D. Su, H.B. Du, *J. Am. Ceramic Soc.* **30**, 2677 (2010).
- [14] M. Cerny, P. Glogar, Z. Sucharda, Z. Chlup, J. Kotek, *Comp. A, Appl. Sci. Manufac.* **40**, 1650 (2009).
- [15] M. Cerny, P. Glogar, Z. Sucharda, *J. Comp. Mater.* **43**, 1109 (2009).
- [16] P. Glogar, M. Cerny, Z. Tolde, *Acta Geodyn. Geomater.* **4**, 27 (2007).
- [17] M. Cerny, Z. Sucharda, A. Strachota, Z. Chlup, P. Glogar, accepted in *Ceramics-Silikaty*.
- [18] Z. Chlup, M. Cerny, A. Strachota, V. Kozak, submitted to *Plastics, Rubber and Composites*.
- [19] *ISO 14577 Instrumented indentation test for hardness and material parameters* (2001).
- [20] M.G. Voronkov, *J. Organometal. Chem.* **557**, 143 (1998).
- [21] J.C. Kleinert, C.J. Weschler, *Analytical Chemistry* **52**, 1245 (1980).

C6 Kozák, V., Chlup, Z., Bridging law shape for long fibre composites and its finite element construction, *Algoritmy 2012*, Slovakia, 1-10.

## BRIDGING LAW SHAPE FOR LONG FIBRE COMPOSITES AND ITS FINITE ELEMENT CONSTRUCTION\*

VLADISLAV KOZÁK † AND ZDENEK CHLUP‡

**Abstract.** Ceramic matrix composites reinforced by unidirectional long fibres are very perspective materials. Especially glass matrix composites reinforced by unidirectional long ceramic fibres are very complicated materials for modelling thanks their common acting of various micromechanisms like pull out, crack bridging, matrix cracking etc. Crack extension is simulated by means of element extinction algorithms. The principal effort is concentrated on the application of the cohesive zone model with the special traction separation law (bridging). Determination of micro-mechanical parameters is based on the combination of static tests, microscopic observation and numerical calibration procedures. The paper is oriented to the construction of the new type of element for FEM program (Abaqus).

**Key words.** finite element method, cohesive elements, bridging law

**AMS subject classifications.** 74S05, 74E30, 74E20

**1. Introduction.** Crack growth modelling achieved during last decade great success and progress. The finite element and boundary element method, molecular dynamic success and actually "ab initio" computation found their use in the material research long time ago. Some of mentioned methods are modified, e.g. parallel approach implementation, which comes into their own in case of the multiprocessor applications. In some cases only the small improvement of the standard procedures is coming. The finite element method as a well known procedure has in this case the special position. It seemed that the boundary of material and geometry nonlinearities will be reached later. Procedures based on the fracture mechanics approach derived benefit from knowledge of global parameters like the stress intensity factor and  $J$  integral are. These parameters were used with the combination of the remeshing ahead the crack tip a bit later.

The special element implementation responding damage and crack growth introduced so-called "damage mechanics". The cohesive elements are similar; the origin can be found in the contact elements and is based on the vanishing elements and the new surface creation [1]. The phenomenological description characterizing material behaviour is realized using the traction-separation law, thanks this the local damage is predicted. Many models published within last five years can be found in literature for laminates, composites, long fibre composites etc.

Although the cohesive zone modelling is used more than one decade, the physical interpretation of the cohesive zone is still discussed. This zone has practically zero thickness which can be in contradiction of the classical fracture mechanic approach. Characteristics of the physical cohesive zones peak traction, critical separation, work of separation  $(T_0, \delta_0, \Gamma_0)$  can be derived by the strain and stress analysis in narrow bands [2]. Since the cohesive model is a phenomenological model, there is no evidence, which form is to be taken for the cohesive law. Thus cohesive law has to be assumed

---

\*This work was supported by Grant No.: P107/12/2445 of the Grant Agency of the Czech Republic.

†Institute of Physics of Materials AS of CR, Brno Czech Republic (kozak@ipm.cz).

‡Institute of Physics of Materials AS of CR, Brno Czech Republic

independently of specific material as a model of the separation process. Most authors take their own formulation for the dependence of the traction on the separation. The exponential model is used by many authors for both the ductile and the cleavage fracture. The  $T - \delta$  response follows an irreversible path with unloading always direct to origin. This model represents all the features of the separation process by: (1) the shape of the cohesive traction-separation curve  $T - \delta$ , (2) the local material strength by the peak traction  $T_0$ , and the work of separation  $\Gamma_0$  given by the area under  $T - \delta$  curve.

Cohesive model use is realized by two types of elements. The first one is described by the classical continuum; the second one is the linking cohesive element. The separation of the cohesive element is computed from the displacement of the standard element. In general terms the separation is dependent on the normal and shear stress constituent and their operation on the linking element [3], [4]. Composite damage modelling on the base of knowledge of crucial micromechanisms is one of the good approaches how to ensure compliance to the prediction and experiment. When the crack is propagates in the composite in the direction perpendicular to the strengthen fibres, the damage is then determined by these basic micromechanisms: matrix cracking, delamination of an interface fibre and matrix, fibre cracking, fibre pull out [5]. The critical problem is to predict interface behaviour between the fibre and the matrix. This interaction plays crucial role in the determination of the final fracture toughness, fracture strength and the general fracture behaviour.

From the micromechanical point a view, every element has its own microstructure, it comes out from the representative volume element (RVE) approach and the material separation and damage is described and determined by the cohesive element. In this manner we separate material behaviour into two distinctively different areas. Crack propagation through the element is described by the fracture mechanic and by the cohesive model. This model is simpler than the classical models and its parameters are determined experimentally [6], [7], [8]. The cohesive models are widely used in case of the crack growth and fragmentation simulation for metals, polymers and ceramics [8], [9].

Outstanding progress in the crack growth modelling has been achieved by onset of the extended finite element method (X-FEM) in the last years. This method seems to be very perspective, no remeshing is used and crack growth goes through the element. By this way one can avoid various numerical problems which is necessary to solve by using the connection elements of interface type [10], [11]. Last innovation for the crack growth modelling without remeshing is the combination of the extended finite element method and application of the cohesive law as a controlling procedure for the crack growth modelling.

**2. Traction-separation law.** For a general constitutive modelling of materials whose fracture may be described by means of a cohesive crack, we need to define three main ingredients: (1) The stress-strain behaviour of the material in absence of cohesive cracks, as described by classical constitutive modelling. (2) The initiation criterion, which determines the conditions in which a crack will form and the orientation of the newly formed cohesive crack. (3) The evolution law for the cohesive crack, which relates the stresses transferred between its faces to the relative displacement between the crack lips.

The cohesive crack model may serve to predict structural behaviour or to analyze experimental results. However, it can also be used to analyze certain wider aspects of material or structural behaviour. This requires, in general, a certain type of spe-

cialization: the type of softening curves and the range of sizes or geometries must be selected and then a systematic analysis carried out from which general conclusions can be drawn about the aspects that have been studied. In the particular model the cohesive elements are surrounded by the classical elements. When the cohesive elements are damaged the crack is extended over the boundaries of the classical elements. In general, the crack is propagated only in areas where the cohesive elements are inserted and the crack growth direction is predicted before the numerical computation.

In common for all cohesive laws: (a) comprises two material parameters  $\delta_0$ ,  $T_0$ , (b) after the material damage the stress becomes zero,  $T(\delta > \delta_0) = 0$ , for normal and tangential separation (this condition is not exactly fulfilled for all cohesive laws). The area below the traction-separation curve whether for tangential or for normal direction gives us the energy dissipated by the cohesive element  $\Gamma_0$ . A schematic diagram for the long fibre composite can be seen in Fig. 2.1. A leading edge up to maximal stress looks like Dirac function; it is clear that from the numerical point a view this shape of the traction-separation law is the source of instabilities and the numerical solution probably is going to diverge. It is necessary this singularity smooth away for  $\Delta u = 0$ , respectively introduce the strength  $J_0$ .

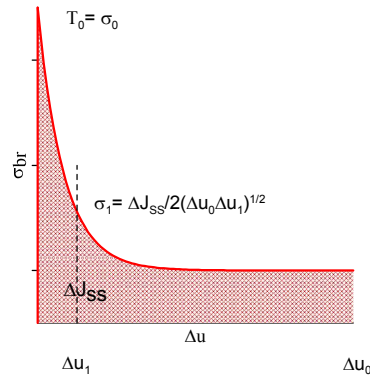


FIG. 2.1. A shape of the bridging law for long fibre composite.

**3. Bridging law and FE modelling.** Let us think over a body having crack perpendicular to the direction of oriented fibres. If we found a relation between the bridging stress  $\sigma_{br}$  and fracture energy, then by means of fracture mechanics one can predict crack growth and propagation. The bridging law in the form of  $\sigma = \sigma(\delta)$  is identical in every point of bridging zone. In case of shock loading the damage of fibres comes straightaway, therefore is inevitable to suppose an existence of characterizing opening  $\delta_0$ , which determines the moment when the bridging effect is vanishing. Contrary of the crack resistance curve ( $R$  curve or  $J - \Delta$  curve) the bridging law is accepted such as the material characteristic. Fracture energy splitting by means of  $J$  integral on the crack surface and the crack vicinity gives:

$$(3.1) \quad J = \int_0^{\delta^*} \sigma(\delta) d\delta + J_{TIP},$$

where  $J_{TIP}$  is the  $J$  integral evaluated around the crack tip (during cracking is equal to the fracture energy of the tip,  $J_0$ ). The total energy is then dissipated in the bringing zone and  $\delta^*$  is the maximum opening of the bridging zone at the notch root.

The bridging law can be determined by differentiating Eq. 3.1:

$$(3.2) \quad \sigma(\delta^*) = \frac{\partial J_R}{\partial \delta},$$

$J_R$  is the value of  $J$  integral during the crack growth. Initially the crack is without the bridging stress and the initiations starts when  $J_R = J_{TIP} = J_0$ . Special shapes of the bridging law can be found in [12]. The shape of the bridging law can be described by Eq. 3.3, it seems to be very suitable for the long fibre composites. When the end opening of the bridging zone reaches  $\delta_0$  the steady state value of fracture energy is reached, see Fig. 3.1,

$$(3.3) \quad J_R(\delta^*) = J_0 + \Delta J_{SS} \left( \frac{\delta^*}{\delta_0} \right)^{1/2}.$$

They are many shapes of the cohesive laws and many ways how to implement this law in the commercial standard FEM package. The authors come out from the long-standing knowledge of Abaqus system, where the user procedure UEL enables very effectively implement the new element into this package and eventually to change the shape of the bridging law. The function in Eq. 3.4 is declared in literature [12] and [13] as a very convenient for the application on the long fibre composites

$$(3.4) \quad \sigma_{br}(\delta) = \frac{\Delta J_{SS}}{2\delta_0} \left( \frac{\delta}{\delta_0} \right)^{-1/2}.$$

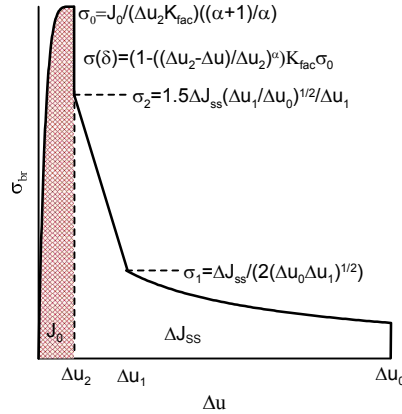


FIG. 3.1. Optimized shape of the bridging law.

The Fig. 3.1 shows the optimized shape of the cohesive law, a leading edge in the chart plays important role for the numerical stability of the interface element. The element is made up of two quadratic line elements for 2D plane elements or two quadratic plane elements for 3D. The node numbering is chosen according to numbering according to Abaqus conventions. Two surfaces of the interface element initially lie together in initial stage; it is in the unstressed deformation state. The relative displacements of the element faces create normal and shear displacements depending on the constitutive equation. Now we suppose the quadratic line element for 2D simulations. This element has 12 degrees of freedom and the nodal displacement vector is given by Eq. 3.5

$$(3.5) \quad \mathbf{d}_N = (d_x^1, d_y^1, d_x^2, d_y^2, \dots, d_x^6, d_y^6).$$

The plane interface element (for 3D) has 48 (3x16) degrees of freedom. The elements ordering follows from the standard conventions, then the opening of the connection element is determined as a difference in displacements between the top (TOP) and bottom (BOT) nodes:

$$(3.6) \quad \Delta \mathbf{u} = \mathbf{u}^{TOP} - \mathbf{u}^{BOT}.$$

Then we can define the interface opening in terms of nodal displacements of paired nodes:

$$(3.7) \quad \Delta \mathbf{u}_N = \Phi \mathbf{d}_N = [-I_{6 \times 6} \mid I_{6 \times 6}] \mathbf{d}_N.$$

where  $I_{6 \times 6}$  is unity matrix with 6 rows and columns,  $\mathbf{u}_N$  is a 6x1 vector. From the nodal positions the crack opening is interpolated to the integration points with the help of standard shape functions. Let  $N_i(\xi)$  be the shape function for node pair  $i$  ( $i = 1, 2, 3$ ), where  $\xi$  stands position in the local coordinate system  $-1 < \xi < 1$ . The relative displacement between the nodes within the elements is then given:

$$(3.8) \quad \Delta \mathbf{u}(\xi) = \begin{pmatrix} \Delta u_x(\xi) \\ \Delta u_y(\xi) \end{pmatrix} = H(\xi) \Delta \mathbf{u}_N,$$

where  $H(\xi)$  is matrix 2x6 containing the quadratic shape function. For 2D element the shape of this matrix is following:

$$(3.9) \quad H(\xi) = \begin{pmatrix} N_1(\xi) & 0 & N_2(\xi) & 0 & N_3(\xi) & 0 \\ 0 & N_1(\xi) & 0 & N_2(\xi) & 0 & N_3(\xi) \end{pmatrix}.$$

As a result, we get

$$(3.10) \quad \Delta \mathbf{u}(\xi) = H(\xi) \Phi \mathbf{d}_N = B(\xi) \mathbf{d}_N,$$

where  $B(\xi)$  has a dimension 2x12 and  $\Delta \mathbf{u}(\xi)$  2x1, thereby describing the continuous displacement field in both direction within the element. For large deformations, the element requires a local coordinate system to compute local deformations in normal and tangential directions. It leads to use the middle points of two element faces. If the coordinates of the initial configuration are given by the vector  $\mathbf{x}_N$  and the deformation state is defined by the vector  $\mathbf{d}_N$ , the reference surface coordinates  $\mathbf{x}_N^R$  are computed by linear interpolation between the top and bottom nodes in their deformed state:

$$(3.11) \quad \mathbf{x}_N^R = \frac{1}{2} (I_{6 \times 6} \mid I_{6 \times 6}) (\mathbf{x}_N + \mathbf{d}_N).$$

The coordinates of the specific point are derived analogically such as in Eq. 3.8:

$$(3.12) \quad \mathbf{x}^R(\xi) = \begin{pmatrix} x^R(\xi) \\ y^R(\xi) \end{pmatrix} = H(\xi) \mathbf{x}_N^R.$$

The differentiation of the vector of global coordinates with respect to local coordinates and dividing its norm we obtain the unit length vector  $\mathbf{t}_1$ . The vector  $\mathbf{t}_n$  perpendicular to the vector  $\mathbf{t}_1$  is derived by the same way:

$$(3.13) \quad \mathbf{t}_1 = \frac{1}{\left\| \frac{\partial \mathbf{x}^R}{\partial \xi} \right\|} \left( \frac{\partial x^R}{\partial \xi}, \frac{\partial y^R}{\partial \xi} \right)^T.$$

The norm of the vector is given by the standard definition:

$$(3.14) \quad \left\| \frac{\partial \mathbf{x}^R}{\partial \xi} \right\| = \sqrt{\left( \frac{\partial x^R}{\partial \xi} \right)^2 + \left( \frac{\partial y^R}{\partial \xi} \right)^2}.$$

The vectors  $\mathbf{t}_1$  and  $\mathbf{t}_n$  represent the direction cosines of the local coordinates system to global one, thus defining transformation tensor  $\Theta$ :

$$(3.15) \quad \Theta = [\mathbf{t}_1, \mathbf{t}_N].$$

This relates the local and global displacements as follows:

$$(3.16) \quad \Delta \mathbf{u}_{loc} = \Theta^T \Delta \mathbf{u}.$$

Subsequently we can mark by symbol  $\mathbf{t}_{loc}$  vector describing the bridging stress relates to the local relative displacement with help of the constitutive relation for interface (cohesive) element:

$$(3.17) \quad \mathbf{t}_{loc} = \begin{pmatrix} \sigma_1 \\ \sigma_N \end{pmatrix} = C_{loc}(\Delta \mathbf{u}_{loc}) \Delta \mathbf{u}_{loc}.$$

The constitutive relation can be expressed by linear displacement for  $\Delta u$  or more complicated, where  $\Delta u$  contains the nonlinear dependence. Just then in this is the trick of good numerical construction and new finite element creation. Preferred procedure depends on the shape of the constitutive equation. In Eq. 3.4 we used the nonlinear equation; it means that we come out from the relation:

$$(3.18) \quad \mathbf{t}_{loc} = \begin{pmatrix} \sigma_1 \\ \sigma_N \end{pmatrix} = C_{loc} \Delta \mathbf{u}_{loc}^{-1/2}.$$

Matrix  $C_{loc}$  is a constant now and does not depend on the displacement. The element stiffness matrix and the vector of the right hand side nodal force must be generated for the users' subroutine UEL.  $\det \mathbf{J}$  is the Jacobian defined by the transformation of the global coordinates to the element coordinates. Jacobian needs to be derived for each integration point; in our case the Eq. 3.4 give us the stability of the computation. The stiffness matrix  $K$  (12x12 for 2D, 48x48 for 3D) is defined:

$$(3.19) \quad K^{el} = - \frac{\partial \mathbf{f}_N^{el}}{\partial \mathbf{d}^{el}},$$

where

$$(3.20) \quad \mathbf{f}_N^{el} = \int_{-1}^1 B^T \Theta \mathbf{t}_{loc} \det \mathbf{J} d\xi.$$

With the derivation one can found:

$$(3.21) \quad K = -W \int_{-1}^1 B^T \Theta D_{loc} \Theta^T B \det \mathbf{J} d\xi.$$

And the stiffness matrix  $D$  is defined:

$$(3.22) \quad D_{loc} = \frac{\partial \mathbf{t}_{loc}}{\partial \Delta \mathbf{u}_{loc}}.$$

Or using Eq. 3.17

$$(3.23) \quad D_{loc} = \frac{\partial C(\Delta \mathbf{u})}{\partial \Delta \mathbf{u}} \Delta \mathbf{u} + C(\Delta \mathbf{u}).$$

**4. Main results.** First material (A) used for the bridging stresses modelling was a commercially available SiC Nicalon fibre reinforced borosilicate glass matrix composite. Properties of the glass matrix, SiC fibres and composite were: Young's modulus 63, 198, 118 GPa, Poisson ratio 0.22, 0.20, 0.21, tensile strength 60, 2750, 600-700 MPa. The fracture toughness determined using the bodies with Chevron notch were  $24.6 \text{ MPam}^{0.5}$ . Experimentally determined values were calibrated and the final values are:  $J_0 = 6200 \text{ J/m}^2$  (experiment),  $\Delta J_{SS} = 18500 \text{ J/m}^2$  (experiment and calibration),  $u_0 = 0.1 \text{ mm}$  (the end of the traction-separation law experiment),  $u_1 = 0.013 \text{ mm}$  (calibration),  $\alpha = 1$  (tested in range  $\langle 1, 5 \rangle$ ). The final shape for the bridging law is in Fig. 4.1.

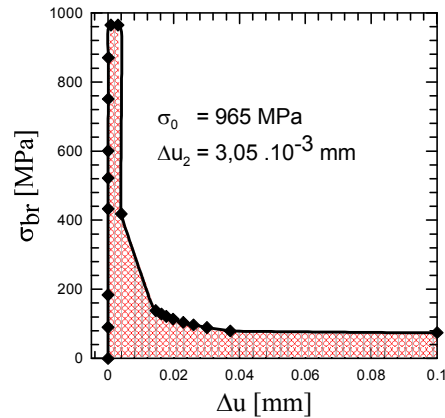


FIG. 4.1. Final shape of the bridging law for material A

Second material (B) used for the bridging stresses modelling was a Nextel 720 fibres reinforced fully pyrolyzed polysiloxane resin. Properties of the resin matrix, Nextel fibres and composite were: Young's modulus 70, 260, 180 GPa, Poisson ratio 0.22, 0.20, 0.21. The fracture toughness determined using the bodies with Chevron notch were  $5 \text{ MPam}^{0.5}$ . Experimentally determined values were calibrated and the final values are:  $J_0 = 5010 \text{ J/m}^2$  (experiment),  $\Delta J_{SS} = 6050 \text{ J/m}^2$  (experiment and calibration),  $u_0 = 0.05 \text{ mm}$  (the end of the traction-separation law experiment),  $u_1 = 0.01 \text{ mm}$  (calibration),  $\alpha = 1$ . The final shape for the bridging law is in Fig. 4.2.

**Conclusions.** The special finite element reflecting the bridging law for the long fibre composites has been created. This interface element was implemented into the standard Abaqus program using the user subroutine UEL. At the same time the experimental techniques needed for obtaining the experimental data were tested. The results can be characterized by following:

- The crack growth modelling for the long fibre composites is dependent on the bridging law shape. The stability of the interface element strongly depends on the first part of the bridging law, on the leading edge.
- The second key role is the mesh size, the application of the RVE seems to be necessary.
- Obtained results of the numerical modelling and running analysis of the microstructure enables combine the extended finite element method with cohesive zone method. The crack branching and crack creations modelling will be closer the material reality.

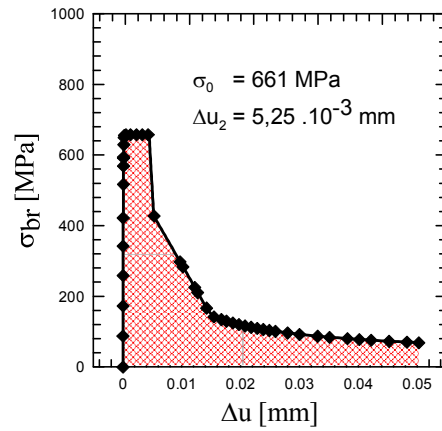


FIG. 4.2. Final shape of the bridging law for material B

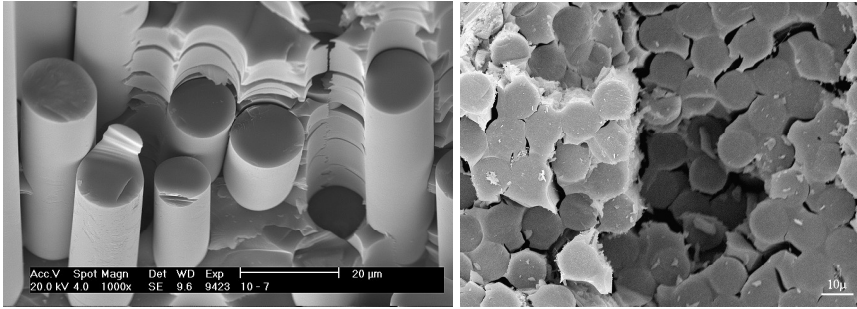


FIG. 4.3. Fracture surface of material A and B

Vanishing elements for the crack growth simulation were tested and numerical stable shape of the traction separation law was suggested for SiC Nicalon fibres reinforced borosilicate glass matrix composite and Nextel 720 fibres reinforced fully pyrolyzed polysiloxane resin.

## REFERENCES

- [1] G. I. BARENBLATT, *Advances in Applied Mechanics*, 7, (1962), pp. 55–129.
- [2] D. S. DUGDALE, *Journal of the Mechanics and Physics of Solids*, 8, (1960), pp. 100–104.
- [3] A. HILLERBORG, M. MODEER, P. E. PETERSON, *Cement and Concrete Research*, 6, (1976), pp. 773–782.
- [4] Z. H. JIN, C. T. SUN, *International Journal of Solids and Structures*, 43, (2006), pp. 1047–1060.
- [5] J. VALA, *Scale Bridging in Diffusive Phase Transformation*, ALGORITMY 2009:18th Conference on Scientific Computing, Slovakia, (2009), pp. 362–371.
- [6] O. RABINOWITCH, *Engineering Fracture Mechanics*, 75, (2008), pp. 2842–2859.
- [7] S. SHET, N. CHANDRA, *Journal of Engng. Materials and Technology*, 124, (2002), pp. 1–11.
- [8] H. LI, N. CHANDRA, *Int. J. of Plasticity*, 19, (2003), pp. 849–882.
- [9] M. WIEWER, R. KABIR, A. CORNEC, K. H. SCHWALBE, *Engineering Fracture Mechanics*, 74, Issue 16, (2007), pp. 2615–2638.
- [10] E. GINER, N. SUKUMAR, et al., *Engineering Fracture Mechanics*, 76, (2009), pp. 347–368.
- [11] N. SUKUMAR, J. H. PRVOST, *Int. Journal of Solids and Structures*, 40, (2003), pp. 7513–7537.
- [12] B. F. SORENSEN, T. K. JACOBSEN, *Composites: Part A*, 29 A, (1998), pp. 1443–1451.
- [13] M. KOTOUK, et al.: *Theoretical and Applied Mechanics*, 49, (2008), pp. 158–170.

C7 Kozák, V., Chlup, Z., Padělek, P., Dlouhý, I., Prediction of traction separation law of ceramics using iterative finite element method, *Solid State Phenomena*, Vol. 258, (2017), 186-189.

## Prediction of the Traction Separation Law of Ceramics Using Iterative Finite Element Modelling

Vladislav Kozák<sup>1\*</sup>, Zdeněk Chlup<sup>1</sup>, Petr Padělek<sup>2</sup> and Ivo Dlouhý<sup>1</sup>

<sup>1</sup>Institute of Physics of Materials AS CR, Žitkova 22, 616 62 Brno, Czech Republic

<sup>2</sup>BUT, Faculty of Mechanical Engineering, Technická 2896/2, 616 69 Brno, Czech Republic

\*kozak@ipm.cz

**Keywords:** cohesive zone model, Si<sub>3</sub>N<sub>4</sub> composite, finite element user's procedure.

**Abstract.** Specific silicon nitride ceramics, the influence of the grain size and orientation on the bridging mechanisms was found. In ceramic matrix composites, crack-bridging mechanisms can provide substantial toughness enhancement coupled with the same and/or increased strength. The prediction of the crack propagation through interface elements based on the fracture mechanics approach and cohesive zone model is investigated. From a number of damage concepts the cohesive models seem to be especially attractive for the practical applications. Within the standard finite element package Abaqus a new finite element has been developed; it is written via the UEL (user's element) procedure. Its shape can be modified according to the experimental data for the set of ceramics and composites. The element seems to be very stable from the numerical point a view. The shape of the traction separation law for four experimental materials is estimated via the iterative procedure based on the FEM modeling and experimentally determined displacement in indentation experiments,  $J$ - $R$  curve is predicted and stability of the bridging law is tested.

### Introduction

Crack growth modelling concepts achieved great success and progress during last decade. The finite element and boundary element method, molecular dynamic success and actually "ab initio" computation found their use in the material research long time ago. Some of the mentioned methods have been modified, e.g. parallel approach implementation, which comes into their own in case of the multiprocessor applications. In some cases only small improvement of the standard procedures is coming. The finite element method as a well developed procedure has in this case a special position. It seemed that the boundary of material and geometry nonlinearities has been reached before. Procedures based on the fracture mechanics approach derived benefit from knowledge of global parameters like stress intensity factor, e.g.  $K_I$ , and  $J$ -integral. These parameters were used with the combination of the remeshing ahead the crack tip a bit later. The special elements corresponding to damage and crack growth were implemented into the Abaqus package.

It is well recognised that the properties of ceramics can be profoundly enhanced by suitably tailoring the microstructure based on intended applications and working conditions. Namely, the effects of the targeted grain structure on the fracture toughness of silicon nitride were demonstrated in [1, 2]. Similarly, the influence of boundary phase manipulation and the effect of grain bridging on the strength and toughness were illustrated in [3]. In order to improve the lifetime of ceramic components and realise cost and energy efficient manufacturing processes, two main issues have to be addressed: (i) materials with increased functionality and optimum properties should be fabricated and tailored for a wide diversity of requirements (materials design and optimisation); (ii) the progress of degradation processes should be predicted and evaluated (damage analysis), focusing in particular on damage mechanisms occurring under realistic operation. This knowledge leads to the design of materials with superior performance in machine components.

Understanding the nature of crack growth in ceramic materials and its relation with the crack resistance curve ( $R$ -curve) behaviour helps to improve the fracture resistance in ceramics [4]. A rising  $R$ -curve behaviour occurs when the microstructure impedes the crack extension. Several microstructural toughening/shielding effects might result in the favourable  $R$ -curve behaviour in

ceramic materials. Such micromechanisms include: microcrack toughening, transformation toughening, brittle particles toughening (including selfreinforcement used in  $\text{Si}_3\text{N}_4$  ceramics), long fibre reinforcement, and chopped fibers or whisker toughening, respectively. Crack-bridging mechanisms can provide substantial toughness enhancement coupled with strength increase. The initial steep rise in crack resistance is attributed to the formation of elastic bridges supposing the reinforcing phase is experiencing no debonding. However, more recently it has been pointed out that those mechanisms do not adequately account for the steep-rising crack resistance curves ( $R$ -curves) observed for some materials [5]. Also, new methods have been proposed for determining the bridging stresses [6] and a mechanism-based constitutive model have been presented for the inelastic deformation and fracture of ceramics [7, 8]. Discrete damage model capable of capturing fragmentation at two size scales is derived by combining a continuum damage model and a discrete damage model for brittle failure [9, 10]. Many authors proposed that the bridging process can be partitioned into five distinct regimes of resistance: propagation, kinking, arrest, stalling, and bridging, e.g. [11].

### Bridging law modelling

Now consider a specimen having a crack with bridging fibres across the crack faces near the tip. The bridging law  $\sigma = \sigma(\Delta u)$  is then taken to be identical at each point along the bridging zone. Since fibres will fail when loaded sufficiently, we assume the existence of a characteristic crack opening  $\Delta u_0$ , beyond which the closure traction vanishes. Shrinking the path of the  $J$  integral to the crack faces and around the crack tip gives

$$J = \int_0^{\Delta u^*} \sigma(\Delta u) d\Delta u + J_{TIP}, \quad (1)$$

where  $J_{TIP}$  is the  $J$  integral evaluated around the crack tip (during cracking is equal to the fracture energy of the tip,  $J_0$ ). The integral is the energy dissipation in the bridging zone and  $\Delta u^*$  is the end-opening of the bridging zone at the notch root. The bridging law can be determined by differentiating Eq. (1)

$$\sigma(\Delta u^*) = \frac{\partial J_R}{\partial \Delta u}. \quad (2)$$

$J_R$  is the value of  $J$  during crack growth. Initially, the crack is unbridged. Thus, by Eq. (1), crack growth initiates when  $J_R = J_{TIP} = J_0$ . As the crack grows,  $J_R$  increases in accordance with Eq. (1). When the end opening of the bridging zone  $\Delta u^*$  reaches  $\Delta u_0$ , the overall  $R$ -curve attains its steady state value  $\Delta J_{SS}$ .

### Bridging law implementation

The preferred option depends on the form of the constitutive equation (Eq. 3) and its numerical implementation:

$$J_R(\Delta u^*) = J_0 + \Delta J_{SS} \left( \frac{\Delta u^*}{\Delta u_0} \right)^{1/2}. \quad (3)$$

$$\sigma_{br}(\Delta u) = \frac{\Delta J_{SS}}{2\Delta u_0} \left( \frac{\Delta u}{\Delta u_0} \right)^{-1/2}. \quad (4)$$

Incorporation of the initial fracture strength  $J_0$  improved traction separation law as can be seen in Fig. 1. Parameter  $\alpha$  is lying in the range  $\langle 1, 100 \rangle$ .

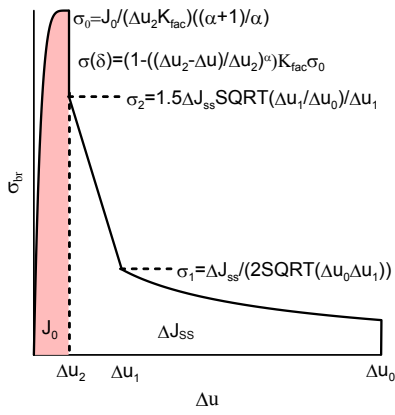


Figure 1: Shape of bridging law

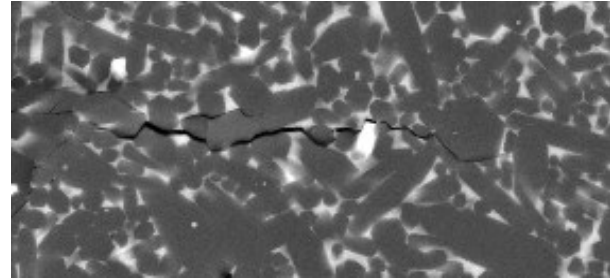


Figure 2: The short crack prepared by the HV1 indentation

**Experiments and determination of material parameters**

The fracture behaviour of short cracks was then observed by applying the indentation technique. This methodology allowed to monitor crack behaviour when cracks are initiating and as well in the stage of crack propagation. The detail of very short crack (having length of several grains) is shown in Fig. 2. Strategy, how to find the best concordance between CTOD versus ( $\Delta a$ ) (experiment versus FEM results) has been selected as follows: a) Increase  $\sigma_0$ , decrease  $\Delta u_0$ , minimize the bridging, and shape – close to jump; b) Decrease  $\sigma_0$ , increase  $\Delta u_0$ , maximize the bridging, shape – close to exponential behaviour with power law softening.

**Stable crack propagation modelling**

The data from Tab. 1 were used for the crack growth modelling (calibrated data). The shape of the moving crack via the FEM can be seen on the following Fig. 3.

Table 1: Data for the bridging law

material	A	B	C	D
$\Delta J_{ss}$ [J/m <sup>2</sup> ]	64	77	67	108
$\Delta u_0$ [ $\mu$ m]	0.30	0.30	0.35	0.35
$\Delta u_1$ [ $\mu$ m]	0.08	0.055	0.045	0.045
$J_0$ [J/m <sup>2</sup> ]	21	24	24	25
$\sigma_0$ [MPa]	1063	1590	1350	1590

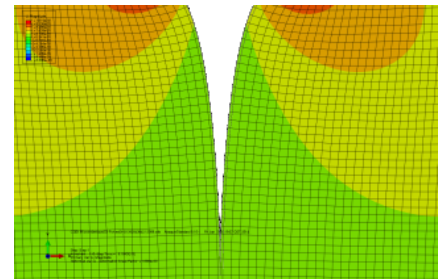


Figure 3: FEM modeling, crack growth

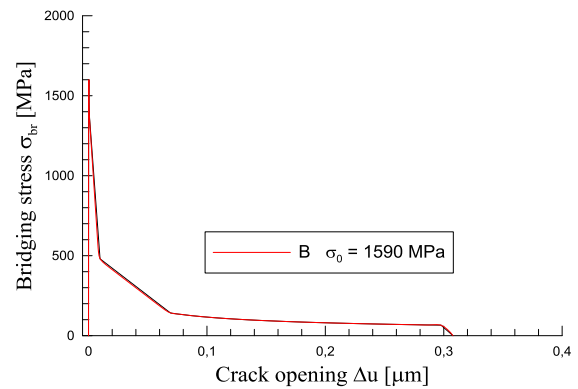
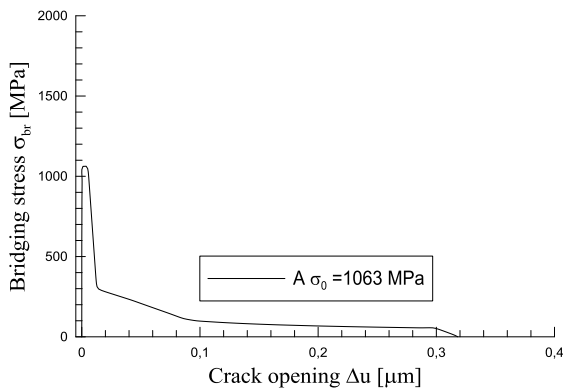


Figure 4: Bridging law after iteration procedure for material A and B

## Summary

Special shape of the bridging law has been tested and implemented into the commercial finite element package Abaqus and  $J - R$  curve was predicted. The following conclusions have been made:

- Crack-bridging mechanisms can provide substantial toughness enhancement coupled with the same strength level in ceramics.
- Saturation in  $J - R$  curve has been reached for XFEM modeling substantially later, usually for the crack length greater than 20  $\mu\text{m}$ ; XFEM model used was without incorporation of the bridging mechanism.
- Saturation in  $J - R$  curve has been reached for cohesive modelling usually for the crack length in interval 10 - 15  $\mu\text{m}$ . It is possible that early real bridging start is probable; due to numerical oscillation the obtained values of  $K$  can be smaller.
- Obtained parameters for traction separation (bridging) law enabled  $J - R$  prediction, for precise prediction seems be essential to determine at least maximum stress  $\sigma_0$  experimentally.

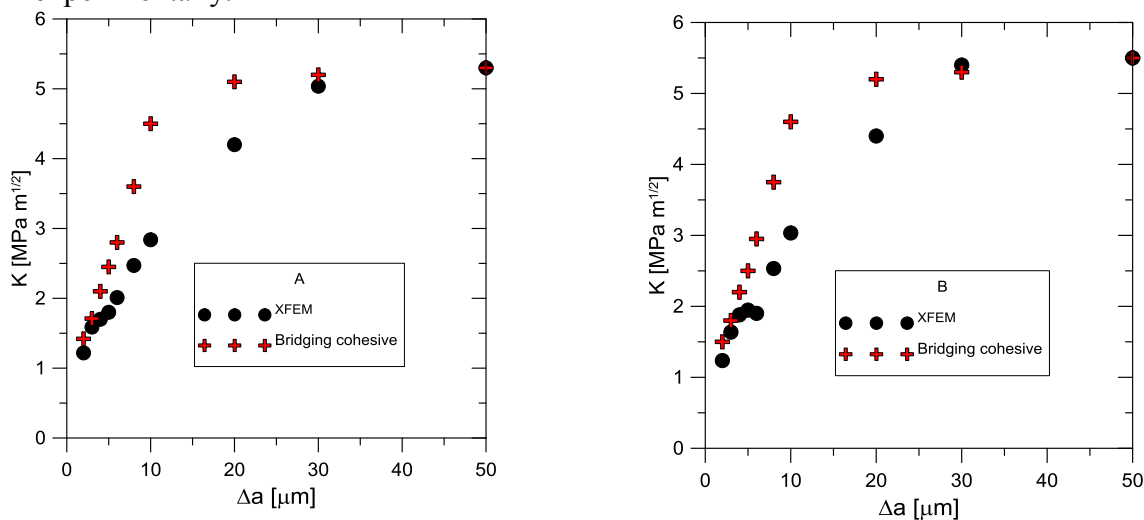


Figure 5: J-R curve prediction for XFEM and cohesive modelling

## Acknowledgements

The research was financially supported by project of Czech Science Foundation (GA CR) 14-11234S.

## References

- [1] M. Lengauer, R. Danzer: J. of the European Ceramic Society 28 (2008), p. 2289–2298
- [2] F.F. Lange: J. of the European Ceramic Society 62 (1979), p. 428–430
- [3] M.J. Hoffmann, G. Petzow: Pure and Applied Chemistry 66 (1994), p. 1807–1814
- [4] Z. Chlup et al: Key Eng. Materials 465 (2011), p. 455–458
- [5] S.F. Fünfschilling, et al: Acta Materialia 59 (2011), p. 3978–3989
- [6] R.B. Greene, S. Gallops, S.F. Fünfschilling, T. Fett, T.J. Hoffmann, J.W. Ager, J.J. Kruzic: J. of the Mechanics and Physics of Solids 60 (2012), p. 1462–1477
- [7] I. Dlouhy et al: J. of Materials Science, 43 (2008), 12, p. 4022–4030
- [8] M. Kotoul et al: Acta Materialia, 56 (2008), 12, p. 2908–2918
- [9] H.D. Espinosa, P.D. Zavattieri, S.K. Dwivedi: J. of the Mechanics and Physics of Solids 56 (2008), p. 3077–3100
- [10] D. Motammedi, S. Mohammadi: Int. J. of Mechanical Sciences 54 (2012), p. 20–37
- [11] J.W. Foulk, R.M. Cannon, G.C. Johnson, P.A. Klein, R.O. Ritchie: J. of the Mechanics and Physics of Solids 55 (2007), p. 719–743

D1 Vala, J., Hobst, L., Kozák, V., Non- destructive detection of metal fibres in cementitious composites, *Advances in Engineering Mechanics and Materials*, Athens: EUROPMENT, (2014), 125-128.

# Non-destructive detection of metal fibres in cementitious composites

Jiří Vala, Leonard Hobst and Vladislav Kozák

**Abstract**—Development of non-destructive methods for the control of metal fibers in cementitious composites concrete is needed to certify the volume fraction of fibers and their directions, crucial for the mechanical properties of a composite. Based on the research experience of authors, namely on the Brno University of Technology, the paper demonstrates advantages and restriction of several useful classes of methods, namely of i) the planar X-ray imaging, with the discrete fast Fourier transform applied to image processing, ii) the magnetic approach, utilizing the Hall probe and advanced considerations on material homogenization (with certain electromagnetic alternative), iii) the computed tomography, as an unique exact method for the detection of volume fraction without breaking the sample, with an information on (an)isotropy as a benefit.

**Index Terms**—Cementitious composites, non-destructive testing, electromagnetic measurements, image processing, computational simulation.

## I. INTRODUCTION

ADVANCED building structures make frequently use of materials as silicate composites, reinforced by metal particles (e. g. steel-fibre-reinforced concrete), preventing the tension stresses and strains as sources of undesirable micro- and macro-cracking. Mechanical properties of such composites are determined by the choice of fibre properties and their volume fraction, location and orientation in the matrix, sensitive to the technological procedures (as special compaction) and to the early-age treatment – cf. [11], as well as by the bond/slip interface relations – cf. [2]. The employment of the destructive approach relies usually on the separation of particles, taken from the early-age matrix, alternatively obtained from the crushed part of the existing structure, in the laboratory; consequently the volume fraction of particles can be evaluated accurately, whereas any information related to the original orientation of particles is missing. Moreover, such experiments with many structures are not allowed by technical standards. This is a strong motivation for the employment of some reliable non- or (at least) semi-destructive measurement methods, applicable in situ, handling homogeneity and isotropy and detecting the volume fraction of fibres in the material structure.

Regardless of the significant progress in this research area in the last decade (for more historical remarks and references see [7]), no inexpensive, robust and reliable method is available, thus all identification approaches rely on a) some indirect measurements and b) non-trivial numerical analysis, to handle a corresponding inverse problem – typically ill-posed, unstable, etc., forcing artificial regularization. Since a) produce quite

other information than needed volume fractions and directional distributions of fibres, typically digital images in pixels or voxels, or electromagnetic quantities detected on the specimen surface, some calibration relations are needed, motivated by the physical and geometrical similarity. Moreover, some reasonable algorithm for the evaluation of effective material properties, using the properties of matrix and particles and the geometrical configuration, as input data, is needed: from simple arguments from the mixture theory to complicated physical and mathematical homogenization techniques (which will be specified later, in connection with electromagnetic measurements).

In this paper we shall pay attention thanks to the research experience of the authors from BUT (Brno University of Technology), namely to three representative approaches:

- i) the planar X-ray imaging, with the discrete fast Fourier transform applied to image processing,
- ii) the magnetic approach, utilizing the Hall probe and advanced considerations on material homogenization (with certain electromagnetic alternative),
- iii) the computed tomography, as an only exact method for the detection of volume fraction without breaking the sample, with an information on (an)isotropy as a benefit.

## II. ANALYSIS OF X-RAY IMAGES

The radiographic approach, developed in [6] for a rather large class of building materials, comes from the gray-scale planar images and some of their post-processing modifications, in particular:

- 1) the reduction of all fibres (whose length and thickness is known) to one-pixel thick black curves, followed by the simplified evaluation of their amount and orientation, by [6],
- 2) the application of the two-dimensional fast Fourier transform by [9], avoiding most artificial image changes, where the same as in 1) can be identified with a special diffraction process: for a the gray level at pixel coordinates  $f(x, y)$ , related to a square image containing  $N \times N$  pixels (with  $N$  tending to  $\infty$  theoretically), the direct and inverse Fourier transforms are

$$F(u, v) = \sum_{x=0}^{N-1} \sum_{y=0}^{N-1} f(x, y) \exp(-2\pi i(ux + vy)/N),$$

$$N^2 f(x, y) = \sum_{u=0}^{N-1} \sum_{v=0}^{N-1} F(u, v) \exp(2\pi i(ux + vy)/N)$$

and the power spectrum  $P(u, v) = |F(u, v)|^2$  contain the useful information, needed for the derivation of the histograms of fibre directions.

J. Vala and L. Hobst are with the Brno University of Technology, Faculty of Civil Engineering, Czech Republic, 602 00 Brno, Veveří 95.

V. Kozák is with the Institute of Physics of Materials, Academy of Sciences of the Czech Republic, 616 62 Brno, Žitkova 22.

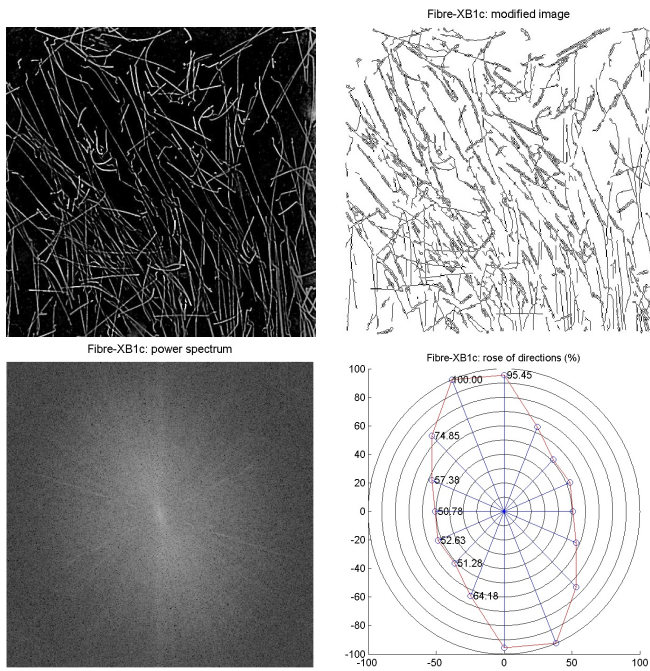


Fig. 1. Evaluation of fibre orientation from the X-ray image: original image (left upper photo), result of fibre localization (right upper image), power spectrum  $P$  (left lower graph), resulting rose of fibre directions (right lower graph).



Fig. 2. X-ray machine EcoRay HF 1040 with digital recording to PC equipment (left photo). PeMaSo-01 depth probe for magnetic measurements (right photo).

Figure 1 presents an example of such MATLAB-supported evaluation of fibre orientation in the fibre concrete specimen; the utilized X-ray equipment is shown on Figure 2. In general, the radiographic analysis gets useful results related to preferential orientations of fibres, although limited to data from planar images, even from several views to cubic specimens. The estimate of volume fraction of fibres is not very precise, at least in the comparison with destructive tests.

### III. NUMERICAL TREATMENT OF MAGNETIC MEASUREMENTS

Magnetic measurements like [20] and [4] rely on the different values of relative permeability of fibres and a matrix, with possible alternative of electrical measurements and relative permittivity. The special experimental configuration usually tries to force a (nearly) stationary process, whose mathematical description works with a differential operator close to the classical Laplace one, to enable non-expensive software simulation. Figure 3 shows the geometrical configuration of such process numerical simulation of such process in COMSOL: the magnetic field is generated by several permanent magnets,

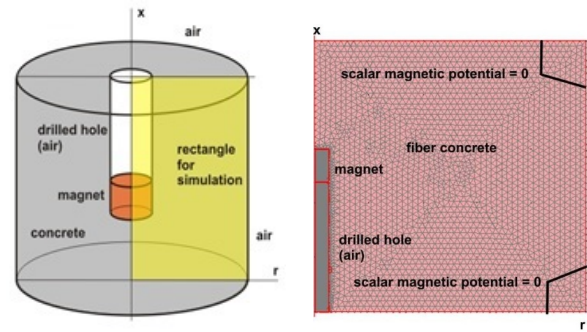


Fig. 3. Radially symmetric geometrical arrangement of the magnetic experiment (left scheme) and computational simplification, including finite/infinite element mesh (right scheme).

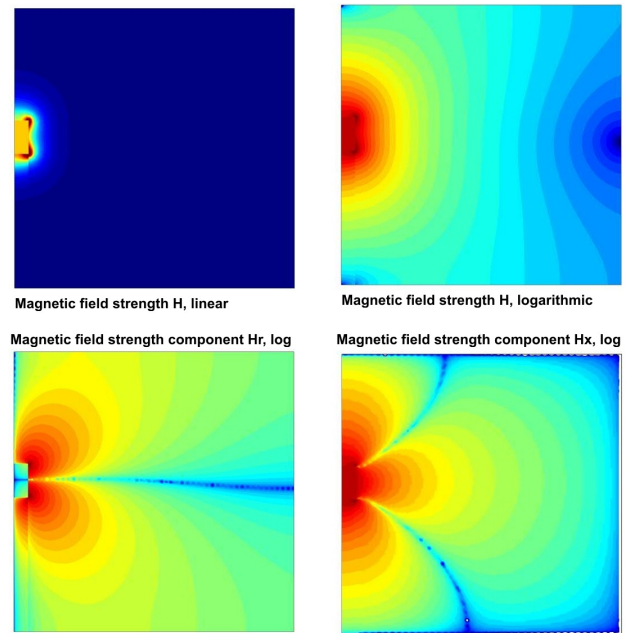


Fig. 4. Results of COMSOL based finite/infinite element simulation of stationary magnetic field strength.

located in the drilled hole (thus this method could be classified as low-invasive, not non-destructive completely), consequently the Hall effect based probe from Figure 2 detects the magnetic field strength. Figure 4 documents the numerical simulation of such experiment, applying the COMSOL supported planar finite/infinite element technique: the influence of the irregularities caused by an artificial hall seems to be not substantial. The comparative simulation, applying only selected functions of *pde* toolbox from MATLAB, leads to the same conclusion.

The crucial problem is now to implement a correct evaluation procedure for an effective relative permeability (or permittivity) using the incomplete data on the material microstructure and on relative permeability of fibres. For spherical particles the classical Maxwell-Garnett mixing formula is available; the generalization of [5] comes from the so-called Bruggeman approach and the repeated usage of similar ellipsoids as reference volume elements, whereas [13] admits the presence of multiple scattering, important for high volume fractions of fibres. No additional physical assumption are needed, again for periodic spheres, in [12]: the auxiliary problem, referring to the mathematical theory of homogenization of elliptic operators,

can be then analyzed (including the existence and uniqueness of solution, the convergence of sequences of approximate solutions, etc.) using the two-scale and similar convergence theorems by [1]; the crucial (seemingly) explicit formula for the evaluation of an effective parameter value, comes from the method of oscillating test functions. In [21] the difficulties with complex particle shapes are handled using the boundary integral approach, thanks to the knowledge of general solutions of the Laplace equation, with Heaviside characteristic functions of particles; [10] admits a priori anisotropic structures. Unfortunately, further generalization of this approach (namely to non-periodic structure, avoiding all mixing tricks), lead to non-trivial (partially still open) problems of mathematical analysis, namely to the convergence using probability measures by [18], thus various alternative statistical approaches, as that with Sobol sensitivity indices and Monte Carlo simulations by [8], have been developed.

The unique material characteristics included here is the magnetic permeability  $\mu$  [Vs/(Am)]; at least in the case of silicate composites used in civil engineering  $\mu$  can be set to 1 for the pure matrix, but no relevant constant is guaranteed by the producers of ferromagnetic fibres. In practice, the dimensionless relative permeability  $\mu_r = \mu/\mu_0$ , using the well-known magnetic constant  $\mu_0 = 4\pi \cdot 10^{-7}$  Vs/(Am), is usually considered; similarly the relative permeabilities  $\mu_c$  for the matrix and  $\mu_s$  for all fibres can be introduced. Fortunately, for a sufficiently slow volume fraction  $\xi$  of fibres ( $\xi \leq 0.05$  in real experiments), following [5], under the assumption of random orientation of fibres, we obtain an explicit monotone and continuous dependence between  $\mu$  and  $\xi$  in the form

$$\xi = 1 - M \frac{\mu_s - \mu_r}{\mu_s - \mu_c} \left( \frac{\mu_c}{\mu_s} \right)^{3L(1-2L)(2-3L)}$$

where the factors

$$M = \left( \frac{M_1}{M_2} \right)^{2(3L-1)^2 / ((2-3L)(1+3L))},$$

$$L = \frac{\varsigma}{4\vartheta^3} \left( 2\varsigma\vartheta + \ln \frac{\varsigma - \vartheta}{\varsigma + \vartheta} \right)$$

are determined using the ratio  $\varsigma$  of lengths of a major and (both) minor axes of ellipsoidal particles (clearly  $\varsigma > 1$ ) for the simplifying notation  $\vartheta = \sqrt{\varsigma^2 - 1}$  and  $M_1 = (1+3L)\mu_c + (2-3L)\mu_s$ ,  $M_2 = (1+3L)\mu_r + (2-3L)\mu_s$ . In particular, for a (theoretically) infinite length and zero diameter of particles we receive  $L = 1/3$ . Unfortunately, all attempts to generalize this result for more complicated distributions of fibre directions lead to unpleasant non-analytical integrals, with the duty of their non-trivial numerical evaluations.

Figure 6 documents the least squares based identification of  $\mu_r$  for 3 input data sets with assumed  $\mu_r = 1$  for pure concrete and uncertain  $\mu_s$  in all other cases, using the above sketched formulae for an isotropic medium. the specimens (unlike the situation in situ) were prepared with exact volume fractions of fibres 0.5%, 1% and 1.5%. Other experiments with comparable results have been performed by the authors' team with magnetic field induced by an electric coil. Moreover, [3] presents a totally non-destructive equipment, applicable

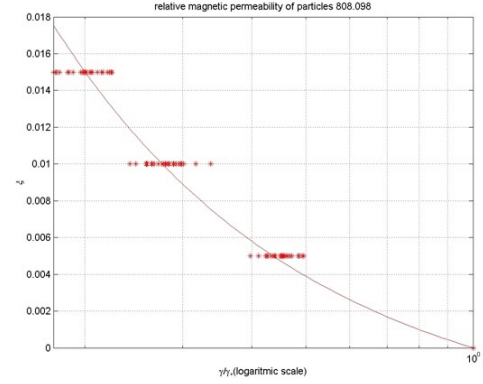


Fig. 5. Application of the least squares technique to the identification of parameters  $\xi$  and  $\mu_s$  from magnetic measurements.

to the surface of a specimen (thus preferring fibres close to such surface). All these result seem to give good estimates of volume fractions (whose improvement using more advanced mathematical analysis is possible), but the differentiating between system and random errors in distributions of fibre directions is difficult.

#### IV. COMPUTED TOMOGRAPHY

A new approach to non-destructive analysis of structures of cementitious composites, motivated by [14] and [19], has been offered by the computed tomography (X-ray CT), generating 3-dimensional images from large series (slices) of 2-dimensional radiographic images taken around a single axis of rotation. The modern industrial tomograph, presented on Figure 6, has been recently installed in the Central European Institute CEITEC of BUT. Unlike most tomographs for medical applications, an analyzed specimen is fixed on the manipulation table of the tomograph, between the radiation source and the surface radiation detector, compound from a matrix of mini-detectors. During the rotation of the table the surface detector records successive changes of X-ray radiation; consequently the specialized computer software is needed to analyze the inner structure of a specimen.

Several types of fibre concrete specimens have been tested using this equipment: whereas some cylindrical specimen is visible on Figure 6, Figure 7 shows the cubic specimen, similar to that from Figure 1, and demonstrates the ability of the specialized software to recognize all fibres completely unlike all approximate estimates from separate planar images. Consequently various forms of histograms or graphical or 3-dimensional roses of directions similar to 2-dimensional ones from Figure 1 can be created. However, this is rather time consuming, expensive and not applicable to the fibre concrete structures in situ. Nevertheless, this seems to be a useful method to obtain a reliable reference basis for all numerical simulation attempts with random positions and orientation of fibres.

#### V. CONCLUSION

This paper should be understood as an introductory comparative study to the most promisable non-destructive approaches



Fig. 6. Tomograph GE phoenix.v|tome|xL 240 (left photo) and a cylindrical specimen fixed in its manipulator (right photo).

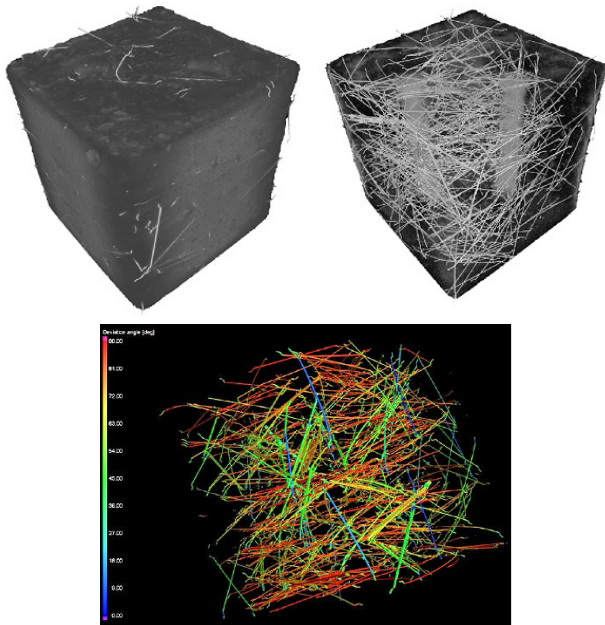


Fig. 7. Cubic fibre concrete specimen, edge length 150 mm, required X-ray tube voltage 300 kV: axonometric view on its surface (left upper image) and inside its structure (right upper image). Axonometric projection of separated fibres in the cube specimen (lower image).

to macroscopic identification of content and random location of fibres in the structure of cementitious composites. However, all introduced approaches have strong restrictions: serious obstacles to get some reasonable estimate of volume fraction of fibres, as the most requested parameter, in the case i), expensive and fastidious experimental setting in the case iii), interpretable as the more sophisticated upgrade of i), both technical and computational difficulties in the case ii).

For the successful computational detection of volume fraction and preferential orientation of fibers, making use of their ferromagnetic properties, both under laboratory and in situ conditions, the crucial point of all considerations is the development of a homogenization procedure, specific to the analyzed class of materials, including its formal verification and its validity range. This leads to non-trivial problems of both physical and mathematical analysis, whose validation seems to be available thanks to the progress in the image processing techniques, consequently their deeper study should belong to the research priorities for the near future.

#### ACKNOWLEDGMENT

The financial support of the FAST-S-14-2490 research project at BUT is acknowledged.

#### REFERENCES

- [1] D. Cioranescu and P. Donato, *An Introduction to Homogenization*. Oxford University Press, 1999.
- [2] V. M. C. F. Cunha, J. A. O. Barros and J. M. Sena-Cruz, An integrated approach for modelling the tensile behaviour of steel fibre reinforced self-compacting concrete. *Cement and Concrete Research* 41, 2011, pp. 64–76.
- [3] M. Faifer, L. Ferrara, R. Ottoboni and S. Toscani, Low frequency electrical and magnetic methods for non-destructive analysis of fiber dispersion in fiber reinforced cementitious composites: an overview. *Sensors* 13, 2013, pp. 1300–1318.
- [4] M. Faifer, R. Ottoboni, S. Toscani and L. Ferrara, Nondestructive testing of steel-fiber-reinforced concrete using a magnetic approach. *IEEE Transactions on Instrumentation and Measurement* 60, 2011, pp. 1709–1711.
- [5] S. Giordano, Effective medium theory for dielectric ellipsoids. *Journal of Electrostatics* 58, 2003, pp. 59–76.
- [6] L. Hobst, O. Anton, J. Vodička and J. Ščučka, Homogeneity detection of fibre-concrete structures by using radiographic technique. In: *Nondestructive Testing of Materials and Structures*, Springer 2013, pp. 323–328.
- [7] L. Hobst and P. Bilek, Various control methods developed for fibre concrete structures. *Recent advances in integrity, reliability and failure – 4-th International Conference in Funchal (Madeira)*, 2013, pp. 721–730.
- [8] Z. Kala, Geometrically non-linear finite element reliability analysis of steel plane frames with initial imperfections. *Journal of Civil Engineering and Management* 18, 2012, pp. 81–90.
- [9] S. Kärkkäinen and E. B. Vedel Jensen, Estimation of fibre orientation from digital images. *Image Analysis and Stereology* 20, 2001, pp. 199–202.
- [10] M. Y. Koledintseva, R.E. DuBroff and R.W. Schwartz, Maxwell-Garnett rule for dielectric mixtures with statistically distributed orientations of inclusions. *Progress In Electromagnetics Research* 99, 2009, pp. 131–148.
- [11] A. Krasnikovs, V. Zaharevskis, O. Kononova, V. Lusi, A. Galushchak and E. Zaleskis, Fiber concrete properties control by fibers motion – investigation in fresh concrete during casting. *Industrial Engineering – 8th International DAAAM Baltic Conference* in Tallin, 2012, Part V: Materials Engineering, #10, 6 pp.
- [12] G. Kristensson, Homogenization of spherical inclusions. *Progress in Electromagnetic Research* 42, 2003, pp. 1–25.
- [13] P. Mallet, C. A. Guérin and A. Sentenac, Maxwell-Garnett mixing rule in the presence of multiple scattering: derivation and accuracy. *Physical Review B* 72, 2005, 14205/1–9.
- [14] P. J. M. Monteiro, C. Y. Pichot and K. Belkebir, Computer tomography of reinforced concrete. In: *Materials Science of Concrete*, Chapter 12, American Ceramics Society, 1998.
- [15] G. Nguetseng and N. Svanstedt,  $\sigma$ -convergence. *Banach Journal of Mathematical Analysis* 5, 2011, pp. 101–135.
- [16] M. Pieper and P. Klein, Application of simple, periodic homogenization techniques to non-linear heat conduction problems in non-periodic, porous media. *Heat and Mass Transfer* 48, 2012, pp. 291–300.
- [17] M. Ya. Sushko, Effective permittivity of mixtures of anisotropic particles. *Journal of Physics D: Applied Physics* 42, 2009, 155410: 9 pp.
- [18] N. Svanstedt, Multiscale stochastic homogenization of convection-diffusion equations. *Applications of Mathematics* 53, 2008, pp. 143–155.
- [19] G. Weidemann, R. Stadie, J. Goebels and B. Hillemeier, Computer tomography study of fibre reinforced autoclaved aerated concrete. *Materials Testing* 50, 2008, pp. 278–285.
- [20] H.-J. Wichmann, H. Budelmann and A. Holst, Determination of steel fiber dosage and steel fiber orientation in concrete. In: *Nondestructive Testing of Materials and Structures*, Springer 2013, pp. 239–245.
- [21] K. W. Whites and F. Wu, Effects of particle shape on the effective permittivity of composite materials with measurements for lattices of cubes *IEEE Transactions on Microwave Theory and Techniques* 50, 2002, pp. 1723–1729.

**Prof. Leonard Hobst** (\*1949) is the head of the Institute of Building Testing at the Brno University of Technology, Faculty of Civil Engineering.

**Prof. Jiří Vala** (\*1956) works at the Institute of Mathematics and Descriptive Geometry at the same faculty as Prof. L. Hobst.

**Dr. Vladislav Kozák** (\*1954) is the scientist at the Institute of Physics of Materials in Brno, a part of the Academy of Sciences of the Czech Republic.

D2 Vala, J., Hobst, L., Kozák, V., Detection of metal fibre composites based on signal and image processing approaches, *WSAS Transaction on Applied and Theoretical Mechanics* 10, (2015), 39-46.

# Detection of metal fibres in cementitious composites based on signal and image processing approaches

Jiří Vala  
Brno University of Technology  
Faculty of Civil Engineering  
Veveří 95, 602 00 Brno  
Czech Republic  
vala.j@fce.vutbr.cz

Leonard Hobst  
Brno University of Technology  
Faculty of Civil Engineering  
Veveří 95, 602 00 Brno  
Czech Republic  
hobst.l@fce.vutbr.cz

Vladislav Kozák  
Academy of Sciences of the CR  
Institute of Physics of Materials  
Žižkova 22, 616 62 Brno  
Czech Republic  
kozak@ipm.cz

*Abstract:* Mechanical properties of cementitious composites, reinforced by metal fibres, are conditioned by the volume fraction and distribution of directions of fibres. However, their reliable non-destructive or low-invasive experimental evaluation is a serious problem. The paper pays attention to three classes of such indirect methods. The first class relies on the planar X-ray imaging, with the discrete fast Fourier transform applied to image processing. The second one applies the magnetic approach, with certain electromagnetic alternative. The last one comes from the computed tomography, as a unique exact method for the detection of volume fraction without breaking the sample, with an information on (an)isotropy as a benefit. Examples related to all sketched methods from the experiments performed at the Brno University of Technology show the advantages and restrictions of particular approaches.

*Key-Words:* Cementitious composites, non-destructive testing, signal and image processing, computational simulation.

## 1 Introduction

Advanced building structures make frequent use of materials as silicate composites, reinforced by metal particles (e.g. steel-fibre-reinforced concrete), preventing the tension stresses and strains as sources of undesirable micro- and macro-cracking. Mechanical properties of such composites are determined by the choice of fibre properties and their volume fraction, location and orientation in the matrix, sensitive to the technological procedures (as special compaction) and to the early-age treatment – cf. [12], as well as by the bond/slip interface relations – cf. [3]. The employment of the destructive approach relies usually on the separation of particles, taken from the early-age matrix, alternatively obtained from the crushed part of the existing structure, in the laboratory; consequently the volume fraction of particles can be evaluated accurately, whereas any information related to the original orientation of particles is missing. Moreover, such experiments with many structures are not allowed by technical standards. This is a strong motivation for the employment of some reliable non- or (at least) semi-destructive measurement methods, applicable in situ, handling homogeneity and isotropy and detecting the volume fraction of fibres in the material structure.

Regardless of the significant progress in this research area in the last decade (for more historical re-

marks and references see [8]), no inexpensive, robust and reliable method is available, thus all identification approaches rely on a) some indirect measurements and b) non-trivial numerical analysis, to handle a corresponding inverse problem – typically ill-posed, unstable, etc., forcing artificial regularization. Since a) produce quite other information than needed volume fractions and directional distributions of fibres, typically digital images in pixels or voxels, or electromagnetic quantities detected on the specimen surface, some calibration relations are needed, motivated by the physical and geometrical similarity. Moreover, some reasonable algorithm for the evaluation of effective material properties, using the properties of matrix and particles and the geometrical configuration, as input data, is needed: from simple arguments from the mixture theory to complicated physical and mathematical homogenization techniques (which will be specified later, in connection with electromagnetic measurements).

In this paper we shall pay attention thanks to the research experience of the authors from BUT (Brno University of Technology), namely to four representative approaches:

1. the planar X-ray imaging, with the discrete fast Fourier transform applied to image processing,

2. the magnetic approach, utilizing the Hall probe and advanced considerations on material homogenization with certain electromagnetic alternative,
3. the computed tomography, as an unique exact method for the detection of volume fraction without breaking the sample, with an information on (an)isotropy as a benefit.
4. the finite element modeling, as a method for exact electromagnetic field modelling based on the random fibre generation and identification.

## 2 First class of methods: analysis of X-ray images

The radiographic approach, developed in [7] for a rather large class of building materials, comes from the gray-scale planar images and some of their post-processing modifications, in particular:

- 1) the reduction of all fibres (whose length and thickness is known) to one-pixel thick black curves, followed by the simplified evaluation of their amount and orientation, by [7],
- 2) the application of the two-dimensional fast Fourier transform by [10] and [15], avoiding most artificial image changes, where the same as in 1) can be identified with a special diffraction process: for a the gray level at pixel coordinates  $f(x, y)$ , related to a square image containing  $N \times N$  pixels (with  $N$  tending to  $\infty$  theoretically), the direct and inverse Fourier transforms are

$$F(u, v) = \sum_{x=0}^{N-1} \sum_{y=0}^{N-1} f(x, y) \exp(-2\pi i(ux + vy)/N),$$

$$N^2 f(x, y) = \sum_{u=0}^{N-1} \sum_{v=0}^{N-1} F(x, y) \exp(2\pi i(ux + vy)/N)$$

and the power spectrum  $P(u, v) = |F(u, v)|^2$  contain the useful information, needed for the derivation of the histograms of fibre directions.

Figure 1 presents an example of such MATLAB-supported evaluation of fibre orientation in the fibre concrete specimen; the utilized X-ray equipment is shown on Figure 2. In general, the radiographic analysis gets useful results related to preferential orientations of fibres, although limited to data from planar images, even from several views to cubic specimens. The estimate of volume fraction of fibres is not very precise, at least in the comparison with destructive tests.

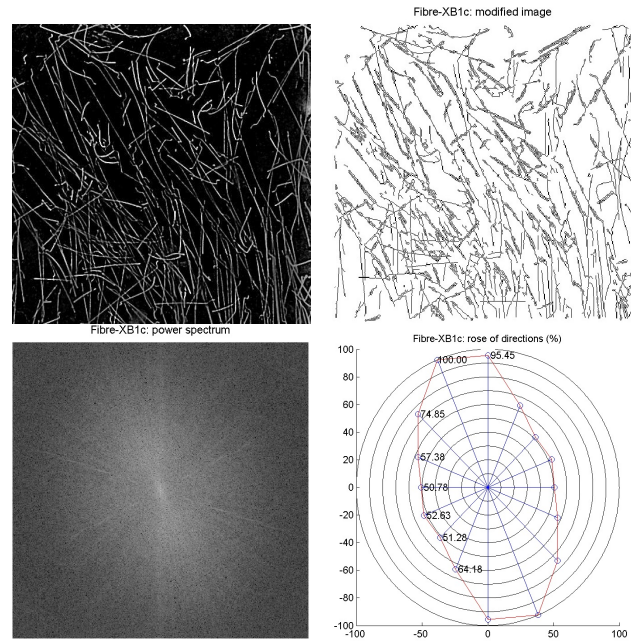


Figure 1: Evaluation of fibre orientation from the X-ray image (images from the left to the right): original image, result of fibre localization, power spectrum  $P$ , resulting rose of fibre directions.



Figure 2: X-ray machine EcoRay HF 1040 with digital recording to PC equipment (left photo). PeMaSo-01 depth probe for magnetic measurements (right photo).

### 3 Second class of methods: numerical treatment of magnetic measurements

Magnetic measurements like [23] and [5] rely on the different values of relative permeability of fibres and a matrix, with possible alternative of electrical measurements and relative permittivity. The special experimental configuration usually tries to force a (nearly) stationary process, whose mathematical description works with a differential operator close to the classical Laplace one, to enable non-expensive software simulation. Figure 3 shows the geometrical configuration of such process numerical simulation of such process in COMSOL: the magnetic field is generated by several permanent magnets, located in the drilled hole (thus this method could be classified as low-invasive, not non-destructive completely), consequently the Hall effect based probe from Figure 2 detects the magnetic field strength. Figure 4 documents the numerical simulation of such experiment, applying the COMSOL supported planar finite/infinite element technique: the influence of the irregularities caused by an artificial hall seems to be not substantial. The comparative simulation, applying only selected functions of *pde* toolbox from MATLAB, leads to the same conclusion.

The crucial problem is now to implement a correct evaluation procedure for an effective relative permeability (or permittivity) using the incomplete data on the material microstructure and on relative permeability of fibres. For spherical particles the classical Maxwell-Garnett mixing formula is available; the generalization of [6] comes from the so-called Bruggeman approach and the repeated usage of similar ellipsoids as reference volume elements, whereas [14] admits the presence of multiple scattering, important for high volume fractions of fibres. No additional physical assumption are needed, again for periodic spheres, in [13]: the auxiliary problem, referring to the mathematical theory of homogenization of elliptic operators, can be then analyzed (including the existence and uniqueness of solution, the convergence of sequences of approximate solutions, etc.) using the two-scale and similar convergence theorems by [2]; the crucial (seemingly) explicit formula for the evaluation of an effective parameter value, comes from the method of oscillating test functions. In [24] the difficulties with complex particle shapes are handled using the boundary integral approach, thanks to the knowledge of general solutions of the Laplace equation, with Heaviside characteristic functions of particles; [11] admits a priori anisotropic structures. Some generalizations are available using the least squares

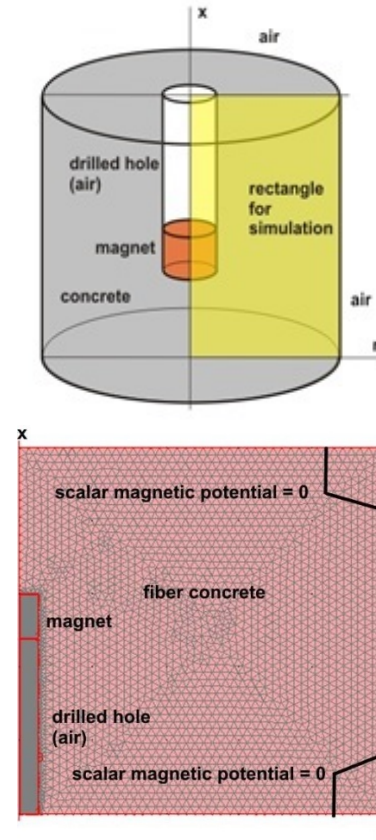


Figure 3: Radially symmetric geometrical arrangement of the magnetic experiment (left scheme) and computational simplification, including finite/infinite element mesh (right scheme).

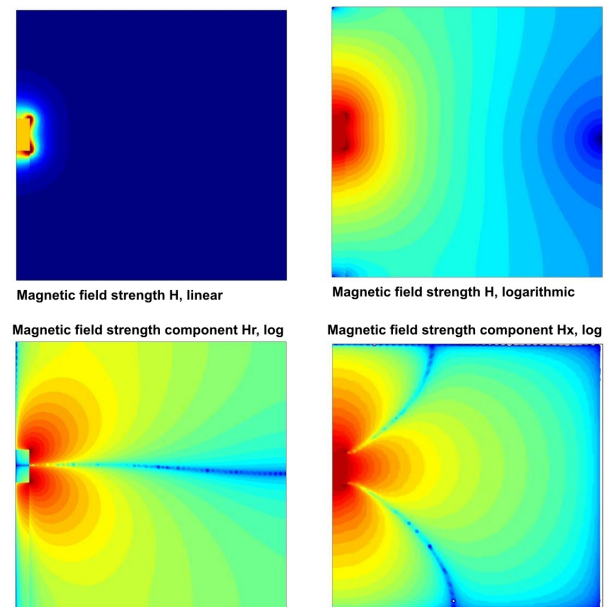


Figure 4: Results of COMSOL based finite/infinite element simulation of stationary magnetic field strength.

and conjugate gradient approaches – cf. [21]. Unfortunately, further substantial generalization of this approach (namely to non-periodic structure, avoiding all mixing tricks), lead to non-trivial (partially still open) problems of mathematical analysis, namely to the convergence using probability measures by [20], thus various alternative statistical approaches, as that with Sobol sensitivity indices and Monte Carlo simulations by [9], have been developed.

The unique material characteristics included here is the magnetic permeability  $\mu$  [Vs/(Am)]; at least in the case of silicate composites used in civil engineering  $\mu$  can be set to 1 for the pure matrix, but no relevant constant is guaranteed by the producers of ferromagnetic fibres. In practice, the dimensionless relative permeability  $\mu_r = \mu/\mu_0$ , using the well-known magnetic constant  $\mu_0 = 4\pi \cdot 10^{-7}$  Vs/(Am), is usually considered; similarly the relative permeabilities  $\mu_c$  for the matrix and  $\mu_s$  for all fibres can be introduced. Fortunately, for a sufficiently slow volume fraction  $\xi$  of fibres ( $\xi \leq 0.05$  in real experiments), following [6], under the assumption of random orientation of fibres, we obtain an explicit monotone and continuous dependence between  $\mu$  and  $\xi$  in the form

$$\xi = 1 - M \frac{\mu_s - \mu_r}{\mu_s - \mu_c} \left( \frac{\mu_c}{\mu_s} \right)^{3L(1-2L)(2-3L)},$$

where the factors

$$M = \left( \frac{M_1}{M_2} \right)^{2(3L-1)^2 / ((2-3L)(1+3L))},$$

$$L = \frac{\varsigma}{4\vartheta^3} \left( 2\varsigma\vartheta + \ln \frac{\varsigma - \vartheta}{\varsigma + \vartheta} \right)$$

are determined using the ratio  $\varsigma$  of lengths of a major and (both) minor axes of ellipsoidal particles (clearly  $\varsigma > 1$ ) for the simplifying notation  $\vartheta = \sqrt{\varsigma^2 - 1}$  and  $M_1 = (1 + 3L)\mu_c + (2 - 3L)\mu_s$ ,  $M_2 = (1 + 3L)\mu_r + (2 - 3L)\mu_s$ . In particular, for a (theoretically) infinite length and zero diameter of particles we receive  $L = 1/3$ . Unfortunately, all attempts to generalize this result for more complicated distributions of fibre directions lead to unpleasant non-analytical integrals, with the duty of their non-trivial numerical evaluations.

Figure 6 documents the least squares based identification of  $\mu_r$  for 3 input data sets with assumed  $\mu_r = 1$  for pure concrete and uncertain  $\mu_s$  in all other cases, using the above sketched formulae for an isotropic medium. the specimens (unlike the situation in situ) were prepared with exact volume fractions of fibres 0.5 %, 1 % and 1.5 %. Other experiments with comparable results have been performed by the authors' team with magnetic field induced by

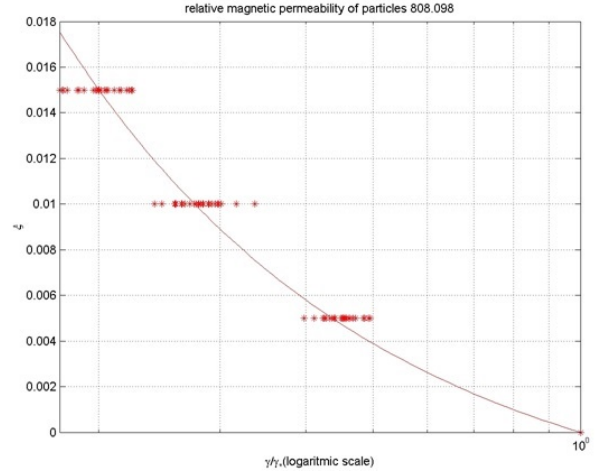


Figure 5: Application of the least squares technique to the identification of parameters  $\xi$  and  $\mu_s$  from magnetic measurements.

an electric coil. Moreover, [4] presents a totally non-destructive equipment, applicable to the surface of a specimen (thus preferring fibres close to such surface). All these result seem to give good estimates of volume fractions (whose improvement using more advanced mathematical analysis is possible), but the differentiating between system and random errors in distributions of fibre directions is difficult.

## 4 Third class of methods: computed tomography

A new approach to non-destructive analysis of structures of cementitious composites, motivated by [16], [22] and [1], has been offered by the computed tomography (X-ray CT), generating 3-dimensional images from large series (slices) of 2-dimensional radiographic images taken around a single axis of rotation. The modern industrial tomograph, presented on Figure 6, has been recently installed in the Central European Institute CEITEC of BUT. Unlike most tomographs for medical applications, an analyzed specimen is fixed on the manipulation table of the tomograph, between the radiation source and the surface radiation detector, compound from a matrix of mini-detectors. During the rotation of the table the surface detector records successive changes of X-ray radiation; consequently the specialized computer software is needed to analyze the inner structure of a specimen.

Several types of fibre concrete specimens have been tested using this equipment: whereas some cylindrical specimen is visible on Figure 6, Figure 7 shows the cubic specimen, similar to that from Figure 1, and demonstrates the ability of the specialized



Figure 6: Tomograph GE phoenix,v|tome|x L 240 (left photo) and a cylindrical specimen fixed in its manipulator (right photo).

software to recognize all fibres completely unlike all approximate estimates from separate planar images. Consequently various forms of histograms or graphical or 3-dimensional roses of directions similar to 2-dimensional ones from Figure 1 can be created. However, this is rather time consuming, expensive and not applicable to the fibre concrete structures in situ. Nevertheless, this seems to be a useful method to obtain a reliable reference basis for all numerical simulation attempts with random positions and orientation of fibres.

## 5 Fourth class of methods: FEM modelling

The current trend of work in micromechanics addresses the industry requirements to decrease the dependence on experimental work, and complement it with new numerical and/or analytical processes capable of providing quickly and efficiently the same information. A highly attractive process to simulate the real behaviour of composite is through finite element analysis. For that, a representative volume element (RVE) of the materials needs to be defined and an equivalent random distribution of fibres generated.

The first issue concerning the use of RVE is its dimension. The RVE cannot be too large as this would

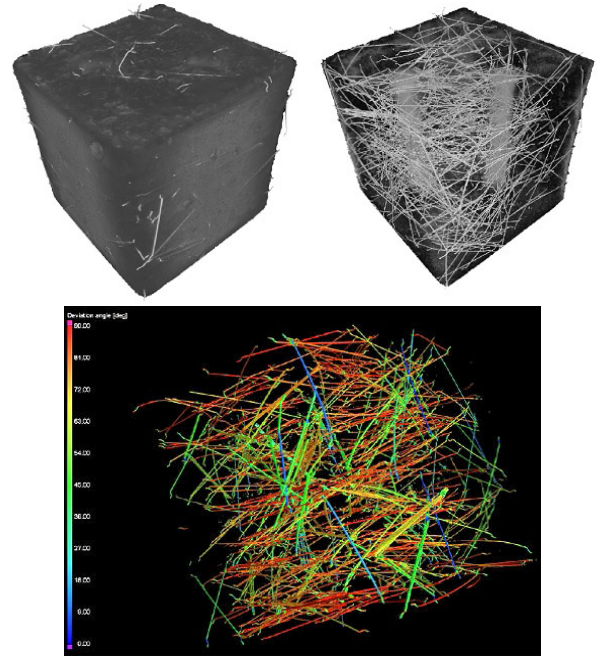


Figure 7: Cubic fibre concrete specimen, edge length 150 mm, required X-ray tube voltage 300 kV (images from the left to the right): axonometric view on its surface, axonometric view inside its structure, axonometric projection of separated fibres in the cube specimen.

endanger the possibility to numerically to analyse it; however, it cannot be too small either as it could not be representative of composite material, see [25]. Trias et al. [26] demonstrates that for long fibre composites a value of 50x the fibre radius should be used.

The second issue involving the use of an RVE is the spatial arrangement of reinforcements which normally is not periodic and is highly dependent upon manufacturing process. [27] using homogenization theory concluded that distribution of reinforcements in the RVE does not affect to macroscopic response, but it significantly affects the microscopic stress distribution and following damage in the matrix.

Good review of some numerical methods for the finite mesh generation can be found in [28] and [29]. Digital image analysis provides a perfect replica of the real composite, but can be extremely time and resource consuming as it requires specific software and hardware. To generate a random distribution of fibres is coupled with a statistical analysis and verified by sets of experiments.

## 6 Conclusion

This paper should be understood as an introductory comparative study to the most promisable non-destructive approaches to macroscopic identification

of content and random location of fibres in the structure of cementitious composites. However, all introduced approaches have strong restrictions: serious obstacles to get some reasonable estimate of volume fraction of fibres, as the most requested parameter, in the first case, expensive and fastidious experimental setting in the third case, interpretable as the more sophisticated upgrade of the first one, both technical and computational difficulties in the second case.

For the successful computational detection of volume fraction and preferential orientation of fibers, making use of their ferromagnetic properties, both under laboratory and in situ conditions, the crucial point of all considerations is the development of a homogenization procedure, specific to the analyzed class of materials, including its formal verification and its validity range. This leads to non-trivial problems of both physical and mathematical analysis, whose validation seems to be available thanks to the progress in the image processing techniques, consequently their deeper study should belong to the research priorities for the near future.

**Acknowledgements:** The financial support of the FAST-S-14-2490 research project at BUT is acknowledged.

#### References:

- [1] N. Baddour, Generalized Fourier diffraction theorem for tomography. *Proceedings of the 6-th WSEAS International Conference on Simulation, Modelling and Optimization* in Lisbon (Portugal), 2006, pp. 411–416.
- [2] D. Cioranescu and P. Donato, *An Introduction to Homogenization*. Oxford University Press, 1999.
- [3] V. M. C. F. Cunha, J. A. O. Barros and J. M. Sena-Cruz, An integrated approach for modelling the tensile behaviour of steel fibre reinforced self-compacting concrete. *Cement and Concrete Research* 41, 2011, pp. 64–76.
- [4] M. Faifer, L. Ferrara, R. Ottoboni and S. Toscani, Low frequency electrical and magnetic methods for non-destructive analysis of fiber dispersion in fiber reinforced cementitious composites: an overview. *Sensors* 13, 2013, pp. 1300–1318.
- [5] M. Faifer, R. Ottoboni, S. Toscani and L. Ferrara, Nondestructive testing of steel-fiber-reinforced concrete using a magnetic approach. *IEEE Transactions on Instrumentation and Measurement* 60, 2011, pp. 1709–1711.
- [6] S. Giordano, Effective medium theory for dielectric ellipsoids. *Journal of Electrostatics* 58, 2003, pp. 59–76.
- [7] L. Hobst, O. Anton, J. Vodička and J. Ščučka, Homogeneity detection of fibre-concrete structures by using radiographic technique. In: *Nondestructive Testing of Materials and Structures*, Springer 2013, pp. 323–328.
- [8] L. Hobst and P. Bílek, Various control methods developed for fibre concrete structures. *Recent advances in integrity, reliability and failure – 4-th International Conference* in Funchal (Madeira), 2013, pp. 721-730.
- [9] Z. Kala, Geometrically non-linear finite element reliability analysis of steel plane frames with initial imperfections. *Journal of Civil Engineering and Management* 18, 2012, pp. 81–90.
- [10] S. Kärkkäinen and E. B. Vedel Jensen, Estimation of fibre orientation from digital images. *Image Analysis and Stereology* 20, 2001, pp. 199–202.
- [11] M. Y. Koledintseva, R.E. DuBroff and R.W. Schwartz, Maxwell-Garnett rule for dielectric mixtures with statistically distributed orientations of inclusions. *Progress In Electromagnetics Research* 99, 2009, pp. 131–148.
- [12] A. Krasnikovs, V. Zaharevskis, O. Kononova, V. Lusi, A. Galushchak and E. Zaleskis, Fiber concrete properties control by fibers motion – investigation in fresh concrete during casting. *Industrial Engineering – 8th International DAAAM Baltic Conference* in Tallin, 2012, Part V: Materials Engineering, #10, 6 pp.
- [13] G. Kristensson, Homogenization of spherical inclusions. *Progress in Electromagnetic Research* 42, 2003, pp. 1–25.
- [14] P. Mallet, C. A. Guérin and A. Sentenac, Maxwell-Garnett mixing rule in the presence of multiple scattering: derivation and accuracy. *Physical Review B* 72, 2005, 14205/1–9.
- [15] N. E. Mastorakis and N. S. Swamy, Spectral transformations for two-dimensional filters via FFT. *IEEE Transactions on Circuits and systems – I: Fundamental Theory and Applications* 49, 2002, pp. 827–831.
- [16] P. J. M. Monteiro, C. Y. Pichot and K. Belkebir, Computer tomography of reinforced concrete. In: *Materials Science of Concrete*, Chapter 12, American Ceramics Society, 1998.
- [17] G. Nguetseng and N. Svanstedt,  $\sigma$ -convergence. *Banach Journal of Mathematical Analysis* 5, 2011, pp. 101–135.

- [18] M. Pieper and P. Klein, Application of simple, periodic homogenization techniques to nonlinear heat conduction problems in non-periodic, porous media. *Heat and Mass Transfer* 48, 2012, pp. 291–300.
- [19] M. Ya. Sushko, Effective permittivity of mixtures of anisotropic particles. *Journal of Physics D: Applied Physics* 42, 2009, 155410: 9 pp.
- [20] N. Svanstedt, Multiscale stochastic homogenization of convection-diffusion equations. *Applications of Mathematics* 53, 2008, pp. 143–155.
- [21] J. Vala, Least-squares based technique for identification of thermal characteristics of building materials. *International Journal of Mathematics and Computers in Simulation* 5 (2011), pp. 126–132.
- [22] G. Weidemann, R. Stadie, J. Goebbels and B. Hillemeier, Computer tomography study of fibre reinforced autoclaved aerated concrete. *Materials Testing* 50, 2008, pp. 278–285.
- [23] H.-J. Wichmann, H. Budelmann and A. Holst, Determination of steel fiber dosage and steel fiber orientation in concrete. In: *Nondestructive Testing of Materials and Structures*, Springer 2013, pp. 239–245.
- [24] K. W. Whites and F. Wu, Effects of particle shape on the effective permittivity of composite materials with measurements for lattices of cubes. *IEEE Transactions on Microwave Theory and Techniques* 50, 2002, pp. 1723–1729.
- [25] L. Mishnaevsky Jr. and S. Schmauder, Continuum Mesomechanical finite element modelling in materials development a state-of-the-art review. *Applied Mechanics Reviews*, 54, 1, 2001, pp. 49–69.
- [26] D. Trias, J. Costa, A. Turon and J. Hurtado, Determination of the critical size of a statistical representative volume element (SRVE) for carbon reinforced polymers. *Acta Mater*, 2006, 54, 13, pp. 3471–3484.
- [27] S. Schmauder and L. Mishnaevsky Jr., Micromechanics and nanosimulation of metals and composites. *Springer*, 2008, 430 pp.
- [28] D. Raabe, Computational materials science: The simulation of materials microstructures and properties. *Wiley*, 1998.
- [29] A. R. Melro, P. P. Camanho and S. T. Pinho, Generation of random distribution of fibres in long fibre reinforced composites. *Composites Science and Technology*, 68, 2008, pp. 2092–2102.

D3 Vala, J., Kozák, V., Computational analysis of quasi-brittle fracture in fibre reinforced cementitious composites, In 9th International Conference Materials Structure & Micromechanics of Fracture (MSMF9), *Procedia Structural Integrity*, Amsterdam: Elsevier, (2019), 328-333.



9th International Conference on Materials Structure and Micromechanics of Fracture

## Computational analysis of crack formation and propagation in quasi-brittle fibre reinforced composites

Jiří Vala<sup>a</sup>, Vladislav Kozák<sup>b,\*</sup>

<sup>a</sup>Brno University of Technology, Faculty of Civil Engineering, Institute of Mathematics and Descriptive Geometry, 602 00 Brno, Veverí 331/95, Czech Republic

<sup>b</sup>Institute of Physics of Materials, Academy of Sciences CR, 616 62 Brno, Žitkova 513/22, Czech Republic

### Abstract

Prediction of quasi-brittle behaviour of structural components from fibre reinforced composites under mechanical loads should incorporate such physical processes as elastic, resp. plastic deformation, crack initiation, crack propagation in a matrix, pull out of fibres and rupture of fibres. The computational model for the practically most important case of cementitious composites containing short intentionally or quasi-randomly oriented steel, ceramic, resp. polymeric fibres with its primary import of suppression of tensile stresses in a matrix will be introduced. Its numerical approach relies on the modified extended finite element technique (XFEM), open to the implementation of the cohesive traction separation law.

© 2019 The Authors. Published by Elsevier B.V.

This is an open access article under the CC BY-NC-ND license (<http://creativecommons.org/licenses/by-nc-nd/4.0/>)

Peer-review under responsibility of the scientific committee of the ICMSMF organizers

*Keywords:* Quasi-brittle fracture; fibre reinforced composites; computational modelling; extended finite element method.

### 1. Introduction

The fibre cementitious composites are in the class of perspective concrete, which increase the mechanical crack resistance, allow for a more subtle and economical construction; thus a new look at creating construction rigs replacing the steel structure is needed. Engineering structures subjected to loading may result in stresses in the body exceeding the material strength and thus results in the progressive failure. Such failures are often initiated by surface or near surface cracks, reducing the strength of the material. In quasi-brittle materials like rocks or concrete this is

\* Corresponding author. Tel.: +420-532-290-364.

E-mail address: [kozak@ipm.cz](mailto:kozak@ipm.cz)

manifested by fracture process zones, in brittle materials like glass or welds in metal structures by discrete crack discontinuities, in elasto-plastic ductile metal or similar materials by shear (localization) bands, see Sumi (2014). Advanced building structures frequently use silicate composites reinforced by metal, plastic or other fibres, preventing undesirable micro- and macro-cracking effects. Mechanical behaviour of such composites is conditioned by the suitable choice of fibre properties, their concentration, localization and orientation in a silicate matrix, influenced by their early-age treatment, see Komárková et al (2017).

Non-destructive testing of material structure is offered by image processing (2D radiographic, 3D tomographic, etc.) and stationary magnetic and non-stationary electromagnetic approaches. The macroscopic material homogenization, Vala (2016), relies then on the semi-analytical mixing formulae for special particle shapes (acceptable namely for their low volume fractions), two-scale homogenization of periodic structures, or alternative results from the asymptotic analysis ( $G$ -convergence,  $H$ -convergence,  $\Gamma$ -convergence, etc.), up to very general (both deterministic and stochastic) results for  $\sigma$ -convergence on homogenization structures, with numerous open problems uncovered by Roubíček (2013). A unified scale-bridging approach covering elastic and plastic behavior together with fracture and other defects results in concept of structured deformation, see Morandotti (2018). The dissipative particle dynamics, Steinhäuser (2008), referring up to the atomistic or molecular scale, can be adopted to handle certain super-particles; this results in the discrete element method, applied namely in soil, rock and concrete mechanics, in the analysis of granular materials and in the dynamic process of initiation and propagation of micro-cracks. The inheritance from dissipative particle dynamics, manifested in the limited offer of particle shapes and sizes, can be overcome with help of two- or three-dimensional reference volume elements, using the combination of finite and discrete element approaches, Munjiza (2004). An autonomous problem is the reliable identification of material parameters at various scales: the relevant computational approaches, Vala (2014), typically suffer from mathematical ill-posedness, numerical instability and need of artificial regularization, together with uncertain or insufficient input data. These difficulties have to be overcome by careful organization of experiments and various special problem-oriented algorithms, Shen et al (2010), Buljak et al (2013).

The extensive use of brittle matrix composite materials requires also appropriate computational models to describe, with adequate accuracy, their mechanical behaviour. From a micromechanical model some macroscopic constitutive equations are derived for intentionally or random oriented fibres Park et al (2010), Brighenti et al (2013), Cerrone et al (2014), Sanjayan et al (2015), accounting for such physical processes as matrix/fibre debonding and fibre rupture. One of possible ways is to adopt a discontinuous-like FE approach to a *lattice model*, see Brighenti & Scorza (2012). An alternative approach refers to special constitutive relations, inspired by continuum mechanics, where crack opening and contact surface sliding are included into the model of plastic damage, using smeared cracking, Jirásek (2011), Edalat-Behbahani et al (2017), together with mesh objective strain localization due to material softening, referring to the thermodynamically irreversible continuum damage mechanics, Le et al (2019), compatible with Nair (2009, especially Chap.14) and open to more general analysis working with tensor calculus and differential geometry, Epstein (2007), Clayton (2015), in particular that leading to a smeared representation of the crack path, Kaliske et al (2012). At least for the practically significant application of self-compacting concrete, supported by both experimental methods and numerical simulations, smeared cracking can be combined with Monte Carlo simulations, which results in the *Variational Multiscale Cohesive Method*, Su et al (2010), whose various implementations differs in the choice of basis functions.

Another approach to the same problems presents the *eXtended Finite Element Method (XFEM)* briefly, Khoei (2015), covering both strong geometrical discontinuities (in function values) and weak ones (in gradients), with the aim of enrichment of the approximation space by all needed types of (especially locally) discontinuous functions, and similar approaches, derived from the *Partition of Unity Method*, namely the *Partition of Unity Finite Element Method*, Babuška & Melenk (1997), the *Generalized Finite Element Method*, Duarte et al (2001), or the *Discontinuous Galerkin XFEM*, Aduloju & Truster (2019). Especially XFEM adds some degrees of freedom in relevant regions during the computation, typically along all curves and surfaces of discontinuities and in singular points, exploiting the *Moving Least Squares* technique: the usual *extrinsic* XFEM works with additional variables and functions, whereas the *intrinsic* XFEM developed by Fries & Belytchko (2006) tries to avoid them, only with one additional shape function in each relevant node. However, although no singularity exist at the tip of cohesive crack, the stresses obtained by differentiation of the displacement are not accurate, and cannot be used to predict accurately the growth of the tip, Ferté et al (2016), Li & Chen (2017).

A possible approach to simulate the propagation of cracks is the application of softening material formulations to continuum elements leading to a smeared representation of the crack path. An alternative discrete approach implements the cohesive finite elements, Kozák & Chlup (2011), Kozák et al (2017), Vala (2017); in this case the crack path must be known a priori, or all element interfaces have to be taken into account, which forces many new degrees of freedom, accompanied also by the risk of non-physical reduction of effective stiffness. The application of XFEM is able to suppress such drawbacks in the simulation of propagation of cohesive cracks; however, it must handle the non-existence of a sharp singularity at the crack tip, with more complicated derivation of required stresses from displacements. In general the complete computational model should involve the formation and propagation of cracks, their bridging by fibres, the loss of cohesion between fibres and matrix, their mutual sliding with friction and the fibre destruction; special functions are necessary e.g. for stress singularities in the case of crack opening and closing. The two-phase composite model of matrix and inclusion, based on the Eshelby solution and on the Mori-Tanaka homogenization scheme, can be adapted to the directional propagation of microcracks, generalized also for long fibres by Bouhala et al (2013), Mihai & Jefferson (2017). Random spatial variability of material parameters can be handled using the stochastic simulation of damage, Eliáš et al (2015).

## 2. Physical, mathematical and computational background

The formulation of the related mathematical problem, incorporating reasonable physical and engineering simplifications as the starting point for a derivation of the effective computational algorithm, comes from the principles of classical thermodynamics, namely from the 1st one of conservation of scalar quantities as energy, (linear and angular) momentum and mass and from the 2nd principle concerning the irreversibility of natural processes, here namely of the damage formation and propagation, which must be respected by semi-empirical (motivated from available information on material micro- and mesostructure) constitutive relationships, together with reasonable initial and boundary conditions. As with a simplified model example (useful just for this short paper), coming from such considerations, we can start with the an abstract (in general nonlinear) quasi-static problem

$$\langle G(\dot{u}), v \rangle + \langle A(u), v \rangle = \langle F, v \rangle \quad (1)$$

where the brackets refer to some dualities for reflexive and separable Banach spaces  $V$  (in particular, to scalar products in Hilbert spaces) for any time  $t$  from some time interval  $I = [0, \tau]$  for a positive  $\tau$  (the limit case  $\tau \rightarrow \infty$  is not forbidden, but not discussed here),  $v \in V$  denotes a virtual quantity, e.g. the displacement related to the reference configuration, the dot means  $\partial/\partial t$ ,  $F$  is a linear functional and  $A(\cdot), G(\cdot)$  are (rather special) mappings defined on  $V$ ; we are seeking for an  $u(t)$  mapping  $I$  to  $V$  coinciding with some prescribed  $u_0 \in V$  for  $t=0$  (a Cauchy initial condition) formally. However, our real aim is to find  $u \in V$  satisfying (1) with the vanished 1st additive term; the main difficulty of the hypothetical direct approach comes from the nonlinearity of  $A(\cdot)$ . Whereas  $G(\cdot)$  can be taken  $G(\cdot)$ , an coercive operator  $A(\cdot)$  may be useful to be decomposed as  $A_*(\cdot, \cdot)$ , linear in the 2nd variable and compact (if possible) in the 1st one, to apply the existence theory for weakly continuous (or pseudomonotone) operators. Consequently (1) can be transferred (accounting for the convergence properties of Rothe sequences) to

$$\langle G(u_s - u_{s-1}), v \rangle + h \langle A_*(u_{s-1}, u_s), v \rangle = h \langle F_s, v \rangle \quad (2)$$

with  $u_s, u_{s-1}$  approximating an unknown  $u$  for  $t = sh$  and  $t = (s-1)h$ , as well as  $F_s$  in the case of known  $F$  (with certain final value); here  $s \in \{1, \dots, m\}$  with  $m = \tau/h$ , considering the limit passage  $h \rightarrow 0$  (thus  $m \rightarrow \infty$ ). Under some additional assumption we are allowed to come from (2) to the estimate, working with the norm  $\|\cdot\|$  in  $V$ ,

$$\|u_s\|^2 + \sum_{r=1}^s \|u_r - u_{r-1}\|^2 \leq c \left( \|u_0\|^2 + h \sum_{r=1}^s \|F_r\|^2 \right) \quad (3)$$

where  $c$  is some generic constant; (3) then manifests the decrease of  $\|u_m - u_{m-1}\|$ , etc., with  $m \rightarrow \infty$  to zero.

In particular, following Pike & Oskay (2005) (with several straightforward generalizations, working with geometrical and physical linearization of elastic matrix and fibre behavior and with a macroscopic view to matrix cracking, let us consider an open set (typically a domain)  $\Omega$  in the 3-dimensional Euclidean space  $R^3$  with an external boundary  $\partial\Omega$ , decomposed to 2 disjoint parts  $\theta$  (for homogeneous Dirichlet boundary conditions) and  $\gamma$  (for non-

homogeneous Neumann ones). Let  $\Omega$  consist of 2 disjoint parts (open sets again):  $\Omega_m$  occupied by a silicate matrix, and  $\Omega_f$  by metal fibres, with contact surfaces  $\kappa$ : the symbol  $[\cdot]$  refers to the difference between function traces on  $\kappa$  from particular sides. It is also useful to introduce the fractured zone  $\Theta$  of  $\Omega$  separately. Then, using the Einstein summation indices  $i, j, k, l \in \{1, 2, 3\}$ ,  $(\cdot)_{,i}$  in the sense  $\partial/\partial x_i$  and the small strain tensors  $\varepsilon_{ij}(v) = (v_{i,j} + v_{j,i})/2$ , etc., the energy conservation with the unknown displacements  $u(x, t) = (u_1(x, t), u_2(x, t), u_3(x, t))$ , the virtual ones  $v(x, t) = (v_1(x, t), v_2(x, t), v_3(x, t))$ , the prescribed surface loads  $q(x, t) = (q_1(x, t), q_2(x, t), q_3(x, t))$  and the prescribed volume loads  $g(x, t) = (g_1(x, t), g_2(x, t), g_3(x, t))$  reads as (1) utilizing

$$\begin{aligned} \langle A_\omega(w, u)(t), v \rangle &= \int_{\Omega} (1 - \alpha(x, w(x, t))) \varepsilon_{ij}(w(x, t)) C_{ijkl}(x) \varepsilon_{kl}(v(x)) dx + \int_{\kappa} \partial \Phi([u(x, t)]) / \partial [u_i(x, t)] v_i(x) ds(x), \\ \langle G(\dot{u})(t), v \rangle &= \int_{\Omega} \alpha(x) \varepsilon_{ij}(\dot{u}(x, t)) C_{ijkl}(x) \varepsilon_{kl}(v(x)) dx, \quad \langle F(t), v \rangle = \int_{\Omega} g_i(x, t) v_i(x) dx + \int_{\gamma} q_i(x, t) v_i(x) ds(x), \end{aligned} \quad (4)$$

whereas  $u(\cdot, t) = (0, 0, 0)$  on  $\theta$ , compatible with a priori known initial displacements  $u(\cdot, 0)$  on  $\theta$ ;  $w$  can be taken as  $u$  here ( $w \neq u$  is admitted because of the computational linearization of (2)).

Serious complications are brought into (1) through constitutive relations, namely those accounting for the significant irreversible processes. Seemingly (1), supplied by standard linearized strain-stress relations, working with the symmetric 4th-order tensors  $C$  of stiffness characteristics (compound from 2 Lamé constants for each material, i.e. fibres and matrix, in the simplest isotropic homogeneous case) and the scalar viscous characteristic  $\alpha$  (often artificial, referring to the Kelvin viscoelastic model) can be handled using the standard theory of linear differential equations of evolution of parabolic type assuming zero-valued  $\omega$  and constant  $\Phi$ . Consequently, using the standard notation of Lebesgue, Sobolev, Bochner, etc. spaces by Roubíček (2013), taking  $V$  as the subspace of all  $\varpi \in W^{1,2}(\Omega, \mathbb{R}^3)$  satisfying  $\varpi = (0, 0, 0)$  for traces on  $\theta$ , under reasonable requirements to such characteristics (such as positive  $\alpha$ , positive definite  $C$ , sufficiently smooth  $\partial\Omega$ , some Lebesgue integrability of  $g$  and Hausdorff integrability of  $q$  in relevant function spaces, needed in embedding and trace theorems, we are able to verify the existence of a unique solution  $u, \dot{u} \in L^2(I, V)$  completely, as well as the convergence of the algorithm induced by (2). Much weaker results (for more general Banach spaces) are available (and complicated, frequently non-constructive proofs occur) in more general cases; this stimulates the proper analysis of the characteristics  $\omega$  and  $\Phi$  and their assessment in (4). Here  $\omega$  refers to certain nonlocal damage function, zero-valued outside  $\Theta$ , motivated by some scale-bridging considerations, whereas  $\Phi$  refers to the interface potential on  $\kappa$ , accounting for the physical deterioration on cohesive interfaces, describing the relationship between the surface traction and material separation between the surfaces, crucial for the reliable study of matrix/fibre debonding.

Since (2) refers in every time step to a linear problem, but still in an infinite-dimensional space, an additional computational discretization (except very special configurations with known analytical or semi-analytical solutions) is needed. Such discretization of (2) can be sketched as

$$u_{si}(x) = u_{sia} \psi_a(x) + u_{sib} \psi_b(x) + u_{sic} \psi_c(x), \quad (5)$$

containing the standard finite element shape functions  $\psi_a(x)$  on  $\Omega$ , the fractured zone enrichment shape functions  $\psi_b(x)$  on  $\Theta$  and the cohesive interface enrichment shape functions  $\psi_c(x)$  on  $\kappa$ ;  $a, b$  and  $c$  are considered as the Einstein summation indices over all corresponding shape function sets here. The favourite choice for the implementation of (5) is  $u_{sia} \approx u_{si}(x_a)$ ,  $u_{sib} \approx u_{si}(x_b)$ ,  $u_{sic} \approx u_{si}(x_c)$  (i.e. just the displacement values in selected points in the role of unknown parameters), corresponding to  $\psi_a(x)$ ,  $\psi_b(x)$  and  $\psi_c(x)$  with small compact supports near  $x_a, x_b$  and  $x_c$ . The optimized choice of both  $x_a, x_b$  and  $x_c$  and  $\psi_a(x)$ ,  $\psi_b(x)$  and  $\psi_c(x)$ , together with the strategy of numerical integration and mesh refinement, determine the efficiency and the robustness of relevant algorithms and stimulate the development of special problem-oriented XFEM (or similar) algorithms.

### 3. Illustrative example

For computational modelling, a specimen with cementitious matrix and steel fibres has been chosen. Numerical results demonstrate the planar crack propagation in a cracked body, depending on the fibre location and material characteristics. The stiffening effect of fibres plays a significant role for the direction of crack propagation.

Figure 1 shows the results of modelling of crack propagation applying the modified XFEM approach, namely the maximum principle stress in various stages of such propagation. The left figure corresponds to the initial state without any crack, the central figure shows the crack passing the stiffening fibres, the right one the similar case with different shear moduli ( $2\times$  higher in the horizontal direction).

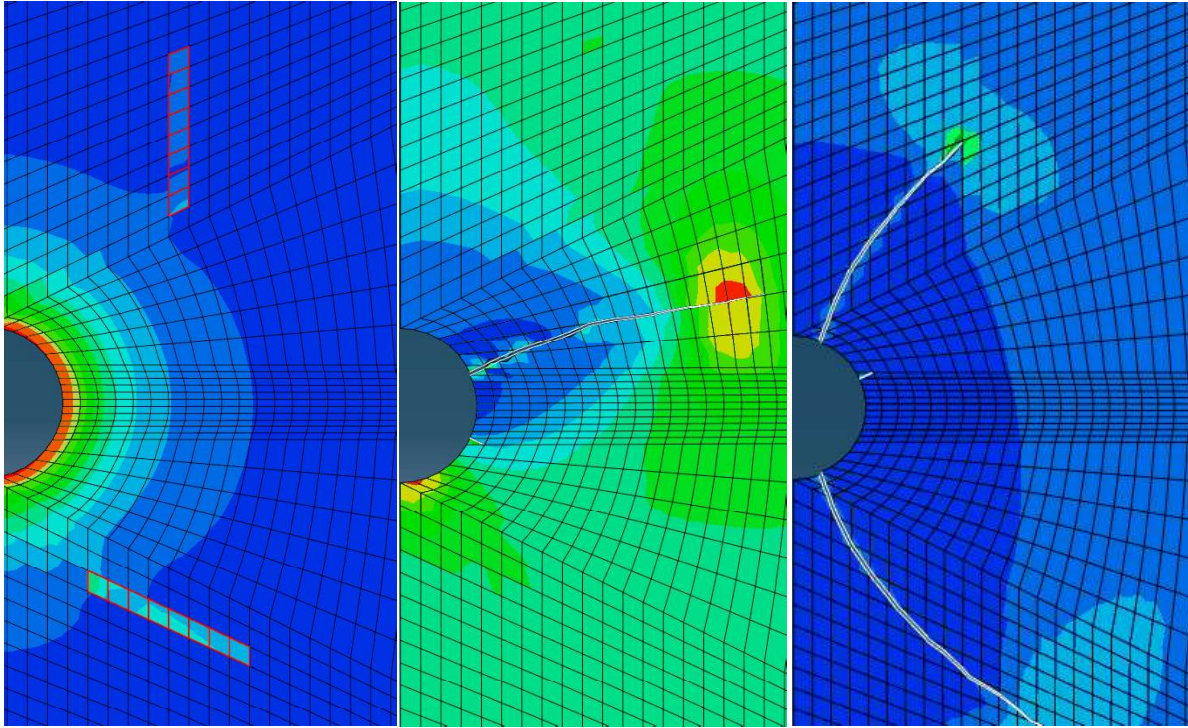


Fig. 1. Modelling of crack propagation applying the modified XFEM approach.

#### 4. Conclusions and generalizations

A model based on FEM and its XFEM modification based on the properties of fibre cementitious composites has been presented. Some criteria for crack propagation coming from both the critical stress values and both the cohesive law ahead the crack tip have been tested. The proposed approaches should contribute to the prediction of fracture behaviour of fibre cementitious composites and to the potential design of constructive structural parts.

#### Acknowledgements

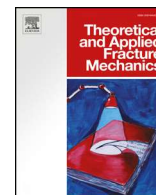
This presentation has been supported from the projects i) of Ministry of Education, Youth and Sports of the Czech Republic *AdMaS UP – Advanced Materials, Structures and Technologies*, National Sustainability Programme I, LO1408, ii) of specific university research at Brno University of Technology FAST-S-19-5878.

#### References

- Aduloju, C., Truster, T. J., 2019. A variational multiscale discontinuous Galerkin formulation for both implicit and explicit dynamic modeling of interfacial fracture. *Computer Methods in Applied Mechanics and Engineering* 343, 602–630.
- Babuška, I., Melenk, J. M., 1997. The partition of unity method. *International Journal for Numerical Methods in Engineering* 40, 727–758.
- Bouhala, L., Makradi, A., Belouettar, S., Kiefer-Kamal, H., Frères, P., 2013. Modelling of failure in long fibres reinforced composites by X-FEM and cohesive zone model. *Composites Part B* 55, 352–361.

- Brighenti, R., Scorza, D., 2012. Numerical modelling of the fracture behaviour of brittle materials reinforced with unidirectional or randomly distributed fibres. *Mechanics of Materials* 52, 12–27.
- Brighenti, R., Carpinteri, A., Spagnoli, A., Scorza, D., 2013. Cracking behaviour of fibre-reinforced cementitious composites: a comparison between a continuous and a discrete computational approach. *Engineering Fracture Mechanics* 103, 103–114.
- Buljak, V., Cocchetti, G., Maier, G., 2013. Calibration of brittle fracture models by sharp indenters and inverse analysis. *International Journal of Fracture* 184, 123–136.
- Cerrone, A., Wawrzynek, P., Nonn, A., Paulino, G. H., Ingrassia, A., 2014. Implementation and verification of the Park-Paulino-Roesler cohesive zone model in 3D. *Engineering Fracture Mechanics* 120, 26–42.
- Clayton, J. D., 2015. *Differential Geometry and Kinematics of Continua*. World Scientific, New Jersey.
- Duarte, C. A., Hamzeh, O. N., Liszka, T. J., Tworzydło, W. W., 2001. A generalized finite element method for the simulation of three-dimensional dynamic crack propagation. *Computer Methods in Applied Mechanics and Engineering* 190, 2227–2262.
- Edalat-Behbahani, A., Barros, J. A. O., Ventura-Gouveia, A., 2017. Three-dimensional plastic-damage multidirectional fixed smeared crack approach for modelling concrete structures. *International Journal of Solids and Structures* 115/116, 104–125.
- Eliš, J., Vořechovský, M., Škoček, J., Bažant, Z. P., 2015. Stochastic discrete meso-scale simulations of concrete fracture: comparison to experimental data, ph{Engineering Fracture Mechanics 135, 1–16.
- Epstein, M., Elzanovski, M., 2007. *Material Inhomogeneities and their Evolution*. Springer, Berlin.
- Ferté, G., Massin, P., Moes, N., 2016. 3D crack propagation with cohesive elements in extended finite element method. *Computer Methods in Applied Mechanics and Engineering* 300, 347–374.
- Fries, T.-P., Belytschko, T., 2006. The intrinsic XFEM: a method for arbitrary discontinuities without additional unknowns. *International Journal for Numerical Methods in Engineering* 68, 1358–1385.
- Jirásek, M. Damage and smeared crack models, 2011. In: *Numerical Modeling of Concrete Cracking* (Hofstetter, G., Meschke, G., eds). Springer: CISM International Centre for Mechanical Sciences 532, 1–49.
- Kaliske, M., Dal, H., Fleischhauer, R., Jenkel, C., Netzker, C., 2012. Characterization of fracture processes by continuum and discrete modelling. *Computational Mechanics* 50, 303–320.
- Khoei, A. R. *Extended Finite Element Method: Theory and Applications*, 2015. J. Wiley & Sons, Hoboken.
- Komárková, T., Láník, J., Dvořák, P., 2017. Influence of dispersed reinforcement on the physico-mechanical properties of the SFRC. *Key Engineering Materials* 755, 75–81.
- Kozák, V., Chlup, Z., 2011. Modelling of fibre-matrix interface of brittle matrix long fibre composite by application of cohesive zone method. *Key Engineering Materials* 465, 231–234.
- Kozák, V., Chlup, Z., Padělek P., Dlouhý, I., 2017. Prediction of the traction separation law of ceramics using iterative finite element modelling. *Solid State Phenomena* 258, 186–189.
- Li, X., Chen, J., 2017. An extensive cohesive damage model for simulation arbitrary damage propagation in engineering materials. *Computer Methods in Applied Mechanics and Engineering* 315, 744–759.
- Li, X., Gao, W., Liu, W., 2019. A mesh objective continuum damage model for quasi-brittle crack modelling and finite element implementation. *International Journal of Damage Mechanic* 28, 24 pp., to appear.
- Mihai, I. C., Jefferson, A. D., 2017. A micromechanics based constitutive model for fibre reinforced cementitious composites. *International Journal of Solids and Structures* 110/111 (2017), 152–169.
- Morandotti, M., 2018. Structured deformations of continua: theory and applications. *Continuum Mechanics Focusing on Singularities (CoMFoS) II – 16th Conference in Fukuoka (2016)*, Proceedings, Springer, 125–138.
- Munjiza, A., 2004. *The Combined Finite-Discrete Element Method*. John Wiley & Sons, Hoboken, 2004.
- Nair, S. *Introduction to Continuum Mechanics*. Cambridge University Press, Cambridge, 2009.
- Pike, M. G., Oskay, C., 2005. XFEM modeling of short microfiber reinforced composites with cohesive interfaces. *Finite Elements in Analysis and Design* 106, 16–31.
- Park, K., Paulino, G. H., Roesler, J. R., 2010. Cohesive fracture model for functionally graded fiber reinforced concrete. *Cement and Concrete Research* 40, 956–965.
- Roubíček, T., 2013. *Nonlinear Partial Differential Equations with Applications*. Birkhäuser, Basel.
- Sanjayam, J. G., Nazari, A., Pouraliakbar, H., 2015. FEA modelling of fracture toughness of steel-reinforced geopolymer composites. *Materials and Design* 76, 215–222.
- Shen, B., Stanciulescu, I., Paulino G. H., 2010. Inverse computation of cohesive fracture properties from displacement fields. *Inverse Problems in Science and Engineering* 18, 1103–1128.
- Steinhauser M. O., 2008. *Computational Multiscale Modeling of Fluids and Solids*. Springer, Berlin.
- Su, X. T., Yang, Z. J., Liu, G. H., 2010. Monte Carlo simulation of complex cohesive fracture in random heterogeneous quasi-brittle materials: a 3D study. *International Journal of Solids and Structures* 47, 2336–2345.
- Sumi, Y., 2014. *Mathematical and Computational Analyses of Cracking Formation*. Springer, Tokyo.
- Vala, J., 2015. Computational approaches to some inverse problems from engineering practice. *Programs and Algorithms of Numerical Mathematics (PANM) – 17th Seminar in Dolní Maxov (2014)*, Proceedings, Institute of Mathematics AS CR, 15, 215–230.
- Vala, J., 2017. Existence and convergence questions in computational modelling of crack growth in brittle and quasi-brittle materials. *Solid State Phenomena* 258, 157–160.
- Vala, J., 2016. Structure identification of metal fibre reinforced cementitious composites. *Algorithmy – 20th Conference on Scientific Computing in Podbanské (2016)*, Proceedings, STU Bratislava, 244–253.

- D4 Vala, J., Kozák, V., Computational analysis of quasi-brittle fracture in fibre reinforced cementitious composites, *Theoretical and Applied Fracture Mechanics* 107, (2020), č. 1, 5501-5510, IF 3,021.



## Computational analysis of quasi-brittle fracture in fibre reinforced cementitious composites

J. Vala<sup>a,\*</sup>, V. Kozák<sup>b</sup>

<sup>a</sup> Brno University of Technology, Faculty of Civil Engineering, Institute of Mathematics and Descriptive Geometry, 602 00 Brno, Veveří 331/95, Czech Republic

<sup>b</sup> Institute of Physics of Materials Czech Academy of Sciences, 616 62 Brno, Žitkova 513/22, Czech Republic

### ABSTRACT

Prediction of quasi-brittle behaviour of structural components from fibre reinforced composites under mechanical loads should incorporate such physical processes as elastic, resp. plastic deformation, crack initiation, crack propagation in a matrix, pull out of fibres and rupture of fibres. The computational model for the practically most important case of cementitious composites containing short intentionally or quasi-randomly oriented steel, ceramic, resp. polymeric fibres with its primary import of suppression of tensile stresses in a matrix will be introduced. Its numerical approach relies on the modified eXtended Finite Element Method, open to the implementation of the cohesive traction separation law. This paper introduces the implementation of some integral-type nonlocal constitutive strain-stress relation. It pays attention namely to the Eringen model for the generation of the multiplicative damage factor, to the related quasi-static analysis, to the existence of a weak solution of the corresponding boundary and initial value problem with a parabolic system of partial differential equation and to the convergence of an algorithm based on 3 types of Rothe sequences. Thus, the article combines the possibilities of the two procedures for modeling crack propagation. Microstructural behavior is contained in the Eringen model, the effect of macro behavior in modified finite element method XFEM.

### 1. Introduction

The fibre cementitious composites are in the class of perspective concrete, which increase the mechanical crack resistance, allow for a more subtle and economical construction; thus a new look at creating construction rigs replacing the steel structure is needed. Engineering structures subjected to loading may result in stresses in the body exceeding the material strength and thus results in the progressive failure. Such failures are often initiated by surface or near surface cracks, reducing the strength of the material. In quasi-brittle materials like rocks or concrete this is manifested by fracture process zones, in brittle materials like glass or welds in metal structures by discrete crack discontinuities, in elasto-plastic ductile metal or similar materials by shear (localization) bands see [69]. Advanced building structures frequently use silicate composites reinforced by metal, plastic or other fibres, preventing undesirable micro- an macro-cracking effects. Mechanical behaviour of such composites is conditioned by the suitable choice of fibre properties, their concentration, localization and orientation in a silicate matrix, influenced by their early-age treatment – see [35]. Non-destructive testing of material structure is offered by image processing (2D radiographic, 3D tomographic, etc.) and stationary magnetic and non-stationary electromagnetic approaches. The macroscopic material homogenization by [70] relies then on the semi-analytical mixing formulae for special particle shapes (acceptable namely for their low

volume fractions), two-scale homogenization of periodic structures, or alternative results from the asymptotic analysis (G-convergence, H-convergence,  $\Gamma$ -convergence, etc.), up to very general (both deterministic and stochastic) results for  $\sigma$ -convergence on homogenization structures, with numerous open problems uncovered by [61]. A unified scale-bridging approach covering elastic and plastic behavior together with fracture and other defects results in concept of structured deformation – see [48].

The dissipative particle dynamics by [68], referring up to the atomistic or molecular scale, can be adopted to handle certain super-particles; this results in the discrete element method, applied namely in soil, rock and concrete mechanics, in the analysis of granular materials and in the dynamic process of initiation and propagation of micro-cracks. The inheritance from dissipative particle dynamics, manifested in the limited offer of particle shapes and sizes, can be overcome with help of two- or three-dimensional reference volume elements, using the combination of finite and discrete element approaches – see [52]. An autonomous problem is the reliable identification of material parameters at various scales: the relevant computational approaches typically suffer from mathematical ill-posedness, numerical instability and need of artificial regularization, together with uncertain or insufficient input data. These difficulties have to be overcome by careful organization of experiments and various special problem-oriented algorithms – see [62] and [8]. The extensive use of brittle matrix composite

\* Corresponding author.

E-mail addresses: [vala.j@fce.vutbr.cz](mailto:vala.j@fce.vutbr.cz) (J. Vala), [kozak@ipm.cz](mailto:kozak@ipm.cz) (V. Kozák).

materials requires also appropriate computational models to describe, with adequate accuracy, their mechanical behaviour. From a micro-mechanical model some macroscopic constitutive equations are derived for intentionally or random oriented fibres by [54], accounting for such physical processes as matrix / fibre debonding and fibre rupture. One of possible ways is to adopt a discontinuous-like FE approach to a lattice model – see [7].

An alternative approach refers to special constitutive relations, inspired by continuum mechanics, where crack opening and contact surface sliding are included into the model of plastic damage, using smeared cracking by [28] and [29], together with mesh objective strain localization due to material softening, referring to the thermodynamically irreversible continuum damage mechanics, by [42], in particular that leading to a smeared representation of the crack path by [32]. At least for the practically significant application of self-compacting concrete, supported by both experimental methods and numerical simulations, smeared cracking can be combined with Monte Carlo simulations, which results in the Variational Multiscale Cohesive Method by [65], whose various implementations differs in the choice of basis functions.

Another approach to the same problems presents the eXtended Finite Element Method (XFEM briefly) by [44] and [33], covering both strong geometrical discontinuities (in function values) and weak ones (in gradients), with the aim of enrichment of the approximation space by all needed types if (especially locally) discontinuous functions, and similar approaches, derived from the Partition of Unity Method (PUM), namely the Partition of Unity Finite Element Method by [3], the Generalized Finite Element Method by [16], or the Discontinuous Galerkin XFEM, by [1]. Especially XFEM adds some degrees of freedom in relevant regions during the computation, typically along all curves and surfaces of discontinuities and in singular points, exploiting the Moving Least Squares technique: the usual extrinsic XFEM works with additional variables and functions, whereas the intrinsic XFEM developed by [26] tries to avoid them, only with one additional shape function in each relevant node. However, although no singularity exist at the tip of cohesive crack, the stresses obtained by differentiation of the displacement are not accurate, and cannot be used to predict accurately the growth of the tip see [24] and [42]. A possible approach to simulate the propagation of cracks is the application of softening material formulations to continuum elements leading to a smeared representation of the crack path. An alternative discrete approach implements the cohesive finite elements by [37]; in this case the crack path must be known a priori, or all element interfaces have to be taken into account, which forces many new degrees of freedom, accompanied also by the risk of non-physical reduction of effective stiffness.

The application of XFEM is able to suppress such drawbacks in the simulation of propagation of cohesive cracks; however, it must handle the non-existence of a sharp singularity at the crack tip, with more complicated derivation of required stresses from displacements. In general the complete computational model should involve the formation and propagation of cracks, their bridging by fibres, the loss of cohesion between fibres and matrix, their mutual sliding with friction and the fibre destruction; special functions are necessary e. g. for stress singularities in the case of crack opening and closing. The two-phase composite model of matrix and inclusion, based on the Eshelby solution and on the Mori-Tanaka homogenization scheme, can be adapted to the directional propagation of microcracks, generalized also for long fibres by [6] and [47]. Random spatial variability of material parameters can be handled using the stochastic simulation of damage cf. [18].

In this paper, exploiting a substantially extended a revised text of [72], we shall pay attention namely to the quasi-brittle damage, realistic for a large class of building materials and composites, with a primarily elastic behaviour. The presence of above sketched effects forces the implementation of some nonlocal strain–stress constitutive relation. Following [13,25,27,29,56], etc., we shall come out from the well-known Eringen model [20] and [21], although numerical results

referring to its pure version are not quite satisfactory, as observed by [60], and its ill-posedness has been recently discovered by [22], except the homogeneous Dirichlet problems and certain simplified 1-dimensional formulations cf. [74], contesting the incomplete existence results by [2]. The remedy suggested by [20] relies on the additive linear combination of the classical local and the nonlocal Eringen model; unlike this, we shall utilize the Eringen approach to the setting of the multiplicative damage factor only, as demonstrated by [29] heuristically.

## 2. A first model problem

For simplicity, to avoid technical difficulties, let us suppose that  $\Omega$  is a union of a finite number of domains with Lipschitz boundaries, whose exterior boundary  $\partial\Omega$  in  $\mathcal{R}^3$  consists of 2 disjoint parts  $\Theta$  (for homogeneous Dirichlet boundary conditions) and  $\Gamma$  (for non-homogeneous Neumann boundary conditions), whereas all interior boundaries, needed for matrix / particle interfaces, generate a set  $\Lambda$  (where certain nonlinear Robin conditions occur); let  $\Theta$  have a non-zero measure on  $\partial\Omega$  (to avoid insufficient support). Let us consider the Cartesian coordinate system  $x = (x_1, x_2, x_3)$  in  $\mathcal{R}^3$  and the time  $t \in I$  where  $I = [0, T]$  for some final time  $T$ ; the limit passage  $T \rightarrow \infty$  will be allowed, too. We shall also use the Hamilton operator  $\nabla = (\partial/\partial x_1, \partial/\partial x_2, \partial/\partial x_3)$ , and the dot symbols instead of  $\partial/\partial t$  for brevity. As the reference variable, let us choose the displacement  $u(x, t) = (u_1(x, t), u_2(x, t), u_3(x, t))$  for any  $x$  from  $\Omega$ , as well as from  $\partial\Omega$  or  $\Lambda$  (in the sense of traces), and arbitrary time  $t \in I$ . For a fixed time  $t$  and any admissible displacement  $v(x) = (v_1(x), v_2(x), v_3(x))$  let us introduce the strain tensor  $\varepsilon(v)$  in the form  $\varepsilon_{ij}(v(x)) = (v_{i,j}(x) + v_{j,i}(x))/2$  where  $i, j \in \{1, 2, 3\}$  and the stress tensor  $\sigma$  of the same type; any comma followed by an index  $k \in \{1, 2, 3\}$  ( $i$  or  $j$  here) must be understood as  $\partial/\partial x_k$  applied to the preceding variable.

We shall start with the heuristic formulation of a model problem, using the standard notations of the linearized theory of elasticity. Let us set the Cauchy initial condition  $u(.,0) = 0$  on  $\Omega$ . Moreover, let us consider some volume loads  $f(x, t) = (f_1(x, t), f_2(x, t), f_3(x, t))$  and some surface loads  $g(x, t) = (g_1(x, t), g_2(x, t), g_3(x, t))$  where  $x \in \Omega$ ,  $x \in \Gamma$  and  $t \in I$ . The physical principle of energy conservation can be then reduced to the Cauchy equilibrium condition on  $\Omega \times I$

$$\sigma_{ij,j} + f_i = 0 \tag{1}$$

for any  $i \in \{1, 2, 3\}$  and an Einstein summation index  $j \in \{1, 2, 3\}$ ; the Neumann boundary condition on  $\Omega \times I$  is

$$\sigma_{ij}n_j = g_i \tag{2}$$

with  $i$  and  $j$  as in (1), whereas the Dirichlet one degenerates to  $u = 0$  on  $\Theta \times I$ . Here  $\sigma_{ik} = \sigma_{ki}$  everywhere for arbitrary  $i, k \in \{1, 2, 3\}$ , as usual in the theory of Boltzmann continuum. The constitutive relation between  $\sigma$  and  $\varepsilon(u)$ , motivated by the classical Kelvin viscoelastic model (containing parallel Hooke and Newton components), on  $\Omega \times I$  reads

$$\sigma_{ij} = \alpha C_{ijkl} \varepsilon_{kl}(\dot{u}) + (1 - \mathcal{D}) C_{ijkl} \varepsilon_{kl}(u) \tag{3}$$

for any  $i, j \in \{1, 2, 3\}$  and Einstein summation indices  $i, j \in \{1, 2, 3\}$ ; here  $C_{ijkl} = C_{jikl} = C_{ijlk} = C_{klij}$  refer to 21 independent material characteristics in the empirical Hooke law (expressible using 2 Lamé coefficients for isotropic materials, or using the Young modulus and the Poisson ratio alternatively),  $\alpha$  forces some energy dissipation in such non-closed physical process and  $\mathcal{D}$  refers to the above announced damage factor, whose reasonable design determines both the well-posedness and the practical validity of the computational model.

Following [29] (slightly generalized, to enable the comparison with other approaches),  $\mathcal{D}$  in (3), as a function of  $t \in I$ , can be set as the maximal value of

$$\omega(l_{\mathcal{A}}(\sigma(.,t))_l) = \omega(l_{\mathcal{A}}(C(.,t)\varepsilon(u(.,t))_l);$$

here  $l_{\mathcal{A}}$  refers to the norm in  $\mathcal{R}^3$  and

$$\mathcal{A}(w(x)) = \int_{\Omega} \mathcal{K}(x, \tilde{x}) w(\tilde{x}) d\tilde{x}. \quad (4)$$

for any  $x \in \Omega$  and integrable functions  $\mathcal{K}$  (real-valued) and  $w$  ( $\mathcal{R}^3$ -valued) in the needed sense. In particular,  $\mathcal{K}$  can be taken as a radial basis function (RBF) (or its interpolation or approximation), as reviewed by [63]. Let us also notice that [22] needs to have  $\mathcal{K}$  as a symmetric positive kernel, whereas [58] formulates 5 requirements to  $\mathcal{K}$ , satisfied by the Gaussian error-like distributions by [23]

$$\mathcal{K}(x, x) = \exp(-|x-x|_3^2)/(4\eta))/((8\pi\eta)^{3/2})$$

automatically where the parameter  $\eta$  should be either set by appropriate experiments or evaluated from the theory of atomic lattice.

The approach of [38] and [39] relies on the theory of dislocations, Burgers vectors, etc., and constructs  $\mathcal{K}(x, x)$  using the Green functions of certain bi-Helmholtz equation, i. e. the generalized Helmholtz equation of the 4th order, exploiting the Bessel function depending on appropriate real constants, whose number can be reduced to 2 in the isotropic case – cf. [36] and [49]; this can be identified with the higher-order strain-gradient formulation in the thermodynamic framework by [41]. However, such considerations may be not realistic especially for concrete-like composites with a complicated non-deterministic structure in general.

Unlike this, [29] introduces

$$\mathcal{K}(x, x) = \exp(-|x - x|_3)/\rho(x)$$

(supplied by an additional normalization step); here  $\rho(x)$  (constant in the first guess) scales the internal length depending on  $|x-x|_3$  with the closest  $x \in \partial\Omega$ . The details of evaluation of  $\rho(x)$  are not unified: namely [29] takes  $\gamma(x)$  as a piecewise linear function, unlike its exponential improvement by [28]. As a quite different example, [56] refers to the (rather complicated) Wendland RBF of the 5th order; for some classes of still other choices (as bell- or conical-shape) cf. [57].

To see the damage progress utilizing  $\mathcal{D}$ , we need now to introduce  $\omega$  properly. Following [29], to force the objectivity, let us set  $w$  in (4) as a vector of principle stress values  $\sigma_k$  with  $k \in \{1, 2, 3\}$ , i. e.  $\sigma_{ij}v_{jk} = \sigma_k v_{ik}$ , using arbitrary indices  $i, k \in \{1, 2, 3\}$  and  $j \in \{1, 2, 3\}$  in the role of an Einstein summation index where  $v_{ik}$  generate an orthonormal matrix from  $\mathcal{R}^{3 \times 3}$  (on  $\Omega$  locally). Consequently we can take  $w$  in (4) as  $(\sigma_1, \sigma_2, \sigma_3)$ , to obtain certain  $\sigma_* = \mathcal{A}(w)$  on  $\Omega$ ; an admissible form of  $\mathcal{A}$  will be discussed later. An appropriate formula for the evaluation of  $\omega$  on  $\Omega$  is then

$$\omega(\sigma_*) = 1 - \exp\left(-\frac{\sigma_*/E - \varepsilon_0}{\varepsilon_f - \varepsilon_0}\right) \quad (5)$$

for  $\sigma_*/E \geq \varepsilon_0$ , zero otherwise; here  $E$  is the (always positive) Young modulus on  $\Omega$  and  $\varepsilon_0$  and  $\varepsilon_f$  are 2 dimensionless parameters (also positive in practice) controlling the peak stress and the slope of the softening part of the strain–stress dependencies.

An useful special relation of this type for an isotropic medium is presented in [29]:

$$\mathcal{A}(\sigma_1, \sigma_2, \sigma_3) = \sqrt{\sigma_{*1}^2 + \sigma_{*2}^2 + \sigma_{*3}^2}$$

where  $\sigma_{*1}$ ,  $\sigma_{*2}$  and  $\sigma_{*3}$  come from the right-hand side of (4) with scalar inputs  $\sigma_1$ ,  $\sigma_2$  and  $\sigma_3$ , whereas various choices of  $\mathcal{K}$  (standard averaging, distance-based averaging, etc.) are allowed. Thus, for certain reference  $\varepsilon_*$ , the linear elastic relation  $\sigma_* = E\varepsilon_*$  valid for  $\varepsilon_* \leq \varepsilon_0$  changes to

$$\sigma_* = E\varepsilon_0 \exp\left(-\frac{\varepsilon_* - \varepsilon_0}{\varepsilon_f - \varepsilon_0}\right)$$

in the case of stiffness decrease  $\varepsilon_* \geq \varepsilon_0$ , as evident from the illustrative Fig. 1.

Let us notice that the slight modification of (5) inserting the multiplicative factor  $1 - \zeta$  with a (usually small) positive  $\zeta < 1$  to its right-

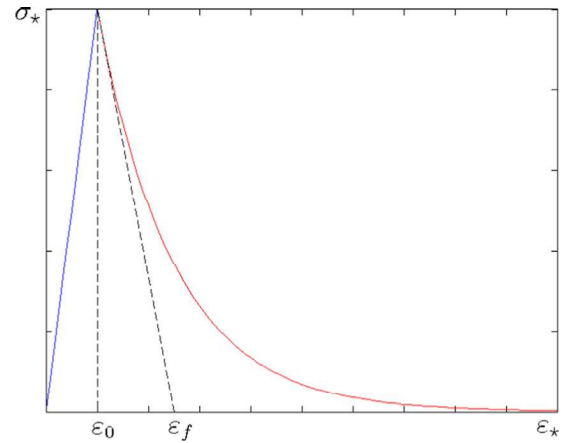


Fig. 1. Stress–strain curve with softening for an isotropic damage model by [29].

hand side, prevents all attempts to explain the total loss of stiffness from the linearized theory. This might be seen as a computational trick only; however, the initiation and development of macroscopic cracks can be expected in this case, as introduced in Section 4.

More generally (in the brief notation), we have  $\mathcal{D} = \mathcal{E}(u)$  finally, with a rather complicated mapping  $\mathcal{E}$ . Assuming  $\zeta$  as above, we receive  $\mathcal{D} \in [\zeta, 1]$  in all cases. In such sense we shall understand the modification of the principle of energy conservation (6), implementing all constitutive relations to obtain (7).

To complete the formulation of a model problem, (6) must be supplied by appropriate constitutive relations for  $\sigma$ ,  $\mathcal{D}$  and  $\mathcal{F}$ , coupling these quantities with  $u$ . In the 1st case we are allowed to use the classical linear Hooke law  $\sigma = C\varepsilon(u)$  on  $\Omega \times I$  with  $C \in L^\infty(\Omega)^{(3 \times 3) \times (3 \times 3)}$ , the announced symmetry, usual in the Boltzmann (non-polar) continuum, means  $C_{ijkl} = C_{jikl} = C_{ijlk} = C_{klij}$  for any  $i, j, k, l \in \{1, 2, 3\}$ . Let us notice that this (in general) admits 21 independent scalar components of  $C$  from  $L^\infty(\Omega)$ , whereas the additional assumption of isotropy leads to their reduction to 2 Lamé coefficients. One more assumption  $C_{ijkl}a_{ij}a_{kl} \geq ca_{ij}a_{ij}$  for all  $a \in \mathcal{R}^{3 \times 3}_{sym}$  with  $i, j, k, l$  taken as Einstein summation indices and with a positive  $c$  independent of the choice of  $x \in \Omega$  will be needed later; the existence of a positive  $\bar{c}$  satisfying  $C_{ijkl}a_{ij}b_{kl} \leq \bar{c}a_{ij}b_{ij}$  for all  $a, b \in \mathcal{R}^{3 \times 3}_{sym}$  is evident. Thus  $\|v\|_{\mathcal{E}}^2 = \|v\|^2 + |\varepsilon(v)|_{\mathcal{E}}^2$  with  $|\varepsilon(v)|_{\mathcal{E}} = |C^{1/2}\varepsilon(v)|$  for each  $v \in V$  generates still another norm in  $V$ .

It is natural to assume  $u \in L^2(I, V, V^*)$  (thus  $u \in L^2(I, V)$ ,  $\dot{u} \in L^2(I, V^*)$ ,  $\nabla u \in L^2(H^2)$ ,  $\varepsilon(u) \in L^2(H^2_{sym})$ , etc.),  $\sigma \in L^2(H^2_{sym})$  and  $\mathcal{D} \in [0, 1 - \zeta]$  with some prescribed real non-negative  $\zeta < 1$ , together with the volume forces  $f \in L^2(I, H)$  and surface forces  $g \in L^2(I, Z_\Gamma)$ . Thus the principle of energy conservation reads

$$\alpha(\varepsilon(v), \dot{\sigma}) + (\varepsilon(v), (1 - \mathcal{D})\sigma) = (v, f) + (v, g)_\Gamma + (\delta v, \mathcal{F})_\Lambda \quad (6)$$

on  $I$  for any virtual displacements  $v \in V$ ; here  $\delta$  refers to the possible matrix / particle jumps in traces of  $v$  and  $\mathcal{F} \in L^2(I, Z_\Lambda)$  introduces the interface tractions. The remaining positive factor  $\alpha$  occurs in the 1st left-hand-side additive terms only, forcing some energy dissipation in such non-closed physical process. The homogeneous Cauchy initial condition  $u(., 0) = (0, 0, 0)$  on  $\Omega$  is supposed; therefore it is reasonable to consider the zero-valued  $f(., 0)$  and  $g(., 0)$ , too, with some final values  $f(., T_0)$  and  $g(., T_0)$  with  $T_0 < T$ , unchanged for any  $t \in [T_0, T]$ .

The 2nd case must be handled using the nonlocal approach. Let us consider a kernel  $\mathcal{K} \in L^2(\Omega \times \Omega)$  and an operator  $\mathcal{A}: L^2(\Omega) \rightarrow L^2(\Omega)$ , introduced by (4); for an isotropic material it can take the very special form by [41], working with 2 additional material coefficients again. Such operator is always compact, as verified (using 2 independent approaches) by [15], pp. 80 and 81. This result can be extended to

$\varepsilon(v) \in H^2$ , replacing  $w \in L^2(\Omega)$  (taking the symmetry of  $\varepsilon$  into account, too), naturally, following [22], as well as to  $C\varepsilon(v) \in H^2$ . Let us consider a continuous bounded non-decreasing function of a non-negative real variable returning values from  $[0, 1 - \zeta]$  such that  $\omega(a) = 0$  for sufficiently small  $a \geq 0$  (where no damage occurs yet). To express the damage progress, using  $\sigma, \varepsilon(u) \in L^2(I, H^2)$ , for any fixed  $t \in I$  then  $\mathcal{D}$  in (6) can be set, following [29], as the maximal value of

$$\omega(\mathcal{D}(\sigma(\cdot, t))|_\varepsilon) = \omega(\mathcal{D}(C(\cdot)\varepsilon(u(\cdot, t)))|_\varepsilon)$$

with  $t \in [0, t]$  where  $|\cdot|_\varepsilon$  denotes the standard norm in  $\mathcal{H}_{sym}^{3 \times 3}$ ; slight modifications, replacing  $|\cdot|_\varepsilon$  by some alternative norm, and / or switching to another rotating local orthogonal coordinate system, e. g. working with the triples of principal strains and stresses by [27], are possible.

In the 3rd case we are allowed to express  $\mathcal{F}$  by its components as  $\mathcal{F}_i = \phi_{ij}(\delta u)\delta u_j$  for any  $i \in \{1, 2, 3\}$ , using the Einstein summation with  $j \in \{1, 2, 3\}$ , assuming that all real continuous cohesion functions  $\phi_{ij}$  of 3 real non-negative variables satisfy  $\phi_{ij}(0, 0, 0) = 0$  and the spectral norm of  $\phi(a)$  in  $\mathcal{H}^{3 \times 3}$  has its upper bound  $\kappa$  independent of  $a \in \mathcal{H}^3$ ; moreover, the components of  $\phi(a)$  tend to zero with a sufficiently large norm of  $a$  in  $\mathcal{H}^3$  in practice (because all cohesion vanishes on large gaps). Let us remark that the components of  $\mathcal{F}$  are frequently formulated in some local coordinate system, related to the normal and tangential directions on  $\Lambda$ , which simplifies these relations namely in the isotropic case, as discussed by [56], deriving  $\delta u$  from differentiation of certain interface potential. Thus we can rewrite (6) as

$$\begin{aligned} & \alpha(\varepsilon(v), C\varepsilon(\dot{u})) + (\varepsilon(v), (1 - \mathfrak{E}(u))C\varepsilon(u)) \\ & = (v, f) + \langle v, g \rangle_\Gamma + \langle \delta v, \phi(\delta u) \rangle_\Lambda \end{aligned} \quad (7)$$

on  $I$  for any  $v \in V$ .

### 3. Existence and convergence properties

We shall use the standard notation of Lebesgue, Sobolev, Bochner, etc. (abstract) function spaces, as introduced by [61] and [71]. Namely we shall need the Hilbert spaces  $H = L^2(\Omega)^3$ ,  $V = \{v \in W^{1,2}(\Omega)^3, v = (0, 0, 0) \text{ on } \Theta\}$  and  $Z = L^2(\partial\Omega \cup \Lambda)^3$  and the corresponding scalar products:  $(\cdot, \cdot)$  both in  $H$  and  $H \times H$ ,  $\langle \cdot, \cdot \rangle$  in  $Z$  and  $\langle \cdot, \cdot \rangle_\Gamma$  or  $\langle \cdot, \cdot \rangle_\Lambda$  the same ones restricted to  $Z_\Gamma = L^2(\Gamma)^3$  or  $Z_\Lambda = L^2(\Lambda)^3$ . Later we shall need also some symbols for standard norms, namely  $|\cdot|$  both in  $H$  and  $H \times H$ ,  $\|\cdot\|$  in  $V$ ,  $|\cdot|_\Gamma$  and  $|\cdot|_\Lambda$  in  $Z_\Lambda$ . We shall use the upper star symbols for dual spaces,  $\mathfrak{C}$  for continuous embeddings,  $\Subset$  for compact embeddings and  $\cong$  for the identification of a space with its dual (following the Riesz representation theorem). Then in the Gelfand triple  $V \subset H \cong H^* \subset V^*$  both inclusions are dense, with the guaranteed embedding  $W^{1,2,2}(I, V, V^*) \subset C(I, H)$ . Moreover  $L^2(I, V^*) \cong L^2(I, V^*)$  holds (thus  $L^2(I, V)$  is reflexive), together with other useful relations  $H \Subset V$  (the Sobolev embedding theorem),  $Z \Subset V$  (the trace theorem), forcing  $|\cdot|_\Gamma \leq \mathfrak{T}|\cdot|$ ,  $|\cdot|_\Lambda \leq \mathfrak{T}|\cdot|$  for any  $v \in V$  with a positive  $\mathfrak{T}$  independent of  $v$ , and  $W^{1,2,2}(I, V, V^*) \Subset L^2(I, X)$  with  $X \in \{H, Z\}$  (the Aubin - Lions lemma). Clearly  $\|\cdot\|^2 = |\cdot|^2 + |\nabla v|^2$  for any  $v \in V$ ; an alternatively norm in  $V$  is generated by  $|\varepsilon(v)|^2$  because  $|\varepsilon(v)|^2 \leq |\nabla v|^2 \leq \|\cdot\|^2$  and  $|\varepsilon(v)|^2 \geq \mathfrak{K}|\cdot|^2$  with a positive  $\mathfrak{K}$  independent of  $v$  (the Korn inequality).

Let us remark that the hypothetical reverse approach, starting from (6) or (7), with the aim to obtain the strong formulation, would be more delicate: it must be understood in the distributive sense, or needs some non-trivial additional regularity assumptions. However, we shall need the following regularization (compactness) property of  $\mathcal{A}$ , taken from  $L^2(\Omega \times \Omega)$ , following (4): if  $\{w^k\}_{k=1}^\infty$  is some sequence converging weakly to  $w$  in  $H$  then, taking  $w = \mathcal{A}(w)$  and  $\hat{w}^k = \mathcal{A}(w^k)$ , up to a subsequence,  $\{w^k\}_{k=1}^\infty$  converges strongly to  $w$  in  $H$ . Indeed,  $\{w^k(x)\}_{k=1}^\infty$  converges locally to  $w(x)$  for almost every  $x \in \Omega$ ; by the Lebesgue dominated convergence theorem is then sufficient to verify the boundedness of  $\{w^k\}_{k=1}^\infty$  in  $H$ , which is guaranteed by the weak

convergence (thus also the boundedness) of  $\{w^k\}_{k=1}^\infty$ , by the Fubini theorem (on multiple integrals) and by the Cauchy - Schwarz inequality; for all details see [15], p. 81. An important consequence is that for a continuous  $\omega$  (not just for the special one by (5)) and for any fixed  $t \in I$  we are able to guarantee the strong convergence of  $\{\mathfrak{E}(u(\cdot, t))\}_{k=1}^\infty$  to  $\mathfrak{E}(u(\cdot, t))$  provided that  $\{u^k(\cdot, t)\}_{k=1}^\infty$  converges weakly to some  $u(\cdot, t)$  in  $V$ .

Let us divide  $I$  into a finite number  $m$  of subsets  $I_s^m = \{t \in I: (s-1)\tau < t \leq s\tau\}$  with  $s \in \{1, \dots, m\}$ , with the final aim  $m \rightarrow \infty$ ;  $\tau(m) = T/m$  is considered here, omitting its argument  $m$  for brevity. Let us consider the Clément quasi-interpolation  $f^m$  of  $f$  in  $L^2(I, H)$  and  $g^m$  of  $g$  in  $L^2(I, Z_\Lambda)$ , defined as

$$\begin{aligned} f^m(t) &= \tau^{-1} \int_{(s-1)\tau}^{s\tau} f(\tilde{t}) d\tilde{t} \\ g^m(t) &= \tau^{-1} \int_{(s-1)\tau}^{s\tau} g(\tilde{t}) d\tilde{t} \end{aligned}$$

for  $t \in I_s^m$ ,  $s \in \{1, \dots, m\}$ . For an unknown  $u$  we can also introduce some  $u^m$ ,  $\bar{u}^m$  and  $\tilde{u}^m$  as  $u^m(t) = u_{s-1}^m + (t - (s-1)\tau)(u_s^m - u_{s-1}^m)$  (linear Lagrange splines),  $\bar{u}^m(t) = u_s^m$  (standard simple functions) and  $\tilde{u}^m(t) = u_{s-1}^m$  (retarded simple functions), which generates 3 different types of the Rothe sequences;  $u_0^m = (0, 0, 0)$ .

The discrete variant of (7) for a fixed  $m$  then reads

$$\begin{aligned} & \alpha(\varepsilon(v), C\varepsilon(\dot{u}^m)) + (\varepsilon(v), (1 - \mathfrak{E}(\tilde{u}^m))C\varepsilon(\bar{u}^m)) \\ & = (v, f^m) + \langle v, g^m \rangle_\Gamma + \langle \delta v, \phi(\delta \tilde{u}^m) \rangle_\Lambda \end{aligned} \quad (8)$$

on  $I$ ; its linearity is evident from its form

$$\begin{aligned} & \alpha(\varepsilon(v), C\varepsilon(u_s^m - u_{s-1}^m)) \\ & + \tau(\varepsilon(v), (1 - \mathfrak{E}(u_{s-1}^m))C\varepsilon(u_{s-1}^m)) \\ & = \tau(v, f_s^m) + \tau \langle v, g_s^m \rangle_\Gamma + \tau \langle \delta v, \phi(\delta u_{s-1}^m) \rangle_\Lambda, \end{aligned} \quad (9)$$

rewritten step-by-step on  $I_s^m$ . Let us set  $v = u_s^m$  in (9). Using the Cauchy - Schwarz inequality, taking an arbitrary positive  $\varpi$ , we have

$$\begin{aligned} & (\varepsilon(u_s^m), C\varepsilon(u_s^m)) = |\varepsilon(u_s^m)|_\mathfrak{C}^2 \geq c\mathfrak{K} \|u_s^m\|^2 \\ & 2(\varepsilon(u_s^m), C\varepsilon(u_s^m - u_{s-1}^m)) \\ & = |\varepsilon(u_s^m)|_\mathfrak{C}^2 + |\varepsilon(u_s^m - u_{s-1}^m)|_\mathfrak{C}^2 - |\varepsilon(u_s^m)|_\mathfrak{C}^2, \\ & |\varepsilon(u_s^m - u_{s-1}^m)|_\mathfrak{C}^2 \geq c\mathfrak{K} \|u_s^m - u_{s-1}^m\|^2, \\ & 2(u_s^m, f_s^m) \leq 2|u_s^m| |f_s^m| \leq \varpi |u_s^m|^2 + \varpi^{-1} |f_s^m|^2, \\ & 2\langle u_s^m, g_s^m \rangle_\Gamma \leq 2|u_s^m|_\Gamma |g_s^m|_\Gamma \leq 2\mathfrak{T} \|u_s^m\| |g_s^m|_\Gamma \\ & \leq \varpi \mathfrak{T}^2 \|u_s^m\|^2 + \varpi^{-1} |g_s^m|_\Gamma^2, \\ & 2\langle \delta u_s^m, \delta u_{s-1}^m \rangle_\Lambda \leq 2\kappa |\delta u_s^m|_\Lambda |\delta u_{s-1}^m|_\Lambda \\ & \leq 2\kappa \mathfrak{T}^2 \|u_s^m\| \|u_{s-1}^m\| \leq \kappa \mathfrak{T}^2 (\|u_s^m\|^2 + \|u_{s-1}^m\|^2). \end{aligned}$$

Thus for any fixed  $r \in \{1, \dots, m\}$ , summing over  $s \in \{1, \dots, r\}$ , we receive

$$\begin{aligned} & \alpha c \mathfrak{K} \|u_r^m\|^2 + \alpha c \mathfrak{K} \sum_{s=1}^r \|u_s^m - u_{s-1}^m\|^2 \\ & + \tau M(\varpi) \sum_{s=1}^r \|u_s^m\|^2 \\ & \leq \tau \varpi^{-1} \sum_{s=1}^r |f_s^m|^2 + \tau \varpi^{-1} \sum_{s=1}^r |g_s^m|_\Gamma^2 \end{aligned} \quad (10)$$

where  $M(\varpi) = 2(1 - \zeta)c\mathfrak{K} - (1 + \mathfrak{T}^2)\varpi$ . Since, up to some multiplicative constants, the right-hand-side additive terms of (10) are just

the squares of norms of  $f^m$  in  $L^2(I, H)$  and of  $g^m$  in  $L^2(I, Z)$  and those left-hand-side ones correspond to the squares of norms of  $\bar{u}^m$  in  $L^\infty(I, V)$  and of  $\sqrt{\tau} \dot{u}^m = \sqrt{\tau} (\bar{u}^m - \tilde{u}^m)$  in  $L^2(I, V)$ , we have  $\{\bar{u}^m\}_{m=1}^\infty$  and  $\{\tilde{u}^m\}_{m=1}^\infty$  bounded in  $L^2(I, V)$  for any  $M(\varpi) > 0$  directly; otherwise this follows from the discrete Gronwall lemma – cf. [61], p. 26, and [15], p. 99. Moreover, using the notation  $[\cdot]$  for the integration over  $I$  here, reformulating (8) with  $w \in L^2(I, V)$  as

$$\begin{aligned} & \alpha[(\varepsilon(w), C\varepsilon(\dot{u}^m))] \\ &= -[(\varepsilon(w), (1 - \mathfrak{E}(\tilde{u}^m))C\varepsilon(\bar{u}^m))] \\ &- [(w, f^m)] - [(w, g^m)], \end{aligned}$$

using the same estimates as above, we can see that the upper bound for  $[(w, \dot{u}^m)]$  is just the norm of  $w$  in  $L^2(I, V)$ , multiplied by a positive constant; thus we have  $\{\dot{u}^m\}_{m=1}^\infty$  bounded in  $L^2(I, V^*)$ , too. Consequently the Eberlein - Shmul'yan theorem by [15], p. 67, implies, up to subsequences, the weak convergence of  $\{\bar{u}^m\}_{m=1}^\infty$  and  $\{\tilde{u}^m\}_{m=1}^\infty$  to some  $\bar{u}$  and  $\tilde{u}$  in  $L^\infty(I, V)$  and of  $\{\dot{u}^m\}_{m=1}^\infty$  to some  $u^\times$  in  $L^\infty(I, V^*)$ .

To verify that both  $\bar{u}$  and  $\tilde{u}$  can be identified with  $u$ , as well as  $u^\times$  with  $\dot{u}$ , let us start with the obvious estimate

$$\begin{aligned} \|u - \bar{u}\| &\leq \|u - u^m\| + \|u^m - \bar{u}^m\| + \|\bar{u}^m - \bar{u}\| \\ &= \|u - u^m\| + \tau\|\dot{u}^m\| + \|\bar{u}^m - \bar{u}\| \end{aligned}$$

on  $I$ . Passing  $m \rightarrow \infty$ , the 2nd additive term vanishes due to the boundedness of  $\sqrt{\tau}\|\dot{u}^m\|$  and the 1st and 3rd ones tend to zero due to the convergence properties in  $L^2(I, H) \subset L^\infty(I, H)$ ; this identifies  $u$  with  $\bar{u}$ . The same arguments can be repeated to identify  $\bar{u}$  with  $\tilde{u}$ , too. Moreover, the integration by parts

$$\begin{aligned} [(w, u^\times)] &= \lim_{m \rightarrow \infty} [(w, \dot{u}^m)] \\ &= - \lim_{m \rightarrow \infty} [(\dot{w}, u^m)] = -[(\dot{w}, u)] \end{aligned}$$

is valid for any  $w$  from the space of distributions  $C_0^\infty(I)$ ; this is sufficient to identify  $u^\times$  with  $\dot{u}$ , as derived by [9], p. 49. Thanks to the compact embeddings we obtain the convergence properties for  $m \rightarrow \infty$ :  $\{\bar{u}\}_{m=1}^\infty$  has its weak limit  $u$  in  $L^\infty(I, V)$ , and its strong limit  $u$  in  $L^2(I, X)$  for  $X \in \{H, Z\}$ , the same holds for  $\{\tilde{u}\}_{m=1}^\infty$ , whereas  $\{\dot{u}\}_{m=1}^\infty$  has its weak limit  $\dot{u}$  in  $L^2(I, V^*)$ . Therefore, taking the continuity of  $\omega$  and  $\phi$  into account, we are allowed to come from (8) to (7).

Let us remark that the presence of  $\mathfrak{E}(\cdot)$  in (9) and (8) brings significant difficulties to most consideration on the uniqueness, regularity, etc., of the solution of (7), including its quasi-static character, as usual in the (both physically and geometrically) linearized elasticity; one can expect some disturbing effects namely for  $\zeta$  decreasing to zero, corresponding to the total loss of stiffness of some part of  $\Omega$ . For example, the artificial evolutionary term with  $\alpha > 0$  should vanish thanks to the setting  $v = u_s^m - u_{s-1}^m$ , the difference of (9) and the same equation with  $s - 1$  instead of  $s$ , provided that  $s > 1$ . If  $f$  and  $g$  are still (nearly) unchanging in time, then the decisive right-hand-side additive term, stemming from (9), reads  $\tau(\varepsilon(u_s^m - u_{s-1}^m), (\mathfrak{E}(u_{s-2}^m) - \mathfrak{E}(u_{s-1}^m))C\varepsilon(u_{s-1}^m))$ . However, to obtain  $|\varepsilon(\dot{u}^m)|$  in (8) and  $|\varepsilon(\dot{u})|$  in (7) decreasing to zero, one needs additional continuity assumptions, related to a rather complicated general form of  $\mathfrak{E}(\cdot)$ .

#### 4. A second model problem

Let us remind that our previous considerations are valid literally only if, from the macroscopic point of view, in the structure of a deformable body, only a (typically cementitious) matrix and some finite particles (usually stiffening ones, e. g. metal fibres), using the common notation  $\Omega$  can be distinguished; the opening / closing of macroscopic cracks is allowed only on internal interfaces  $\Lambda$ , whereas the effect of microcracking relies on certain damage factor; this is compatible with [29] and [56]. We shall now demonstrate that the same approach can handle initiation and development of macroscopic cracks inside  $\Omega$ , too, using

nearly the same existence and convergence theory.

Up to now,  $\Omega$  here consists of a finite number of certain simply connected subdomains  $\Omega_*$ , whose boundaries in  $\mathcal{R}^3$  generate  $\Lambda$ ,  $\Theta$  and  $\Gamma$ . Moreover, following [37], let us consider the decomposition of  $\Omega_*$  to a finite number of subdomains  $\Omega_*^\times$ . Let us assume that all such subdomains have Lipschitz boundaries and the properties of their interfaces are prescribes in the same sense as above, i. e. not only for matrix / particle interfaces, but also for certain mutual grain ones. Thus  $\Theta$  and  $\Gamma$  generated by  $\Omega_*^\times$  (instead of  $\Omega_*$ ) stay unchanged, whereas  $\Lambda$  can be much more rich. Consequently all derivations of Section 3 can be performed with the analogous results. The more detailed analysis of such configurations with several examples have been prepared for [73] recently.

#### 5. Some generalizations

Let us start with the remark that, being ready to overcome some technical difficulties in proofs, numerous assumptions in our model problem could be weakened, e. g. the choice of  $f$  and  $g$  would be able to use the embeddings  $L^{(6-\varepsilon)}(\Omega) \in V$  (the Sobolev embedding theorem) and  $L^{4-\tilde{\varepsilon}}(\Gamma) \in V$  (the trace theorem) for any positive  $\varepsilon$  and  $\tilde{\varepsilon}$  instead of those with  $\varepsilon = 4$  for  $H$  and  $\tilde{\varepsilon} = 2$  for  $Z$ ; even the boundary of  $\Omega$  need not to be just the Lipschitz one, as analyzed by [10], generalizing the deep classical results of [46]. Still other generalizations, e. g. the linear growth of selected material characteristics instead of their boundedness, could be enabled using the results of [61], pp. 7, 201, 210 and 213, applying the weak star convergence, the formal introduction of very weak solutions and the Alaoglu - Bourbaki theorem (or the Banach selection principle), some general dualities instead of scalar products above, etc., although some complicated non-constructive proof steps, combining the properties of Rothe sequences with the Faedo - Galerkin arguments, obstruct the development of relevant computational algorithms.

Most extensive calculations concentrate on the matrix / particle interfaces and in their vicinity. To avoid this phenomenon, various continuum “smeared crack” approaches have been developed; the concepts and history of such research activities from the late 1960s to recent achievements can be assessed by [4], [55] and [74]. In some very simplified formulations more numerical stable exact or fundamental solutions can be implemented than those generated by Green functions, e. g. in the special problem of [40], coupling the Timoshenko beam on elastic medium with the Eringen model of nonlocal Euler - Bernoulli nanobeams. The cooperation of plasticity and damage is also available, following [53].

Nevertheless, the theory of linear elasticity in the simple quasi-static context as the basis of all our considerations has some limitations, namely for real physical processes far from such simplification, generating various nonlinear contributions to corresponding differential equations. Thus the implementation of infinitely many potential crack surfaces, as well as the total loss of stiffness due to microcracking, does not seem to be overcome in a simple way.

Alternative research directions rely on the computational peridynamics, avoiding all gradient evaluations – cf. [19], [31] and [43], or on statistical physics, handling extremal dynamics in random threshold systems – see [59]. Numerous open questions still occur in the case of multiple scale bridging, i. e. of the computational homogenization at several (typically macro- and micro-) levels, namely for the non-periodic problems.

#### 6. Assertion of XFEM

Computational analysis of initiation and time development of fracture in brittle and quasi-brittle materials and composites needs to handle i) weak discontinuities, such as material interfaces, ii) strong discontinuities, related to cracks, and iii) near-tip behaviour of basic characteristics of (elastic, plastic, etc.) fracture mechanics. This

represents a serious problem, in addition to those connected with the convergence of Rothe sequences, as discussed above; for extensive historical remarks cf. [67].

Namely [5] relies on the strain smoothing technique, including finite order piecewise polynomials, applied to simple elements, divided into subcells. [12] pays attention to an important partial problem of effective computation of integrals of polynomials over finite-dimensional simplices and general polytops, up to software implementation details. A special hexahedral cutting algorithm for the 3-dimensional geometrical configuration is designed and implemented in [14]. [17] introduces the so-called Finite Cell Method (FCM) as certain combination of the (in general) higher-order FEM and the fictitious domain technique, with application just to tetrahedral grids. For the tetrahedral version of FCM, [64] develops a flexible ad hoc integration technique. [30] attempts to extend such approach to arbitrarily broken elements, connected with various modifications of PUM in the sense of [66], as the Generalized Finite Element Method or XFEM (as introduced above); optimization of the Gauss - Legendre quadrature points and weights becomes then a rather complicated auxiliary problem. In particular, the detailed results on generalized Gaussian rules on arbitrary (2-dimensional) polygons are derived in [51] and [50]. Three general approaches are employed to handle integrals of homogeneous functions over arbitrary polytops in [11]: a) tessellation of the domain into simplices, b) application of the generalized Stokes theorem to reduce the volume integral to a surface one, c) utilization of some moment fitting method. Useful results on multilinear and quasilinear forms with homogeneous polynomials come from [34]. An alternative approach of [45], starting with orthogonal polynomials, generates some other classes of weighted quadrature rules.

Switching back to (9), upgraded due to the considerations from Section 4, we are able to convert it into the form

$$\begin{aligned} & \alpha(\varepsilon(v_h), C\varepsilon(u_{hs}^m - u_{hs-1}^m)) \\ & + \tau(\varepsilon(v_h), (1 - \mathcal{E}(u_{hs-1}^m))C\varepsilon(u_{hs-1}^m)) \\ & = \tau(v_h, f_s^m) + \tau(v_h, g_s^m) \quad (11) \\ & + \tau(\delta v_h, \phi(\delta u_{hs-1}^m))_\Lambda \end{aligned}$$

on  $I_s^m$  ( $s \in \{1, \dots, m\}$ ,  $m \in \{1, 2, \dots\}$  again), for all  $v_h$  from certain  $V_h$ . Here  $h$  is some positive number, characterizing the element size in the FEM decomposition of  $\Omega$ , thus the limit passage  $h \rightarrow 0$  is needed;  $V_h$  is then an appropriate approximation of  $V$ , converging to  $V$  in some reasonable sense, especially in the norm

$$\lim_{h \rightarrow 0} \|v_h - v\| = 0 \quad (12)$$

for any  $v \in V$  provided that  $V_h \subset V$ . Consequently  $u_{hs}^m$  should be found in  $V_h$ , too. More generally, (12) can be modified using  $v_h^*$  instead of  $v_h$ , with certain image  $v_h^*$  of  $v_h \in V_h$  into  $V$  such that

$$\lim_{h \rightarrow 0} \|v_h^* - v\| = 0. \quad (13)$$

Various XFEM and similar approaches differs in the choice of  $V_h$  for (11) and its potential modification (robust, effective and non-expensive if possible) with increasing  $s$ , i. e. in the adaptive mesh and choice of test functions strategy.

Let us remind that (3) can be understood as certain regularization of progressive microcracking in above mentioned materials in order to obtained objective results; for monotonic loading the steady-state version of (3) relies on its vanishing 1st right-hand-side additive term. In such sense a modified nonlocal regularization method described in [27] that takes the stress state into account has been used as a default nonlocal approach for our solution. The question arises to try to combine some advantages of nonlocal approach and a modified finite element method. The simple and uncomplicated solution was used for the numerical modelling in the following section, referring to the implementation of the two-dimensional XFEM application containing

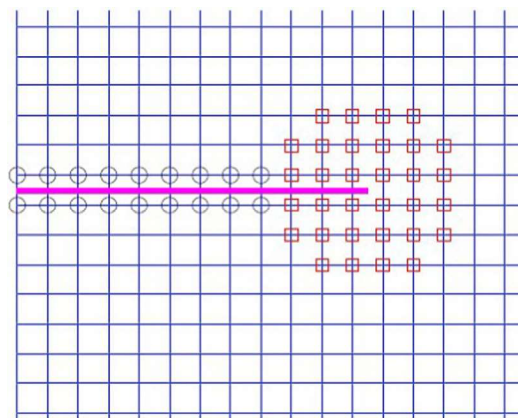


Fig. 2. Schematic diagram of crack propagation, stress in elements in enriched zone is determined via damage model.

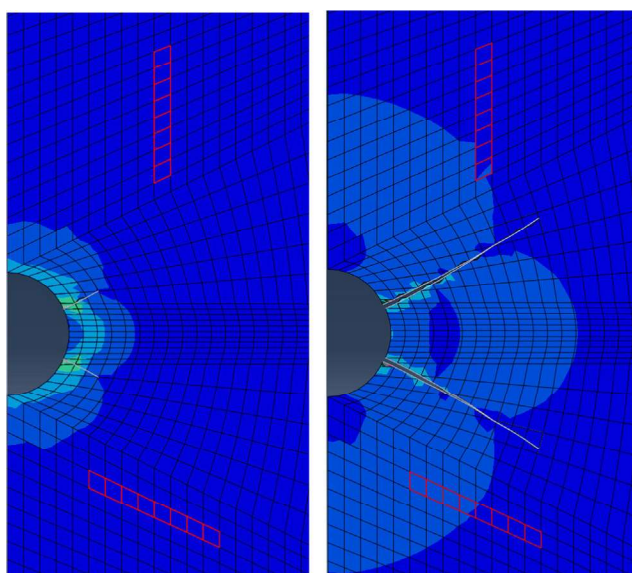


Fig. 3. Modelling of crack propagation applying the XFEM approach.

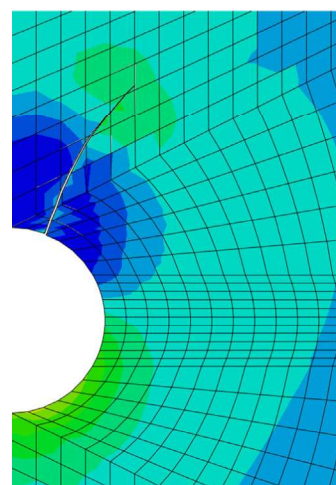


Fig. 4. Modelling of crack propagation for low value of damage parameter.

single or multiple cracks. In comparison to the classical finite element method, XFEM provides significant benefits in the numerical modelling, based on the enrichment of the FE model with additional degrees of freedom that are tied to the nodes of the elements intersected by the

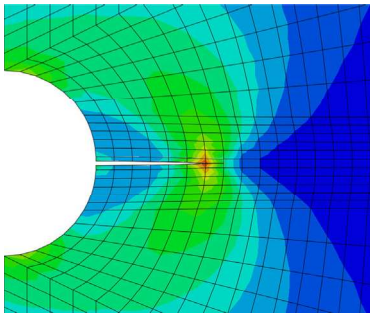


Fig. 5. Modelling of crack propagation for exponential damage parameter.

crack, e. g. on a special adaptive choice of  $V_h$  respecting (13), see Fig. 2.

## 7. Numerical computations

To demonstrate the practical implementation of most considerations from previous sections in some details, let us introduce the 2-dimensional crack propagation in a steel fibre reinforced cementitious specimen, using the above introduced quasi-static approach together with the XFEM technique and user implemented subroutine for Abaqus. Crack initiation and growth was tested in a plate with hole, where the uniform stress was applied. To describe the material, the following data for modelling were used: elastic modulus of the hardened paste  $E = 3.2$  GPa, Poisson constant  $\mu = 0.3$ , tensile strength  $\sigma_* = 10$  MPa; elastic modulus of steel fibres  $E = 190$  GPa, Poisson constant  $\mu = 0.3$ .

Some crack development is visible on Fig. 3 showing the results of modelling of crack propagation by XFEM. For computational modelling, a specimen with cementitious matrix and steel fibre has been chosen. Both figures demonstrates the planar crack propagation in a body with fibres. The left figure shows the crack propagation passing the stiffening fibres, the second one the similar case with different shear moduli (2x higher in the horizontal direction). The stiffening effect of fibres plays a significant role for direction of crack propagation.

Another crack development is presented by Figs. 4 and 5 for simple combination of above mentioned approaches, which is nonlocal and XFEM approach. Fig. 4 describes the situation for damage parameter  $\mathcal{D}$  below 0.1, Fig. 5 was obtained for its exponential dependence varying from 0.1 to 0.3.

## 8. Conclusion

The extensive use of fibre reinforced cementitious materials requires appropriate computational models to describe, with adequate accuracy, their mechanical behaviour. A possible choice of such model has been introduced in this paper, including the development of both micro- and macrocracks, working with the adaptive XFEM discretization modified with damage law, mainly for monotonic loading in elastic visco-plastic regime has been introduced in this paper. Its mathematical verification has been discussed, including numerous references to still open problems. Simplified numerical computations demonstrate some advantages of such approach for engineering practice, although its deeper analysis, covering more complex 3-dimensional simulations, can be seen as the research challenge for the near future.

## Acknowledgment

The authors appreciate the support from the projects i) of Ministry of Education, Youth and Sports AdMaS UP (Advanced Materials, Structures and Technologies), National Sustainability Programme I, LO 1408, Czechia, and ii) of the specific university research at Brno University of Technology FAST-S-19-5878, Czechia.

## References

- [1] C. Aduloju, T.J. Truster, A variational multiscale discontinuous Galerkin formulation for both implicit and explicit dynamic modeling of interfacial fracture, *Comp. Meth. Appl. Mech. Engrg.* 343 (2019) 602–630.
- [2] S. Altan, Existence in nonlocal elasticity, *Arch. Mech.* 41 (1989) 25–36.
- [3] I. Babuška, J.M. Melenk, The partition of unity method, *Int. J. Num. Meth. Engrg.* 40 (1997) 727–758.
- [4] R. de Borst, Fracture in quasi-brittle materials: a review of continuum damage-based approaches, *Eng. Fract. Mech.* 69 (2002) 95–112.
- [5] S.P.A. Bordas, S. Natarajan, P. Kerfriden, Ch.E. Augarde, D.R. Mahapatra, T. Rabczuk, S. Dal Pont, On the performance of strain smoothing for quadratic and enriched finite element approximations (XFEM/GFEM/PUFEM), *Int. J. Num. Meth. Engrg.* 86 (2011) 637–666.
- [6] L. Bouhala, A. Makradi, S. Belouettar, H. Kiefer-Kamal, P. Frères, Modelling of failure in long fibres reinforced composites by X-FEM and cohesive zone model, *Composites B* 55 (2013) 352–361.
- [7] R. Brighenti, D. Scorza, Numerical modelling of the fracture behaviour of brittle materials reinforced with unidirectional or randomly distributed fibres, *Mech. Mater.* 52 (2012) 12–27.
- [8] V. Buljak, G. Cocchetti, G. Maier, Calibration of brittle fracture models by sharp indenters and inverse analysis, *Int. J. Fract.* 184 (2013) 123–136.
- [9] J.K. Bunkure, Lebesgue-Bochner spaces and evolution triples, *Int. J. Math. Appl.* 7 (2019) 41–52.
- [10] A. Cianchi, V.G. Maz'ya, Sobolev inequalities in arbitrary domains, *Adv. Math.* 293 (2016) 644–696.
- [11] E.B. Chin, J.B. Lasserre, N. Sukumar, Numerical integration of homogeneous functions on convex and nonconvex polygons and polyhedra, *Comput. Mech.* 56 (2015) 967–981.
- [12] J.A. De Loera, B. Dutra, M. Köppe, S. Moreinis, G. Pinto, J. Wu, Software for exact integration of polynomials over polyhedra, *Comput. Geom.* 46 (2013) 232–252.
- [13] R. Desmorat, F. Gatuingt, F. Ragueneau, Nonlocal anisotropic damage model and related computational aspects for quasi-brittle materials, *Eng. Fract. Mech.* 74 (2007) 1539–1560.
- [14] Ch. Dick, J. Georgii, R. Westermann, A hexahedral multigrid approach for simulating cuts in deformable objects, *IEEE Trans. Visual. Comput. Graphics* 17 (2011) 1663–1675.
- [15] P. Drábek, I. Milota, *Methods of Nonlinear Analysis*, Birkhäuser, Basel, 2013.
- [16] C.A. Duarte, O.N. Hamzeh, T.J. Liszka, W.W. Tworzydło, A generalized finite element method for the simulation of three-dimensional dynamic crack propagation, *Comp. Meth. Appl. Mech. Engrg.* 190 (2001) 2227–2262.
- [17] S. Duczek, F. Duvigneau, U. Gabbert, The Finite Cell Method for tetrahedral meshes, *Finite Elements in Analysis and Design* 121 (2016) 18–32.
- [18] J. Eliáš, M. Vořechovský, J. Skoček, Z.P. Bažant, Stochastic discrete meso-scale simulations of concrete fracture: comparison to experimental data, *Eng. Fract. Mech.* 135 (2012) 1–16.
- [19] E. Emmrich, D. Puhst, Measure-valued and weak solutions to the nonlinear peridynamic model in nonlocal elastodynamics, *Nonlinearity* 28 # 285 (2015) 1–25.
- [20] A.C. Eringen, *Theory of Nonlocal Elasticity and Some Applications*, Princeton Univ. report (1984, tech.) 62.
- [21] A.C. Eringen, *Nonlocal Continuum Field Theories*, Springer, New York, 2002.
- [22] A. Evgrafov, J.C. Bellido, From non-local Eringen's model to fractional elasticity, *Math. Mech. Solids* 24 (2019) 1935–1953.
- [23] G.E. Fasshauer, Q. Ye, Reproducing kernels of generalized Sobolev spaces via a Green function approach with distributional operators, *Numer. Math.* 119 (2011) 585–611.
- [24] G. Ferté, P. Massin, N. Moës, 3D crack propagation with cohesive elements in extended finite element method, *Comp. Meth. Appl. Mech. Engrg.* 300 (2016) 347–374.
- [25] S. Fichant, Ch. La Borderie, G. Pijaudier-Cabot, Isotropic and anisotropic descriptions of damage in concrete structures, *Mech. Cohes.-Frict. Mater.* 4 (1999) 339–359.
- [26] T.-P. Fries, T. Belytschko, The intrinsic XFEM: a method for arbitrary discontinuities without additional unknowns, *Int. J. Numer. Meth. Engrg.* 68 (2006) 1358–1385.
- [27] C. Giry, F. Dufour, J. Mazars, Stress-based nonlocal damage model, *Int. J. Solids Struct.* 48 (2011) 3431–3443.
- [28] P. Grassl, D. Xenos, M. Jirásek, M. Horák, Evaluation of nonlocal approaches for modelling fracture near nonconvex boundaries, *Int. J. Solids Struct.* 51 (2014) 3239–3251.
- [29] P. Havlásek, P. Grassl, M. Jirásek, Analysis of size effect on strength of quasi-brittle materials using integral-type nonlocal models, *Eng. Fract. Mech.* 157 (2016) 72–85.
- [30] S. Hubrich, P. Di Stolfo, L. Kudela, S. Kollmannsberger, A. Schröder, A. Düster, Numerical integration of discontinuous functions: moment fitting and smart octree, *Comput. Mech.* 60 (2017) 863–881.
- [31] A. Javili, R. Mosarata, E. Oterkus, *Peridynam. Rev. Mathematics and Mechanics of Solids* 24 (11) (2019) 3714–3739.
- [32] M. Kaliske, H. Dal, R. Fleischhauer, C. Jenkel, C. Netzker, Characterization of fracture processes by continuum and discrete modelling, *Comput. Mech.* 50 (2012) 303–320.
- [33] A.R. Khoei, *Extended Finite Element Method: Theory and Applications*, John Wiley & Sons, Hoboken, 2015.
- [34] M. Khosravifard, M. Esmaili, H. Saidi, Extension of the Lasserre - Avrachenkov theorem on the integral of multilinear forms over simplices, *Appl. Math. Comput.* 212 (2009) 94–99.
- [35] T. Komárková, J. Láňk, P. Dvořák, Influence of dispersed reinforcement on the

- physico-mechanical properties of the SFRC, *Key Eng. Mater.* 755 (2017) 75–81.
- [36] C. Ch. Koutsoumaris, K.G. Eptameris, A research into bi-Helmholtz type of nonlocal elasticity and a direct approach to Eringen's nonlocal integral model in a finite body, *Acta Mech.* 229, 2018, pp. 3629–3649.
- [37] V. Kozák, Z. Chlup, Modelling of fibre-matrix interface of brittle matrix long fibre composite by application of cohesive zone method, *Key Eng. Mater.* 465 (2011) 231–234.
- [38] M. Lazar, G.A. Maugin, E.C. Aifantis, On a theory of nonlocal elasticity of bi-Helmholtz type and some applications, *Int. J. Solids Struct.* 43 (2006) 1404–1421.
- [39] M. Lazar, G.A. Maugin, E.C. Aifantis, Dislocations in second strain gradient elasticity, *Int. J. Solids Struct.* 43 (2006) 1787–1817.
- [40] G.P. Lignola, F.R. Spena, A. Prota, G. Manfredi, Exact stiffness-matrix of two nodes Timoshenko beam on elastic medium – an analogy with Eringen model of nonlocal Euler-Bernoulli nanobeams, *Comput. Struct.* 182 (2017) 556–572.
- [41] C.W. Lim, G. Zhang, J.N. Reddy, A higher-order nonlocal elasticity and strain gradient theory and its applications in wave propagation, *J. Mech. Phys. Solids* 78 (2015) 298–313.
- [42] X. Li, W. Gao, W. Liu, A mesh objective continuum damage model for quasi-brittle crack modelling and finite element implementation, *Int. J. Damage Mech.* 28 (2019) 1299–1322.
- [43] R.W. Macek, S.A. Silling, Peridynamics via finite element analysis, *Finite Elem. Anal. Des.* 43 (2007) 1169–1178.
- [44] S. Mariani, U. Perego, Extended finite element method for quasi-brittle fracture, *Int. J. Numer. Meth. Engng.* 58 (2003) 103–126.
- [45] M. Masjed-Jamei, A new type of weighted quadrature rules and its relation with orthogonal polynomials, *Appl. Math. Comp.* 188 (2007) 154–165.
- [46] V.G. Maz'ya, S.L. Prostranstva, Soboleva, Leningrad (St. Petersburg) Univ., 1985, in Russian.
- [47] I.C. Mihai, A.D. Jefferson, A micromechanics based constitutive model for fibre reinforced cementitious composites, *Int. J. Solids Struct.* 110 (111) (2017) 152–169.
- [48] M. Morandotti, Structured deformations of continua: theory and applications, in: 16th Int. Conf. Continuum Mechanics Focusing on Singularities (CoMFoS) II in, Conf. Proc, Springer, 2016, pp. 125–138.
- [49] S.E. Mousavi, Dislocation-based fracture mechanics within nonlocal and gradient elasticity of bi-Helmholtz type, *Int. J. Solids Struct.* 87, 2016, pp. 222–235, and 92–93, 2016, pp. 105–120.
- [50] S.E. Mousavi, N. Sukumar, Numerical integration of polynomials and discontinuous functions on irregular convex polygons and polyhedrons, *Comput. Mech.* 47 (2011) 535–554.
- [51] S.E. Mousavi, H. Xiao, N. Sukumar, Generalized Gaussian quadrature rules on arbitrary polygons, *Int. J. Num. Meth. Engng.* 82 (2010) 99–113.
- [52] A. Munjiza, *The Combined Finite-Discrete Element Method*, John Wiley & Sons, Hoboken, 2004.
- [53] N.S. Ottosen, M. Ristinmaa, Thermodynamically based fictitious crack / interface model for general normal and shear loading, *Int. J. Solids Struct.* 50 (2013) 3555–3561.
- [54] K. Park, G.H. Paulino, J.R. Roesler, Cohesive fracture model for functionally graded fiber reinforced concrete, *Cement Concr. Res.* 40 (2010) 956–965.
- [55] T. Rabczuk, Computational methods for fracture in brittle and quasi-brittle solids: state-of-the-art review and future perspectives, *ISRN, Appl. Math.* # 849231 (2013, 2013,) 1–38.
- [56] M.G. Pike, C. Oskay, XFEM modeling of short microfiber reinforced composites with cohesive interfaces, *Finite Elem. Anal. Des.* 106 (2015) 16–31.
- [57] C. Polizzotto, Nonlocal elasticity and related variational principles, *Int. J. Solids Struct.* 38 (2001) 7359–7380.
- [58] Yu.Z. Povstenko, The nonlocal theory of elasticity and its applications to the description of defects in solid bodies, *J. Math. Sci.* 97 (1999) 3840–3845.
- [59] P. Ray, Statistical physics perspective of fracture in brittle and quasi-brittle materials *Phil. Trans. R. Soc. A* #20170396 (377, 2019,) 1–13.
- [60] G. Romano, R. Baretta, M. Diaco, F.M. de Sciarra, Constitutive boundary conditions and paradoxes in nonlocal elastic nanobeams, *Int. J. Mech. Sci.* 121 (2017) 151–156.
- [61] T. Roubíček, *Nonlinear Partial Differential Equations with Applications*, Birkhäuser, Basel, 2005.
- [62] B. Shen, I. Stanculescu, G.H. Paulino, Inverse computation of cohesive fracture properties from displacement fields, *Inverse Prob. Sci. Eng.* 18 (2010) 1103–1128.
- [63] V. Skala, A practical use of radial basis functions interpolation and approximation, *Investigacion Operacional* 37 (2016) 137–144.
- [64] A. Stavrev, L.H. Nguyen, R. Shen, V. Varduhn, M. Behr, S. Elgeti, D. Schillinger, Geometrically accurate, efficient, and flexible quadrature techniques for the tetrahedral finite cell method, *Comp. Meth. Appl. Mech. Engrg.* 310 (2016) 646–673.
- [65] X.T. Su, Z.J. Yang, G.H. Liu, Monte Carlo simulation of complex cohesive fracture in random heterogeneous quasi-brittle materials: a 3D study, *Int. J. Solids Struct.* 47 (2010) 2336–2345.
- [66] N. Sukumar, J. Dolbow, A. Devan, J. Yvonnet, F. Chinesta, D. Ryckelynck, P. Lorig, I. Alfaro, A. Martinez, E. Cueto, M. Doblaré, Meshless methods and partition of unity finite elements, *Int. J. Forming Proc.* 8 (2005) 409–427.
- [67] N. Sukumar, J.E. Dolbow, N. Moës, Extended finite element method in computational fracture mechanics: a retrospective examination, *Int. J. Fract.* 196 (2015) 189–206.
- [68] M.O. Steinhauser, *Computational Multiscale Modeling of Fluids and Solids*, Springer, Berlin, 2008.
- [69] Y. Sumi, *Mathematical and Computational Analyses of Cracking Formation*, Springer, Tokyo, 2014.
- [70] J. Vala, Structure identification of metal fibre reinforced cementitious composites. 20th Int. Conf. Algorithmy in Podbanské (2016), Conf. Proc. (STU Bratislava), 2016, pp. 244–253.
- [71] J. Vala, Remarks to the computational analysis of semilinear direct and inverse problems of heat transfer, 24th Int. Conf. Thermophysics in Smolenice (2019), AIP Conf. Proc. 2170, 2019, 020023/1–6.
- [72] J. Vala, V. Kozák, Computational analysis of crack formation and propagation in quasi-brittle fibre reinforced composites, 9th Int. Conf. Materials Structure and Micromechanics of Fracture (MSMF) in Brno (2019), *Procedia Struct. Integrity*, 2020, 6 pp., to appear.
- [73] J. Vala, V. Kozák, K možnostem výpočtové predikce kvazikřehkého porušení cementových kompozitů rozšířenou metodou konečných prvků, 18th Conf. Maltoviny in Brno, 2019, Conf. Proc., 2019, pp. 5–13, in Czech.
- [74] R. Zaera, Ó. Serrano, J. Fernández-Sáez, On the consistency of the nonlocal strain gradient elasticity, *Int. J. Eng. Sci.* 138 (2019) 65–81.

D5 Vala, J., Kozák, V., Nonlocal damage modelling of quasi-brittle composites, accepted for publication *Applications of Mathematics*, January (2021), to appear, IF 0,544.

# NONLOCAL DAMAGE MODELLING OF QUASI-BRITTLE COMPOSITES

JIŘÍ VALA, Brno, VLADISLAV KOZÁK, Brno

(Received September 30, 2020. Revised March 18, 2021.)

*Abstract.* Most building materials can be characterized as quasi-brittle composites with a cementitious matrix, reinforced by some stiffening particles or elements. Their massive exploitation motivates the development of numerical modelling and simulation of behaviour of such material class under mechanical, thermal, etc. loads, including the evaluation of the risk of initiation and development of micro- and macro-fracture. This paper demonstrates the possibility of certain deterministic prediction, applying the dynamical approach using the Kelvin viscoelastic model and cohesive interface properties. The existence and convergence results rely on the semilinear computational scheme coming from the method of discretization in time, using several types of Rothe sequences, coupled with the extended finite element method (XFEM) for practical calculations. Numerical examples refer to cementitious samples reinforced by short steel fibres, with increasing number of applications as constructive parts in civil engineering.

*Keywords:* quasi-brittle composites, steel fibre concrete, micro- and macro-fracture, non-local viscoelasticity, cohesive interfaces, partial differential equations of evolution, method of discretization in time, extended finite element method.

*MSC 2020:* 74R10, 74H15, 74S05, 74S20, 74E30.

## 1. INTRODUCTION

Study of behaviour of quasi-brittle composites under mechanical, thermal, etc. loads belongs to research priorities in civil engineering, utilizing such composites as constructive parts of buildings and engineering structures. These parts are often made from a material with a cementitious matrix, reinforced by some stiffening (e. g. various metal, glass or plastics as polyethylene or polypropylene fibres), with the

---

This research has been supported by the project FAST-S-20-6294 of specific university research at Brno University of Technology.

aim to reduce the danger of cracking in tension: cf. [22] for the fibre reinforced concrete technology, [30] for the review of steel fibre reinforced composites (as the most frequently applied ones) and [25] for certain simplified methodology of computational design of such fibre composites, with the relevant software support [12]. However, a proper computational prediction of strain, stress, etc. development in such composites cannot be based on simple calculations well-known from linear elasticity and related fracture mechanics. Following [54], two stages of damage can be recognized: i) formation of micro-fractured zones, reducing the stiffness of a structure, ii) creation of macro-cracks, whose later opening and closing is conditioned by the cohesive characteristics of new interfaces. At least the following scales should be distinguished: matrix particles (at  $10^{-3}$  m), hardening fibres (at  $10^{-2}$  m) and laboratory samples (at  $10^{-1}$  m) or real structures in situ (even greater). Consequently a reasonable setting of material parameters on the macroscopic scale, supported by appropriate experiments, producing some (typically incomplete) data on material structure, as random or intentionally oriented fibre directions, may be complicated in general. Selected problems of this kind, preferring non-destructive or low-invasive testing approaches, namely direct photographic, roentgenographic and tomographic ones, and indirect electromagnetic ones, relying on certain changes in stationary magnetic or harmonic electromagnetic fields, are discussed in [57], with numerous further references.

Various arguments on the non-negligible non-deterministic character of both input data and relevant physical processes motivate some authors to the attempts to handle the evolution of damage by stochastic considerations, genetic algorithms or other soft computing approaches like [53], [14] or [41], by statistical physics using [48], or by computational peridynamics, avoiding all gradient evaluations, following [38], [15] and [27]. Unlike such approaches, in this paper we shall try to develop a rather simple deterministic physical, mathematical and computational model, up to its software implementation, based on the principle of energy conservation from classical mechanics, incorporating the kinetic and deformation energy, similarly to [37], together with certain energy dissipation (structural and mass damping).

However, the detailed description and computational analysis of particular micro-cracks cannot be performed easily in most engineering applications. The thermodynamic approach of [51] and [40], especially in Part 4.3, introduces additional internal variables to displacements and temperature and combines a fully implicit discretization, based on both Galerkin and Rothe methods, with the analysis of nonlinear Nemytskiĭ operators and enthalpy transformation to verify the existence of certain energetic solution of a needed initial and boundary value problem. In our paper, initiation and development of particular micro-cracks will be incorporated using the

damage zone representation by [21] and [28], utilizing numerous ideas of [47], adopting the nonlocal model from [16]. This model was later reformulated by [17] and is frequently referred as the Eringen one in the last 2 decades. Fortunately the recent result [18] on the ill-posedness of the nonlocal approach [17], referring to the incomplete existence analysis of [1], for boundary conditions significant in practical applications, is not addressed to our formulation, as explained by [58]. Moreover, according to [55], such conception can be considered as a suitable procedure for a multi-scale approach, avoiding any interpolation between macro- and micro-scale variables. For the strain-stress relations we shall work with the viscoelastic Kelvin law, generating the so-called structural damping, accompanied by the mass damping due to the Rayleigh model in the sense of [43].

The above sketched considerations will be incorporated in our model problem. As its natural generalization, we shall consider also a finite set of matrix / fibre interfaces, as well as of interfaces inside the matrix, or even inside any fibre, depending on the process of activation of macro-cracks. All such interfaces will be assumed to satisfy the cohesive model, developed by [46], [32], [6] (for various types of fibre composites), [33] (for ceramics) and [36] (for a rather general class of damage propagation).

For most existence and convergence proofs we shall use the method of discretization in time, based on the convergence properties of Rothe sequences, following [49], devoted to linear problems. Moreover we need to handle 2 types of nonlinear terms, coming from i) and ii), as introduces above. For practical evaluations of fully discretized problems we shall prefer the extended finite element method (XFEM), working with the adaptive enrichment of the set of base functions near geometric singularities. This method, including numerous modifications with their special names and specific notations, as generalized finite element method (GFEM) or partition of unity method (PoUM), has its own rich history; the progress in several decades can be traced from the comparison of pioneering works [2], [3] and [19] with the later monograph [31] and the recent articles [37] and [56].

However, we shall pay attention namely to the convergence properties independent of the choice of XFEM adaptive strategies, as discussed by [29].

## 2. PHYSICAL AND MATHEMATICAL PRELIMINARIES

For our first model problem, let us consider a domain  $\Omega$  in the 3-dimensional Euclidean space  $\mathbb{R}^3$ , whose exterior Lipschitz boundary  $\partial\Omega$  consists of 2 disjoint parts  $\Theta$  (for homogeneous Dirichlet boundary conditions) and  $\Gamma$  (for non-homogeneous Neumann boundary conditions),  $\Theta$  having a non-zero measure on  $\partial\Omega$  (to avoid insufficient support). Let  $\mathbb{R}^3$  be supplied by a Cartesian coordinate system  $x = (x_1, x_2, x_3)$ . Moreover we shall work with the time  $t \in I$  from an interval  $I = [0, T]$  with some

final time value  $T$ , assumed as finite here. For the brevity of notation we shall work with the Hamilton operator  $\nabla = (\partial/\partial x_1, \partial/\partial x_2, \partial/\partial x_3)$  and with upper dots instead of  $\partial/\partial t$ . Moreover any comma followed by  $k \in \{1, 2, 3\}$  will be seen as  $\partial/\partial x_k$  applied to the preceding variable: e.g.  $2\varepsilon_{ij}(v) = v_{i,j} + v_{j,i}$  with  $i, j \in \{1, 2, 3\}$  can be understood as the definition of linearized strain, applicable to any differentiable virtual displacement  $v(x) = (v_1(x), v_2(x), v_3(x))$ , related to an initial configuration. The Einstein summation rule for indices  $i, j, k, l \in \{1, 2, 3\}$  will be active, too.

The introduction of Lebesgue, Sobolev and Bochner spaces of functions on  $\Omega$  and  $\partial\Omega$  and abstract functions mapping  $I$  to them is compatible with [50]. To present our approach as simple as possible now, we shall work namely with the special Hilbert spaces  $H = L^2(\Omega)^3$ ,  $Z = L^2(\partial\Omega)^3$ ,  $Z_\Gamma = L^2(\Gamma)^3$  and  $V = \{v \in W^{1,2}(\Omega)^3 : v = O \text{ on } \Theta\}$ , supplied with norms denoted by  $|\cdot|$  both in  $H$  and  $H \times H$ ,  $|\cdot|_\Gamma$  in  $Z_\Gamma$  and  $\|\cdot\|$  in  $V$ , as well as with scalar products  $(\cdot, \cdot)$  both in  $H$  and  $H \times H$ , together with  $\langle \cdot, \cdot \rangle_\Gamma$  in  $Z_\Gamma$ ;  $O$  means the zero vector from  $\mathbb{R}^3$  here. Slight natural generalizations (which may bring technical difficulties in proofs), motivated by much more detailed references from [50], are left to the curious reader. We shall also utilize upper star symbols for dual spaces,  $\subset$  for continuous embeddings,  $\Subset$  for compact embeddings,  $\cong$  for the identification of a space with its dual in the sense of the Riesz representation theorem.

The following properties of the above introduced spaces (for all notations see [50] again) will be needed:

**Lemma 2.1** (Sobolev embedding).  $V \Subset H$ . *Consequently: from any weakly convergent sequence in  $V$  a strongly convergent subsequence in  $H$  can be selected.*

*Proof.* See [50], p. 16, and [13], p. 40. □

**Lemma 2.2** (trace operator).  $V \Subset Z$ ;  $|v|_\Gamma^2 \leq \mathfrak{T}\|v\|^2$  for any  $v \in V$  with a positive  $\mathfrak{T}$  independent of  $v$ . *Consequently: from any weakly convergent sequence in  $V$  a strongly convergent subsequence in  $Z$  can be selected.*

*Proof.* See [50], p. 17, and [13], p. 275. □

**Lemma 2.3** (Korn). *There holds  $|\varepsilon(v)|^2 \geq \mathfrak{K}\|v\|^2$  for any  $v \in V$  with a positive  $\mathfrak{K}$  independent of  $v$ . Consequently: to the standard norm  $\|v\|^2 = |v|^2 + |\nabla v|^2$  an alternative norm is generated by  $|\varepsilon(v)|^2$  in  $V$ .*

*Proof.* For the inequality see [50], p. 22. The consequence follows from the obvious estimate, referring to linear elasticity,  $\mathfrak{K}\|v\|^2 \leq |\varepsilon(v)|^2 = (v_{i,j} + v_{j,i})(v_{i,j} + v_{j,i})/4 \leq v_{i,j}v_{i,j} = |\nabla v|^2 \leq \|v\|^2$ . □

**Lemma 2.4** (Eberlein - Shmul'yan). *All spaces  $H, V, L^2(I, H)$  and  $L^2(I, V)$  are reflexive. Consequently: from any bounded sequence in such space a weakly convergent subsequence can be selected.*

*Proof.* For  $H$  and  $V$  see [50], p. 15.  $L^2(I, H)$  can be interpreted as  $L^2(\Omega \times I)$  with the quite similar result. For the details on duality pairing  $L^2(I, V)^* \cong L^2(I, V^*)$  see [50], p. 201. For the consequence cf. [50], pp. 5 and 210, with [13], p. 67.  $\square$

**Lemma 2.5** (Gelfand triple). *In the triple  $V \subset H \cong H^* \subset V^*$  both inclusions are dense;  $W^{1,2,2}(I, V, V^*) \subset C(I, H)$ .*

*Proof.* See [50], p. 190;  $W^{1,2,2}(I, V, V^*)$  here denotes a Bochner-Sobolev space of abstract functions from  $L^2(I, V)$  with time derivatives belonging to  $L^2(I, V^*)$ .  $\square$

**Lemma 2.6** (Aubin - Lions).  *$W^{1,2,2}(I, V, V^*) \Subset L^2(I, X)$  with  $X \in \{H, Z\}$ .*

*Proof.* See [50], p. 194.  $\square$

### 3. A MODEL PROBLEM WITH MICRO-CRACKS

Let us introduce a displacement in a deformable body (a priori unknown), occupying the domain  $\Omega$ ,  $u(x, t) = (u_1(x, t), u_2(x, t), u_3(x, t))$ , related to the reference initial configuration (at  $t = 0$ ), such that the homogeneous Cauchy initial conditions  $u_1(x, 0) = u_2(x, 0) = u_3(x, 0) = 0$  and  $\dot{u}_1(x, 0) = \dot{u}_2(x, 0) = \dot{u}_3(x, 0) = 0$  are satisfied for almost every  $x \in \Omega$ . We shall assume that  $u \in \mathcal{V} = W^{1,2,2,2}(I, V, V, V^*)$ ; thus  $u(\cdot, t), \dot{u}(\cdot, t) \in V$  and  $\ddot{u}(\cdot, t) \in V^*$  for any  $t \in I$  - cf. (3.22) in the proof of Theorem 3.1, including the identification of particular limits below. Both initial conditions can be written as

$$(3.1) \quad u(\cdot, 0) = O, \quad \dot{u}(\cdot, 0) = O \quad \text{on } \Omega.$$

Analogous simplified notations will be used for further functions, too. Let us remark that just the zero-valued  $u(\cdot, 0)$  and  $\dot{u}(\cdot, 0)$  in (3.1), referring to certain stationary initial status, are considered in numerous engineering applications; if needed, the following considerations can be repeated for a non-homogeneous form of (3.1) without substantial difficulties.

For an arbitrary  $v \in V$  the energy conservation for our model problem can be presented as

$$(3.2) \quad (v, \rho \ddot{u}) + \beta(v, \rho \dot{u}) + \alpha(\varepsilon(v), \dot{\sigma}) + (\varepsilon(v), (1 - \mathfrak{D}) \sigma) = (v, f) + \langle v, g \rangle_{\Gamma} \quad \text{on } I$$

where  $\rho \in L^\infty(\Omega)$  is the material density and  $\sigma \in L^2(I, L^2(\Omega)_{\text{sym}}^{3 \times 3})$  refers to all stress components. Its symmetry comes from the assumptions on Boltzmann continuum;

for much more general considerations of this type, including constitutive laws, cf. [4], p.18. The energy dissipation in (3.2), driven by the prescribed body forces  $f \in L^2(I, H)$  and surface forces  $g \in L^2(I, Z_\Gamma^3)$ , is taken into account using the positive damping factors  $\alpha$  for structural damping due to the parallel Kelvin viscoelastic model, and the real non-negative factor  $\beta$  for mass damping, compatible with the Rayleigh damping model by [43]. We shall assume that  $\rho \geq \rho_0$  on  $\Omega$  for some positive constant  $\rho_0$ . Finally  $\mathfrak{D}$  can be presented as some local damage factor with values between 0 and  $1 - \varsigma$ , using an additional positive constant  $\varsigma$ ;  $\mathfrak{D} = 0$  holds always for  $t = 0$  (no micro-cracking is present). This factor should depend on  $\sigma$ , or  $\varepsilon(u)$  directly, non-increasing in time  $t \in I$ , which can be guaranteed by its evaluation in the form

$$(3.3) \quad \mathfrak{D}(u)(t) = \max_{\xi \in [0, t]} \mathfrak{D}_*(u(\xi))$$

etc., for particular  $t \in I$ . Its practical design, namely the form of the continuous mapping  $\mathfrak{D}_*$  from  $V$  to  $L^\infty(\Omega)$ , based on the nonlocal Eringen theory, will be discussed later.

Let us notice that the strong formulation corresponding to (3.2) can be derived, at least in the sense of distributions, from integration by parts. Following the approach of [58] (where the quasi-static case is discussed in all details), for each  $i$  (respecting the brief notation  $\sigma_{ij,j}$  forcing divergence  $\partial\sigma_{ij}/\partial x_j$ , etc.) we receive

$$(3.4) \quad \begin{aligned} \rho(\ddot{u}_i + \beta\dot{u}_i) - \sigma_{ij,j} &= f_i & \text{on } \Omega \times I, \\ \sigma_{ij}\nu_j &= g_i & \text{on } \Gamma \times I, \\ u_i &= O & \text{on } \Theta \times I \end{aligned}$$

where  $\nu = (\nu_1, \nu_2, \nu_3)$  means the local unit normal vector associated with  $\Gamma$ . In addition to the 1st evolution equation of (3.4), referring to the classical Cauchy equilibrium condition, we can see both an explicit Neumann boundary condition in the 2nd equation and a Dirichlet one in the 3rd equation.

The local stress-strain relation can be taken in the simple form

$$(3.5) \quad \sigma = (1 - \mathfrak{D})C\varepsilon(u) + \alpha C\varepsilon(\dot{u})$$

with  $C \in L^\infty(\Omega)_{\text{sym}}^{(3 \times 3) \times (3 \times 3)}$ , containing (in general) 21 material parameters,  $C(x)$  being positive definite in the sense  $C_{ijkl}(x)a_{ij}a_{kl} \geq C_0 a_{ij}a_{ij}$ , involving some positive constant  $C_0$ . In particular, for an isotropic homogeneous medium, setting  $\alpha = 0$  formally (the needed generalization with  $\alpha > 0$  is straightforward) and zero-valued  $\mathfrak{D}$  (no damage occurs yet), using the Kronecker symbol  $\delta_{ij} = 1$  for  $i = j$ , 0 otherwise,

we have  $\sigma_{ij} = 2\lambda_1 \varepsilon_{ij}(u) + \lambda_2 \delta_{ij} \varepsilon_{kk}(u)$  with only 2 positive Lamé factors  $\lambda_1$  and  $\lambda_2$ ; frequently they are expressed as  $\lambda_1 = \mu E / (1 + \mu) / (1 - 2\mu)$ ,  $2\lambda_2 = E / (1 + \mu)$ , utilizing the well-known Young modulus  $E$  and the Poisson ratio  $\mu$ ; such characteristics will be referenced e. g. from Section 5.

Inserting (3.5) into (3.2), taking (3.3) into account (without explicit highlighting), we obtain

$$(3.6) \quad \begin{aligned} & (v, \rho \ddot{u}) + \beta(v, \rho \dot{u}) + \alpha(\varepsilon(v), C\varepsilon(\dot{u})) \\ & + (\varepsilon(v), (1 - \mathfrak{D}) C\varepsilon(u)) = (v, f) + \langle v, g \rangle_\Gamma \quad \text{on } I. \end{aligned}$$

Let  $I$  be divided into a finite number  $m$  of subsets  $I_s^m = \{t \in I : (s-1)\tau < t \leq s\tau\}$  where  $s \in \{1, \dots, m\}$ , with the final aim  $m \rightarrow \infty$ ;  $\tau(m) = T/m$  is considered (the argument  $m$  will be omitted formally). We are able to work with the Clément quasi-interpolation  $f^m$  of  $f$  in  $L^2(I, H)$  and  $g^m$  of  $g$  in  $L^2(I, Z_\Gamma)$ , assuming  $t \in I_s^m$ ,  $s \in \{1, \dots, m\}$ , i. e.  $f^m(t) = f_s^m$  and  $g^m(t) = g_s^m$  where

$$f_s^m = \frac{1}{\tau} \int_{(s-1)\tau}^{s\tau} f(\xi) \, d\xi, \quad g_s^m = \frac{1}{\tau} \int_{(s-1)\tau}^{s\tau} g(\xi) \, d\xi.$$

This yields

$$(3.7) \quad \begin{aligned} \tau \sum_{s=1}^m |f_s^m|^2 &= \frac{1}{\tau} \sum_{s=1}^m \left| \int_{(s-1)\tau}^{s\tau} f(\xi) \, d\xi \right|^2 \leq \int_I |f(\xi)|^2 \, d\xi \\ \tau \sum_{s=1}^m |g_s^m|_\Gamma^2 &= \frac{1}{\tau} \sum_{s=1}^m \left| \int_{(s-1)\tau}^{s\tau} g(\xi) \, d\xi \right|_\Gamma^2 \leq \int_I |g(\xi)|_\Gamma^2 \, d\xi, \end{aligned}$$

which will be needed later, cf. (3.17).

For any unknown  $u^m$ , introducing the differences  $Du_s^m = u_s^m - u_{s-1}^m$  with  $s \in \{1, \dots, m\}$ , taking  $u_0^m = O$  and  $Du_0^m = O$  formally, due to (3.1), we can set some linear Lagrange splines

$$(3.8) \quad u^m(t) = u_{s-1}^m + \frac{t - (s-1)\tau}{\tau} Du_s^m$$

and standard and retarded simple functions

$$(3.9) \quad \bar{u}^m(t) = u_s^m, \quad \check{u}^m(t) = u_{s-1}^m$$

for  $t \in I_s^m$ . Let us recall that  $u^m(t)$  and  $\bar{u}^m(t)$  for  $m \in \{1, 2, \dots\}$  by (3.8) and (3.9) are just 2 classical sequences of Rothe, as introduced in [49]. To handle the 1st additive term of (3.6) properly, we need also certain quadratic interpolation

$$(3.10) \quad U^m(t) = u_{s-1}^m + \frac{t - (s-1)\tau}{2\tau} (Du_s^m + Du_{s-1}^m) + \frac{(t - (s-1)\tau)^2}{2\tau^2} D^2 u_s^m$$

where  $D^2u_s^m = Du_s^m - Du_{s-1}^m$ . Thus we are able to rewrite (3.6) in its time-discretized form

$$(3.11) \quad \begin{aligned} & (v, \rho \ddot{U}^m) + \beta(v, \rho \dot{u}^m) + \alpha(\varepsilon(v), C\varepsilon(\dot{u}^m)) \\ & + (\varepsilon(v), (1 - \check{\mathfrak{D}}^m) C\varepsilon(\bar{u}^m)) = (v, f^m) + \langle v, g^m \rangle_\Gamma \end{aligned}$$

where  $\check{\mathfrak{D}}^m$  refers to the evaluation of  $\mathfrak{D}$  with  $\check{u}^m$ , instead of  $u$  by (3.6); this is a simple function with certain values  $u_{s-1}^m$ , denoted  $\mathfrak{D}_{s-1}^m$  for brevity, cf. (3.12). For any step-by-step evaluation with  $s \in \{1, \dots, m\}$ , taking  $t \in I_s^m$  only, (3.11) gets the form

$$(3.12) \quad \begin{aligned} & \frac{1}{\tau^2} (v, \rho D^2 u_s^m) + \frac{\beta}{\tau} (v, \rho D u_s^m) + \frac{\alpha}{\tau} (\varepsilon(v), C\varepsilon(D u_s^m)) \\ & + (\varepsilon(v), (1 - \mathfrak{D}_{s-1}^m) C\varepsilon(u_s^m)) = (v, f_s^m) + \langle v, g_s^m \rangle_\Gamma. \end{aligned}$$

The following theorem guarantees the solvability of (3.6) assuming (3.1), utilizing the computational construction of sequences by (3.12).

**Theorem 3.1.** *Let us consider a damage factor by (3.3). There exist a solution  $u \in \mathcal{V}$  satisfying (3.6) for any  $v \in V$  together with the Cauchy initial condition (3.1). Moreover  $u, \dot{u} \in C(I, H)$  and, up to subsequences,*

$$(3.13) \quad \begin{aligned} \{\ddot{U}^m\}_{m=1}^\infty & \text{ converges weakly to } \ddot{u} \text{ in } L^2(I, V^*), \\ \{\dot{u}^m\}_{m=1}^\infty & \text{ converges weakly to } \dot{u} \text{ in } L^2(I, V), \\ \{\dot{u}^m(t)\}_{m=1}^\infty & \text{ converges weakly to } \dot{u} \text{ in } H \text{ for any } t \in I, \\ \{\bar{u}^m(t)\}_{m=1}^\infty & \text{ converges weakly to } u \text{ in } V \text{ for any } t \in I, \\ \{\check{u}^m(t)\}_{m=1}^\infty & \text{ converges weakly to } u \text{ in } V \text{ for any } t \in I, \\ \{\check{u}^m(t)\}_{m=1}^\infty & \text{ converges strongly to } u \text{ in } H \text{ for any } t \in I, \\ \{\dot{U}^m\}_{m=1}^\infty & \text{ converges strongly to } \dot{u} \text{ in } L^2(I, H), \end{aligned}$$

using the sequences  $\{u^m\}_{m=1}^\infty$ ,  $\{\bar{u}^m\}_{m=1}^\infty$ ,  $\{\check{u}^m\}_{m=1}^\infty$  and  $\{U^m\}_{m=1}^\infty$ , induced by (3.8), (3.9) and (3.10), for the time-discretization scheme (3.11).

*Proof.* Let us choose  $v = Du_s^m$  in (3.12), with the aim to derive some a priori bounds for the above introduced sequences generated by  $U^m$ ,  $u^m$ ,  $\bar{u}^m$  and  $\check{u}^m$  with integer  $m$ . We receive

$$(3.14) \quad \begin{aligned} & \frac{1}{\tau^2} (Du_s^m, \rho D^2 u_s^m) + \frac{\beta}{\tau} (Du_s^m, \rho D u_s^m) + \frac{\alpha}{\tau} (\varepsilon(Du_s^m), C\varepsilon(Du_s^m)) \\ & + (\varepsilon(Du_s^m), (1 - \mathfrak{D}_{s-1}^m) C\varepsilon(u_s^m)) = (Du_s^m, f_s^m) + \langle Du_s^m, g_s^m \rangle_\Gamma. \end{aligned}$$

The same results remain true with arbitrary  $r \in \{1, \dots, s\}$ , instead of  $s$ . Using the obvious relation  $2a(a-b) = a^2 - b^2 + (a-b)^2$ , valid for any real  $a$  and  $b$ , the sum of all equations (3.14), understanding  $r$ , as well as  $p \in \{1, \dots, s-1\}$  (needed in the following 6th left-hand-side additive term exclusively), as Einstein summation indices, is then

$$\begin{aligned}
(3.15) \quad & \frac{1}{2\tau^2}(Du_s^m, \rho Du_s^m) + \frac{1}{2\tau^2}(D^2u_r^m, \rho D^2u_r^m) \\
& + \frac{\beta}{\tau}(Du_r^m, \rho Du_r^m) + \frac{\alpha}{\tau}(\varepsilon(Du_r^m), C\varepsilon(Du_r^m)) \\
& + \frac{1}{2}(\varepsilon(u_s^m), (1 - \mathfrak{D}_{s-1}^m)C\varepsilon(u_s^m)) + \frac{1}{2}(\varepsilon(u_p^m), (\mathfrak{D}_p^m - \mathfrak{D}_{p-1}^m)\varepsilon(u_p^m)) \\
& + \frac{1}{2}(\varepsilon(Du_r^m), (1 - \mathfrak{D}_{r-1}^m)C\varepsilon(Du_r^m)) = (Du_r^m, f_r^m) + \langle Du_r^m, g_r^m \rangle_\Gamma.
\end{aligned}$$

All left-hand-side additive term are non-negative, namely the 6th one thanks to (3.3), thus the 2nd, 3rd and 6th ones can be bounded by zero from below. The more precise estimates for the 1st, 4th and 5th terms, applying Lemma 2.3 to the 4th and 5th ones, are

$$\begin{aligned}
(3.16) \quad & \frac{1}{2\tau^2}(Du_s^m, \rho Du_s^m) \geq \frac{\rho_0}{2\tau^2}|Du_s^m|^2, \\
& \frac{\alpha}{\tau}(\varepsilon(Du_r^m), C\varepsilon(Du_r^m)) \geq \frac{\alpha C_0 \mathfrak{K}}{\tau} \delta_{rr} \|Du_r^m\|^2, \\
& \frac{1}{2}(\varepsilon(u_s^m), (1 - \mathfrak{D}_s^m)C\varepsilon(u_s^m)) \geq \frac{\varsigma C_0 \mathfrak{K}}{2} \|u_s^m\|^2.
\end{aligned}$$

Using the Cauchy - Schwarz and the Young inequalities, the 1st and 2nd righthand-side terms of (3.14) then admit the estimates

$$\begin{aligned}
(3.17) \quad & (Du_r^m, f_r^m) \leq |Du_r^m| |f_r^m| \leq \frac{\epsilon}{2\tau} \delta_{rr} |Du_r^m|^2 + \frac{\tau}{2\epsilon} \delta_{rr} |f_r^m|^2 \\
& \leq \frac{\epsilon}{2\tau} \delta_{rr} \|Du_r^m\|^2 + \frac{\tau}{2\epsilon} \delta_{rr} |f_r^m|^2, \\
& \langle Du_r^m, g_r^m \rangle_\Gamma \leq |Du_r^m|_\Gamma |g_r^m|_\Gamma \leq \frac{\epsilon}{2\tau} \delta_{rr} |Du_r^m|_\Gamma^2 + \frac{\tau}{2\epsilon} \delta_{rr} |g_r^m|_\Gamma^2 \\
& \leq \frac{\epsilon \mathfrak{T}}{2\tau} \delta_{rr} \|Du_r^m\|^2 + \frac{\tau}{2\epsilon} \delta_{rr} |g_r^m|_\Gamma^2
\end{aligned}$$

where  $\epsilon$  is an arbitrary positive constant; the constant  $\mathfrak{T}$  in the last inequality comes from Lemma 2.2. Comparing (3.16) and (3.17) with respect to (3.7), we obtain

$$(3.18) \quad \frac{1}{\tau^2}|Du_s^m|^2 + \frac{1}{\tau} \delta_{rr} \|Du_r^m\|^2 + \|u_s\|^2 \leq c$$

where  $c$  is some positive constant independent of  $\tau$  (as well as of  $m, s$ , etc.). The evident consequences of (3.18) are

$$(3.19) \quad \begin{aligned} \{\dot{u}^m\}_{m=1}^\infty & \text{ is bounded in } L^2(I, V), \\ \{\dot{u}^m(t)\}_{m=1}^\infty & \text{ is bounded in } H \text{ for any } t \in I, \\ \{\bar{u}^m(t)\}_{m=1}^\infty & \text{ is bounded in } V \text{ for any } t \in I, \\ \{\check{u}^m(t)\}_{m=1}^\infty & \text{ is bounded in } V \text{ for any } t \in I, \end{aligned}$$

Moreover, from (3.11), converted to the form

$$(3.20) \quad \begin{aligned} (v, \rho \ddot{U}^m) &= -\beta(v, \rho \dot{u}^m) - \alpha(\varepsilon(v), C\varepsilon(\dot{u}^m)) \\ &\quad - (\varepsilon(v), (1 - \check{\mathfrak{D}}^m) C\varepsilon(\bar{u}^m)) + (v, f^m) + (v, g^m)_\Gamma, \end{aligned}$$

we are able to derive an additional estimate for  $\ddot{U}^m$ , using the dual space to  $L^2(I, V)$ , as suggested by [50], p. 205; cf. also the comment to the proof of Lemma 2.4. Taking  $\|v\| \leq 1$ ,  $(v, \rho \ddot{U}^m)$  in (3.20) can be bounded from its right-hand side again, using the Cauchy-Schwarz inequalities and further arguments similarly to (3.17), together with the knowledge of all results (3.19); thus we have  $(v, \rho \ddot{U}^m) \leq \hat{c}$  for some positive constant  $\hat{c}$  and consequently

$$(3.21) \quad \{\rho \ddot{U}^m\}_{m=1}^\infty \text{ is bounded in } L^2(I, V^*).$$

Let us notice that (3.21) remains true without the positive multiplier  $\rho \in L^\infty(\Omega)$ .

From (3.21) and (3.19) we can now conclude, following Lemma 2.5, up to subsequences,

$$(3.22) \quad \begin{aligned} \{\dot{U}^m\}_{m=1}^\infty & \text{ converges weakly to } u'' \text{ in } L^2(I, V^*), \\ \{\dot{u}^m\}_{m=1}^\infty & \text{ converges weakly to } \hat{u} \text{ in } L^2(I, V), \\ \{\dot{u}^m(t)\}_{m=1}^\infty & \text{ converges weakly to } u' \text{ in } H \text{ for any } t \in I, \\ \{\bar{u}^m(t)\}_{m=1}^\infty & \text{ converges weakly to } \bar{u} \text{ in } V \text{ for any } t \in I, \\ \{\check{u}^m(t)\}_{m=1}^\infty & \text{ converges weakly to } \check{u} \text{ in } V \text{ for any } t \in I, \\ \{\check{u}^m(t)\}_{m=1}^\infty & \text{ converges strongly to } \check{u} \text{ in } H \text{ for any } t \in I, \\ \{\dot{U}^m\}_{m=1}^\infty & \text{ converges strongly to } u^\diamond \text{ in } L^2(I, H), \end{aligned}$$

etc., where  $u'', \hat{u}, u', \bar{u}$  and  $\check{u}$  are some elements of corresponding spaces; see Lemma 2.6 for the last proposition, too. The strong convergence of  $\{\check{\mathfrak{D}}^m\}_{m=1}^\infty$ , seemingly as in that for  $\{\check{u}^m(t)\}_{m=1}^\infty$  in the 6th proposition of (3.22), is inherited from the formal introduction of  $\mathfrak{D}$  here and will need more detailed analysis.

In particular, considering  $t \in I$ , by Lemma 2.6  $u^\diamond(t)$  coincides with  $\int_0^t u''(\xi) d\xi$ ; also further limits can be unified. The 2nd and 3rd propositions (3.22) manifest the weak convergence of the same sequence both to  $\hat{u}$  and to  $u'$  e.g. in  $L^2(I, H)$ , thus  $\hat{u} = u'$ . The obvious estimate  $\max_{t \in I} (|u^m(t) - \bar{u}^m(t)|, |u^m(t) - \check{u}^m(t)|) \leq \max_{s \in \{1, \dots, m\}} |Du_s^m| \leq \sqrt{c}\tau$ , referring to (3.18), implies  $u = \bar{u} = \check{u}$  and  $\dot{u} = u'$  where  $u(t) = \int_0^t u'(\xi) d\xi$ . Thus it remains to identify  $u''$  with  $\ddot{u}$  only, as the most delicate task. Let us work with symbols  $[\cdot]$  for integration over  $I$  for brevity. The following integration by parts, inspired by [50], p. 210, can be helpful:

$$\begin{aligned}
(3.23) \quad [(w, u'')] &= \lim_{m \rightarrow \infty} [(w, \ddot{U}^m)] = - \lim_{m \rightarrow \infty} [(\dot{w}, \dot{U}^m)] \\
&= - \lim_{m \rightarrow \infty} [(\dot{w}, \dot{U}^m - \dot{u}^m)] - \lim_{m \rightarrow \infty} [(\dot{w}, \dot{u}^m)] \\
&= - \lim_{m \rightarrow \infty} [(\dot{w}, \dot{U}^m - \dot{u}^m)] - [(\dot{w}, \dot{u})]
\end{aligned}$$

is valid for each  $w$  from the space of distributions  $C_0^\infty(I)$ . Moreover for arbitrary  $t \in I_s^m$ ,  $s \in \{1, \dots, m\}$ , we can write

$$\begin{aligned}
(3.24) \quad \dot{U}^m - \dot{u}^m &= \frac{t - (s-1)\tau}{\tau^2} D^2 u_s^m + \frac{1}{2\tau} (Du_s^m + Du_{s-1}^m) - \frac{1}{\tau} Du_s^m \\
&= \frac{t - (s-1)\tau}{\tau^2} D^2 u_s^m + \frac{1}{2\tau} (Du_{s-1}^m - Du_s^m) \\
&= \frac{t - (s-1/2)\tau}{\tau^2} D^2 u_s^m = (t - (s-1/2)\tau) \ddot{U}^m.
\end{aligned}$$

Let us remind that  $0 \leq t - (s-1/2)\tau \leq \tau/2$  here. Thus, inserting (3.24) into the result of (3.23), the limit in its 1st additive term vanishes, whereas the 2nd additive term is sufficient to identify  $u''$  with  $\ddot{u}$ , etc., as explained by Buncure [7], p. 49. Thus the modified form of (3.22) is just (3.13); also the convergence of  $\{\check{\mathfrak{D}}^m\}_{m=1}^\infty$  can work with  $u$ . This enables the limit passage from (3.11) to (3.6) finally;  $u, \dot{u} \in C(I, H)$  follows from Lemma 2.5.  $\square$

Let us recall that the crucial step for the design of a model with micro-cracks is the reasonable choice of the damage factor  $\mathfrak{D}$ . Here we shall demonstrate how to express it as an appropriate function of  $\sigma$ , with certain regularizing properties. This can be done using some kernel (typically radial basis or similar) operator  $K \in L^2(\Omega \times \Omega)$ , introduced as

$$(3.25) \quad A(w(x)) = \int_{\Omega} K(x, \tilde{x}) w(\tilde{x}) d\tilde{x}$$

for  $x \in \Omega$  and  $w \in H$  by [17]. From the mathematical point of view, such nonlocal approach to engineering mechanics relies on the properties of compact linear operators, discussed in [13], Part 2.2, in details; for its computational implementation

cf. [5] and [39], The following regularization (compactness) property of the kernel  $K$ , taken from  $L^2(\Omega \times \Omega)$ , is useful: if  $\{w^k\}_{k=1}^\infty$  is some sequence converging weakly to  $w$  in  $H$  then, taking  $\tilde{w} = A(w)$  and  $\tilde{w}^k = A(w^k)$ , up to a subsequence,  $\{\tilde{w}^k\}_{k=1}^\infty$  converges strongly to  $\tilde{w}$  in  $H$ . Two different ways of verification of this result can be found in [13], pp. 80 and 81.

The needed generalization, introduced by [20], for  $w \in L^2(\Omega)_{\text{sym}}^{3 \times 3}$ , or that for  $w \in H$ , referring to principal stresses by [23], Part 1.5, is straightforward. Namely [34] works with  $K(x, \tilde{x}) = \mathcal{K}(|x - \tilde{x}|_3)$  where  $|\cdot|_3$  means the norm in  $\mathbb{R}^3$  and  $\mathcal{K}(|x - \tilde{x}|_3)$  is obtained using Green functions of a special bi-Helmholtz equation; for certain class of brittle fracture this can be traced up to atomistic considerations, working with dislocation and disclination defects. However, for more complicated material structures such transparent theory is not available; e.g. for practical computational simulations of behaviour of fibre-reinforced concrete structures under mechanical loads [12] recommends the “generalized Mazars model” with several heuristic parameters, respecting anisotropy together with different behaviour under tension and pressure like [28] and [24], inspired by [44], [45] and [21].

Thus we are ready, using  $\sigma$  from (3.5), for any fixed time  $\xi \in I$ , to derive (at least theoretically) all nonlocal stress values

$$(3.26) \quad \tilde{\sigma}(\xi) = A(\sigma(\xi)),$$

belonging to  $L^2(\Omega)_{\text{sym}}^{3 \times 3}$ . Thanks to (3.26), it remains only to set

$$(3.27) \quad \mathfrak{D}_*(u(\xi)) = \omega(|\tilde{\sigma}(\xi)|_{3 \times 3}),$$

taking  $\omega$  as some real continuous non-decreasing function (containing some additional experimentally validated parameters typically) for the right-hand side of (3.3);  $|\cdot|_{3 \times 3}$  here means the norm in  $\mathbb{R}^{3 \times 3}$ . Clearly the resulting damage factor  $\mathfrak{D}$ , obtained from (3.3) with (3.27), depends on  $u$  from (3.2) in a rather complicated way. Nevertheless, such formulation of (3.3) together with (3.25) enables us to exploit the results on Nemytyskiĭ mappings by [13], p. 134: if some sequence converges weakly to  $u \in V$  for a fixed  $t \in I$ , together with the sequence or corresponding time derivatives converging to  $\dot{u}$ , then, thanks to (3.5), the operator  $A$  generates a weakly convergent sequence to  $\tilde{\sigma} \in H$ , after the regularization (3.26) the same, up to a subsequence, converges strongly to  $\tilde{\sigma} \in H$ , etc. Consequently, thanks to the continuity of  $\omega$  by (3.27), we are allowed to come to the strong limit of the corresponding sequence induced by (3.3), which may be helpful to overcome the nonlinearity of our model problem. However, the design of a sufficiently general class of functions  $\omega$  admitting all above sketched mathematical considerations and applicable in engineering practice (regardless of both physical and geometrical linearizations, connected with the

existence of a positive  $\varsigma$ ) cannot be seen as a closed problem; for some particular examples cf. [28] and [58].

#### 4. IMPLEMENTATION OF MACRO-CRACKS

Instead of one domain  $\Omega$ , as introduced in the Section 3, let us consider a union of a finite number of adjacent domains, denoted by  $\Omega$  again, whose boundary  $\partial\Omega$  consists of 3 parts: of 2 exterior ones, analogical to  $\Gamma$  and  $\Theta$ , and of a set of internal interfaces  $\Lambda$ . Such notion of interfaces can cover both potential locations of macro-cracks, as well as existing interfaces between particular components of a composite, e. g. between a cementitious matrix and stiffening fibres in building applications.

For simplicity, let us consider a material specimen occupying an open set  $\Xi$  with its boundary  $\partial\Xi$  in the 3-dimensional Euclidean space  $\mathbb{R}^3$ , compound from a finite number of domains  $\Omega_\times$  with their boundaries  $\partial\Omega_\times$  in the following sense:

- a) The union of closures of all domains  $\Omega_\times$  is identical with the closure of the domain  $\Omega$  in  $\mathbb{R}^3$ .
- b) Every boundary  $\partial\Omega_\times$  consists of a part belonging to  $\partial\Xi$  (external boundary) and from that non-belonging to  $\partial\Xi$  (internal boundary); the 1st one will be denoted by  $\Psi_\times$ , the 2nd one by  $\Lambda_\times$ . (Some of them can be empty.) Cohesive interface conditions will be applied later on  $\Lambda_\times$ .
- c) Every boundary part  $\Psi_\times$  is the union of its disjoint subsets  $\Theta_\times$  and  $\Gamma_\times$ . (Some of them can be empty.) Homogeneous Dirichlet boundary conditions will be then prescribed on  $\Theta_\times$  (supported boundary part), unlike Neumann boundary conditions (inhomogeneous in general) on  $\Gamma_\times$  (unsupported boundary part).
- d) The unions of above introduced sets  $\Theta_\times$ ,  $\Gamma_\times$  and  $\Lambda_\times$  are certain sets  $\Omega$ ,  $\Gamma$  and  $\Lambda$ . Similarly the union of all  $\Omega_\times$  generates an open set  $\Omega$  (i. e.  $\Xi$  without interior boundaries) with its boundary  $\partial\Omega$ .

We shall also work with the notation  $\delta v(x)$  for the differences of triples of values  $v(x)$  from the neighbour domains  $\Omega_\times$ ; the same notation is applicable to arbitrary  $\tilde{v}(x, t)$ , dependent also on  $t \in I$ , replacing  $v(x)$  here.

One can notice that such rather extensive list of assumptions tries to save the validity of Lemmas 2.1, ..., 2.6, to be able to adopt the proof of Theorem 3.1 without serious difficulties. The potential modification of this approach for another finite dimension than 3 (namely as 2 in illustrative examples) is left to the patient reader. Evidently a model problem with macro-cracks could be studied separately; however, we shall now try to implement macro-cracking to the results of Section 3 directly.

All notations need certain extensions. Namely we shall utilize also the Hilbert space  $Z_\Lambda = L^2(\Lambda)^3$ , its norm  $|\cdot|_\Lambda$  and its scalar product  $\langle \cdot, \cdot \rangle_\Lambda$ . For the analysis of potential opening and further behaviour of cracks let us consider such surface tractions  $\mathcal{T} \in L^2(I, Z_\Lambda)$  that

$$(4.1) \quad \mathcal{T} = \lambda(\delta u)$$

on  $\Lambda \times I$ ; possible forms of a just introduced function  $\lambda$  can be found in [32] and [33]. Especially  $\lambda(\delta u) = \lambda_0 \delta u$  with a real constant  $\lambda_0 \rightarrow \infty$  forces  $\delta u \rightarrow 0$  on  $\Lambda$ , i. e. the continuity of  $u$  without no active macro-cracking. In general we shall assume the Lipschitz continuity of  $\lambda$  in the sense

$$(4.2) \quad |\lambda(\delta v)|_\Lambda \leq \lambda_* |\delta v|_\Lambda$$

for any  $v \in V$  and a positive  $\lambda_*$ . For certain finite  $N$  independent of  $v$  from (4.2) we have:

$$(4.3) \quad |\delta v|_\Lambda \leq N\sqrt{\mathfrak{I}}\|v\|, \quad |\lambda(\delta v)|_\Lambda \leq \lambda_* N\sqrt{\mathfrak{I}}\|v\|.$$

The existence of  $N$  comes from b), d) above: traces by the analogy of Lemma 2.2 are related to any  $\Omega_\times$  at most  $N$ -times, from corresponding cohesive boundary parts  $\Lambda_\times$ . In the proof of Theorem 4.1 below we are allowed to take only  $\mathfrak{I}$  instead of  $N^2\mathfrak{I}$  formally, without any loss of generality.

Thus we obtain the slight modification of (3.2)

$$(4.4) \quad \begin{aligned} & (v, \rho \ddot{u}) + \beta(v, \rho \dot{u}) + \alpha(\varepsilon(v), \dot{\sigma}) + (\varepsilon(v), (1 - \mathfrak{D}) \sigma) \\ & = (v, f) + \langle v, g \rangle_\Gamma + \langle \delta v, \mathcal{T} \rangle_\Lambda \quad \text{on } I. \end{aligned}$$

Inserting (4.1) into (4.4), we receive the analogy of (3.2)

$$(4.5) \quad \begin{aligned} & (v, \rho \ddot{u}) + \beta(v, \rho \dot{u}) + \alpha(\varepsilon(v), \dot{\sigma}) + (\varepsilon(v), (1 - \mathfrak{D}) \sigma) \\ & = (v, f) + \langle v, g \rangle_\Gamma + \langle \delta v, \lambda(\delta u) \rangle_\Lambda \quad \text{on } I. \end{aligned}$$

In most following equations, unlike (4.4) extending (3.2) and (4.5) extending (3.6), we shall discuss only additional righthand-side terms for brevity. In particular, this means  $\langle \delta v, \lambda(\delta \ddot{u}^m) \rangle_\Lambda$ , in (3.11),  $\langle \delta v, \lambda(\delta u_{s-1}^m) \rangle_\Lambda$  in (3.12); no improved linearization will be considered, although the evaluation of  $\lambda(\cdot)$  is typically less complicated as that of  $\mathfrak{D}(\cdot)$ . Such approach will be useful in the proof of the following theorem, too.

**Theorem 4.1.** *Let us consider a damage factor by (3.3) and a cohesive interface by (4.1), (4.2). There exist a solution  $u \in \mathcal{V}$  satisfying (4.5) for any  $v \in V$  together with the Cauchy initial condition (3.1). Moreover  $u, \dot{u} \in C(I, H)$  and, up to subsequences, (3.13) remains valid.*

*Proof.* All common ideas are the same as in the proof of Theorem 3.1. The above announced additional terms are  $\langle \delta Du_s^m, \lambda(\delta u_{s-1}^m) \rangle_\Lambda$  in (3.14) and  $\langle \delta Du_r^m, \lambda(\delta u_{r-1}^m) \rangle_\Lambda$  in (3.15) (involving the sum over  $r \in \{1, \dots, s\}$ ). The extension of (3.17), making use of (4.3), reads

$$(4.6) \quad \langle \delta Du_r^m, \lambda(\delta u_r^m) \rangle_\Lambda \leq |\delta Du_r^m|_\Gamma |\delta u_{r-1}^m|_\Gamma \leq \frac{\epsilon}{2\tau} \delta_{rr} |\delta Du_r^m|_\Gamma^2 + \frac{\tau}{2\epsilon} \delta_{rr} |\delta u_{r-1}^m|_\Gamma^2 \\ \leq \frac{\epsilon \mathfrak{T}}{2\tau} \delta_{rr} \|Du_r^m\|^2 + \frac{\tau \mathfrak{T}}{2\epsilon} \delta_{rr} \|u_{r-1}^m\|^2.$$

The last right-hand-side additive term of (4.6) causes the modification of (3.18)

$$(4.7) \quad \frac{1}{\tau^2} |Du_s^m|^2 + \frac{1}{\tau} \delta_{rr} \|Du_r^m\|^2 + \|u_s\|^2 \leq c + c\tau \delta_{rr} \|u_r\|^2.$$

However, the 2nd right-hand-side additive term can be removed from (4.7), using the Gronwall lemma by [13], p. 99; its simple discrete version from [9] is sufficient here. Thus we come back to (3.18), with some larger value of  $c$ . All remaining steps can be then performed following the proof of Theorem 4.1 with obvious modifications.  $\square$

## 5. COMPUTATIONAL STRATEGY WITH ILLUSTRATIVE EXAMPLES

The computational scheme (3.12) by Section 3, including its extension by Section 4, for the evaluation of  $u_s^m$ ,  $s \in \{1, \dots, m\}$  refers to the numerical analysis of  $m$  elliptic problems of infinite dimension. In practical calculations, instead of  $v$  in (3.12) from an infinite-dimensional space  $V$ , we consider a finite number  $n$  of test functions  $\phi_i^n$  where  $i \in \{1, \dots, n\}$  refers to a new Einstein summation index; the approximation of  $u_s^m$  from (3.12) with  $n$  unknown parameters can be then constructed as

$$(5.1) \quad u_s^m(x) = u_{is}^{nm} \phi_i^n(x)$$

for any  $x$  from  $\Omega$  or its suitable approximation. Consequently, step-by-step with  $s \in \{1, \dots, m\}$ , by (3.12) and (5.1) we choose  $\phi_i^n$  as particular elements from a basis of certain finite-dimensional space  $V^n$ , approximating  $V$  (which can be a subspace of  $V$  in a special case).

Typically  $\phi_i^n$  are functions with small compact support, applicable in  $\Omega$ , as well as on  $\Theta$ ,  $\Gamma$  and  $\Lambda$ , or their approximations, to create a sparse system of linear algebraic equations, and  $u_{is}^{nm}$  refer to nodal displacement values. The guarantee of solvability

of such system, together with the convergence properties for  $n \rightarrow \infty$ , depend on certain (semi-)regularity of such decomposition due to the XFEM-based adaptive enrichment functions, namely near geometric singularities. Here we shall apply the approach of [29] to demonstrate the possibility of effective numerical simulations.

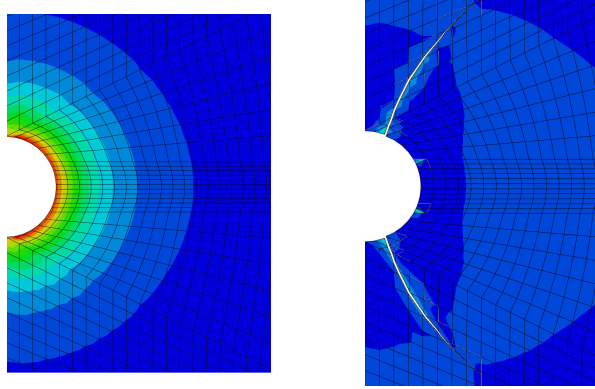


FIGURE 1. Principal stresses in the pure cement paste.

As an illustrative 2-dimensional example, the test task is a relatively simple body with an a priori crack of a circular shape (fulfilling the plane strain condition). A uniform load was applied to the surface of this a priori crack, and thus the formation of the following cracks emanating from this stress concentrator is assumed using

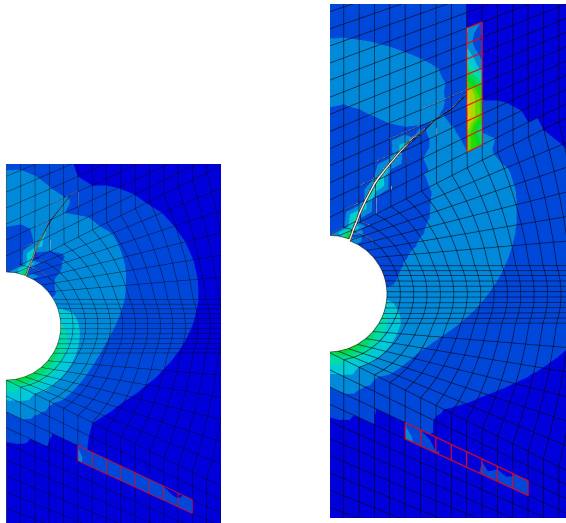


FIGURE 2. Principal stresses near 1 or 2 stiffening fibres.

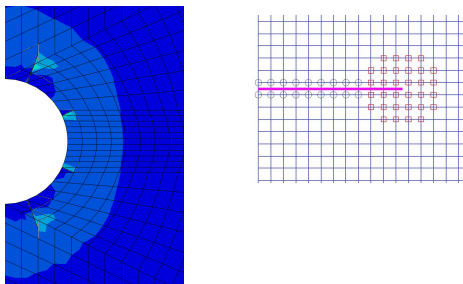


FIGURE 3. Nonlocal handling of stress near the crack tip.

XFEM. The basic calculation system was the commercial software Abaqus 2018, into which a user subroutine in the Fortran 90 language was implemented, realizing the modelling of matrix damage using exponential law, based on the planar element CPE4. The following basic input data corresponding to reinforced cement paste were used for this task: the Young modulus  $E = 3.2$  GPa, the Poisson constant  $\mu = 0.3$  and the tensile strength 10 MPa – cf. the discussion under (3.5) on some special structures of  $C$ . For approximately 20 mm long and 3 mm thick circular steel fibres, the Young modulus  $E = 190$  GPa and the same Poisson constant  $\mu = 0.3$  were used.

All figures show some typical distribution of principal stresses under plain strain conditions. Figure 1 shows the distribution for quasi-static loads in certain representative time for the pure cement paste. In the initial period, four germs of initial cracks are formed evenly distributed along the circular initiator. The germs closer to the plane of symmetry are running first as expected. Directions that are not blocked by the fibres will run. Figure 2 presents the comparable result near 1 or 2 stiffening fibres, where reinforcing metal fibres are introduced into the structure. The influence of fibre blocking and their orientation is clear. Directions that are not blocked by the fibres will run. Figure 3 demonstrates the non-local handling of stress near the crack tip. Its left part attempts to illustrate the algorithm used to calculate the stress concentrators in front of the crack tip. This picture has a schematic character, indicates how the stresses are calculated with the help of a non-local approach. The question is from which distance from the crack front it is appropriate to calculate the stress distribution ahead the crack tip. Figure 4 reflects the Mazars model, evaluating the stress by certain exponential formula (cf. [44] and [21]). The former Mazars model has gaps in the modelling of the behaviour of concrete during loading; the new formulation was proposed to improve behaviour in bi-compression

and shearing. It was reached by introduction of one new internal variable into the classical Mazars model. It corresponds to the maximum of equivalent deformation reached during loading. The damage factor is dependent on the stress concentration in front of the local crack, therefore the real stress value is essential for the prediction of the crack growth, especially the non-local approach can give credible direction of damage. Figure 5 tries to implement some homogenized material structure with “smeared cracks”, inspired by [28], where reinforcement has the influence to the whole structure. XFEM approach reflects the increasing strength of structure.

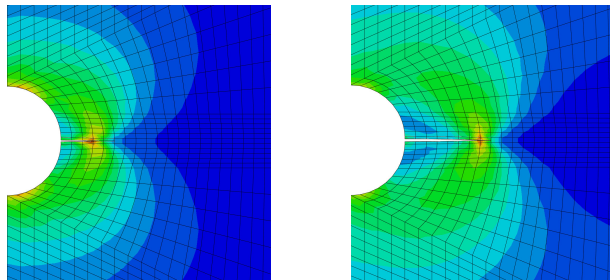


FIGURE 4. Application of Mazars model.

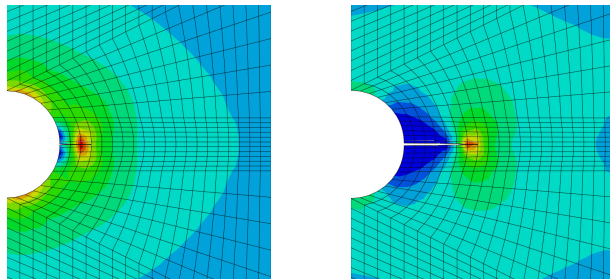


FIGURE 5. Application of crack homogenization.

## 6. SOME MODIFICATIONS AND GENERALIZATIONS

Numerous computational tools in fracture mechanics ignore the first couple of additional terms in (3.2), which switches to a quasi-static problem where the time evolution of damage relies on the 3rd additive term; even in our illustrative examples the 1st and 2nd terms are not dominant. Clearly the 2nd condition (3.1) is not applicable. Some estimates from Sections 3 and 4 degenerate, namely the 1st inequality (3.16) to  $0 = 0$ . Thus less regular results in comparison with the above discussed

dynamic case can be expected and their derivation cannot be repeated quite easily. The remedy is to seek for  $u \in W^{1,2,2}(I, V, V^*)$ , instead of  $u \in W^{1,2,2,2}(I, V, V, V^*)$ ; all details of such approach can be found in [58].

Other seemingly useful generalization ideas can rely on the removal of too strict assumptions, e. g. that on the Lipschitz boundary for Lemmas 2.1, . . . 2.6, thus also for Theorems 3.1, 4.1. Indeed, results like [26] (on Sobolev embedding on arbitrary domains), [7] (on improved trace operators), etc. offer this way. However, we have ignored it here, at least from three reasons: i) the original version of this paper, prepared for the (rarely physical) discussion at the seminar PANM (Programs and Algorithms of Numerical Mathematics) in Hejnice (Czech Republic) in June 2020 was intended to be as reader-friendly as possible, ii) numerous technical difficulties in proofs have to be overcome, often those occurring in practical modelling and simulation software tools exceptionally, iii) such generalizations do not handle more significant limitations of our approach: iii-1) the nonlocal damage factor implemented into certain linearized model, working with small strains and linearized empirical constitutive (strain-stress) relations in the case of micro-cracking, iii-2) the careful description of geometrical properties of  $\Omega$ ,  $\Lambda$ , etc., admitting the macroscopic cracks only at a finite number of prescribed interfaces. Because of iii-1) we are not able to detect a total loss of stiffness in some part of  $\Omega$  properly, whereas iii-2) may not cover some practical XFEM techniques correctly. Certain inspiration for a future (much more complicated) proper finite-strain formulation can be found in [40], Part 4.2.4, in confrontation with [11] and [35], together with the scale-bridging using structured deformation, following [10], [42] and [52].

## 7. CONCLUSION

We have demonstrated the possibility of simultaneous deterministic study of dynamics of micro- and macro-cracking in quasi-brittle composites, using the standard linearized viscoelastic model with two nonlinear terms, covering i) the nonlocal evaluation of damage factor  $\mathfrak{D}$  for micro-cracking and ii) the cohesive behaviour of macroscopic cracks. Some unclosed problems occur even in such linearized theory, namely in the physically and mathematically proper interpretation of  $\mathfrak{D}$ , ad hoc implemented in available software packages.

The limitations of the presented approach, sketched in the preceding section, can be seen as motivations for continuing research in the near future. Its possible aim of high practical importance can be the development, verification and validation of the computational tool for prediction of quasi-brittle behaviour of structural components from fibre reinforced composites under mechanical loads, with methodology based on the physical model incorporating most significant physical processes, namely elastic

and plastic deformation, crack initiation and propagation in a matrix and alternative debonding and rupture of fibres.

#### REFERENCES

- [1] *S. Altan*: Existence in nonlocal elasticity. *Arch. Mech.* **41** (1989), 25–36.
- [2] *I. Babuška, J. M. Melenk*: The partition of unity method. *Int. J. Numer. Methods Eng.* **40** (1997), 727–758. Zbl 0949.65117, MR1429534.
- [3] *T. Belytchko, T. Black*: Elastic crack growth in finite elements with minimal remeshing. *Int. J. Numer. Methods Eng.* **45** (1999), 601–620.
- [4] *A. Bermúdez de Castro*: Continuum Thermomechanics. Birkhäuser, Basel, 2005.
- [5] *G. S. Bhatia, G. Arora*: Radial basis function methods for solving partial differential equations – a review. *Indian Journal of Science and Technology* **9** (2016), #45/1–17.
- [6] *L. Bouhala, A. Makradi, S. Belouettar, H. Kiefer-Kamal, P. Frères*: Modelling of failure in long fibres reinforced composites by X-FEM and cohesive zone model. *Composites Part B* **55** (2013), 352–361.
- [7] *J. K. Bunkure*: Lebegue-Bochner spaces and evolution triples. *Int. J. Math. Appl.* **7** (2019), 41–52.
- [8] *A. Cianchi, V. Maz'ya*: Sobolev inequalities in arbitrary domains. *Adv. Math.* **293** (2016), 644–696. MR4074620.
- [9] *D. S. Clark*: Short proof of a discrete Gronwall inequality. *Discrete Appl. Math.* **16** (1987), 279–281.
- [10] *G. Del Piero, D. R. Owen*: Structured deformations of continua. *Arch. Rat. Mech. Anal.* **124** (1993), 99–155.
- [11] *G. Dal Maso, G. Lazzaroni*: Crack growth with non-interpenetration: a simplified proof for the pure Neumann problem. *Discrete Contin. Dyn. Syst.* **31** (2011), 1219–1231.
- [12] *L. Dlouhý, S. Pouillon*: Application of the design code for steel fibre-reinforced concrete into finite element software. *Beton* **116** (2020), 8–13.
- [13] *P. Drábek, J. Milota*: Methods of Nonlinear Analysis – Applications to Differential Equations. Birkhäuser, Basel, 2013. Zbl 1264.35001, MR3025694.
- [14] *J. Eliáš, M. Vořechovský, J. Skoček, Z. P. Bažant*: Stochastic discrete meso-scale simulations of concrete fracture: comparison to experimental data. *Eng. Fract. Mech.* **135** (2015), 1–16.
- [15] *E. Emmrich, D. Puhst*: Measure-valued, weak solutions to the nonlinear peridynamic model in nonlocal elastodynamics. *Nonlinearity* **28** (2015), #285/1–25.
- [16] *A. C. Eringen*: Theory of Nonlocal Elasticity and Some Applications. Princeton University Press, 1984, technical report 64.
- [17] *A. C. Eringen*: Nonlocal Continuum Field Theories. Springer, New York, 2002. Zbl 1023.74003.
- [18] *A. Evgrafov, J. C. Belido*: From nonlocal Eringen’s model to fractional elasticity. *Mathematics and Mechanics of Solids* **24** (2019), 1935–1953. Zbl 1425.74093.
- [19] *T.-P. Fries, T. Belytschko*: The intrinsic XFEM: a method for arbitrary discontinuities without additional unknowns. *Int. J. Numer. Methods Eng.* **68** (2006), 1358–1385.
- [20] *Z. Gao, L. Zhang, W. Yu*: A nonlocal continuum damage model for brittle fracture. *Eng. Fract. Mech.* **189** (2018), 481–500.
- [21] *C. Giry, F. Dufour, J. Mazars*: Stress-based nonlocal damage model. *Int. J. Solids and Struct.* **48** (2011), 3431–3443.
- [22] *S. Grija, D. Shanthini, S. Abinaya*: A review of fibre reinforced concrete. *International Journal of Civil Engineering and Technology* **7** (2016), 386–392.
- [23] *K. Hashiguchi*: Elastoplasticity Theory. Springer, Berlin, 2014.
- [24] *P. Havlásek, P. Grassl, M. Jirásek*: Analysis of size effect on strength of quasi-brittle materials using integral-type nonlocal models. *Eng. Fract. Mech.* **157** (2016), 72–85.
- [25] *A. Hoekstra*: Design methodologies for steel-fibre-reinforced concrete and a new methodology for a real time quality control. *Beton* **116** (2020), 44–49.

- [26] *C. O. Horgan*: Eigenvalue estimates and the trace theorem. *J. Math. Anal. Appl.* **69** (1979), 231–242.
- [27] *A. Javili, R. Mosarata, E. Oterkus*: Peridynamics review. *Math. Mech. Solids* **24** (2019), 3714–3739. MR4000179.
- [28] *M. Jirásek*: Damage and smeared crack models, in: *Numerical Modeling of Concrete Cracking* (G. Hofstetter, G. Meschke, eds.). Springer: CISM International Centre for Mechanical Sciences 532, Udine, 2011, 1–49.
- [29] *M. Kaliske, H. Dal, R. Fleischhauer, C. Jenkel, C. Netzker*: Characterization of fracture processes by continuum and discrete modelling. *Comput. Mech.* **50** (2012), 303–320.
- [30] *P. Kawde, A. Warudkar*: Steel fibre reinforced concrete: a review. *International Journal of Engineering Sciences and Research Technology* **6** (2017), 130–133.
- [31] *A. R. Khoei*: *Extended Finite Element Method: Theory and Applications*. J. Wiley & Sons, New York, 2015.
- [32] *V. Kozák, Z. Chlup*: Modelling of fibre-matrix interface of brittle matrix long fibre composite by application of cohesive zone method. *Key Engineering Materials* **465** (2011), 231–234.
- [33] *V. Kozák, Z. Chlup, P. Padělek, I. Dlouhý*: Prediction of the traction separation law of ceramics using iterative finite element modelling. *Solid State Phenomena* **258** (2017), 186–189.
- [34] *M. Lazar, G. A. Maugin, E. C. Aifantis*: On a theory of nonlocal elasticity of bi-Helmholtz type and some applications. *Int. J. Solids and Struct.* **43** (2006), 1404–1421.
- [35] *G. Lazzaroni*: Quasistatic crack growth in finite elasticity with Lipschitz data. *Ann. Mat. Pura Appl.* **190** (2011), 165–194.
- [36] *X. Li, J. Chen*: An extensive cohesive damage model for simulation arbitrary damage propagation in engineering materials. *Comput. Methods Appl. Mech. Eng.* **315** (2017), 744–759.
- [37] *X. Li, W. Gao, W. Liu*: A mesh objective continuum damage model for quasi-brittle crack modelling and finite element implementation. *Int. J. Damage Mech.* **28** (2019), 1299–1322.
- [38] *R. W. Macek, S. A. Silling*: Peridynamics via finite element analysis. *Finite Elem. Anal. Des.* **43** (2007), 1169–1178.
- [39] *Z. Majdišová, V. Skala*: Radial basis function approximations: comparison and applications. *Appl. Math. Modell.* **51** (2017), 728–743. Zbl 07166287, MR3694560.
- [40] *A. Mielke, T. Roubíček*: *Rate-Independent Systems*. Springer, New York, 2015.
- [41] *M. Moradi, A. R. Begherieh, M. R. Esfahani*: Constitutive modeling of steel fiber-reinforced concrete. *Int. J. Damage Mech.* **29** (2020), 388–412.
- [42] *M. Morandotti*: Structured deformation of continua: theory and applications. *Mathematical Analysis of Continuum Mechanics and Industrial Applications II – Proceedings of CoMFoS16 (Continuum Mechanics Focusing on Singularities)* in Kyushu (2016), Springer, Singapore, 2018, 125–136.
- [43] *N. Nakamura*: Extended Rayleigh damping model. *Frontiers in Built Environment* **2** (2016), #14/1–13.
- [44] *R. H. J. Peerlings, R. de Borst, W. A. M. Brekelmans, M. Geers*: Gradient enhanced damage modelling of concrete fracture. *Int. J. Numer. Anal. Methods Geomech.* **3** (1998), 323–342.
- [45] *G. Pijaudier-Cabot, J. Mazars*, Damage models for concrete, in: *Lemaitre Handbook of Materials Behavior Models* (J. Lemaitre, ed.), Section 6.13, 500–512. Academic Press, London, 2001.
- [46] *M. G. Pike, C. Oskay*: XFEM modeling of short micro-fiber reinforced composites with cohesive interfaces. *Finite Elem. Anal. Des.* **106** (2005), 16–31.
- [47] *Yu. Z. Povstenko*: The nonlocal theory of elasticity and its application to the description of defects in solid bodies. *Journal of Mathematical Sciences* **97** (1999), 3840–3845.
- [48] *P. Ray*: Statistical physics perspective of fracture in brittle and quasi-brittle materials. *Phil. Trans. R. Soc. A* **377** (2019), #20170396/1–13.
- [49] *K. Rektorys*: *The Method of Discretization in Time and Partial Differential Equations*. D. Reidel, Dordrecht, 1982. Zbl 0505.65029, MR0689712.
- [50] *T. Roubíček*: *Nonlinear Partial Differential Equations with Applications*. Birkhäuser, Basel, 2005. Zbl 1087.35002, MR2176645.

- [51] *T. Roubíček*: Thermodynamics of rate-independent processes in viscous solids at small strains. SIAM J. Math. Anal. **42** (2010), 256–297. Birkhäuser, Basel, 2005. Zbl 1213.35279, MR2596554.
- [52] *M. Šilhavý*: The general form of the relaxation of a purely interfacial energy for structured deformations. Mathematics and Mechanics of Complex Systems 5 (2017), 191–215. Zbl 1447.49026, MR3669123.
- [53] *X. T. Su, Z. J. Yang, G. H. Liu*: Monte Carlo simulation of complex cohesive fracture in random heterogeneous quasi-brittle materials: a 3D study. Int. J. Solids Struct. **47** (2010), 2336–2345. Zbl 1194.74313.
- [54] *Y. Sumi*: Mathematical and Computational Analyses of Cracking Formation. Springer, Tokyo, 2014.
- [55] *E. Svaning, F. Larsson, M. Fagerström*: A two-scale modeling framework for strain localization in solids: XFEM procedures and computational aspects. Comput. Struct. **219** (2019), 43–54. Zbl 1386.74129.
- [56] *R. F. Swati, L. H. Wen, H. Elahi, A. A. Khan, S. Shad*: Extended finite element method (XFEM) analysis of fiber reinforced composites for prediction of micro-crack propagation and delaminations in progressive damage: a review. Microsyst. Technol. **25** (2019), 747–763.
- [57] *J. Vala*: Structure identification of metal fibre reinforced cementitious composites. Algoritmy – 20th Conference on Scientific Computing in Podbanské (2016), Proceedings, STU Bratislava, 2016, 244–253.
- [58] *J. Vala, V. Kozák*: Computational analysis of quasi-brittle fracture in fibre reinforced cementitious composites. Theor. Appl. Fract. Mech. **107** (2020), #102486/1–8.

*Authors' addresses: Jiří Vala, Vladislav Kozák*: Brno University of Technology, Faculty of Civil Engineering, Institute of Mathematics and Descriptive Geometry, Brno, Czech Republic, e-mail: [vala.j@fce.vutbr.cz](mailto:vala.j@fce.vutbr.cz), [kozak.v@fce.vutbr.cz](mailto:kozak.v@fce.vutbr.cz).